VERÖFFENTLICHUNGEN
des Instituts für Geotechnik
der Technischen Universität Bergakademie Freiberg

Herausgeber: H. Konietzky

Heft 2024-3

53. Geomechanik-Kolloquium

Freiberg – 15. November 2024

Freiberg 2024

Veröffentlichungen des Instituts für Geotechnik der TU Bergakademie Freiberg

Herausgeber: Prof. Dr.-Ing. habil. Heinz Konietzky

Anschrift: TU Bergakademie Freiberg
Institut für Geotechnik
Gustav-Zeuner-Straße 1
09596 Freiberg
Telefon: 03731 39-2458
Fax: 03731 39-3638
E-Mail: gmk@ifgt.tu-freiberg.de
Internet: https://tu-freiberg.de/geotechnik

Herstellung: Medienzentrum TU Bergakademie Freiberg
Printed in Germany

ISSN 1611-1605

Wir danken unseren Unterstützern und Mitorganisatoren !
Thanks to our supporters and co-organizers !

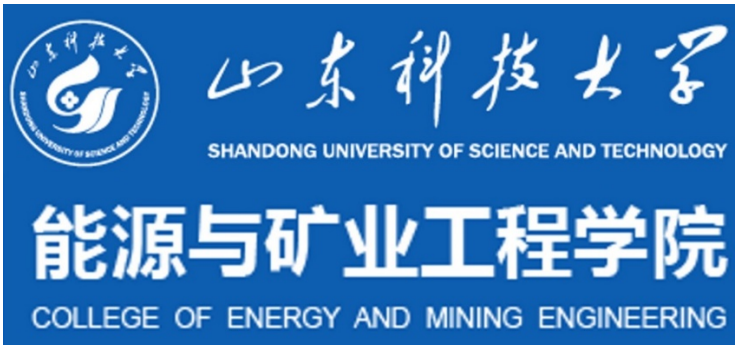

Aussteller / Exhibitors

DESOI®

DSI UNDERGROUND

GEOBRUGG®
BRUGG
Safety is our nature

SOLEXPERTS

WEBAC®
Unsere Formel – Ihre Lösung

Table of content

Integrity Criteria for Operation and Abandonment of Gas- and Fluid-Filled Salt Caverns under Consideration of Effective Stresses

Integritätskonzepte für Betrieb und Verwahrung von Gasspeicher- und lösungserfüllten Kavernen im Salzgebirge unter Berücksichtigung effektiver Spannungen

Markus Knauth, Christoph Lüdeling, Ralf-Michael Günther
Institut für Gebirgsmechanik GmbH
Leipzig, Germany

Abstract

Salt caverns are utilized for the underground storage of hydrocarbons due to the essentially impermeable nature of salt under appropriate pressure conditions. Consequently, designing and operating these caverns safely and economically necessitates a thorough understanding of the hydromechanical behavior of rock salt. This paper examines fluid transport in rock salt, criteria for maintaining hydraulic integrity, and the interaction with mechanical deformations. Drawing on decades of experience in both conventional and solution mining, a comprehensive understanding of fluid transport in salt has been established, identifying pressure-driven percolation as the primary mechanism. The paper presents conceptual frameworks, numerical investigations, and both laboratory and field data. We specifically review published in situ examples and demonstrate their consistency with our general analysis. By exploring various conceptual approaches, evaluating evidence from laboratory and large-scale in situ tests, and recalculating these findings using computational models, we offer evaluation criteria and propose a hierarchical structure for increasingly complex numerical modeling approaches suited to the specific application.

Zusammenfassung

Salzkavernen werden für die unterirdische Speicherung von Fluiden und Gasen genutzt, da Salz unter geeigneten Druckbedingungen im Wesentlichen undurchlässig ist. Daher erfordert die sichere und gleichzeitig wirtschaftliche Auslegung dieser Kavernen ein umfassendes Verständnis des hydromechanischen Verhaltens von Steinsalz. Diese Arbeit untersucht den Fluidtransport im Steinsalz, Kriterien zur Aufrechterhaltung der hydraulischen Integrität und ihre Wechselwirkung mit mechanischen Verformungen. Auf der Grundlage jahrzehntelanger Erfahrung sowohl im konventionellen als auch im Lösungsbergbau wurde ein umfassendes Konzept des Fluidtransports im Salz entwickelt, wobei die druckgetriebene Perkolation als Hauptmechanismus identifiziert wurde. Der Artikel präsentiert den konzeptionellen Rahmen, numerische Untersuchungen sowie Labor- und Felddaten. Wir überprüfen veröffentlichte In-situ-Beispiele und zeigen deren Konsistenz mit unserer allgemeinen Analyse. Durch die Untersuchung verschiedener konzeptioneller Ansätze, die Bewertung von Labor- und großmaßstäblichen In-situ-Tests und die Nachrechnung dieser Ergebnisse mit Hilfe von Computermodellen ordnen wir bestehende Bewertungskriterien ein und schlagen eine hierarchische Struktur für zunehmend komplexere numerische Modellierungsansätze vor, die für die jeweilige Anwendung geeignet sind.

1 Introduction

Salt caverns have a wide range of applications, including the storage of natural gas, crude oil, and liquid petroleum. The unique properties of salt, most importantly its extremely low porosity and permeability, make it an ideal material for stable and secure underground storage caverns (Fig. 1). The storage of natural gas in salt caverns allows for the smooth regulation of supply and demand in the gas market, ensuring a stable and consistent supply of natural gas to consumers.

However, the unique sealing capacity of salt rocks is tied to certain conditions, which determine the macroscopic permeability of the material. Under undisturbed conditions, typical rock salt only has a porosity below 1% and this pore space is distributed to predominantly isolated pores in the corner pockets of viscoplastic salt grains, so that initially there is no interconnected flow network, thus resulting in the low permeabilities found in laboratory experiments of the order of 10^{-22} – 10^{-21} m^2 [1]. It has been widely established that a significant increase in permeability in salt rocks can then occur only by mechanical damage to the salt (dilatancy) or when an applied gas or fluid pressure exceeds the local normal stress on grain boundaries [1], [2], [3]. This process, in which fluids push open a pathway into the material, is called pressure driven percolation.

The pioneering efforts of Bérest collaborators [4], [5] have significantly influenced the understanding of the thermo-hydro-mechanical interactions around salt caverns after abandonment. The interpretation of several long-term in situ tests proposed the existence of a so-called “equilibrium pressure”, which is (in some cases significantly) lower than the lithostatic stress at cavern depth and at which the effects of fluid loss through the cavern contour and the pressure increase due to convergence will compensate indefinitely.

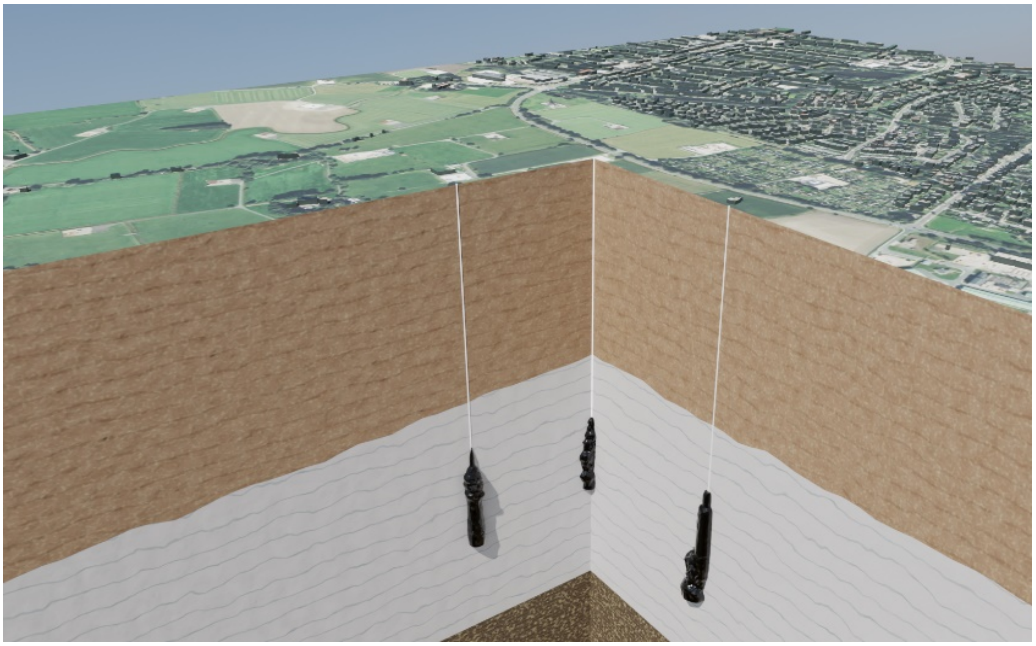

Fig. 1: Exemplary depiction of oil storage in caverns in a salt layer.

At first glance, this apparently contradicts the established criteria and assumptions for the assessment of rock salt integrity, since it seems to show that the caverns are potentially losing stored gases/fluids at surprisingly low pressures. In many discussions pertaining cavern-related projects, this has not only led to general doubts on the validity of current general assumptions in the evaluation of cavern integrity and sealing capacity within the scientific community, but it has also created insecurities among licensing authorities and public interest groups.

The apparent disagreement will be explained and discussed extensively in this paper. From our point of view, confusions predominantly arise from a conflation of the virgin lithostatic stress and the actual local stress state as well as from the assumptions for the salt rock permeability at fluid pressures clearly below the minor principal stress and the onset of the increase at higher pressures.

The paper aims to show that the supposed counterexamples actually are consistent with the fluid transport mechanisms discussed above when the basic rock-mechanical behavior of the rock mass is properly accounted for. In conclusion, we argue that these mechanisms form the basis for assessments of cavern integrity. We present practical numerical assessment methods, classified into a hierarchical structure with increasing complexity but also accuracy.

2 Fluid Transport Mechanisms in Rock Salt & Established Integrity Criteria

2.1 Established Fluid Transport Mechanisms

Fluid flow through rock masses and soils is often modelled using Darcy's law. The conceptual basis is the laminar flow through an existing, static pore space network in which the flow *q* is:

$$q \sim K \cdot \Delta p,$$

i.e., it is proportional to the difference in fluid pressure between input and output multiplied by the permeability *K,* which is a constant parameter characterizing the material.
Undisturbed rock salt, on the other hand, is a polycrystalline viscous material with vanishingly low permeability, which in its natural state does not sustain a connected pore space in which bulk water can flow. Creep deformation of the grains will close grain boundaries, and pressure gradients are different in the rock mass and in bulk fluids. Hence, the equilibrium state is one where the stress state in the rock mass is close to isotropic, and fluids are enclosed in isolated pores, with fluid pressure equal to the average stress in the rock mass. Rock salt thus has a vanishing (Darcy-type) permeability in the undisturbed state.
However, there are two main fluid transport mechanisms in rock salt that can induce an increased macroscopic permeability, which are verified in lab and field situations:

- Stresses exceeding the dilatancy boundary will lead to the formation of microscopic defects that can accumulate and coalesce into larger fractures. These cracks act as secondary porosity, turning rock salt into a porous medium; macroscopically, this porosity manifests itself in an increase in volume, i.e. dilatancy. Due to the preferred orientation of the cracks forming in a deviatoric stress state, even small amounts of volumetric strain can form connected pathways, so that less than one percent of dilatancy can cause permeabilities in the order of 10^{-17} m² [6], [7], [8].

- If fluid pressure exceeds the normal stress on a grain boundary (plus, potentially, a tensile strength), the fluid can open a flow path, in the process of pressure-driven percolation (Minkley et al. 2012). Hence, in undamaged salt, there is a threshold pressure below which there will be no flow. If the threshold is exceeded, the fluid will predominantly open grain boundaries where the normal stress is low. In a rock mass, this corresponds to a directed motion orthogonal to the minor principal stress. It is important to note that both the threshold and the preferred direction are not parameters of the rock but depend on the stress state.
  Note that this implies that a violation of barrier integrity can result from changes both in the fluid pressure and in the rock mass stress state.

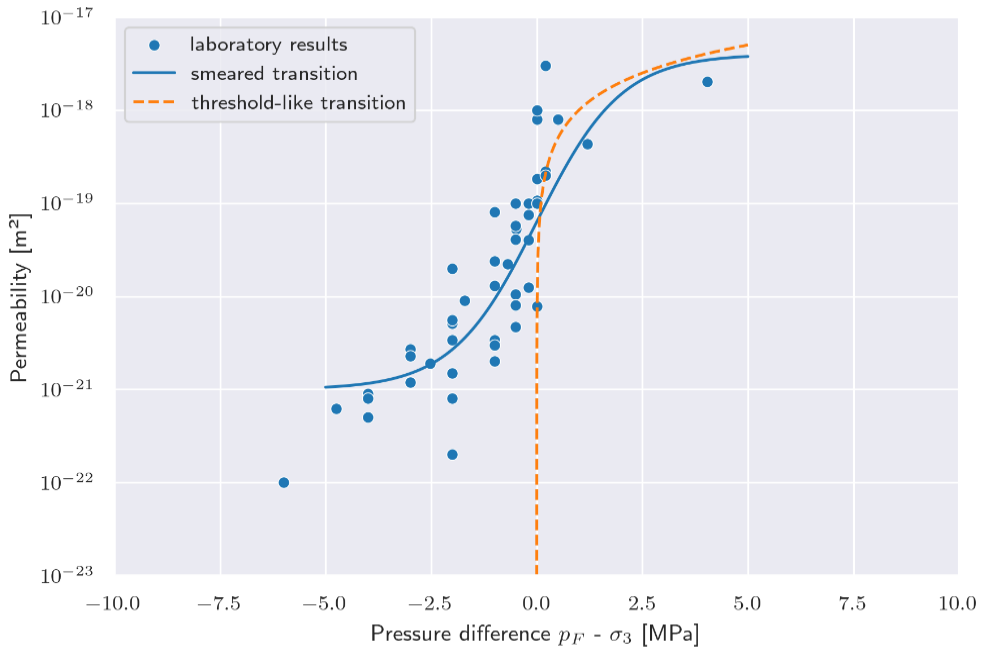

Fig. 2: Laboratory results of hydro-mechanically coupled permeability measurements performed at the IfG for different fluid pressures in relation to the minor principal stress. Solid curve as a possible smeared transition function in comparison to the dashed approach for a threshold-like transition.

Additional transport mechanisms had been proposed for very high temperatures and pressures [9], but these have been refuted both on the basis of corresponding laboratory measurements [10] as well as theoretical considerations on flow path geometries [11].

We should point out that the name “percolation” is applied to other possible modes of fluid transport that do not share these properties. Pressure-driven percolation derives its name from percolation theory which deals with the connectivity of graphs, and the percolation threshold (expressed in terms of fluid pressure and rock stress) is analogous to the percolation threshold as link occupation probability, as it divides connected and non-connected graphs, i.e. intact and failed barriers. Fig. 2 shows the measured permeabilities of rock salt in laboratory gas permeation tests under different stress and pressure conditions for a variety of rock salt samples from German salt domes. There is a clearly observable transition from permeabilities of the order of 10^{-21} m² to 10^{-18} m² around the region where the gas pressure compensates for the minor principal stress in the sample. This supports the general notion that this is the critical threshold at which the infiltrating medium can open the grain boundaries and penetrate the sample. Since compressive stresses are usually used with negative signs in the field of geomechanics, please note that here and in the subsequent discussion the "minor" principal stress means the least compressive principal stress and not the algebraically smallest (most negative) stress.

Undisturbed salt rocks could therefore be treated as entirely impermeable in the region of fluid pressures clearly below the minor principal stress and the small measured permeabilities are then understood as mere remnants of sample damage and/or unrepresentative sampling (grain size vs. sample size). Since the permeabilities lower than 10^{-19} m^2 in this region are many magnitudes lower than what many textbooks would still classify as a hydraulically tight material [12], this might appear more of an academic debate at first glance. However, in the timescales required for long-term safety evaluations of cavern abandonment or nuclear waste disposal, the distinction between impermeability and very low permeability becomes essential and can lead to different results [13].

The issue becomes more interesting at pressures slowly approaching the least compressive stress. Some laboratory studies show an increase in permeability already at 0,5 - 1 MPa below the minor principal stress. Since the exact behavior and position of this threshold is critical for the evaluation and assessment of hydraulic barriers and cavern integrity, this would suggest that an increase in permeability may already be observed at pressures below the minor principal stress. This approach has been taken in various empirical permeability relations employed in the numerical analysis of cavern integrity and abandonment [14] and has the benefit of a conservative treatment of the hydraulic sealing capacity.

Investigations on the size dependence of mathematical percolation patterns (Fig. 3) in the context of oil field performance [15] and CO2 storage [16] shed a different light on this "premature" increase, discussing it as a necessary consequence of the small sample size in comparison to in situ scales. In this view, a small sample size means that there is a higher probability that local impurities and damage patterns create a connected flow path under conditions below the percolation threshold, where, by definition, no connected path should exist. With increasing sample size, the transition becomes increasingly sharp since connected random local defects will no longer be able to cross the sample. So, the argument can be made that the low baseline permeability in laboratory studies is inherently connected to the sample size and may not be present at the in situ scale. Given this assumption, rock salt would then act essentially impermeable below the percolation threshold (defeating the general concept of an intrinsically permeable medium), which would be more compatible with the established criteria for the assessment of hydraulic integrity of caverns (see section 2.3).

To investigate this important region of the curve in Fig. 2, an obvious step is to look at the results of large scale in situ tests and to determine which permeability relations can be brought in a good agreement to the observed behavior. However, what these attempts can gain by observing the hydro-mechanical properties of salt in a large-scale system is unfortunately often impaired by a lower degree of control and knowledge over the exact technological and geological boundary conditions, e.g. cavern shape, precise stress conditions and material inhomogeneities. Another issue with many long-term in situ cavern studies is the purely economic fact that such investigations rarely take place in "good" storage caverns, but predominantly in somewhat flawed caverns since those have little other value to their owners and hence are more likely to be provided for scientific studies. Therefore, the interpretations of some important in situ - tests used for validation of the permeability relation in section 3 must be inevitably also tied to these reservations.

2.2 Integrity Criteria

The most widely used type of criteria are simple stress-based assessments, which have been established since the 1990s: The dilatancy criterion and the minor principal-stress criterion [17], [18], [19]. The minor principal-stress criterion (subsequently abbreviated as MPS criterion) is also sometimes referred to as the "fluid pressure criterion". These criteria aim to cover the two fundamental mechanisms by which an intrusion of fluid or gas into the grain structure may occur.

The dilatancy criterion covers the effects of mechanical damage, which may create internal fractures and thereby induce a connected porous network within the material, which in turn will lead to a sharp increase in permeability already at very small amounts of damage [6], [7].

In numerical modeling, this is typically related to the evaluation of a complex constitutive model of salt rocks, which will allow an assessment of damaged areas [20], [21], [22], [23]. Although this is certainly of practical relevance, especially in conditions where solution mining occurs in large extraction ratios and a small remaining rock salt barrier [2], [24], violations of this criterion are typically limited to the immediate vicinity of underground voids (Fig. 3).

In practice, the MPS criterion is usually the most relevant criterion for the assessment of barrier integrity and boundary conditions on the mining operation, such as e.g. allowable cavern operation pressures. As previously stated, it is based on the general notion that the undamaged grain boundary network is impermeable against an attacking fluid or gas pressure, as long as this pressure is lower than the normal stress pressing the grain boundaries together.

The normal stress on a grain boundary depends on its orientation in the stress field. In a first conservative approach, the normal stress can be taken to be the minor principal stress. Numerical models are used to verify that the mining-induced stress redistribution does not reach a state where the fluid pressure of a groundwater column is higher than the minor principal stress on a connected path from the top of the salt down to the mining level (Fig. 4, left panel). Within the context of cavern storage, this typically amounts to verifying that the pressure within the cavern is below the minor principal stress (multiplied by safety factor) in a sufficiently thick salt mass above the cavern, so that the cavern retains its storage functionality (Fig. 4, right panel). Using these criteria, numerical studies on a wide variety of applications in conventional mining, solution mining and nuclear waste disposal are performed and assessed to determine, for example, safe pillar dimensions [25], optimization strategies or cavern pressure conditions [26].

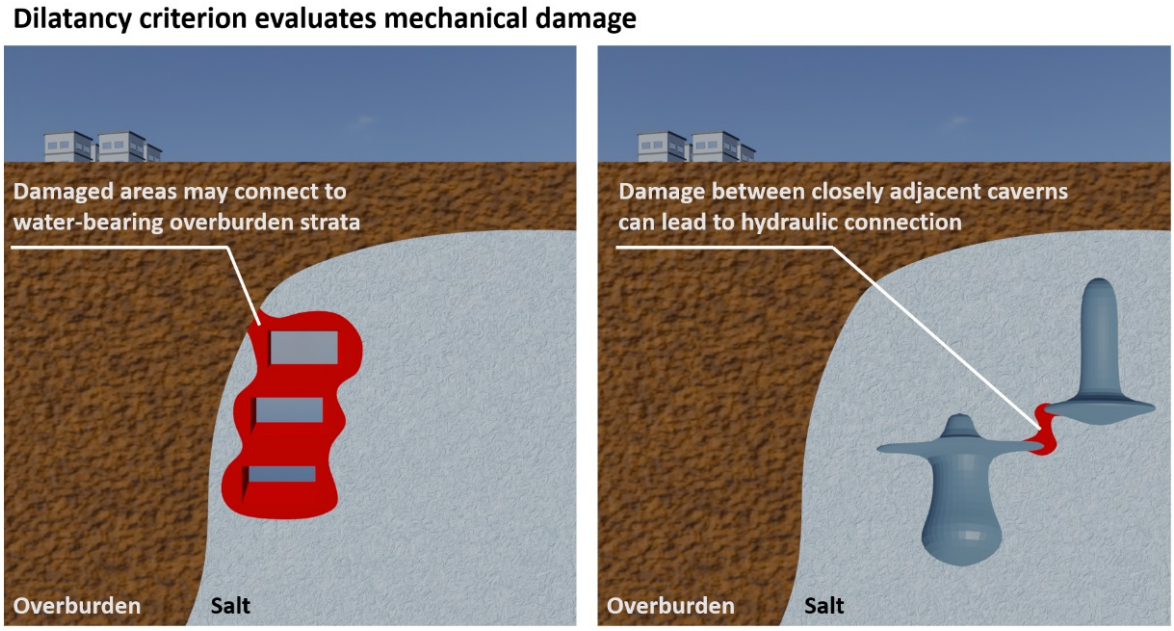

Fig. 3: Schematic examples for the practical relevance of the dilatancy criterion in the numerical assessment of geotechnical problems. Dilatant areas around mined rooms (left) and possible connection of unfavorably leached caverns near each other (right). Violation areas in red.

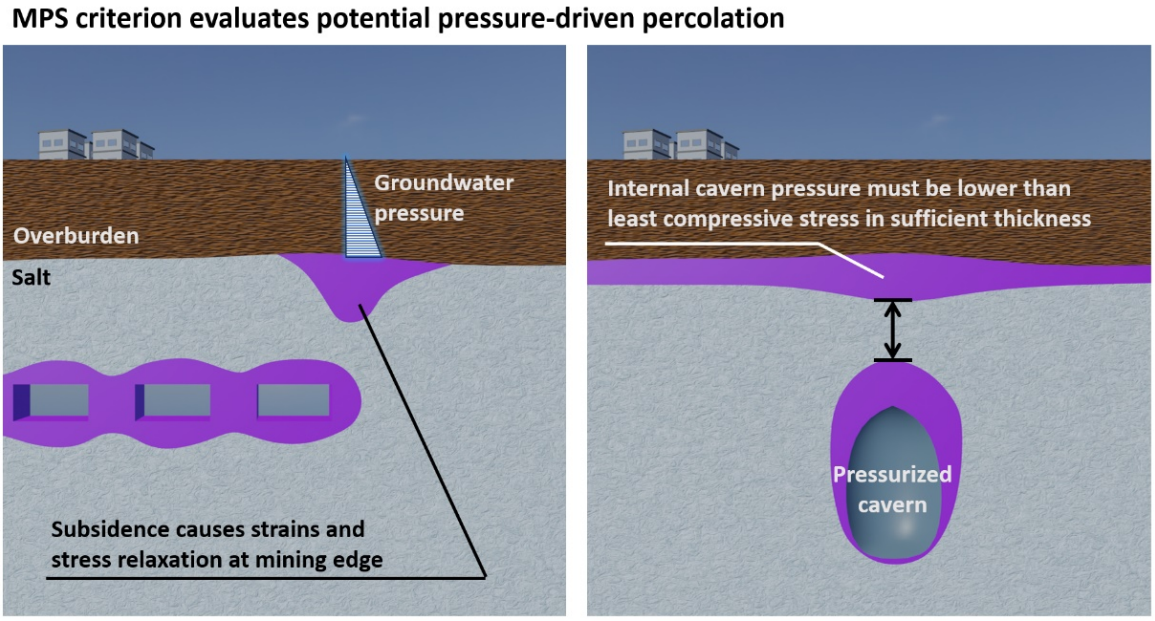

Fig. 4: Schematic example for applications of the MPS criterion in the numerical assessment of geotechnical problems. Possible groundwater inflow over the stress-relaxed mining edge (left) and determination of maximum allowable cavern pressure (right). Violation areas in purple.

3 Coupled numerical 3D-modeling of cavern storage and abandonment

In this section, we will show that the application of the principal mechanisms previously discussed in theoretical, laboratory, and in situ conditions will suffice to replicate the observations made in several cavern abandonment studies using hydro-mechanically coupled numerical modeling. The general idea of the common framework used for this modeling was already hinted at: Instead of treating rock salt as a permeable medium and misleadingly comparing cavern pressures with a hypothetical lithostatic stress, both laboratory and in situ evidence suggest that one has to consider the local stress field around the cavern and a step-function-like permeability assumption, which may either vanish or have a very low baseline at pressures below the minor principal stress. These simple assumptions are then sufficient to replicate the pressure behavior of the cavern abandonment tests discussed without having to resort to the notion of a general unconditional fluid loss in the cavern contour.

3.1 Numerical approach

During these simulations performed within FLAC3D alternating mechanical and hydraulic steps are calculated, where the mechanical part uses the Minkley-model [22] for the elasto-visco-plastic behavior of salt and a custom explicit finite-volume solver updates the zone saturations and pressures according to the dynamic permeabilities depending on the local stress and pressure. The general modeling sequence then iteratively followed the schematic depicted in Fig. 5.

During the calculation of the fluid percolation, we dynamically evaluate an (isotropic) permeability in dependence of the local stresses and fluid pressures. For each face between finite volume zones i and j the local permeability k_{ij} is calculated as (compressive stresses negative, σ_{min} as the least compressive stress):

$$k_{ij} = f(x) = \begin{cases} k_0 \cdot \max\left[\left(p_j + \sigma_{min,i}\right), \left(p_i + \sigma_{min,j}\right)\right], & p_{i/j} > \sigma_{min,j/i} \\ 0, & \text{otherwise} \end{cases}$$

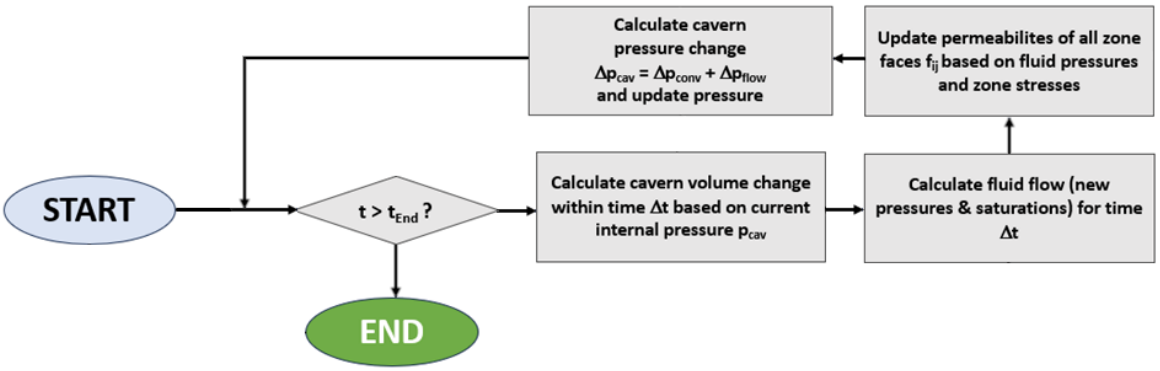

Fig. 5: Schematic flowchart of the hydro-mechanically coupled numerical modeling of cavern abandonment.

Since the general notion for the percolation process describe here is an opening of previously closed/inaccessible pore space, the approach assumes an induced secondary porosity, which may be possibly filled. Values for this secondary porosity are hard to determine but are generally assumed to be in the order of 0,2 – 1 %. For the numerical studies given here, we assume a value of 1%.

Note that while we have discussed that the percolation process may be highly oriented by following the plane perpendicular to the least compressive stress, the application of an isotropic permeability in this study (albeit dependent on pressure and stresses) is still a good approximation for the case of cavern abandonment, since the increasing pressure will most likely lower the tangential stresses, thus allowing outflow away from the cavern.

3.2 Validation through recalculations of large-scale in situ tests

To validate the proposed numerical approach and the underlying implications given by the assumed permeability behavior of rock salt, the obvious choice is to try to model the results found in large-scale in situ – tests. Numerous large-scale tests on boreholes and caverns in salt have been performed over the years. However, what these attempts can gain by observing the hydro-mechanical properties of salt in a large-scale system is unfortunately often impaired by a lower degree of control and knowledge over the exact technological and geological boundary conditions, e.g. cavern shape, precise stress conditions and material inhomogeneities. (Recall somewhat flawed caverns with little economic value are preferentially available for long-term tests.) Therefore, the interpretations of some important in situ - tests in the following paragraphs must be inevitably also tied to these reservations.

Here, pressure-tests in real salt caverns are divided into two groups: active and passive. Active mechanical integrity tests (MITs) are essential for evaluating the mechanical stability and safety of salt caverns used for hydrocarbon storage, waste disposal, and other underground applications (and are generally required by regulators). These tests involve injecting fluid into the cavern and monitoring its pressure response over time. The injection pressure response is analyzed to determine the integrity of the cavern, including the presence of any leaks or other mechanical anomalies. The most used MIT is the brine injection test, which involves the injection of brine into the cavern at a constant rate while monitoring the pressure response.

During passive tests, the cavern is plugged, and the convergence of the sealed cavern itself is the driving force for a subsequent increase in pressure. The corresponding pressure development is then (neglecting thermal effects) mainly determined by an increasing term due to the salt creep rate at the given internal cavern pressure and a decreasing term caused by a potential loss of fluid into the cavern wall. Many experiments on cavern abandonment also employ a mixed form of these two test regimes, by manually introducing certain pressure levels and then observing the subsequent undisturbed pressure behavior.

For a given cavern, the computed lithostatic stress at the top of the cavern generally is a good approximation of the virgin stress at the cavern roof before leaching. It may serve as an upper bound on the normal stress on grain boundaries during cavern operation and abandonment and is therefore often used as a reference value in the determination of the maximum allowable cavern pressure. The origin of this approximation is again related to the percolation threshold, which translated to this simplified notion that a cavern will be hydraulically tight until the internal pressure approaches the lithostatic stress. As with all generalizations, this is obviously not accurate for all circumstances — basic rock mechanics implies that excavations change the stress state in the rock mass. Rapid changes in internal cavern pressure will produce elastoplastic stress responses, which can potentially lower local stresses in the vicinity of the cavern below the internal cavern pressures even at pressures clearly below lithostatic stress. Depending on cavern geometry and pressure this may locally lead to contour areas where the fluid pressure is higher than the minor principal stress even at stresses clearly below the lithostatic stress level of the cavern. This behavior will be more pronounced the shallower a cavern is located, since then the creep deformation rates will be much smaller. This mechanism has obviously already been described in theory decades ago at the SMRI [27] and was accordingly confirmed in numerical models [28], but is apparently still not widely appreciated in its significance, since even 40 years later recent papers discuss it within the framework of "unexpected features of salt cavern behavior" (Gordeliy, 2022).

3.3 Stassfurt S102 Pressure Test

During a pressure test supported by the SMRI, the cavern was actively pressurized to a brine pressure of approximately 90% of the estimated lithostatic stress level at the top of the cavern and then closed while the pressure evolution was observed [30]. Naively, it could be expected that the cavern pressure would subsequently increase because of the remaining convergence rate of the cavern, but instead the pressure dropped slightly before reaching an apparently stable asymptotic level (Fig. 6). After a (unplanned) technical pressure drop, the pressure again increased, which led to the postulation of an "equilibrium" pressure level, below the lithostatic stress, at a wellhead pressure of approximately 30 bar, which was attributed to the general rock salt permeability already increasing below reaching the lithostatic stress, therefore leading to a stable state where the pressure loss by fluid permeation is compensated by the pressure increase due to cavern convergence.

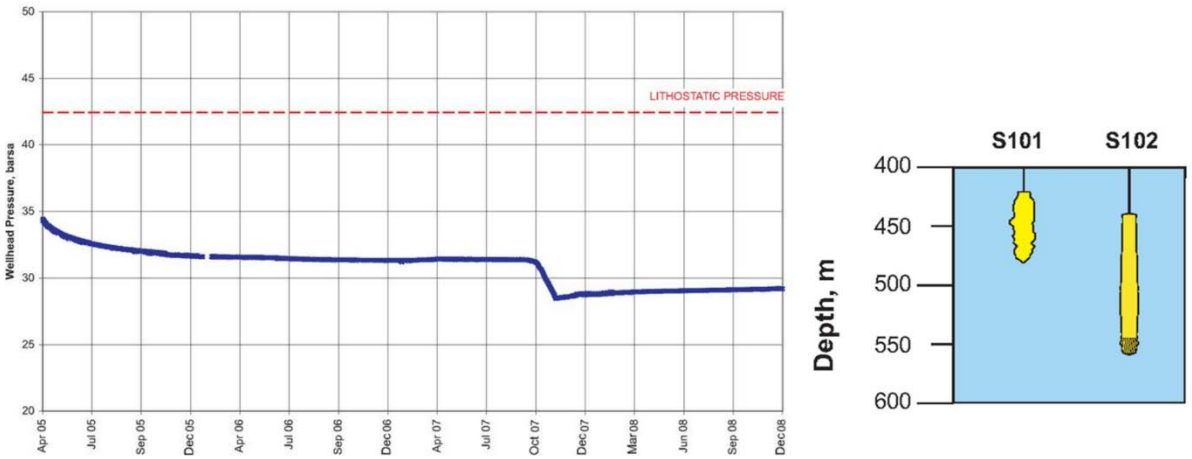

Fig. 6: Wellhead pressure of the S102 test.

For the recalculation of this test simple continuum-mechanical model for the Stassfurt cavern K102 was used to demonstrate this using hydro-mechanically coupled numerical modeling. Cavern leaching is modeled by slowly reducing the inner pressure gradient from lithostatic (0.025 MPa/m or 1.1 psi/ft) to brine gradient (0.012 MPa/m or 0.53 psi/ft) over two years. To replicate the abandonment test, the cavern head pressure is then increased to 35 bar

instantaneously. Afterwards, the cavern is regarded as plugged, so that the pressure is only determined by an increasing term due to volume convergence increment $\Delta\epsilon_V$ and the system stiffness K,

$$\Delta p_{conv} = -K \cdot \Delta \epsilon_v \,,$$

and a decreasing term due to fluid volume loss by percolation ΔV_{perco} ,

$$\Delta p_{perco} = -K \cdot \frac{\Delta V_{perco}}{V_{cavern}} \,.$$

The modeling cycle depicted in Fig. 5 is then repeated until the desired total modeling time is reached. (Recall that a sharp percolation threshold and no residual Darcy-type permeability was assumed in the calculations.) For this example, we will not consider thermal effects caused by brine warming and assume a system at thermal equilibrium. Brine warming will however be considered in the subsequent section. The results of the numerical modeling in Fig. 7 show a very good agreement of the result of the modeled pressure curve compared to the in situ test using the assumptions mentioned above regarding the hydraulic behavior of the salt. As a result of the rapid pressure increase, the elastoplastic stress redistribution leads to a small amount of brine being pressed into the cavern contour since the least compressive stresses there are lower than the fluid pressure even though the overall cavern pressure is still below lithostatic pressure. This leads to the observed small decrease in pressure. Since the convergence-driven pressure increment is very low at pressure close to the lithostatic level, the pressure curve seems to approach a constant level. The reaction to the small pressure drop is captured again with our simplified numerical model.

The right side of Fig. 7 then indicates an interesting behavior, suggesting that the “equilibrium pressure” interpretation of the multiple years long in situ - test does not hold over longer times. Since the secondary porosity induced in the surrounding volume of the cavern slowly fills up, the flow rate out of the cavern slowly decreases (as a result of a dropping pressure gradient), while the small convergence-driven pressure increments are still adding up. Therefore, the numerical models indicate that the pressure evolution even in those long-term tests could just be a snapshot within the time frames that might be relevant for cavern abandonment. It must be noted that the final conclusions regarding the safety of cavern abandonment remain unaffected, since the results still show that the flow rates are exceedingly small therefore and no macroscopic fracturing can occur.

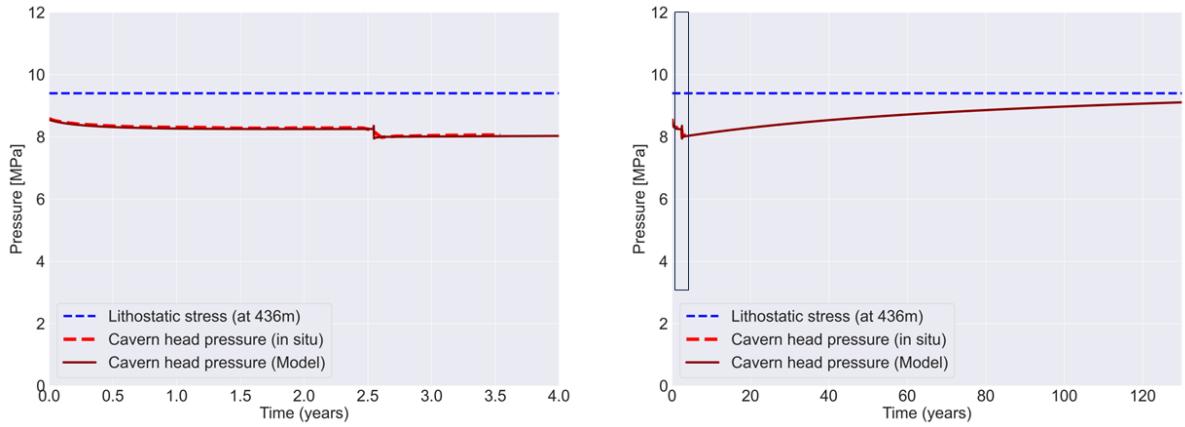

Fig. 7: Results of the hydro-mechanically coupled numerical modeling of the Stassfurt abandonment test. Timespan of the "long-term" test on the left with apparent equilibrium pressure, while the numerical model still shows a slow but steady pressure increase for even longer times.

These numerical modeling results show that the pressure behavior of salt caverns can be reproduced with the assumptions discussed above, without resorting to a premature permeability increase below the minor principal stress level. This conclusion was also drawn in an extensive review of in situ observations, where the KEM-17 research study (Phase 2) also found that *"the salt permeability does not necessarily need to be increased to reach a pressure equilibrium lower than the lithostatic pressure"* (Brouard, 2019), which again supports the notion that an increased salt permeability not necessarily needs to be assumed to explain those in situ findings.

For the sake of brevity, this example shall suffice as a proof of concept for the hydro-mechanically coupled 3D-modeling. Other examples of such recalculations are published in [32]. Also, additional validation examples of other long-term abandonment tests (e.g. Etrez EZ53) are currently being performed to further refine the approach.

3.4 Application to the modeling of hydrogen storage in salt caverns

The same principles presented in the numerical modeling examples of the preceding sections can in principle also be applied for storage operation with the additional complexity of thermodynamical calculations for gas caverns, to capture the effects of the cooling and heating of the gas during pressure changes. Given desired or actual gas flow rates during injection and withdrawal in a specific cavern, thermodynamic calculations may be carried out to determine a corresponding good approximation of the pressure and temperature behavior of the gas within the cavern. Several software packages with such functionality for the estimation of temperature evolution have been developed in the cavern storage community, such as SCTS [33] or TSCW-GACA. At the IfG we use our own custom code called CavTemp for this application, which is based on the open-source "coolProp engine" [34] and has been validated against the results of the established codes.

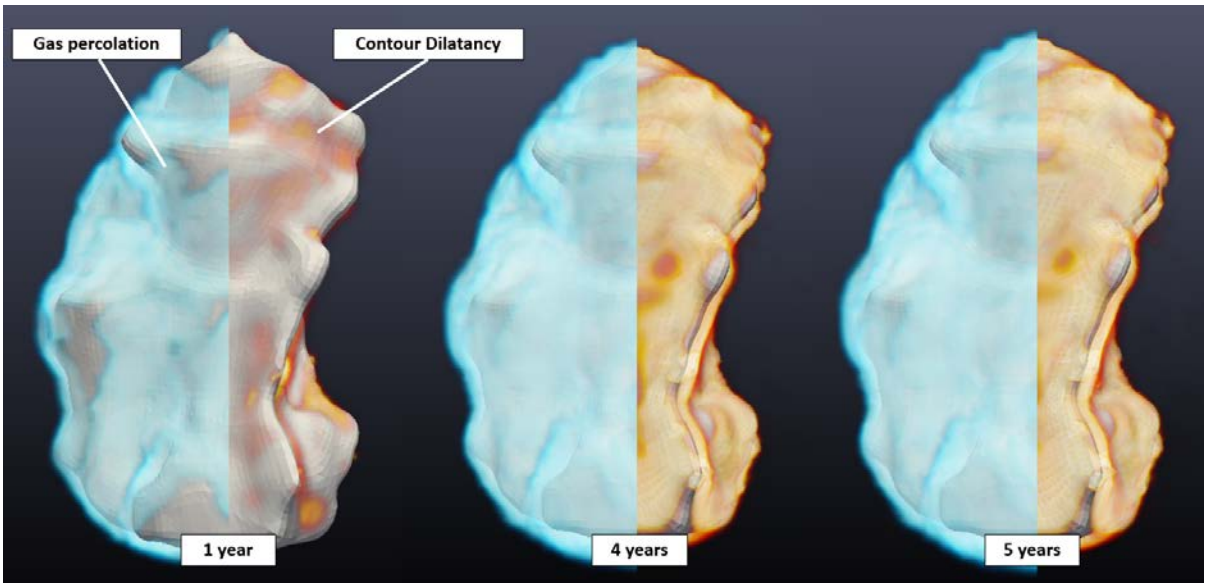

Fig. 8: Generic example of modeled contour dilatancy and fluid percolation regions around a fictitious cavern after seasonal cyclic hydrogen storage operation.

Given these input parameters, we can then use a similar workflow as presented in Fig. 5, only inserting a corresponding thermal part for the calculation of the changes in temperature field around the cavern because of the gas temperature change.

An additional point of consideration, which is generally ignored in most assessments of cavern stability, is the application of an effective stress concept for the calculation of material strength.

While it is well-known and always applied in general soil mechanics that the presence of a fluid pressure decreases the strength of a material, this is usually not applied in salt caverns. Since we aim to underline the general tightness of rock salt against fluid/gas pressures under suitable pressure and stress conditions, this seems to be an appropriate assumption, since then there is no pressurized pore network that may reduce the material strength. However, in dilatant regions at the immediate cavern contour as well as in those regions where e.g. the minor principal stress criterion is violated, one must assume that a fluid pressure is acting in the grain boundary network, countering against the normal stresses on the grain boundaries and therefore reducing the strength of the rock mass. The inclusion of such effects is predominantly important for the local contour behavior and could in principle explain previous overestimations of long-term stability of large-diameter cavern roofs as well as spalling effects at the contour of deep caverns. Therefore, in the coupled simulations presented herein, the regions into which a pressurized gas or fluid has percolated are assigned a corresponding pore pressure, which reduces the effective minor principal stress.

To illustrate a typical result of such an investigation Fig. 8 shows the calculated contour dilatancy and fluid percolation in a realistic, but fictitious cavern after 5 years of a sinusoidal yearly gas pressure regime. In the modeling, a pressure-driven filling of geometrically unfavorable regions occurs very fast during the initial high pressure. In the times around each pressure minimum, a clear increase of accumulating dilatancy in the cavern contour is observed, which is then usually subsequently filled with gas, when the pressure increases again. However, for the given pressure course in this generic model, these effects can be shown to be confined to a limited region around the cavern contour, which eventually does not extend any further. Please note that this model and its pressure/temperature curve was synthetically constructed to show the principal mechanisms in hydro-mechanically coupled calculations in a generic case, therefore deliberately without discussing the specific operation pressures and material properties, which were based on realistic values, but at last were entirely arbitrary for this fictitious cavern.

3.5 Limitations and the Role of Inhomogeneities.

The previously discussed properties applied for the rock salt (and the derived methodology for the assessments) are valid for a reasonably homogeneous rock salt without significant internal impurities and laminations. Based on the recalculations of in situ – cavern behavior this appears to be a valid approximation, especially for the cavern scale, where local impurities may lead to small local differences without significantly affecting the global system behavior. However, if the cavern site contains significant inhomogeneities, a simple continuum-mechanics approach with a large-scale homogenized salt stratum is likely to miss potential failure modes. In particular, bedding planes and fractured layers of other rocks (e.g., carbonates, shales or anhydrite) may present preferential flow paths for fluids. In such cases a thorough geological exploration to determine the presence of significant inhomogeneities and, if necessary, their hydromechanical properties, is advisable. If such structures are present, a more advanced numerical approach that can account for localized fluid motion along bedding planes, fractures or intercalations is required to provide a robust assessment of cavern integrity.

4 A Hierarchy of Approaches for Cavern Assessment

When it comes to evaluating the stability and hydraulic integrity of salt caverns, there are certain established geomechanical investigations and tasks whose completion is necessary for its successful operation, e.g. the laboratory confirmation of the site-specific mechanical and hydraulic salt properties and the determination of safe, but efficient, operational parameters. However, due to their natural geological setting each cavern comes with its own set of challenges and characteristics. To tackle these challenges, we have different levels of numerical modeling, ranging from simple to more complex. This approach (see table 1) offers great flexibility and helps us address the various issues we might encounter in cavern storage and abandonment.

The basic level of sophistication contains the simple 2D modeling of an ideal cavern enveloping the actual or the planned cavern and can comparatively quickly evaluate standard integrity and stability criteria as well as define initial cavern operation parameters at the cost of a strong simplification of cavern geometry and overestimation of cavern volume. Therefore, the corresponding results e.g. the derived maximum/minimum allowable operation pressures and other constraints in pressure increase/decrease rates are potentially very conservative. Also, the influence of other caverns in the field in terms of minimum pillar width between caverns and potential stress influences due to potentially varying cavern depths, heights and operation types of neighboring caverns cannot be accurately described in simplified 2D models. As a compromise it is then possible to use a 3D system of idealized caverns. In the case of gas storage, already at this stage a thermo-mechanical coupling taking the cooling & heating of the stored gas into account is necessary to accurately predict the cavern behavior, which adds an additional layer of complexity already to the most basic numeric models.

To alleviate some of the conservativities inherent to the idealized 2D models, but also to identify potential challenges with the real solution-mined cavern, a more complex modeling approach using the sonar measurements as the basis for a realistic 3D modeling of the actual cavern shape and available geologic layer data is used. These models can then be employed to optimize the basic operational parameters given the actual cavern shape and volume, while also assessing the potential likelihood of contour damage due to unfavorably leached configurations or geological particularities. While these numerical modeling tasks demand a certain amount of additional work for mesh generation and computational power, the current advances in pre-processing tools and numerical codes allow for much more complex models at manageable times and cost for this additional insight into the cavern behavior.

In the most complex state of modeling, fully thermo-hydro-mechanically modeling task like the ones described in the previous sections may be performed to replace the qualitative evaluation of the minor-principal-stress criterion with a realistic modeling of the gas or fluid percolation into the salt barrier and the investigation of the time- and pressure-regime-dependent depth of penetration into the cavern contour. This is currently already used for the modeling of cavern abandonment scenarios, which cannot be evaluated with the standard criteria for cavern operation (see section 3), but also has the potential to be beneficial in the assessment of cavern storage operations, especially under complex geological and geotechnical boundary conditions.

The three layers of complexity for numerical studies presented in this paper offer a degree of flexibility for cavern operators, licensing authorities, and geomechanical experts to select an approach that aligns with their specific objectives and requirements.

5 Summary / Zusammenfassung

In this paper we have reviewed the general notions and conceptual approaches regarding the permeability characteristics of rock salt under varying confining stresses and fluid pressures. We have tried to show that there is a common framework to unify some seemingly contradictory views on the subject by presenting a concise overview and discussing the difference of lithostatic stress and the actual local stress field within the context of assumptions for the salt rock permeabilities at fluid pressures clearly below the minor principal stress, and the onset of the increase at higher pressures. Most importantly we have shown that the findings of key in situ experiments can be replicated using hydro-mechanically coupled numerical models without having to assume an increase in salt permeability before the fluid pressure exceeds the least compressive stress around the cavern. Thus, all evidence is consistent with the notion that rock salt is essentially impermeable, and that fluid transport in rock salt is possible only when either secondary porosity, i.e., dilatancy, is generated, or if the fluid pressure exceeds the minor principal stress, i.e., by pressure-driven percolation.

Potential counterexamples, which indicate an “equilibrium pressure” for salt caverns significantly below the lithostatic stress, do not contradict this idea once stress redistributions and appropriate creep behavior is considered.

In diesem Beitrag haben wir die allgemeinen konzeptionellen Ansätze hinsichtlich der Permeabilitätseigenschaften von Steinsalz unter variierenden Einspannungen und Fluiddrücken diskutiert. Wir haben versucht zu zeigen, dass eine Beschreibung der makroskopischen Permeabilitätsentwicklung basierend auf diesen Vorstellungen existiert, die einige scheinbar widersprüchliche Ansichten zu diesem Thema vereint. Ein zentrales Ergebnis der Untersuchungen ist, dass die Ergebnisse wichtiger In-situ-Experimente mit hydro-mechanisch gekoppelten numerischen Modellen repliziert werden können, ohne dass eine Erhöhung der Salzpermeabilität angenommen werden muss, bevor der Fluiddruck den geringsten Kompressionsdruck um die Kaverne überschreitet. Die Beschreibung ist damit konsistent mit der seit Jahrzehnten in der Praxis bewährten Vorstellung, dass homogenes, ungestörtes Steinsalz im Wesentlichen undurchlässig ist und dass ein praktisch relevanter Fluidtransport im Steinsalz nur möglich ist, wenn entweder sekundäre Porosität, d.h. Dilatanz, erzeugt wird oder wenn der Fluiddruck den geringsten Hauptspannungsdruck überschreitet, d.h. durch druckgetriebene Perkolation.

Die in diesem Kontext oft angeführten „Gegenbeispiele“, die auf einen Gleichgewichtsdruck für Salzkavernen hinweisen, der deutlich unter dem lithostatischen Druck liegt, widersprechen dieser Idee also ausdrücklich nicht, sondern folgen sogar völlig zwanglos, sobald Spannungsumlagerungen und das Kriechverhalten der Salzgesteine im sekundären Spannungsfeld berücksichtigt werden.

6 Literaturverzeichnis

[1] K. L. Kuhlman und E. N. Matteo, „Porosity and Permeability: Literature Review and Summary“, in *Mechanical Behavior of Salt IX*, Hannover, Germany, 2018, S. 291–120.

[2] W. Minkley, D. Brückner, und C. Lüdeling, „Percolation in salt rocks“, in *Mechanical Behavior of Salt IX*, Hannover, Germany, 2018, S. 29–44.

[3] W. Minkley, M. Knauth, D. Brückner, und C. Lüdeling, „Integrity of saliferous barriers for heat-generating radioactive waste - natural analogues and geomechanical requirements“, in *Mechanical Behavior of Salt VIII*, Rapid City, USA, Mai 2015, S. 159–170.

[4] P. Bérest *u. a.*, „Cavern abandonment: three in situ tests.“, in *SMRI Fall Meeting 2013*, Avignon, 2013.

[5] P. Bérest, B. Brouard, und G. Hévin, „Twelve-year monitoring of the idle Etrez salt cavern“, *International Journal of Rock Mechanics and Mining Sciences*, 2011, doi: 10.1016/j.ijrmms.2010.07.004.

[6] C. J. Peach und C. J. Spiers, „Influence of crystal plastic deformation on dilatancy and permeability development in synthetic salt rock“, *Tectonophysics*, Bd. 256, Nr. 1, S. 101–128, 1996, doi: https://doi.org/10.1016/0040-1951(95)00170-0.

[7] T. Popp, H. Kern, und O. Schulze, „Evolution of dilatancy and permeability in rock salt during hydrostatic compaction and triaxial deformation“, *Journal of Geophysical Research*, 2001.

[8] J. Urai, Z. Schléder, C. Spiers, und P. Kukla, „Flow and transport properties of salt rocks“, *Dynamics of complex intracontinental basins: The central European basin system*, S. 277–290, 2008.

[9] S. Ghanbarzadeh, M. A. Hesse, M. Prodanović, und J. E. Gardner, „Deformation-assisted fluid percolation in rock salt“, *Science*, Bd. 350, Nr. 6264, S. 1069–1072, 2015, doi: 10.1126/science.aac8747.

[10] C. Lüdeling, D. Naumann, und W. Minkley, „Investigation of fluid transport in rock salt under repository-relevant conditions – the PeTroS project“, in *The Mechanical Behavior of Salt X*, J. H. P. de Bresser, M. R. Drury, P. A. Fokker, M. Gazzani, S. J. T. Hangx, A. R. Niemeijer, und C. J. Spiers, Hrsg., Utrecht, The Netherlands: CRC Press, 2022, S. 200–211. doi: 10.1201/9781003295808.

[11] C. J. A. Sinn, P. Giacomel, C. J. Peach, S. J. T. Hangx, und C. J. Spiers, „Effects of Plastic Deformation on the Transport Properties of Rocksalt“, in *Mechanical Behavior of Salt IX*, Hannover, Germany, 2018, S. 101–120.

[12] J. Jaeger, N. Cook, und R. Zimmerman, „Fundamental of Rock Mechanics“, 2007. doi: 10.1017/CBO9780511735349.

[13] P. Cosenza und M. Ghoreychi, „Effects of very low permeability on the long-term evolution of a storage cavern in rock salt“, *International Journal of Rock Mechanics and Mining Sciences*, Bd. 36, Nr. 4, S. 527–533, 1999, doi: https://doi.org/10.1016/S0148-9062(99)00018-2.

[14] K. Staudtmeister und D. Zander-Schiebenhöfer, „Abandonment of caverns in rock salt mass“, in *Numerical Methods in Geotechnical Engineering*, Graz, Austria, Sep. 2006, S. 347–352.

[15] M. Masihi, P. R. King, und P. Nurafza, „Fast Estimation of Connectivity in Fractured Reservoirs Using Percolation Theory“, *SPE Journal*, Bd. 12, Nr. 02, S. 167–178, Juni 2007, doi: 10.2118/94186-PA.

[16] C. L. Petrovitch, L. J. Pyrak-Nolte, und D. D. Nolte, „Laboratory to Field: Critical Scaling of Single Fractures“, in *Proceedings of the 47th US Rock Mechanics/Geomechanics Symposium*, San Francisco, USA, Juni 2013.

[17] W. Minkley, M. Knauth, und D. Brückner, „Discontinuum-mechanical behaviour of salt rocks and the practical relevance for the integrity of salinar barriers“, in *Proceedings of the 47\textsuperscriptth US Rock Mechanics/Geomechanics Symposium*, J. F. Labuz, E. Detournay, W. Pettitt, L. Petersen, und R. Sterling, Hrsg., Minneapolis, Minnesota, USA, Juni 2013.

[18] W. Minkley, M. Knauth, und U. Wüste, „Integrity of salinar barriers under consideration of discontinuum-mechanical aspects“, in *Mechanical Behavior of Salt VII*, Paris, France: Taylor and Francis Group, Apr. 2012, S. 469–478.

[19] M. Rahmig, C. Lerch, N. Müller-Hoeppe, M. Polster, T. Schröpfer, und B. Stielow, „Derivation of a non-local criterion to assess functionality and robustness of rock salt barrier“, in *The Mechanical Behavior of Salt X*, J. H. P. de Bresser, M. R. Drury, P. A. Fokker, M. Gazzani, S. J. T. Hangx, A. R. Niemeijer, und C. J. Spiers, Hrsg., Utrecht, The Netherlands: CRC Press, 2022, S. 262–271. doi: 10.1201/9781003295808.

[20] R.-M. Günther, „Erweiterter Dehnungs-Verfestigungs-Ansatz - Phänomenologisches Stoffmodell für duktile Salzgesteine zur Beschreibung primären, sekundären und tertiären Kriechens“, Dissertation, TU Bergakademie Freiberg, Freiberg, 2009.

[21] P. Labaune und A. Rouabhi, „Dilatancy and tensile criteria for salt cavern design in the context of cyclic loading for energy storage“, *Journal of Natural Gas Science and Engineering*, Bd. 62, S. 314–329, 2019, doi: 10.1016/J.JNGSE.2018.10.010.

[22] W. Minkley, „Gebirgsmechanische Beschreibung von Entfestigung und Sprödbrucherscheinungen in Carnallitit“, Habilitation, TU Bergakademie Freiberg, Freiberg, 2004.

[23] R. Wolters *u. a.*, „WEIMOS: Laboratory investigation and numerical simulation of damage reduction in rock salt“, in *The Mechanical Behavior of Salt X*, J. H. P. de Bresser, M. R. Drury, P. A. Fokker, M. Gazzani, S. J. T. Hangx, A. R. Niemeijer, und C. J. Spiers, Hrsg., Utrecht, The Netherlands: CRC Press, 2022, S. 190–199. doi: 10.1201/9781003295808.

[24] W. P. Kamlot, R.-M. Günther, G. Gärtner, und L. Teichmann, „Geomechanical stability proof of the Asse II mine and forecast of the further development using an extensive 3D-model“, in *Mechanical Behavior of Salt IX*, Hannover, Germany, 2018.

[25] W. Minkley, J. Mühlbauer, und C. Lüdeling, „Dimensioning principles in potash and salt mining to achieve stability and integrity“, in *Rock Mechanics and Rock Engineering*, Springer Verlag Wien, 2016.

[26] W. Minkley, T. Fabig, M. Knauth, und N. Farag, „Stability of salt caverns under consideration of hydro-mechanical loading“, in *Mechanical Behavior of Salt VIII*, Rapid City, USA, Mai 2015.

[27] M. Wallner, „Frac-pressure risk in rock salt“, in *Proc. SMRI Fall Meeting*, Amsterdam, 1986.

[28] H. Djizanne, P. Bérest, und B. Brouard, „Tensile Effective Stresses in Hydrocarbon Storage Caverns“, in *SMRI Fall 2012 Technical Conference*, Bremen, Germany, Okt. 2012.

[29] E. Gordeliy und P. Bérest, „Unexpected features of salt cavern behavior“, in *The Mechanical Behavior of Salt X*, J. H. P. de Bresser, M. R. Drury, P. A. Fokker, M. Gazzani, S. J. T. Hangx, A. R. Niemeijer, und C. J. Spiers, Hrsg., Utrecht, The Netherlands: CRC Press, 2022, S. 372–383. doi: 10.1201/9781003295808.

[30] A. Banach und M. Klafki, „Staβfurt Shallow Cavern Abandonment Field Tests.“, SMRI Research Report RR 2009-01, 2009.

[31] P. Brouard, „Over-pressured caverns and leakage mechanisms. Phase 2 - Cavern scale“, Brouard Consulting, Paris, France, Research Project KEM-17, 2019.

[32] M. Knauth, C. Lüdeling, und R. M. Günther, „Rock Salt: Hydraulic Integrity and Creep for Safe and Efficient Cavern Operations.“, in *SMRI Spring 2024 Technical Conference*, Krakow, Poland, Apr. 2024.

[33] J. Nieland, „Salt cavern thermal simulator version 2.0 user’s manual“, *RESPEC Topical Report RSI-1760, Ed. by RESPEC, Rapid City, South Dacota*, 2004.

[34] I. H. Bell, J. Wronski, S. Quoilin, und V. Lemort, „Pure and Pseudo-pure Fluid Thermophysical Property Evaluation andthe Open-Source Thermophysical Property Library CoolProp“, *Industrial & Engineering Chemistry Research*, Bd. 53, Nr. 6, S. 2498–2508, 2014, doi: 10.1021/ie4033999.

A Novel Method for Rock Permeability Determination Based on Numerical Optimization of Inverse Problems

Eine neuartige Methode zur Bestimmung der Felspermeabilität basierend auf numerischer Optimierung inverser Probleme

Dongyu Li[1,2,3], Qingquan Liu[1,2,3,4], Biao Lv[1,2,3], Heinz Konietzky[4]
[1]State Key Laboratory of Coal Mine Disaster Prevention and Control, China University of Mining & Technology, Xuzhou 221116, China
[2]Key Laboratory of Coal Methane and Fire Control, Ministry of Education, China University of Mining & Technology, Xuzhou 221116, China
[3]National Engineering Research Center for Coal Gas Control, China University of Mining & Technology, Xuzhou 221116, China
[4]Geotechnical Institute, TU Bergakademie Freiberg, Freiberg, Germany

Abstract

Rock permeability is a critical parameter for assessing the ability of rocks to facilitate fluid flow. The pressure pulse decay method, renowned for its short testing duration and high accuracy, is extensively utilized for permeability testing of low-permeability rocks. However, the theoretical solution relies on the seepage cross-sectional area and length, which cannot be applied to rocks that are challenging to shape into regular samples, such as soft rocks. To address limitations, this paper proposes a novel approach to permeability determination based on inverse problem numerical optimization. This method involves constructing a mathematical model that accurately describes the entire process of determining permeability using the pressure pulse decay method: the sample's pressure differential data is used as a penalty function, and the sample permeability is calculated by combining numerical optimization of inverse problems. Comparative analysis with experimental data reveals that pressure differential data calculated through the new model's inverse optimization closely aligns with experimentally measured pressure differentials on regular samples, with a high fitting accuracy (R^2=0.9820). The simulated permeability is determined to be 0.148 mD, showing minimal deviation from the theoretically derived permeability of 0.142 mD, demonstrating the new model's ability to accurately describe experimental processes using the pressure pulse decay method and obtain precise permeability. Furthermore, experiments were conducted on irregularly shaped samples, and numerical simulations using the new solution model showed a high degree of consistency between inverted pressure difference data and actual measurements; however, the permeability differed significantly from those obtained through theoretical solutions due possibly to limitations in sample processing methods. This newly proposed approach effectively overcomes restrictions imposed by theoretical solutions on sample shape during permeability testing, providing a fresh avenue for measuring rock permeabilities. Additionally, the convenience offered by numerical experiments presents an efficient means for studying competitive effects among factors influencing rock permeabilities.

Zusammenfassung

Die Permeabilität von Gesteinen ist ein Schlüsselparameter zur Bewertung der Fähigkeit von Gesteinen, Flüssigkeiten hindurchzulassen. Die Methode der transienten Druckimpulsprüfung wird aufgrund ihrer kurzen Testzeit und hohen Testgenauigkeit häufig zur Bestimmung der Permeabilität von Gesteinen mit geringer Durchlässigkeit eingesetzt. Da bei der Berechnung der Permeabilität mit dieser Methode theoretische Lösungen die Querschnittsfläche und Fließlänge der Probe berücksichtigen müssen, kann sie jedoch nicht direkt für die Permeabilitätstests von Gesteinen wie Weichgestein oder Weichkohle verwendet werden, bei denen es schwierig ist, regelmäßige Proben herzustellen. Um diese Einschränkung zu überwinden, wird in diesem Artikel eine neue Methode zur Bestimmung der Permeabilität anhand der Optimierung eines inversen Problems vorgeschlagen: Durch den Aufbau eines mathematischen Modells, das den gesamten Prozess der Bestimmung der Permeabilität mittels der Methode der transienten Druckimpulsattenuierung realistisch beschreibt, wird anhand der gemessenen Druckdifferenzdaten an den Ein- und Austrittsstellen des Samples eine Zielfunktion erstellt. In Kombination mit der numerischen Optimierung des inversen Problems wird die Permeabilität des Samples berechnet. Der Vergleich der Simulationsresultate mit Experimentaldaten zeigt, dass die basierend auf dem neuen Modell umgekehrten optimierten Druckdifferenzdaten eine hohe Übereinstimmung mit den gemessenen Druckdifferenzdaten von regelmäßigen Proben aufweisen, wobei die Anpassungsgenauigkeit R^2 bis zu 0,9820 beträgt. Die ermittelte Permeabilität beträgt 0,148 mD, was nur geringfügig von der auf Basis der theoretischen Lösung berechneten Permeabilität von 0,142 mD abweicht. Dies beweist, dass das neu vorgeschlagene Modell den Prozess der transienten Druckimpulsprüfung genau beschreiben kann und es in der Lage ist, die Permeabilitätsparameter präzise zu ermitteln. Darüber hinaus wurden Experimente zur Permeabilität von Proben in unregelmäßiger Form durchgeführt, und das neue Lösungsmodell wurde für numerische Tests verwendet. Die inversen Druckdifferenzdaten weisen eine hohe Übereinstimmung mit den gemessenen Druckdifferenzdaten der unregelmäßigen Proben auf, jedoch weichen die spezifischen Permeabilitätslösungen erheblich von den auf Basis der theoretischen Lösung ermittelten Permeabilitätswerten ab. Dies könnte auf Mängel bei der Probenbehandlung zurückzuführen sein. Die Etablierung neuer Methoden kann effektiv die Einschränkungen der theoretischen Lösungen bezüglich der Probenform bei der Durchlässigkeitstests lösen und bietet einen neuen Ansatz zur Messung der Durchlässigkeit von Gesteinen. Die Bequemlichkeit numerischer Experimente eröffnet zudem einen neuen, effizienten Weg zur Erforschung der wettbewerbsseitigen Einflüsse von Faktoren auf die Durchlässigkeit.

1 Introduction

Permeability is a fundamental parameter that characterizes the ability of porous media to facilitate fluid flow. It reflects the migration and distribution of fluids underground and is a crucial parameter across various fields such as energy and geology. For instance, in the development of unconventional oil and gas resources, permeability is key to assessing reservoir conditions and production(Wang et al. 2016; Zou et al. 2012; Jia et al. 2012). In CO_2 geological storage projects(Busch et al. 2008; Aminu et al. 2017) and deep-ground energy storage technologies(Matos et al. 2019; Epelle et al. 2022), permeability is essential for evaluating the sealing integrity of caps and long-term safety. Therefore, the accurate measurement of permeability is a focal point in these studies.

The determination methods for rock permeability can be classified into on-site measurements at production sites and laboratory measurements based on the location of the experiments. Since gas permeability varies with changes in reservoir conditions, it is difficult to provide a comprehensive description on-site(Sander et al. 2017). In contrast, laboratory testing is the primary means to obtain rock permeability parameters and study factors influencing permeability.

Currently, the commonly used methods are mainly classified into steady-state methods(Jones and Meredith, 1998) and unsteady-state methods(Gensterblum et al. 2015). Steady-state methods are generally applicable to rocks with higher permeability, requiring the measurement and recording of the stable volumetric flow rate at the fluid outlet. However, for dense rocks such as granite, the process of measuring a stable volumetric flow rate can be prolonged, and there is a high demand for sensor precision(Cui et al. 2009).To address the inadequate performance of steady-state methods in measuring permeability in low-permeability rocks, Brace et al. (1968) proposed a new transient pressure pulse decay method. Brace was the first to apply this method to determine the permeability of granite, demonstrating its superior performance compared to steady-state methods for testing low-permeability rocks. After its introduction, scholars in the field widely accepted and used this method, making various simplifications and improvements. Dicker and Smits (1988), in their study of permeability in tight rocks using transient methods, found that if the volumes of the upstream and downstream gas chambers in the testing apparatus are inconsistent, the relationship between pressure decay and time may no longer be a single exponential relationship. This increases the complexity of data analysis. Therefore, setting the volumes of the upstream and downstream gas chambers to be the same not only simplifies the processing of experimental data but also reduces the impact of changes in pore volume compression on the experiment. Furthermore, Ma et al. (2016), in researching shale permeability, suggested increasing sensitivity to pressure changes in experiments by minimizing the volumes of gas chambers and pipelines, thereby reducing testing time.

However, regardless of the laboratory experimental method mentioned above, when conducting permeability tests, it is necessary to use regular "cylindrical" or "rectangular" specimens. This is because when calculating the permeability of the sample using theoretical solutions, parameters such as the flow cross-sectional area and flow length are required. For the convenience of data processing, the permeability test apparatus is designed to require specimens with regular shapes such as cylinders or rectangular prisms. However, in practical engineering, some soft rocks may lack sufficient strength, making it difficult to obtain samples with regular shapes directly. Alternatively, sampling conditions may be unfavorable, as in the case of core sampling during geological exploration, where irregular fractured samples often exist(Liu et al. 2017; Cheng et al. 2021). In these situations, the theoretical solution using the transient pressure pulse method cannot be directly applied to calculate the permeability of irregularly shaped samples. Therefore, for soft rock permeability determination, the test is typically conducted by crushing the rock to the specified particle size and then pressing it into a briquette under high pressure.

Nevertheless, such test results are insufficiently accurate to characterize the permeability characteristics of strata(Liu et al. 2016; Jasinge et al. 2012).

Fig. 1: Rock samples that are difficult to produce regularly shaped samples.

Given the limitations of theoretical solutions, this paper proposes a numerical simulation method for determining the permeability of irregularly shaped rocks. In this approach, laser scanning is used to obtain the appearance of the sample, combined with upstream and downstream pressure differential data from pressure pulse decay tests are required. The permeability of the samples can then be derived through optimization analysis of the inverse problem. This paper constructs a mathematical model that accurately describes the testing process of the pressure pulse decay method, determines the permeability of regularly and irregularly shaped samples with laboratory experiments and numerical simulations, and analyzes the results to verify the novel method.

2 Principle of Pressure Pulse Decay Testing and Gas Flow Models

2.1 Principle of pressure pulse decay testing

The common experimental system for testing permeability using the transient pressure pulse method is illustrated in Fig. 2. In the diagram, the sample is enveloped in a rubber sleeve and supported within the apparatus. The clamping device can apply confining pressure and axial pressure to the sample, and there is an equally sized gas tank on the upstream and downstream sides of the sample. During the experiment, the test gas flows through the sample from the upstream gas tank to the downstream gas tank through a porous medium.

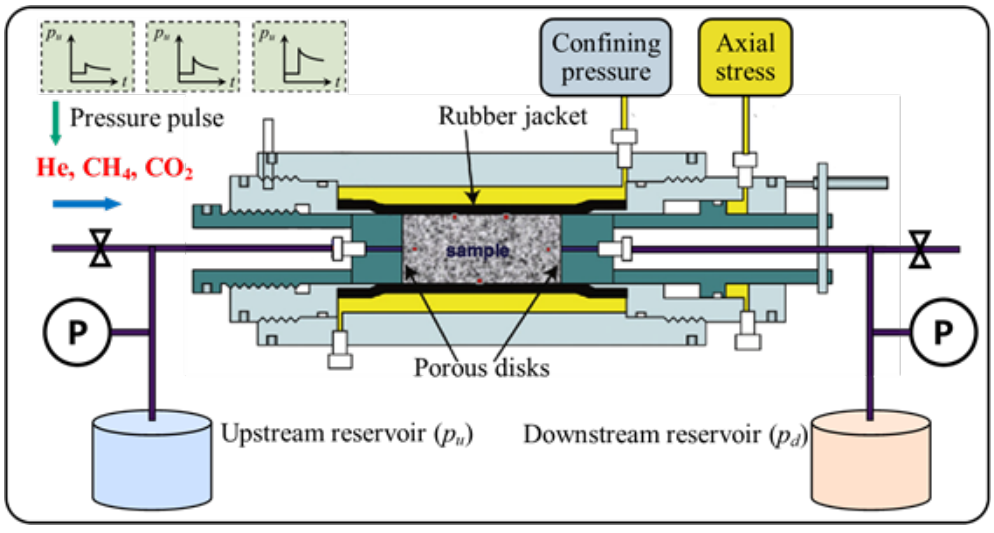

Fig. 2 Common testing device of pressure pulse decay method.

The experimental process and principle of the pressure pulse decay method are illustrated in Fig. 3. During the experiment, after allowing a period for the pressure equilibrium between the test sample and the upstream and downstream gas tanks, the pressure inside the upstream gas tank suddenly increased. Under the influence of the pressure gradient between the upstream and downstream, gas will form one-dimensional permeation within the sample. Subsequently, the pressure in the upstream gas tank gradually decreases, while the pressure in the downstream gas tank increases gradually, leading to a gradual reduction in the pressure difference.

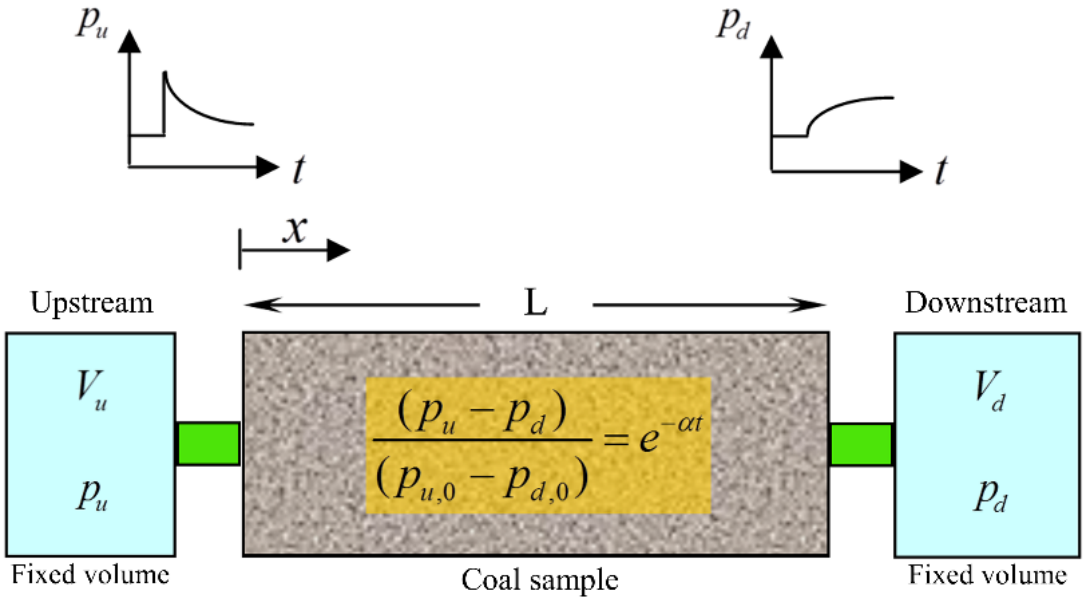

Fig. 3: Principle of pressure pulse decay method.

The pressure difference between the upstream and downstream gas tanks is collected and stored in real-time by a pressure differential sensor, data acquisition card, and computer. The typical curve depicting the variation of the pressure difference over time during the experiment is shown in Fig. 4.

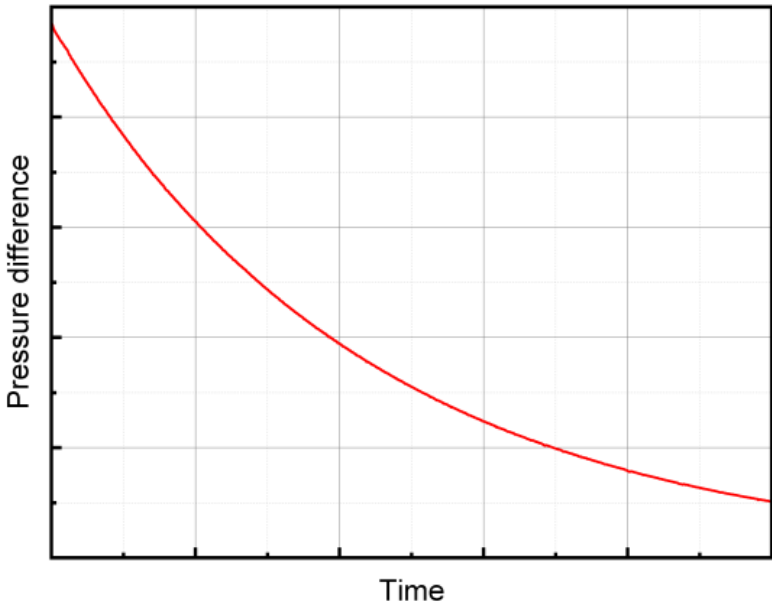

Fig. 4: Typical pressure difference decay curve.

2.2 Gas mass transfer models of pressure pulse decay testing

2.2.1 Gas free flow control equation

In the gas storage tanks upstream and downstream of the permeability testing apparatus, the flow state of the gas conforms to the description of the Navier-Stokes equations. The Navier-Stokes equations are fundamental equations describing fluid motion in fluid mechanics. They establish a connection between Newton's second law and the motion and deformation of fluids. Widely applied in the fields of fluid mechanics, meteorology, fluid dynamics, and others, the equations are expressed as follows:

$$\rho\left(\frac{\partial v}{\partial t}+v\bullet\nabla v\right)=-\nabla p+\nabla\bullet\left(\mu\left(\nabla v+\left(\nabla v\right)^{T}\right)-\frac{2}{3}\mu\left(\nabla\bullet v\right)I\right)+F \quad (1)$$

$$\rho\frac{\partial v}{\partial t}+\rho\left(v\bullet\nabla\right)v=-\nabla pI+\nabla\bullet\left(K\right)+F \quad (2)$$

$$K=\mu\left(\nabla v+\left(\nabla v\right)^{T}\right)-\frac{2}{3}\mu\left(\nabla\bullet v\right)I \quad (3)$$

v… velocity of helium [m/s]
ρ… density of helium [kg/m^3]
p… pressure of helium [Pa]
F… external force on helium [N]

Eq. 1 is referred to as the Navier-Stokes equations, or the N-S equations for brevity. In practical applications, when the Reynolds number of a fluid is small, the influence of inertial forces on fluid flow is significantly less than that of viscous forces and can be neglected. Consequently, Eq. 2 can be modified accordingly:

$$\rho\frac{\partial u}{\partial t}=-\nabla pI+\nabla\bullet\left(K\right)+F \quad (4)$$

By the transient pressure pulse method experiment examining the flow characteristics of helium within the gas chamber, high-speed flow conditions are absent throughout the process. Consequently, the flow of helium within the gas chamber can be regarded as low-speed flow, characterized by a small Reynolds number. Thus, the inertial term can be neglected, aligning with the Stokes flow described by Eq. 4.

2.2.2 Gas permeability control equation in porous media

In the process of the pressure pulse decay method for testing the permeability of coal samples, the upstream gas storage tank releases gas pulses of a predetermined pressure into the equipment. The gas flows through the coal sample and enters the downstream gas storage tank. As coal is a typical dual-porosity medium, the flow of helium in the coal sample during testing involves both seepage and diffusion movements, accompanied by adsorption and desorption processes(Liu et al. 2016; Liu et al. 2015). However, considering the complexity of solving multi-field coupled models, conventional theoretical solutions for the pressure pulse decay method have not taken into account the effects of diffusion and adsorption-desorption. This study also opts to neglect their influence. Consequently, the gas movement in the coal sample during the pressure pulse decay method for the permeability testing process is simplified to pure seepage, with its governing equation represented by Eq. 5:

$$\frac{\partial m}{\partial t}=-\nabla\left(\rho\bullet v\right) \quad (5)$$

m… mass of helium participating in the flow

Helium flow velocity *v* can be obtained by Darcy's law, as shown in Eq. 6:

$$v = -\frac{k}{\mu}\nabla p \tag{6}$$

In a single-porosity medium, the mass of gas participating in the flow, denoted as *m*, can be calculated based on the Langmuir equation and the ideal gas state equation, as given in Eq. 7:

$$m = \frac{V_L p}{p + p_L} \bullet \frac{M_g}{V_M}\rho_c + \varphi\rho \tag{7}$$

V_L... Langmuir volume [m^3/t]
P_L... Langmuir pressure [Pa]
M_g... molar mass of helium [g/mol]
V_M... molar volume of helium [L/mol]
ρ_c... apparent density of coal [kg/m^3]
φ… porosity of coal

According to the ideal gas state equation, the density of helium during the flow process can be determined based on the helium pressure, as given by Eq. 8:

$$\rho = \frac{M_g}{RT}p \tag{8}$$

R… ideal gas constant [J/(mol·K)]
T… experimental temperature [K]

By substituting Eq. 6, 7, 8 into Eq. 5, the equation describing gas flow in the single-porosity medium model can be obtained, as shown in Eq. 9:

$$\left[\frac{p_L V_L \rho_c}{\left(p + p_L\right)^2 V_M} + \frac{\varphi}{RT}\right]\frac{\partial p}{\partial t} = \nabla\left(\frac{k}{\mu RT}p \bullet \nabla p\right) \tag{9}$$

2.2.3 Initial and boundary conditions

For completeness, the standard boundary and initial conditions are defined as follows. The initial conditions for gas flow in the domain are defined as:

$$p = p_0 + p_p \quad \text{in} \quad \Omega_1 \tag{10}$$

$$p = p_0 \quad \text{in} \quad \Omega_2 \quad \text{and} \quad \Omega_3 \tag{11}$$

p_0... gas pressure at equilibrium [Pa]
p_p... instantaneous pulse pressure [Pa]
Ω_1 … upstream gas free flow space
Ω_2 … sample space
Ω_3 … downstream gas free flow space

The gas flow conditions on the boundaries are defined as:

$$\frac{k}{\mu}\cdot\nabla p\cdot\vec{n} = 0 \quad \text{on} \quad \sum\Omega_1, \quad \sum\Omega_2 \quad \text{and} \quad \sum\Omega_3 \tag{12}$$

$\vec{n}$ … outward unit normal vector on the boundary

The initial conditions and boundary conditions apply to both regular and irregular samples, thus the solution domain can be utilized in the test of both samples.

2.3 Theoretical solution of pressure pulse decay method

Brace et al. (1968) developed a theoretical solution to calculate the permeability by deriving the seepage process during the pressure pulse decay test. Since gas is a compressible fluid, a pressure gradient exists, Darcy's law can be applied:

$$q = -\left(\frac{kA}{\mu}\right)\left(\frac{\partial P}{\partial x}\right) \tag{13}$$

q… volume flow rate of gas [m^3/s]
A… cross-sectional area of the sample [m^2]
μ … viscosity of the fluid [$N \cdot s/m^2$]
k… permeability of rock [mD]

Simplify the compressibility of coal mass(Brace et al. 1968) and the pressure distribution was found to be consistent with:

$$\frac{\partial^2 P}{\partial x^2} = 0 \tag{14}$$

Therefore, although the pressure gradient in the sample varies over time, it remains constant in the longitudinal direction. To simplify the transient model, as shown in Fig. 5, it is assumed that all pore volumes (V_P) within the rock are concentrated in the center, with V_R representing the volume of the non-porous coal body, V_d representing the volume of the downstream gas tank and the pipeline, and V_u representing the volume of the upstream gas tank and the pipeline.

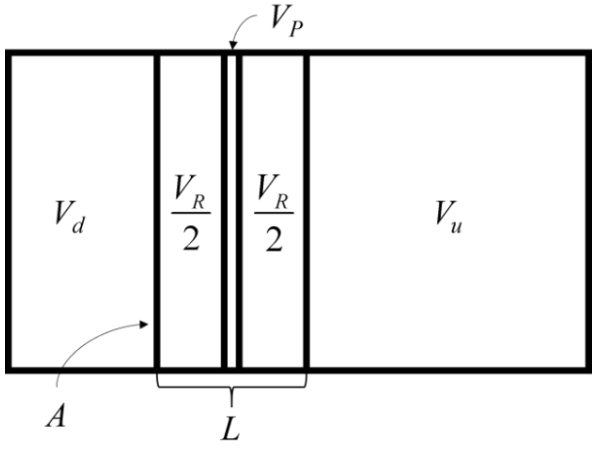

Fig. 5: Simplified model of pressure decay method.

Derive mathematically from the simplified model(Brace et al. 1968) and obtain the flow equation Eq. 15 for the pressure pulse decay method test process:

$$\frac{(P_u - P_f)}{(P_d - P_f)} = \frac{V_d e^{-\alpha t}}{(V_u + V_d)} \tag{15}$$

P_f… gas pressure at the final equilibrium [Pa]

The index coefficient α is given by Eq. 16:

$$\alpha = \left(\frac{k\mu}{\beta L^2} \right) \frac{V_R (V_u + V_d)}{V_u V_d} \tag{16}$$

β … gas compression coefficient

After conversion, the theoretical solution for permeability(*k*) can be calculated using Eq. 17:

$$k = \frac{\alpha \mu L V_u V_d}{A P_0 \left(V_u + V_d \right)} \tag{17}$$

The specific method for determining the permeability of rock using theoretical analysis is as follows: By utilizing the pressure decay data in experiments, with the pressure difference between the upstream and downstream gas tanks plotted on the vertical axis and time on the horizontal axis, a pressure decay curve can be constructed that shows how the pressure difference changes over time. This allows for the fitting of the coefficient *α*, which can then be used in Eq. 17 to calculate the permeability *k*.

Through the analysis of Eq. 17, the theoretical solution equation for permeability involves parameters such as channel length *L* and cross-sectional area *A*. This is why the pressure pulse decay method requires the sample itself to have a regular shape. In the above situation, the determination of permeability in irregularly shaped rocks cannot be directly calculated using the equation.

3 Experimental work

3.1 Novel method validation overall plan

This paper selects coal samples to verify the reliability of the novel permeability-determining method. The verification plan has two parts as Fig. 6. First, preparation of the regularly shaped coal column for pressure pulse decay tests to obtain the pressure difference decay data. The benchmark permeability of coal samples can be obtained by directly calculating using the theoretical solution. Comparing the benchmark permeability with simulation results for the validation of the novel method for regularly shaped coal columns. Secondly, preparation and processing of the irregularly shaped coal samples from the coal column. Collection of the pressure difference decay data under the same experimental conditions for simulations to yield the permeability. Similarly, comparing the results with the benchmark permeability to evaluate the performance of the novel method for irregularly shaped.

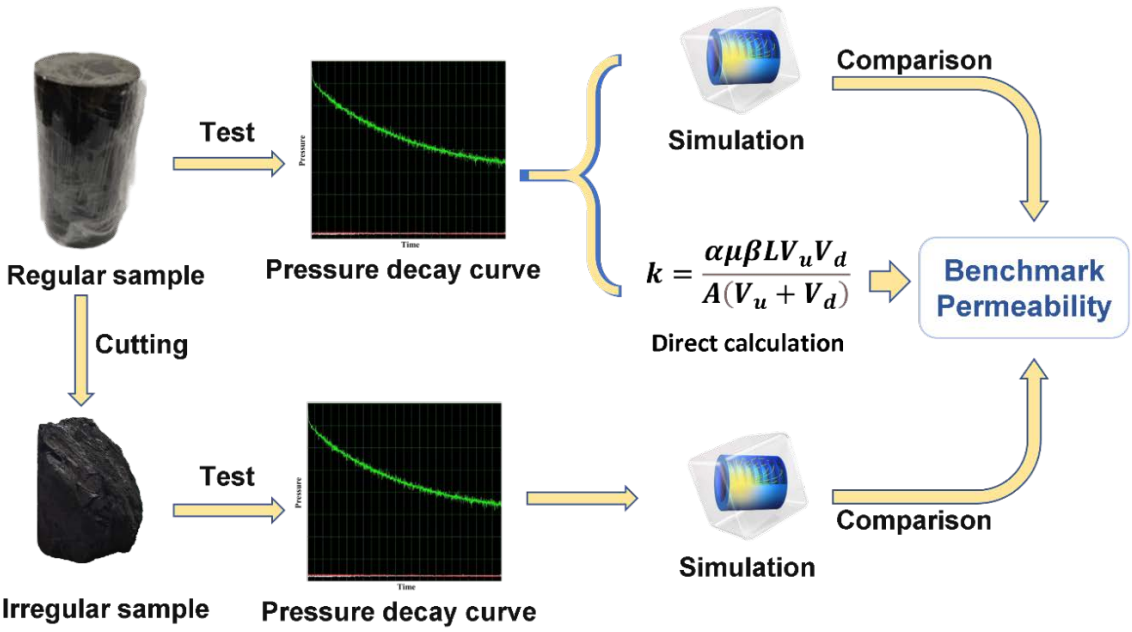

Fig. 6: The verification plan of the novel method.

3.2 The experiment by novel method

All permeability determination tests described in this chapter utilize a coupled testing system for coal and rock, integrating "adsorption-permeation-mechanics" shown in Fig. 7. The system primarily consists of three parts: a loading module and a flow module. Detailed preparations for the measurements and operating steps can be found in previously published papers by the research group(Liu et al. 2017; Liu et al. 2016; Liu et al. 2015).

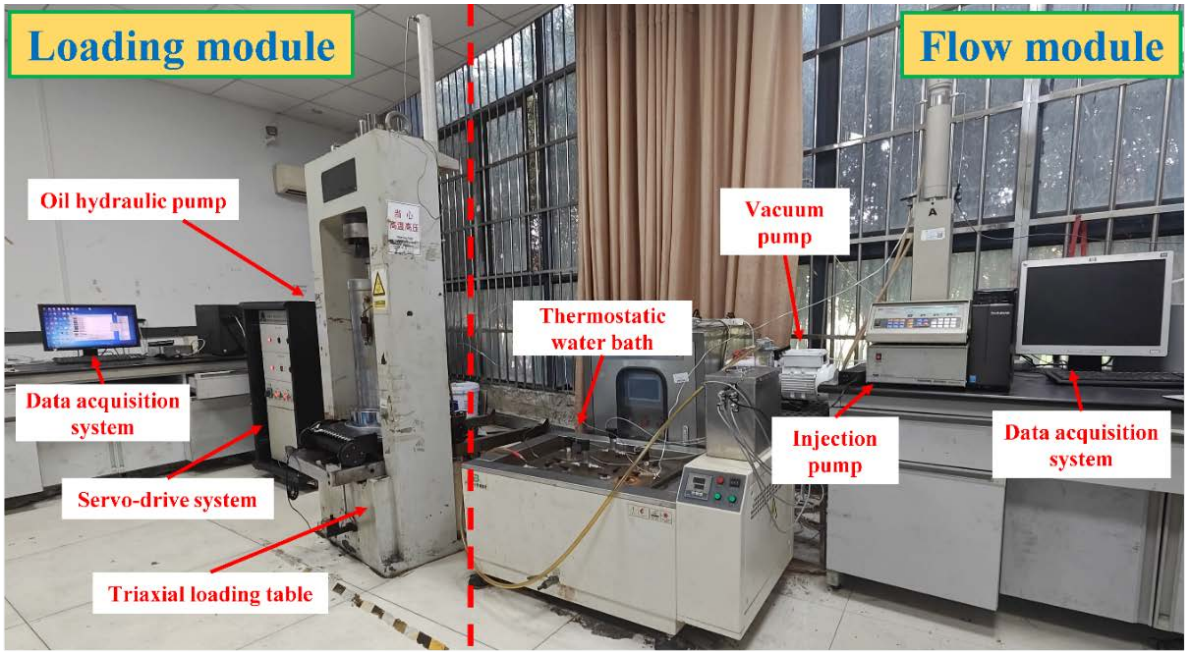

Fig. 7: Permeability test instrument.

The pressure and flow of the experimental gas are controlled by an injection pump (Teledyne ISCO, Model 500D). The injection pump applies a maximum gas pressure of 40 MPa to the coal sample. Pressure sensors are installed in the upstream and downstream gas tanks of the experimental apparatus to monitor the pressure changes in each tank. Additionally, a pressure differential sensor is installed between the upstream and downstream gas tanks to transmit the gas pressure difference data. In a typical experimental test, a gas pressure pulse is applied to the upstream gas tank, and the pressure difference between the upstream and downstream gas tanks is recorded over a certain period.

To avoid the interference of the hard coal (raw coal)'s heterogeneity on the experimental results, the experiment supplements the testing of the soft coal (briquette) as an auxiliary. As shown in the Fig. 8, the preparation methods for coal samples are as follows:

Drilling coal columns from the appropriate large lump of coal with a 50 mm inner diameter drill rod during underground coal mining. Polishing both ends of the extracted coal to achieve a hard coal column Y1 with approximately Φ50×100 mm. The remaining coals are broken and screened to obtain coal particles of specific sizes. After spraying a little distilled water into the coal particle and stirring evenly, it is placed into a double-headed pressing mold for compression. Then perform pressurization, stabilization, and depressurization operations. Remove the mold once the pressure unloading is complete. Polishing both ends and placing in a vacuum drying oven to yield a soft coal sample X1 with approximately Φ50×100 mm.

Fig. 8: Preparation process of regularly shaped coal columns.

Conduct the permeability tests on the regularly shaped coal columns obtained hereinabove. Helium gas was used as the test gas under various helium pressures and confining pressures, with a pressure pulse of 100 kPa applied to the upstream gas tank to obtain differential pressure decay data. The experimental scheme is shown in Tab.1.

Tab. 1: Test scheme for permeability testing of regularly shaped coal.

Sample	Confining pressure(MPa)	Gas pressure(MPa)	Test number
Regularly shaped hard coal Y1	3	1	#Y1-1
	5	1	#Y1-2
	5	2	#Y1-3
Regularly shaped soft coal X1	3	1	#X1-1
	5	1	#X1-2
	7	1	#X1-3

After the permeability test, irregularly shaped coal samples were produced from Y1 and X1. For Y1, loose areas of the raw coal were removed using the hammer, leaving the hardest part to obtain the irregularly shaped coal sample Y2. For X1, due to its softer texture, a steel saw was used for cutting and the surface was polished. Due to the uneven stress during the pressing process resulting in an uneven density distribution in coal samples, the cutting was performed along the upper, middle, and lower sections, resulting in irregularly shaped soft coals: X-UP, X-MID, and X-DOWN. The maximum width of irregularly shaped coals was 3-4 cm. The cutting results are shown in Fig. 9.

Fig. 9: Irregularly shaped coal from cutting.

To construct the physical model of the irregularly shaped samples, a 3D scan was conducted to obtain the appearance model, which was then processed for further modeling in COMSOL. The 3D scanning was carried out using a ZEISS COMET 5M 3D scanning imager, as illustrated in Fig. 10.

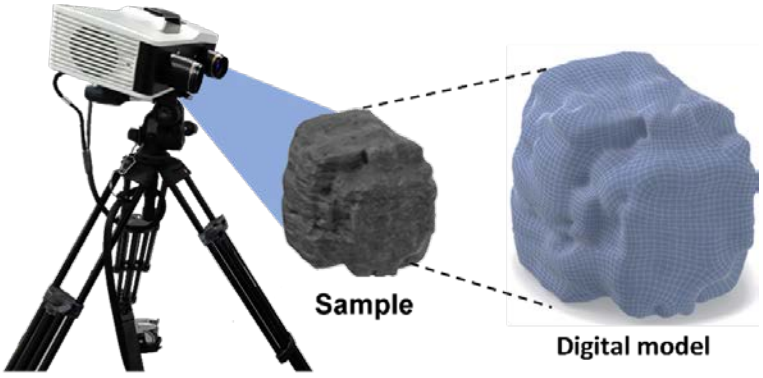

Fig. 10: The scanning imager.

Before scanning, the developing agent was sprayed on the surface of the samples. After performing preheating and calibration, scan the various surfaces of the sample and conduct post-processing operations until the model is complete. The models obtained from 3D scanning are overly complex, which complicates the solution process. Therefore, it is necessary to simplify the model by removing unnecessary details, reducing the number of triangular facets, and streamlining the mesh structure in preparation for simulation. The scanned and the simplified models are shown in Fig. 11.

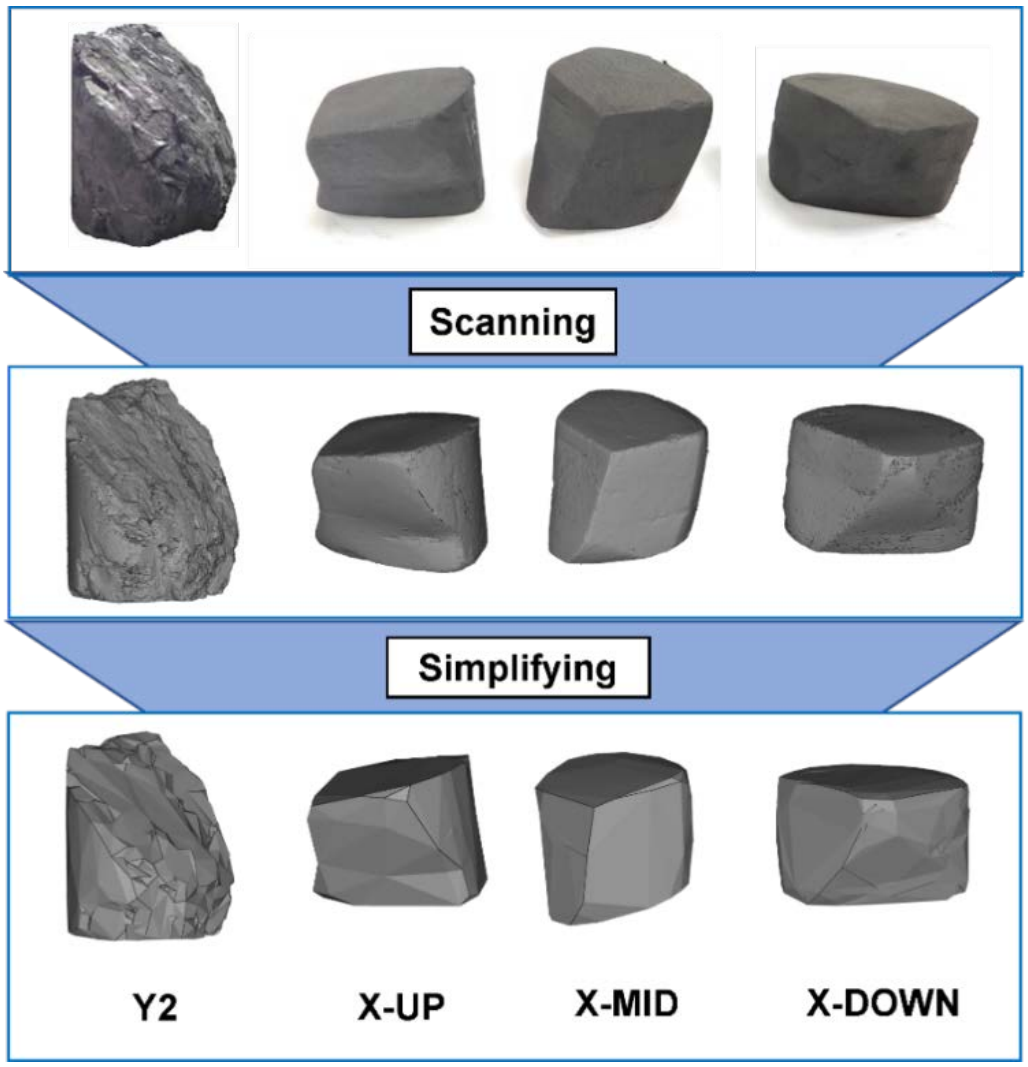

Fig. 11: Scanning model and simplified model of irregularly shaped coal.

Next, encapsulate the coal with glue to create samples suitable for testing equipment. 704 silicone is applied to the surface of the coal for protection, after which epoxy resin adhesive is mixed in a mass ratio of glue A: glue B = 3:1 and then poured into a Φ50 mm×100 mm cylindrical silicone mold. During the pouring process, a base layer is poured first, followed by the placement of the sample, and pouring to the desired height. Each pouring should be less than 40 g. Once fully cured, the holes at both ends are drilled at the center of the cylinder using a 10 mm diameter drill, ensuring that it contacts the coal. Subsequently, a steel pipe with an outer diameter of 3/8" and a wall thickness of 1 mm is inserted into the hole to protect the gas channel. The completed products of test samples are shown in Fig. 12.

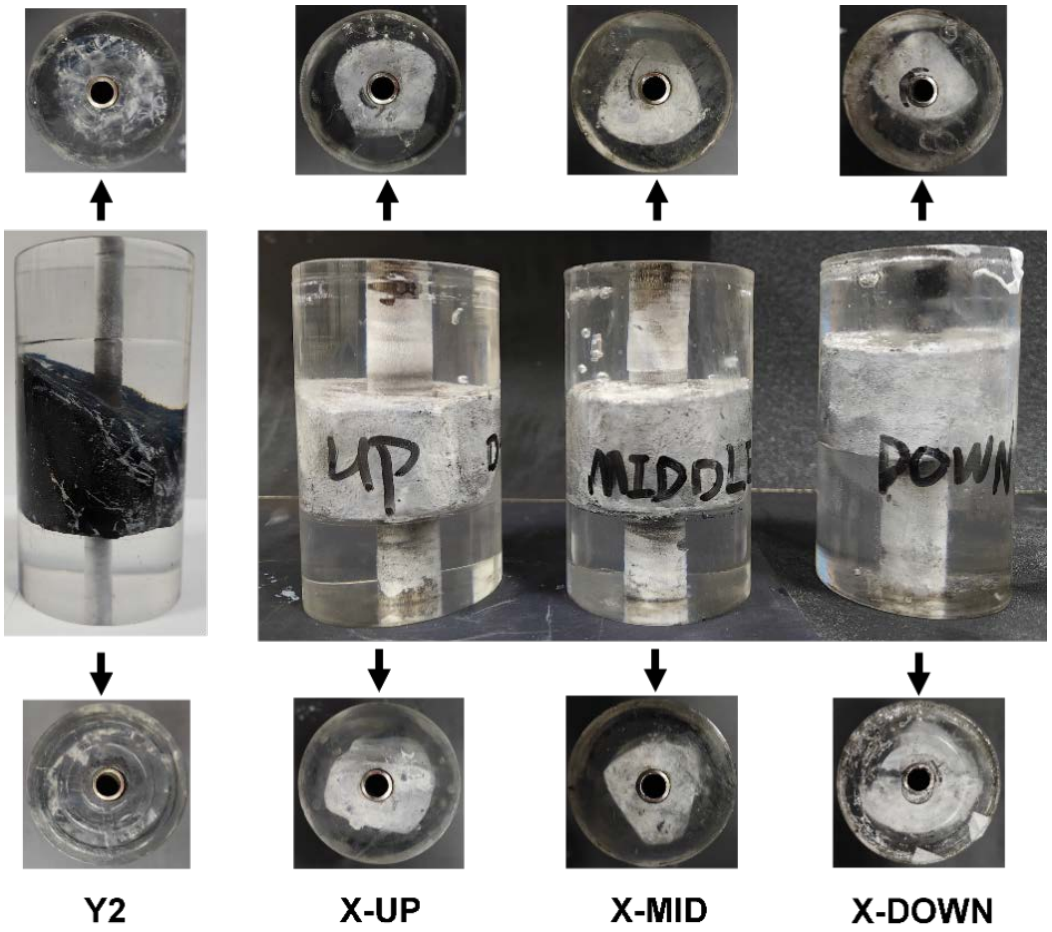

Fig. 12: Irregularly shaped coal samples for test.

After processing according to the above content, conduct the permeability testing on irregularly shaped coal samples under the same experimental conditions of regularly shaped coal according to the experimental plan in Tab. 2.

Tab. 2: Test scheme for permeability testing of irregularly shaped coal.

Sample number	Confining pressure (MPa)	Gas pressure (MPa)	Test number	Corresponding test
Y2 From Y1	3	1	#Y2-1(T)	#Y1-1
	5	1	#Y2-2(T)	#Y1-2
	5	2	#Y2-3(T)	#Y1-3
X-UP From X1	3	1	#X-UP-1(T)	#X1-1
	5	1	#X-UP-2(T)	#X1-2
	7	1	#X-UP-3(T)	#X1-3
X-MID From X1	3	1	#X-MID-1(T)	#X1-1
	5	1	#X-MID-2(T)	#X1-2
	7	1	#X-MID-3(T)	#X1-3
X-DOWN From X1	3	1	#X-DOWN-1(T)	#X1-1
	5	1	#X-DOWN-2(T)	#X1-2
	7	1	#X-DOWN-3(T)	#X1-3

3.3 Experimental results

Fig. 13 illustrates the pressure difference decay curves of regularly shaped coal under different confining pressures and gas pressures, along with the fitted curves based on the theoretical solution. The fitting accuracy of the theoretical solution, indicated by R^2, exceeds 0.97, demonstrating a good-fitting effect.

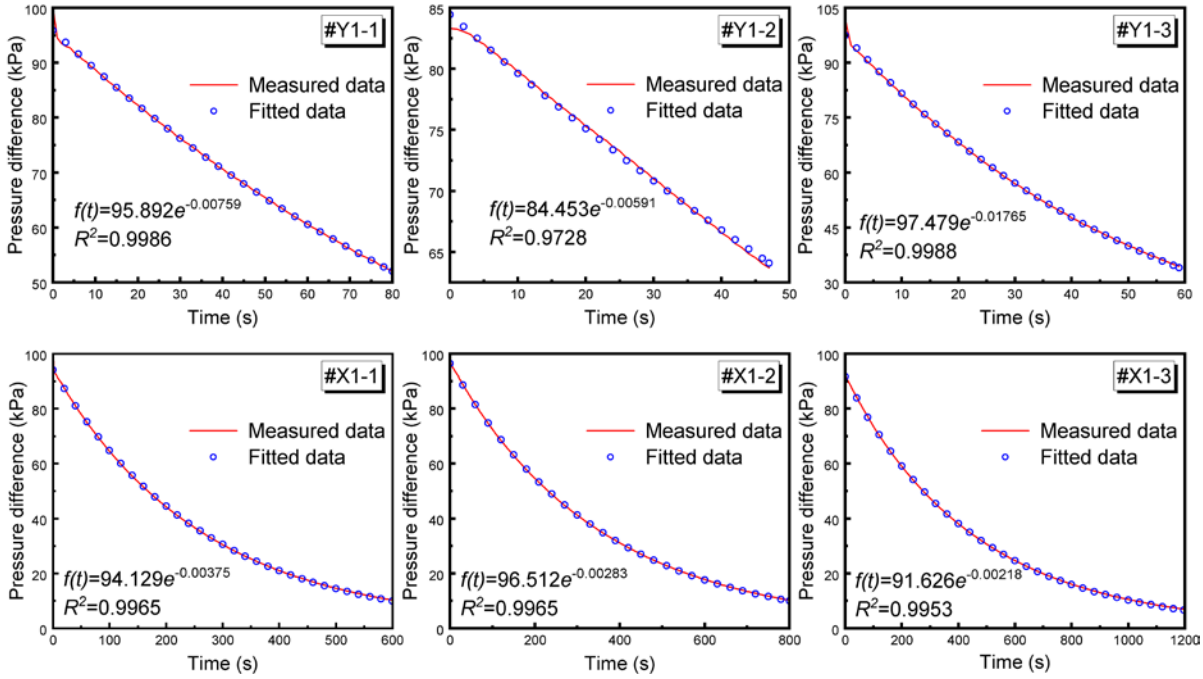

Fig. 13: Measured and fitted pressure difference data of regularly shaped coal.

According to Eq. 17, the permeability results of the theoretical solution and related parameters are presented in Tab. 3. The testing gas, helium, is non-adsorptive; therefore, effective stress is the sole determinant of permeability. A smaller effective stress results in a higher permeability of coal. Under constant loading conditions of the coal samples, effective stress increases with increasing confining pressure and decreases with increasing helium pressure. Consequently, the permeability of coal decreases with increasing confining pressure while it increases with rising helium pressure. This trend aligns with conclusions from the previous study(Li et al. 2009).

Tab. 3: Theoretical solution results of permeability of regularly shaped coal.

Test number	Length(L) and Cross-sectional area diameter (D)	α	Permeability(mD)
#Y1-1	L=100.40 mm D=50.40 mm	0.00759	0.375
#Y1-2		0.00591	0.295
#Y1-3		0.01765	0.439
#X1-1	L=99.56 mm D=49.63 mm	0.00375	0.190
#X1-2		0.00283	0.143
#X1-3		0.00218	0.111

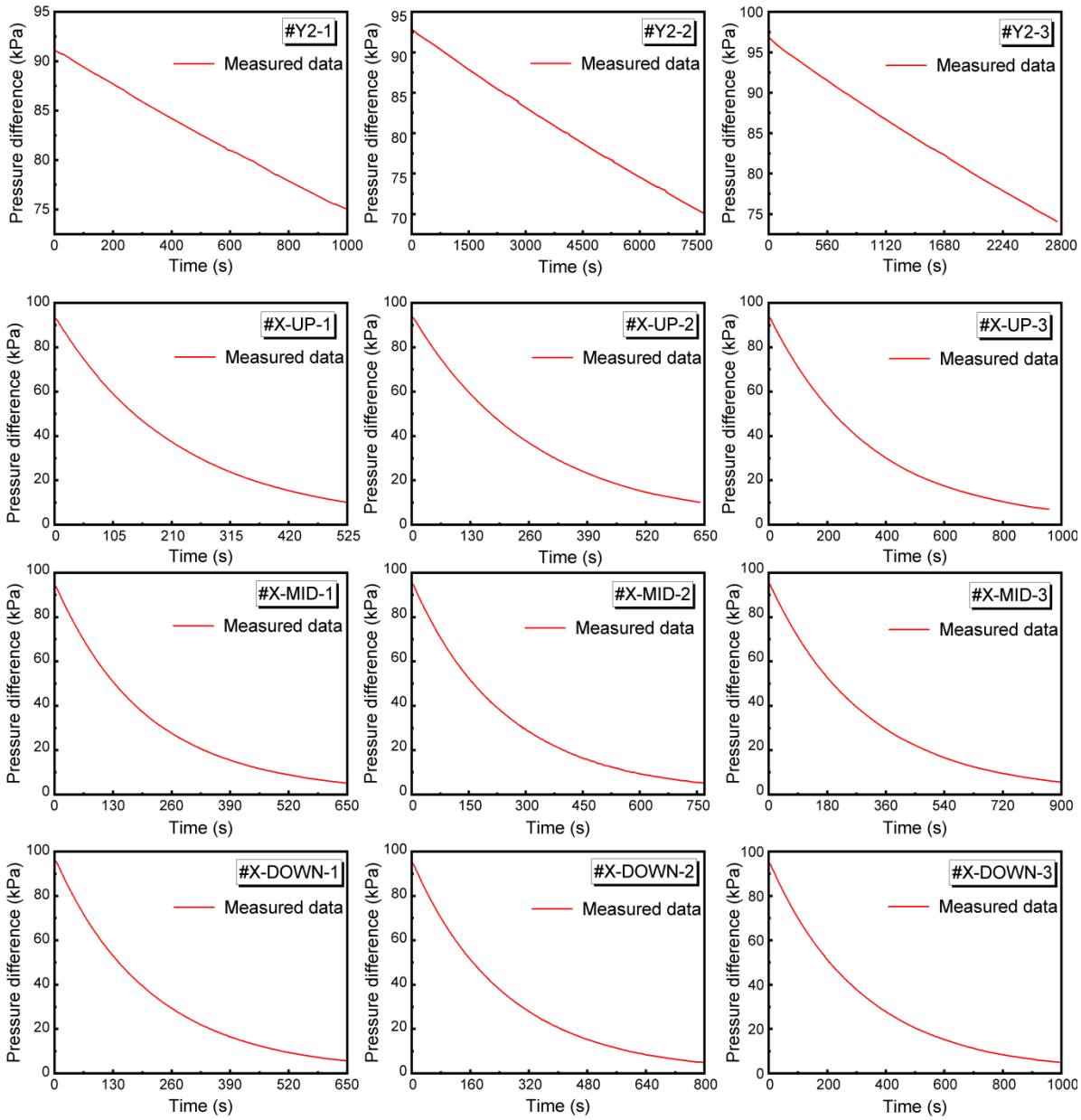

Fig. 14: Measured data of irregularly shaped coal.

Similarly, the pressure difference decay curves for irregularly shaped coal are shown in Fig. 14. Since irregularly shaped coal cannot be directly calculated using the equation, these data serve solely as the objective function for the optimization of the inverse problem.

4 Solution and Result Analysis of Permeability Based on Numerical Inverse Problem Method

4.1 Numerical models and simulation schemes

The premise and key to solving inverse problems through optimization is to construct a model that replicates the experimental conditions of the laboratory. Utilizing actual data already measured in the laboratory, the model is employed to deduce the physical parameters of the experimental object. The previous chapter provided the measured data, and the following section will outline the numerical solution model:

Based on the experimental principles of pressure pulse decay methods, this paper employs COMSOL Multiphysics to implement the same mechanism for numerical simulations. This enables the simulation for both regularly and irregularly shaped samples using pressure pulse decay methods to determine permeability. Without compromising the accuracy of results, the geometric model has been simplified, as illustrated in Fig. 15. The components of the geometric model are, from top to bottom: the upstream gas tank (and the steel pipe), the coal pillar sample, and the downstream gas tank (and the steel pipe). The length and cross-sectional area of the coal pillar model correspond to those of the experimental samples, while the lengths of the upstream and downstream gas tanks are denoted as L_u and L_d, which are calculated using Eq. 18 in conjunction with the cross-sectional diameter D of the regular samples. For the irregularly shaped samples, the physical model is realized by importing a simplified 3D model.

$$\begin{cases} L_u = \dfrac{4V_u}{\pi D^2} \\ L_d = \dfrac{4V_d}{\pi D^2} \end{cases} \tag{18}$$

$L_{u...}$ length of the upstream tank [m]
$L_{d...}$ downstream tank length [m]
D… radius of the sample [m]

In the model, gas flows through the upstream and downstream gas channels, moving from the upstream gas tank through the coal sample into the downstream gas tank. The gas inside the upstream and downstream gas tanks (and steel pipes) freely flows, while the gas in the middle specimen follows Darcy's law for permeable flow. The boundary between the gas tanks and the coal column is set as a free-flowing boundary. The external boundary of the specimen in the model is set as a no-flow boundary. The boundary between the gas tanks and the coal is a free-flowing boundary. The external boundary of the specimen in the model is set as a no-flow boundary.

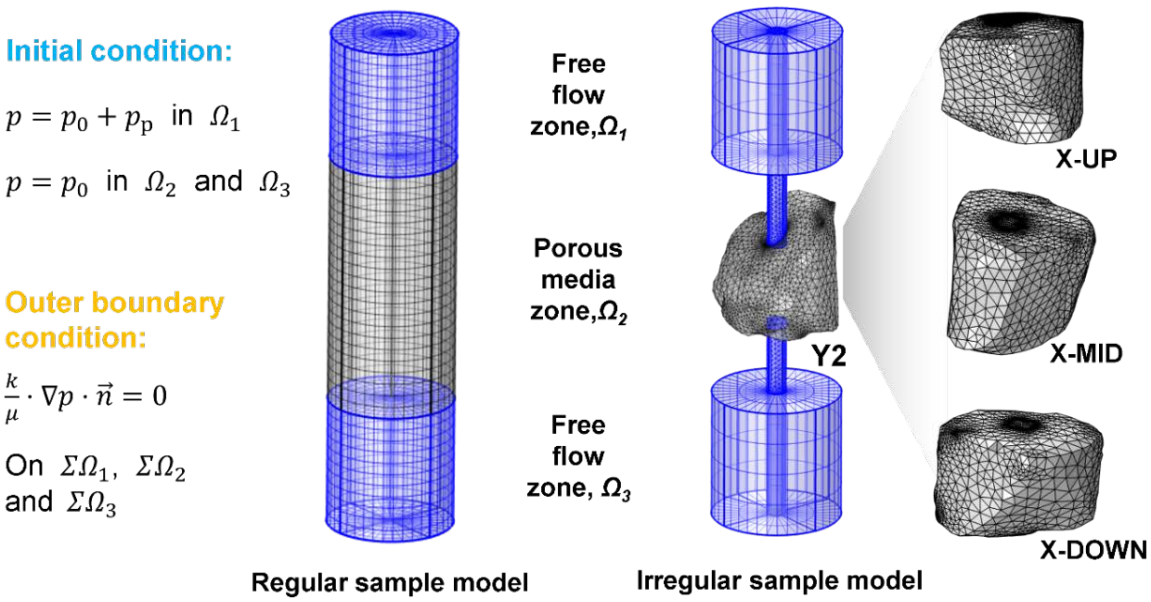

Fig. 15: Schematic diagram of the geometric model for simulation.

The principle of inverse problem-solving for permeability can be summarized as follows: optimization algorithms generate test parameters, a simulation model calculates this set of parameters, and the results are fed back to the optimization algorithm. After multiple iterations, the optimal solution is obtained.

For nonlinear least squares problems, Gauss-Newton (G-N) iteration and Levenberg-Marquardt (L-M) iteration methods are commonly used to find the minimum point x*. The basic idea of the G-N iteration method is to linearize the function f(x) and expand it into a Taylor series around the point xk, as shown in Eq. 19:

$$f(x) \approx f_D(x^k)(x - x^k) + f(x^k) \tag{19}$$

The iterative formula for the Gauss-Newton (G-N) iteration method is obtained through transformation operations and is expressed as Eq. 20:

$$x^{k+1} = x^k - \left[f_D^T(x^k) f_D(x^k)\right]^{-1} f_D^T(x^k) f(x^k) \tag{20}$$

Let：

$$\begin{cases} G(x) = f_D^T(x) f_D(x) \\ g(x) = f_D^T(x) f(x) \end{cases} \tag{21}$$

Therefore, Eq. 20 can be expressed as follows:

$$x^{k+1} = x^k - G^{-1}(x^k) g(x^k) \tag{22}$$

In order to prevent the iteration matrix (G(x_k)) from becoming singular or ill-conditioned in the Gauss-Newton iteration format, an additional damping term (μkI) is introduced, thus considering:

$$L(x) = G(x^k) + \mu_k I \tag{23}$$

Therefore, Eq. 22 transforms into:

$$x^{k+1} = x^k - L^{-1}(x^k)g(x^k) \quad (24)$$

The equation represents the iterative format of the Levenberg-Marquardt (L-M) method. L-M method represents a nonlinear optimization approach that sits between Newton's method and gradient descent. It's less sensitive to over-parameterization issues and efficiently handles problems with redundant parameters. By doing so, it significantly reduces the chance of the cost function getting trapped in local minima(Tan et al. 2005).

However, during the process of solving inverse problems, there's always the possibility of getting stuck in local optimal solutions. Despite L-M's ability to mitigate such scenarios, careful consideration in selecting initial values and the scope of solving is still crucial to ensure that the calculated parameters closely match the actual scenario.

In the numerical simulation experiments for determining the permeability of coal samples using the transient pressure pulse method, the simulation parameters utilized are presented in Tab. 4. With the exception of certain specific parameters which are known constants, the remaining parameters are obtained through experimental means.

Tab. 4: Permeability simulation parameters.

Serial number	Parameter name	Parameter value
1	Upstream gas tank capacity, V_u	97.27 mL
2	Upstream gas tank capacity, V_d	97.93 mL
3	Inner diameter of steel pipe, L_p	7.53 mm
4	Length of hard coal column, L_h	100.40 mm
5	Diameter of hard coal column, D_h	50.50 mm
6	Length of soft coal column, L_s	99.56 mm
7	Diameter of soft coal column, D_s	49.63 mm
8	Langmuir volume, V_L	20 m^3/t
9	Langmuir pressure, P_L	1 MPa
10	Fissure ratio, Φ_f	0.01314
11	The molar mass of helium gas, M_g	4 g/mol
12	Ideal gas constant, R	8.314 J/(mol·K)
13	Test temperature, T	298.15 K
14	Kinetic viscosity of helium gas, μ	1.99×10^{-5}Pa·s
15	Molar volume of helium gas, V_M	22.4 L/mol
16	Pressure pulse, p_p	100 kPa

4.2 Permeability determination simulation and novel model validation for regularly shaped samples

The experimental data from #X1-1 is used to validate the reliability of the gas mass transfer model under the pressure pulse mechanism. Initially, the permeability parameter is directly set to the theoretical solution result of 0.143 mD to perform a forward calculation. The flow field map is shown in Fig. 16. The distribution of streamlines is controlled by flow velocity, while the color of the streamlines is influenced by pressure. It can be observed that the overall distribution of streamlines is uniform, indicating that gas flows uniformly within the regular coal body model. The gas pressure exhibits a diminishing trend from top to bottom, aligning with the pressure gradient outlined in Darcy's law.

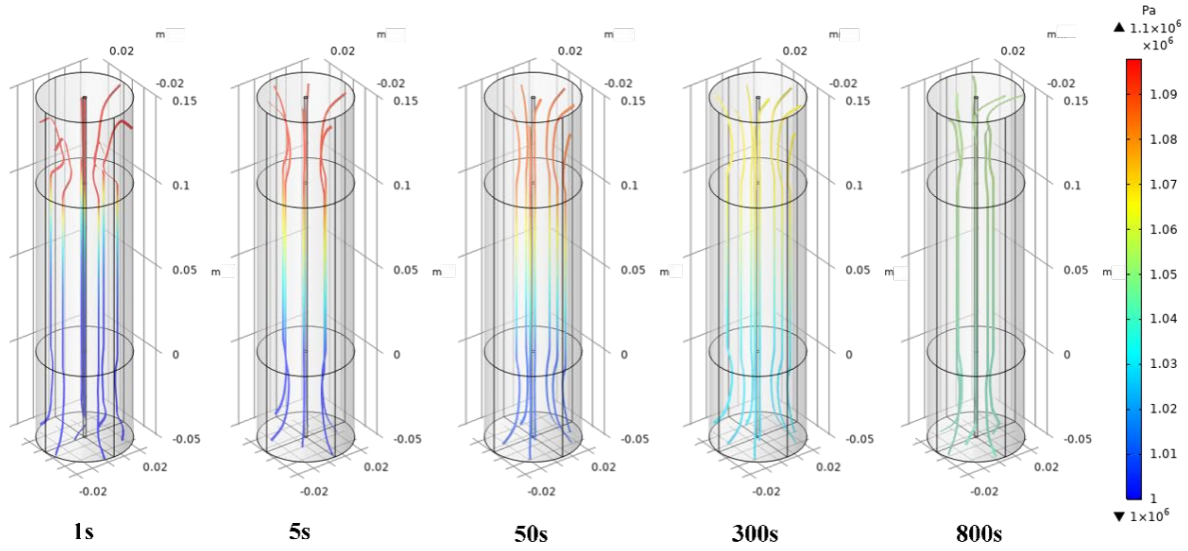

Fig. 16: Gas pressure and flow state changes in regularly shaped coal simulating.

Next is the optimization solution of the inverse problem. To avoid the modeling and computation of inverse problems from the challenge of potentially converging to locally optimal solutions, it is essential to determine reasonable initial values and the size of the range for the inverse problem target before formally proceeding with the modeling and computation of the inverse problem.

As shown in Fig. 17, the permeability parameters are initially set to 10, 1, and 0.1 (mD), followed by selections of 0.2, 0.4, 0.6, and 0.8 (mD). The red line in Fig. 17 represents the measured data curve, while the point graph depicts the simulated data curve. Based on the information in the figure, it can be determined that the coarse value range is 0.1-1 (mD), and the refined value range is 0.1-0.2 (mD), with the initial value set at 0.15 (mD).

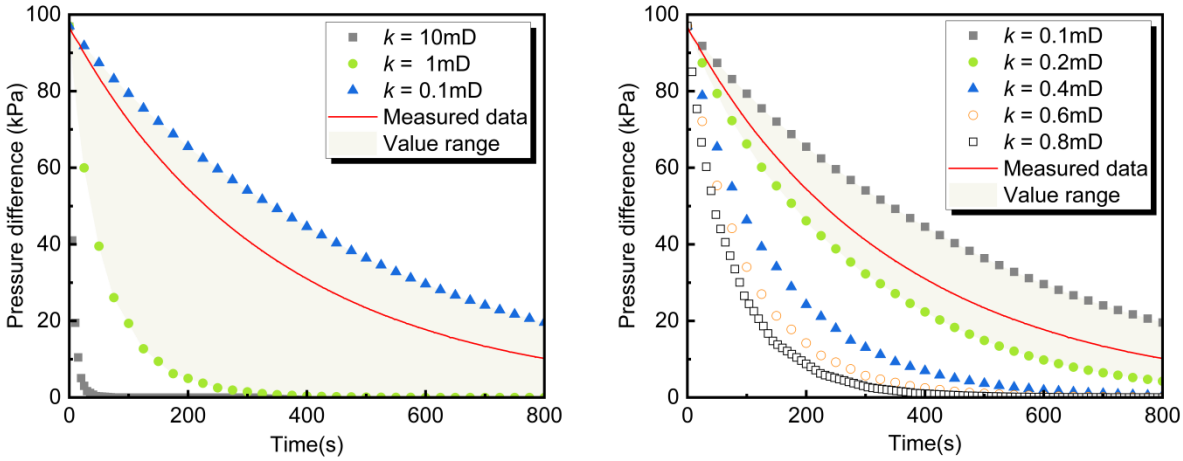

Fig. 17: Determination of the range of initial values.

The laboratory-measured 800 s pressure difference decay data curve from section 3.2 is used as the objective function to conduct simulated inverse calculation experiments, thereby deriving the permeability for the coal.

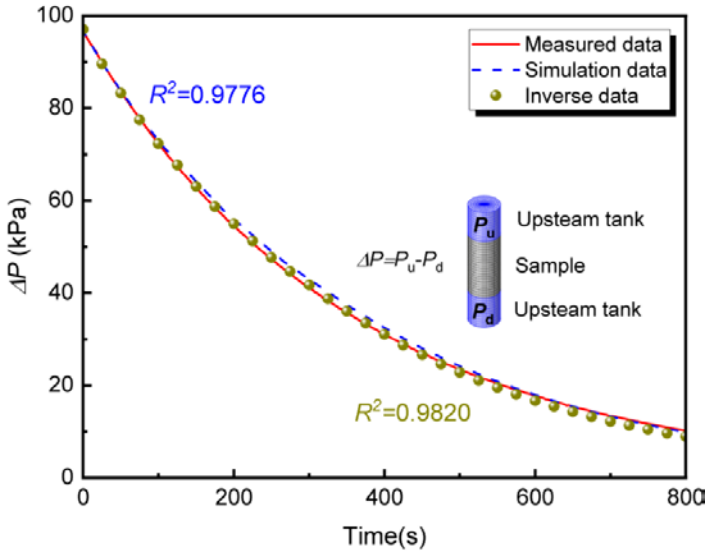

Fig. 18: Measured, simulation, and inverse pressure difference data of regularly shaped coal.

The simulated computational outcomes from both the forward model and the inverse problem-solving calculations were contrasted with experimental data and illustrated in Fig. 18. The red data line represents the pressure decay data obtained from laboratory measurements of a regularly shaped sample. The blue data line and green data points respectively represent the upstream and downstream gas cylinder pressure decay data obtained from numerical simulation forward calculations and inverse optimization solutions.

From Fig. 18, it is evident that both the laboratory-measured data and the simulated data show consistent trends, with pressure data exhibiting a decay trend over time. The goodness of fit calculations for the measured data and the simulated data from both forward and inverse calculations yield R^2 values of 0.9776 and 0.9820, respectively. This indicates that the gas mass transfer model proposed in this study for testing rock permeability accurately reflects real-world conditions. The new model effectively describes the transient pulse method for testing rock permeability. Through the inverse problem-solving model, the permeability parameter for the coal sample is determined to be 0.148 mD, which differs numerically by only 0.005 mD from the calculated permeability value of 0.143 mD based on measured data. This demonstrates the high accuracy of the inverse problem-solving model.

4.3 Permeability determination simulation and solution strategy for irregularly shaped samples

4.3.1 Simulation results analysis

The permeability determination of irregularly shaped samples using the pressure difference decay data obtained in Section 3.2 as the objective function for the inverse problem optimization. Subsequently, assess the degree of matching between the permeability parameters obtained from reverse solving and the permeability solution results obtained from the benchmark permeability, thus verifying whether the novel method is applicable to samples of irregular shape as well. The specific strategy remains the same as the regularly shaped sample.

The results simulated from #X-UP-1(S) illustrate variations in gas pressure and flow patterns, as shown in Fig. 19. The distribution of streamlines is influenced by flow velocity, while the color of the streamlines is determined by gas pressure. There are pressure gradient variations within the irregular model, consistent with the characteristics of pressure distribution in porous media seepage. Streamlines are densely concentrated in the middle region of the coal, indicating that the gas flows at the highest velocity at the center.

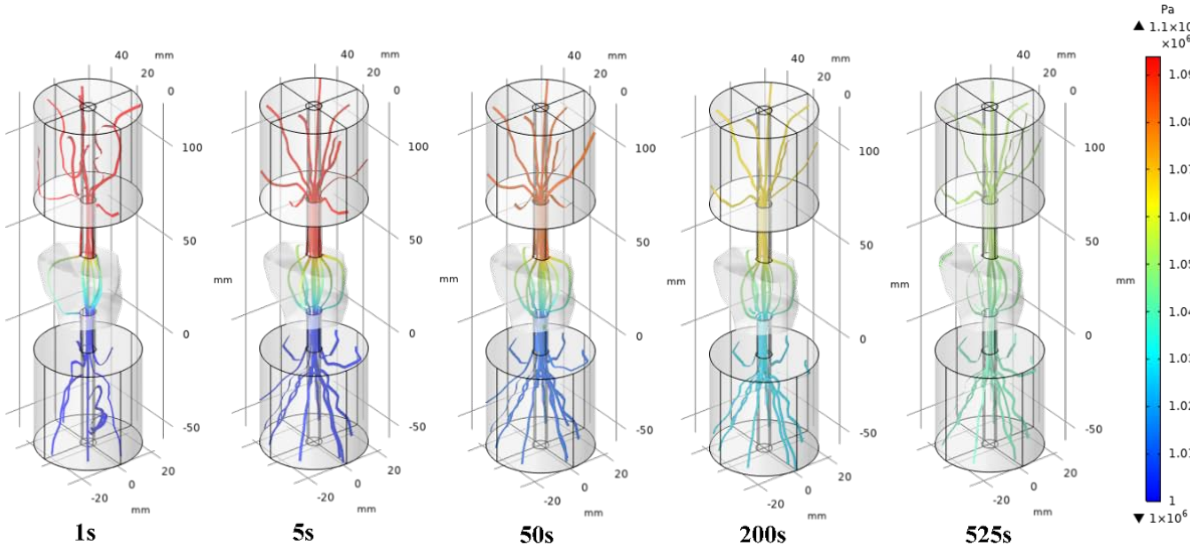

Fig. 19: Gas pressure and flow state changes in irregularly shaped coal simulating.

The simulated computation results of the model inverse problem-solving are compared with experimental data and presented in Fig. 20. The red data points represent the pressure difference decay data obtained from experiments, while the blue data line indicates the pressure difference decay data of upstream and downstream gas tanks acquired through inverse optimization based on the new model. It is evident from Fig. 20 that the fitting accuracy (R^2) of the simulation data is above 0.9659, indicating a good fitting effect.

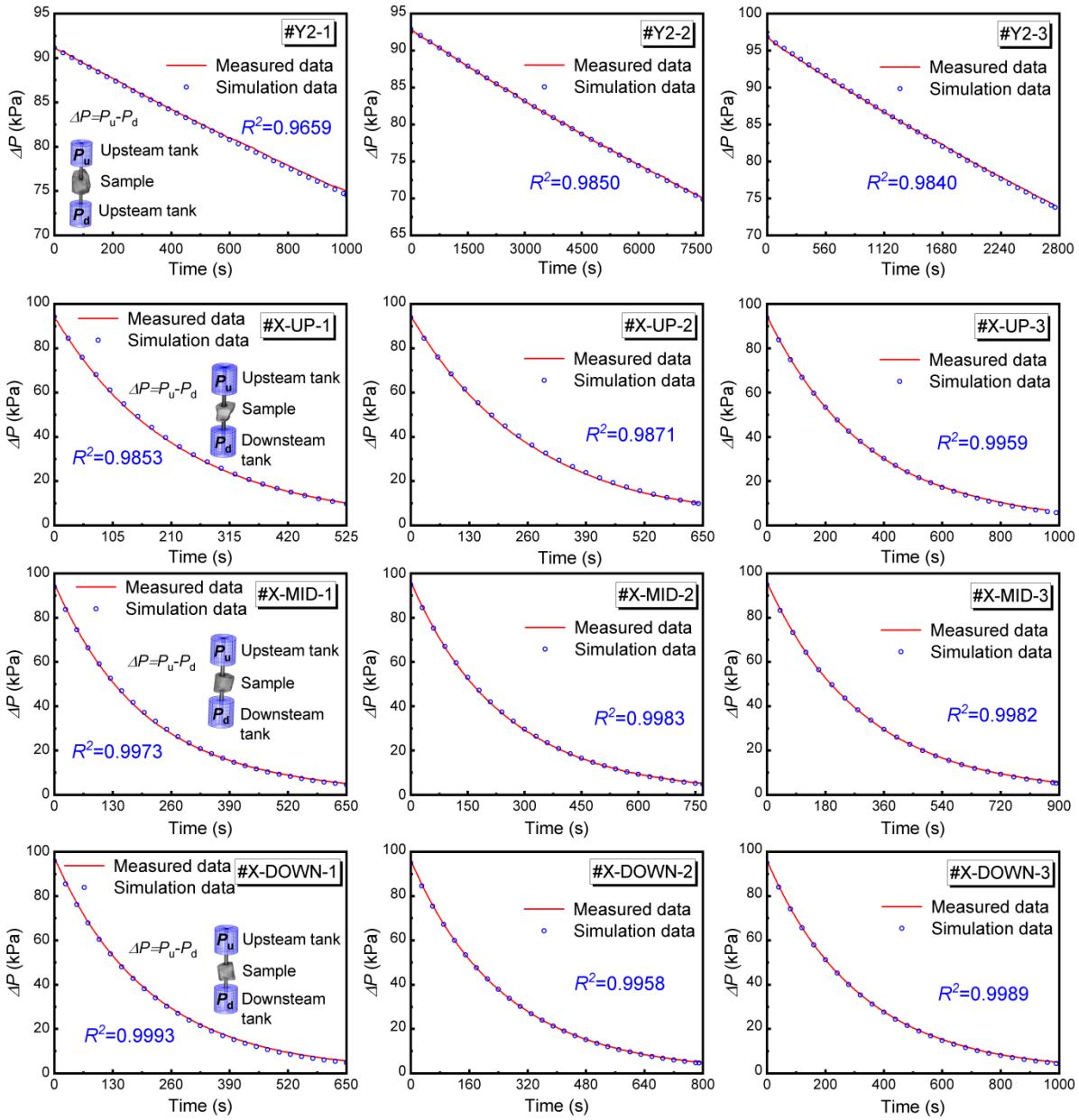

Fig. 20: Simulation and measured pressure difference data of irregularly shaped coal.

The results obtained will be compared with the benchmark permeability, as shown in Tab. 5. From the table, it is evident that the ratio of the numerical solution for the irregularly shaped hard coal to the benchmark permeability ranges from 0.00973 to 0.0458. For the irregularly shaped soft coal, this ratio varies from 2.668 to 3.432.

The permeability results of irregularly shaped hard coal numerical solutions are significantly lower than the benchmark permeability. This may be attributed to the removal of brittle and soft portions during the preparation of irregularly shaped raw coal, leaving only the hardest and densest parts, which leads to a considerable reduction in permeability. The results of irregularly shaped soft coal exhibit higher permeabilities than the benchmark permeability. This difference may arise from coal particles loosening and increasing fissure rates after intense cutting movements, thereby enhancing the permeability.

Tab. 5: Comparison of permeability results.

Simulation number	Permeability simulation result（mD）	Benchmark permeability（mD）	Ratio (Simulation/Benchmark)
#Y2-1(S)	0.0172	0.375	0.0459
#Y2-2(S)	0.00319	0.295	0.0108
#Y2-3(S)	0.00432	0.439	0.00984
#X-UP-1(S)	0.507	0.190	2.668
#X-UP-2(S)	0.412	0.143	2.881
#X-UP-3(S)	0.322	0.111	2.900
#X-MID-1(S)	0.531	0.190	2.795
#X-MID-2(S)	0.445	0.143	3.112
#X-MID-3(S)	0.371	0.111	3.342
#X-DOWN-1(S)	0.566	0.190	2.979
#X-DOWN-2(S)	0.470	0.143	3.287
#X-DOWN-3(S)	0.381	0.111	3.432

4.3.2 Numerical permeability determination strategy for irregularly shaped rocks

The study analyzes and summarizes the aforementioned laboratory tests and numerical simulations, leading to the complete process of the novel method for determining the permeability of irregularly shaped rocks, as shown in Fig. 21.

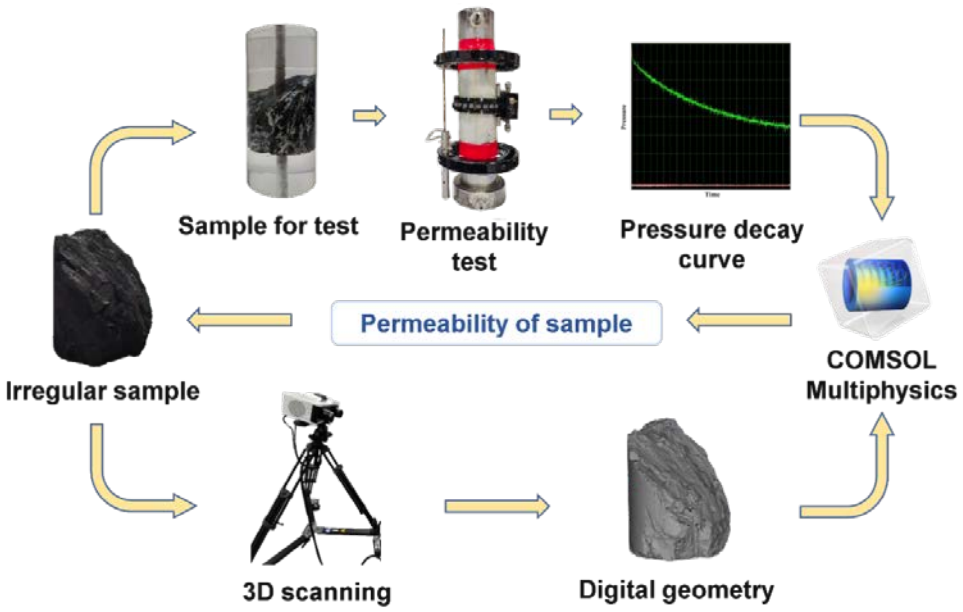

Fig. 21: The strategy for determining the permeability of irregular samples.

After extracting soft rock from the mine, a three-dimensional scanning technique is utilized to obtain its 3D appearance model. The samples are then processed into cylindrical or rectangular shapes using the glue as epoxy resin, and holes are drilled at the centers of both ends to create gas flow channels. In simulation software, an inverse problem permeability-solving model is established, with the pressure difference data obtained from permeability tests based on the pressure pulse decay method serving as the objective function for the inverse problem calculation, ultimately yielding the permeability through simulation.

The newly proposed method of combining physical experiments with numerical models, as mentioned above, can be applied not only to permeability testing of irregularly shaped samples but also provides an efficient approach for conducting experimental studies on competitive factors influencing permeability. By utilizing the new numerical model, various factors, such as gas type(Wang et al. 2019), effective stress(Somerton et al. 1975), and adsorption expansion(Jasinge et al. 2012), affecting permeability can be studied. This allows for further analysis of the sensitivity of permeability to different factors and the competitive interactions between influencing factors. The simulation results of numerical experiments lay the foundation for conducting physical experiments on related influencing factors, making the devised experimental plans more scientifically sound while saving a significant amount of time.

5 Conclusions

This study proposes a novel method for testing the permeability of rock that combines laboratory experiments with numerical simulations, providing an efficient approach to address the limitations of traditional methods in handling irregularly shaped rocks. Through theoretical analysis, comparative experiments, and numerical simulations, we have drawn the following conclusions:

1. This paper pioneers the construction of a mathematical model that accurately describes the entire process of determining permeability using transient pressure pulse decay testing. Accordingly, this paper proposes a novel method for irregularly shaped rock permeability determination: by acquiring a 3D scanned model of the sample's appearance, using the measured pressure difference decay data obtained from the upstream and downstream as the objective function, and integrating inverse problem optimization for to determine the permeability.

2. For regularly shaped samples, forward simulation and backward deductions are conducted. The simulated fitting accuracy (R^2) values were 0.9776 and 0.9820, respectively, and the inversely derived permeability was 0.148 mD, which closely aligns with the 0.143 mD obtained through theoretical solutions. This indicates that the newly proposed model can accurately describe the experimental process of the transient pressure pulse method and reliably obtain permeability parameters.

3. Furthermore, this study conducts permeability tests on irregularly shaped samples and simulates using the novel model. The inversely obtained pressure difference decay data showed a high degree of correlation with the measured data, with each group's fitting accuracy (R^2) exceeding 0.9659. The permeability of the corresponding regularly shaped sample calculated by the theoretical solution serves as the benchmark. The permeability determined from the irregularly shaped hard coal sample ranged from 0.00319 to 0.0172 mD, with a ratio difference compared to the benchmark permeability of 0.00973 to 0.0459. For the irregularly shaped soft coal, the permeability results were between 0.322 and 0.566 mD, yielding a ratio of 2.668 to 3.432 compared to the benchmark permeability. The discrepancies observed may be attributed to improper processing methods for the irregularly shaped samples.

4. The integration of physical experiments with numerical models offers an efficient means for research. In the future, numerical models can be utilized to investigate the effects of various factors on permeability, further analyzing the effect of permeability on these factors and the competitive interactions among influencing variables.

6 Acknowledgments

The authors are grateful for the financial support from projects funded by the National Natural Science Foundation of China (No. 52274238, No. 42211540389, No. 52311530336), and the Fundamental Research Funds for the Central Universities (No. 2021YCPY0110). Qingquan Liu thanks the Alexander von Humboldt Foundation for a fellowship and financial support (3.5-CHN-1235634-HFST-E).

7 References

Aminu, M. D., Nabavi, S. A., Rochelle, C. A., & Manovic, V. (2017). A review of developments in carbon dioxide storage. *APPLIED ENERGY*, 208, 1389-1419. doi: 10.1016/j.apenergy.2017.09.015

Brace, W. F., Walsh, J. B., & Frangos, W. T. (1968). Permeability of granite under high pressure. *Journal of Geophysical Research*, 73(6), 2225-2236. doi: 10.1029/JB073i006p02225

Busch, A., Alles, S., Gensterblum, Y., Prinz, D., Dewhurst, D. N., Raven, M. D.,... Krooss, B. M. (2008). Carbon dioxide storage potential of shales. *International Journal of Greenhouse Gas Control*, 2(3), 297-308

Cheng, Y. & Lei, Y. (2021), Causality between tectonic coal and coal and gas outbursts. *Journal of China Coal Society*, 46(01), 180-198. doi: 10.13225/j.cnki.jccs.YG20.1539

Cui, X., Bustin, A. M. M., & Bustin, R. M. (2009). Measurements of gas permeability and diffusivity of tight reservoir rocks: different approaches and their applications. *Geofluids*, 9(3), 208-223. doi: https://doi.org/10.1111/j.1468-8123.2009.00244.x

Dicker, A. I., & Smits, R. M. (1988*A Practical Approach for Determining Permeability From Laboratory Pressure-Pulse Decay Measurements*. Paper presented at the International Meeting on Petroleum Engineering.

Epelle, E. I., Obande, W., Udourioh, G. A., Afolabi, I. C., Desongu, K. S., Orivri, U.,... Okolie, J. A. (2022). Perspectives and prospects of underground hydrogen storage and natural hydrogen. *Sustainable Energy & Fuels*, 6(14), 3324-3343. doi: 10.1039/D2SE00618A

Gensterblum, Y., Ghanizadeh, A., Cuss, R. J., Amann-Hildenbrand, A., Krooss, B. M., Clarkson, C. R.,... Zoback, M. D. (2015). Gas transport and storage capacity in shale gas reservoirs – A review. Part A: Transport processes. *Journal of Unconventional Oil and Gas Resources*, 12, 87-122. doi: https://doi.org/10.1016/j.juogr.2015.08.001

Jasinge, D., Ranjith, P. G., Choi, X., & Fernando, J. (2012). Investigation of the influence of coal swelling on permeability characteristics using natural brown coal and reconstituted brown coal specimens. *Energy*, 39(1), 303-309. doi: https://doi.org/10.1016/j.energy.2012.01.010

Jia, C., Zheng, M. & Zhang, Y. (2012), Unconventional hydrocarbon resources in China and the prospect of exploration and development, *Petroleum Exploration and Development*, 39(02), 129-136. doi: 10.1016/s1876-3804(12)60026-3

Jones, C., & Meredith, P. (1998*An Experimental Study of Elastic Wave Propagation an Isotropy and Permeability an Isotropy In an Illitic Shale.* Paper presented at the SPE/ISRM Rock Mechanics in Petroleum Engineering.

Li, Z. Q., Xian, X. F., & Long, Q. M. (2009). Experiment Study of Coal Permeability Under Different Temperature and Stress. *Journal of China University of Mining & Technology*, 38(4), 523-527

Liu, Q., Cheng, Y., Haifeng, W., Hongxing, Z., Liang, W., Wei, L.,... Hongyong, L. (2015). Numerical assessment of the effect of equilibration time on coal permeability evolution characteristics. *Fuel*, 140, 81-89. doi: https://doi.org/10.1016/j.fuel.2014.09.099

Liu, Q., Cheng, Y., Jin, K., Tu, Q., Zhao, W.,... Zhang, R. (2017). Effect of confining pressure unloading on strength reduction of soft coal in borehole stability analysis. *Environmental Earth Sciences*, 76, 1-11

Liu, Q., Cheng, Y., Ren, T., Jing, H., Tu, Q.,... Dong, J. (2016). Experimental observations of matrix swelling area propagation on permeability evolution using natural and reconstituted samples. *Journal of Natural Gas Science and Engineering*, 34, 680-688

Ma, Y., Pan, Z., Zhong, N., Connell, L. D., Down, D. I., Lin, W.,... Zhang, Y. (2016). Experimental study of anisotropic gas permeability and its relationship with fracture structure of Longmaxi Shales , Sichuan Basin, China. *FUEL*, 180, 106-115. doi: 10.1016/j.fuel.2016.04.029

Matos, C. R., Carneiro, J. F., & Silva, P. P. (2019). Overview of Large-Scale Underground Energy Storage Technologies for Integration of Renewable Energies and Criteria for Reservoir Identification. *The Journal of Energy Storage*, 21(FEB.), 241-258

Sander, R., Pan, Z., & Connell, L. D. (2017). Laboratory measurement of low permeability unconventional gas reservoir rocks: A review of experimental methods. *Journal of Natural Gas Science and Engineering*, 37, 248-279. doi: 10.1016/j.jngse.2016.11.041

Somerton, W. H., Söylemezoğlu, I. M., & Dudley, R. C. (1975). Effect of stress on permeability of coal. *International Journal of Rock Mechanics and Mining Sciences & Geomechanics Abstracts*, 12(5), 129-145. doi: https://doi.org/10.1016/0148-9062(75)91244-9

Tan, D. & Xiao, R. (2005), Static parameter identification of bridge structure based on Levenberg-Marquardt algorithm. *Journal of Traffic and Transportation Engineering*, 5(3), 56-59. doi: 10.3321/j.issn:1671-1637.2005.03.012

Wang, F., Jiao, L., Lian, P., & Zeng, J. (2019). Apparent gas permeability, intrinsic permeability and liquid permeability of fractal porous media: Carbonate rock study with experiments and mathematical modelling. *Journal of Petroleum Science and Engineering*, 173, 1304-1315. doi: https://doi.org/10.1016/j.petrol.2018.10.095

Wang, J., Mohr, S., Feng, L., Liu, H., & Tverberg, G. E. (2016). Analysis of resource potential for China ' s unconventional gas and forecast for its long-term production growth. *ENERGY POLICY*, 88, 389-401. doi: 10.1016/j.enpol.2015.10.042

Zou, C., Zhu, R., Wu, S., Yang, Z., Tao, S., Yuan, X.,… Wang, L. (2012), Types, characteristics, genesis and prospects of conventional and unconventional hydrocarbon accumulations: taking tight oil and tight gas in China as an instance, *Acta Petrolei Sinica*, 33(02), 173-187. doi: 10.7623/syxb201202001

Pragmatic, empirical swelling pressures in sulphate bearing rock masses

Pragmatisch empirische Quelldrücke in Sulfat führendem Gebirge

Walter Steiner
B+S AG
Bern, Switzerland

Abstract

Construction work in sulphate bearing rock is challenging and these rocks have to be detected early in the planning phases such that their effects may be avoided or at least mitigated during construction. The types of sulphates (Anhydrite or gypsum) and the clay types must be known and investigated. Mineralogical investigations are required. If swelling sulphates the appropriate construction procedures must be selected. The use of the observational method for determining the support is strongly discouraged, support must have sufficient structural resistance to prevent uncontrolled swelling. In-situ swelling pressures empirically determined are less than swelling pressures from laboratory swelling tests. The author started in 1988 to compile experience and swelling pressures from case histories: swelling pressures and construction behavior. In-situ swelling pressures of 1.5 to 2 MPa have been estimated since then. The clay minerals influence the swelling pressures, the above-mentioned values are valid for clays with smectite or corrensite. Illitic clay show lower swelling pressures of about 0.5 MPa. New insights have been gained.

Zusammenfassung

Untertagebauten in Sulfat führendem Ton Mischgesteinen stellen grosse Herausforderungen beim Bau, deshalb müssen diese Gesteine frühzeitig in der Planung entdeckt und identifiziert werden, um diesen Gebirgsabschnitten entweder auszuweichen oder die Auswirkungen gering zu halten. Die Art der Sulfatgesteine spielt eine Rolle, handelt es sich um Anhydrit oder Gips und die mitwirkenden Tongesteine, handelt es sich um Smectite oder Corrensit oder um weniger quellfähigen Illit. Die Quellfähigkeit des Ton-Sulfatgesteins wird von der Kombination beeinflusst. Die anzubringenden Stützmassnahmen müssen vorgängig ausreichend bemessen werden, dazu dienen empirisch ermittelte Quelldrücke. Die Beobachtungsmethode darf nicht zur Bemessung verwendet werden. Für Mischgesteine aus Sulfat und hochaktivem Ton (Smectit. Corrensit) betragen die empirischen Quelldrücke 1.5 bis 2 MPa, Für Mischgesteine mit Illit sind dies niedriger (0.5 MPa).

Aus der Analyse von unterschiedlichen Messtechniken der Quelldrücke konnten neue Erkenntnisse über deren Wirkung im Gebirge gefunden werden.

1 Introduction

Tunnels in rock with a mixture of sulphates and clay rocks have caused many problems during tunnelling and require substantial support and resisting lining. In addition to sufficient mechanical resistance the structure must be resistant against chemical attack as the rock mass may contain corrosive agent like sulfates and other minerals.

The author has been involved in the design and repair work for several decades and tunnels and has compiled the experience from these tunnels until 1988 (Steiner & Metzger, 1988) and later from other projects and publications. Here a list of reference on case histories is included and a general analysis and synthesis of the main issues is presented, followed by the most important factors to be considered.

2 Experience from case histories

Tunnelling through swelling rocks started with the construction of railway during the 19th century, the knowledge in rock and soil mechanics was inexistent and experience was gained with the construction of the tunnels. The author started to assemble the experience from case histories (Steiner & Metzger, 1988; Steiner, 1993) and continues to collect published experience. Experience shows that different factors led to problems with the tunnels. In some cases, it is a single cause, in other cases it is a combination of different causes. The experience from several case histories had been discussed be Steiner (2007) since then new experience was gained and will be discussed here. . The experience from two cases with major problems will be discussed in more detailed: the Wagenburgtunnel (Stuttgart, 1957, Wichter, 1989 & 1991; Paul & Wichter, 1996) in Stuttgart, Germany, built 1954 – 1957 and the Chienbergtunnel of the Sissach By-Pass Road in Switzerland built 2000 – 2006 with continued works (Chiavero and Püschner, 2024). Experience from other cases will also be interpreted. Other cases exist that are not discussed in detail here.

2.1 Insufficient design loads

Analyzing case histories (Steiner, 2020) one notes that the loads on the structure were initially not estimated, mostly the lining in the crown and sidewalls was built from masonry. The invert mas mostly flat and was trimmed when heave occurred, such a method was possible with railways as ballast could be rather easily adjusted.
From the following tunnels the design loads are known.

2.1.1 Wagenburgtunnel in Stuttgart

The pilot tunnel of the northern tube of the Wagenburgtunnel was constructed 1942 to 1943 (Stuttgart, 1957) during World War II. During the war this pilot tunnel and the full section at the western end were used as bomb shelter. Construction resumed 1954 to 1957 for the southern tube, with a special support system the “Kunz’sche Rüstung” or the *Kunz Scaffolding*. The invert was designed for a swelling pressure equal to 350 kPa. The invert arch made with reinforced concrete with blast furnace slag cement had a thickness of 0.5 m and an interior radius of 5m and the concrete a cube compressive strength β_{w28} = 42….45 MPa. The lining in the crown had an exterior lining of 1.1 m thickness and an interior lining d =0.6m at side walls. Soon after opening of the tunnel cracks were developing below the roadway in the fresh air channel (Paul & Wichter, 1996). From 1957 until 1990 the tunnel lifted from 200 to 300 mm between stations 380 to 410m. From 1978 heave was measured on the ground surface between tunnel chainage 300 and 500 m, with 46 mm heave at station 400 m at the ground surface and 70 mm at the tunnel crown.

With extensometers in the invert swelling was detected to 10 m below the invert. The tunnel structure suffered heave but can still be used and requires maintenance and repair. The initial geologic longitudinal section (Stuttgart, 1957) did not show the “anhydrite level” below which was determined later (Paul & Wichter, 1996). The anhydrite line lies mostly in the cross section of the tunnel and reaches the crown. The rock above the anhydrite level has poorer mechanical properties (Rauh, 2009). The overburden stress is about 1 MPa or less, which is less than the swelling stress. Wichter (1989a) has proposed the existence of high horizontal stresses in the ground, which will lead to larger mean normal stresses and could resist higher swelling pressures. The tunnel excavation changed the stress state in the ground and swelling may start heaving the entire tunnel.

2.2 Insufficient structural resistance

The lining in the crown of an old railway tunnel was often several decimeters or a meter thick, made from natural stone, limestone, sandstone or similar sedimentary stones locally available. Often no invert was placed and the heave under the railway bed was trimmed periodically. The lining suffered little damage.

With the 20th century concrete became available, and inverts were cast in concrete. The concrete often had rather low strength and the invert ruptured. In case of the Hauenstein Base tunnel, during the first repair works Invert arches made from granite blocks with tailored sides were used to form an arch of 5 m interior diameter and 0.5 m thickness.

The next major tunnel constructed was the Belchen Tunnel of the north-south motorway N2 through the Jura mountains (Grob, 1972). The initial invert had a thickness of d= 0.45 m and an interior radius of 10.4 m, which gives a resistance of radial pressure 1.2 MPa. In sections the lining had to be replaced (Werder, 1989) and the side walls were reinforced. From 2001 to 2004 an extension of service life of the tunnel was achieved by strengthening parts of the lining.

In the Wagenburgtunnel sections of the reinforced invert arch had to be replaced around 1986, some 30 years after construction (Paul & Wichter, 1996). The slab of the road was also reinforced. Loading was also from differential heave in the longitudinal direction.

2.3 Issues caused by the construction procedure

The construction of newer tunnels required the excavation of several openings in sequence. The crown heading was followed by the bench and the invert. The length from the face to invert closure might extend over one to two hundred meters. During this advance and stoppages of the tunnel advance heave of the temporary invert in the top heading or the final invert may occur (Chiaverio et al., 2024). Heave also occurred during the construction of the Wagenburg tunnel (Stuttgart, 1957) and the Belchen Tunnel (Grob, 1972, 1976). At the Wagenburgtunnel a central pilot tunnel had been built, followed by the excavation of the top heading and finally the invert. The ring closure came a long time after the initial excavation. These were construction procedures known then.

For the construction of the initial Belchentunnel, (Grob, 1972) two side drifts were constructed first, followed by the upper part under the protection of a semi-circular shield and then by the invert. After placement of the first invert with R = 10.4 m and d = 0.45m rapid heave of the invert occurred. A new stronger invert was placed.

2.3.1 The Chienbergtunnel, Sissach By-pass Road, Switzerland

The Chienbergtunnel (Hofer et al., 2007; Chiaverio et al. 2007; Chiaverio and Püschner, 2024) was built with a pilot drift, followed by the top heading and benching. The 1443 m long tunnel forms part of the by-pass of the town of Sissach. Approximately 780 m of the western section are in Gipskeuper (Sulfate-clay rock). The first 340 m have small overburden of about 35 m, with the invert in non-altered sulphate clay rock (Anhydrite with clay) and weathered rock, with soil-like characteristics, In the upper part of the tunnel.

A pilot tunnel in the crown preceded the widening to top heading, followed by bench and invert in the lateral zones with smaller overburden of 35 m. Some roof collapses occurred, which led to standstill of the excavations. The floor of the heading was partly flooded, which led to uncontrolled heave of the tunnel floor by 1.5 m. The unreinforced interior concrete liner is nearly circular with a thickness of 0.7 m in the crown and 1.1 m in the invert. About 4 months after the final placement of the liner, heave was detected and a rupture in the invert. A first heave zone of 90 m length (Chainage 100 to 190 m) and a second 140 m long heave zone (Chainage 370 to 510 m) were detected. The inverts in these zones were substituted by a modular yielding system (Hofer et al., 2007). Every meter of tunnel four rock anchors with 1500 kN admissible loads were installed with a sliding anchor that limited the swelling pressure to an average of 0.6 MPa and allowed a controlled heave of the floor.

In the first heave section the heave could be stopped. In the second section the heave could not be stopped. The rate of heave in the crown was reduced from 6.5 mm/a to 2.5 mm/a, which is larger than estimated from other tunnels (Fig. 10).

The observations show also lateral swelling in the lower zone (side walls) of the tunnel, this also indicates the presence of high horizontal stresses.

2.4 Comparison of the experience from Wagenburg and Chienberg tunnels.

The tunnels have been built more than forty years apart, but they suffer from similar issues and have also have some differences. Both tunnels have small overburden of 30 to 40 m in the crown and the anhydrite level lies in the cross section of the tunnel. Both tunnels experienced heave underneath the tunnel section of about a decimeter. The Wagenburg has a reinforced concrete liner also an invert arch. The liner was loaded to a substantial larger load than designed and required repairs in 1986. The Chienberg was designed to 6 MPa, but the liner ruptured, and a new yielding support was installed that still heaves.
In both tunnels the overburden stress is less than the in-situ swelling stress and horizontal stresses may have an influence. These stresses are difficult to measure but they can be inferred from soil mechanics considerations for over consolidated clays (Steiner, 2007). The ground conditions appear to be similar for both tunnel with small overburden and high horizontal stresses.

3 Swelling pressures

In this section some key observations on swelling pressures observed in laboratory tests and in-situ observations are summarized.

3.1 Laboratory tests for swelling rocks in tunnels

The swelling problems during the construction of the Belchen Tunnel of motorway N2 in Switzerland led to the use of swelling tests (Huder & Amberg,1070; Grob, 1972). These tests were derived from soil mechanics tests that are used for compressing soil and unloading the ground beneath a horizontal surface, they are called oedometer tests. There is the test developed by Huder-Amberg (1970) where the loading in dry conditions (no water added) are determined when the sample is loaded to the natural stress and then water is added and the deformation under unloading measured. In the swelling pressure test the vertical dimensions of the sample are kept constant, the deformation of the loading frame is compensated, and the swelling pressure is measured (ISRM, 1989 & 1999) for no vertical strain. The test procedure for clay rocks and for rocks with sulphates are different. Rauh (2009) has compiled a comprehensive study on laboratory tests,

3.1.1 The determination of swelling pressures for pure argillaceous rock

The swelling pressure (Huder & Amberg, 1970) determined with the direct measurement of swelling pressure and with the incremental loading and decremental loading should give the same swelling pressure. However, there are deviations between the two methods that were investigated at EPFL and comparisons were compiled over years (Steiner et al, 2023). A modified method for determining the swelling pressures from the incremental loading and unloading test has been proposed.

3.1.2 Swelling tests for sulphatic rocks

For sulphatic rocks only tests for swelling pressures under restraint heave must be used and the deformation of the loading frame must not be reset (ISRM. 1999). The samples in the swelling tests are alimented by water with a sulfate content close to saturation and may last several years.

3.1.3 Observations on swelling tests in the laboratory with sulphate clay rock.

For swelling pressure tests on sulphate bearing rock the deformation of the loading frame must not be compensated, as this would mean that crystallized gypsum should be reversed, this procedure results in higher pressures. In the area where the stresses in the lining of the Hauensteintunnel were measured for the design of the Wisenbergtunnel several swelling free and stress tests and mineralogical investigations (Nüesch et al.,1995) were conducted on specimens from the same core sample (400 mm long core) in the same boring. The measured swelling stress after several years of testing varied from 1.8 to 4.8 MPa and appeared to continue after several years. The back-figured average swelling stresses from flat jack measurements in the lining were in the order of 1.7 MPa (Steiner, 1989; Steiner et al. 1989), thus nearly one third lower than the test on specimens in the laboratory.

The content of different minerals was determined along the 20 m long core from the horizontal boring, about every 0.5 to 1.0 m where the anhydrite content varied from 50 to 75%, the gypsum content varied from a few to 28 percent and the clay content from 5 to 35%. The results for the seven swelling strain tests and the four available swelling stress tests are summarized in Tab. 1. no correlation could be developed.

Tab. 1: Compiled mineral contents of specimens prior to test and after swell strain or swell stress tests.

Case	Gypsum	Anhydrite	Clay	Gypsification
	%	%	%	%
Prior to Test	3…..28	50…..75	5 …..35	Not determined
Swelling strain test	15…..61	17…...56	7…..14	21…...78
Swelling stress test	7…..21	56…...63	5…...18	10…...25

For other tunnels swelling pressure teste were carried out by Kirschke, (1996, 2010) for the Freudenstein Tunnel and Noher et al. (2006) for the Adlertunnel. After a several years of swelling the reached stresses (8 MPa) were released, but the samples immediately started to build-up the swelling stresses again. With this stress release the swelling stresses could not be reduced. The formation of crystallized gypsum was also observed on specimens from a test tunnel in the Belchen tunnel (Amman et al. 2013) and the Gotschnatunnel (Krähenbühl, 2014).

3.1.4 Effect of texture and microstructure of clay sulphate rocks

Nüesch et al. (1995) and Nüesch (1995) had carried out extensive investigation on samples from a boring in the Hauenstein base tunnel. The texture of these specimens with 50 mm width and 30 mm height were inspected.
One principal aim was to differentiate between texture developed during the swelling test from gypsum derived during geological time scale, Texture controls the formation of Gypsum. Layered shale containing anhydrite has presumably higher permeability, whereas massive anhydrite has low permeability and does not swell. The deformation of shale and intercalated anhydrite is different. Fissuring may start in clay and increase water conductivity.

In the swelling stress samples primary structures were observed like anhydrite nodule, called “chicken-wire”. Gypsum crystals formed tectonically and during the swell stress tests. The gypsum crystals formed tectonically showed a preferred orientation, whereas in the swell stress test they were randomly oriented. The formation of gypsum crystals was close to zones rich in clay minerals. Clay clasts (lumps) may be present. Gypsum crystals adjacent to clay minerals show a fine-grained margin which was interpreted as reaction seam. The reaction front ends when there are no clay minerals available.

There are differences between swelling strain and stress tests. In swelling strain tests anhydrite will transform more into gypsum, in stress tests only little anhydrite is transformed into gypsum. This can be translated into the dimensions of tunnels, if the resisting pressure is insufficiently large, possibly uncontrollable heave may occur. With sufficient counterpressure deformations can be minimized. The texture of clay sulphate rocks varies in the range of centimeters, concentrated swelling pressures will appear in the same extensions, in between the swelling pressure will be smaller. This is in accordance with the observation with measurements with in-situ stress cells (5.2).

3.2 Direct in-situ measurements of swelling stresses in sulphate bearing rock

3.2.1 Measurement with hydraulic contact stress cells

Field measurements of swelling stresses were carried out for the Belchentunnel with hydraulic contact pressure cells. The measured stresses varied from 1.5 to 4 MPa (Grob,1972). Additional contact stress cells installed in lining of the vertical ventilation shaft gave very high stresses (> 8 MPa) that appeared not plausible.

In the Wagenburgtunnel (Paul & Wichter, 1996) some sections required repairs and new instrumentation was installed around 1986. The contact stress cells showed a large scatter from 1 to 6 MPa. The measured tangential concrete stresses do not confirm the high radial stresses.

In the Freudensteintunnel (Fecker & App,1992; Fecker,1996) extensive instrumentation had been installed with different support systems in 1986. The measurements for 4 to 10 years had been published. The test tunnel with about 8 m diameter had different test sections of 5.5 m length with resisting liner and liner thickness of 0.3, 0.6 and 0.85 m. Radial contact stresses were measured with hydraulic stress cells (Glötzl type) in the invert and the crown, Stresses in the lining were measured with vibrating wire strain gauges and stress cells. The radial contact stresses in the invert showed large variation from 0.5 to 6 MPa. With the strain gauges in the liner the stresses and the forces could be back calculated, the resulting radial stresses were in the order of 1.5 to 2 MPa. In the Main tunnel of the Freudensteintunnel a single measurement of contact stresses between compressible layer and concrete was found (Kirschke, 2010) with a nearly constant value of 0.7 MPa.

In the Lilla Tunnel near Tarragona, Spain (Alonso et al, 2013) similar observations were made with high stresses in contact stress measurements (0.5 to 6 MPa) and lower backfigured stresses from strain measurements on the reinforcement. (0.2 to 0.5 MPa).

The measurement with contact stress cells show discrepancies will be discussed below.

3.2.2 Measurement of contact stresses with a steel plate fixed to a steel pipe

The 5300 m long Adler Tunnel (Noher et al. 2006) in Switzerland was excavated with an open rock TBM in a simple shield over 4264 m and lined with a segmental liner, with a thickness of 0.65 m in the invert and 0.35 m in the upper part. The tail void was grouted, thus stress cells placed on the extrados of the segments would be shielded from the swelling stress from the ground. The system shown Fig. 9 was installed. in Boreholes of 120 mm diameter (Sambeth, 2024) were drilled through the segments and grout and a steel plate of at least,10 mm thickness was fixed to a 100 mm diameter pipe were inserted into the borehole. The contact zone was filled with grout. The strain in the pipe were measured with vibrating wire strain gauges and the contact stresses calculated.

The initial results had been published in 2005. 15 Stress measurement varied from1 to 1.9 MPa, with a mean of 1.3 MPa and one outlier. The further readings until 2022 remained constant. Some devices were post-tensioned and then showed erratic behavior and extreme increments to 4 MPa, we exclude these values. The average measurements remained stable. These measurements with a stiff plate show substantially less scatter than the measurements with hydraulic cells with a steel membrane. The lining of the tunnel had been designed for 4 MPa and the actual loading is half of the design load.

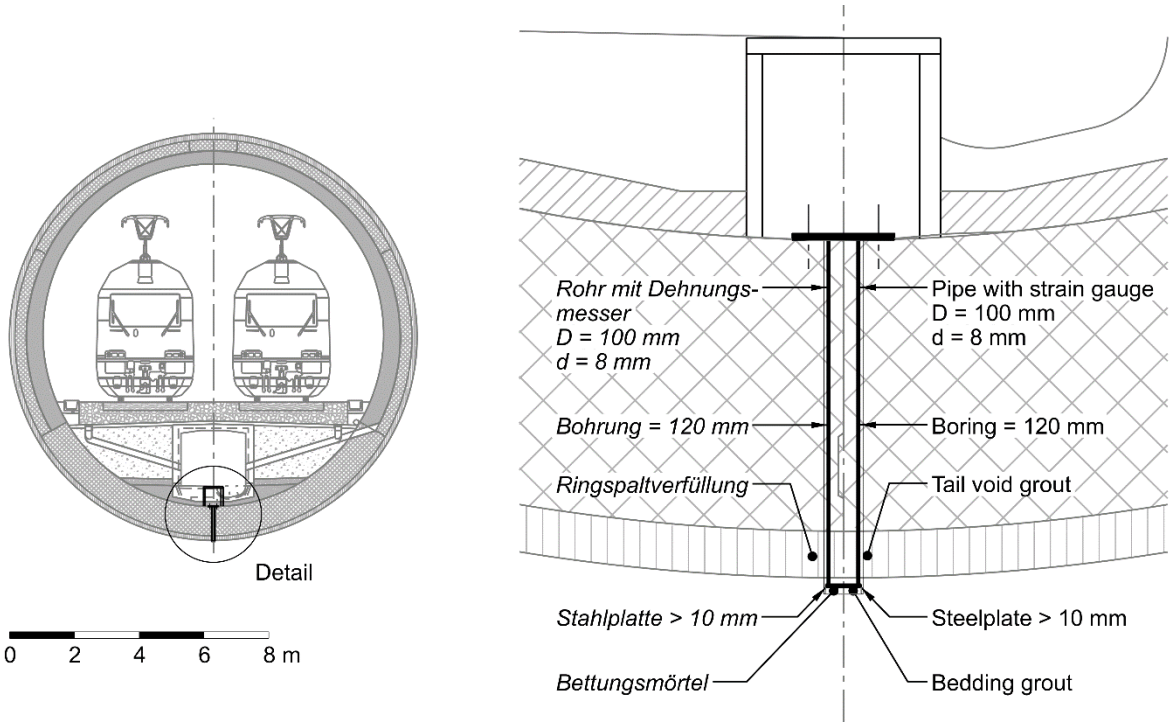

Fig. 9: Stress measurements in the Adler Tunnel with a steel plate fixed to a steel pipe and the tunnel lining (Sambeth, 2024 and Chiaverio, 2024). In one measurement section five stress measurement devices are installed along the tunnel, spaced one meter in the same area.

3.2.3 Probable causes of the differences.

Laboratory tests indicate large variations of measured swelling stresses in oedometer cells. Samples in these cells with a ring are alimented with sulfate bearing water and can swell forever. In the rock mass the swelling closes fissures in the rock and the alimentation with sulfate bearing water and other water inflow will stop and swelling. Different parts of the rock mass will swell but produce locally different pressures. These rocks are mixtures of clay and sulfates. Crystallization will occur mainly at the boundaries between the different minerals (Amann et al. 2014, Krähenbühl, 2014), the crystallization pressure will compress clay and water flow will stop. The mechanism in-situ is different from laboratory tests, as the alimentation with water ceases.

3.2.4 Creation of point loads on cell membranes

When measuring with hydraulic cells (mostly called Glötzl cells) with a thin metallic membrane at the location of the crystallization localized high pressures will develop and spread the pressure over the entire cell. The measurement with the steel plates will not lead to a point load, the load will be more evenly distributed as shown by the measurement at the Adlertunnel (see section 3.2.2). There are load cells with thicker plates (10 mm) on the market that reduce the effect of point loads, these cells are used for coarse grained soil and the measurement of stresses between railway ties and the ballast.

3.3 In-situ stresses back-figured from strains (or stresses) in the lining.

3.3.1 Limits of measurement systems

Within a liner the strains are measured and then the stresses computed, this requires that the relation between the strain is known, usually it is linear or elastic. If concrete is loaded close to the strength the behavior may become inelastic and the material may creep. The requirements are then no longer fulfilled.

3.3.2 Measurement with strain gauges.

Vibrating wire strain gauges can be easily used in concrete segments and cast concrete liner and give usually reliable results. In a cross section two or three strain gauges should be used such that normal forces and bending moments can be captured. Such arrangements were used in sections of test tunnel in the Freudenstein tunnel, which gave good results. In several sections of the Freudenstein Test tunnel a circular concrete lining with different wall thickness d =0.3, 0.6 and 0.85 m, equipped with two or three vibrating-wire strain gauges or stress cells were installed. Based on a few results measured after 4 years (Fecker, & App, 1992, Fecker, 1996) radial stresses of 1.5 to 1,9 MPa were back figured. For the 0.3 m thick lining concrete stresses from 10 to 20 MPa were measured. In the thicker lining they were by a factor 2 less. These back calculated swelling pressures agree with the stresses the load relief sections

3.3.3 Stress measurements with flat jacks

The author has been involved in carrying out flat jack measurements in the lining of the Hauenstein base tunnel (Steiner, 1989, Steiner et al. 1989, Steiner 2020) that yielded valuable information on the stresses in the lining and the acting swelling pressures. The back figured swelling pressure required interpretation of the measured stresses in the lining which were very high at some places (30 to 50 MPa). The average swelling pressures were 1.5 to 2.0 MPa.

Flat jack measurements were carried out in the section of the Gotschna tunnel (Steiner and Schwalt, 2019) with a sufficiently strong invert, that gave swelling pressures of 0.5 MPa in sulfate illitic clay.

3.4 Estimation of swelling pressures under constant load with deformations

In several tunnels the observation was made that with insufficient support the invert heaved at a nearly constant rate of heave for different resisting pressures.

3.4.1 Observations in the Gotschnatunnel

In the Gotschnatunnel three sections with different invert support in the “Rauhwacke” had been constructed (Steiner and Schwalt, 2019). The rates were plotted as function of structural resistance in the invert. (Fig. 10). The pressure to stop swelling was 0.5 MPa in this formation of sulphatic rock mixed with illitic clay.

3.4.2 Observation from the Freudenstein test tunnel

In the Freudenstein Test tunnel sections were equipped where the support pressure could be kept constant, and deformations measured. This was achieved by manually releasing the displacement with constant loads. The measurements were presented as pressure vs. displacement at different times (Wittke et al. 2007). The data have been transformed in rates of heave for different time periods and replotted on Fig. 10 in parallel to the data from the Gotschnatunnel. Extrapolating the displacement rate data, one finds a swelling pressure of 1.5 MPa for no displacement of the clay-sulfate rock at the Freudenstein Tunnel. These swelling pressures agrre well with the one determined directly with strain gauges (see section 3.3.2).

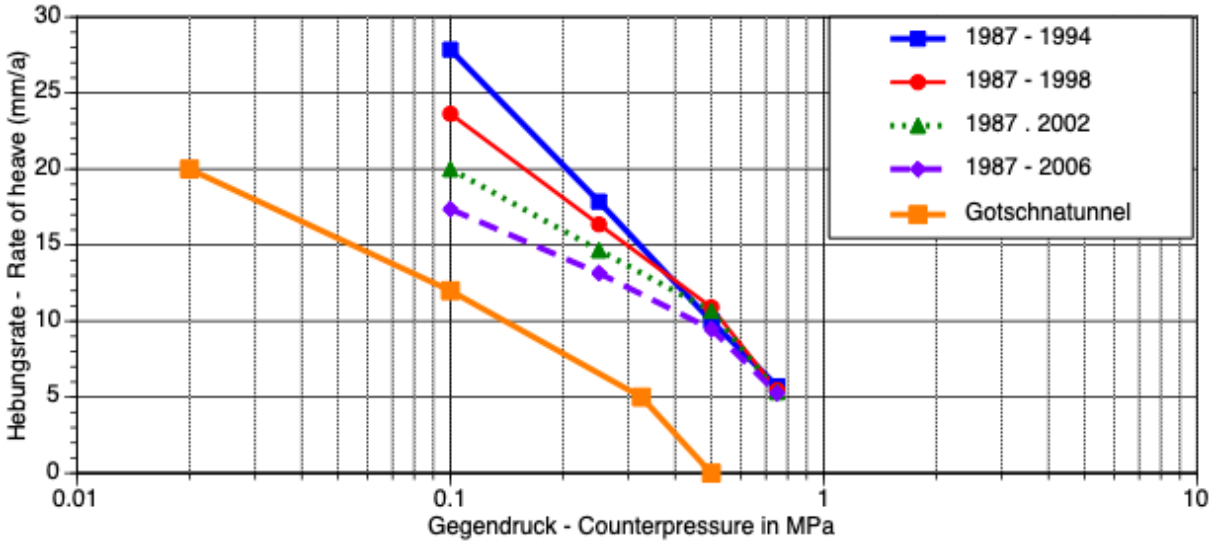

Fig. 10: Rate of heave for invert in Gotschnatunnel and) and test section in Freudensteintunnel (Wittke et al. 2007) with constant resistance.

3.4.3 Contact stresses at contact compressible layer to concrete in the invert of the Freudensteintunnel

From the Freudenstein Tunnel a single measurement of contact stresses between concrete invert and compressible layer was published (Kirschke, 2010). The measurements started on November 1, 1997, and increased to 0.6 MPa until November 1999, then increased to 0.7 MPa in November 2002 and remained constant thereafter, with the last reading in 2010. The compressible layer was designed to be activated at 1 MPa compressive stress. The compressible layer was not activated and proved not necessary.

3.5 Relieving swelling pressures by allowing displacements

A theory was proposed by Kovari et al. (1987) that swelling pressures can be reduced by allowing deformations. This technique has been applied in several cases and the success was varied and was either not successful or not necessary in practice.

1. Hauenstein Base tunnel, Tecknau – Olten, Switzerland:
   A compressible packing had been applied by the contractor Julius Berger, during the construction of the Hauenstein Base tunnel in 1914. As Wiesmann (1917) reported grouting of the 100 m long zone was already started in 1916. The section had to be rebuilt 1919 – 1923 (Etterlin et al.,1986; Steiner, 1989) with granite blocks as lining.
2. Laboratory tests reported by Kirschke (2010) and Noher (2006) show that when the swelling stresses in a lab oratory apparatus are released by some percentage and test apparatus is mechanically blocked again and the swelling pressure build-up restarted.
3. Field observation of invert heave for different support pressure indicate that the rate of heave decreases with higher support pressure (Fig. 10) until to cease completely.
4. Freudenstein Tunnel: The few published measurement from the Freudenstein tunnel show that in test sections all back figured swelling pressures are from 1.5 to 2.0 MPa. In the main tunnel (Kirschke, 2010) with compressible zone the recorded pressure (0.7 MPa) is below the pressure to activate the compressible layer and was not necessary.
5. In the Engelberg tunnel (A81, Leonberg near Stuttgart) a compressible zone was installed after problems with the construction of a resisting invert (Erdmann et al. 2019). The tunnel did not perform satisfactorily, and the lining was reinforced to resist the swelling pressure., in particular horizontal stresses.

With compressible layers placed between the rock and lining in some parts the bedding conditions of the lining are modified. The swelling loads in anhydritic rocks are large. This may lead to large bending moments in the lining and damage to the tunnel.

3.6 Drainage of the rock mass

Observation of the rock mass have shown that alimenting the rock mass with water will lead to swelling. There was the hypothesis developed that draining the rock mass will stop swelling. To verify this a 275 m long test tunnel was constructed between two crosscuts in the Belchen tunnel at a level below the two road tunnels. Drainage borings were drilled and initially brought some water. Later water ceased but swelling continued. No technical scientific publication had been written, but a press communication was published (Kanton Basel-Land; 2007).

4 Measurements of deformation in the invert.

Measurement of heave (deformation) in the invert is carried out with multipoint extensometers or incremental extensometers. In the above cited cases with large heave this is recorded often to the depth of one diameter depth.

The measurements carried out in the Adler tunnel are particularly interesting had been initially published by Noher et al. 2006). The author had insights in the newest series of measurements in this tunnel excavated 25 years ago with a Shield TBM and segmental lining. The displacements measured occurred only over the first two meters of the extensometer below the concrete liner from 2000 to 2005 the displacements were 2 mm and increased to 8 mm until 2022.

The swelling is about one meter thick. To swell the rock has to change its permeability. Brittle failure is necessary (Steiner et al, 2011, Kaiser et al., 2010, Amann et al. 2010) analyses for a circular tunnel gave a failure zone of one meter thickness. Water could flow through this fissured rock and the swelling process by sulfate transport starts. As the swelling pressure built-up the fissures were closed and the swelling process stopped with the attained stresses. The development of crystallization had been observed in the test tunnel at Belchen (Amann et al (2013) and in the Gotschnatunnel (Krähenbühl, 2014).

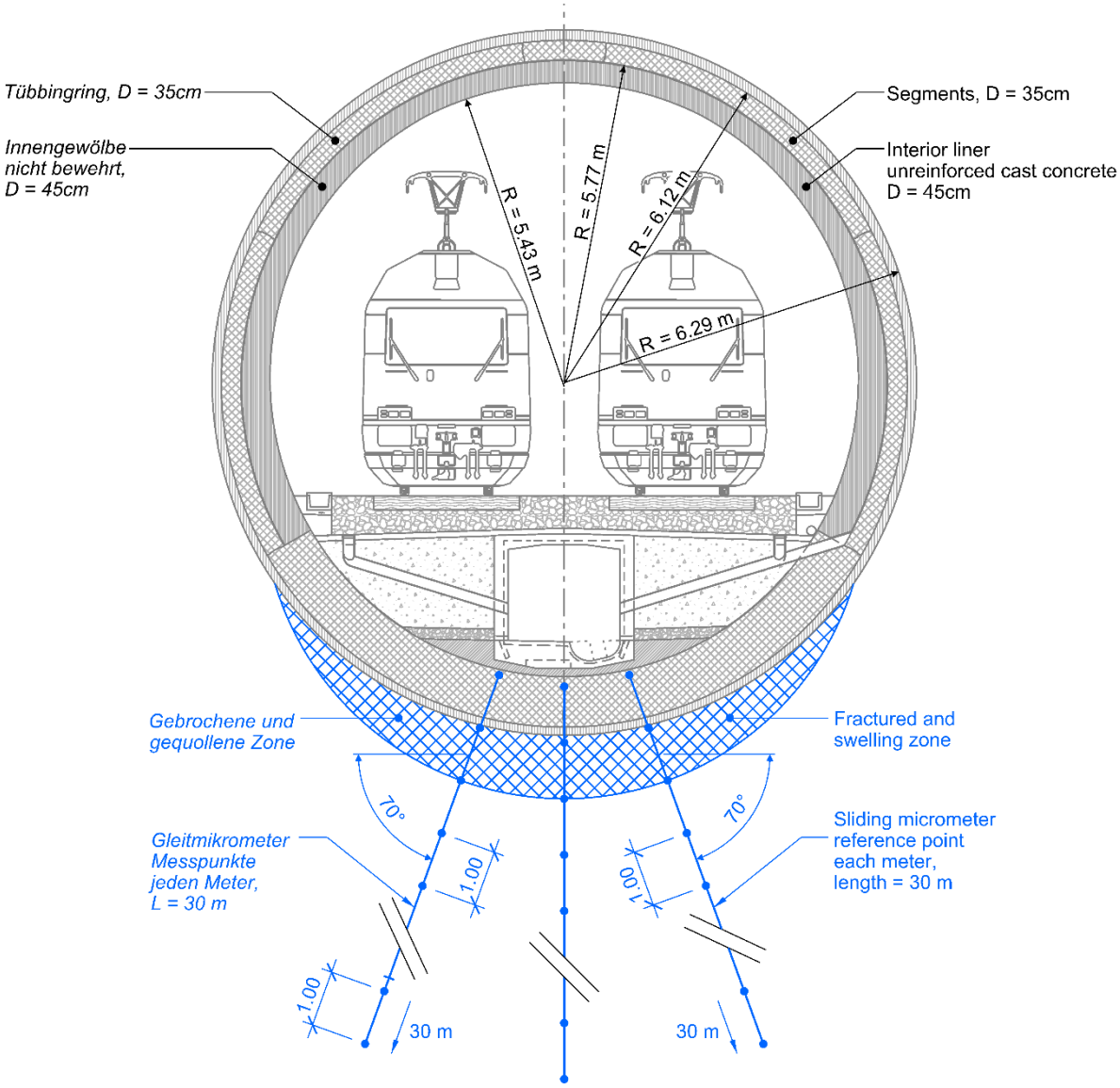

Fig. 11: Measurement of deformation in the Adler Tunnel. Three sliding micrometers were installed from the channel in the invert. One vertical and two inclined at 70° dip sliding micrometers were installed. Measuring marks were installed every meter over 30 meters length. The about one meter thick zone, first fractured and after water entered the fissures, has swollen.

5 Discrepancies between swelling pressures from laboratory test and field measurements

The compilation of experience from laboratory tests and field measurements shows contradictions and inconsistencies.

5.1 Laboratory tests on clay-sulphate rocks.

As discussed above measured swelling stresses in one-dimensional swelling teste from the same rock mass may differ significantly and the swelling may continue with no clearly defined termination of the swelling or crystallization process.

5.2 Discrepancies between measurements with different types of stress cells.

Laboratory tests show large variation of swelling pressures on samples of 60 mm diameter. As elaborated above, crystallization may produce point loads in the rock mass. In addition, the crystallization pressure will compress the clay zone and compress the fissures that opened during the mechanical stress redistribution. The stresses on the liner will and cell membrane vary within a few centimeters. The load determined by membrane pressure (http://www.gloetzl.de/en/products/sensors/pressure-and-stress.htm#c290) cells will indicate the point loads from crystallization on a local area. These swelling pressures correspond to the swell pressures measured in the laboratory. One can thus explain that within the rock mass will vary with the mineralogy of the rock and the that the stresses are heterogeneous.

With stiff steel plates as applied in the Adlertunnel (see 3.2.2) the point loads were distributed on the average stresses measured. In practice there exist also hydraulic stress cells with stiff plates (https://www.geokon.com/4815) that will distribute the point loads, similar as for use in granular soil or measuring the stresses under ties of railway track and the contact with the ballast.

In the case of swelling in tunnels, the explanation of the differences between the two types of the measured stresses leads to a better understanding of the rock structure and the swelling process governed by crystallization.

5.3 Comparison to stresses measured in the structure

Stresses in the structure have been measured with strain-gauges and stress measurement cells and gave rather consistent values of 1.5 to 1.9 MPa. These also agree with the values of the direct measurements with the steel plates from the Adler tunnel.

5.4 Effect of clay type in sulphate rocks

There exist field observations in sulfate rock with smectite or corrensite clay (Lippmann, 1976; Hauber et al. 2005) that indicate swelling pressures around 1.5 MPa to 2 MPa such as

- Hauenstein, (Nüesch et al. 1995)
- Belchen, (Grob, 1972 & 1976;
- Adlertunnel in Switzerland; and
- Wagenburg, (Stadt Stuttgart, 1957; Paul & Wichter, 1996; Henke K.F, 1975)
- Freudenstein, (Fecker & App, 1992; Fecker, 1996; Kirschke, 1996, 2010)
- Heslach, (Henke et. al, 1979)
- Kappelesberg Tunnel (Kurz & Spang, 1984)
- Weinsberger Tunnel (Gremminger & Spang, 1978); Lorenz et al. (2006)
- and other Tunnels near Stuttgart, Germany.

In contrast Tunnels with illitic clay and sulphates like Gotschnatunnel (Steiner and Schwalt, 2019) and Lilla tunnel (Alonso et al., 2013) in Spain indicate smaller in-situ swelling stresses of 0.5 MPa.

6 Method to design the lining based on computed rock behavior.

The design of tunnels in sulfate rock with. numerical methods is difficult and challenging. Different processes of mechanical behavior, flow behavior, material transport and crystallization interact. There are methods applied to solve these problems that are based mostly on proprietary numerical codes that are not easily traceable by external persons or are not accessible. Publications exist that indicate that the analyses should work. However, successful analysis requires that the results can be compared to measured (monitored) behavior of the tunnel.

6.1 Design method by WBI (Wittke Consulting Engineers)

The design method developed by WBI (Wittke Consulting Engineers) started in 1979 (Wittke & Pierau) with later publications (Wittke, M. 2010; Wittke et al. 2007) have been summarized by Wittke, M (2021), are based on proprietary numerical codes and require the input of many parameters. There are results for the design of the tunnel with different boundary conditions. The swelling pressures are very high 1.7 MPa, 5.9 MPa and 7.9 MPa. No measurement results for these tunnels built already several years ago have been published. However, two of these computed values largely exceed values back figured for earlier tunnels in this area that perform satisfactorily.

6.2 Design method developed by UPC (Universitat Politechnica de Catalunya)

The Department of Civil Engineering of the Universitat of Catalunya developed a numercal method to simulate hydraulic, chemical and mechanical processes with sulphate swelling. This research was a continuation of the work after the problems constructing the Lilla Tunnel near Tarragona, Spain of the High-speed railway line AVE to Madrid (Ramon et., 2018). The elaborate model considers at least 22 parameters, which is still a simplification of complex reality. Model predictions were made on the behavior of the horizontal tunnel floor after initial excavation, A second analysis considered the construction of the invert in the test section and computed the development of the contact stresses in contact stress cells and the heave of the invert. The limits and shortcomings of the analyses are discussed. The swelling pressure were computed for the contact pressures, which are too high. The analyses give insight in the processes but not all details can be explained.

7 Conclusions and Recommendations

7.1 Design of tunnels

For a proper design of tunnels in swelling rocks the loading conditions by swelling must be known in size and location. The swelling pressures are resisted by the structure of the tunnel and the ground, the types and location of the ground must be known. For the case of shallow tunnels at the Anhydrite – Gypsum interface this is particularly important.

The analyses of experience from case histories leads to the conclusion that in-situ average swelling pressures of 1.5 to 2 MPa act. These findings are in accordance with earlier publications (Steiner,1989, 1993; 2007 and 2020). For the design of the structural liner the higher value should be used. To explain the swelling processes with shallow overburden the lower value may apply in zones of lower overburden. The clay also plays a role for the swelling pressures.

7.1.1 Confirmation of swelling pressures and deformations

The information on swelling pressures has been compiled from various case histories with different field measurements. Some case histories give a rather complete picture of measured stresses and deformations. In other cases, only pieces of measurements or single measurements have been published and had to collected. No complete set of measurements are available from several cases and had to be complied from fragments of information. For the understanding of the in-situ swell pressures and deformations field measurements are mandatory and must be made accessible or published.

There are also cases where no monitoring systems for loading (stresses) have been installed, in these cases it is not possible to evaluate the state of loading in the liner and the margin of safety cannot be evaluated.

7.1.2 Structural resistance and soil-structure interaction

Near the transition zone from Anhydrite to Gypsum not only the swelling potential also the mechanical properties of the ground change. The soil-structure interaction must be considered. The fracturing of the rock (brittle failure) should be minimized.

7.2 Planning and site investigation

Rocks containing sulfates should be identified already in the planning stage with mineralogical investigations which types of sulfates and clays are present.

7.3 Selection of alignment

Tunnels though sulphatic rocks may cross different types of rocks, a typical cross section through a hill or mountain is shown in Fig. 12. The cover with weathered rock behaves like soil and construction methods to cope with such conditions must be applied. With more cover the invert will be in unleached clay-sulphate rock which has swelling potential. The overburden over the base of the invert is 40 to 50 m, which corresponds to an overburden stress of about 1 MPa, which is slightly less than the swelling pressures. As discussed by Steiner (2007) high horizontal stresses may be present that give higher mean normal stress. The underground is naturally in a precarious equilibrium regarding swelling. Below the anhydrite line the rock mass is not swollen and in a meta stable condition.

The construction of a tunnel in this “limiting” equilibrium may trigger heave of the entire rock mass, as observed in several cases.

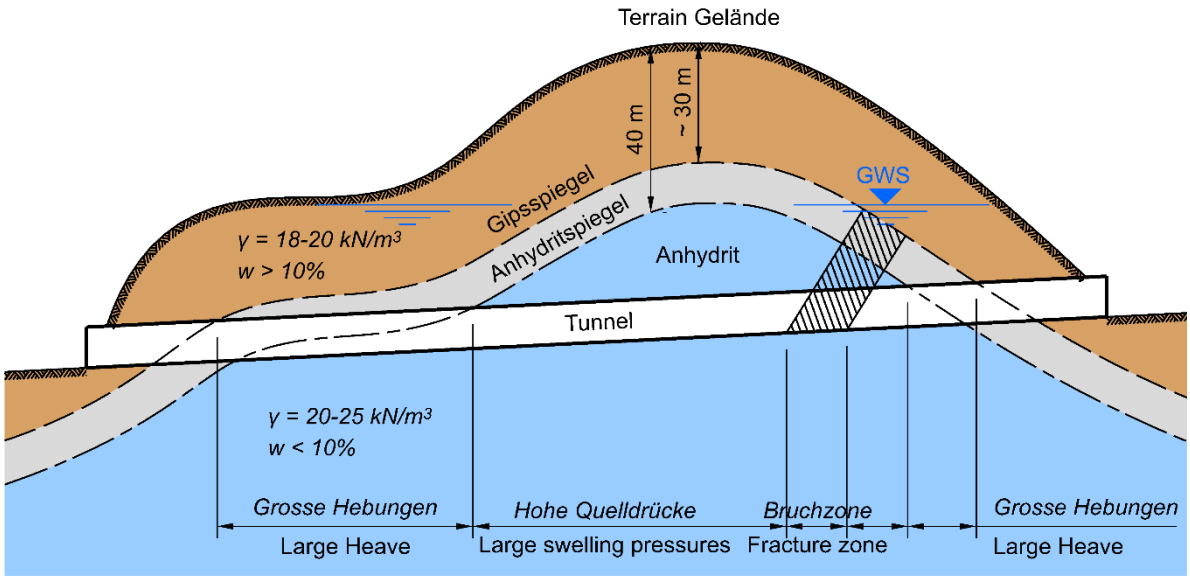

Fig. 12: Section across a hill (Mountain) made from clay-sulfate rock. On top is weathered rock, mainly soil like clay, this is about 30 to 40 m thick, limited by gypsum line. Another about 10 m follow with less weathered gypsum and clay. Anhydrite is essentially impervious, but the weathered rock above is pervious as are fracture zones and may be water bearing.

7.4 Selection of construction procedure

The stress state in the underground should be disturbed as little as possible. However, ground conditions may be variable and different excavation procedure may be required.

7.4.1 Excavation with a full face TBM

The experience from the Adler tunnel illustrates that with a TBM a single shield and segmental lining the ground may be supported safely. Problems may arise when the tunnel face my become unstable. The causes may be more discontinuous or jointed zones (Fault zones), the presence of water. These zones extend only over short sections of the tunnel, thus a closed face TBM is not the solution. The zone ahead of the tunnel be reached by borings, these could be drainage borings to drain the fractured zone, borings for placing fiberglass 1bolts or borings for grouting.

7.4.2 Excavation in mixed face conditions

In mixed face conditions with altered (leached) rock in the crown and swelling rock in the invert a procedure should be used that a near full-face excavation is possible. The use of long top headings followed by benching and excavation the invert should be avoided. With a moving platform near the face the invert may be constructed close to the face and the ring constructed shortly thereafter, Ring closure is possible at a short distance from the face

8 Literature

Alonso, E. E., Berdugo, I. R., Ramon, A.: Extreme expansive phenomena in anhydritic gypsiferous claystone: the case of Lilla tunnel. Géotechnique 63 (2013), No. 7, pp. 584–612.

Amann, F., Kaiser, P. K., Steiner, W.: Triggering swelling potential of anhydrite clay rocks by brittle failure processes. Eurock (2010), Lausanne, Switzerland, S. 339–342.

Amann, F., Ömer Ü., Löw S., Kaiser, P.: Fracture processes and in-situ fracture observation in Gipskeuper. Research contract ASTRA 2011/006 (2013), ASTRA Report No. 1422.

Amann, F., Ömer Ü., Kaiser, P. 2013. Crack initiation and Crack Propagation in Heterogeneous Sulfate-Rich Clay Rocks. Rock Mechanics and Rock Engineering, No. 10.

Chiaverio, F., Thut, A.: Chienberg Tunnel: Instandsetzung der Hebungsstrecke im Gipskeuper mit Knautschkörpern. Chienberg Tunnel: Rehabilitations using yielding elements of the section in Keuper sediments affected by heave. Geomechanics and Tunnelling 3, (2010) Nr.5, S. 573–582.

Chiaverio, F.; Püschner, U.R. Sixteen years of operation of a road tunnel in swelling rock – results of special measures. Sechzehn Jahre Betrieb eines Strassentunnels in Gipskeuper – Ergebnisse von Spezialmassnahmen. Geomechanics and Tunnelling 17, (2024) Nr.3, S. 111–124.

Chiaverio, F.: Chienberg Tunnel: Umfahrung Sissach: Tunnel im quellhaften Juragestein. SGBF, 145 (2002), S. 27–36.

Dauwe, L., Fröhlich, B.: Weinsberger Tunnel – Teilerneuerung eines alten Eisenbahntunnels in quellendem Gebirge. Mitt. Institut für Geotechnik TU Darmstadt 71 (2005), S. 71– 81.

Etterlin A. Herausgeber 1986, Sanierung des Hauenstein Basistunnels. Luzern, 117p.

Erdmann,P., Frenzl, R.,Buba, R., Berger, S., 2019, Engelbergbasistunnel: Ertüchtigung der Innenschale durch eine grundlegende Änderung der Lastableitung im quellenden Gbeirge – Vorversuche, bauliche und betriebstechnischen Optimierungen, STUVA_Tagung 2019, 148 – 152.

Fecker, E.: Untersuchungen von Schwellvorgängen und Erprobung von Auskleidungskonzepten beim Freudensteintunnel. Taschenbuch Tunnelbau, DGGT, Verlag Glückauf (1996), S.165–182. & Fecker & App U. 1992. TAE Esslingen, 21 p.

Gremminger, G., Spang, J.: (1978) Instandsetzung des Weinsbergertunnels, Eisenbahningenieur 29. 1.

G*rob, H.*: (1972), Schwelldruck im Belchen Tunnel. Int. Symposium on Underground Construction S. 99–119.

Grob, H.: (1976), Swelling and heave in Swiss tunnels. Bull. Int Assoc. Eng. Geology, 13 pp. 55–60.

Hauber,L., Jordan, P., Madsen, F., Nüesch, R., Vögtli, B. (2005).: Tonminerale und Sulfate als Ursachen für druckhaftes Verhalten von Gesteinen: Ursachen und Wirkungen des Quellvorganges. Forschungsauftrag ASTRA 1966/039 Bericht 1162, VSS Zürich.

Henke, K.F. Herausgeber: (1975), Durchführung eines felsmechanischen Grossversuchs in der Nordröhre des Wagenburgtunnels in Stuttgart. Forschungsbericht Nr. 184, Forschungsprogramm des Bundesverkehrsministeriums, Bonn 195 S.

Henke, K.F., Kaiser, W., Beiche, H. (1979)*:* Verhalten von Tunnelbauwerken in quellfähigen Schichten des Gipskeupers. 2. Nat. Tagung Ingenieurgeologie, DGEG, S. 135– 142.

Hofer, R., Chiaverio, F., Kovari, K. (2007): Chienberg Tunnel – Tunnel heave due to swelling. In German: Chienberg Tunnel Sissach – Tunnelhebung infolge Quellen. Proc. Swiss Tunnel Congress, S. 94–100.

Kaiser, P. K. with contributions by Amann, F. and Steiner, W.: (2010), How highly stressed brittle rock failure impacts tunnel design. Eurock Lausanne, Switzerland, S. 27–38.

Kanton Basel-Landschaft (2007) Pressemitteilung der Belchenkommission, Tiefbauamt des Kantons Basel-Landschaft, 25. Juni 2007.

Kirschke, D. (1996) Neue Versuchstechniken und Erkenntnisse zum Anhydritschwellen. Taschenbuch Tunnelbau, DGGT, Verlag Glückauf, S.203 – 225

Kirschke, D.: (2010), Lösungsansätze für den Tunnelbau in quell- und schwellfähigem Gebirge. Geomechanik und Tunnelbau 3 H. 5, S. 547–556.

Kovari, K.; Amstad, Ch. Anagnostou, G. (1987) Tunnelbau in quellfähigem Gebirge, Mitteillungen der Schweizerischen Gesellschaft für Boden und Felsmechanik, No. 115, pp. 19 - 26.

Krähenbühl, R.:2014 Geologischer Bericht Untersuchungen, mit Fokus auf Anhydrit führende Gesteine. Interner Bericht Bundesamt für Strassen, Bern, Schweiz.

Kurz, G., Spang J.: Instandsetzung und Erneuerung des Kappelesberg-Tunnels. Bautechnik 11 (1984), Berlin.

Lippmann, F.: Corrensite, a swelling clay mineral and its influence of floor heave in tunnels in the Keuper formation. Bull. Int Assoc. Eng. Geology 13 (1976), S. 65–70.

Lorenz, S., Dauwe, L., Fröhlich, B.: Teilerneuerung und Stadtbahnverkehr, Eisenbahningenieur 57 (2006), Nr. 5, S. 14–20.

Noher, H. P., Meyer, M., Zeh, R.M.: (2010) The anhydritic surface – cause of problems in tunnel constructions (new results based on measurements and observations). Eurock), Lausanne, Switzerland, Taylor & Francis, London, S. 343–346.

Noher, H.P., Vögtli, B., Kister, B.: 2006) Swelling – a geotechnical problem at the Adler Tunnel, Switzerland – monitoring results and their interpretation. Proc. Eurock Liège, Belgium.

Nüesch, R., Steiner, W., Madsen, F.: (1995) Long time swelling of anhydritic rock, mineralogical and microstructural evaluation. Proc. 8th Int. Conf. on Rock Mechanics, ISRM, Tokyo, Japan, pp. 133–138.

Nüesch, R. (1995) Laboratory investigation on clay sulphate rocks from the Hauenstein Basetunnel for the design of the Wisenberg tunnel, unpublished report of IGT-ETH for Swiss railways, in German. 69 pp.

Paul, A.; Wichter, L.: (1996), Das Langzeitverhalten von Tunnelbauten im quellenden Gebirge – Neuere Messergebnise vom Stuttgarter Wagenburgtunnel. Taschenbuch Tunnelbau, Glückauf S. 125–164.

Ramon, A., Alonso, E.E., Olivella, S, (2017) Hydro-chemo-mechanical modelling of tunnels in sulfated rocks, *Géotechnique 67,* No. 11, pp. 968 – 982.

Rauh, F.: Untersuchungen zum Quellverhalten von Anhydrit und Tongestein im Tunnelbau. Münchner Geowissenschaftliche Abhandlungen, Reibe B, 11, Verlag Friederich Pfeil, München, S.110.

Sambeth, U. (2024) Dimensions of Plate load device in the Adler Tunnel. Pers. Communication.

Schwalt, M., Steiner, W.: (2020), Behaviour of sulphate-bearing rock: lessons from the Gotschna and other tunnels. EUROCK Trondheim, Norway.

Stadt Stuttgart: Der Wagenburgtunnel in Stuttgart. 1957, 66 S.

Steiner, W. und Schwalt, M.: In situ swelling pressure in sulphate bearing rocks. Findings from field observations. Rock mechanics for Natural Resources and Infrastructure Development, ISBN 978-0-42284-4, ISRM Congress September 2019, Iguaçu (Brasil).

Steiner, W., Kaiser P. K., Spaun, G.: (2010), Role of brittle fracture on swelling behaviour evidence from Tunnelling case histories*.* Geomechanics and Tunnelling 3 H. 5, S. 583-596.

Steiner, W., Kaiser, P. K., Spaun, G.: (2011) Role of brittle fracture on swelling behaviour of weak rock tunnels: evidence from tunnelling case histories. Geomechanics and Tunnelling 4, Nr. 2, S. 141–156.

Steiner, W., Metzger, R.:(1988) Experience from tunnels in swelling rock. Projekt Wisenbergtunnel, Bahn 2000, Bericht an die Schweizerischen Bundesbahnen.

Steiner, W.; Madsen, F., Mathier, J.-F. (2023) Swelling pressures of clay rocks from laboratory tests: experience and improvements. Proc. 15th ISRM Congress and 72nd Geomechanics Colloquium, Salzburg, paper 1575.

Steiner, W.; Rossi P.P. and Devin, P.: (1989) Flat Jack Measurements in the Lining of the Hauenstein Tunnel as a Design Base for the New Wisenberg Tunnel. Proc. Int. Congress on Tunneling, Toronto.

Steiner, W.: (1989), Wisenbergtunnel, Bahn 2000. Tagung Juradurchquerungen, Délemont, SIA-FGU, Zürich D 037, S. 69–80.

Steiner, W.: (2020) Verhalten von Sulfatgestein im Tunnelbau: Erfahrungen aus Feldbeobachtungen und in-situ Quelldrücke; Sulphate bearing rocks in Tunnels: Lessons from field observations and in-situ swelling pressures. Geomechanics and Tunnelling 13, Nr.3, S. 286–301.

Steiner, W.:(1993) Swelling rock in tunnels: Characterization, effect of horizontal stresses and Construction Procedures. Int. Jour. of Rock Mech. and Min. Sci., 30, No. 4, pp. 361–380.

Werder, F.: (1989), Sanierungs- und Erneuerungsarbeiten im Belchentunnel. Tagung Juradurchquerungen, Délemont, SIA-FGU, D 037, Zürich, S. 53–57

Wichter, L.: (1989) Quellen anhydrithaltiger Tongesteine. Bautechnik 66.

Wichter, L.: (1991) Horizontal stresses in anhydriceous rocks, Proc. 7th ISRM, Aachen.

Wiesmann, E.: Der Bau des Hauenstein-Basistunnels. Kümmerly & Frey AG, Bern.

Wittke, M. (2020) Stuttgart 21 – 17 km Kilometres Tunnelling in Anhydrite: Lessons Learned. Tunnel 2020/2, 12 – 25.

Wittke, M., Wittke-Gattermann, P.: Tunnelbau im quellfähigen Gipskeuper. Geotechnik 33 (2010), S. 104–108.

Wittke, M., Wittke, P., Wahlen, R.: Möglichkeiten der Optimierung des Tunnelbaus in quellfähigem Gipskeuper durch Berücksichtigung der Selbstabdichtung. Geotechnik 30 (2007), Nr. 4, Essen, S. 247–255.

Wittke, W., Pierau, B.: Fundamentals for the design and construction of tunnels in swelling rock. Proc. 4th ISRM Conf., Montreux, Switzerland (1979), Vol. 2, S. 719–729.

Unexpected Phenomena in the 3D Modelling of a Segment-Lined Gallery during Undercutting at Skew Angle

Unerwartete Phänome bei der 3D-Modellierung der schiefwinkligen Unterfahrung eines tübbingverkleideten Stollens

Jörg-Martin Hohberg
IUB Engineering AG
Eigerhaus, Belpstraße 48, 3007 Bern / Schweiz

Abstract

In Switzerland, currently a flood relief tunnel is driven by TBM through the Zimmerberg Freshwater Molasse ridge separating the Sihl river from Lake Zurich to protect the city of Zurich against inundation by diverting 330-440 m^3/s of a 500-yrs. flood event into the lake. The future Zimmerberg Base Tunnel II to the city of Zug – part of the Gotthard northern approach line along Lake Zug – will cross this gallery at close distance and oblique angle.

The influence of this twin tunnel onto the segmental lining of the gallery – and vice versa any potential threat to the railway tunnel drive – was investigated in a large FEM model with the software ZSOIL. The paper discusses the unexpected twisting deformation of the gallery lining due to the skew crossing angle and the predicted continuing elastoplastic crown settlement in the railway twin tunnel, which appears to be artificial and due to the boundary conditions of the model.

Zusammenfassung

Zurzeit wird in der Schweiz mittels TBM durch die Obere Süßwassermolasse des Zimmerbergrückens ein Hochwasserentlastungsstollen vorgetrieben, um die Stadt Zürich gegen Überschwemmung zu schützen, indem 330-440 m^3/s eines HQ_{500}-Sihlhochwassers in den Zürichsee umgeleitet werden. Der zukünftige Zimmerbergbasistunnel II – Teil der Gotthard-Nordzulauflinie entlang des Zuger Sees – wird den Stollen in geringem Abstand schiefwinklig unterqueren.

Der Einfluß des zweiröhrigen Bahntunnel auf die Tübbingauskleidung des Stollens – und umgekehrt die Frage einer allfälligen Erschwernis des Vortriebs – wurde in einem großen FEM-Modell mit der Software ZSOIL abgeklärt. Der Beitrag diskutiert das unerwartete tordierende Deformationsverhalten des Stollens aufgrund der schiefwinkligen Kreuzung und die vorhergesagte anhaltende elastoplastische Firstsetzung in den Bahntunnelröhren, die artifizieller Natur ist und von den Randbedingungen des Modells abhängt.

1 Overall situation

1.1 The flood relief gallery Thalwil

Numerous towns in Switzerland were founded at the end of lakes, where the outflowing river provided energy for water mills. Quite often a second river, bypassing the lake, joins there and deposits stream sediments with ensuing risks of flooding the town. A proven concept of flood protection consists of diverting the mountain stream into the lake, which acts a buffer and smoothes the discharge peak, like that of the Kander into Lake Thun (1714) and the Aare-Handeck Canal into Lake Biel (1878).

The same concept is now being applied to the Sihl river, which flows under the main SBB railway station of Zurich into the Limmat river and threatens to flood large parts of the suburbs and Sitzerlands largest railway station (Fig. 1), similarly to what happened in Dresden in 2002. Moreover, for a hydropower station of the Swiss railways, in 1937 the artificial Sihl reservoir was created upstream, and if the earth dam were overtopped and eroded, the flood wave arriving at Zurich would be 8 m high.

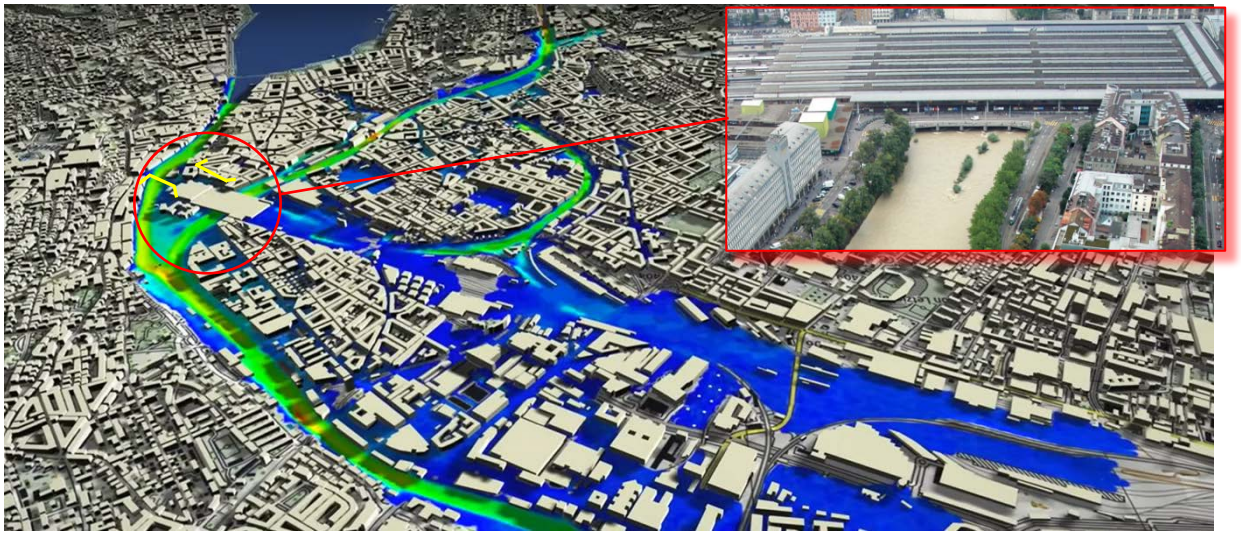

Fig. 1: Inundation of Zurich's quarters lying on the Alluvial fan of the Sihl river [1]; insert shows the Sihl water level at 300 m^3/s under the SBB railway terminal in 2005.

One option to improve the situation might have been to increase the discharge capacity of the Etzel hydropower station during its planned modernisation. But the Canton Zurich decided to go ahead with their own solution of a flood relief gallery for diverting about 50% of the 500-years flood (HQ_{500} = 600 m/s) into Lake Zurich (Fig. 2).

Fig. 2: Model view of Lake Zurich with the Sihl river, the penstock gallery of the existing Etzel hydropower station, and the new free-flow gallery at Thalwil [1].

The cross-section of the unpressurized gallery has been designed to ∅ 6.6-6.8 m with a functional specification of the hydraulic radius, leaving it to the building contractors to offer a precast segmental lining or in-situ shotcreting as alternative. The groundwater level is several meters above the crown with a very low permeability of the Upper Freshwater Molasse, apart from the possible presence of stress relaxation fissures.

The gradient of the 2.1 km long gallery is bilinear with 1.26 % in the upper part and 3.33 % in the lower part, with a pronounced kink at the anticipated under-passing of the future SBB railway tunnel (Fig. 3). The steep decline to the outlet structure at the shore of Lake Zurich requires a large covered tumbling box in the slope and a subsurface outlet into lake Zurich, to avoid currents endangering nearby swimmers and boats.

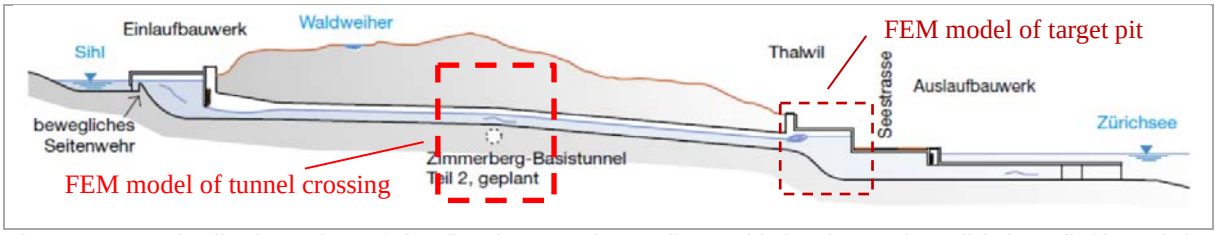

Fig. 3: Longitudinal section of the flood protection gallery with intake at the Sihl river (left) and the outlet structure at Lake Zurich (right).

The last few meters approaching the target pit, which is later to become the excavation for the tumbling box housing, the gallery is driven under the main SBB railway line Zurich – Chur. For the basic design a large 3D FEM model had been used to analyze the stability of the weathered rock layer between railway line and gallery crown, while slowly pulling the TBM out for dismantling (Fig 4). The horizontal schistosity of the Molasse rock was modelled as multilaminate material with a Mohr-Coulomb (M-C) matrix, capturing the strength anisotropy while neglecting the stiffness anisotropy. Rock anchors were modelled explicitly, reducing the rock strength parameters till failure.

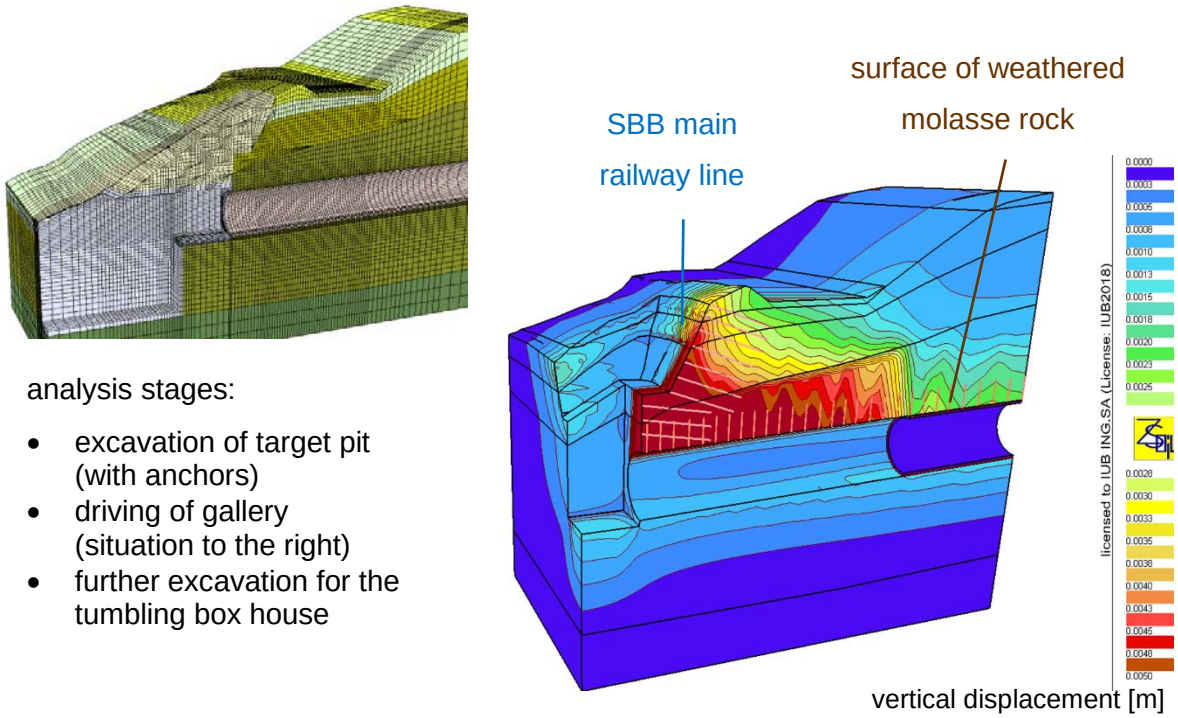

analysis stages:

- excavation of target pit (with anchors)
- driving of gallery (situation to the right)
- further excavation for the tumbling box house

Fig. 4: Symmetric FEM model of the target construction pit in Thalwil [2].

To mitigate the risk to the railway tracks, if the hauling of the TBM were delayed, a counter-drive protected by a pipe umbrella was chosen during detail design.

1.2 Crossing with the future Zimmerberg Base Tunnel II

The Swiss Federal Railways (SBB) plan for 2030/35 the construction of the “Zimmerberg Base Tunnel II” (ZBT II) between Zurich and Zug to further speed-up the train connection via the Gotthard base tunnel to Milano. For the approval process of the flood protection gallery, SBB demanded that the compatibility of the two projects be investigated from the rock mechanical point of view. It is to be assured that the later twin-tube railway tunnel underpassing the gallery would not cause settlement and subsequent leakage of the precast lining elements in the gallery. Nor must the ca. 8 m thick roof between tunnel and gallery become so fragmented as to potentially block the cutting wheel of the TBM. The envisaged angel of crossing is 48° (Fig. 5).

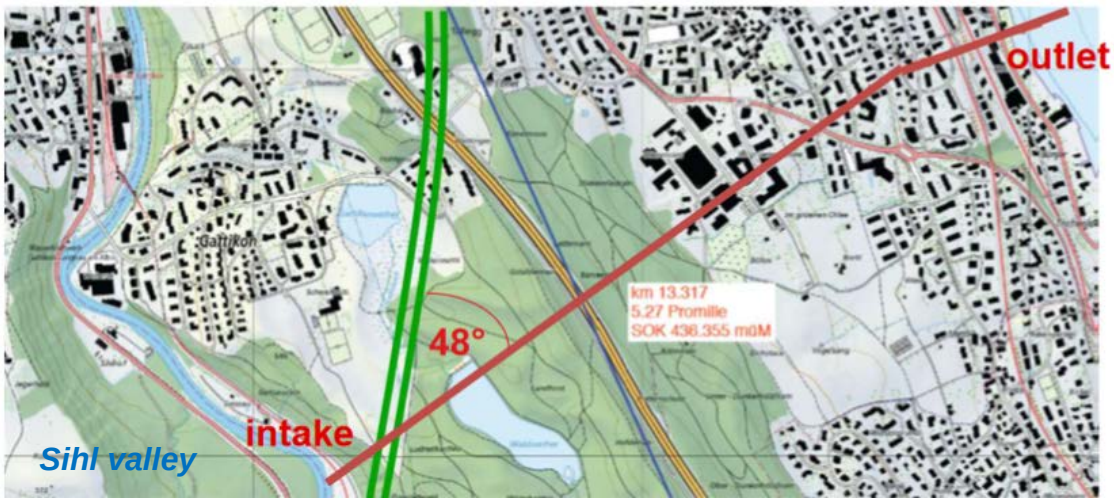

Fig. 5: Situation of the railway twin tunnel crossing the flood protection gallery

Compared to the preliminary assumption in 2017, the alignment of the railway tunnel was shifted more to the west towards the intake structure (Fig. 6). Because of the gallery's inclination with the intake as highest point, the vertical distance between gallery and railway tunnel is now larger than anticipated.

Fig. 6: The Sihl valley in spring 2023: cofferdam for building the intake structure; starting pit for TBM assembly, crossed by the provisional bridge for a local railway line; in the background to the right the existing driftwood rake at the outside bank [1].

Also, the overburden is less than at the maximum elevation of the Zimmerberg ridge (Fig. 4) for which the gallery had been dimensioned. The ground water in the dense Molasse rock is neglected and the gallery is assumed to be empty during the short period of driving the railway tubes underneath.

The initial state of interest is the one after completion of the flood relief gallery ("secondary stress state"). This depends on the primary stress state in the rock mass and on the simulation of the gallery construction sequences. Because of this rather lengthy preparatory computation it is good advice to thoroughly check the geometry, the gallery excavation and the installation of the segmental lining in a series of linear-elastic test runs (immediate convergence), before material nonlinearity is activated.

Since the objective of the study is to ascertain the behaviour of the gallery and the effect on the future railway tunnel drive, structural details of the railway tunnel lining are neglected and replaced by supporting pressure (generated from the excavated rock elements) for deformation control. Gradually reducing this support pressure yields characteristic deformation lines for selected observation points.

2 FEM model

2.1 Domain size, boundary conditions and mesh generation

The size of the modelled domain is chosen to 200 m of the gallery, a 70 m strip to either side, and 100 m in vertical direction (Fig. 7). The usual boundary conditions were applied, allowing for vertical sliding to activate the primary stress state due to self-weight and overburden load. The "settlement" due to gravity activates isotropic lateral pressures of $\sigma_H = K_0 \cdot \sigma_V$ according to the Poisson's ratio chosen.

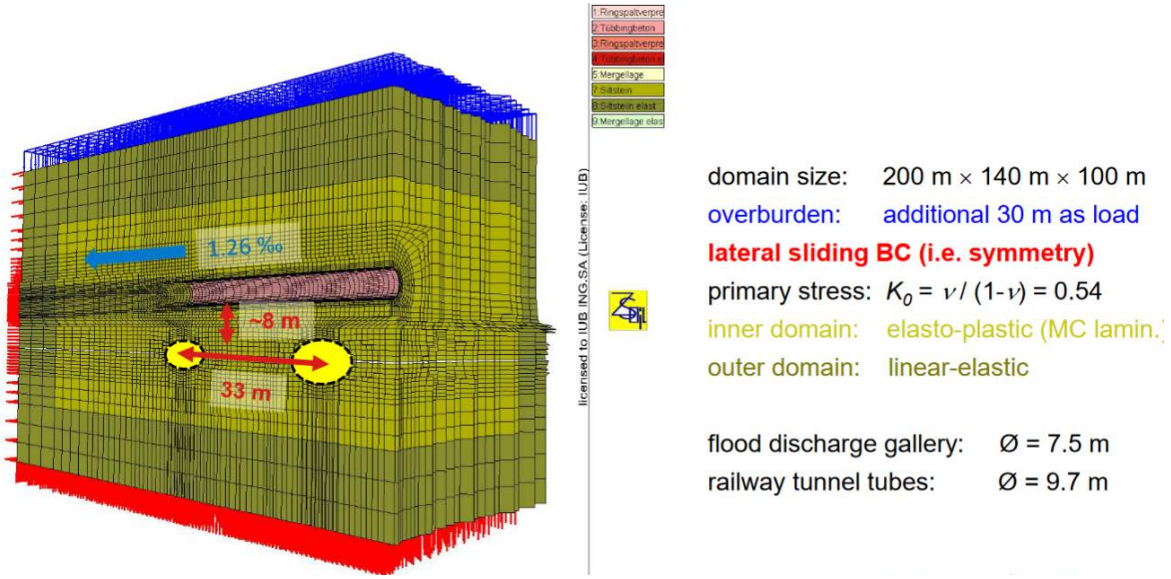

Fig. 7: Cut-away view of about 40% of the FE mesh, showing the inclined gallery with lining (pink) and the skew location of the future railway twin tunnel in the mesh.

The main challenge of the mesh generation are the differing extrusion directions of the upper and the lower part, and how to "glue" these two meshes. The software package ZSOIL offers global constraints for the purpose of blunt mesh refinement, i.e. tying a coarse far-field mesh to a fine near-field mesh. As no experience is available of how the interpolated node-to-face constraint formulation alters local stresses, it was decided not to apply this method in the rock roof between gallery and railway tunnel. The alternative is the use of a row of twisted macro elements (Fig. 8), which are later subdivided into finite elements ("real mesh").

It is known that twisting quadrilaterals does not affect the Jacobian matrix, linking strain interpolation to nodal displacements.

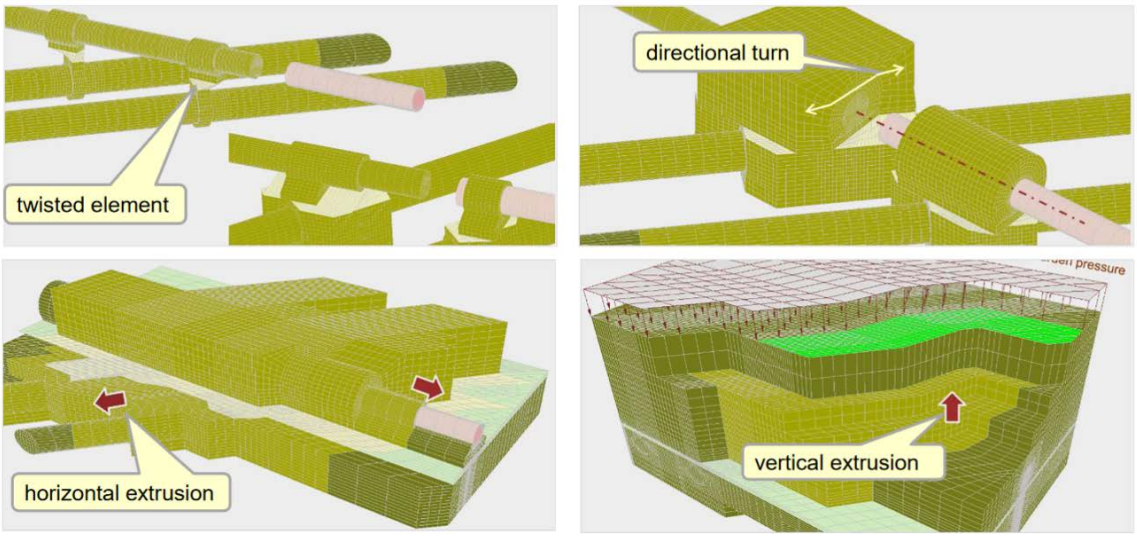

Fig. 8: Sequences of mesh building in the ZSOIL preprocessor, starting with twisted elements in the two connecting points, followed by individual horizontal extrusion of the upper and the lower near-field mesh and subsequent vertical extrusion.

The twisted macros appear in Fig. 8 in light colours. Twisting was done by drawing macro vertices to points of the opposite macro mesh and merging them before extrusion. Macro wedges were used to arrive at boundaries perpendicular to the global coordinate directions in which the boundary conditions are formulated.

Two problems were encountered: picking the extrusion vector from two points in the macro mesh may introduce errors in the 5th or 6th digit, which leads to non-negligible variations in coordinates over longer distances and requires repetitive drawing and merging of macro points. The second challenge is that generating a mesh inside-out makes it difficult to control the resulting total number of nodes and DOF. When the run times of the first meshing attempt turned out to be prohibitive – resulting in several minutes for each solving of the equation system – more errors creeped in during coarsening of the virtual mesh. Although merging is again done on the level of nodes after generating the “real mesh”, this cannot repair undetected incompatibilities in the virtual mesh.

Large mesh incompatibilities result in gapping element interfaces, severe stress jumps and very poor numerical convergence of equilibrium iterations. To a large part they become visible on the outside of the domain already in the primary stress state, but still require several mesh dissections to trace the origin of the problem. Smaller mesh incompatibilities also slow down the convergence somewhat and result in non-physical local stress concentration, but without invalidating the principal computational solution. If outside the zone of interest, they can be accepted unresolved.

2.2 Simulation of the gallery drive

From the experience with the 3D model of the target pit (Fig. 4) it was feared that starting the tunnel drive at the boundary in elastoplastic material may exhibit convergence problems due to the lacking restraint by the vertically sliding boundary and non-existent longitudinal arching from the tunnel face to the tunnel support. The far-field mesh, marked by darker colours in Fig. 7, was given elastic properties, which in hint-side was found to be overly prudent for relatively competent molasse rock.

This avoided integration point iterations in the far-field and allows to distinguish elastic from plastic contributions to cavity deformation. However, more iterations where required at the transition from the elastic to the elastoplastic material zone.

Two different sets of existence functions were defined for simulating the excavation and lining of the gallery (Fig. 9):

- Set 1 employed larger advancement steps over several macros (Fig. 9) by virtue of a supporting pressure on the excavation contour, diminishing with the distance to the tunnel face. Such spreading of the primary stress relaxation over some distance speeds up the numerical convergence [3].
- Set 2 adopts the alternative philosophy of complete relaxation during every excavation step, waiving the use of support pressure. This set was motivated by the fact that the annular gap around the TBM shield is going to be larger than the magnitude of deformations at the excavation contour.

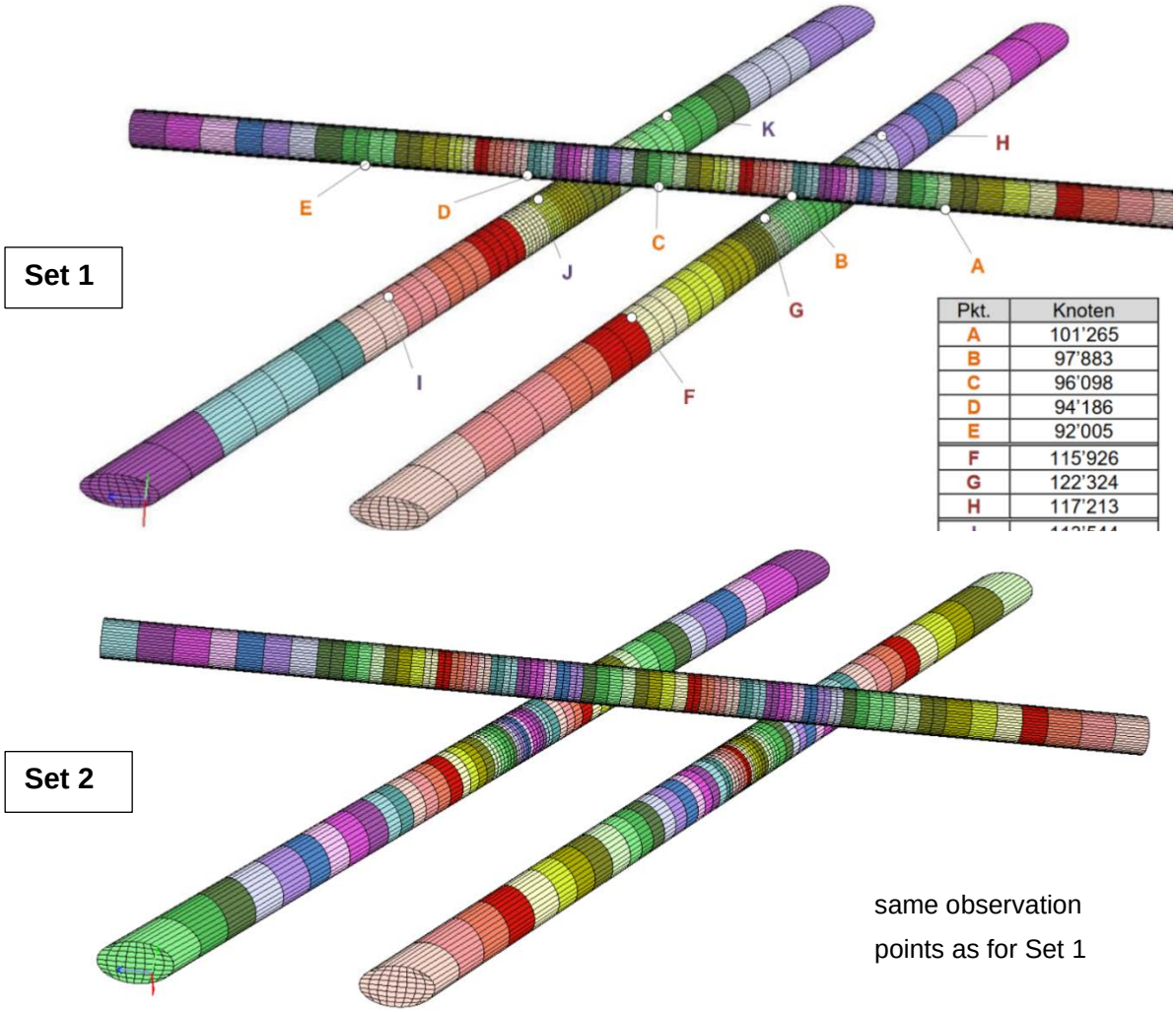

Fig. 9: Different existence functions, spanning several element groups (Set 1 with gradual stress relaxation) or just a single excavation step (Set 2 with immediate stress relaxation); the observation points are later used for time-history plots at selected stages.

For the railway tunnel it is assumed that the west tube (points F÷H) is driven first, and that the eastern drive (points I÷K) reaches the model domain after the western drive has left it. As the focus of attention lies on the two crossing points B/G and D/J, the excavation steps there are considerably smaller than near the domain edges.

The gallery lining is modelled with two continuum elements across the thickness of the lining and one continuum element for the annular ring.

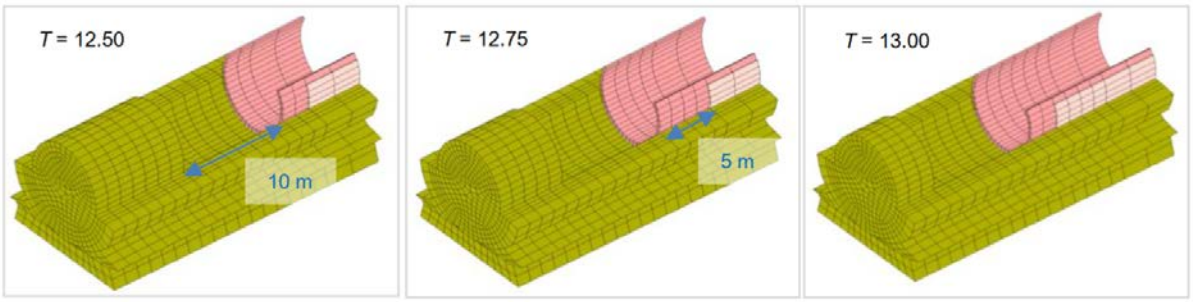

Fig. 10: Model of the lining installation, example: during the step T = 12.5 → 12.75 both the gallery face and lining front advance 2.5 m; during the step T = 12.75 → 13.00 both the gallery face and lining front advance another 2.5 m, the annular filling 5 m.

The first lining element is supposed to be placed 10 m and filling of the annular gap to occur 15 m behind the face. In each sub-step excavation and lining installation are advanced by 2.5 m, whereas every other step the annular filling is completed for 5 m (Fig. 10). Towards the more coarsely modelled far-field, several segments are combined in one step (see Fig. 9), increasing the computational step size to 5 m and 10 m.

During advancement the cross-section varies from the unstructured mesh of the rock core to the lining elements before and after filling of the annulus (Fig. 11).

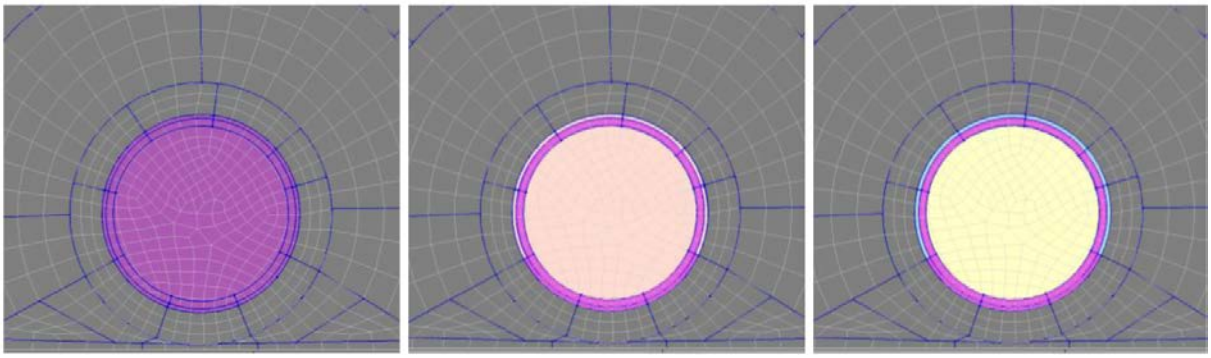

Fig. 11: Mesh change during gallery advancement (two meshes superimposed).

In circumferential direction the quadrilaterals were arranged according to the design length of the lining segments, with the idea that eventually interface elements might be inserted to account for opening and friction in the joints between segments.

2.3 Constitutive model

ZSOIL does not offer elastic anisotropy. For dimensioning of the lining in the basic project stage, the alternating layers of sandstone, siltstone and bedding joints with marl were approximated by an isotropic equivalent stiffness, accepting a certain overestimation of the horizontal ovalization of the lining. The present model, however, only considers the strength anisotropy by means of a multilaminate model with horizontal schistosity and employs for the rock matrix the low elastic modulus of siltstone:

Matrix:	E_r = 3.8 GPa, ν_r = 0.35;	φ_r = 46°, c_r = 2,500 kPa
Schistosity:		φ_r = 22°, c_r = 1.9 kPa

The constitutive model is Mohr-Coulomb with an additional plasticity criterion for the horizontal schistosity. The dilatancy angle was assumed to φ - 30°, i.e. zero in the schistosity. No tensile strength was assumed throughout.

The precast lining segments are delivered to site with their design strength. The fill of the annulus ring might be grouted, but the gradual hardening was neglected. Both the concrete lining and the annular fill are also given Mohr-Coulomb plasticity with zero tension cut-off to allow for plasticity in compression and shear:

Concrete:	E_c = 30 GPa, ν_c = 0.2; φ_c = 45°, c_c = 8.3 MPa
Grout injection:	E_g = 10 GPa, ν_g = 0.2; φ_g = 35°, c_g = 5.2 MPa
Pearl gravel:	E_f = 10 GPa, ν_f = 0.2; φ_f = 25°, c_f = 0 MPa

The M-C parameters were chosen to match 40 MPa uniaxial compressive strength for concrete and 20 MPa for the grout respectively, according to the formula:

$$\sigma_c = 2\, c \cdot \cos \varphi / (1 - \sin \varphi).$$

Due to Poisson's ratio under radial rock pressure the annular fill mostly experiences three-dimensional compression, such that the uniaxial strength does not govern the behaviour of the lining. For the same reason the difference in results between grout and pearl gravel was found to be marginal.

3 Results for immediate stress relaxation

3.1 Deformation behaviour

In earlier computations using an equivalent isotropic stiffness with only E_r = 1.5 GPa the elastic contribution was almost of the same magnitude as the nonlinearity resulting from the opening of the schistosity planes [3]. However, the total deformation was still too small to justify the assumption of a temporary support pressure exerted by the TBM shield ("Set 1"). This is why the assumption of a brittle response with immediate stress relaxation and shorter excavation distances ("Set 2") was preferred.

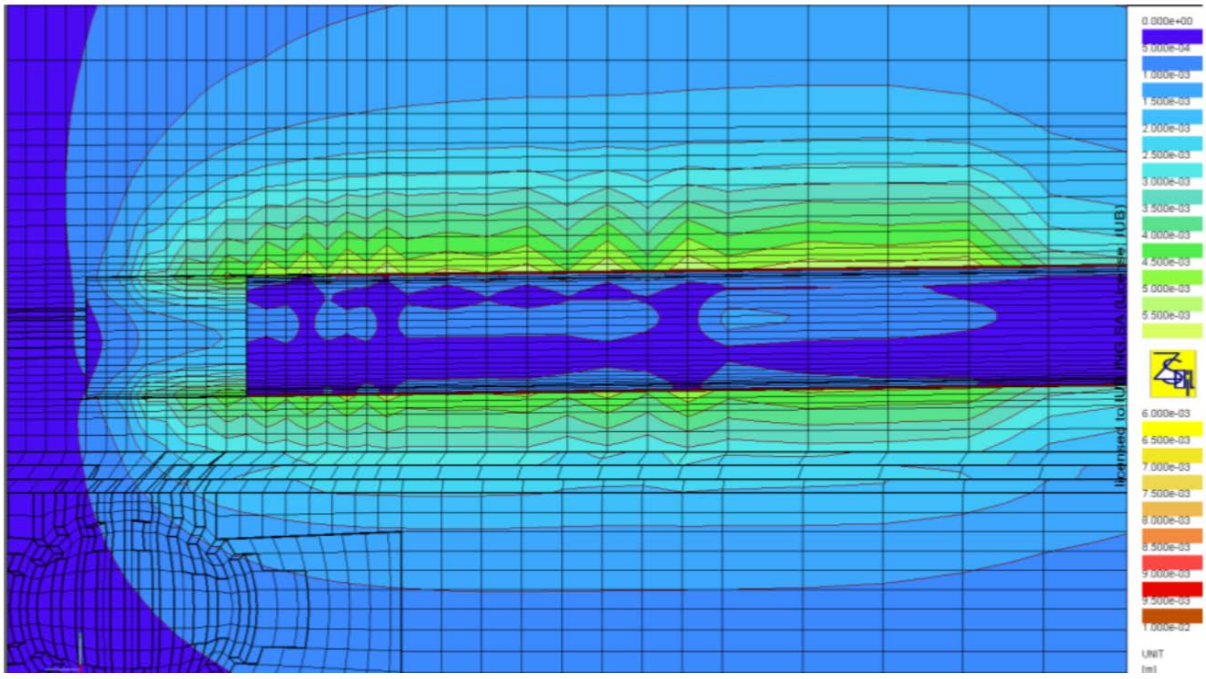

Fig. 12: Absolute vertical displacements behind the gallery face [range 0…10 mm].

The effect of the schistosity planes opening up becomes apparent in the unsupported space between excavation face (extreme left) and lining, with only a minor increase over the distance where the annulus has not yet been grouted (Fig. 12). The total deformation amounts to about 6 mm, with an elastic contribution of about 3 mm. Note that the floor heaves slightly less than the crown settles.

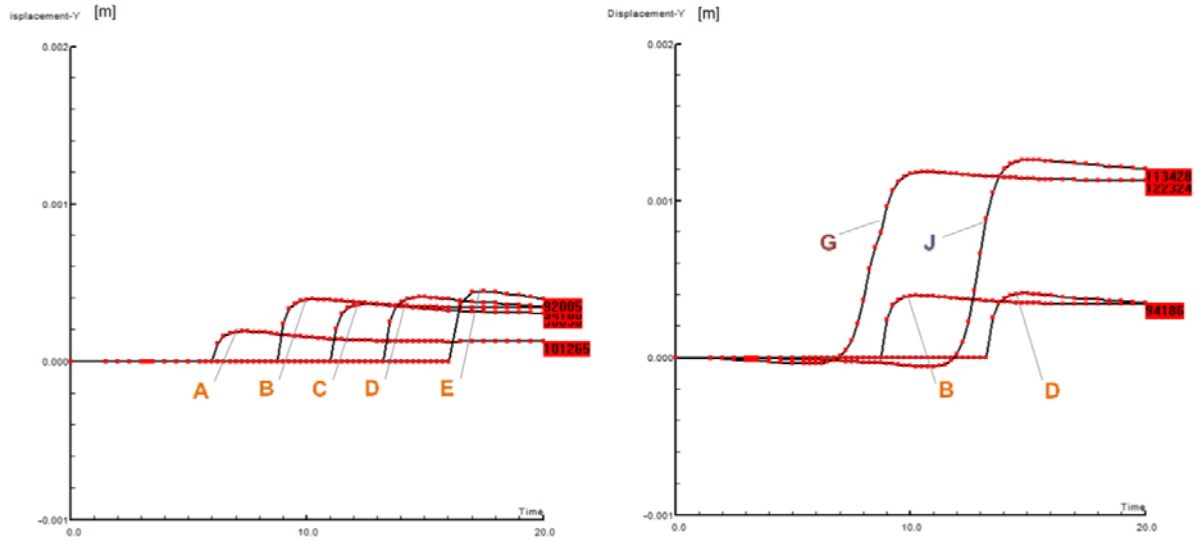

Fig. 13: Vertical displacement history during gallery drive [range 0…2 mm till T=20].

The history plots of the observation points reveal two more features (Fig. 13):

- The points A÷E show correctly first a heave of the invert due to buoyancy, which is subsequently reduced by the vertical stress transmitted through the grouted lining. The deformation is unsymmetric, with point A showing the smallest and point E the largest amount. Since the points are situated at the concrete invert, no deformation is indicated before placing of the lining, i.e. the overall settlement has already progressed when the points B and following spring into life.
- The points G and J, situated in the deeper rock below the gallery, experience the heave even before the excavation face. The much larger magnitude is partly due to this earlier start of accumulating displacements, partly because of the smaller stiffening effect of the concrete lining at that depth.

Thus, the railway tunnel tubes are excavated in a ground which has experienced heave before. Therefore, one must distinguish between total displacements and those relative to the finished flood protection gallery ("secondary initial state").[1]

[1] *While the software sets diplacements due to primary gravity loading automatically to zero, those accumulated during excavation of the gallery must explicitely be declared as reference state in the postprocessing, if relative stresses are to be evaluated.*

The difference becomes apparent in the following comparison of the final state after complete excavation of the railway twin tunnel (Fig. 14):

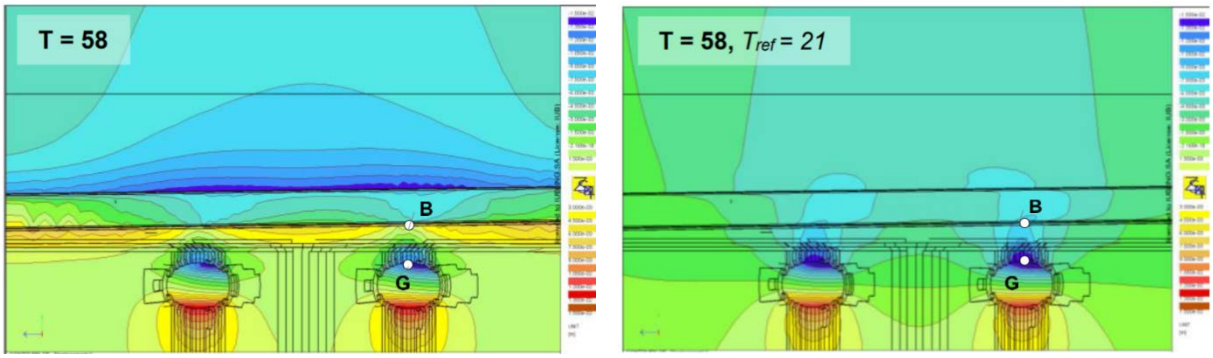

Fig. 14: Displacement pattern at the end of computation [range -15…+15 mm]: in total displacements with overall sagging caused by the gallery excavation (left) and in relative displacements with local sagging above the crown of each tunnel tube (right); relative displacements of the points B and G are larger, since the prior heave is deducted.

The history plots can merely show total displacements. Continuing the plot in Fig. 13 for T > 21 with drive of the railway twin tunnel, a strange phenomenon becomes apparent (Fig 15): The settlement, so-to-speak, continues long after the tunnel face has passed the point of observation, and this is happening to all points.

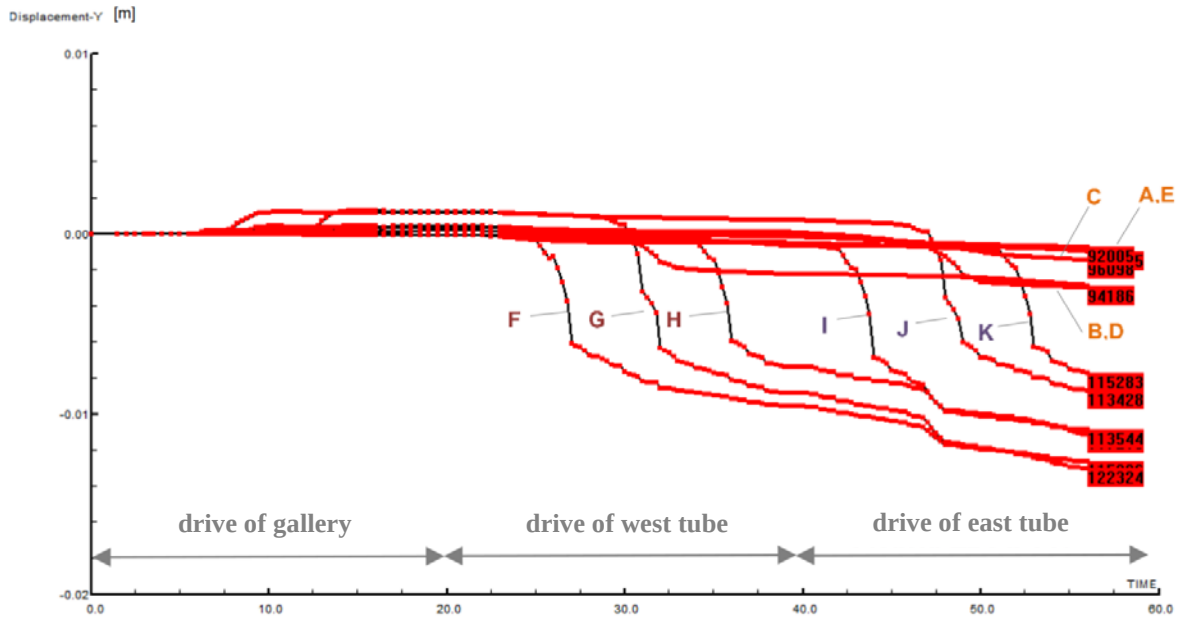

Fig. 15: Vertical displacement history for the complete computation [range -20…+10 mm till T=60].

This can also be observed in a cut-away plot of the western crossing point (Fig. 16): after the drive of the west tube has left the modeled domain (T = 38), the downwards displacement of the crown in the west tube increases further while the east tube is driven (till T = 50). Apparently, the entire domain undergoes a settlement as more and more cavities are created.

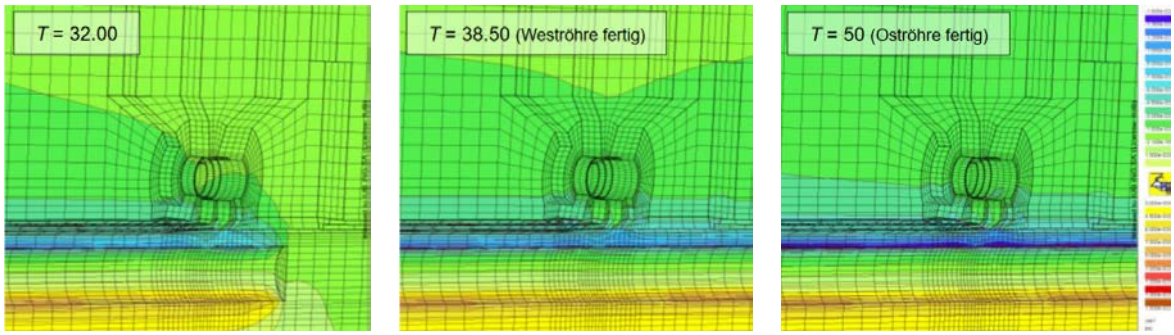

Fig. 16: Continuing relative crown displacement with further excavation [range -15…+15 mm].

4 Stress and strain patterns

Stresses are plotted as total stresses accumulated since the primary stress state for assessing the present degree of nonlinearity. As plausibility check, total strains may also be of interest, and relative strains might indicate plastic loading or unloading.

Of particular interest is the moment when the drive of the railway tunnel approaches the crossing point. As seen in Fig. 17, the maximum additional loading is reached some distance behind the tunnel face, when the 3D supporting effect has subsided. This is expected, but obviously the excavation of the second tube causes an additional loading on the first tube through an elastic coupling, confer step T = 54. Regarding mesh quality it is reassuring to see that the twisting of elements between the gallery and the tunnel does not appear to disturb the stress and strain fields (T = 29 and 31 resp.).

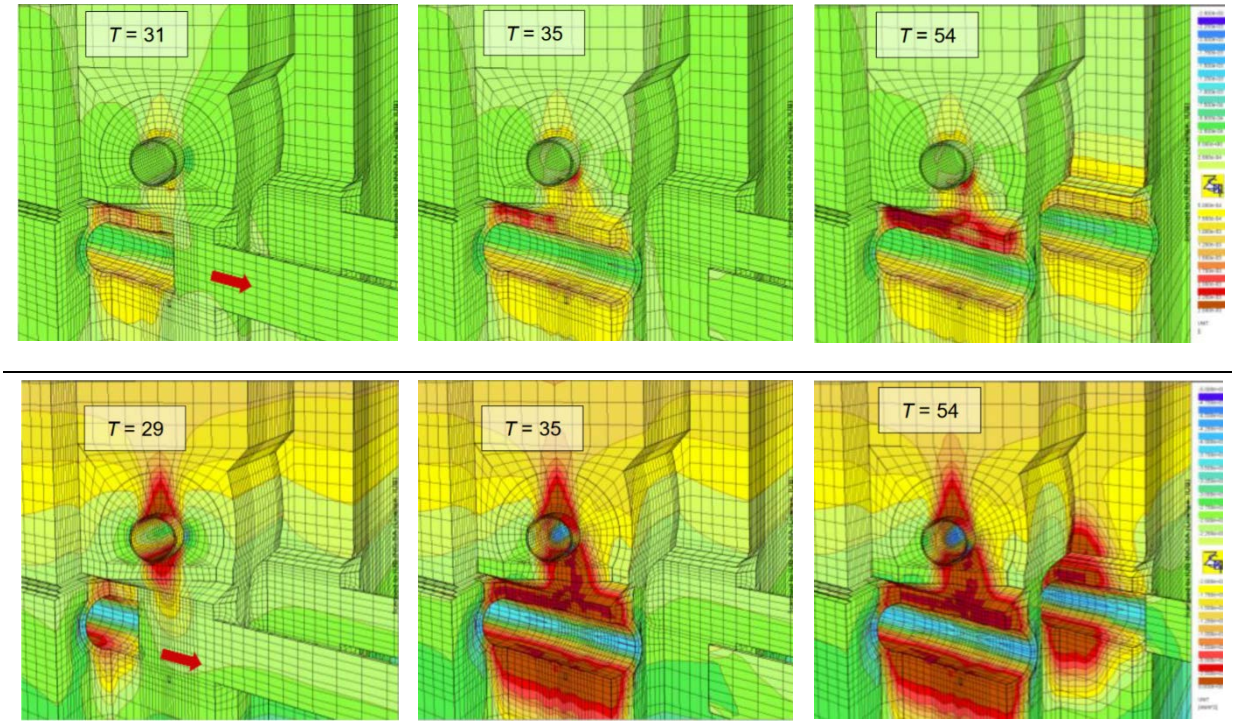

Fig. 17: The west tube of the railway tunnel crossing the flood relief gallery: vertical strain [range -2.5…+2.5 mm/m] (top) and vertical stress [range -5…0 MPa] (bottom).

To search deeper for the reason of this interaction between the two tubes of the twin tunnel, the *relative* vertical and volumetric strains are looked at more closely in Fig. 18. This was done with factorized rock properties by γ_φ = 1.3 and γ_c = 1.5, in order to ascertain that even with strength reduced to design level the roof above the railway tunnel remains stable.

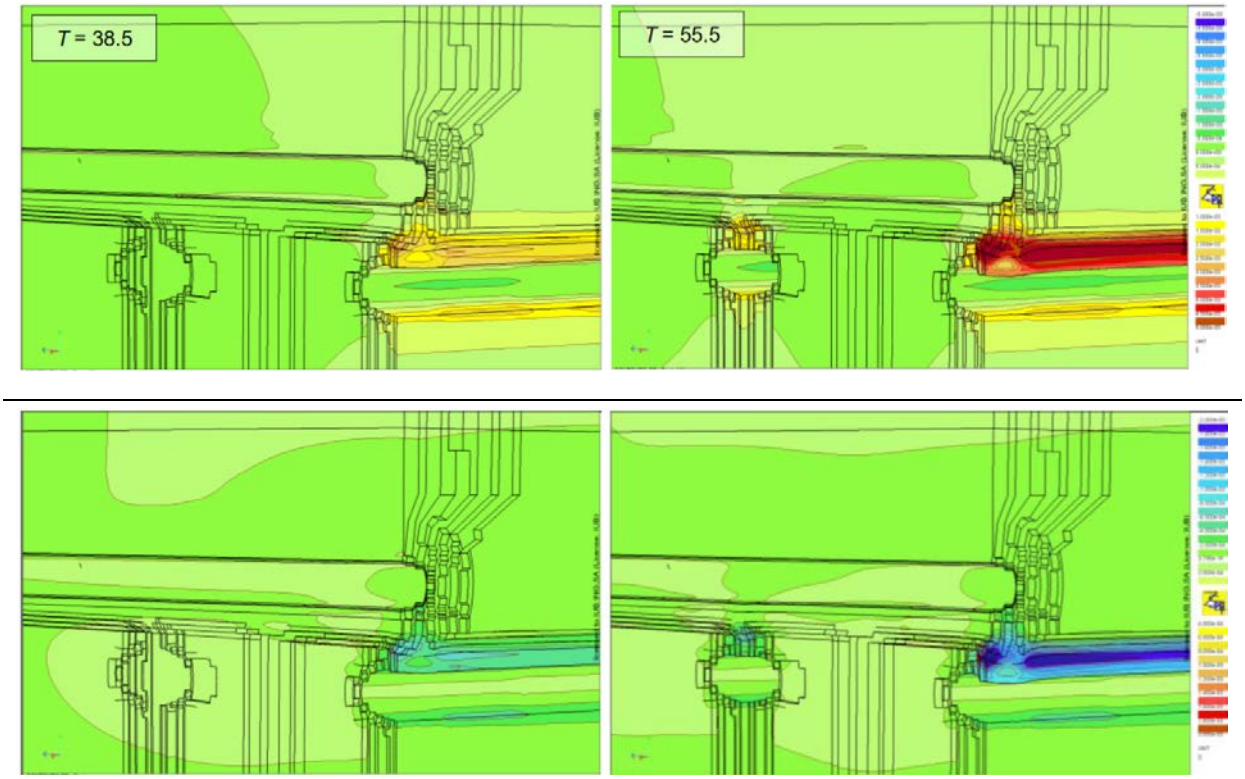

Fig. 18: Relative vertical strain and stress since completion of the gallery: at T = 38.5, when the west tube has left the domain (left), and at T = 55.5, when the east tube has left the domain; vertical strain [range -5…+5 mm/m] (top) and vertical stress [range -2.5…+2.5 MPa] (bottom); strength at design level, deformed mesh.

The excavation of the west tube doubles the vertical strain change in the crown of the east tube, whereas the invert is not affected at all. With characteristic strength parameters the elastic deformation dominates, leading almost point-symmetric behaviour of the railway tunnel around the center of the modelled domain. However, with strength parameters reduced to design level, the plastic part of the crown deformations becomes more apparent and was found to be path-dependent, e.g. it matters to the west tube in which direction the east tube is driven (whether a second TBM follows in some distance, or by turning the TBM after completion of the west tube). Of course, early lining installation and backfill in the railway tunnel will suppress this effect.

Searching for an explanation as to why an elastic coupling can aggravate the opening of the schistosity in the crown of a previously excavated cavity, the answer is found in the change of confinement pressure (Fig. 19): In large magnification of the stress scale one can detect that the drive of the east tube leads to a small change in the stress pattern around the existing west tube, compressive at the walls but decompressive at the crown and invert.

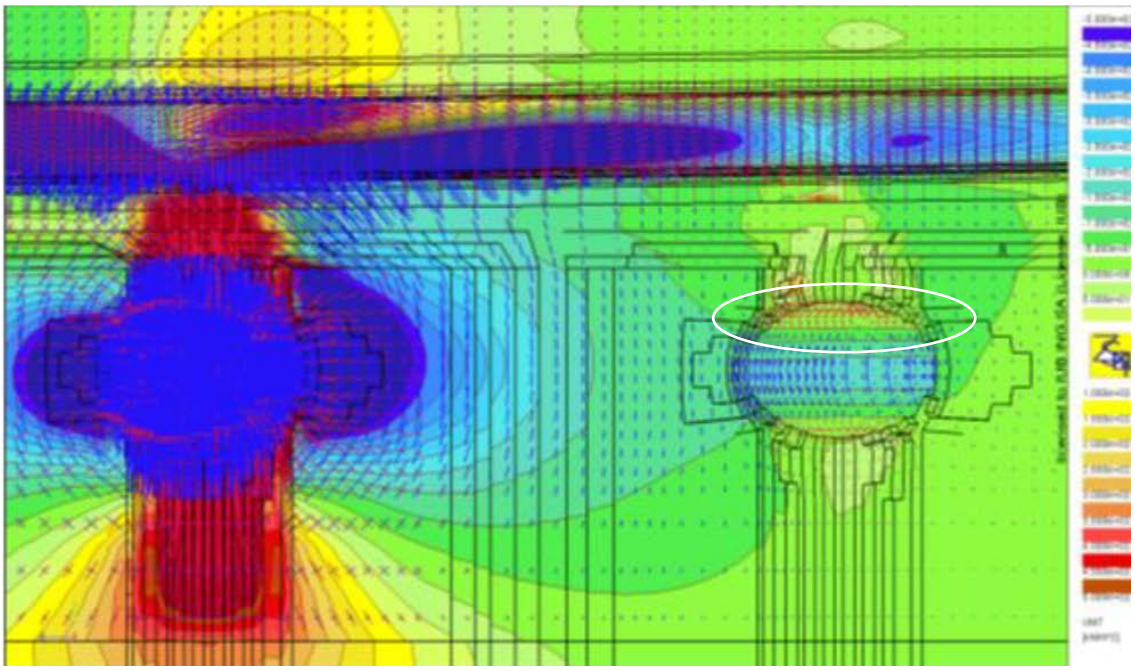

Fig. 19: Stress change due to excavation of east tunnel (left) with small elastic effects on the stress state at the existing west tube (stress increments in red indicating decompression); colour contours are that of vertical stress change [range -500…+500 kPa].

5 Influence of boundary conditions

5.1 Settlement of the entire domain

The vertically sliding «roller» boundary conditions (Fig. 7) are necessary to activate the primary stresses due to selfweight.[2] If they are not blocked lateron, it is clear that progressing underground excavation leads to additional compression in the rock pillars between cavities and, consequently, to additional settlement governed by the elastic modulus. This is demonstrated in Fig. 20 for the case of the rather low equivalent modulus of the molasse rock (E_r = 1.5 GPa). The deformations at the domain faces are smaller due the elastically assumed material behaviour in the far field.

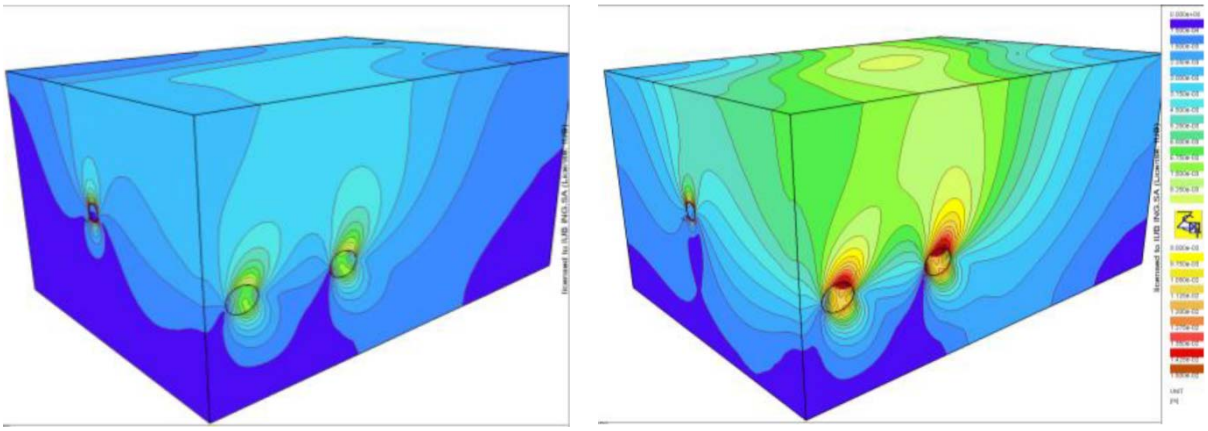

Fig. 20: Total absolute displacement for the equivalent molasse modulus [range 0…15 mm] due to excavation of gallery and railway tunnel with 40% support pressure (left); increase due to reduction of the support pressure in the railway tunnel to 0% (right).

[2] As an alternative with rigid boundaries on all domain faces, the primary stresses would need to be defined as imposed initial stress field with three spatial components and a depth-dependent gradient.

Not considered was the fact that vertical roller bearings are also a symmetry condition! Hence, when starting the drive of a tunnel at the face of the modelled domain in a direction pointing inwards, a virtual second «mirror» drive is started pointing outwards. The maximum displacement occurs in principle at the mirror plane (Fig 21); but in the present case this was somewhat disguised by limiting plasticity to the near-field domain.

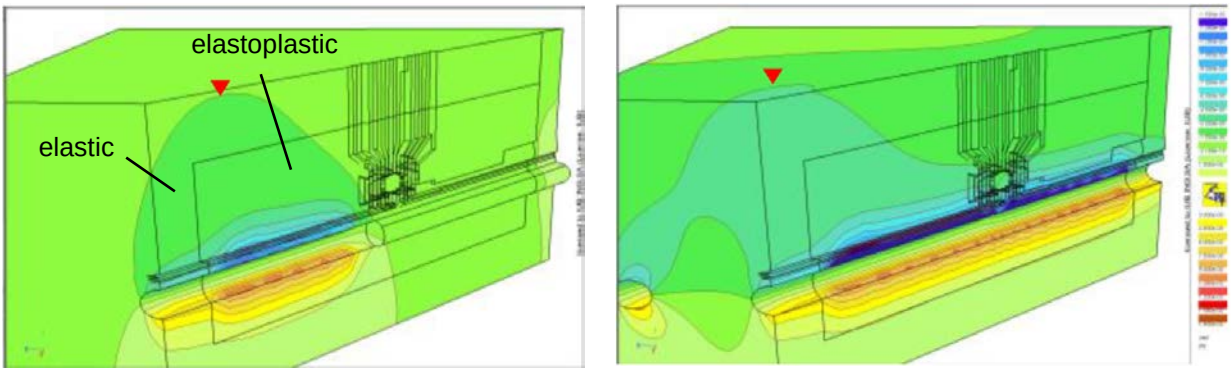

Fig. 21: Relative vertical displacement due to driving the railway tunnel: west tube driven half-way through (left), both tubes completed unsupported (right) [range -15 …+15 mm]; no vertical restraint at the lateral domain boundaries («roller bearings»).

This unwelcome effect can be moderated by adding infinite boundary elements, which act as external shear beams. Depending on the shear stiffness, the vertical restraint at the lateral faces of the domain can be varied from complete sliding to complete fixity. Infinite elements also reduce the deformation magnitude in the interior of the domain, reducing the elastic coupling between the east and the west tube of the railway tunnel.

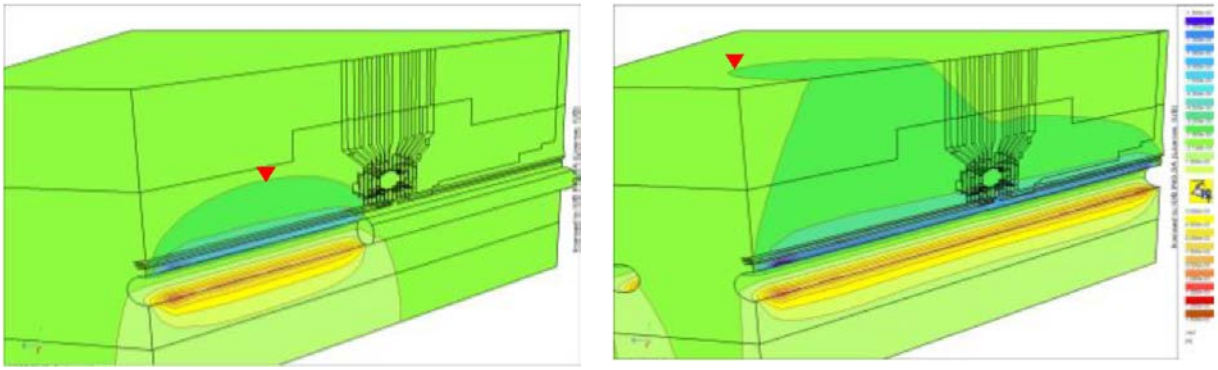

Fig. 22: Same as Fig. 21, but with infinite elements added to the outside faces of the domain [range -15…+15 mm]; silt stiffness with immediate stress relaxation (Set 2).

6 Handling of infinite elements

The infinite elements are connected to all outside faces of the FE mesh (Fig. 23) and fixed on their remote side.

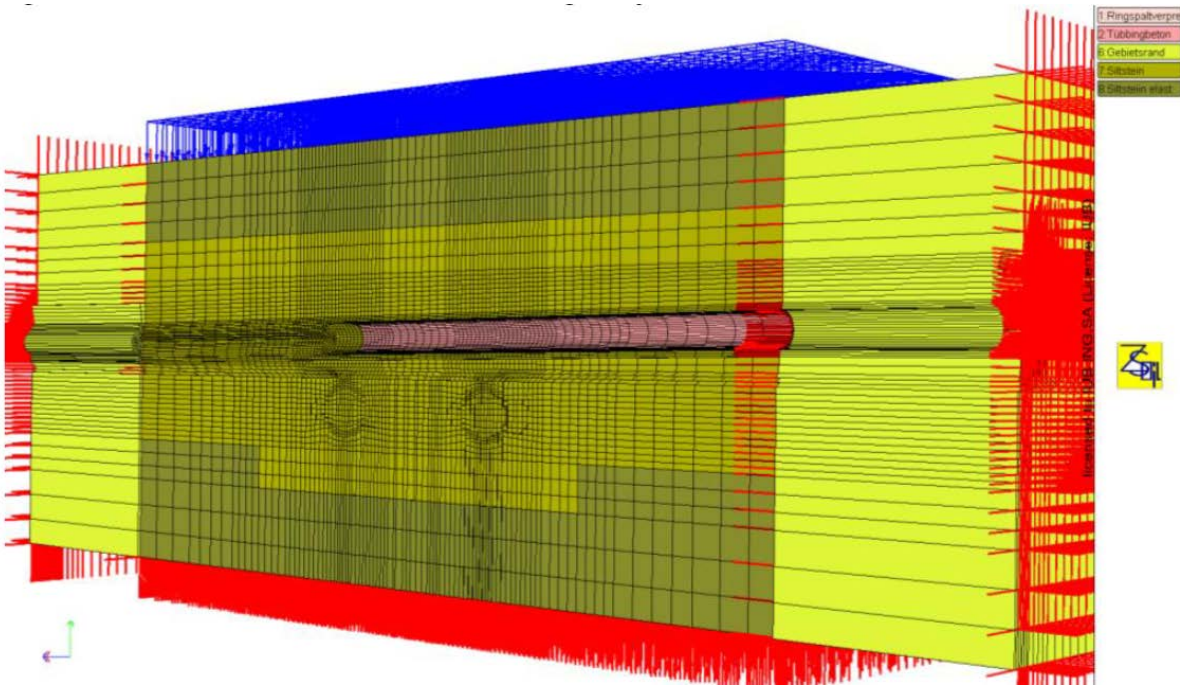

Fig. 23: View of the FE mesh with added infinite elements (in yellow), longitudinal section in the center plane through the flood protection gallery (lining in pink).

The elastoplastic material model can be extended sidewards to the boundaries, as the infinite elements provide enough stabilization at the beginning of the tunnel drive. Important is that the infinite elements are defined inactive during the computation of the primary stress due to gravity and activated after nullifying the initial displacements.

7 Behaviour of the segmental lining

7.1 Effects of the skew crossing with the railway tunnel

When the tunnel drive approaches the gallery, the thicker pillar in the obtuse angle is stiffer and takes more additional load than the pillar in the acute angle. This becomes apparent in the more deformable rock with E_r = 1.5 GPa. By gradually reducing the support pressure in the railway tunnel, the loosening in the tunnel roof progresses toward the obtuse angle (Fig. 24).

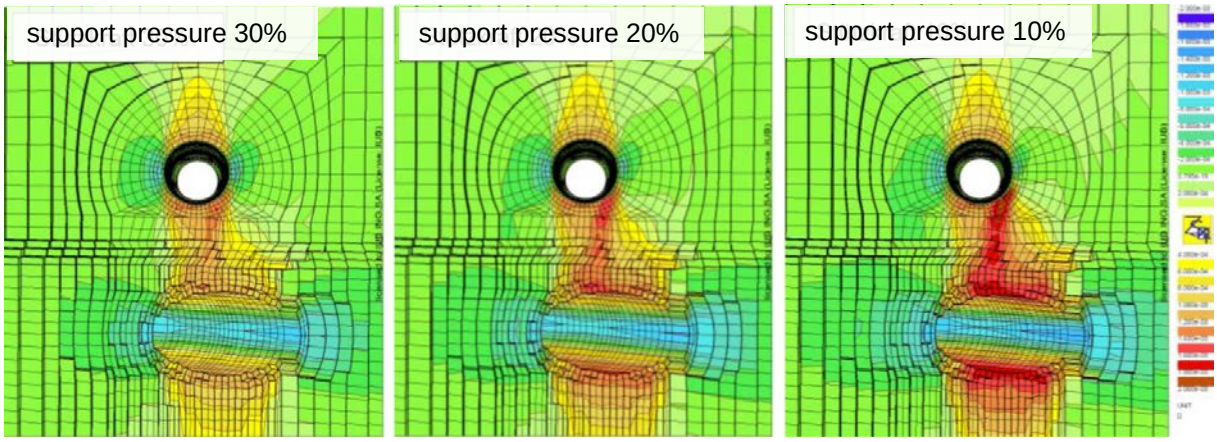

Fig. 24: Development of vertical strain with reduced support pressure [range -2…+2 mm/m].

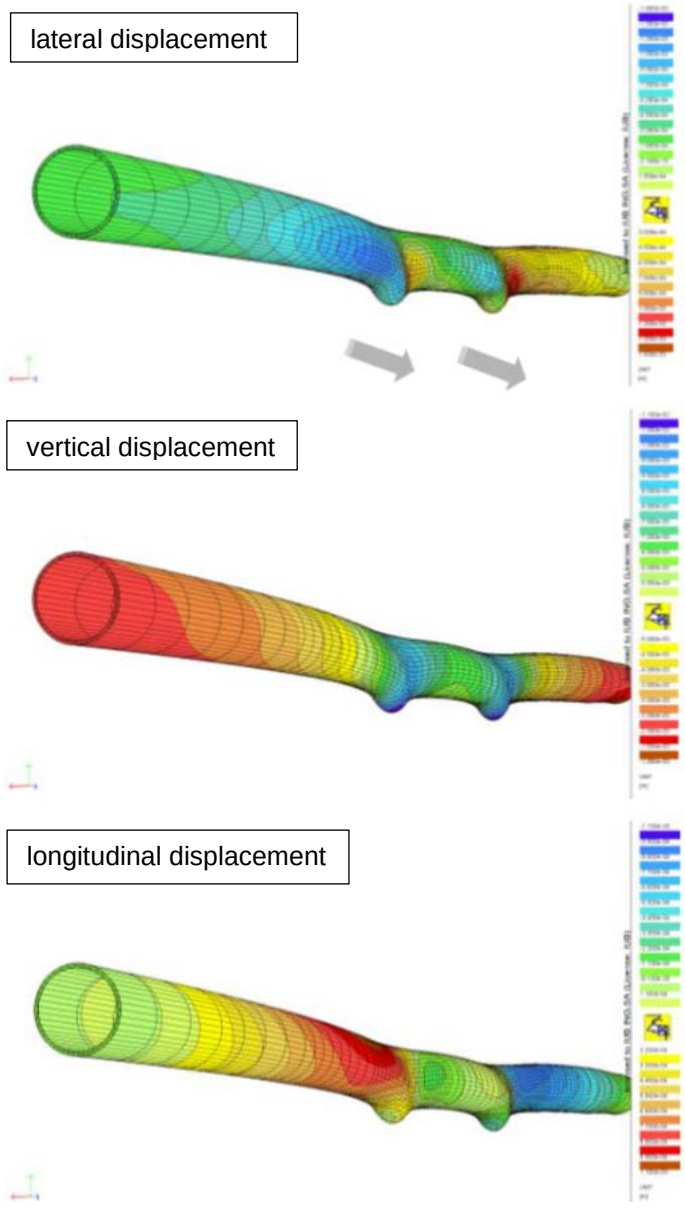

Fig. 25 Distorsion of the gallery lining (soft ground).

As a result of the skew crossing the gallery experiences a peculiar twisting, in which the lining in the acute angle moves laterally forward, in the obtuse angle backwards, with different magnitude above the west tube and the east tube. The vertical displacements are also unsymmetric, with slight heave in the acute angle and sagging in the obtuse angle. In longitudinal direction, the tube reacts with extension in front of the west tube and compression behind the east tube. Immediately above the crossing, as expected, the deformed mesh exhibits a pronounced downwards movement of equal amount.

It should be noted that the deformation of the segmental lining is not elastic but with a no-tension Rankine criterion to curb tensile stresses. Whether the joints between segments open up, depends on both the longitudinal prestress – which, in turn, is determined by the radial pressure exerted by the relaxing rock in combination with Poisson's effect in the lining – and the local bending due to sagging immediately above the railway twin tunnel. All plots for Set 1 (E_r = 1.5 GPa).

7.2 Stresses in the gallery lining

As just explained, the stress level in the lining is lower in stiff ground (silt model), with less prestress in the longitudinal joints but also smaller sagging of the invert (Fig. 26).

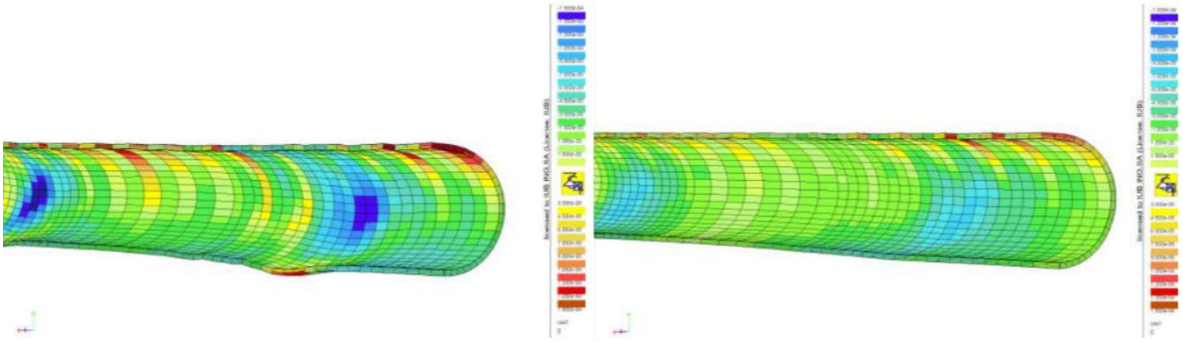

Fig. 26: Total longitudinal strain (i.e. incl. construction of the gallery) for the soft molasse model (Set 1, left) and the stiffer silt model (Set 2, right) [range -0.15…+0.15 mm/m].

The local sagging leads to inclined principal stresses, of which any tensile component is cancelled by the no-tension criterion. The inclined compression field bridges the local weakness of the ground support caused by the railway tunnel below. Because of the skew angle, the pattern of principal stress is unsymmetric (Fig. 27).

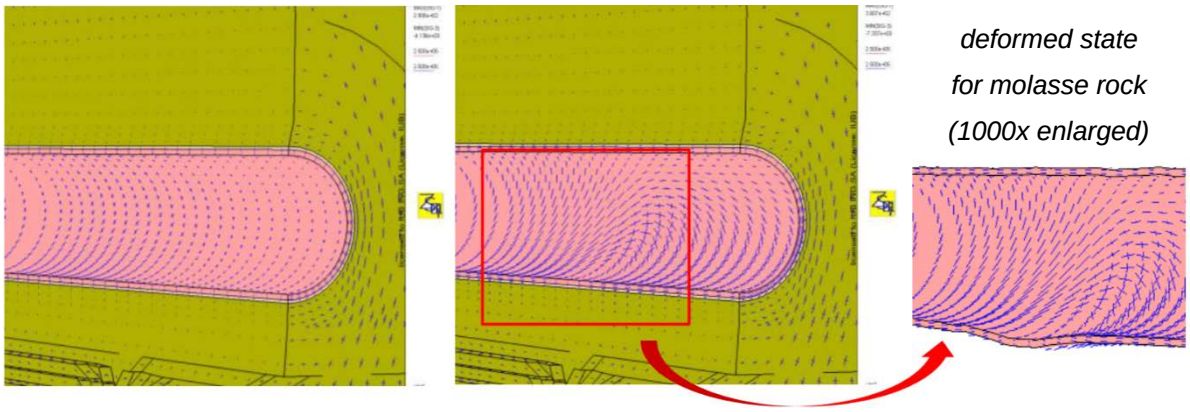

Fig. 27: Crosses of principal stress after completion of the gallery (left) and after driving the west tube of the railway tunnel (right).

Plotting the longitudinal and the circumferential stress magnitudes in the deformed mesh, together with the crosses of principle stresses, illustrates the torsional stress trajectories around the crossing points (Fig. 28). Actually, the bending is twofold: ovalization of the lining ring due to difference between vertical and horizontal rock pressure (over the entire length of the gallery), and the effect of local bending in two directions due to sagging of the lining at the crossing points.

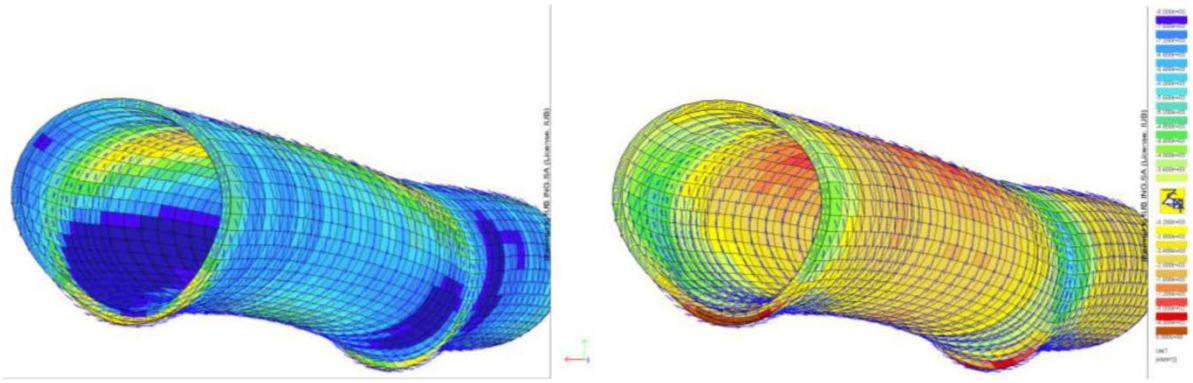

Fig. 28: Circumferential stress (left) and longitudinal stress (right) for soft molasse rock (Set 1) [range -8…0 MPa], deformed mesh 400x enlarged.

With just two continuum elements across the lining thickness, the bending stresses are in effect stress couples from the inner and the outer lining elements. To check lining for flexural opening across the wall thickness, the averaging of stresses across element boundaries need be switched off.

Taking the maximum principal stress σ_3 for the circumferential stress, immediately after completion of the gallery (T = 21) the stress increase at the sides of the gallery and the ear-shaped plastic zones due to shear can be identified (Fig. 29 top left). The longitudinal stress shows the relaxation above and below the gallery (Fig. 29 top right), which is that of the vertical stress multiplied by the Poisson's number of the rock. The concrete stresses in the liner are quite even across the liner thickness and do hardly exhibit any bending.

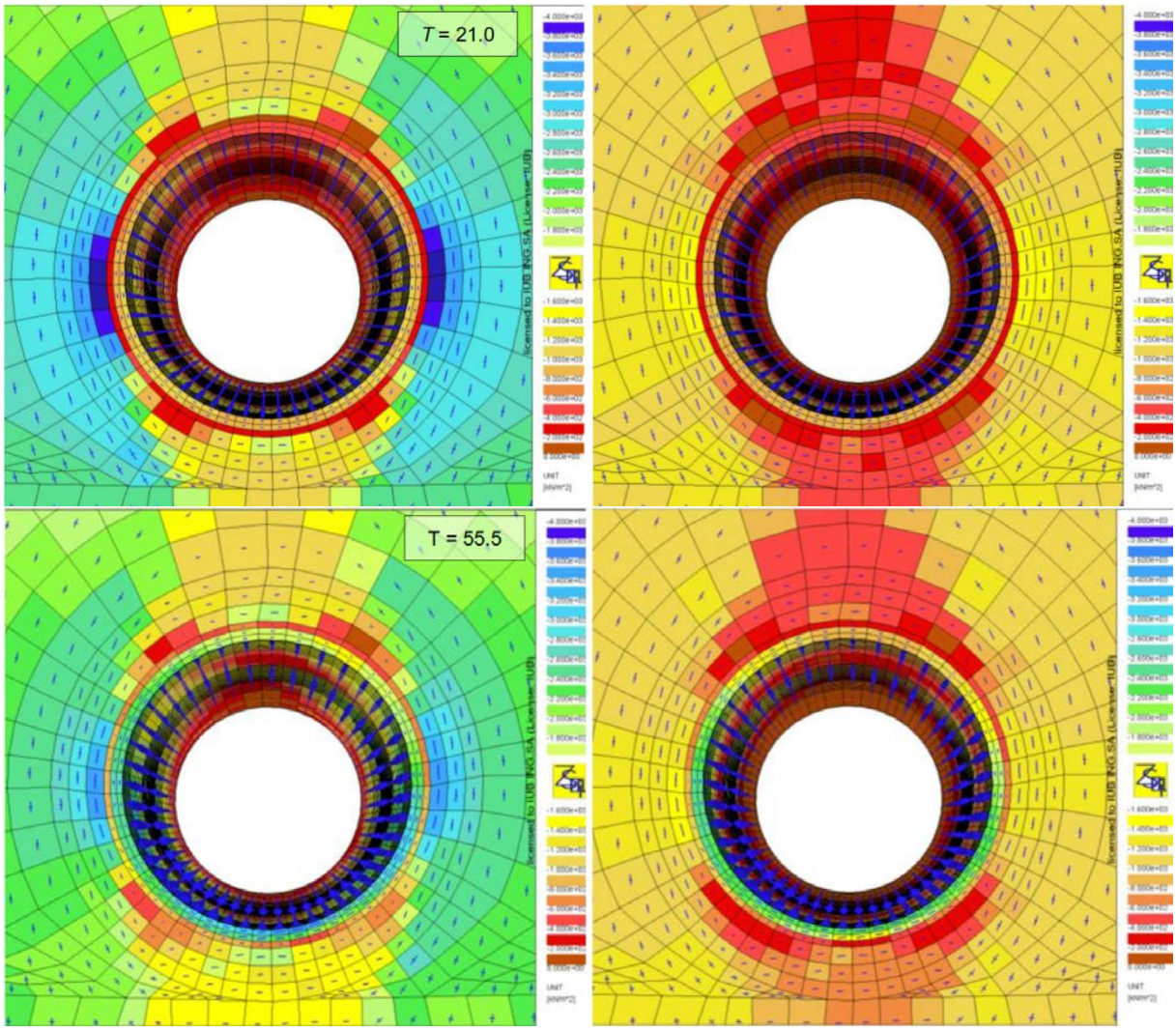

Fig. 29: Cross-section of the gallery above the western crossing point: circumferential stress (left) and longitudinal stress (right) for stiff silt rock (Set 2) [range -4…0 MPa], after completion of the flood relief gallery at T = 21 (top) and after driving of the railway twin tunnel at T = 55.5 (bottom)

After driving of the railway twin tunnel (T = 55.5), the following stress changes can be observed:

- The circumferential stress in the rock is reduced due to stress relaxation caused by the presence of the railway tunnel; but the gallery lining is stressed more in an undulating pattern, which reflects the distortion of the circular shape due to ring flexure (confer the deformed mesh in Fig. 28).
- The longitudinal stress in the gallery lining shows an overall increase in compression (from orange to yellow and green), which is due to overall longitudinal bending of the gallery; in the invert the two element rows across the liner thickness have a different colour (green and yellow), which indicate local bending, but no complete decompression of the outer element.

Note that in non-cohesive ground, the global effect of the gallery lining as a stiff element with a kind of string behaviour would be much more pronounced than here. Because of the only moderate decompression in molasse rock, a closer investigation of the potential dislocation of lining segments during the advancement of the railway tunnel does no longer seem necessary and the tightness of the liner appears to be not impaired. The integrity of the rock roof over the railway tunnel appears to be preserved with a residual minimum compression of about -850 kPa; only some surface layers in the crown might detach.

8 Conclusions

The design of the Sihl flood relief gallery enabled interesting rock mechanical studies with large 3D finite element meshes over a planning duration of several years. Such studies with 500,000+ to 950,000 degrees of freedom are about the maximum of what can be computed on a PC today, given the slow convergence of multilaminate material models subject to delamination, where only initial stiffness iterations converge.

Moreover, as one computation is no computation, various parameter sets had to be studied, and it was found that different failure modes result [2]. In the present problem of a railway twin tunnel crossing the gallery, the interplay between global reaction and local bending at the crossing points does hardly permit an educated guessing of whether softer or stiffer rock response is the more critical. Bracketing the results by different assumptions is a reassuring strategy to be prepared to deviating rock responses encountered on site during construction.

In this presentation the importance of looking at both total and relative displacements and deformations was emphasized – after a time-consuming computation of the “secondary initial state”, which is the one after completion of the flood protection gallery and before starting the excavation simulation of the railway tunnel. For the purpose of comparing in-situ measurements with computational predictions, it is even more complicated as the zero measurement must await accessibility of an observation point.

Not many analyses of tunnel crossings are known to the author, except a few from Aisa, where the crossing was assumed to be at right angle and symmetry was exploited. As shown here for a crossing at skew angle, some surprising results may show up, regarding invalid symmetry, required mesh size, fictitious stresses due to boundary conditions, and elastic cross-influence between cavities fueling non-linear response.

To explore the reserve strength in rock mechanics, it is expedient to run a stability analysis with strength reduction. However, this was not feasible in the present case, because if delamination occurs everywhere along the tunnel crown – and the crossing point is not the most critical one – numerical convergence will fail, as too many integration points are active alike. Rather, the computation was repeated with factorized strength parameters to demonstrate stability of the crown of the railway tunnel.

9 References

[1] Baudirektion Kanton Zürich: Entlastungsstollen Sihl – Zürichsee. Animation (in German), https://www.youtube.com/watch?v=46CCkN5tVQI, 2013.

[2] J.-M. Hohberg: 3D FEM analysis of the construction pit for a TBM-driven flood discharge gallery. 46th Foundation Engineering Conf., Brno/CZ 2018. *Acta Polytechnica CTU Proc.* **23**: 31-37, 2019.

[3] J.-M. Hohberg: On 3D modelling of tunnels crossing at close distance. ISRM sponsored 15th International Conf. on Underground Construction, Prague/CZ, May 2023.

Advancements in Intelligent Rock Bolt Measurement: A General Approach

Fortschritte in intelligenter Ankermesstechnik: Generelles Vorgehen

Michel Varelija, Pauline Vailhé, Philipp Hartlieb
Montanuniversitaet Leoben,
8700 Leoben, Austria,

Abstract

This paper presents a comprehensive overview of recent advancements in intelligent rock bolt systems and their measurement outcomes, along with potential applications and uses. It delves into the core principles of intelligent rock bolts, explaining their functionality, and addresses the challenges encountered during their development. Additionally, it examines the advantages and drawbacks of current installation methods. Furthermore, it explores the implications of these advancements for the future of ground support systems, highlighting opportunities for further research and innovation. Through a thorough analysis of the strengths and limitations of existing technologies, this paper identifies key areas for improvement and optimization, with the overarching goal of enhancing safety and efficiency in underground operations. In contributing to the ongoing discourse on the optimization of ground support systems, this paper provides invaluable insights for researchers, engineers, and industry professionals. By setting theoretical foundations, practical considerations, and prospects, it aims to propel the understanding and implementation of intelligent rock bolt technology toward the creation of safer and more sustainable underground environments.

Zusammenfassung

Dieser Artikel präsentiert einen umfassenden Überblick über aktuelle Entwicklungen bei sogenannten „intelligent rock bolts“ oder „intelligenten Gebirgsankern“, sowie deren Anwendungspotenzial. Dabei werden die grundlegenden Prinzipien von intelligenten Gebirgsankern erklärt, sowie deren Funktionsweise und Herausforderungen bei der Entwicklung näher dargelegt. Auch werden die Vor- und Nachteile unterschiedlicher Installationsarten dargestellt. Darüber hinaus werden die Auswirklungen der Technologie für die Zukunft von Stützmaßnahmen diskutiert und Möglichkeiten für weitere Forschung und Entwicklung gezeigt. Durch eine gründliche Analyse der Stärken und Schwächen existierender Methoden werden in diesem Artikel Schlüsselbereiche für Verbesserungen aufgezeigt, die dem übergeordneten Ziel der allgemeinen Verbesserung der Sicherheit und Effizienz im Bergbau dienen sollen. Als Beitrag zum laufenden Diskurs leistet dieser Artikel Erkenntnisse für Forscher, Ingenieure und Fachleute aus der Industrie. Durch die Definition theoretischer Grundlagen, praktischer Erwägungen und Perspektiven zielt er darauf ab das Verständnis und die Umsetzung der intelligenten Gebirgsanker voranzutreiben.

1 Introduction

Rock bolts are important for ensuring the stability of underground structures Click or tap here to enter text. and with technological advancement intelligent rock bolts have emerged as an approach to improve monitoring and control of ground support. An intelligent rock bolt is a system comprising of standard rock bolt and sensors as monitoring technologies to continuously assess the structural integrity of the steel bar (Feiel et al. 2023; Nöger et al. 2021; Varelija et al. 2023). By capturing real-time data this innovative system offers invaluable insights into rock bolt behaviour and facilitates early detection of potential failure. Moreover, intelligent rock bolts enable adaptive and responsive support strategies, thereby optimizing safety and operational efficiency in dynamic underground environments.

This paper summarizes recent advancements in the intelligent rock bolt measurement and support system, with a focus on a general approach to implementation and utilization. Fundamental principles underlying intelligent rock bolt technology are presented and key questions such as their functionality, development challenges, and current possibilities are addressed. Through an examination of case studies and installation experience, the advantages and disadvantages of the installation method are presented. Additionally, this paper delves into the implications of advancements in intelligent rock bolts for the future of underground ground support systems. Through critical analysis of the strengths and limitations of existing technologies, opportunities for further research are identified and innovation is aimed at overcoming current obstacles and maximizing the potential of intelligent rock bolts to ensure safer and more sustainable underground operations. By combining theoretical foundations, practical considerations, and prospects, the aim is to contribute to the pursuit of safer and more efficient underground environments.

A mine is a complex environment where numerous processes occur simultaneously involving both workers and machinery (Brady and Brown 2006). These activities take place in a partially unknown environment—the rock mass. Stress environment and resulting movements are constantly expected, particularly around excavation areas susceptible to potential instabilities (Bagdassarov 2021; Hoek 2006). Depending on the scale, instabilities can occur locally and regionally, with local and regional rock mass behaviour intertwined. Signs of local instabilities could also serve as precursors to regional problems. An increase in geotechnical events in certain areas could stem from larger underlying issues (Terzaghi 1946; Hoek and Brown 1980). It is very important to monitor the rock mass stability during the mine development to ensure safety. Measurements hold significant potential for implementation as they can indicate specific conditions in the mine or prevent dangerous situations. Moreover, they provide valuable information about current rock mass conditions and the integrity of the rock support system. The detection of indicators, precursors, and causal circumstances drives the necessity for a mine-wide geotechnical monitoring system. Objective measurements of rock mass response and support function are derived from deformation measurements. Early detection of dangerous situations is feasible, but it is also crucial to accumulate knowledge to enable better modelling and design, ultimately leading to a safer environment in the long run. Asking questions about the gathered data is vital as it can help understand how to enhance the safety of miners and mining operations. By comprehending the potential of instrumented rock bolts for monitoring support function, more cost-effective solutions can be developed to provide early warnings to miners about increasing roof fall risks. Analysing data from instrumented rock bolts can help identify potential problems and improve safety measures.

The purpose of a monitoring system using intelligent rock bolts should encompass two tasks within this context: Firstly, providing information for assessing the integrity of the rock support system to ensure safe conditions on a local scale. Secondly, gathering fundamental information to assist engineers in detecting deeper-seated issues. Despite advancements, there remains a need for engineers to determine whether certain areas are safe due to the complexity of rock mass behaviour. As a result, the project provides data and analysis based on deformation in specific areas where the measuring bolts are installed.

2 Definition and functionality of the intelligent rock bolt system

The intelligent rock bolts are an example of persistent creativity and a dedication to overcoming obstacles. The system has come a long way from its early iterations, and its current form is a result of meticulous work in sensor printing and prototype development (Figure 1). Prototype development and other concepts are assessed in the first phase concerning their system components to satisfy the requirements for successful deformation readings. Sensor behaviour needs to follow the steel and stay intact till the steel breaks, otherwise, information would be false. Basecoat and topcoat also need to be ductile enough that they don't break too early. The current intelligent bolt contains a three-layer system basecoat, conductive ink and top coat.

Fig. 13: Tensile testing of the 75cm sample without topcoat, here the sensor ink (grey stripe) and white basecoat are visible.

The intelligent rock bolt works on the principle of strain gauge. The loop goes through the sensor and goes back through the steel. Figure 2 shows the intelligent rock bolt principle (Feiel et al. 2023).

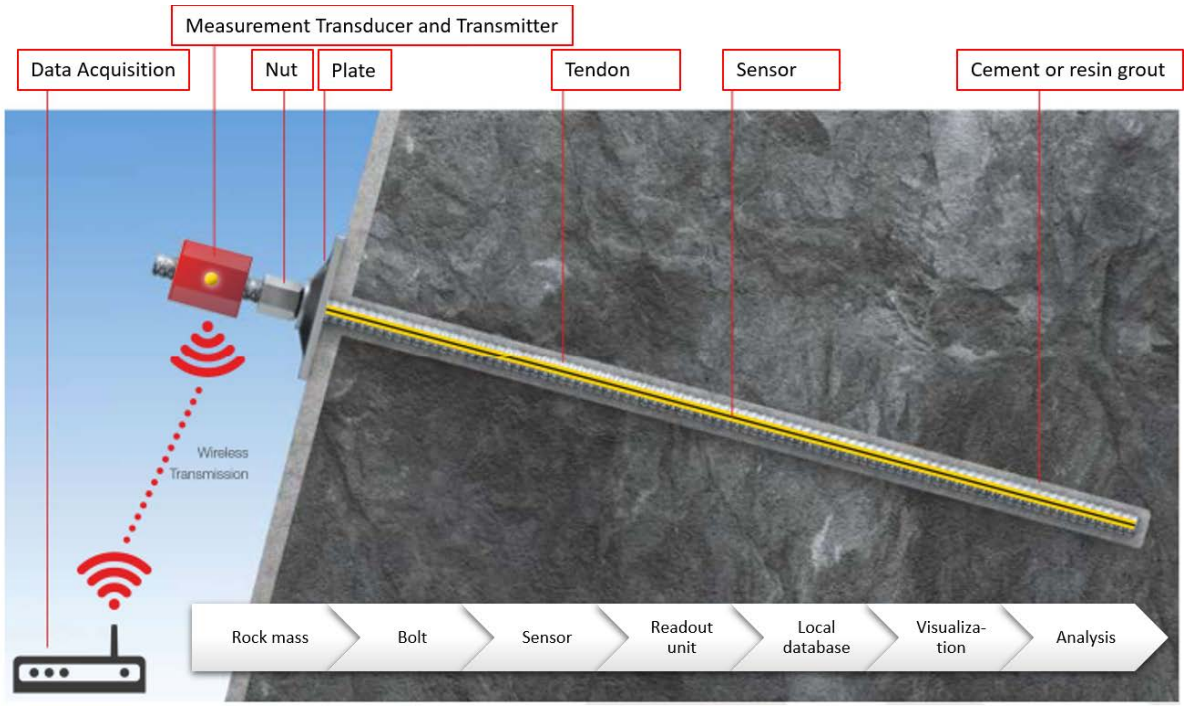

Fig. 14: Graphical description of intelligent rock bolt principle (Nöger et al. 2022).

3 Development, challenges and potential solutions

The study started by identifying conductive materials suitable for the development of the sensor. Initially, the focus was on exploring silver-based inks for printed sensor fabrication. Leveraging the expertise of the polymeric department in screen-printing techniques, the selection process naturally gravitated towards inks compatible with this method.

A comprehensive evaluation encompassing various criteria such as tensile strength, durability under extended strain, and performance in diverse climatic conditions were considered. This assessment identified six potential silver inks, each distinguished by its technological attributes and intended applications.

Through conducted material experimentations, the number of inks was systematically narrowed down. Subsequently, two silver ink formulations emerged as suitable for application onto rock bolts, thus meeting the requirements of the intended sensor deployment.

Following this, attention turned to identifying the appropriate substrate for printing. Similar to the ink evaluation process, various substrates underwent testing to ascertain their compatibility and efficacy. The goal was to affix the printed sensor onto the bolt using adhesive means.

As the development of the system progressed, it became apparent that the initially planned method of printing the sensor on the substrate and attaching it to the bolt on-site encountered unforeseen challenges. It was discovered that the prototype experienced significant creep between the sensor and bolt, leading to unreliable data. The assembly procedure was redesigned to overcome this issue, and a new method was developed in place of the traditional approach to attaching the sensor to the bolt. The breakthrough came with the realization that direct printing of the sensor onto the bolt offered the most reliable bond. This critical decision required an in-depth exploration of materials, ensuring their compatibility and properties matched the requirements.

The development of a basecoat was crucial to isolate the steel from the conductive silver ink and provide an optimal surface for printing. Extensive testing with various materials led to the identification of the most effective basecoat solution compatible with the silver inks. Later stages involved carefully reviewing printing mechanisms and inks, which presented an important challenge due to the bolt's circular cross-section.

A specially designed printing pen emerged as the standout solution, offering the best line quality and thickness while maintaining simplicity of use. To protect the entire system, an additional protective coating—top coat—was introduced, designed to be scratch-resistant and shield the sensor from humidity. Throughout this intricate process, numerous tests were conducted, primarily to assess each material's ability to deform under tensile force without microfractures. The interaction between materials, coupled with multiple curing cycles, further added complexity to the development. The handmade process also imposes inherent problems of human precision and error possibilities (Figure 3). Despite these challenges, the dedicated effort invested in prototype development and sensor printing underscored the commitment to achieving an innovative, reliable, and cost-effective solution.

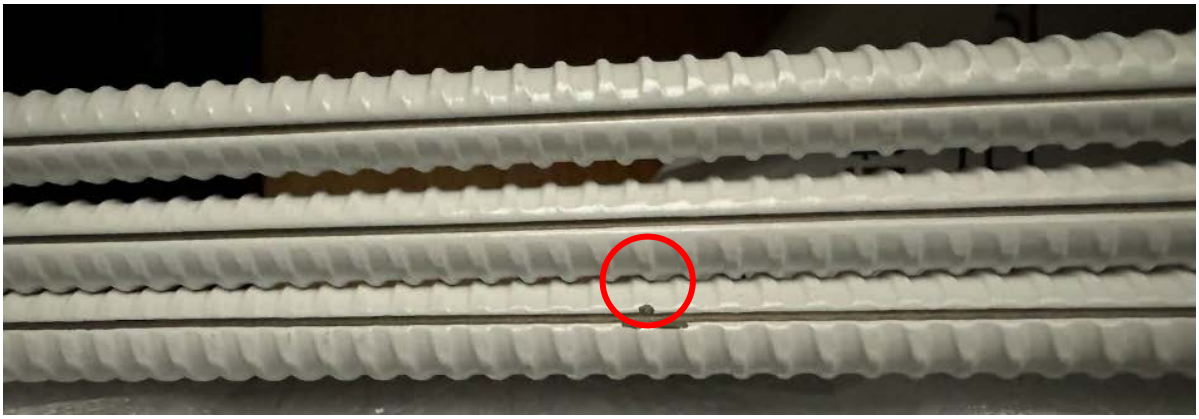

Fig. 15: Error in the printing of the ink due to the handmade process.

4 Conducted tests

The first conducted tests included only one material at a time to check the tensile deformation possibility of each. At that stage, the initial base coat and ink were chosen. Afterwards, a method for the application of materials on the bolt itself is chosen, in the beginning, an idea was to print a strain gauge sensor on the stripe and then attach it to the bolt. However, that idea turned out to have some inherent problems discovered during the tensile testing phase. As a solution to that problem, the whole design had to be changed and new materials had to be chosen since the old ones would not work with the new system design. This process involved many tensile tests in different material combinations until one worked. The last iteration of the intelligent bolts is presented in Figures 1 and 2. The final test results are presented in Figures 4 and 5.

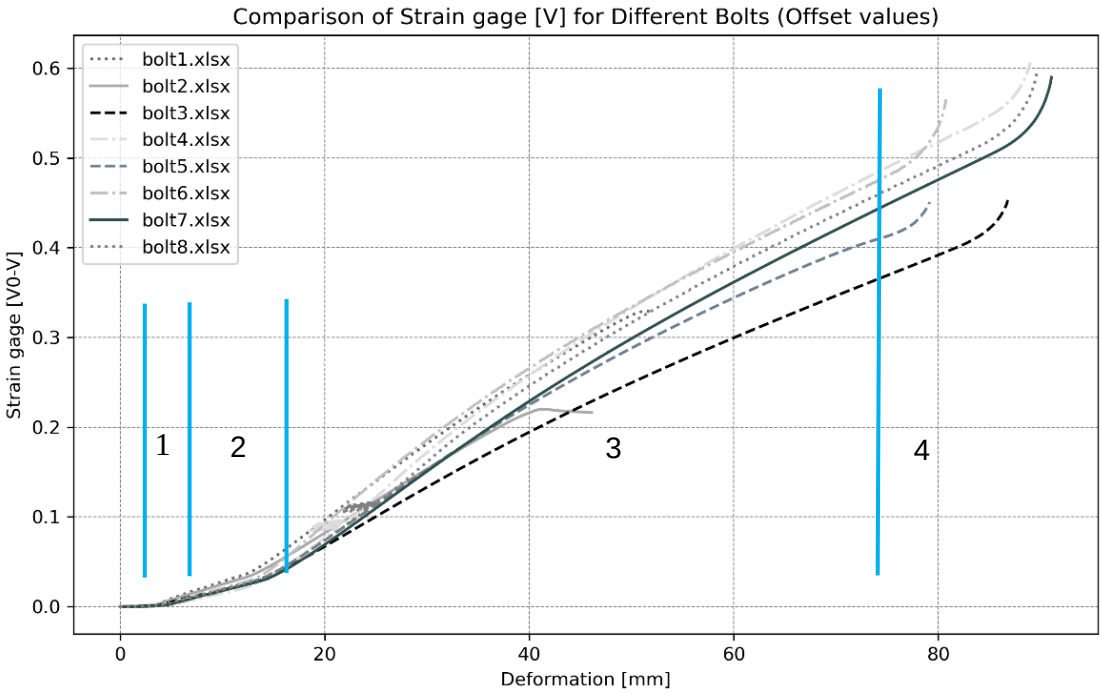

Fig. 16: Comparison of different sensors in the V-V_0 - deformation graph (laboratory tests).

Figure 4 shows the tensile test laboratory result from 8 bolts 75cm in length, deformation is shown in mm and comes from the testing machine, and strain gauge readings in V_0 -V (the sensor is not a strain gauge but it works on a similar principle). It shows that sensor behaviour follows the same pattern, there are 4 stages in the graph: the first one is the linear elastic phase which is almost horizontal, the second stage corresponds to the bolt-yielding phase and the steepness of the curve increases, this stage is linear behaviour, third stage corresponds to the plastic deformation of the bolt and it is not linear anymore, here are the most deviations in the curves, probably due to the handmade system that is not always perfectly precise – deviations in the ink thickness that affects the resistance is the most likely cause for that deviation. The fourth stage is a failure, when a failure occurs voltage increases. Two of the bolts had a problem with the testing setup, which is why two lines around 40mm deformation just ending - here the nut that was holding the bolt slipped, and there was no failure of the bolt since the nut damaged rebars of the bolt, the test could not be continued on those two samples. After fixing the setup other bolts had no such problems.

Fig. 17: Intelligent rock bolts prepared for the curing process.

Figure 5 shows 3m long rock bolts prepared for drying in the oven at 100°C. This system was installed directly in the mine for onsite testing since testing this long bolt is more difficult to conduct in the laboratory. The result of these long bolts is not presented in this paper since it is still under investigation.

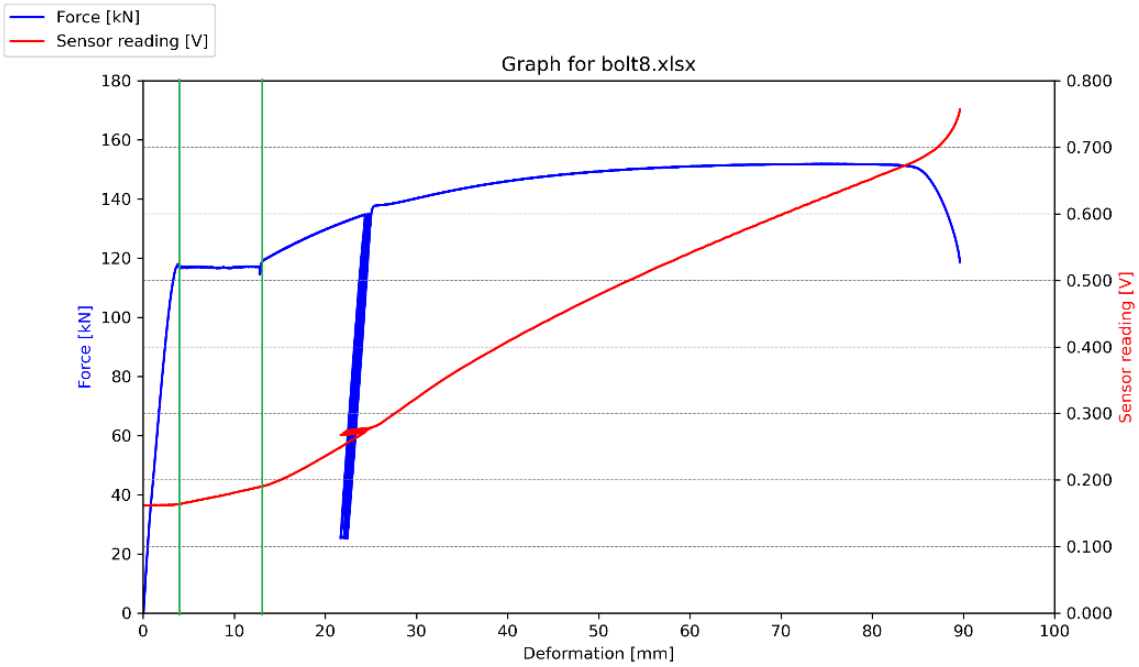

Fig. 18: Bolt nr. 8, force-deformation and deformation-Volt graph (laboratory test).

Figure 6 shows tensile test data from one of the bolts. This graph shows a comparison of the force [kN] on the left side (blue line) and sensor reading [V] on the right side (red line) Here is also visible that the behaviour of the sensor follows the bolt, again four stages, elastic, yielding, plastic and failure. This bolt was tested with the loop in the plastic phase where the force decreased to 25kN and then returned it to 130kN, this is also seen in the sensor response.

5 Usage possibilities and innovations

Currently, all the possibilities of data usage and analysis are being explored. Few numerical models have been created to test the potential of the system with precise readings and concluded that the final product will have the ability to detect joints in the rock mass and gravity-driven roof failures (Varelija et al. 2023; Nöger et al. 2022). More information on that will be followed in the next publication that is still pending a review process.

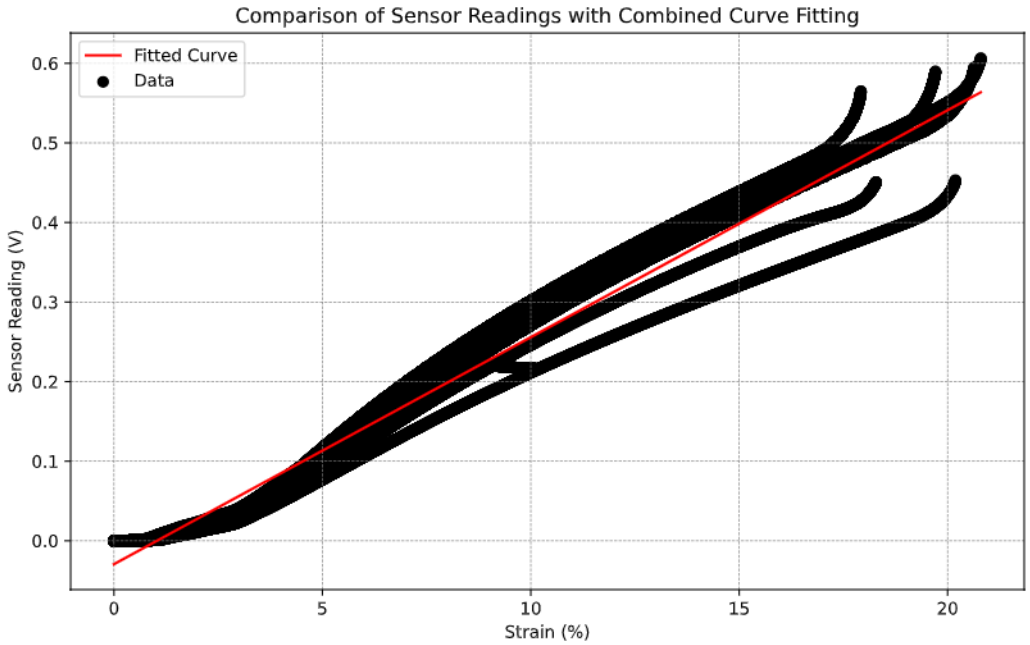

Fig. 19: Linear curve fitting to the sensor reading (laboratory test) data and strain.

Figure 7 shows one way to simply convert volts to strain- by linear curve fitting, the black lines are test results and the red line is the linear fitting. If the sensor were perfectly precise and accurate, the fitted curve would have a better match with the data points. In such a scenario, the errors between the fitted values and the actual values would be closer to zero, resulting in the following values for the precision and accuracy metrics. For a better fitting the formula or the fitting needs to be divided into 3 phases, the first two parts are linear, and the plastic part can be approximated by the least square's method, however, the fastest way to calculate is with the linear fitting formula (1).

Sensor reading [V] = 0.028533749896243 * Strain [%] - 0.029548260489301006 (1)

It is difficult to achieve perfect accuracy in real measurements due to various factors such as noise, measurement errors, and model assumptions. Therefore, while aiming for more accurate values of these metrics is desirable, it's essential to consider the inherent limitations and uncertainties in the data and the modelling process.

Tab. 2: With formula (1) following error values.

		Perfect fit	Calculated value
Mean Absolute Error	MAE	0.00	0.01965
Mean Squared Error	MSE	0.00	0.00060
Root Mean Squared Error	RMSE	0.00	0.02463
R-squared	R^2	1.00	0.97816

6 Installation Considerations

Intelligent rock bolts have been installed in 3 European mines, all bolts are still functional and providing data. Installations were conducted manually due to the low amount of available intelligent rock bolts. Automatic installation would require first big amounts of intelligent rock bolts to be available and then designing the system or machine that could do it automatically. Installation of the bar itself is not that much different from the standard one – mechanically anchored one, it just requires a bit gentler approach so the sensor doesn't get damaged. Figure 8 shows the first prototype installed on-site and the readout unit.

Fig. 20: The first prototype installation on-site.

7 Comparison with available measuring rock bolt system

For the system comparison, two measuring rock bolt systems are installed in the same drift. Measurement devices from Yield Point company (YieldPoint Inc. 2024) have a function of wireless connection via Bluetooth with the ability to save information to data loggers and thus deliver a vast amount of data with a low risk of losing data. Compared to the intelligent bolts produced by Montanuniversitaet Leoben which are still in the early stage of development and are prototypes. However, there is a possibility to do a wireless connection, it was just not tested at this stage. Hence the difference in the amount of data. More data also offers a better temporal distribution – if looking into a specific case: data collected around the blast date shown in YP bolts (Figure 9) has better temporal and spatial resolution since more points are showing an anomaly when compared to prototype "intelligent rock bolt" bolts which have only one reading that is significantly higher than the others. One outlying reading doesn't seem so significant in this context, since several different errors could result in the same or similar outcome. Otherwise, a larger array of sensor readings could be interpreted more reliably. Another big difference is the number of sensors that are applied on one single bolt: YP has 6, and the prototype "intelligent rock bolt" has 1. That gives a difference in readings of deformation distribution along the tendon. One sensor gives only one deformation reading for the whole bolt, while 6 sensors show which points on the bolt and how much they are deformed.

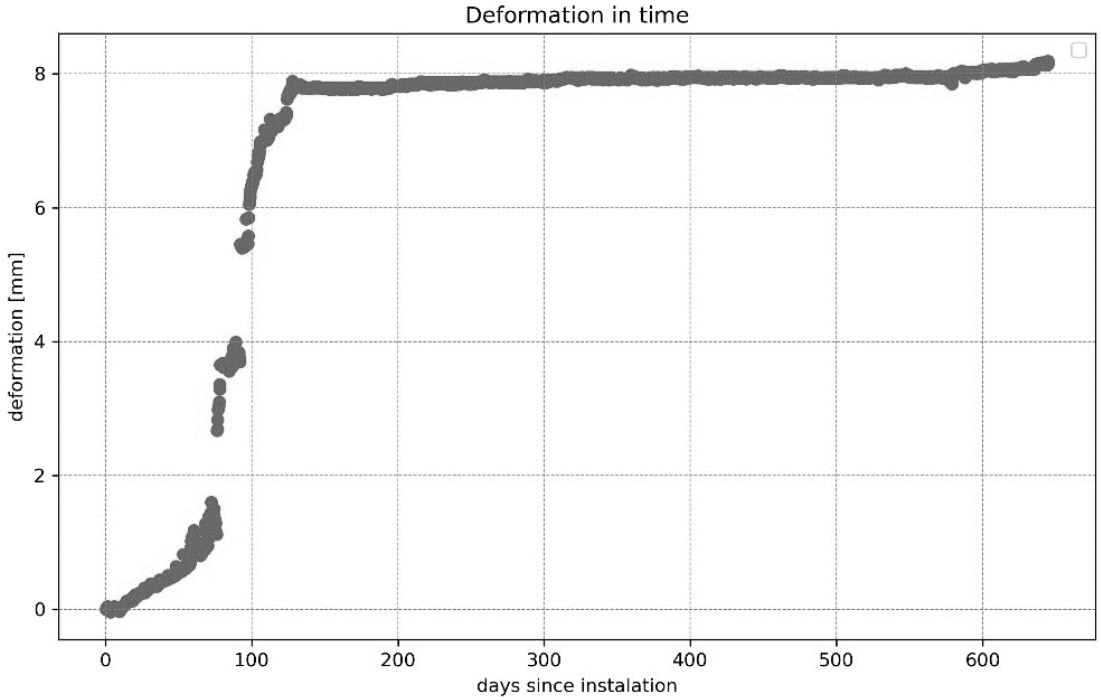

Fig. 21: Data gathered from the mine drift using Yield point measuring bolt.

8 Conclusion

Intelligent rock bolts represent a novel combination of established technologies in the field of mining and underground construction. Strain gauges, which measure strain in materials, have been utilized for decades, while traditional rock bolts have been employed in mining and construction for much longer. The convergence of these technologies within the framework of intelligent rock bolts offers an innovative solution to the pressing need for enhanced safety and automation in underground environments. Modern mining and underground construction are leaning towards automated processes and increasing safety standards. One effective approach is to embed sensors within rock bolt support systems. This integration offers real-time monitoring of structural integrity, enabling remote assessment of ground support systems from a central location. Through this technology, engineers can analyze the capacity utilization of the support systems, determining whether they are over- or under-designed, thus enabling more informed decision-making.

However, the adoption of intelligent rock bolt technology is not without challenges. As it stands, this system is still in its early days and requires further development and rigorous testing to ensure reliability and robustness. Additionally, the current cost of implementation remains high, which could deter widespread adoption. Nevertheless, the benefits of intelligent rock bolts far outweigh the drawbacks. As technology evolves, these systems could become fully automated, incorporating machine learning algorithms to predict rock behaviour, thereby preventing failures and accidents. They could also contribute to the identification of rock mass structures and fault lines, providing critical data for enhanced safety and planning.

The primary strength of intelligent rock bolts lies in their potential to provide continuous, real-time monitoring of underground support systems. This capability can significantly reduce the risk of structural failure and improve safety for workers in mines and underground construction sites. Moreover, the data generated by these sensors can inform maintenance schedules and design adjustments, leading to cost savings and increased efficiency.

However, the technology's limitations must be considered. The primary limitation is the cost, both in terms of the sensors themselves and the infrastructure required to support data collection and analysis. Additionally, the technology is still in a relatively early stage, with potential issues relating to sensor reliability, calibration, and data interpretation. These factors are still the problem for the broader adoption of intelligent rock bolts. To overcome these limitations, further research and development are needed in several key areas: cost reduction, reliability and durability, data analytics and integration with other systems.

The advancement of intelligent rock bolt technology could have profound implications for the future of ground support systems in mining and underground construction. By enabling predictive maintenance and real-time monitoring, these systems could revolutionize safety standards and operational efficiency. Furthermore, the integration of machine learning and artificial intelligence could facilitate predictive modelling, allowing engineers to anticipate and mitigate risks before they occur. As the technology matures, intelligent rock bolts could become an indispensable component of modern mining and construction practices, paving the way for safer, more efficient underground environments.

9 Acknowledgement

We would like to thank the Boliden employees for their assistance and availability in providing us with their mine for prototype testing and for diligently delivering data from the bolts for additional research. We would also like to thank DSI for all of their help with the creation and testing of this intelligent bolt system, as well as the custom production of readout units. We thank Gerold Wölfler for all the support with printing and designing printing tools. It was a pleasure working with all of you.

The paper was prepared within the framework of, IlluMINEation project, European Union’s Horizon 2020 research and innovation program under grant agreement no. 869379.

10 Publication bibliography

Bagdassarov, N. (2021): Stresses in Rocks. In N. Bagdassarov (Ed.): Fundamentals of Rock Physics: Cambridge University Press, pp. 66–112.

Brady, B. H. G.; Brown, E. T. (2006): Rock mechanics for underground mining. 3rd ed. B.H.G. Brady, E.T. Brown. Dordrecht, London.

Feiel, S.; Kern, W.; Griesser, T.; Moser, P. (2023): Gebirgsanker mit sensor zur messung mechanischer spannung. Patent no. EP3927942C0.

Hoek, E. (2006): Practical Rock Engineering. Rock bolts and cables.

Hoek, E.; Brown, E. T. (1980): Underground excavations in rock. London: The Institution of Mining and Metallurgy.

Hoek, E.; Kaiser, P. K.; Bawden, W. P. (1995): Support of Underground Excavation in Hard Rock.

Nöger, M.; Hartlieb, F.; Fimbinger, E.; Mansouri, S. S.; Marcin, P.; Bursa, B.; Sörensen, J. (2021): Data assessment for safe zone classification - Deliverable D4.1.

Nöger, M.; Varelija, M.; Hartlieb, F.; Paterek, M.; Kobylanska, M.; Pikuła, M. et al. (2022): D4.4 The safe zone concept. Improved safety and environmental performance.

Terzaghi, K. (1946): Rock defects and loads on tunnel supports.

Varelija, M.; Nöger, M.; Hartlieb, F.; Dendl, D.; Moser, P. (Eds.) (2023): The effect of different rock mass properties on deformation distribution detected with intelligent rock bolts in underground mining. 15th ISRM Congress 2023 & 72nd Geomechanics Colloquium. Salzburg.

YieldPoint Inc. (2024): Measurement Rock Bolts. Available online at https://www.yieldpoint.com/, checked on 4/30/2024.

Influence of injection protocols on the development of Enhanced Geothermal Systems

Einfluss von Injektionsparametern auf die Entwicklung von Enhanced Geothermal Systems

Hannes Hofmann[1,2], Yinlin Ji[1], Arno Zang[1,3], Günter Zimmermann[1,2], Gergö Hutka[1,2], Supeng Zhang[1], Mauro Cacace[1]

[1]Helmholtz Centre Potsdam German Research Centre for Geosciences,
Telegrafenberg, 14473 Potsdam
[2]Technische Universität Berlin,
Straße des 17. Juni, 10623 Berlin
[3]Universität Potsdam,
Am Neuen Palais 10, 14469 Potsdam

Abstract

In the development of Enhanced Geothermal Systems (EGS) by hydraulic stimulation we face two major challenges. First, how to create flow paths between multiple wells with sufficient permeability while avoiding early thermal breakthrough. Second, how to mitigate the risk of large magnitude injection-induced seismic events. One main parameter that influences both questions is the injection protocol. Here we summarize our laboratory-scale, field-scale and numerical research on the influence of the injection protocol on the slip behaviour (induced seismicity) and permeability of pre-existing fractures and faults that was conducted in the framework of the Helmholtz Young Investigator Group “Advanced reservoir engineering concepts for a controlled utilization of deep geothermal energy in urban areas” (ARES) together with collaborators. Injection parameters include pressurization rate at the start of injection, depressurization rate at the end of injection, flow rate, (cyclic) injection protocols and hydraulic energy. Overall, we find that the injection protocol can influence the stimulation results to a certain degree within the site-specific geological boundary conditions. Future work will focus on feedback-controlled injection to optimize injection protocols and the use of proppants and acids to keep fractures open and influence their slip behaviour.

Zusammenfassung

Bei der Entwicklung von Enhanced Geothermal Systems (EGS) durch hydraulische Stimulation stehen wir vor zwei großen Herausforderungen. Erstens: Wie können Fließwege zwischen mehreren Bohrlöchern mit ausreichender Durchlässigkeit geschaffen und gleichzeitig ein frühzeitiger thermischer Durchbruch vermieden werden? Zweitens: Wie kann das Risiko von seismischen Ereignissen, die durch die Injektion ausgelöst werden, gemindert werden? Ein Faktor, der beide Fragen beeinflusst, ist das Injektionsprotokoll. Hier fassen wir unsere Forschung im Labor- und Feldmaßstab sowie numerischen Modellierungen zum Einfluss des Injektionsprotokolls auf das Scherverhalten (induzierte Seismizität) und die Durchlässigkeit bereits bestehender Klüfte und Verwerfungen zusammen, die im Rahmen der Helmholtz-Nachwuchsgruppe "Advanced reservoir engineering concepts for a controlled utilization of deep geothermal energy in urban areas" (ARES) zusammen mit Partnern durchgeführt wurde. Zu den Injektionsparametern gehören die Drucksteigerungsrate am Anfang der Injektion, die Druckentlastung am Ende der Injektion, die Injektionsrate, (zyklische) Injektionsprotokolle und hydraulische Energie. Insgesamt kann das Injektionsprotokoll die Stimulationsergebnisse bis zu einem gewissen Grad innerhalb der jeweiligen standortspezifischen geologischen Randbedingungen beeinflussen. Zukünftige Arbeiten werden sich auf rückkopplungsgesteuerte Injektion zur Optimierung von Injektionsprotokollen und den Einsatz von Stützmitteln und Säuren konzentrieren, um Risse offen zu halten und ihr Gleitverhalten zu beeinflussen.

1 Introduction

Deep geothermal energy can have a significant contribution to the energy transition as a local and renewable energy source. However, most of this heat is stored in deep formations with low permeability which need reservoir engineering methods to improve subsurface fluid flow. Despite decades of research and development today still no fully commercial geothermal heating or power plant exists in such a so called Enhanced Geothermal System (EGS). This is mainly due to insufficient flow and some of these projects had to be stopped due to injection-induced seismicity. The long-term vision of EGS research is to develop solutions for the safe, reliable and economic development of the enormous potential of hot, low permeability rocks – known as petrothermal energy systems - using EGS technologies. The challenges in the development of EGS can be summarized in two main aspects:

1) How to create and maintain sufficiently high permeability, heat exchange area and near-uniformly distributed flow between multiple wells in an otherwise low permeability rock mass?
2) How to assess, monitor and mitigate injection-induced seismic hazard?

Both questions can only be answered based on a sound understanding of the behavior of fractures and faults under varying pressures, stresses, temperatures and geochemical conditions. The underlying long-term research questions are therefore: What is the dynamic behavior of fractures and faults under different geological and operational conditions? How can this behavior be influenced (or engineered)? And what conditions are favorable for EGS development? To answer these questions, we pursue a multi-scale approach involving laboratory, mine and field-scale experiments in different geological settings, accompanied by theoretical considerations and numerical modelling studies. Some of our main findings in this key research area are outlined below. We focus here on stimulation of pre-existing fractures and faults as oppose to hydraulic fracturing and on induced seismicity rather than permeability enhancement.

2 Materials and methods

2.1 Laboratory experiments

At the Geoenergy section at GFZ Potsdam a triaxial cell (MTS 815) is used for laboratory shear-flow experiments (Fig. 1). It can provide a hydrostatic confining pressure of up to ~140 MPa. Two Quizix fluid pumps (C6000-10K-HC-AT) can supply pore fluid pressure of up to 70 MPa. Heating stripes can control the cell temperature up to 140°C. Extensometers can be used to measure the axial and circumferential strains and we also have the possibility to feed fibre optic cables through the end plate of the MTS and for additional pressure, temperature and strain measurements. As shear-flow experiments have not been conducted in this setup before, the first step for us was to test the equipment for our purposes, establish the new workflows and address methodological concerns.

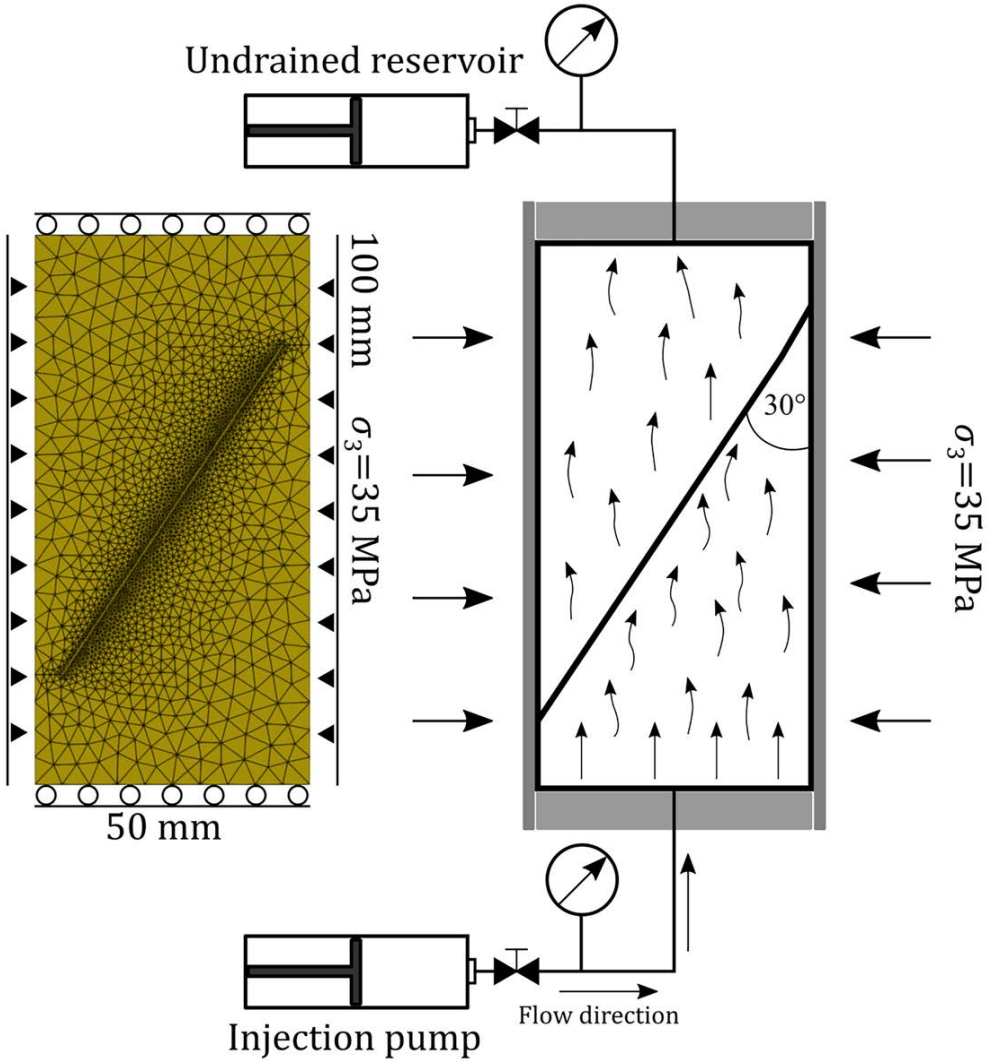

Fig.1: Typical setup of a shear-flow experiment (right) and the corresponding numerical model (left). In this example the fluid flows through the endcaps towards a high permeability sandstone into the fracture. In low permeability rock such as granite small holes are drilled from the end caps into the fault to direct the fluid flow into the fracture (Hutka et al., 2023a).

First, we reviewed laboratory experiments investigating fault behavior in geoenergy systems including the current state-of-the-art on injection-induced seismicity from the laboratory perspective (Ji et al., 2022a). The review includes basic fault behavior, a description of common laboratory methods and an overview of the effects of injection protocol, fault properties, stress state, temperature, fluid physics and fluid chemistry on injection-induced seismicity, as well as open questions.

We then determined the effects of external temperature and dead volume of the pore pressure system on the measurement of pore pressure and injected volume in a rock fracture and proposed a correction method for these effects (Ji et al., 2022b). We also compared different methods to determine the permeability of elliptical rock fractures with a source and sink hole in the triaxial shear-flow setup and identified an error in a classical equation derived by Rutter and Mecklenburgh (2018), which we corrected in collaboration with Prof. Ernest Rutter (Ji et al., 2022c).

While we have previously established fibre optic pressure measurements at a single point at the end of the fibre (Nicolas et al., 2020, Ji et al., 2022b), we have recently developed the experimental setup and data analysis procedure to measure the strain at the outer surface of our cylindrical samples by fibre optics and applied the setup to conventional triaxial tests (Miao et al., submitted), which is now a new feature of our experimental setup of shear-flow tests.

2.2 Numerical models

We implemented the numerical simulation of shear slip behavior and associated induced seismicity in the open-source finite element code GOLEM (Cacace and Jacquey, 2017), which is based on the multi-physics general modelling framework MOOSE (Permann et al., 2020). A classical slip tendency analysis workflow was already available (Blöcher et al., 2018), and we used it to assess the impact of geological and operational parameters on the stability of a single fault in typical Dutch geothermal reservoirs (Mathur et al., 2024). Hutka et al. (2023a) added a rate-and-state friction formulation including a tailored time-stepping algorithm, validated it against a set of laboratory shear-flow experiments (Fig. 1). Hutka et al. (2023b) then applied it to a field scale modeling case in the Netherlands. This workflow allows us to simulate the dynamic change of the friction coefficient and slip velocity/displacement of complex three-dimensional fault structures as an indicator for seismic hazard. Additionally, Cacace et al. (2021) developed a new mathematical approach for induced seismic hazard prediction based on the Seismogenic Index (Shapiro et al., 2007, 2010) and Coulomb Failure Stress changes, implemented it in GOLEM and validated the approach against field data of the Groß Schönebeck EGS (Blöcher et al., 2018). The model was then applied to Dutch geothermal reservoirs (Hutka et al., 2023b). Previous statistical approaches to predict induced seismic hazard accounted for the physics of pore pressure increase only (Shapiro et al., 2010). Cacace et al. (2021) generalized this approach for arbitrary injection/production protocols and physical processes.

We also setup a two-dimensional field scale finite element model in COMSOL to investigate the influence of temperature-enhanced fault closure on post-injection seismicity (Ji et al., 2023a). The model was validated against laboratory results from flow-through experiments at elevated temperatures, together with analytical solutions for fluid diffusion. An alternative modeling approach for hydraulic shearing treatments is the Displacement Discontinuity Method (DDM). Sabah et al. (2022) validated their two-dimensional DDM model against analytical solutions and used it to investigate the influence of fluid injection protocols on the seismic behavior of a thermo-hydro-mechanically coupled rate-and-state-governed fault.

In addition to 2D/3D coupled numerical models at multiple scales we performed analytical studies to investigate fracture flow, fracture slip and fracture permeability for fast and simple use, benchmarking and straightforward interpretation. An important question we have answered with such an approach is how a cyclic pressure signal is transmitted through a fault with effective stress dependent permeability. The finite element model setup for this investigation was validated against laboratory-scale experiments and multi-scale analytical solutions and the results have significant implications for field-scale cyclic injection design (Ji et al., 2023b). Another question was how the permeability of a fracture changes during fluid injection. The transient permeability of a fracture depends not only on the well-known effect of effective normal stress and shear displacement, but also on other, previously less constrained factors, such as the fault slip velocity. We confirmed the slip velocity dependence of fracture permeability with laboratory injection experiments on a fractured granite sample and corrected the previously published semi-analytical velocity-dependent aperture model (Fang et al., 2017; Samuelson et al., 2009) in Ji et al. (2023c). We also constrained the constitutive parameters required to calculate the transient aperture change with such displacement and slip velocity dependent aperture models and found that the combined displacement- and velocity-dependent aperture model can better reproduce the measured apertures compared to the displacement-dependent aperture model (Zhang et al., 2024a).

3 Results

3.1 Pressurization rate

Our laboratory experiments on a naturally fractured granite sample (Ji et al., 2023c) and rate-and-state friction based numerical models of a saw-cut fault in a high permeability sandstone (Hutka et al., 2023a; Fig. 2) indicate that a higher fluid pressurization rate leads to faster slip events and thus a higher injection-induced seismic hazard. The Coulomb Failure stress models by Cacace et al. (2021) confirm this by predicting higher seismicity rates resulting from higher pressurization rates. At the same time, a higher pressurization rate enhances the transient permeability of a fracture as shown by our laboratory experiments and the updated semi-analytical aperture model dependent on both slip displacement and velocity (Ji et al., 2023c; Zhang et al., 2024a). We find that this effect may be more significant for smooth fractures at high slip velocities under low effective normal stresses (Zhang et al., 2024a).

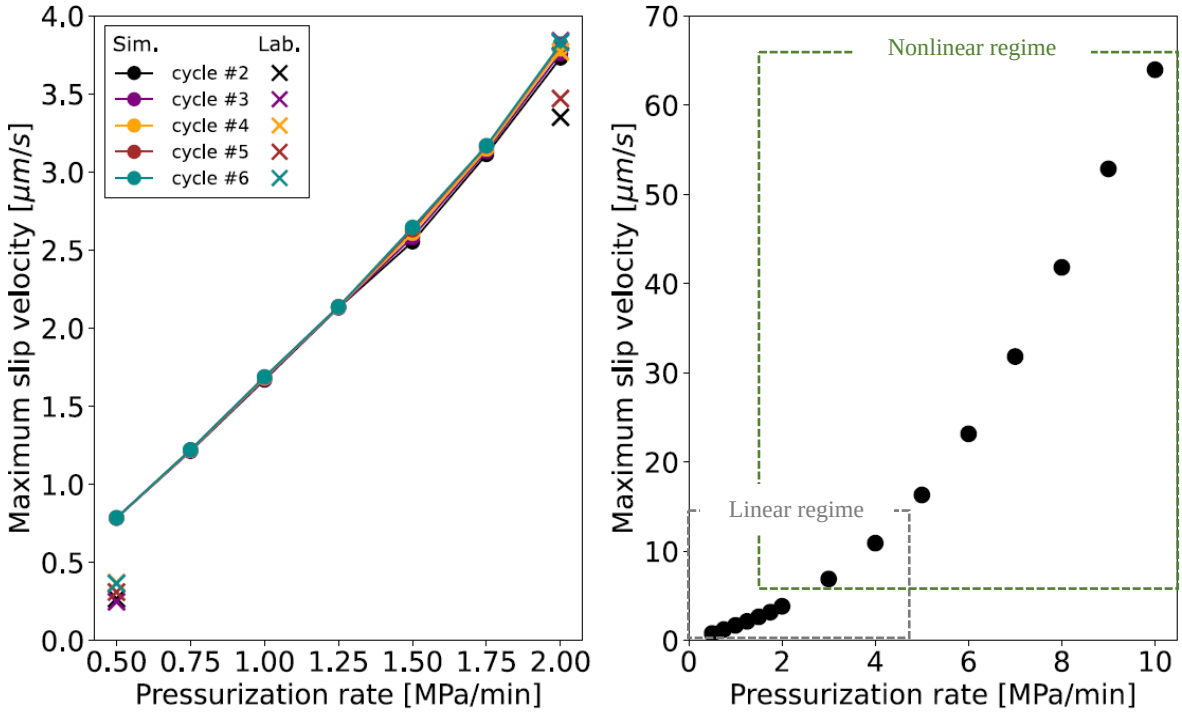

Fig.2: Measured and simulated maximum slip velocities depending on the fluid pressurization rate in laboratory fluid injection experiments of permeable sandstone samples containing a saw-cut fault (modified from Hutka et al., 2023a). Laboratory experiments were interpolated (left) and extrapolated (right) by the numerical modelling results. At low pressurization rates this relationship is linear and may be interpreted as unconditionally stable with slow shear fracture growth and seismic energy release during injection. At high pressurization rates this relationship becomes nonlinear which may be interpreted as an unstable regime eventually leading to runaway instabilities with acceleration in shear fracture growth and seismic energy release also after injection.

3.2 Depressurization rate at the end of injection

Induced earthquakes occurring after the end of fluid injection activities are a major concern for EGS projects. These events can primarily be linked to continued pressure diffusion after stop of injection (Baisch et al., 2010), poroelastic stress relaxation on faults which are compressed during injection (Segall and Lu, 2015), far-field pressure increase due to near-well fracture closure resulting from wellbore pressure reduction (Ucar et al., 2017), and Coulomb stress transfer from seismic and aseismic fault slip (Ge and Saar, 2022). However, recommendations for well shut-in strategies to mitigate this post-injection seismicity are limited. Therefore, we performed laboratory-scale fluid depressurization experiments on a granodiorite sample and combined these findings with field-scale modelling of the Pohang EGS site (Ji et al., under review, Fig. 3). Our results suggest that immediate flowback of the injected water is the preferred strategy to reduce the likelihood of occurrence of large magnitude post-injection seismic events in reservoirs where poroelastic effects are negligible, such as the typical low-permeability crystalline rock most relevant to EGS. The reason for the reduced seismic hazard potential is that flowback reduces the pore pressure in nearby fault zones, thereby reducing 1) pore pressure-induced fault slip and 2) Coulomb static stress transfer resulting from pore pressure-induced seismic and aseismic fault slip. On the other hand, tapered injection may reduce post injection seismic hazard in reservoirs with significant poroelastic effects (Segall and Lu, 2015). At the same time, we found that the hydraulic diffusivity of the fracture was reduced the most in the experiments with the highest fluid production rate after shut-in (Ji et al., under review). With our Coulomb Failure Stress models, we also show how the injection scheme can influence the decay of post-injection seismicity (Cacace et al., 2021). We additionally performed numerical simulations to analyse the relative importance of poroelasticity, heat transfer, and thermoelasticity in post-injection fault closure and pressure diffusion, and the resulting post-injection induced seismic hazard. We found that out of these three effects, poroelastic fault closure near the well has the strongest effect on the far-field pore pressure increase, heat transfer can slightly increase this effect primarily due to changes in the fluid viscosity and thermo-elastic effects are negligible (Ji et al., 2023a). Based on our cyclic injection models of stress sensitive faults we also introduce the concept of a fluid pressure pocket to explain the limited influence operators have on the far-field seismic hazard especially during later stages of fluid injection and when injecting into a low permeability fault (Ji et al., 2023b). The prediction and control of post-injection-induced seismicity therefore remains an important future research topic.

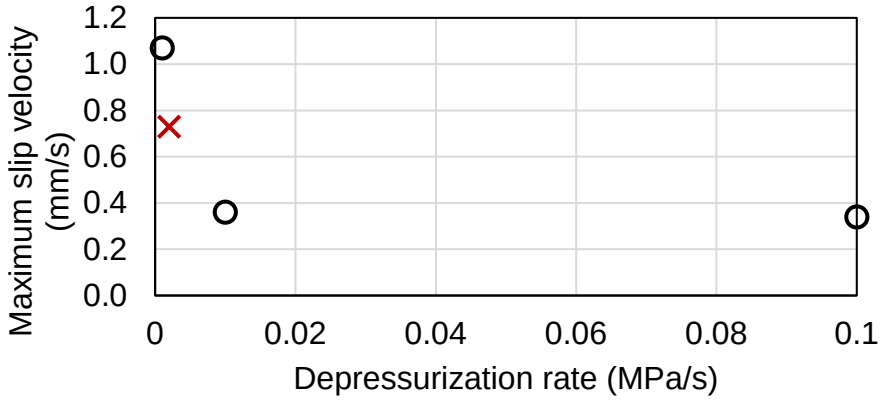

Fig.3: Relationship between depressurization rate and maximum slip velocity measured during laboratory-scale fluid depressurization shear-flow experiments in a saw-cut fault of a granitic rock sample (based on data from Ji et al., under review). The red X indicates the depressurization rate representative for the shut-in scenario. Lower rates represent tapered shut-in (with continued injection) and higher rates represent active production (pumping). While the slip velocity decreases significantly with increasing pressurization rate close to the shut-in scenario, further excessive increase in depressurization rate by one order of magnitude from 0.01 MPa/s to 0.1 MPa/s does not further decrease the maximum slip velocity in these experiments.

3.3 Flow rate

To study the effect of fluid injection rate on the seismic hazard we performed a series of fluid injection experiments on cylindrical granite samples with a critically stressed sawcut fault monitored by an array of six local strain gauges close to the fault. With these experiments we systematically demonstrated that higher injection rates increase the seismic hazard (i.e., higher peak slip rates and larger fault slip displacements) by shrinking the earthquake nucleation length and that initially stable fault patches subject to low injection rates may be reactivated by increasing injection rates (Ji et al., 2022d, Fig. 4). On the other hand, we know from field experience that higher fluid injection rates also tend to increase the productivity and/or injectivity of a well (e.g., Hofmann et al., 2021).

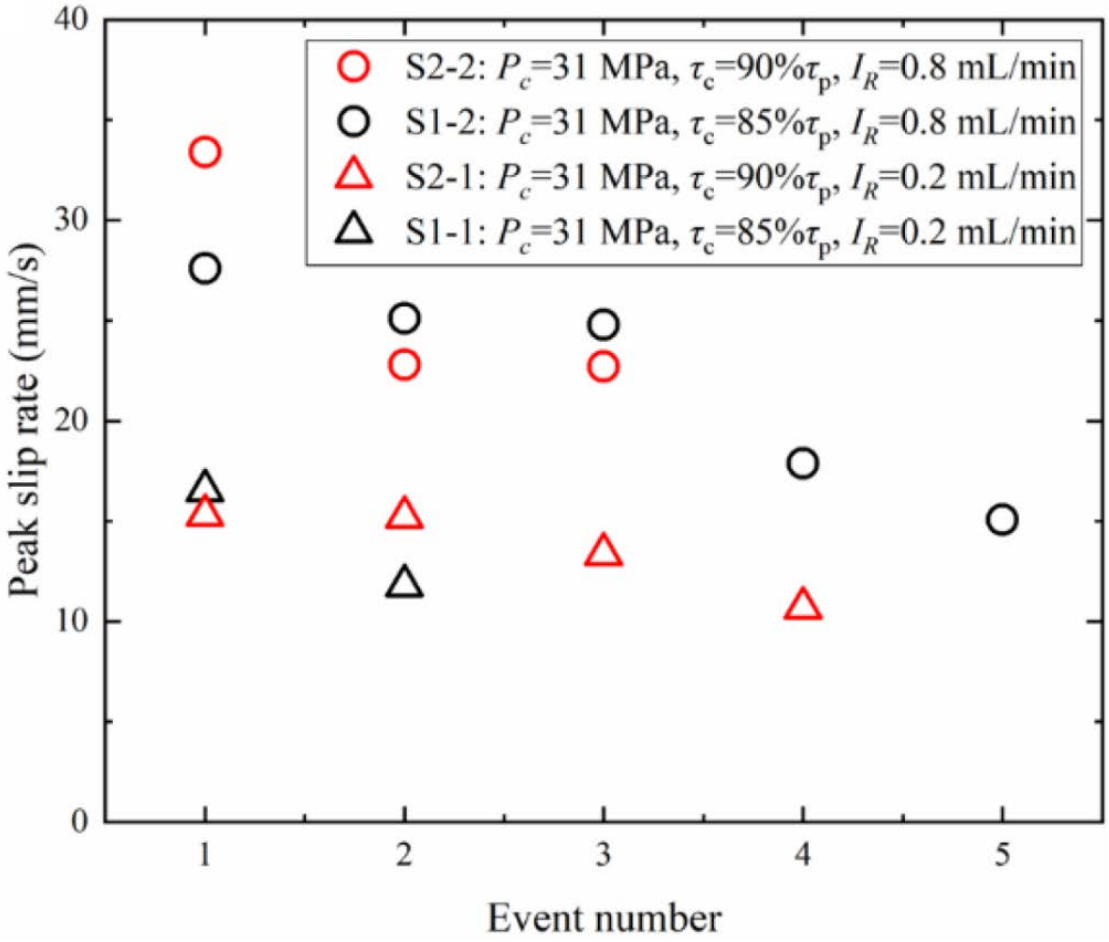

Fig.4: Comparison of peak slip rate of shear-flow laboratory experiments performed with high injection rate (0.8 mL/min, circles) and low injection rate (0.2 mL/min, triangles) in saw-cut granodiorite samples. P_c , τ_c , τ_p and I_R are the confining pressure, initial shear stress, peak shear strength and injection rate, respectively (Ji et al., 2022e).

3.4 Cyclic injection protocols

Previous laboratory shear-flow experiments with naturally fractured granite have shown that the same displacement (which may be an indication for fracture permeability change) can be achieved with lower peak slip rates by cyclic injection schemes compared to monotonic injection (Ji et al., 2021; Fig. 5.). Our numerical simulations of a cyclic pressure perturbation in a field-scale stress-sensitive fault show that a lower initial fault permeability, a smaller stress sensitivity coefficient and a higher injection frequency lead to a stronger attenuation of the injection pressure, i.e. a smaller amplitude ratio and a larger phase shift, while being independent of the pressure amplitude (Ji et al., 2023b).

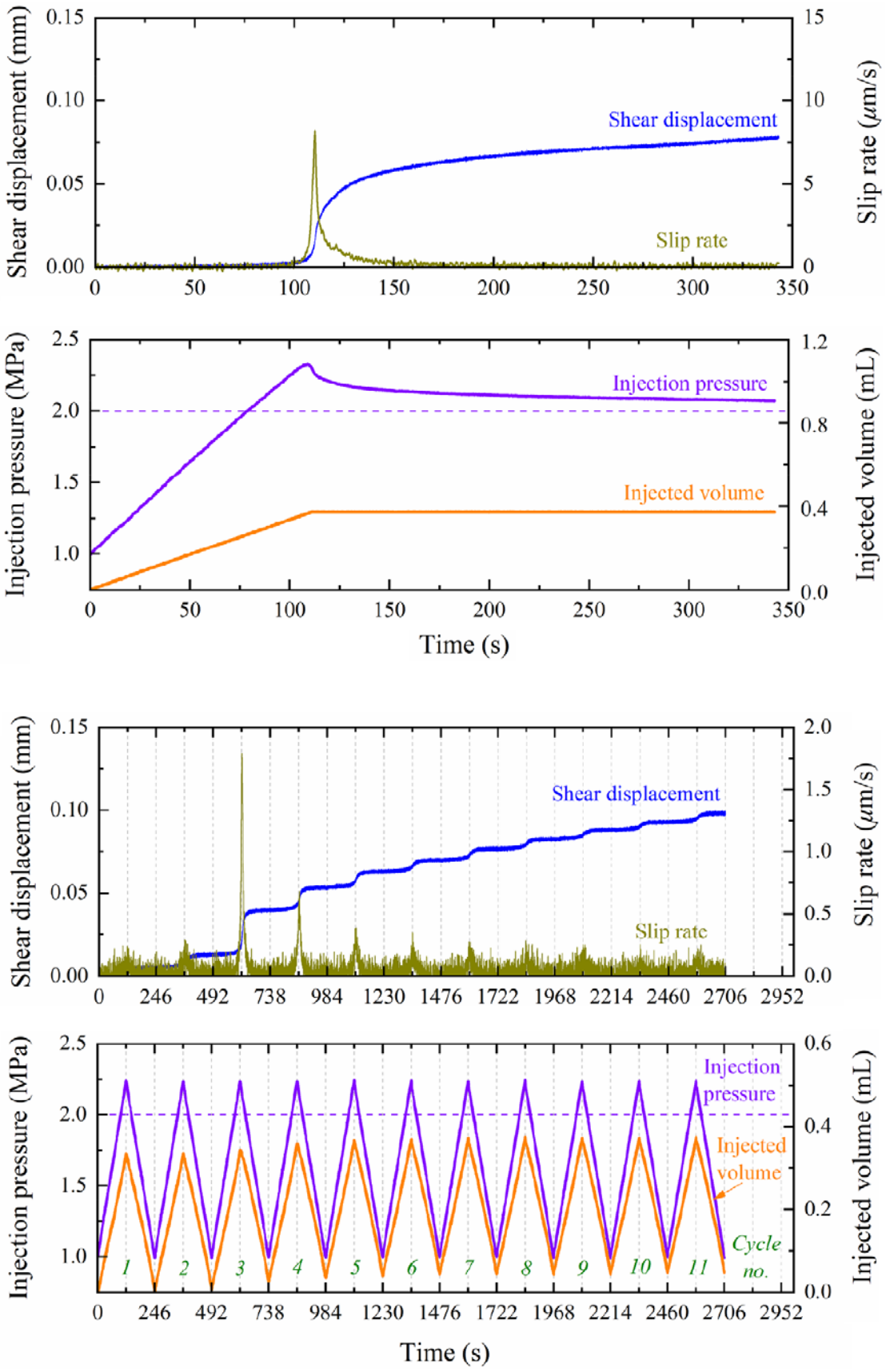

Fig.5: Evolution of shear displacement and slip rate during monotonic (top) and cyclic (bottom) injection shear-flow experiments in a granite sample containing an inclined natural fracture (modified from Ji et al., 2021).

3.5 Hydraulic energy

It is well known that the maximum expected injection-induced seismic moment magnitude increases with injection volume (McGarr, 2014; van der Elst, 2016; Galis et al., 2017) and that local magnitude-net volume relationships (Hofmann et al., 2018) as well as cumulative hydraulic energy-seismic injection efficiency relationships (Bentz et al., 2020) have been used to manage injection-induced seismic hazard (Kwiatek et al., 2019; Broccardo et al., 2020; Hofmann et al., 2018, 2019, 2021).

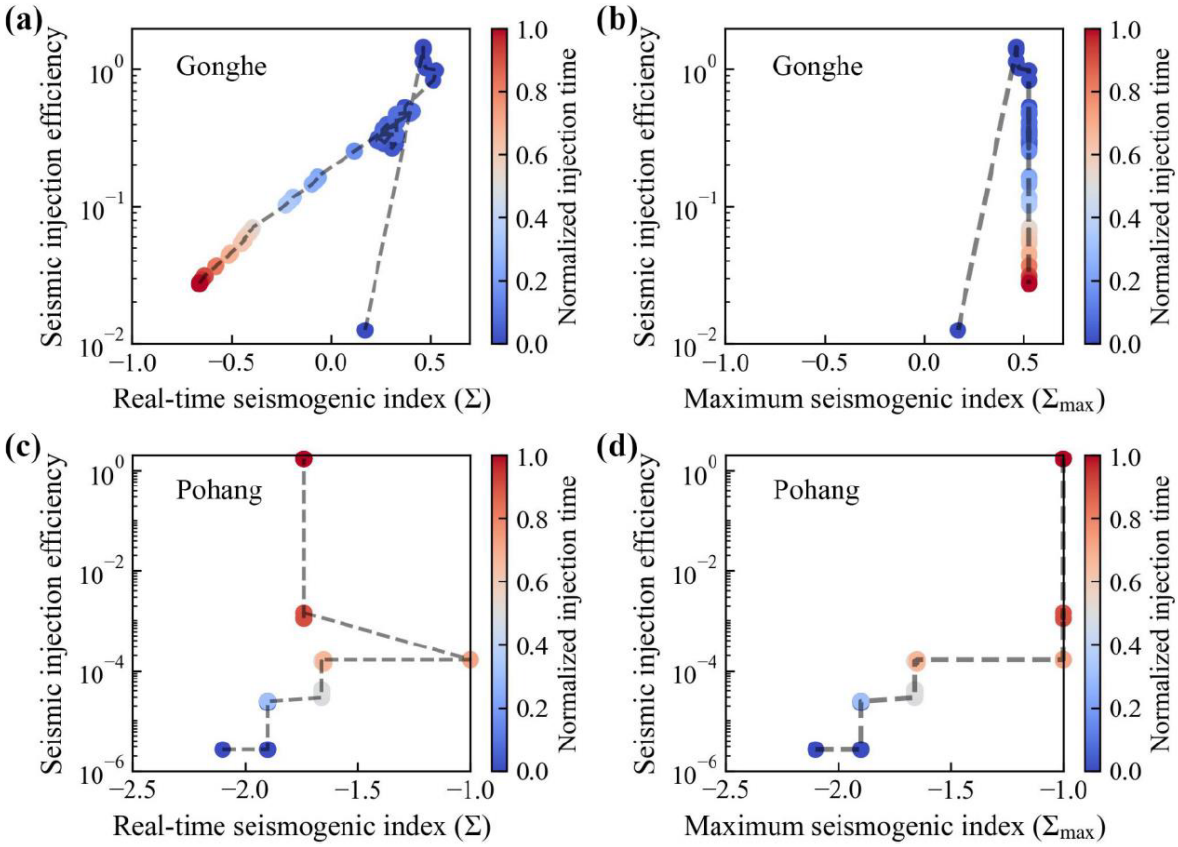

Fig.6: Seismic injection efficiency as a function of real-time seismogenic index (left) and maximum seismogenic index (right) for Gonghe, China (top) and Pohang, Korea (bottom). Real-time seismogenic index – seismic injection efficiency data may be feasible for seismic hazard assessment in relatively stable EGS reservoirs characterized by decreasing seismogenic index and seismic injection efficiency. Maximum seismogenic index – seismic injection efficiency data may be suitable to describe the seismic behavior of relatively unstable EGS reservoirs characterized by generally increasing seismogenic index and seismic injection efficiency (Zhang et al., under review).

We applied these relationships now to the Gonghe EGS in China and the Pohang EGS in Korea and propose to use the relationship between seismogenic index and seismic injection efficiency as an additional indicator for the management of injection-induced seismic hazard. Specifically, we compared the maximum magnitude estimated from the real-time seismogenic index with the maximum magnitude estimated from the maximum seismogenic index and concluded that using the real-time seismogenic index seems more feasible for stable EGS reservoirs (with decreasing seismogenic index and seismic injection efficiency, such as Gonghe) and the use of the maximum seimogenic index appears to be more suitable for unstable reservoirs (with increasing seismogenic index and seismic injection efficiency, such as Pohang) (Zhang et al., under review; Fig. 6). Overall, we recommend that such relationships could be included as standard procedures for seismic risk assessment and mitigation during hydraulic stimulation treatments, and we have the idea of using them for automated injection protocols as described later.

4 Discussion

Note, that the effects of the individual injection parameters could not be described in all their complexity here. We therefore refer to the publications provided in the text for further reading. Additionally, some of these effects are not entirely clear yet, there are partly contradicting observations reported in the literature and the underlying processes can vary significantly from site to site. More experiments are therefore needed at all scales and the experience from the hydrocarbon industry should be better integrated into EGS developments. Nevertheless, much improvement has been made in recent years in the fields of seismic risk mitigation and controlled permeability enhancement as for example shown in the Blue Mountain EGS demonstration project in the USA (Norbeck and Latimer, 2023).

The focus of this publication is the influence of injection parameters on hydraulic shear stimulation results. However, we note that also other effects, such as the effect of well placement/completion (Mathur et al., 2024) and geological boundary conditions, including reservoir temperature (Cacace et al., 2021; Ji et al., 2022e; Fig. 7), in-situ stress state (Ji et al., 2022d; Mathur et al., 2024) and fault properties (Ji et al., 2023c; Zhang et al., 2022), may even be more important.

In our laboratory experiments on sawcut faults in cylindrical granite samples we observed that besides elevated injection rates, also elevated normal stresses reduce the earthquake nucleation length which results in higher slip velocities and slip displacements and thus a higher seismic hazard (Ji et al., 2022d). Systematic sensitivity analyses of our Dutch geothermal reservoir models have confirmed that increased stress/depth increases the seismic hazard potential (Hutka et al., 2023b; Mathur et al., 2024). However, experiments performed by Zhang et al. (2022) showed a transition from velocity strengthening (stable) to velocity weakening (unstable) behavior of faults during fault slip experiments when decreasing the effective confining pressure. At the same time, it is well known that elevated effective normal stresses on fractures lead to a reduction in permeability (e.g., Hofmann et al., 2016). Awareness of the effective in-situ stresses in relation to fractures and faults is therefore critical in managing injection-induced seismicity and permeability enhancement.

On the one hand, fractures and faults are a potential geothermal development target due to elevated heat and fluid flow. On the other hand, fluid injection into large faults carry the risk of hosting large injection-induced seismic events. Obviously, staying away from faults thus significantly reduces the seismic risks (e.g., Mathur et al., 2024), even though our laboratory experiments highlight that injecting adjacent to faults can also cause induced seismic hazards due to the high fluid pressure required to create new fractures in intact rock matrix (Zhang et al., 2024b). At the same time, natural fracture networks influence hydraulic stimulation treatments, for example by promoting the development of more complex fracture networks and thus a larger heat exchange area (Farkas et al., 2023; Li et al., 2022). For example, in our phase field models, we found that as the strength contrast between natural fractures and the rock mass increases, complex fracture networks are more likely to form, and stronger cemented fractures require higher pressures to open compared to an unfractured intact rock mass (Li et al., 2022). The fault slip experiments performed by Zhang et al. (2022) also showed that an increasing Chlorite content in a fault stabilizes slip, but reduces frictional strength. This highlights the importance of the presence and properties of fractures and faults when planning hydraulic stimulation treatments.

The goal of the Helmholtz Young Investigator Group ARES is to develop a comprehensive understanding of injection-induced seismicity and permeability enhancement in EGS. From this understanding we want to derive geothermal reservoir engineering concepts for different geological conditions and apply them in field-scale EGS demonstrators. Additionally, we want to use new mine-scale experiments to assess how the influence of injection parameters and geological boundary conditions, which we have identified mainly from laboratory experiments and validated numerical models in recent years, can be translated to complex geological

systems. In the long term, the geothermal underground laboratory GeoLaB, which is currently in the exploration phase, can for example serve as a mine scale laboratory to demonstrate EGS technologies under well monitored and controlled conditions. After we have investigated the effects of individual operational parameters and some geological constraints in the past years, we want to investigate the potential of adaptive stimulation control approaches on the efficient permeability enhancement and seismic hazard mitigation. Therefore, we will investigate the influence of rock and fracture properties of isotropic (e.g., granites) and anisotropic (e.g., metamorphic rock) rock, including the effects of mineralogy and mineral size distribution on fault permeability and stability. The newly acquired true triaxial cell at the GFZ will be a key device for this. We would also like to investigate other stimulation techniques such as chemical stimulation and hydraulic stimulation with proppants and other environmental impacts of geothermal, such as drinking water contamination.

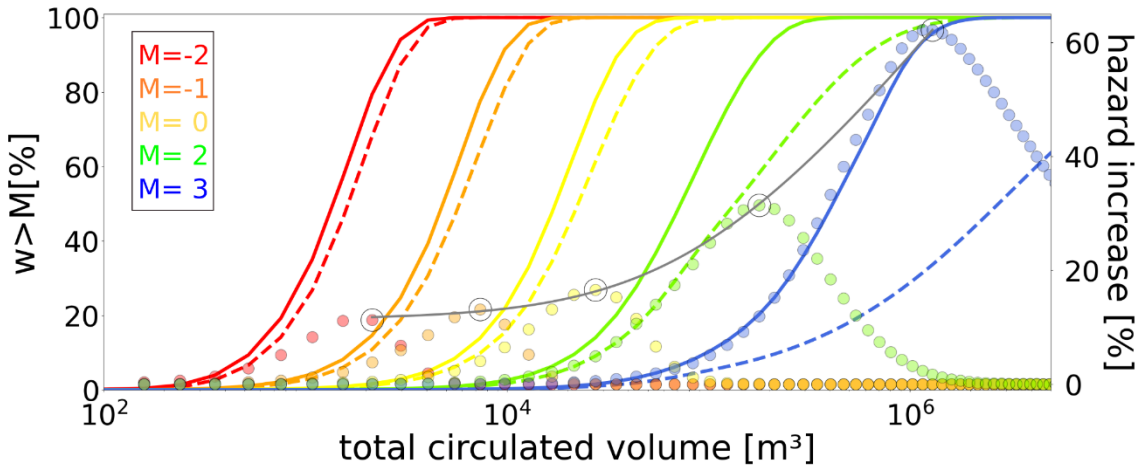

Fig.7: Cumulative exceedance probability of a given moment magnitude (w>M) for a simulated geothermal well doublet during 30 years of continuous operation. Solid lines represent the coulomb failure stress model in GOLEM with porothermoelastic stress transfer. Dashed lines show the results with poroelastic stress transfer witout thermal effects. Points indicate the increase in seismic hazard for a given volume of injected fluid and the grey curve is the fitting curve of ttheir maximum, indicating a power law increase in seismic hazard with respect to the expected maximum moment magnitude and circulated volume (based on Cacace et al., 2021).

5 Conclusions

Overall, we find that field operations that tend to promote more efficient permeability enhancement also tend to increase seismic hazard. However, our research suggests that the evolution of permeability and seismicity for geothermal energy applications can, to some extent, be engineered through controlled fluid injection protocols that take into account local geological conditions. While the geological conditions appear to have the strongest influence on the success of stimulation treatments in terms of permeability enhancement and induced seismicity, careful design of the injection protocol can at least improve the balance between permeability enhancement and seismic hazard at a particular site within the local geological constraints.

6 Acknowledgements

We kindly acknowledge the financial support of the Helmholtz Association's Initiative and Networking Fund for the Helmholtz Young Investigator Group ARES (contract number VH-NG-1516).

7 References

Bentz, S., Kwiatek, G., Martinez-Garzon, P. et al. (2020). Geophysical Research Letters, https://doi.org/10.1029/2019GL086185

Blöcher, G., Cacace, M., Jacquey, A.B. et al. (2018): Rock Mechanics and Rock Engineering, https://doi.org/10.1007/s00603-018-1521-2

Baisch, S., Vörös, R., Rothert, E. et al. (2010): A numerical model for fluid injection induced seismicity at Soultz-sous-Forêts. International Journal of Rock Mechanics and Mining Sciences, https://doi.org/10.1016/j.ijrmms.2009.10.001

Broccardo, M., Mignan, A., Grigoli, F. et al. (2020): Natural Hazards and Earth System Sciences, https://doi.org/10.5194/nhess-20-1573-2020

Cacace, M., Hofmann, H., Shapiro, S.A. (2021): Scientific Reports, https://doi.org/10.1038/s41598-021-02857-0

Cacace, M., Jacquey, A. B. (2017): Solid Earth, https://doi.org/10.5194/se-8-921-2017

Fang, Y., Elsworth, D., Wang, C. et al. (2017): Journal of Geophysical Research: Solid Earth, https://doi.org/10.1002/2016jb013435

Farkas, M. P., Hofmann, H., Zimmermann, G. et al. (2023): Acta Geotechnica, https://doi.org/10.1007/s11440-022-01648-9

Galis, M., Ampuero, J.P., Mai, P.M. et al. (2017): Science Advances, https://10.1126/sciadv.aap7528

Ge, S., Saar, M. O. (2022): Review: Induced Seismicity During Geoenergy Development—A Hydromechanical Perspective. Journal of Geophysical Research: Solid Earth, https://doi.org/10.1029/2021JB023141

Hofmann, H., Zimmermann, G., Huenges, E. et al. (2021): Geothermics, https://doi.org/10.1016/j.geothermics.2021.102146

Hofmann, H., Zimmermann, G., Farkas, M. et al. (2019): Geophysical Journal International, https://10.1093/gji/ggz058

Hofmann, H., Zimmermann, G., Zang, A. et al. (2018): Geothermal Energy, https://doi.org/10.1186/s40517-018-0114-3

Hofmann, H., Blöcher, G., Milsch, H. et al. (2016): International Journal of Rock Mechanics & Mining Sciences, http://dx.doi.org/10.1016/j.ijrmms.2016.05.011

Hutka, G., Cacace, M., Hofmann, H., et al. (2023a): Scientific Reports, https://doi.org/10.1038/s41598-023-30866-8

Hutka, G., Cacace, M., Hofmann, H., et al. (2023b): Geologie en Mijnbouw - Netherlands Journal of Geosciences, https://doi.org/10.1017/njg.2023.7

Ji, Y., Zhang, S., Hofmann, H. et al. (under review): The 2017 Mw 5.5 Pohang earthquake could have been mitigated by an adjusted shut-in strategy. Submitted to Nature Communications.

Ji, Y., Chen, Y., Hofmann, H. et al. (2023a): Deep Underground Science and Engineering, https://doi.org/10.1002/dug2.12053

Ji, Y., Zhang, W., Hofmann, H., et al. (2023b): Geophysical Journal International, https://doi.org/10.1093/gji/ggac416

Ji, Y., Zhang, W., Hofmann, H.et al. (2023c): Geophysical Research Letters, https://doi.org/10.1029/2023GL104662

Ji, Y., Hofmann, H., Duan, K. et al. (2022a): Earth-Science Reviews, https://doi.org/10.1016/j.earscirev.2021.103916

Ji, Y., Kluge, C., Hofmann, H. et al. (2022b): Journal of Rock Mechanics and Geotechnical Engineering, https://doi.org/10.1016/j.jrmge.2021.12.007

Ji, Y., Hofmann, H., Rutter, E. H. et al.(2022c): Rock Mechanics and Rock Engineering, https://doi.org/10.1007/s00603-022-02797-9

Ji, Y., Wang, L., Hofmann, H. et al. (2022d): Geophysical Research Letters, https://doi.org/10.1029/2022GL100418

Ji, Y., Hofmann, H., Rutter, E. H. et al. (2022e): Geophysical Research Letters, https://doi.org/10.1029/2022GL101212

Ji, Y., Zhuang, L., Wu, W. et al. (2021): Rock Mechanics and Rock Engineering, https://doi.org/10.1007/s00603-021-02438-7

Kwiatek, G., Saarno, T., Bluemle, T.A. (2019): Science Advances, https://doi.org/10.1126/sciadv.aav7224

Li, X., Hofmann, H., Yoshioka, K., et al. (2022): Rock Mechanics and Rock Engineering, https://doi.org/10.1007/s00603-022-02970-0

Mathur, B., Hofmann, H., Cacace, M. et al. (2024): Geologie en Mijnbouw - Netherlands Journal of Geosciences, https://doi.org/10.1017/njg.2023.12

McGarr, A. (2014): Journal of Geophysical Research: Solid Earth, https://doi.org/10.1002/2013JB010597

Miao, S., Zang, A., Ji, Y. et al. (submitted): Transient strain rate response and deformation heterogeneity in granite during stress relaxation: insights from distributed optical fiber measurements. Submitted to Journal of Geophysical Research: Solid Earth

Nicolas, A., Blöcher, G., Kluge, C. (2020): Geomechanics for Energy and the Environment, https://doi.org/10.1016/j.gete.2020.100183

Norbeck, J.H., Latimer, T.M. (2023): Commercial-scale demonstration of a first-of-a-kind Enhanced Geothermal System. Preprint submitted to EarthArXiv. https://doi.org/10.31223/X52X0B

Permann, C. J., Gaston, D.R., Andrs, D. et al. (2020): SoftwareX, https://doi.org/10.1016/j.softx.2020.100430

Rutter, E.H., Mecklenburgh, J. (2018): Journal of Geophysical Research: Solid Earth, https://doi.org/10.1002/2017JB014858

Sabah, M., Ameri, M. J., Hofmann, H. et al. (2022): Geothermics, https://doi.org/10.1016/j.geothermics.2022.102481

Samuelson, J., Elsworth, D., Marone, C. (2009): Journal of Geophysical Research, https://doi.org/10.1029/2008jb006273

Segall, P., Lu, S. (2015): Journal of Geophysical Research: Solid Earth, https://doi.org/10.1002/2015JB012060

Shapiro, S.A., Dinske, C. & Kummerow, J., 2007. Probability of a givenmagnitude earthquake induced by a fluid injection. Geophysical Research Letters 34(22): L22314.

Shapiro, S.A., Dinske, C., Langenbruch, C. et al. (2010): Leading Edge, https://doi.org/10.1190/1.3353727

Ucar, E., Berre, I., Keilegavlen, E. (2017): Postinjection Normal Closure of Fractures as a Mechanism for Induced Seismicity. Geophysical Research Letters, https://doi.org/10.1002/2017GL074282

Van der Elst, N.J., Page, M.T., Weiser, D.A. et al. (2016): Journal of Geophysical Research: Solid Earth, https://doi.org/10.1002/2016JB012818

Zhang, S., Ji, Y., Hofmann, H. et al. (under review): Evaluation of injection-induced seismic hazards in Enhanced Geothermal Systems: Lessons learned from the comparison of Gonghe and Pohang. Submitted to Seismological Research Letters.

Zhang, S., Ji, Y., Hofmann, H. (2024a): Geophysical Journal International, https://doi.org/10.1093/gji/ggae156

Zhang, S., Ji, Y., Hofmann, H., Li, S. et al. (2024b): Philosophical Transactions of the Royal Society A, in print. https://doi.org/10.1098/rsta.2023.0186

Zhang, F., Huang, R., An, M. et al. (2022): Journal of Geophysical Research – Solid Earth, https://doi.org/10.1029/2022JB024310

Implementation and test of an extended Hoek-Brown-based anisotropic constitutive model for fractured crystalline rock

Implementierung eines erweiterten Hoek-Brown-basierten anisotropen Stoffgesetzes für geklüftetes kristallines Gestein

Rocio Paola León Vargas[1], Max Friedel[2], Tymofiy Gerasimov[1], Alireza Hassanzadegan[1], Heinz Konietzky[2] and Fabian Weber[2]
[1]BGE TECHNOLOGY GmbH, Eschenstraße 55, 31224 Peine, Germany
[2]Geotechnical Institute, TU Bergakademie Freiberg, Gustav-Zeuner-Str. 1, 09599 Freiberg, Germany

Abstract

Crystalline rocks are considered as potential host rock formation for deep geological repositories (DGRs) for nuclear waste in many countries (Rutqvist & Tsang 2024; Kroner et al. 2021; Faybishenko et al. 2016). Ensuring the long-term integrity of DGRs requires advanced numerical models capable to accurately simulating the complex behavior of fractured crystalline rocks (Müller et al. 2023). A critical question remains: which constitutive models are best suited for capturing the mechanical and hydraulic interactions within both fractured and intact crystalline rocks, especially for proving the integrity of the geological barrier?

This paper introduces the BARIK model, which extends the Hoek-Brown constitutive model to simulate the anisotropic behavior of fractured crystalline rock common in DGR environments. The BARIK model can handle matrix anisotropy and up to three different fracture systems each with its own strength properties and failure criteria. These considerations are essential for assessing the strength-reducing effects of fractures on the integrity of the geological barrier, highlighting the critical role they play in evaluating the barrier's structural stability.

The BARIK model is implemented in two different computational platforms: FLAC3D and OpenGeoSys, enabling cross-validation and enhancing its robustness. This dual integration enables the identification and correction of discrepancies between software tools. The model supports a range of calculations, from isotropic-elastic to orthotropic-elasto-plastic, making it a powerful tool for site selection and long-term safety assessments of barriers for geological repositories.

The development of the BARIK model signifies a substantial advancement in understanding the complex material behavior of fractured crystalline rock. This study supports the ongoing evaluation of barrier integrity by providing important information on how to create, test, and use models.

Zusammenfassung

Kristalline Gesteine werden in vielen Ländern als potenzielle Wirtsgesteine für die Endlagerung radioaktiver Abfälle in Betracht gezogen (Rutqvist & Tsang 2024; Kroner et al. 2021; Faybishenko et al. 2016). Die langfristige Integrität von einem Tiefenlager erfordert fortschrittliche numerische Modelle, die das komplexe Verhalten von geklüftetem kristallinem Gestein präzise simulieren können. Eine entscheidende Frage bleibt: Welche konstitutiven Modelle eignen sich am besten, um die mechanischen Wechselwirkungen sowohl in geklüftetem als auch in intaktem kristallinem Gestein, insbesondere während der Integritätsprüfung der geologischen Barriere, zu erfassen?

In dieser Arbeit wird das BARIK-Modell vorgestellt. Es erweitert das Hoek-Brown-Modell, um das anisotrope mechanische Verhalten von geklüftetem kristallinem Gestein zu simulieren. Das BARIK-Modell kann Matrixanisotropie und bis zu drei verschiedene Schwächeflächensysteme mit jeweils eigenen Festigkeitseigenschaften und Versagenskriterien verarbeiten. Diese Überlegungen sind wesentlich, um die festigkeitsmindernden Effekte von Klüften auf die Integrität der geologischen Barriere zu bewerten, da sie eine kritische Rolle bei der Beurteilung der strukturellen Stabilität der Barriere spielen.

Das BARIK-Modell wird auf zwei verschiedenen Rechenplattformen implementiert: FLAC3D und OpenGeoSys, wodurch eine Kreuzvalidierung und Erhöhung der Robustheit des Modells ermöglicht wird. Diese duale Implementierung erlaubt die Identifizierung und Korrektur von Abweichungen zwischen den Software-Tools. Das Modell unterstützt eine Vielzahl von Berechnungen, von isotrop-elastischen bis zu orthotrop-elasto-plastischen Modellen, und stellt somit ein vielseitiges Werkzeug für die Standortwahl und langfristige Sicherheitsbewertungen von Barrieren für geologische Tiefenlager in kristallinem Wirtsgestein dar.

Die Entwicklung des BARIK-Modells stellt einen bedeutenden Fortschritt in Bezug auf das komplexe Materialverhalten von geklüftetem kristallinem Gestein dar. Diese Arbeit liefert wichtige Erkenntnisse zur Implementierung, Prüfung und Anwendung geomechanischer Stoffgesetze. Die Ergebnisse tragen zur umfassenderen Diskussion über Rechenmethoden und Mehrbarrierensystembewertungen in Tiefenlagern bei und zeigen, wie wichtig die mechanische Integrität für die sichere Entsorgung radioaktiver Abfälle, insbesondere in geologischen Tiefenlagern in kristallinem Wirtsgestein, ist.

1 Introduction

1.1 Background and Motivation

Over the past few decades, extensive research has been done in Germany and abroad on the safe disposal of radioactive waste, focusing on safety assessments and long-term containment strategies for deep geological repositories (DGRs). A key element in ensuring repository safety is the identification of an effective containment zone, which must isolate waste for up to one million years (StandAG vom 05.05.2017). Previous studies, such as the CHRISTA and CHRISTA-II, have advanced the methodologies for proving the integrity of such geological barriers (Jobmann et al. 2021). However, a critical challenge remains: translating qualitative safety criteria into quantifiable terms, especially for fractured crystalline rock.

The BARIK project emerges from the need to develop advanced models that accurately simulate the complex mechanical and hydraulic behavior of fractured crystalline rock. By extending the Hoek-Brown (HB) constitutive model, BARIK addresses the anisotropic nature of these rocks, providing robust tools for assessing barrier integrity. This research is vital for supporting the safe disposal of nuclear waste and refining long-term safety assessments in DGR environments.

1.2 Objectives of the Study

The objective of the BARIK research project is to develop and test an enhanced three-dimensional HB constitutive model capable of capturing the anisotropic strength behavior of fractured crystalline rock. In particular, this model takes into account how multiple fracture systems in the rock mass weaken it. These effects are very important for checking the strength of geological barriers in DGRs.

The primary focus of this paper is on the model implementation in FLAC3D and OpenGeoSys (OGS) and on the laboratory tests. These implementations allow for cross-validation between different computational codes, helping to identify and correct discrepancies that may arise from their use.

The BARIK model features a non-linear elasto-plastic formulation for the crystalline matrix with up to three weakness planes (joints). Additionally, it includes softening functions for post-failure behavior. The validation is based on the calculation of benchmark tests, with the ultimate goal of applying the model as a dilatancy criterion for long-term safety assessments in DGR environments. The BARIK model's ability to capture the complex behavior of fractured rock under various loading conditions could make it a valuable tool for predicting rock mass response in DGRs. It is also pursued to incorporate hydro-mechanical coupling through the Biot coefficient in the BARIK model, accounting for the effective stress in fractured rock.

2 Development of the BARIK Model

2.1 Theoretical formulation of the Extended Hoek-Brown Criterion

Crystalline rock has a predominantly brittle fracture behavior and is only to a small extent characterized by dilatant deformation (Chang 2017; Mahabadi et al. 2014; Agharazi et al. 2012). Mechanical loading could result in the development of microcracks, fissures, and fractures, leading to anisotropic, non-linear behavior that is highly dependent on the loading path due to the presence of these discontinuities (see Fig. 1). But even without loading and damage some crystalline rocks behave anisotropic.

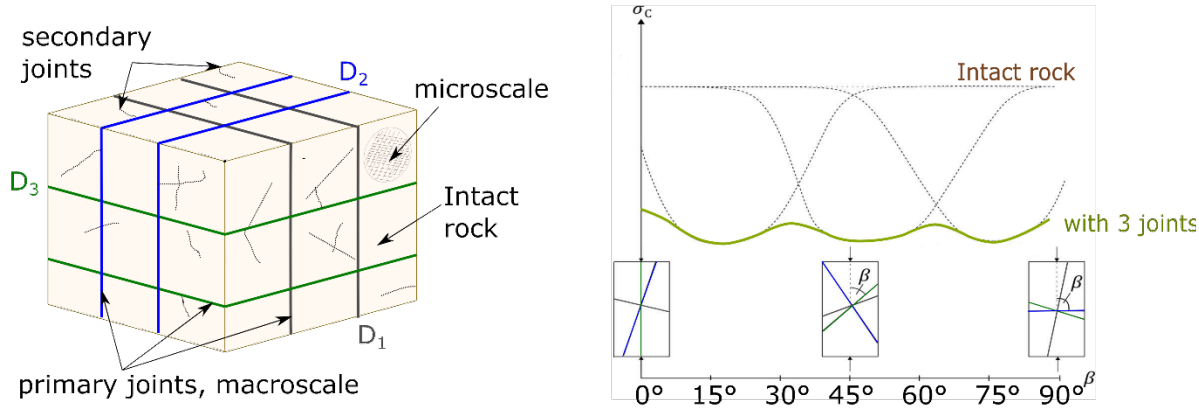

Fig. 22: Schematic of the rock matrix with multiple fracture systems (D_i) for the BARIK model (left) and the strength-reduction effects of fractures on rock mass (right), adapted from León Vargas et al. (2023).

The extended HB criterion describes how the strength of fractured crystalline rock changes with different orientations and magnitudes of stress. This formulation is based on the empirical HB failure criterion (Hoek & Brown 2019; Eberhardt 2012; Hoek et al. 2002) and its theoretical derivation (Zuo et al. 2015). The original Hoek-Brown criterion is expressed in Equation 2-1.

$$\sigma_1' = \sigma_3' + \sigma_{ci}\left(m_b \cdot \frac{\sigma_3'}{\sigma_{c0}} + s\right)^a \qquad 2\text{-}1$$

where:

σ_{ci}… uniaxial compressive strength of intact rock
σ_1'… maximum effective principal stress
σ_3'… minimum effective principal stress

$$m_b = m_i \cdot e^{\left(\frac{GSI-100}{28-14D}\right)} \qquad 2\text{-}1$$

$$s = e^{\left(\frac{GSI-100}{9-3D}\right)} \qquad 2\text{-}2$$

$$a = \frac{1}{2} + \frac{1}{6}\left(e^{-GSI/15} - e^{-20/3}\right) \qquad 2\text{-}3$$

m_i… material constant
GSI… Geological Strength Index (GSI = 1, …,100)

The BARIK constitutive model extends the HB criterion by incorporating anisotropic failure behavior. This model can capture the directional dependence of strength and deformation by considering both matrix anisotropy and the properties of up to three distinct and independent joints. Anisotropic deformation of the elastic material is caused by orthotropic elastic properties in three main directions that are not coupled to the direction of the joints. This decoupling is required for assessing the strength-reducing effects of fractures on rock mass, which improves the model's predictive capabilities under various loading conditions.

The Mohr-Coulomb criterion (MC) is used to model how the weakness planes fail, while the extended HB criterion controls how the rock matrix fails. Each component of the rock mass (matrix and fractures) follows its own failure criterion, and their combined effect determines the overall strength and deformation response of the system. This enables a detailed representation of the anisotropic mechanical behavior of fractured crystalline rocks.

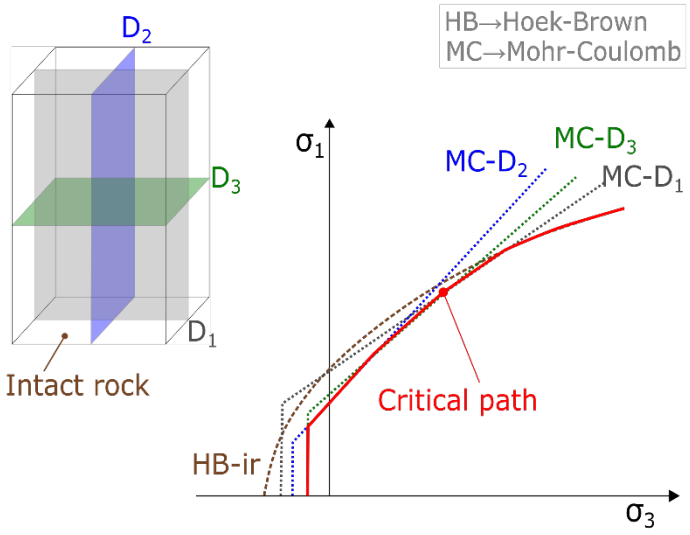

Fig. 23: Critical path of matrix (HB) and fracture/weakness plane (MC) failure criteria, adapted from León Vargas et al. (2023).

Due to its complexity, the implementation of the BARIK constitutive model follows a certain sequence (See Fig. 24). The first step focuses on the anisotropic elastic deformation behavior, where the model is set up to capture the directional differences in the material's elastic response.

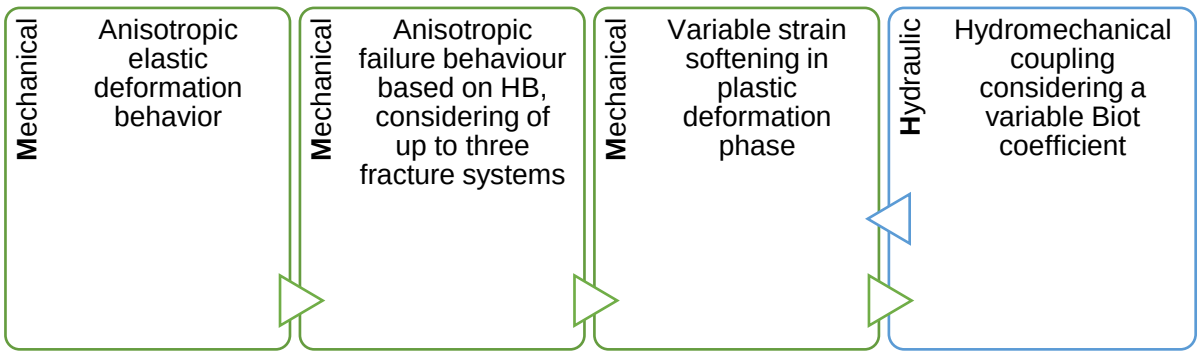

Fig. 24: Basic structure of the constitutive model BARIK, a multiple anisotropic HB constitutive model with strain softening in the post-failure region.

The second step considers up to three weakness planes and extends the model to include anisotropic failure behavior based on the HB criterion. In this step, the model simulates the failure process, considering the influence of these fractures on the overall strength and behavior of the rock. The third step introduces variable strain softening during the plastic deformation phase, allowing the model to adjust the strength of the material as it deforms after failure, ensuring that the loss of strength is adequately captured. Finally, the fourth stage incorporates hydromechanical coupling, where a variable Biot coefficient is considered.

2.2 Implementation of the BARIK Model in FLAC3D

The technical implementation of the BARIK model was conducted in Visual Studio using C++, and the compiled code was loaded into FLAC3D as a Dynamic Link Library (.dll). This implementation allows the BARIK model to be utilized as a User-Defined Model (UDM) in FLAC3D. The UDM builds upon the existing Hoek-Brown-PAC constitutive model for the matrix and utilizes the in-built Columnar-Basalt (COMBA) Model to represent the three weakness planes.

The implementation process in FLAC3D involved several stages. In the first stage, the HB model was modified to replace the isotropic elastic formulation with an orthotropic elastic approach. This adaptation allows to consider anisotropic elastic properties of the matrix. Following this, a comprehensive validation and verification phase was conducted. The second step was to add the joint sets to the model. The strength of each joint set is modeled using the MC criterion with a tension cut-off. The in-built COMBA Model in FLAC3D was utilized to incorporate the presence of the weakness planes.

The BARIK model facilitates simulations ranging from isotropic-elastic to orthotropic-elasto-plastic behavior of the matrix. This flexibility enables the detailed analysis of the complex, non-linear, and anisotropic behavior of fractured crystalline rock, which depends on the loading paths and variable properties of the fractures. The resulting implementation of the BARIK model in FLAC3D captures the complex mechanical and coupled hydro-mechanical behavior of fractured crystalline rock and allows for a realistic simulation of anisotropic failure mechanisms.

2.3 Implementation of the BARIK Model in OpenGeoSys using MFront

The BARIK model was also implemented in OpenGeoSys (OGS) using MFront, an open-source code generator for constitutive models, which is integrated with the TFEL (Toolbox for Finite Elements and Life) library. This tool chain enabled the translation of material models described in high-level domain-specific languages into efficient C++ code, making it suitable for integration into finite element solvers (Helfer et al. 2015). MFront has been widely used in OGS to implement custom constitutive models, supporting the development of constitutive laws in multiple programming languages (Silbermann et al. 2021; Helfer & Marois 2020; Simo et al. 2020; Helfer et al. 2015).

Since the HB failure criterion, including its regularized and twice continuously differentiable version of interest, was not originally available in OGS as of 2023, it had to be implemented using MFront. To ensure a comprehensive description of the deformation behavior of fractured rock masses under complex stress conditions, the BARIK model incorporates orthotropic elasticity. The orthotropic elastic behavior, coupled with the non-linear failure characteristics of the HB criterion, allows the model to simulate the anisotropic response of the rock matrix under different loading paths.

Similar to the implementation procedure in FLAC3D, the HB model in MFront required a detailed mathematical formulation of the yield criterion. The generalized version of the classical HB yield function (Equation 2-5) from Hoek & Brown (1980), along with its smoothed or regularized counterpart (Hoek & Brown 2019; Dai et al. 2018), was satisfactorily implemented to capture the complex failure mechanisms of fractured crystalline rock.

$$F = \frac{I_1 \cdot m_b \cdot {\sigma_{ci}}^{-1+\frac{1}{a}}}{3} - s \cdot {\sigma_{ci}}^{\frac{1}{a}} + \sqrt{J_2} m_b \cdot {\sigma_{ci}}^{-1+\frac{1}{a}} \left(-\frac{\sqrt{3}\sin\theta}{3} + \cos\theta \right) + \left(2\sqrt{J_2}\cos\theta\right)^{\frac{1}{a}} \quad \text{2-4}$$

Where:

σ_{ci}… uniaxial compressive strength of intact rock
I_1… first deviatoric stress invariant
J_2… second deviatoric stress invariant
θ… Lode angle

The MFront implementation includes fundamental computational plasticity algorithms, such as the evaluation of the Jacobian matrix, stress-update algorithms, and return-mapping procedures.

To simulate the behavior of fractures within the rock mass in OGS, the BARIK model incorporates three orthogonal joint sets (or weak planes). Each joint set is defined by its normal vector’s orientation relative to a global basis. Initially, due to implementation constraints, the rotation was applied uniformly across the entire joint system, limiting the ability to specify arbitrary orientations for each joint plane. To address this limitation, separate local coordinate systems were introduced, allowing for an accurate and independent representation of each joint set's orientation.

The failure behavior of the matrix is represented using the HB failure criterion, while the failure of the ubiquitous joint sets is modeled using the MC failure criterion with a non-associated flow rule. This approach enables the BARIK model to incorporate three independent joint sets and elastic orthotropy to account for directional variations in the stiffness of the rock matrix. In this setup, the ubiquitous joint model was employed as a basis for representing the mechanical interactions between the joints and the surrounding rock matrix.

After completion of the mathematical formulation of the HB criterion and the joint sets, MFront was used to translate these relations into C++ code. The resulting numerical routines were linked to OGS as a UDM, allowing the BARIK model to be utilized in various geomechanical simulations of fractured crystalline rock formations.

2.4 Complementary laboratory program

The complementary laboratory program was developed as part of the BARIK research project to provide a comprehensive dataset for validation and verification of the BARIK constitutive model. This dataset is essential for accurately representing the anisotropic mechanical behavior of fractured crystalline rock, as required for DGRs. The laboratory tests were conducted on Freiberger Gneiss, a rock type selected due to its pronounced anisotropic properties in terms of deformation and strength, as well as its availability for obtaining a sufficient amount of sample material.

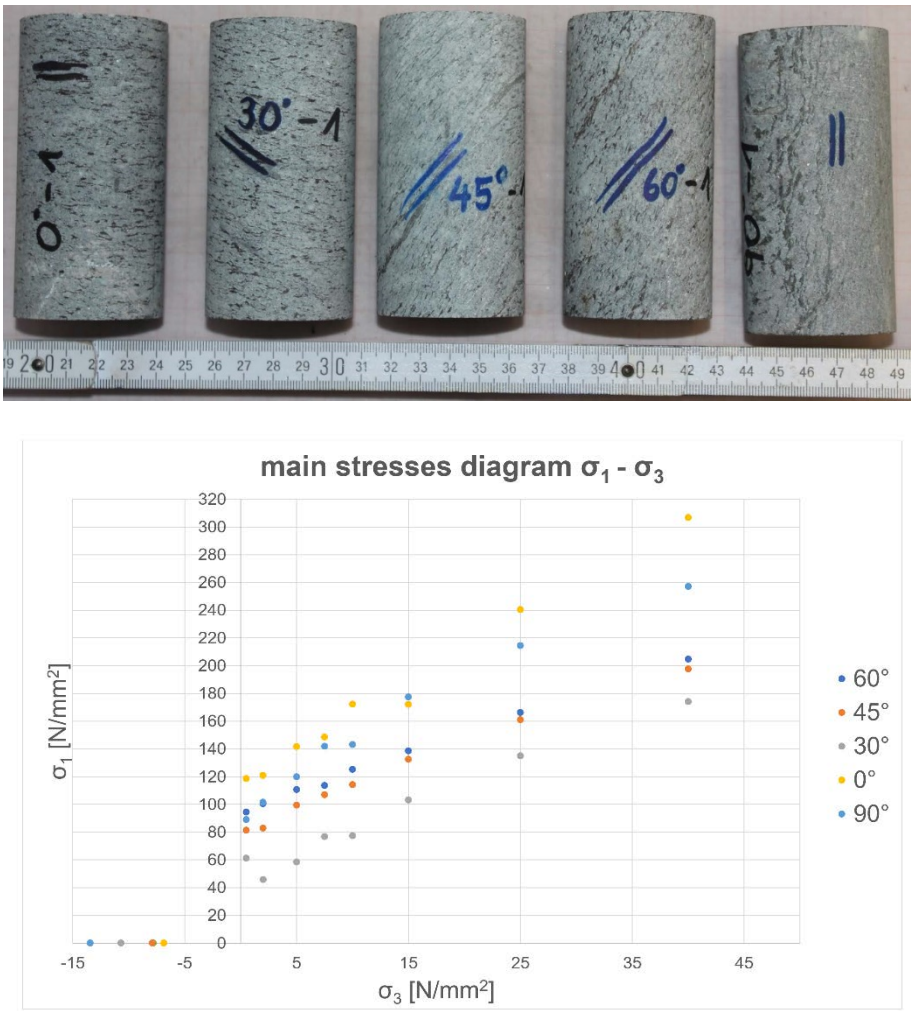

Fig. 25: Gneiss samples tested under different loading angles regarding the weakness planes and corresponding triaxial strength curves.

The first phase of the laboratory program was structured into two primary test categories:

- Basic Testing:
  - Determination of density and porosity of the samples.
  - Measurement of dynamic elastic constants through ultrasonic wave velocity testing to derive parameters such as Young's modulus and Poisson's ratio.
  - Determination of static elastic constants and uniaxial strength under uniaxial compression conditions.
  - Brazilian tests for the determination of tensile strength.
  - Uniaxial compression strength tests to establish baseline strength properties.

- Extended Testing:
  - Mechanical single-stage and multi-stage triaxial compression tests incorporating strain softening to capture the post-failure behavior of the material.
  - Hydromechanical (HM) coupled single-stage triaxial compression tests aimed at evaluating the evolution of permeability and the Biot coefficient, which are critical for quantifying changes in effective stress under saturated conditions.
  - Mechanical uniaxial compression tests on special prepared samples with distinct weakness planes filled with gypsum under different orientation angles.

The purpose of these primary tests was to obtain a robust dataset about deformation and strength properties, that reflects the anisotropic nature of Freiberger Gneiss under various loading directions (0°, 30°, 45°, 60°, and 90°). The experimental program includes tests with different orientations of the rock's structural planes (weakness planes) relative to the loading direction to capture the directional dependence of its mechanical properties and fracture mechanisms.

Fig. 26: Gneiss samples with distinct discontinuities before preparation and after testing.

Subsequently, the mechanical triaxial tests were finished and assessed, offering important data for the mechanical validation of the BARIK model. The HM-coupled triaxial tests are also finished. Their main goal was to figure out how the micromechanical damage processes change Biot coefficient and effective stresses in saturated rock samples.

The evaluation of the HM-coupled tests involved two main stages:

- Quantification of the damage state and derivation of the dilatancy boundary.
- Determination of the Biot coefficient under the corresponding stress conditions.

To proof that the gneiss samples are nearly fully saturated, Skempton-B-Tests have been performed before each HM-coupled test was started. For further validation of the BARIK model, uniaxial compression tests were conducted using samples with two distinct weakness planes. The tests were designed to verify the model's ability to simulate the complex mechanical behavior of fractured rock. The current focus is on evaluating the results of these tests to finalize the validation process. This extensive laboratory program formed a critical component of the BARIK project, providing the empirical foundation necessary for the successful implementation and validation of the BARIK constitutive model.

3 Verification and Validation

3.1 Verification in FLAC3D

The verification calculations were carried out for different matrix configurations and joint failure scenarios, focusing on shear and tensile failure behavior. The simulations considered a range of material configurations, including isotropic-elastic, transversely isotropic-elastic, transversely isotropic-elasto-plastic, and orthotropic-elastic matrices. Each configuration was compared with existing built-in models in FLAC3D, such as the Ubiquitous-Joint model (Ubi), the Anisotropic-Elasticity Ubiquitous-Joint model (UANISO), and the COMBA model, using various dip and dip direction (DD) angles for the matrix and joint systems.

For the isotropic-elastic matrix with shear failure in the joint systems, the results were compared between the BARIK model and the built-in Ubi and UANISO models. The simulations were performed for different dip and DD angles of matrix and joint. Exemplary results are presented in Fig. 27.

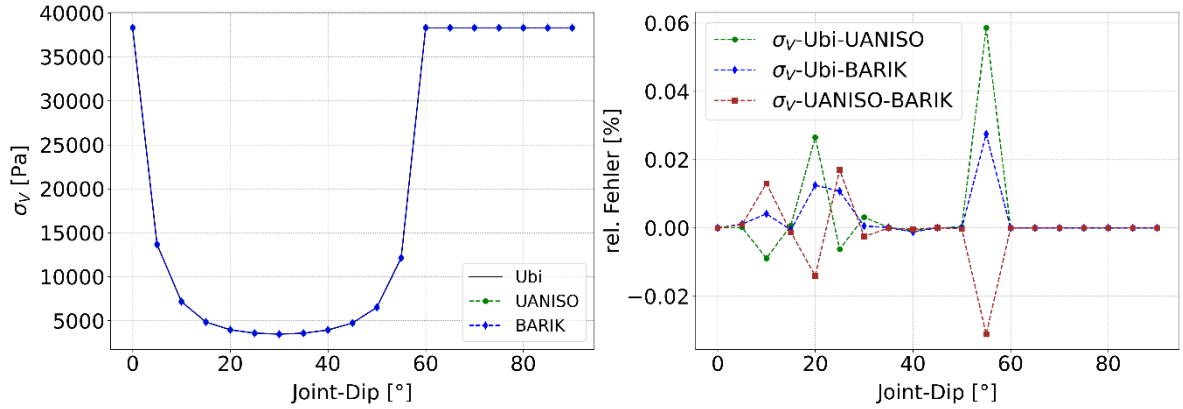

Fig. 27: Verification results for isotropic-elastic matrix with shear failure on weakness planes.

In the case of the transversely isotropic-elastic matrix comparison involved the BARIK model versus the UANISO model, with the weakness plane aligned in the direction of anisotropy (i.e., matrix dip = joint dip). Joint dip and joint DD angles were varied to evaluate the anisotropic response, and exemplary results are depicted in Fig. 28

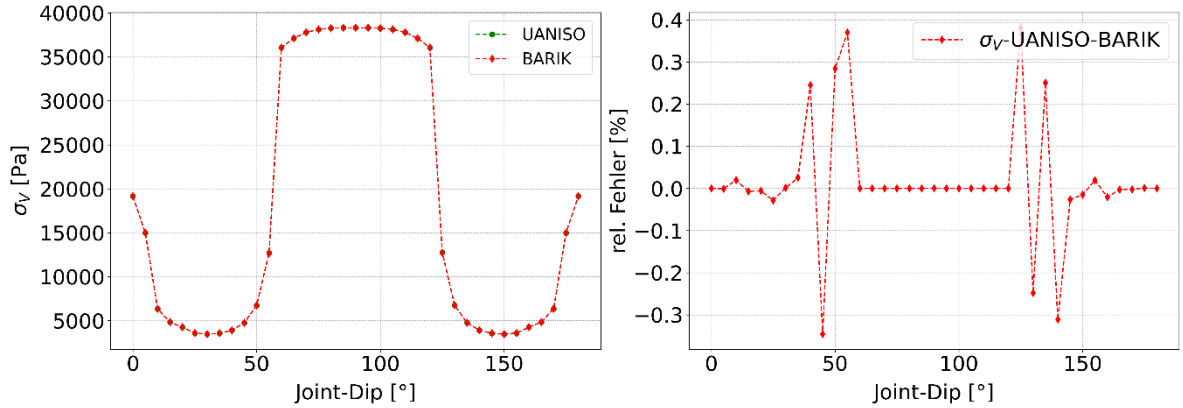

Fig. 28: Verification results for transversely isotropic-elastic matrix with shear failure in the weakness planes.

For the transversely isotropic-elasto-plastic matrix, uniaxial compression tests were simulated based on laboratory experiments using gneiss samples, described in 2.4. The evaluation focused on the strength behavior of the material under varying conditions of plasticity. The corresponding results are illustrated in Fig. 29.

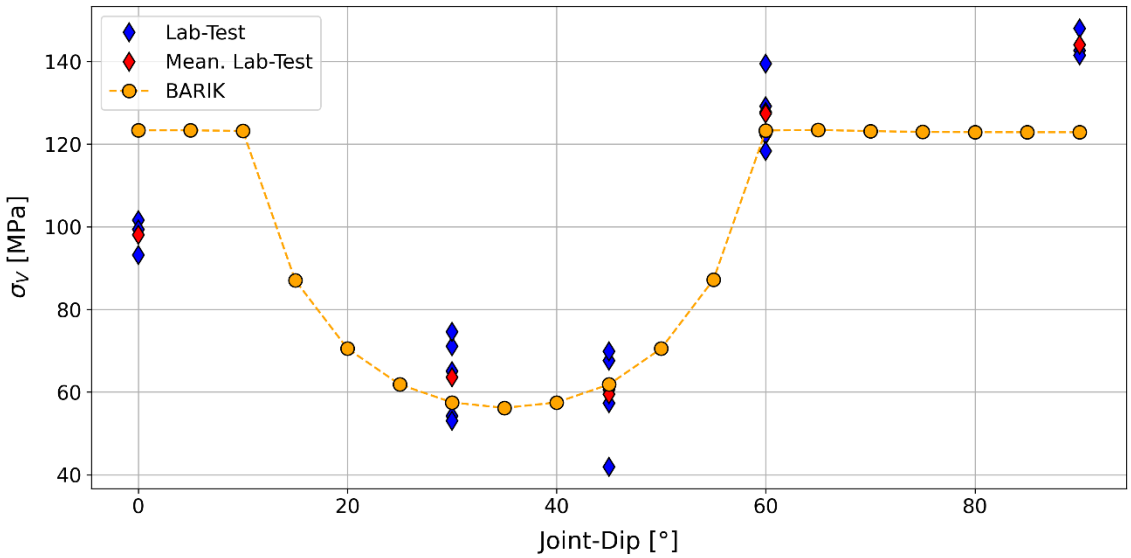

Fig. 29: Simulation results of uniaxial compression tests on gneiss samples with transversely isotropic-elasto-plastic matrix exhibiting shear failure in the weakness planes and HB failure in the matrix.

For verification of matrix and joint interaction, a plane strain tunnel model considering anisotropic material properties and in-situ stress was analyzed using the BARIK and COMBA models. The tunnel, with a radius of 1 meter is considered including orthogonal joint sets to represent rock mass discontinuities. Fig. 30 compares the final plastic states for different dip angles of joint no. 3 (0° and 60°) using both models. The results exhibited symmetrical plasticity patterns as joint orientation varied, confirming the models' capability to simulate the effects of different joint orientations on the tunnel's elasto-plastic response.

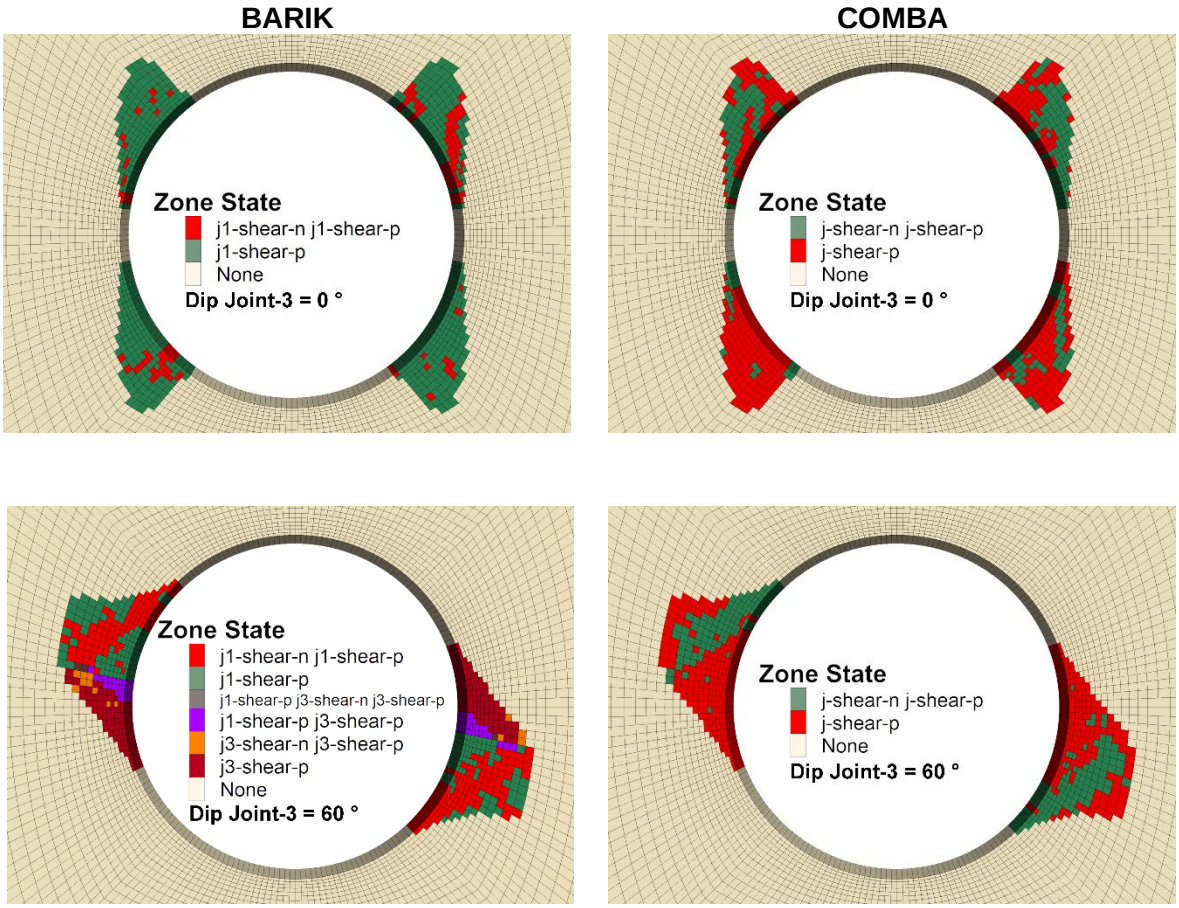

Fig. 30: Final plasticity comparison between BARIK and COMBA models in a jointed anisotropic elastic tunnel model, highlighting the influence of dip angles (0° and 60°).

The verification process yielded successful results across the test cases, with minor error deviations (less than 2-4%). These results show that the BARIK model in FLAC3D is reliable and accurate for simulating complex mechanical interactions in fractured crystalline rock.

3.2 Verification in OGS

The implementation of the BARIK model in OGS followed its successful integration into FLAC3D, which enabled a consistent verification approach across both platforms. The verification methodology initially developed for FLAC3D was adapted to validate the OGS implementation, ensuring consistency between the results obtained from the BARIK model in these two different numerical environments (explicit finite difference approach versus implicit finite element approach).

The verification process began with reproducing benchmark tests previously performed in FLAC3D. These tests included uniaxial and triaxial compression tests using cubic rock samples to evaluate the deformation and failure behavior under different loading conditions. As depicted in Fig. 31, the numerical results obtained in OGS demonstrate a high degree of agreement with the FLAC3D solution, indicating that the implementation of the BARIK model in OGS correctly captures the mechanical response of fractured crystalline rock.

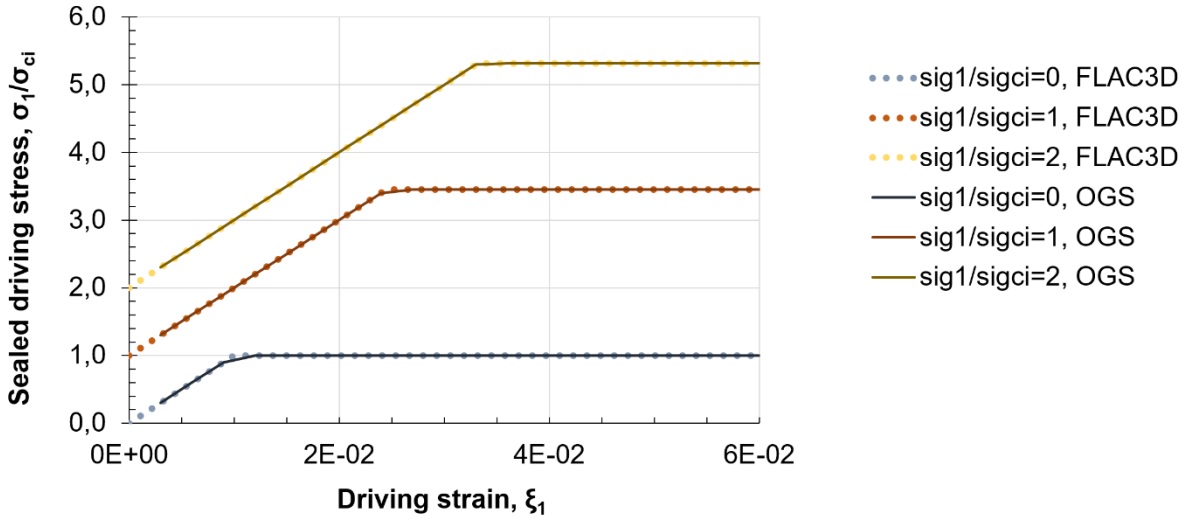

Fig. 31: Stress-strain plots obtained from triaxial compression tests using the implemented BARIK model in OGS, compared with FLAC3D solution.

3.3 Validation and Comparison of the results with FLAC3D and OGS

The validation focused on comparing results of the BARIK model implemented in OGS and FLAC3D considering different stress states, using scenarios derived from the benchmarks defined by Dai et al. (2018), which are based on the work of Carranza-Torres & Fairhurst (1999). Three specific validation scenarios were analyzed.

a) *Uniaxial Compression Test on a Cylindrical Rock Specimen:* A uniaxial compression test was selected as a basic example to verify the initial implementation of the HB criterion in the BARIK model. The results from OGS exhibited minor discrepancies compared to the FLAC3D results, which were attributed to variations in numerical schemes between the two platforms.

b) *Triaxial Compression Test on a Cylindrical Rock Specimen:* This test was conducted at confining pressures of 0 MPa, 20 MPa, and 50 MPa, as shown in Fig. 32. The triaxial test served as a more complex scenario to evaluate the model's capability to simulate the response of fractured crystalline rock under various confining pressures. The results from OGS, FLAC3D, and Dai et al. (2018) were compared, showing excellent agreement in terms of stress-strain behavior and failure patterns.

c) *Plane Strain Model of a Circular Tunnel:* The third validation scenario involved a plane strain model of a circular tunnel. The stability of the tunnel was assessed under varying in-situ stress conditions, and the results were compared to both the analytical solution of Carranza-Torres & Fairhurst (1999) and the numerical solution obtained by Dai et al. (2018). As illustrated in Fig. 33 and Fig. 34 the comparison showed good agreement in terms of displacement magnitude and stress distribution, further validating the correct implementation of the HB criterion in the BARIK model.

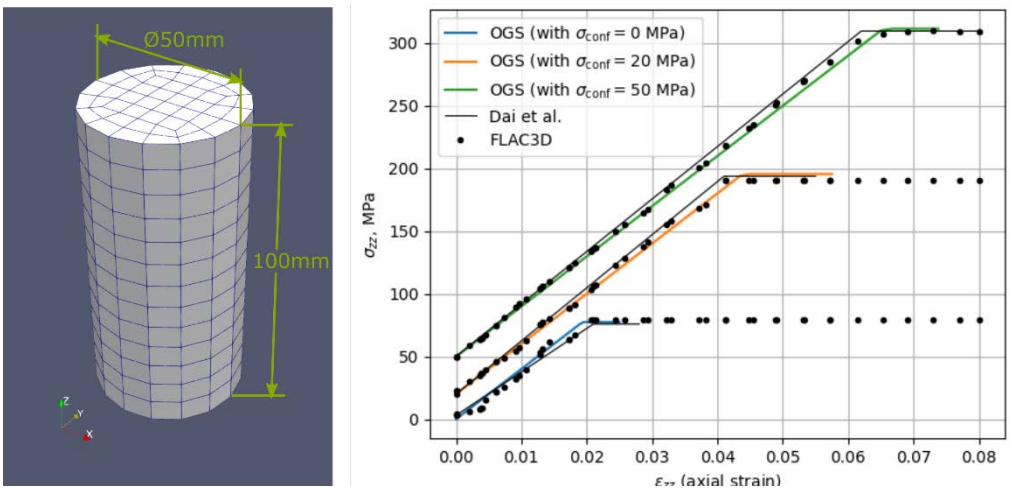

Fig. 32: Results from triaxial compression tests at 0 MPa, 20 MPa and 50 MPa confining pressures (Dai et al. 2018) using the BARIK model in FLAC3D and OGS.

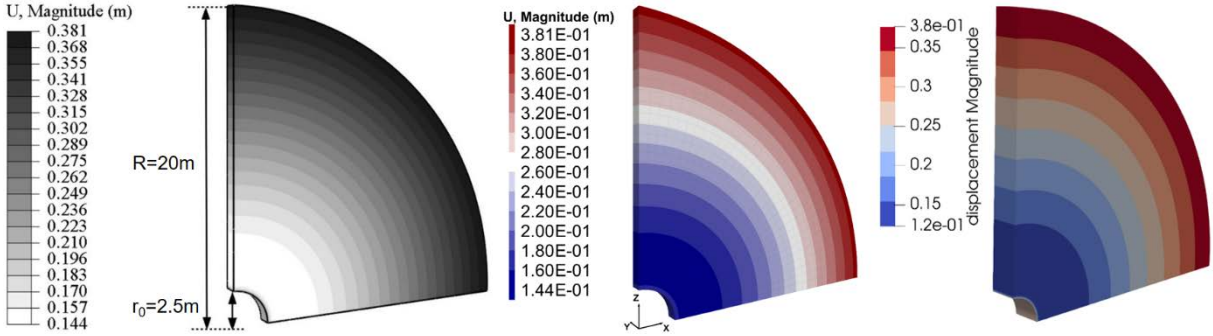

Fig. 33: Contour of displacement magnitude for a circular tunnel, comparing the results of Dai, (left), FLAC3D (middle) and OGS (right).

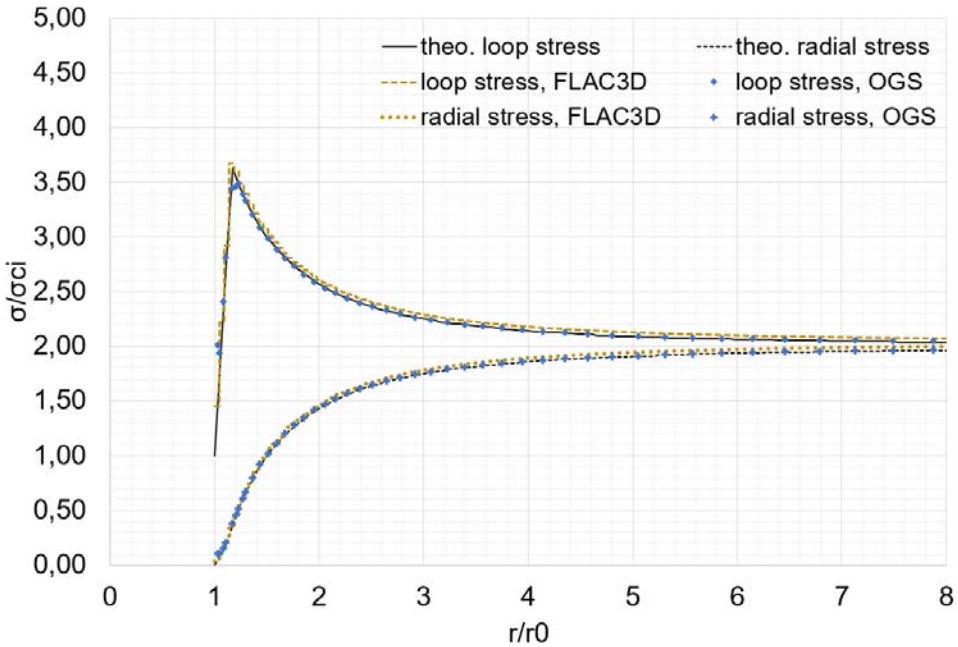

Fig. 34: Comparison of radial and loop stresses obtained from FLAC3D, OGS and the theoretical solution.

The verification process demonstrated that the BARIK model is capable of accurately simulating complex mechanical interactions in orthotropic rock masses, making it a reliable tool for assessing the stability and integrity of underground structures and barriers under different stress conditions.

4 Conclusions and Outlook

This paper introduces development and implementation of the BARIK model, an extended HB-based anisotropic constitutive model developed for simulating the complex mechanical and hydro-mechanical behavior of fractured crystalline rock masses. By incorporating up to three distinct fracture systems and orthotropic elastic properties, the model effectively captures the anisotropic, non-linear deformation and failure characteristics inherent in such geological materials.

The BARIK model is successfully implemented in FLAC3D and OGS, enabling cross-validation and demonstrating its robustness and adaptability across different computational environments. Verification exercises involving isotropic and anisotropic elastic matrices, as well as elasto-plastic scenarios with shear and tensile failure in weakness planes, showed very good agreement between the BARIK model and existing built-in models like Ubi, UANISO, and COMBA within FLAC3D. The minimal deviations observed confirm the model's accuracy in representing the mechanical interactions between rock matrix and fracture systems.

Validations were performed to replicate benchmarks tests, including uniaxial and triaxial compression tests, as well as plane strain tunnel models. The BARIK model's numerical results closely matched analytical solutions and previous numerical studies, affirming its capability to simulate the behavior of jointed, orthotropic rock masses under various loading conditions.
The complementary laboratory program provided essential empirical data for calibrating and validating the model. Tests conducted on Freiberger Gneiss samples have revealed the anisotropic mechanical properties under diverse loading conditions and weakness plane orientations, thereby enriching the model's parameter set and enhancing its predictive capabilities.

Future work will focus on further enhancing the BARIK model's capabilities and applicability. This includes:

- *Variable Strain Softening Behavior:* Advanced post-failure behavior modeling has been incorporated and is currently under testing. This will enhance the representation of post-failure behavior, especially in the transition from brittle to ductile deformation regimes.
- *Variable Biot Coefficient:* The inclusion of hydromechanical coupling through a variable Biot coefficient will further refine the model, allowing it to account for effective stress changes in saturated fractured rock masses.
- *Reformulation of the Dilatancy Criterion for Crystalline Host Rocks:* Utilizing the BARIK model to redefine the dilatancy criterion specific for crystalline rocks used as host formations in geological repositories for radioactive waste. By accurately simulating these conditions, the BARIK model can contribute significantly to ensuring the long-term integrity of geological barriers.
- *Coupled Hydro-Mechanical Simulations:* Providing deeper insights into the interactions between mechanical deformation and fluid flow in fractured rock masses, which is crucial for long-term safety assessments in DGR environments.
- *User Accessibility and Integration:* Enhancing the user-friendliness of the model within FLAC3D and OGS, along with comprehensive documentation, will facilitate its adoption by the geomechanical engineering community.

The development of the BARIK model represents a significant advancement in numerical modeling for geotechnical applications, particularly in the context of nuclear waste disposal. Its ability to accurately simulate the anisotropic strength and deformation behavior of fractured crystalline rocks is crucial for designing effective containment strategies and ensuring the long-term integrity of DGRs. The reformulation of the dilatancy criterion using the BARIK model, could enhance our understanding of how mechanical stresses impact the integrity and containment capabilities of host rocks, thereby improving safety assessments and regulatory compliance.

Continued collaboration between computational modeling, laboratory testing, and field investigations will be essential to further refine the model and expand its applicability to a broader range of geomechanical challenges.

5 Acknowledgements

This research has been supported by the Bundesministerium für Wirtschaft und Energie (grant no. FKZ 02E11890A-B), represented by the Project Management Agency Karlsruhe (PTKA).

6 References

Agharazi, A.; Tannant, D. D.; Derek Martin, C. (2012): *Characterizing rock mass deformation mechanisms during plate load tests at the Bakhtiary dam project*. International Journal of Rock Mechanics and Mining Sciences, Bd. 49. S. 1–11. ISSN 1365-1609. DOI: https://doi.org/10.1016/j.ijrmms.2011.10.002

Carranza-Torres, C. & Fairhurst, C. (1999): *The elasto-plastic response of underground excavations in rock masses that satisfy the Hoek–Brown failure criterion*. International Journal of Rock Mechanics and Mining Sciences, Bd. 36 (6). S. 777–809. ISSN 1365-1609. DOI: https://doi.org/10.1016/S0148-9062(99)00047-9

Chang, L. (2017): *Behavior of jointed rock masses: numerical simulation and lab testing*. Ph.D. Thesis. Technische Universität Bergakademie Freiberg, Freiberg

Dai, Z.-H.; You, T.; Xu, X.; Zhu, Q.-C. (2018): *Removal of Singularities in Hoek-Brown Criterion and Its Numerical Implementation and Applications*. International Journal of Geomechanics, Bd. 18 (10). DOI: https://doi.org/10.1061/(ASCE)GM.1943-5622.0001201

Eberhardt, E. (2012): *The Hoek–Brown Failure Criterion*. Rock Mechanics and Rock Engineering, Bd. 45 (6). S. 981–988. ISSN 1434-453X. DOI: https://doi.org/10.1007/s00603-012-0276-4

Faybishenko, B.; Birkholzer, J.; Persoff, P.; Sassani, D.; Swift, P. (2016): *International Approaches for Nuclear Waste Disposal in Geological Formations: Report on Fifth Worldwide Review.* Fifth worldwide review. DOI: https://doi.org/10.2172/1431439

Helfer, T. & Marois, G. (Hrsg.) (2020): *Overview of TFEL-3.4 and MGIS-1.2. 6th MFront User Day*, online. 25. November 2020. Manosque: cea

Helfer, T.; Michel, B.; Proix, J.; Salvo, M.; Sercombe, J.; Casella, M. (2015): *Introducing the open-source mfront code generator: Application to mechanical behaviours and material knowledge management within the PLEIADES fuel element modelling platform*. Comput. Math. Appl., Bd. 70. S. 994–1023. DOI: https://doi.org/10.1016/J.CAMWA.2015.06.027

Hoek, E. & Brown, E. T. (1980): *Empirical Strength Criterion for Rock Masses*. Journal of the Geotechnical Engineering Division, Bd. 106 (9). S. 1013–1035. DOI: https://doi.org/10.1061/AJGEB6.0001029

Hoek, E. & Brown, E. T. (2019): *The Hoek-Brown failure criterion and GSI - 2018 edition*. 16747755, Bd. 11 (3). S. 445–463. ISSN 16747755. DOI: https://doi.org/10.1016/j.jrmge.2018.08.001

Hoek, E.; Carranza-Torres, C.; Corkum, B. (2002): *Hoek-Brown failure criterion - 2002 Edition*. In: R. Hammah (Hrsg.)*NARMS-TAC 2002,* Toronto, Ontario, Canada, 7 - 10 July. Toronto: University of Toronto Press, Bd. 1. S. 267–273

Jobmann, M.; Burlaka, V.; Guevara Morel, C.; Flügge, J.; Mrugalla, S.; Frank, T.; Müller, C.; Frenzel, B.; Noseck, U.; Hassanzadegan, A.; Rübel, A.; Johnen, M.; Simo, E.; Krumbholz, M.; Sönnke, J.; León Vargas, R.; Stark, L.; Lommerzheim, A.; Thiedau, J.; Maßmann, J.; Weihmann, S.; Mayer, K.-M.; Weitkamp, A.; Meleshyn, A.; Wolf, J. (2021): *Methodisches Vorgehen zur sicherheitlichen Bewertung von Endlagersystemen im Kristallin in Deutschland.* Synthesebericht des FuE Projekts CHRISTA-II. BGE TEC 2021-17. BGE TECHNOLOGY GmbH (BGE TEC); Gesellschaft für Anlagen- und Reaktorsicherheit (GRS) gGmbH; Bundesanstalt für Geowissenschaften und Rohstoffe (BGR). Peine

Kroner, U.; Hallas, P.; Müller, F. (2021): *The anisotropic properties of granites – effects of tectonic emplacement mode on potential crystalline host rocks for nuclear waste deposits in Germany*. Safety of Nuclear Waste Disposal, Bd. 1. S. 67–68. DOI: https://doi.org/10.5194/sand-1-67-2021

León Vargas, R. P.; Friedel, M.; Hassanzadegan, A.; Rahmig, M.; Weber, F.; Konietzky, H. (2023): *BARIK: an extended Hoek–Brown-based anisotropic constitutive model for fractured crystalline rock*. In: J. Ahlswede; M. Becker; F. Czerwinski; C. Dietl; S. Hellebrandt; A. Kaufhold; T. Oesch & T. Weyand (Hrsg.)*Interdisciplinary Research Symposium on the Safety of Nuclear Disposal Practices safeND 2023,* Berlin, Vom 13. bis 15. September 2023. Berlin: Copernicus

Mahabadi, O. K.; Tatone, B. S. A.; Grasselli, G. (2014): *Influence of microscale heterogeneity and microstructure on the tensile behavior of crystalline rocks*. Journal of Geophysical Research: Solid Earth, Bd. 119 (7). S. 5324–5341. ISSN 2169-9313. DOI: https://doi.org/10.1002/2014JB011064

Müller, C.; Burlaka, V.; Flügge, J.; Gafoor, A.; Hassanzadegan, A.; Herold, P.; Johnen, M.; Zhao, H. (2023): *Challenges and best practices for modelling fractures in geological repositories*. Safety of Nuclear Waste Disposal, Bd. 2. S. 121. DOI: https://doi.org/10.5194/sand-2-121-2023

Rutqvist, J. & Tsang, C.-F. (2024): *Modeling nuclear waste disposal in crystalline rocks at the Forsmark and Olkiluoto repository sites – Evaluation of potential thermal–mechanical damage to repository excavations*. Tunnelling and Underground Space Technology, Bd. 152. DOI: https://doi.org/10.1016/j.tust.2024.105924

Silbermann, C. B.; Kern, D.; Naumov, D.; Parisio, F.; Nagel, T. (2021): *Implementing geomechanical models in MFront/OpenGeoSys for hydrogeological and geotechnical applications Importance of elasto-plastic material models in geoscience*. In: CEA Cadarache (Hrsg.)*7th MFront user meeting,* Paris, 21. Oktober 2021. Paris: CEA Cadarache. DOI: https://doi.org/10.13140/RG.2.2.12541.90086

Simo, E.; Helfer, T.; Nagel, T.; Mašín, D.; Mánica, M.; Herold, P. (2020): *Implementation of clay rock and bentonite models using Mfront*. In: T. Helfer & G. Marois (Hrsg.)*6th MFront User Day,* online, 25. November 2020. Manosque: cea

StandAG: Gesetz zur Suche und Auswahl eines Standortes für ein Endlager für hochradioaktive Abfälle

Zuo, J.; Liu, H.; Li, H. (2015): *A theoretical derivation of the Hoek-Brown failure criterion for rock materials*. 16747755, Bd. 7 (4). S. 361–366. ISSN 16747755. DOI: https://doi.org/10.1016/j.jrmge.2015.03.008

Design of Support Structures for Underground openings in a future HLW repository in claystone

Entwicklung von Ausbaukonzepten von Grubenbauen für ein HAW-Endlager im Tongestein

Philipp Herold[1] (Editor), Sven Bock[2], Ajmal Gafoor[1], Andreas Hucke[2], Jürgen te Kook[2], Eric Simo[1], Axel Studeny[2], Benedikt Wöhrl[2]

[1] BGE TECHNOLOGY GmbH,
Eschenstr. 55, 31224 Peine
[2] DMT GmbH & Co. KG,
Am TÜV 1, 45307 Essen

Abstract

The German site selection process for a future high-level waste (HLW) repository is ongoing, and claystone is one of the potential host rock formations under consideration. From a long-term safety perspective, claystone offers several beneficial properties, such as low permeability and high sorption capacity. However, from an operational safety standpoint, the geomechanical properties of claystone must be evaluated more carefully. The relevant claystone formations exhibit low to moderate strength and demonstrate changes in properties depending on water content and time (including rheological behaviour). These conditions imply the need for regular support structures inside all underground openings throughout their operational life.

Furthermore, the complexity of a deep geological repository (DGR) project introduces a wide range of requirements for all safety-relevant structures, systems, and components (SSCs), including the support structures. The direct transfer and implementation of standardized concepts, as known from mining and tunnelling, are not feasible. The specific characteristics of an HLW DGR require specialized solutions. BGE TECHNOLOGY GmbH, together with DMT GmbH & Co. KG, is investigating technical concepts for these support structures. This work includes the preliminary design of segmental linings with compressible grouting between the rock and the liner, which is preferred for long living main drifts with large diameters, as well as the design of intersections between different drifts and the interaction between the rock and the support structures in the proposed underground layout.

Zusammenfassung

Das deutsche Standortauswahlverfahren für ein zukünftiges Endlager für hochaktive Abfälle läuft und Tonstein ist neben anderen Gesteinsformationen eines der möglichen Wirtsgesteine. Unter dem Gesichtspunkt der Langzeitsicherheit bietet Tonstein mehrere vorteilhafte Eigenschaften, wie z.B. eine geringe Permeabilität oder eine Sorptionsfähigkeit. Unter dem Gesichtspunkt der Betriebssicherheit müssen die geomechanischen Eigenschaften differenzierter bewertet werden. Die relevanten Tonsteinformationen weisen eine geringe bis mäßige Festigkeit auf und zeigen Eigenschaftsänderungen, die sowohl vom Wassergehalt als auch von der Zeit abhängen (rheologisches Verhalten). Diese Bedingungen erfordern einen regelmäßigen Ausbau innerhalb aller unterirdischen Grubenräume sowie während deren gesamter Betriebsdauer.

Darüber hinaus führen die komplexen regulatorischen Vorgaben an ein solches Endlagerprojekt zu einer Vielzahl von Anforderungen an alle sicherheitsrelevanten Systeme, einschließlich des Ausbaus. Die direkte Übertragung und Implementierung von standardisierten Ausbausystemen, wie sie aus dem Berg- und Tunnelbau bekannt sind, ist nicht ohne weiteres möglich. Die spezifischen Eigenschaften eines Endlagers für hochradioaktive Abfälle erfordern eigens angepasste Ausbaukonzepte. Die BGE TECHNOLOGY GmbH hat gemeinsam mit der DMT GmbH & Co. KG damit begonnen, technische Konzepte für solche Ausbausysteme zu untersuchen. Die Arbeiten umfassen die Entwicklung eines Tübbingausbaus mit kompressibler Hinterfüllung zwischen Gebirge und starrer Innenschale, wie er für langlebige Strecken mit großen Durchmessern bevorzugt wird, die Planung der Kreuzungen zwischen verschiedenen Strecken sowie die Untersuchung der geomechanischen Wechselwirkungen zwischen Gebirge und Ausbau.

1 Material properties of clay rock formation

As part of Step 1 of Phase I of the German site selection procedure in accordance with the StandAG, nine sub-areas were identified in the host rock clay (BGE, 2020). The sub-areas cover a total area of approximately 130,000 km² and belong to different geological eras in terms of their genesis. Accordingly, it is expected that the clay formations exhibit a wide variation in their geomechanical properties. In the site selection process, a rough distinction is made between tertiary and pre-tertiary clay formations. The latter were also considered as potential host rocks in various generic R&D projects. For the analysis presented in this paper, these tertiary formations were considered as a reference point as well. For the development of suitable support structures, the first step was to compile rock properties based on literature data of clay formations from various locations and depths. The main findings can be summarized as follows:

- The formations considered are located in a depth between 200 and 800 m
- The rock density is between 2.1 and 2.5 g/cm³ and increases with depth
- The pore volume (porosity) of the rock generally decreases with increasing depth
- The water content of the rock generally decreases with increasing depth
- The decrease in water content correlates with an increase in strength
- Unconfined compressive strengths are between 3 and 30 MPa
- Cohesion (1.0 to 4 MPa) and internal Internal friction angle (14 to 27°) tend to increase with depth
- Poisson's ratio is between 0.26 and 0.32 and decreases with depth
- Modulus of elasticity increases with depth

In summary, it can be stated that the various rock parameters tend to improve with increasing depth in terms of their geomechanical properties. However, this advantage is offset by the disadvantage that the rock pressure increases with increasing depth, which leads to a greater load on underground mine workings.

2 Assessment of different support structure concepts

A more detailed investigation of the relationship between rock and support structure was carried out using numerical calculations. The calculations include variations of:

- the rock pressure
- the structure inside the rock formation (strata)
- the geomechanical properties
- different types of support structures
- different shapes of the drifts

The analysis allowed for an assessment of damage within the rock as well as an assessment of the effects on the support structures. Three basic drift shapes — rectangular, arch-shaped, and circular — were considered. Based on this, a variation of the support systems for each respective shape was conducted in parallel with the variation of the rock mass properties. Fig. 35 provides an overview of selected comparative calculations.

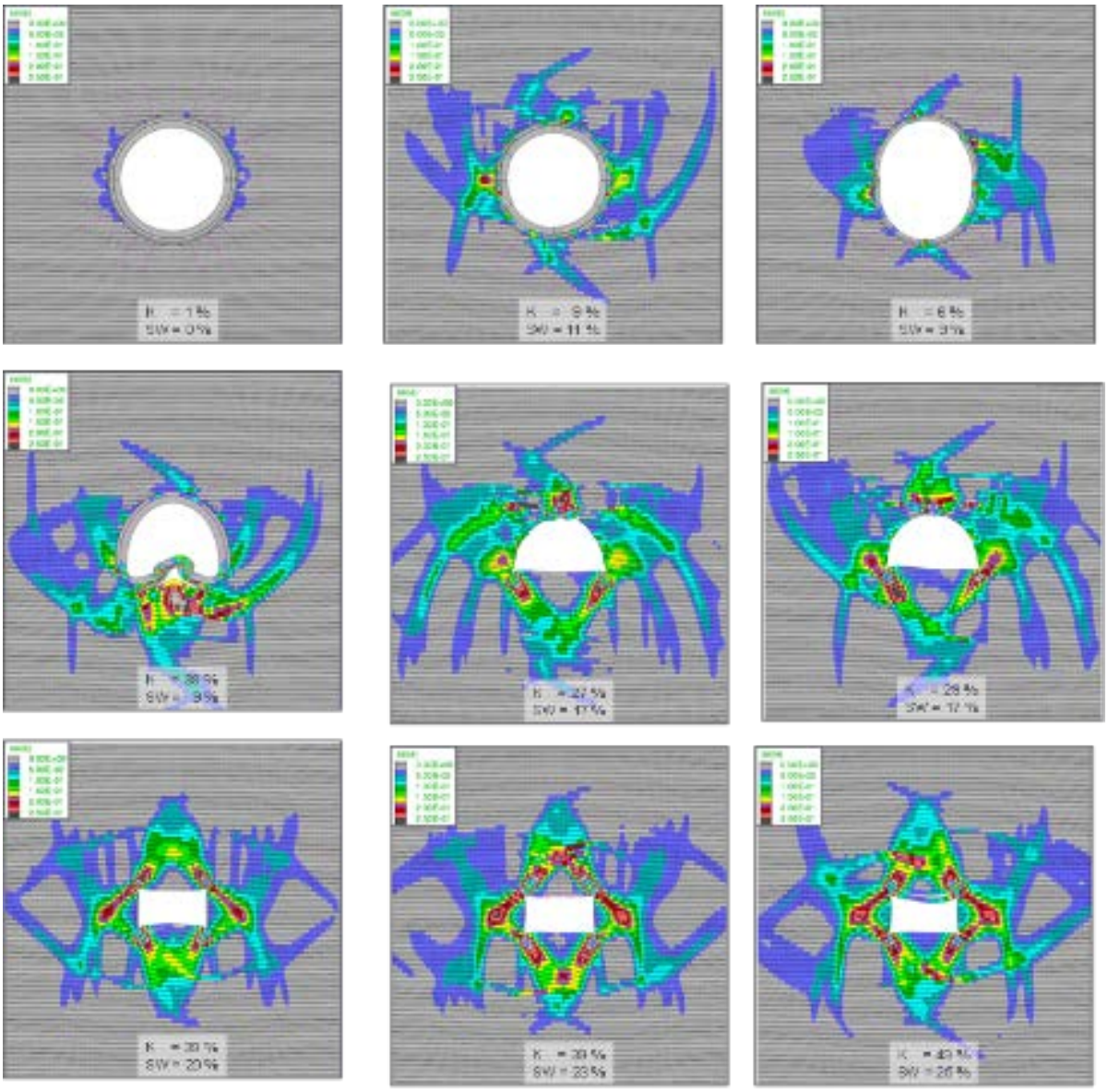

Fig. 35: Comparative calculations of different drift shapes in an isotropic stress state (1,000 m depth, UCS=15 MPa, horizontal bedding, thickness of strata = 30 cm).

These first comparative calculations clearly showed that rectangular-shaped drifts, widely used in some branches of mining, are not suitable for the present application. Arch-shaped drifts, also commonly used in the mining industry, can be considered suitable but only in conjunction with appropriate support structures and favourable geomechanical conditions. For example, a single arch-shaped drift with a concrete lining (30 cm shell thickness, 20 MPa concrete strength) and an assumed rock strength of more than 15 MPa provides an acceptable level of deformation, at least from a rock mechanics point of view. Drift deformations of up to 10% of the initial width are expected to be tolerable, and dinting work (re-cutting of the floor) can be carried out, respectively is tolerated.

Accordingly, further analyses were based on arched drifts with a concrete lining (30 cm, 20 MPa). Furthermore, the required pillar width was examined as a function of three predefined levels of depth (500 m, 750 m, 1000 m) and rock strengths (15 MPa, 20 MPa, 28 MPa). By considering a pillar width of twice the maximum drift width, the application limits of the system can be identified. Fig. 36 provides an overview of the models. In the areas marked in red, the pillars are too small, indicating that the distance between the drifts needs to be increased due to persistent shear zones in the pillars.

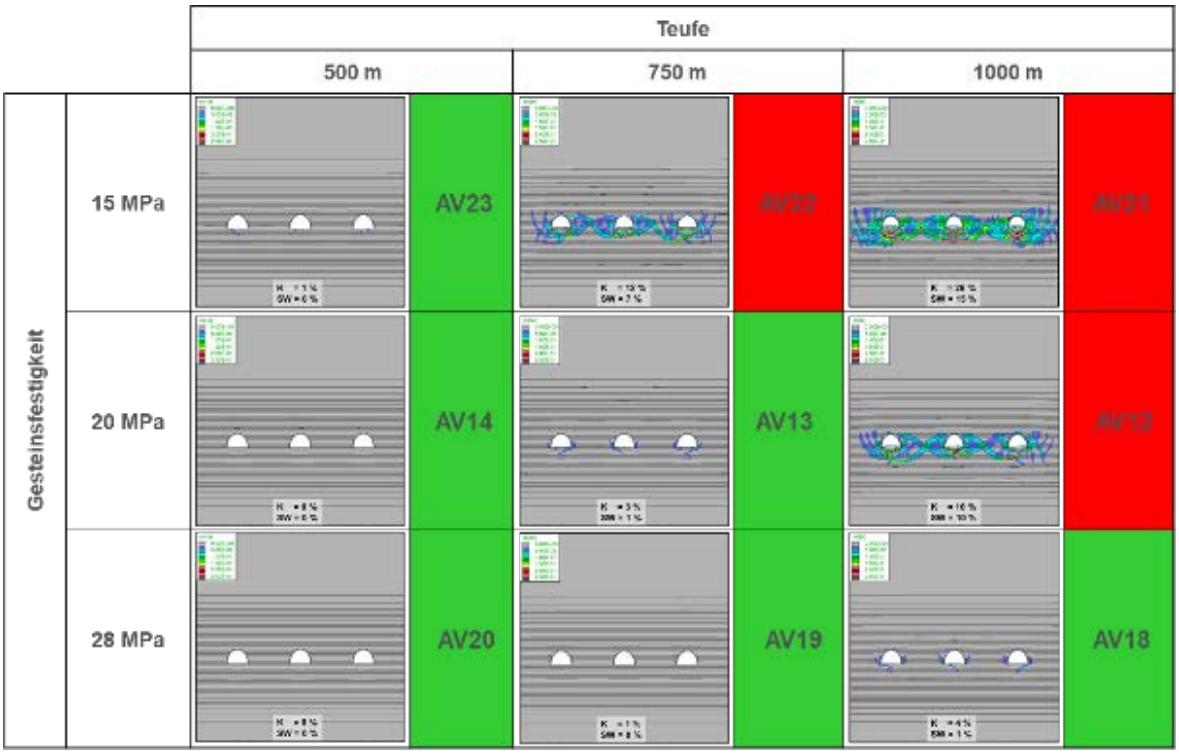

Fig. 36: Results of the model calculations with a pillar width = 2*section width for various depths and rock strengths (presentation of shear deformations).

Disposal drifts are characterized by a short service lifetime (less than two years) and immediate backfilling after disposal. Main drifts**,** on the other hand, have a much longer service life, potentially up to several decades (approximately 50 years or more). For this reason, circular cross-sections are considered for the main drifts. Since refurbishing the drifts is generally regarded as unfavourable due to radiological requirements, it can be assumed that highly load-bearing or strongly deformable support systems must be used to guarantee safety and serviceability over such a long period.

The analyses have shown that claystone with a strength of more than 15 MPa can be managed with high-strength support systems, even at depths of 1000 m, as long as no swelling effects or significant deformations occur. However, due to the long service life of the drifts and the current lack of knowledge about the actual rock properties, these effects cannot be completely ruled out. To meet the requirements, the support system of the main drifts must be designed to withstand rheological effects unless these can be ruled out by future rock investigations.

In summary, it can be stated that challenging requirements and high impact loads are expected for support structures in main drifts maintain the stability and serviceability of the drifts for a long period. For example, high-strength concretes in combination with yielding layers offer the possibility of absorbing high loads over extended periods. As a result, a rigid inner shell made of concrete segments combined with a compressible backfill is defined as the preferred option for this type of drift. However, it has also been shown that there are conditions in which even these systems reach their limits. For instance, very high concrete strengths and lining thicknesses are required, especially in cases of pronounced rheological behaviour, to guarantee the stability of the lining over long periods. The extent to which these effects occur in clay rock formations still needs to be clarified in the future.

In conclusion, it can be stated that, from a rock mechanics perspective, care should be taken to avoid a combination of various “unfavourable” factors when searching for a repository in clay formations. For example, large and non-uniform rock stresses increase the deformation rates, which have a very unfavourable effect, especially in clay that is prone to deformation. This also applies to low-strength or heavily fractured rock. In this case, it is recommended to limit the depth of a possible repository. If, on the other hand, firmer clays with lower creep properties are encountered, significantly greater depths are feasible for a repository.

3 Segmental pre-cast liner for long living main drifts

3.1 Concrete tubbings

For the long lining main drifts segmental pre-cast liner was identified as a favourable option. The design and stability is investigated with numerical models.

With the developed material model and the determined basic parameters, a three-dimensional model was created in FLAC3D, in which a planned main section with a defined support system was analysed. The three-dimensional code FLAC3D (Fast Lagrangian Analysis of Continua) uses an explicit finite difference solution scheme. The finite difference method (FDM) has certain advantages over the finite element method (FEM) in geotechnical problems. The FDM uses a time-marching explicit solution scheme in which physical instability (such as collapse) does not lead to numerical instability or lack of convergence. The FLAC3D code, developed by Itasca Consulting Group Inc., allows the simulation of three-dimensional structures made of soil, rock, or other materials that may undergo plastic flow once their strength is exceeded. The DMT has enhanced FLAC3D with Python-based functions for stability analysis in accordance with international standards and additional automation tools.

A segmental lining with a backfill was used as the lining system for the long living main drifts. Since the segmental precast liner is composed of individual segments, the overall structural behaviour can vary significantly based on the design of the joints, see Fig. 37.

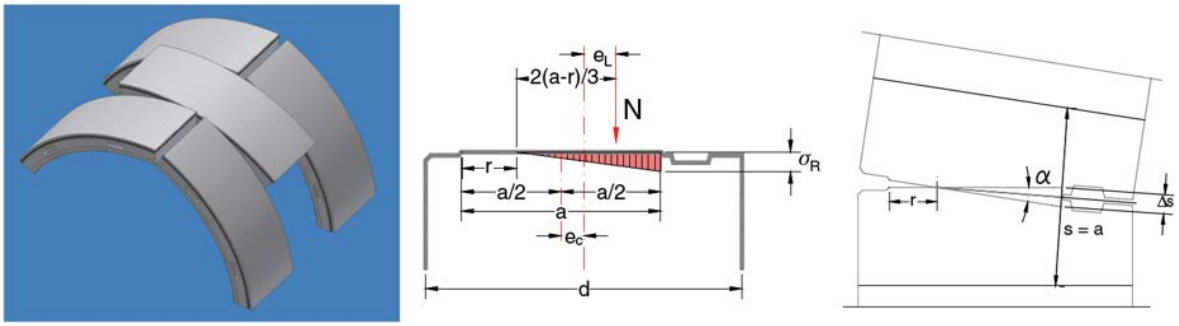

Fig. 37: Different deformation of individual segments, greatly exaggerated (DAUB, 2014).

Considering the importance of joint behaviour, it was decided that the FLAC3D model should be coupled with a 3DEC model to ensure a realistic simulation of the segmental lining system. The 3DEC allows for a hybrid (DEM + continuum) simulation to model blocks of discontinuous material (such as jointed rock or masonry bricks). Discontinuous methods are promising for applications in rock and soil mechanics. The main difference between discontinuous and continuous methods is the former’s ability to rotate and even detach blocks during the deformation process. The 3DEC blocks may be rigid or deformable (zoned) and can slide, rotate, and move apart from or towards each other, see Fig. 38.

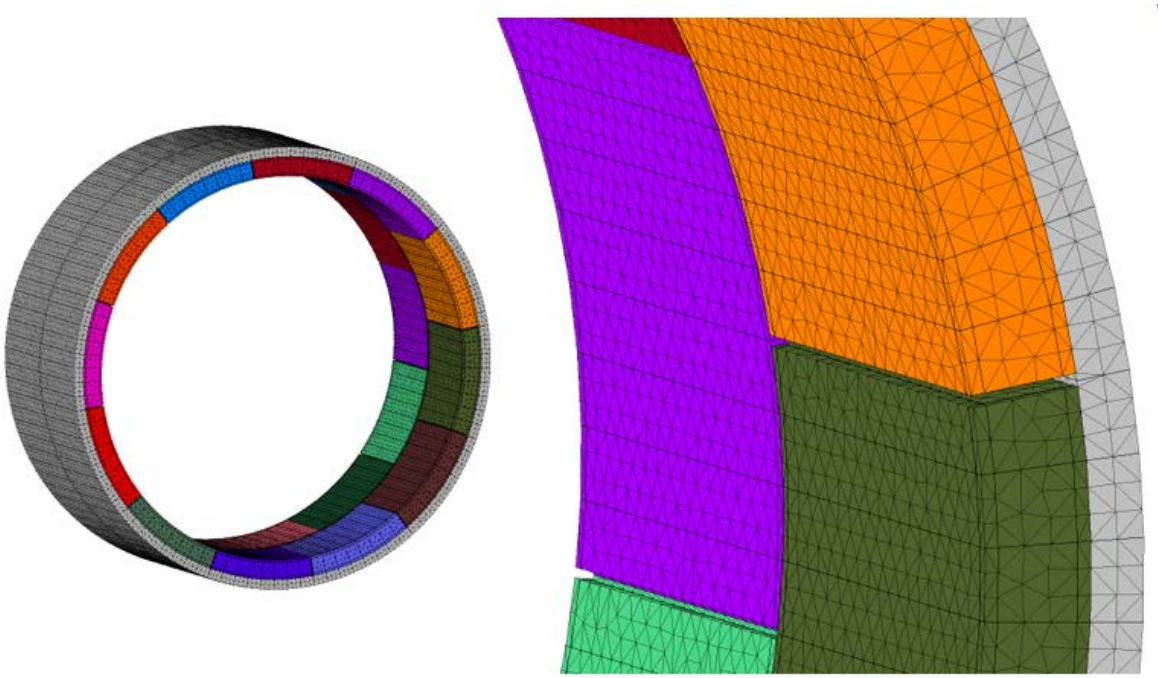

Fig. 38: Automatically generated mesh of pre-cast segment liner (coloured) according to the input geometry of the joints, segments, and the compressible backfilling (grey).

A basic FLAC3D model of a main drift is shown in Fig. 39. Similar to 3DEC, the support structure is modelled by a segmental concrete lining with backfill, to derive the most realistic loads for the coupling process possible. In FLAC3D, the radial and longitudinal joints between tubing segments are modelled as plane contact areas. A detailed simulation of the contact behaviour, considering a realistic joint profile (e.g., including notches for sealing elements), is performed in 3DEC.

Prior to the modelling, the necessary support was estimated using a rock-support interaction diagram and a longitudinal displacement profile (see Fig. 40). The analysis of the interaction behaviour showed that the support must be installed at least 1.5 m behind the excavation face to achieve a safety factor of more than 1.5 for the concrete structures.

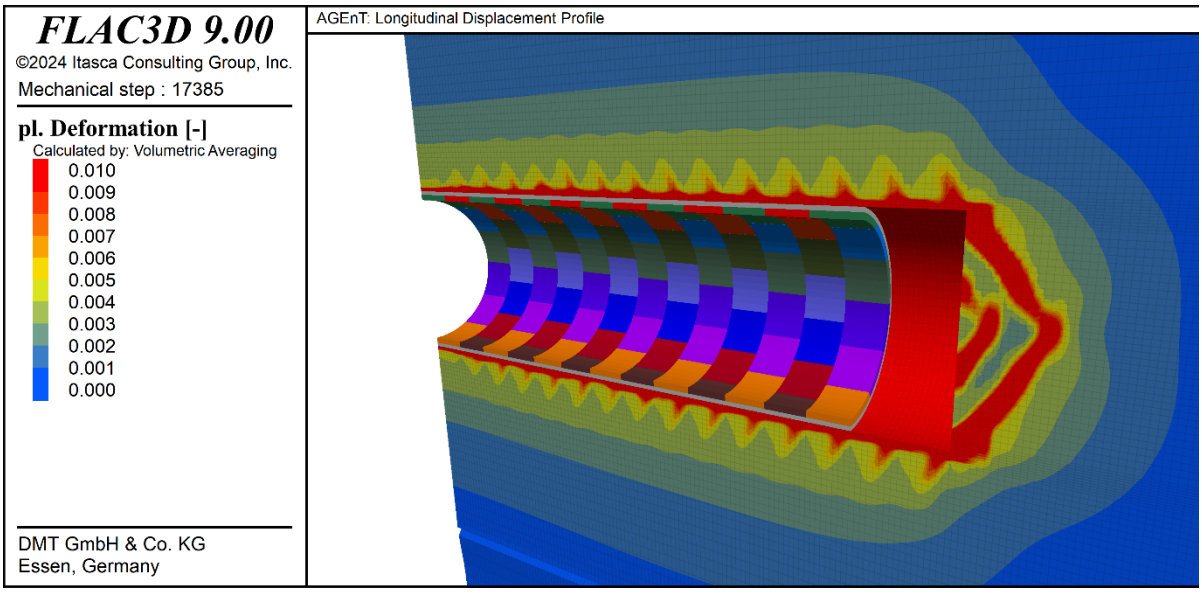

Fig. 39: FLAC3D model of a main drift considering concrete tubbings as a support and plastic deformation of the surrounding rock mass.

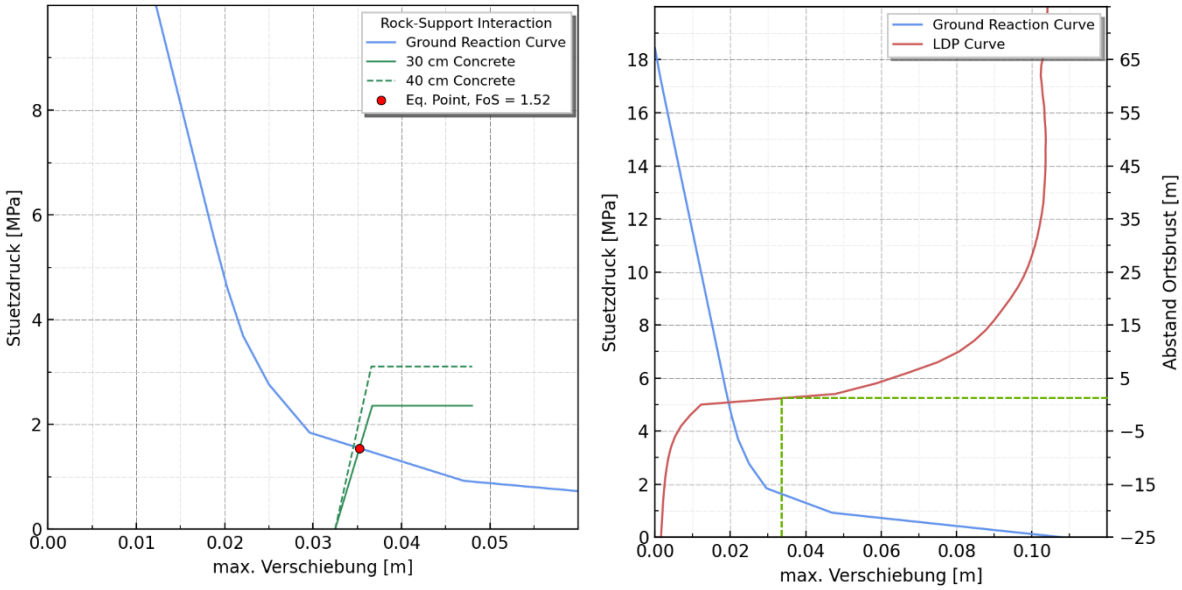

Fig. 40: Rock-support-interaction diagram for two lining thicknesses (left) and the combination with a longitudinal displacement profile (right). The dashed green lines relate the estimated displacement at the time of support installation with a distance to the excavation face.

For the calculations of the segmental pre-cast liner for the main drifts, the loads from the FLAC3D model on the lining were determined at different stages (during excavation, after completion of excavation, and taking creep processes into account) and were transferred to the 3DEC model. Initial difficulties arose at the beginning of the investigations because slightly irregular loads, determined from the FLAC3D model, significantly affected the behaviour of the segmental lining and led to very uneven deformations. Consequently, adjustments had to be made to the support modelling in FLAC3D to equalize the loads.

4 Compressible backfilling to moderate the interaction between rock and rigid support structures

The basic concept of a rigid inner shell combined with a compressible backfill was further investigated using coupled hydro-mechanical model calculations. These simulations do not represent the conditions of a specific site. The parameter set used was derived from the literature review mentioned earlier and summarized in (Herold et al., 2020). The simulations provide an improved understanding of the system and offer qualitative insights into the behaviour of the support system and its interaction with the host rock. Various conclusions can be drawn from the obtained results.

It is well known that the development of the excavation damaged zone (EDZ) as well as the excavation disturbed zone (EdZ) depends on many factors, such as the rock properties (especially its material anisotropy), the initial stress state, the geometry of the excavation spaces, the excavation method, and time. The numerical analysis indicates that the characteristics of the support system also play a major role in the development of local deformations. Displacements are considerably reduced by the presence of the support structure, which is not surprising. Not only the size but also the characteristics of the displacement field can be influenced by the support structure. The compressible backfill provides the possibility of controlling interactions between the rock mass and the support structure. Backfilling can limit the load transferred to the inner ring and thus significantly reduce the internal forces in the segments. However, this results in further loosening of the rock, which leads to a larger EDZ and EdZ (see Fig. 41). The results show that using a compressible backfill can optimize the interaction between the damage in the rock and the magnitude of the internal forces in the lining.

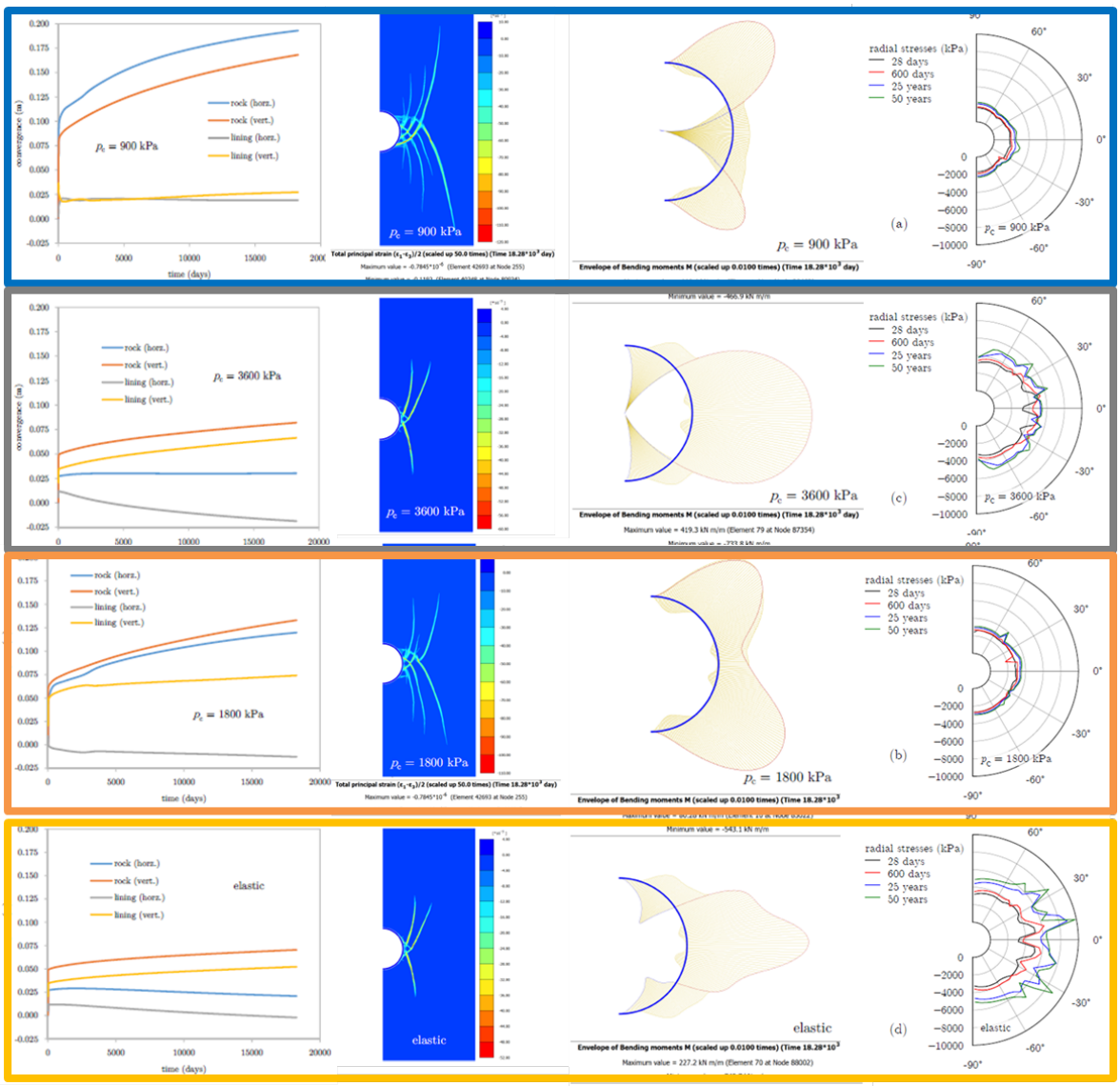

Fig. 41: Variation of the compressibility of the backfill in comparison, from the top to the bottom: the stiffness increases, deformation (left) and extension of the EDZ (middle) reduces but internal loads in the inner rigid ring of concrete segments increases (right).

5 Support structures at drift intersections

The use of a support structure made of concrete-based precast segments is a standard approach in tunnelling. However, for a mine or a repository, it is not always possible to use such standardized support structures. The regular crossings and intersections between different types of drifts necessitate additional support structures. The underground facility can be described as a network of short-lived drifts for disposal, in addition to the long living main infrastructure drifts or cross passages. Therefore, special considerations are required for the design of support structures for such main drifts and cross passages of the repository. This section discusses the numerical modelling and design of intersections between long living drifts, such as an exemplary intersection between the main drift and a cross passage. It is assumed that both drifts meet at right angles at the intersection. A conceptual design of the excavation and support structure installation method has been developed, and a suitable support structure has been designed. Three different modelling programs are used to investigate the mechanical deformation behaviour of the intersecting drifts located at a depth of 750 m and to design a suitable support structure. A continuum-based modelling approach used for simulating rock behaviour is discussed here.

6 Continuum-based approach for rock simulation

To understand the mechanical deformation behaviour, a continuum-based approach, similar to that used in the KONRAD project (Stahlmann et al., 2014), was employed to study the rock behaviour and to understand the development of secondary stress states after excavation. To avoid high stress concentrations at the intersection, a suitable corner radius was introduced at the intersection based on a parametric investigation. To model the anisotropic host rock behaviour, the ubiquitous-softening model was used to represent the rock matrix, considering the bedding direction, while the Mohr-Coulomb model was used only at the drift contour to avoid any numerical instabilities close to the opening. The in-situ state was established by setting up initial stresses and relevant boundary conditions. In addition, the convergence-confinement method was employed to obtain the ground reaction behaviour, see Fig. 42.

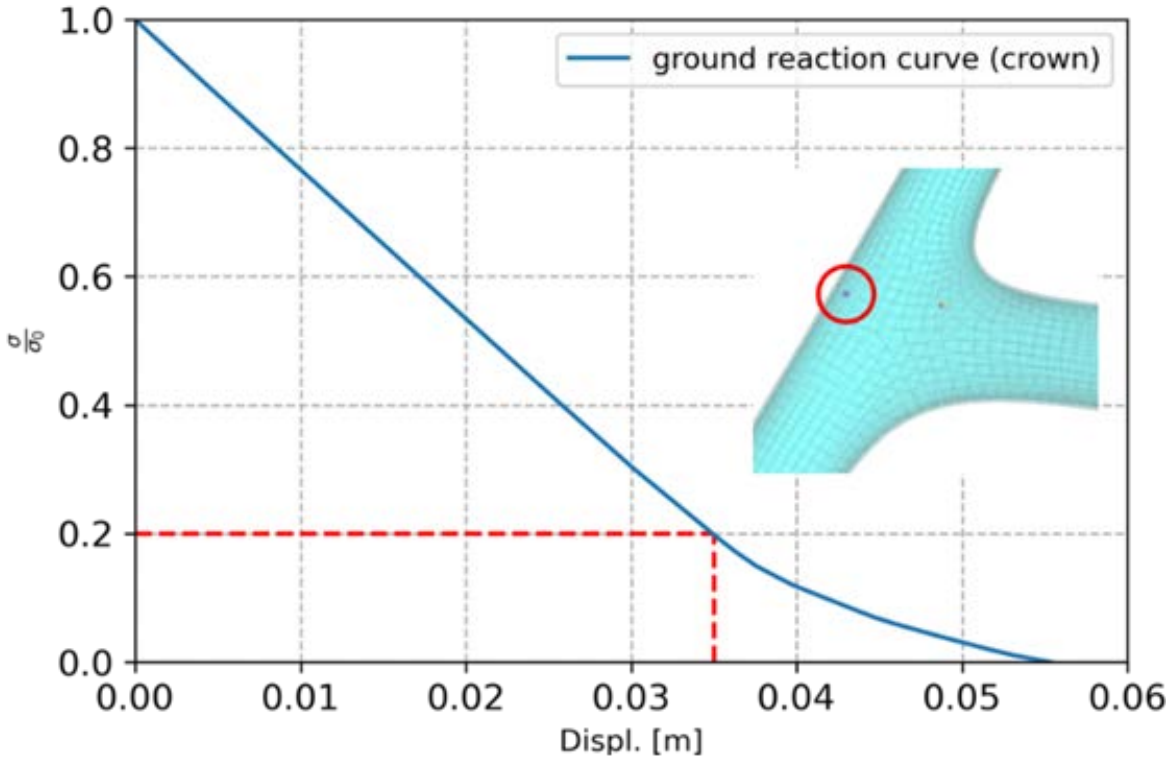

Fig. 42: Ground reaction curve measured at the crown of the main drift intersecting with the cross passage; red dashed lines refers to the 80% relaxation state.

Fig. 43 shows the results of a secondary stress state from the rock simulation, where 80% relaxation of the rock mass is achieved during the simultaneous excavation process. The secondary stress state is evaluated using the utilization factor, defined as the ratio between the actual stress in the system and the failure stress of the material. The plastic deformation of the rock matrix bedding and the corresponding rock state are also evaluated based on the utilization factor.

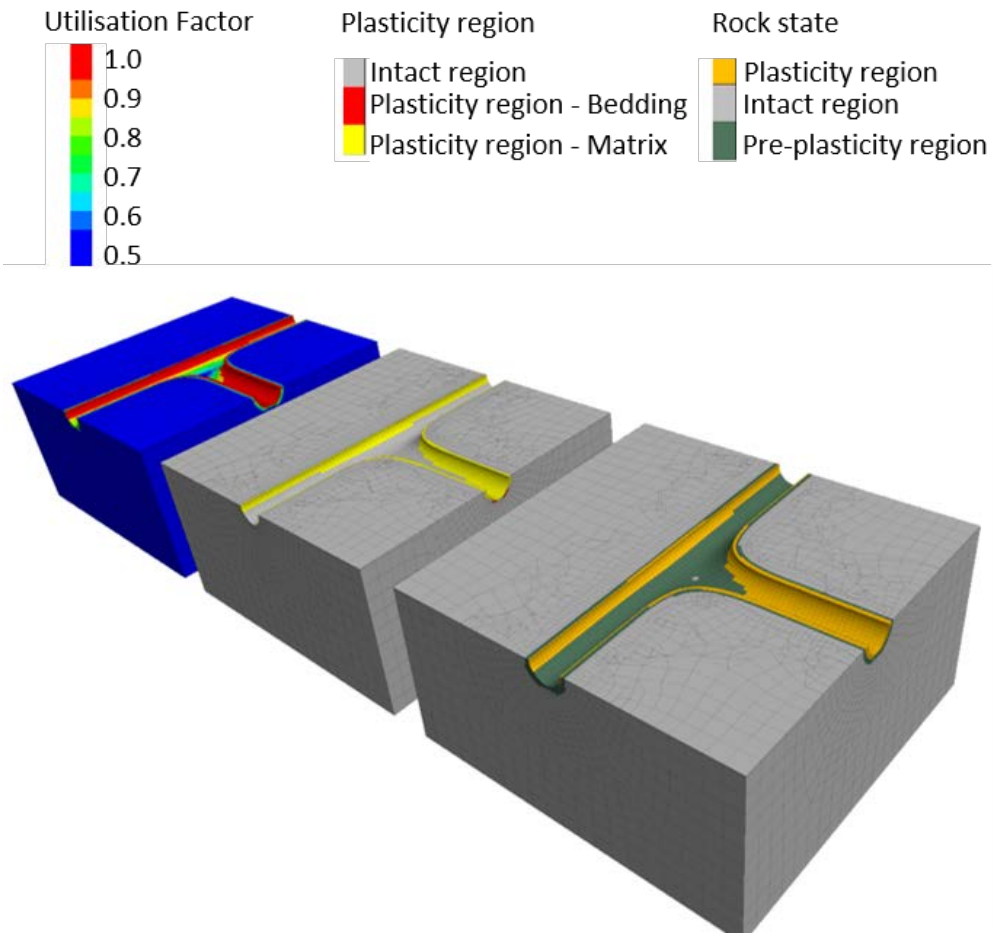

Fig. 43: An exemplary sectional view of intersection between the main infrastructure drift and a cross passage located at a depth of 750 m.

7 Successive excavation and support installation process

To understand the mechanical deformation behaviour of the host rock and its reaction during successive excavation and installation of the support structure, a host rock model with the designed intersection is considered for the simulation of this entire process. Excavation is performed in 5-meter intervals from the front side of the main drift, and a supporting radial pressure of 2 MPa, corresponding to a concrete lining of 50 cm thickness, is applied to the drift contour. The system is then brought to an equilibrium state. Likewise, the main drift is excavated first, followed by the excavation of the cross passage. During the excavation of the first 20 meters of the cross passage, each half of the drift is excavated in 5-meter segments, with the left half excavated and supported before progressing with the second half. Finally, the next 20 meters of the cross passage are excavated and supported successively. The development of secondary stresses and plastic deformation during the successive excavation and application of support pressure are shown in Fig. 44. Downward crown displacements are recorded at the locations of the main and cross passage drifts are highlighted in Fig. 45. The crown displacements at the cross passage decrease because of radial support and in the same manner, the extent of the plastic zone decreases if compared with excavation process without radial support. Moreover, the excavation of the main drift (excavation length 0–100 m) causes a slower development of crown convergence at the entry of cross passage but faster convergence occurs once the excavation of cross passage progresses.

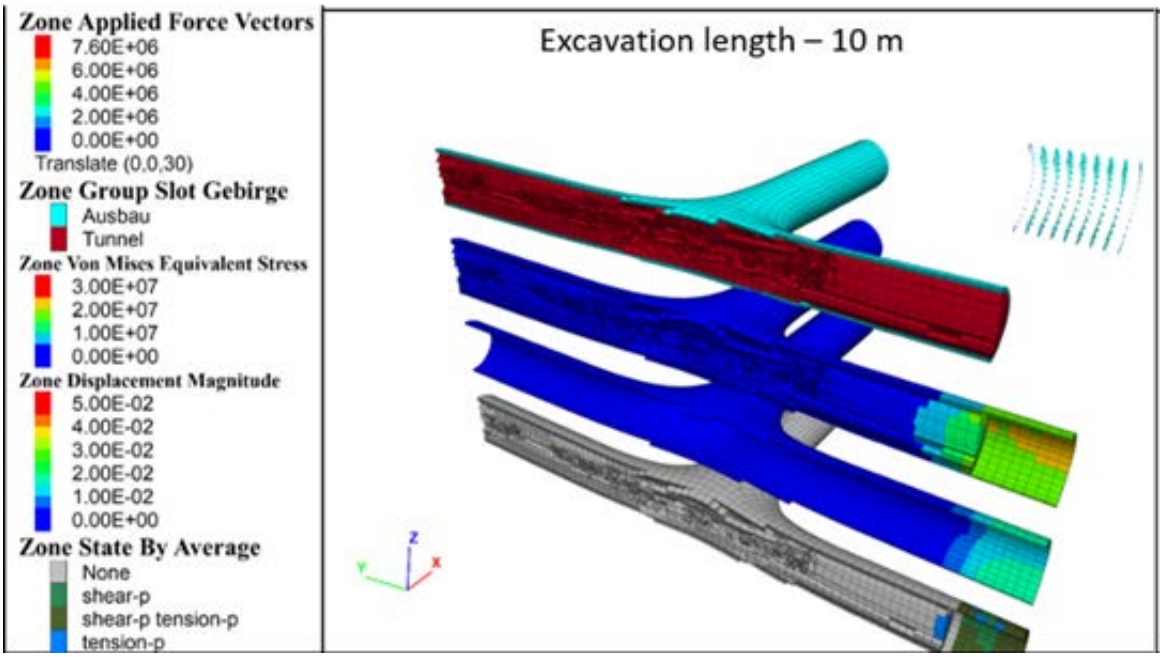

Fig. 44: Successive excavation and support installation process, example at an excavation length of 10 m.

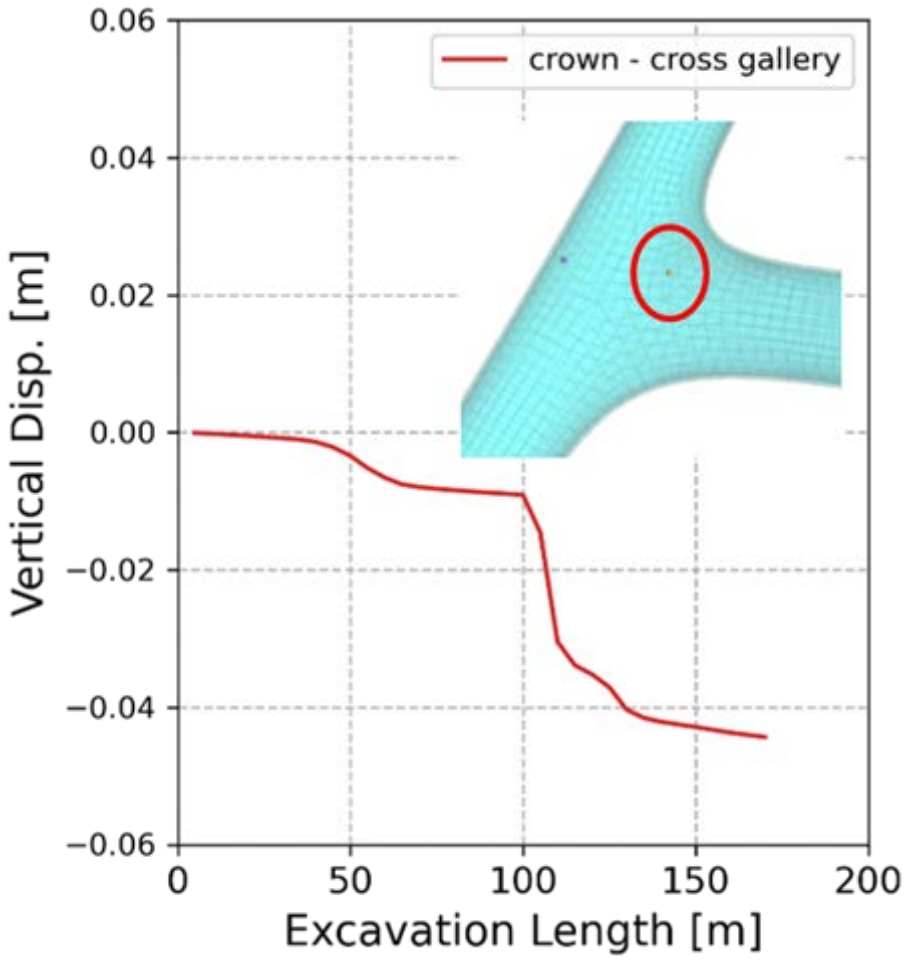

Fig. 45: Downward vertical displacements at crown location on contour of cross passage during excavation and support installation process.

Parallel investigations of structural analyses and the design of concrete shell lining, as well as the post-peak/long-term behaviour of concrete shell liners, are in progress. As part of a master thesis, the structural analyses and the design of concrete lining using spring modulus approach is performed in the software SOFISTIK. In parallel a nonlinear finite element analysis in the software ATENA is performed. For these analyses, the forces acting on the concrete shell structure are derived from the rock mechanics simulation carried out using a continuum-based approach.

8 Summary

The paper summarizes the conceptual considerations for support structures in a future German HLW repository in claystone. In terms of long-term behaviour, claystone offers several beneficial properties, such as low permeability and high sorption capacity. However, from an operational safety perspective, the geomechanical properties need to be evaluated more thoroughly. The relevant claystone formations exhibit low to moderate strength and show changes in properties depending on water content and time (rheological behaviour). These conditions imply the need for a robust support structure within all underground openings throughout their operational life.

Initial analyses were performed to determine suitable drift shapes and types of support structures within a defined geological setting and range of geomechanical parameters. The data set used was generic, based on literature. Arch-shaped drifts are suitable under favourable geomechanical conditions and for small, short-lived drifts. Emplacement drifts meet these criteria, and a support structure consisting of shotcrete, mesh, and bolts appears sufficient. For large, long living drifts, a circular cross-section combined with a concrete shell (segmental per-cast lining) and compressible backfill was identified as a suitable option. More detailed numerical analyses have improved the understanding of interactions between the rock mass and the support structure. The authors continue this work, now focusing on specific elements such as intersections and the segmental lining itself.

The authors gratefully acknowledge the support and project funding for the projects AGENT (German acronym for: Development of mine workings for a HAW repository in clay rock) and AGENT002 (German acronym for: Continuation of the development of mine workings for a HAW repository in clay rock) at the German Federal Ministry for the Environment, Nature Conservation, Nuclear Safety and Consumer Protection (BMUV) as well as the Project Management Agency Karlsruhe (PTKA).

9 References

BGE (2020) Zwischenbericht Teilgebiete gemäß §1 13 StandAG, Stand 28.09.2020, Bundegesellschaft für Endlagerung mbH, Peine

DAUB (2014) Recommendations for the design, production and installation of segmental rings, Deutscher Ausschuss für unterirdisches Bauen e. V. (DAUB), Köln

Herold, Philipp; Simo, Eric; Räuschel, Hannes; Engelhardt, Hans-Joachim; te Kook, Jürgen; Pflüger, Bernd et al. (2020): AGEnT. Ausbau von Grubenbauen für ein HAW-Endlager in Tongestein, Abschlussbericht, BGE TEC 2020-26, BGE TECHNOLOGY GmbH, Peine

Stahlmann, J.; Missal, C.; Hahn, P.; Edel, T. (2014): Geotechnische Bedingungen in der Schachtanlage Konrad – Auffahrungen von Strecken und Kammern im druckhaften Gebirge, geotechnik 37 (2014), Heft 2

EUROCODE-7 Second generation: Implications for underground rock engineering

EUROCODE-7 Zweite Generation: Auswirkungen auf die Fels- und Gebirgsmechanik

Heinz Konietzky
TU Bergakademie Freiberg
Geotechnical Institute
Gustav-Zeuner-Str. 1, 09599 Freiberg, Germany

Abstract

The EUROCODE is a binding set of regulations for civil and structural engineering in Europe. However, it has not established itself in rock engineering, especially for underground structures. The second generation of the EUROCODE (2024 published and valid latest in 2027) considers some special elements of rock engineering, so that a partial application is possible. This paper describes the general procedure according to the 2nd generation of the EUROCODE-7 and indicates the special features for the application in rock engineering. Nevertheless, a widespread application in rock engineering, especially for underground structures, is still not or only to a limited extend possible.

This short paper provides a general overview and a personal (private) opinion. Please note, that currently the 2nd generation of EC-7 is not yet finalized at the national level.

Zusammenfassung

Der EUROCODE bildet ein verbindliches Regelwerk für das Bauwesen und die Tragwerksplanung in Europa. Er hat sich aber bisher in der Fels- und Gebirgsmechanik, insbesondere für untertägige Bauwerke, noch nicht durchgesetzt. Die zweite Generation des Eurocodes (2024 publiziert und spätestens ab 2027 gültig) berücksichtigt nun einige spezielle Elemente der Fels- und Gebirgsmechanik, so dass zumindest eine partielle Anwendung möglich ist. Der Beitrag beschreibt das generelle Vorgehen gemäß EUROCODE-7 der zweiten Generation und weist auf die Besonderheiten bei der Anwendung für fels- und gebirgsmechanische Aufgabenstellungen hin. Eine umfassende Anwendung in der Fels- und Gebirgsmechanik, insbesondere für untertägige Bauwerke, ist allerdings immer noch nicht oder nur in einem begrenzten Umfang möglich.

Der Beitrag liefert einen groben Überblick und eine persönliche (private) Stellungnahme dazu. Es ist zu beachten, dass die zweite Generation des EC-7 gegenwärtig auf nationaler Ebene noch nicht abgeschlossen ist.

1 Introduction

The Eurocode is obligatory for the European Community, but also used in other countries worldwide. So far the EUROCODE is not applied for underground rock engineering structures. However, the second generation (latest date for publication is 2027) considers besides soils now also rocks and rock masses, respectively.

The complete set of EUROCODES (EC) consists of the following documents

- EN 1990 EUROCODE-0: Basis of structural design
- EN 1991 EUROCODE-1: Actions on structures
- EN 1992 EUROCODE-2: Design of concrete structures
- EN 1993 EUROCODE-3: Design of steel structures
- EN 1994 EUROCODE-4: Design of composite steel and concrete structures
- EN 1995 EUROCODE-5: Design of timber structures
- EN 1996 EUROCODE-6: Design of masonry structures
- EN 1997 EUROCODE-7: Geotechnical design
- EN 1998 EUROCODE-8: Design of structures for earthquake resistance
- EN 1999 EUROCODE-9: Design of aluminium structures

For geotechnical design EC-0 and EC-7 are the most important ones. The EC-7 itself consists of three parts:

- EN 1997-1:2024 (Geotechnical design, Part 1: General rules)
- EN 1997-2:2024 (Geotechnical design, Part 2: Ground investigation)
- EN 1997-3:2024 (Geotechnical design, Part 3: Geotechnical structures)

As already in the past, the EC demands two different verifications:

- Ultimate Limit State (ULS) verification
- Service Limit State (SLS) verification

To conduct the verifications, the EC offers the following general procedures:

- Calculations using the partial factor method or other realiability based methods
- Prescripting rules (defined in national annexes or by national authorities)
- Testing (proof by large-scale in-situ testing)
- Observational method (Konietzky, 2024a)

Most important for rock engineering are the observational method and the partial factor calculation method. Please note, that the EC-7 includes also national annexes, which contain for instance specific (different) partial factors valid for each country.

2 General procedure

The design process according to EN 1990 and EN 1997 comprises in general 4 tasks:

(1) Reliability management: establishing geotechnical complexity classes, consequence classes and geotechnical categories

(2) Ground modelling: determination of geological, hydrological and geotechnical conditions

(3) Design verification: verification of ULS and SLS

(4) Implementation of design: supervision, inspection, monitoring, maintenance during execution and design service time

Within the first step (reliability management) Consequence Class (CC) and Geotechnical Complexity Class (GCC) have to be specified. Based on these classifications the Geotechnical Category (GC) can be deduced (see Tab. 1 to 3). The deduced GC is important to determine the partial factors for ULS and SLS.

Tab. 1: Consequence classes (CC).

Consequence class	Loss of human life or personal injury	Economic, social or environmental consequences	Examples	Consequence factor
CC4	Extrem	Huge	Dams, nuclear power plants	Not yet specified
CC3	High	Very great	Highrise buildings, concert halls	1.1
CC2	Medium	Considerable	Buildings not covered by CC1 and CC3	1.0
CC1	Low	Small	Storage buildings	0.9
CC0	Very low	Insignificant	Elements other than structural	Not yet specified

Tab. 2: Geotechnical complexity classes (GCC).

Geotechnical complexity classes	Complexity	General features
GCC3	Higher	Considerable uncertainty regarding ground conditions, Highly variable or difficult ground conditions, Significant sensitivity to groundwater and surface water conditions, Significant complexity of the ground-structure interaction
GCC2	Normal	GCC2 applies of GCC1 and GCC2 are not applicable
GCC1	Lower	Negligible uncertainty regarding ground conditions, Uniform ground conditions, Low sensitivity to groundwater and surface water conditions, Low complexity of the ground-structure interaction

Tab. 3: Geotechnical categories (GC).

Consequence classes	Geotechnical complexity classes		
	GCC1	GCC2	GCC3
CC3	**GC2**	**GC3**	**GC3**
CC2	**GC2**	**GC2**	**GC3**
CC1	**GC1**	**GC2**	**GC2**

The second step is the ground modeling (the term ground comprises soils, rock and rock masses). The content/results of the ground investigations which comprise in-situ and lab investigations and the deduction of ground properties have to be documented in a so-called Ground Investigation Report (GIR).

The third step is the design verification for ULS and SLS. In case of using the partial factor concept according to GC and the Verification Case (VC) partial factors have to be determined for actions and resistance.

For geotechnical ULS design the following is valid in terms of the partial factors (see exemplary Tab. 4.):

- VC3: partial factors are put only on unfavourable variable actions
- VC4: partial factors are applied to action effects

There are 2 options to consider partial factors (for geotechnical engineering MFA is normally used):

- Partial factors on material strength parameters (Material Factor Approach = MFA)
- Partial factors on resistance directly (Resistance Factor Approach = RFA)

The 2nd generation of the EC explicitly recommends the application of probabilistic methods for design. Theoretically, this is the most appropriate method. However, it is complicated to apply this procedure due to several reasons, especially in the field of rock engineering:

- It is difficult to determine the distribution functions for material properties and actions.
- It is difficult to define an acceptable probability level of failure
- For most cases the computer run-time by applying probabilistic analysis (e.g. Monte Carlo simulation or Point-Estimation method) exceeds by far the currently available computer power and would lead to unacceptable long total run times even by using optimised sampling algorithms, especially if we have to consider many parameters

Tab. 4: Example: Partial factors for different verification cases (Lamas et al., 2023).

Action or effect *Einwirkungen oder Auswirkung von Einwirkungen*				**Partial factors γ_F and γ_E for verification cases** *Teilsicherheitsfaktoren γ_F und γ_E für Überprüfungsfälle*				
Type *Art*	**Group** *Gruppe*	**Symbol** *Symbol*	**Resulting effect** *Auswirkung*	**Structural resistance** [a] *Struktureller Widerstand* [a]	**Static equilibrium and uplift** [b] *Statisches Gleichgewicht und Auftrieb* [b]		**Geotechnical design** *Geotechnische Bemessung*	
Verification case / *Nachweisfälle*				**VC1** [a]	**VC2(a)** [b]	**VC2(b)** [b]	**VC3** [c]	**VC4** [d]
Permanent action (G_k) *Dauerhafte Wirkung* (G_k)	All [f] *Alle* [f]	γ_G	unfavourable / destabilizing *ungünstig / destabilisierend*	1.35 k_F	1.35 k_F	1.0	1.0	G_k is not factored *G_k wird nicht berücksichtigt*
	Water [l] *Wasser* [l]	γ_{Gw}		1.2 k_F	1.2 k_F	1.0	1.0	
	All [f] *Alle* [f]	$\gamma_{G,stb}$	stabilizing [g] *destabilisierend* [g]	not used	1.15 [e]	1.0	not used	
	Water [l] *Wasser* [l]	$\gamma_{Gw,stb}$			1.0 [e]	1.0		
	All *Alle*	$\gamma_{G,fav}$	favourable [h] *günstig* [h]	1.0	1.0	1.0	1.0	
Prestressing (P_k) *Vorspannung* (P_k)		γ_P [k]						
Variable action (Q_k) *Veränderliche Wirkung* (Q_k)	All [f] *Alle* [f]	γ_Q	unfavourable *ungünstig*	1.5 k_F	1.5 k_F	1.5 k_F	1.3	$\gamma_{Q,red}$ [j]
	Water [l] *Wasser* [l]	γ_{Qw}		1.35 k_F	1.35 k_F	1.35 k_F	1.15	1.0
	All Alle	$\gamma_{Q,fav}$	favourable	0	0	0	0	0
Effects of actions (E) *Auswirkungen von Einwirkungen (E)*		γ_E	unfavourable *ungünstig*	γ_E is not applied *γ_E wird nicht verwendet*				1.35 k_F
		$\gamma_{E,fav}$	favourable *günstig*					1.0

[a] Verification case VC1 is used both for structural and geotechnical design. / *Der Nachweisfall VC1 wird sowohl für die statische als auch für die geotechnische Bemessung verwendet.*

[b] Verification case VC2 is used for the combined verification of strength and static equilibrium, when the structure is sensitive to variations in permanent action arising from a single-source. Values of γ_F are taken from VC2(a) or VC2(b), which ever gives the less favourable outcome. / *Der Nachweisfall VC2 wird für den kombinierten Nachweis der Festigkeit und des statischen Gleichgewichts verwendet, wenn das Bauwerk gegenüber Schwankungen der ständigen Einwirkungen aus einer einzigen Quelle empfindlich ist. Die Werte für γ_F werden aus VC2(a) oder VC2(b) entnommen, je nachdem, welcher Fall das ungünstigere Ergebnis liefert.*

[c] Verification case VC3 is typically used for the design of slopes and embankments, spread foundations, and gravity retaining structures. See the relevant part of EN 1997 for details. / *Der Nachweisfall VC3 wird in der Regel für die Bemessung von Böschungen und Dämmen, Flachgründungen und Schwerkraft-Stützbauwerke verwendet. Einzelheiten sind dem entsprechenden Teil von EN 1997 zu entnehmen.*

[d] Verification case VC4 is typically used for the design of transversally loaded piles and embedded retaining walls and (in some countries) gravity retaining structures. See EN 1997 (all parts) for details. / *Der Nachweisfall VC4 wird in der Regel für die Bemessung von quer belasteten Pfählen und eingebetteten Stützwänden sowie (in einigen Ländern) für Schwerkraft-Stützbauwerke verwendet. Für Einzelheiten siehe EN 1997 (alle Teile).*

[e] The values of $\gamma_{G,stb}$ = 1.15 and 1.0 are based on $\gamma_{G,inf}$ = 1.35 ρ and 1.2 ρ with ρ = 0.85. / *Die Werte von $\gamma_{G,stb}$ = 1,15 und 1,0 basieren auf $\gamma_{G,inf}$ = 1,35 ρ and 1,2 ρ mit ρ = 0,85*

[f] Applied to all actions except water actions. / *Angewandt auf alle Einwirkungen außer Wassereinwirkungen.*

[g] Applied to the stabilizing part of an action originating from a single source. / *Angewandt auf den stabilisierenden Teil einer Einwirkung, die aus einer einzigen Quelle stammt.*

[h] Applied to actions whose entire effect is favourable and independent of the unfavourable action. / *Angewandt auf Aktionen, deren gesamte Wirkung günstig und unabhängig von der ungünstigen Aktion ist.*

[j] $\gamma_{Q,red} = \gamma_{Q,1} / \gamma_{G,1}$ where $\gamma_{Q,1}$ = corresponding value of γ_Q from VC1 and $\gamma_{G,1}$ = corresponding value of γ_G from VC1. / $\gamma_{Q,red} = \gamma_{Q,1} / \gamma_{G,1}$ *mit $\gamma_{Q,1}$ = entsprechender Wert von γ_Q aus VC1 und $\gamma_{G,1}$ = entsprechender Wert von γ_G aus VC1.*

[k] For the definition of γ_P where γ_P is materially dependent, see other relevant Eurocodes. / *Für die Definition von γ_P, wenn γ_P materialabhängig ist, siehe andere relevante Eurocodes.*

[l] For water actions induced by waves and currents. / *Für Wassereinwirkungen durch Wellen und Strömungen.*

3 Implications for underground rock engineering

Although the 2nd generation of the EC is also considering rocks and rock masses in an explicit manner – in contrast to the first generation -, the applicability for underground rock engineering structures, e.g. underground mines, caverns, tunnels etc. is limited. Nevertheless, some hints to perform ULS and SLS verifications can be deduced from the EC and will be discussed in this chapter.

The 2nd generation of EC has explicitly included the following items (recommendations) directly related to rock engineering:

- Use of rock mass classification schemes to characterize rock masses, to consider scale effects and to determine parameters (RMR-system, Q-system and RMi-system are recommended)
- Use of numerical simulation tools to perform ULS and SLS verification are recommended
- Special significance of rock discontinuities for the overal rock mass behavior is explicitly noticed
- Special failure criteria for rock matrix and rock discontinuities (joints etc.) are recommended, for instance the Hoek-Brown-criterion or the Barton-Bandis-criterion
- ISRM suggested methods or tests according to ASTM are recommended

The general understanding so far is, that the use of partial factors on both sides (actions and resistance) for rock engineering projects in the classical way (like done in civil engineering) is questionable, mainly due to two reasons:

(1) The in-situ state of stress has to be considered as the main action/load. However, this is a tensor value which cannot be handled by a single factor. May be that several special tensor values like invariants, stress deviators or single critical stress values (e.g. tensile stresses) can be used depending on the project/task. Also, depending on the chosen stress component and project, different partial factors may have to be defined.

(2) Rock and rock mass properties act as resistance. Each rock/rock mass is unique and the variance of rock properties is quite different. The same holds for the interaction between support measures and the rock/rock mass. The use of rock mass classification schemes to scale-down strength and stiffness parameters obtained by lab test results on intact rock samples is a possibly and often applied solution strategy. However, one should be aware, that rock mass classifications include subjective assessments and qualitative evaluations, although clear to determine quantitative values are necessary.

(3) Resistance may be load-depending and vice versa (for instance: rocks can show strain-hardening or strain-softening). Therefore, the specification of partial factors is questionable. May be they have to be replaced by functions instead of beiing single values.

(4) ULS and SLS may be difficult to specify exactly. We can distinguish different levels of local and global failure as well as different criteria and levels in respect to acceptable service states.

Due to these reasons, the application of the partial factor approach in rock engineering needs specific definitions for partial factors depending on rock type and project.

In rock engineering, typically numerical calculations using the shear strength reduction technique extended by a simultaneous tensile reduction approach are applied to verify the ULS (Konietzky, 2023b). To verify temporary stability often factor-of-safety values between 1 and 1.5 – depending on considered timespan and type of project- have to be documented and long-term stability is given by factor-of-safety values of about 2 or bigger (Konietzky, 2023c). However, the question arises how the shear strength reduction should be performed (reduction of all parameters with the same factor ? linear or non-linear failure envelope ? etc.). Based on current available studies it seems, that the use of the HB-criterion and the application of the strength reduction considering the local (apparent) stress state is the most appropriate according to backanalysis of failure events (Illeditsch, 2023).

Based on the 2nd generation of EC-7 the observational method in combination with numerical verifications of ULS and SLS seems to be the only way to incorporate the EC system into practise.The determination and application of partial factors for the numerical simulations is depending on several aspects:

- Type of Project
- Rock mass characteristics
- Responsible authority
- Practical experience

According to the 2nd generation of EC-7 for underground rock engineering structures (mines, tunnels, caverns etc.) the following may be applicable:

- CC2 + GCC3 which leads to GC3

Based on this categorization and Tab. 4, the verification case 4 (VC4) should be applied, which defines not partial factors for permanant loads/actions, but partial factors of 1.11 and 1.35 for unfavourable variable loads/actions and unfavourable effects of loads/actions.

For radioactive waste disposal the 2nd generation of EC-7 is not applicable because it should belong to CC4 and for this consequence class, GC and consequence factors are not specified.

For the third generation of EUROCODE-7 (scheduled for 2035) it is planned to involve rock engineering for underground structures in an even more explicit manner.

4 References

Illeditsch, M. (2023): Procedures for assessing the hazard posed by rock slopes, PhD Thesis, TU Wien

Konietzky, H. (2024a): Observational method, ebook, www.geotechnics.webador.de

Konietzky, H. (2024b): Factor-of-safety calculations in geomechanics, ebook, www.geotechnics.webador.de

Konietzky, H. & Schleinig, J.-P. (2024c): Geomechanical issues in room and pillar mining, ebook, www.geotechnics.webador.de

Lamas, L. et al. (2023): Rock engineering design in tomorrow's geotechnical toolbox: Eurocode and the basis of structural and geotechnical design (the second generation of EN 1990 and EN 1997), Geomechanics and Tunneling, 16(5): 469-490

Walter, H. et al. (2023): Rock engineering design in tomorrow's geotechnical toolbox: Eurocode 7 – General rules (EN 1997-1:2024), Geomechanics and Tunneling, 16(5): 491-509

Geotechnical stability analysis under mining supervision – Legal bases and practise in nonmetallic mineral mining

Geotechnische Standsicherheitsberechnungen in der Bergaufsicht – Rechtsgrundlagen und Praxis im Steine-Erden-Bergbau

Martin Herrmann, Robert Kaschkat
Sächsisches Oberbergamt,
Kirchgasse 11, 09599 Freiberg

Abstract

Geotechanical stability calculations form an important working basis for both mining companies and the Saxon Chief Mines Inspectorate as the licensing and supervisory authority. It is therefore essential that the quality of the stability calculations is guaranteed. In order to meet this requirement, both the federal government and the state of Saxony have issued a series of legal regulations, which regulate the legal requirements for a geotechnical expert. The first part of the lecture deals with the legal framework that is relevant in Saxony. Following the legal basis, the second part uses practical examples to show how diverse the tasks and requirements of a geotechnical expert are, especially in opencast solid rock mining.

Zusammenfassung

Geotechnische Standsicherheitsberechnungen bilden eine wichtige Arbeitsgrundlage sowohl für die Bergbauunternehmer, als auch für das Sächsische Oberbergamt als Zulassungs- und Aufsichtsbehörde. Daher ist es unabdingbar, dass die Qualität der Standsicherheitsberechnungen gewährleistet ist. Um dieser Anforderung gerecht zu werden, wurden sowohl vom Bund, als auch vom Land Sachsen eine Reihe von Rechtsvorschriften erlassen, in welchen die rechtlichen Voraussetzungen an einen Sachverständigen für Geotechnik geregelt werden. Im ersten Teil des Vortrags werden die rechtlichen Randbedingungen, welche hierfür in Sachsen einschlägig sind, behandelt. Der zweite Teil zeigt dann im Anschluss an die rechtlichen Grundlagen, anhand von Praxisbeispielen wie vielfältig die Aufgaben und Anforderungen eines Sachverständigen für Geotechnik gerade im Festgesteinstagebau sind.

1 Einführung

Die geotechnische Sicherheit eines Bergbaubetriebs stellt eine Kernanforderung für die Zulassung eines Betriebsplans nach dem BBergG dar. Bereits im Gesetzeszweck bestimmt § 1 Nr. 2 BBergG, dass die Sicherheit der Betriebe und der Beschäftigten im Bergbau zu gewährleisten und Vorsorge gegen Gefahren, die sich aus bergbaulicher Tätigkeit für Leben, Gesundheit und Sachgüter Dritter ergeben, zu verstärken ist. Diese rechtlichen Grundanforderungen sind letztlich abstrakte Schutzziele. Deren Umsetzung basiert demgegenüber auf einer Anwendung dieser Regeln im Einzelfall, die regelmäßig außerhalb des eigentlichen Betriebsplans durch einen Geotechniker oder andere für das Sachgebiet befähigte Personen als Planungsgrundlage erarbeitet wird und nur in einfach gelagerten Fällen pauschalen Ansätzen genügen darf. Geotechnische Standsicherheitseinschätzungen sind insoweit Planungsgrundlagen und werden mit der späteren Zulassung eines Betriebsplans durch die Bergbehörde verbindlich.

Im laufenden Betrieb sind dieselben Berechnungs- und Beurteilungsgrundlagen als allgemein anerkannte Regeln der Sicherheitstechnik heranzuziehen. Allerdings ändert sich hier der Blickwinkel: Entstehen Zweifel an der Standsicherheit einer Gewinnungsböschung, z.B. durch bisher unbekannte Störungszonen im Gebirge, durch geotechnische Ereignisse oder schlichtweg Abweichungen vom Betriebsplan, muss der Istzustand bewertet werden, ob Gefahren bestehen und Gegenmaßnahmen erforderlich werden. Da diese Prüfungen durch die zuständige Bergbehörde veranlasst werden, sind Abnahmen und Prüfungen eines anerkannten Sachverständigen eng mit der Bergaufsicht verknüpft. Dies gilt natürlich erst recht, wenn aufgrund der Empfehlungen des Sachverständigen die Bergbehörde Anordnungen zur Gewährleistung der geotechnischen Sicherheit erlässt.

Nachfolgend werden die rechtlichen Randbedingungen zu geotechnischen Standsicherheitsberechnungen anhand der Rechtsverhältnisse in Sachsen dargestellt und im zweiten Teil praxisnah mit Anwendungsbeispielen aus dem Steine-Erden-Bergbau untersetzt. Insbesondere die Verschränkung zwischen bergaufsichtlichen Befugnissen der Bergbehörde und Arbeitsergebnissen der Sachverständigen stehen dabei im Vordergrund.

2 Rechtliche Grundlagen für die allgemein anerkannten Regeln der Sicherheitstechnik im Bergbau

Eine Zulassung von Betriebsplänen für Aufsuchungs-, Gewinnungs- oder Wiedernutzbarmachungsbetriebe setzt voraus, dass in Hinblick auf die Vorsorge gegen Gefahren für Leben, Gesundheit und zum Schutz von Sachgütern Dritter den allgemein anerkannten Regeln der Sicherheitstechnik entsprechende Maßnahmen getroffen und die bergrechtlichen Vorschriften eingehalten werden (§ 55 Abs. 1 Nr. 3 BBergG). Daneben ist auch der Schutz der Oberfläche im Interesse der persönlichen Sicherheit und des öffentlichen Verkehrs (§ 55 Abs. 1 Nr. 5 BBergG) zu beachten sowie die Vorsorge zur Wiedernutzbarmachung der Oberfläche (§ 55 Abs. 1 Nr. 7 BBergG) zu treffen. Auf unmittelbar gesetzlicher Ebene sind damit nur Schutzziele geregelt, anders als beim einleitend genannten Gesetzeszweck allerdings als harter Versagungsgrund für einen Zulassungsantrag. Für die Prüfung dieses Zulassungskriteriums bedarf es deshalb einer Konkretisierung, welche allgemein anerkannten Regeln der Sicherheitstechnik für die konkrete Planung und Prüfung bergbaulicher Maßnahmen heranzuziehen sind.

2.1 Bergverordnungen des Bundes

In erster Linie werden bergbauspezifische Regeln der Technik durch Bergverordnungen normiert, die grundsätzlich durch die Landesregierungen oder die von den Ländern bestimmten Stellen erlassen werden, soweit nicht das Bundeswirtschaftsministerium zuständig ist (§ 68 Abs. 1 BBergG). Dieser bundesrechtliche Vorrang für den Erlass von Bergverordnungen hat seit Inkrafttreten der Allgemeinen Bundesbergverordnung (ABBergV) 1996 erheblich an Bedeutung gewonnen und die bis dahin geltenden detaillierten Landesbergverordnungen für bestimmte Bergbauzweige wie den Braunkohlenbergbau oder den Steinkohlenbergbau oder bestimmte Tätigkeiten und Anlagen wie Tiefbohrungen oder Schacht- und Schrägförderanlagen aufgehoben. Hintergrund war damals die Umsetzung von Europarecht in Gestalt der Arbeitsschutzrahmenrichtlinie und darauf gestützter weiterer Einzelrichtlinien (Keusgen S. 60 ff). In den neuen Bundesländern hatte dies zur Folge, dass sämtliche nach dem Einigungsvertrag als Bergverordnungen fortgeltende untergesetzliche Bergbauvorschriften der ehemaligen DDR gegenstandslos wurden (Herrmann, Anhang Einigungsvertrag RN 58).

Eine weitere – und für die Bestimmung des Standes der Technik entscheidende – Rechtsfolge war dabei, dass sich die europäische Regelungsphilosophie bei den für die Arbeitssicherheit maßgeblichen Regeln auch im Bergbau durchsetzte. Diese geht davon aus, dass sowohl die staatlichen Rechtsnormen als auch die behördlichen Aufsichtsbefugnisse nur vergleichsweise allgemeine Schutzziele vorgeben, die dann der Unternehmer individuell durch betriebliche Pläne und Maßnahmen untersetzen muss. Eine normative Konkretisierung des Standes der Technik durch Bundesbergverordnungen ist also schon aus diesen systematischen Gründen nicht möglich: Dies verdeutlicht das Beispiel der geotechnischen Sicherheit von Tagebauen: Anstelle der umfangreichen ABAO 122/1 der DDR, die in den neuen Bundesländern bis zum Inkrafttreten der ABBergV 1996 als Landesbergverordnung angewendet wurde, trat ein einziger Paragraf, nämlich § 14 ABBergV für „Arbeitsstätten zur übertägigen Aufsuchung, Gewinnung und Aufbereitung, Wiedernutzbarmachung“ mit der Kernforderung, wonach „Höhe und Neigung des Böschungssystems“ der Standfestigkeit der Gebirgsschichten sowie dem Abbauverfahren angepasst sein müssen.

2.2 Bergverordnungen des Landes

Ganz so konsequent erfolgte die Neuordnung des untergesetzlichen Bergrechts aber nun doch nicht. Die Verordnungsermächtigungen im Bundesberggesetz zum Erlass von Landesbergverordnungen zugunsten der Länder ermöglichen zumindest in den Bereichen, die nicht durch den Bund zur Umsetzung europäischer Rechtsvorschriften besetzt wurden, Spielräume. Länder wie Bayern und Hessen in den alten Bundesländern sowie Sachsen in den neuen Bundesländern haben insoweit nach 1996 neue Landesbergverordnungen erlassen, die an die ABBergV angepasst sind und für bestimmte sicherheitstechnisch relevante Bereiche zwei wesentliche Fragen klären: Welche zwingenden Regeln der Technik sind z.B. bei Tiefbohrungen oder Schachtanlagen einzuhalten und welche Prüfungen und Abnahmen müssen durch hierfür anerkannte Sachverständige vorgenommen werden. Auch diese Bergverordnungen verzichten dabei auf detailgenaue Regeln der Technik auf normativer Ebene, sie stellen damit einen Kompromiss zwischen den sehr allgemeinen Schutzzielen der ABBergV und detaillierten Regeln der Technik dar, wie sie zum Teil in Landesbergverordnungen, v.a. aber in untersetzenden Richtlinien der Bergbehörden geregelt waren. Sachsen hat diesen Spielraum in Hinblick auf die geotechnische Sicherheit von Tagebauen im Übrigen weitergehender als andere Bundesländer genutzt, da die vom Sächsischen Oberbergamt erlassene Sächsische Bergverordnung Kerninhalte der früheren Richtlinie Geotechnik und Anwendungserfahrungen zur ABAO 122/1 und der Sachverständigenanordnung der DDR in das sächsische Landesrecht übernommen hat. Sie enthält in §§ 6 bis 8 sowie in der Anlage pauschale Mindestanforderungen an die Standsicherheit von Böschungen im Fest- und Lockergestein, noch wesentlicher in Praxis aber

auch Regelungen zu Prüfungen und Abnahmen, die von einem vom Oberbergamt anerkannten Sachverständigen für Geotechnik vorgenommen werden müssen.

Auch das sächsische Landesrecht regelt also keineswegs umfassend die allgemein anerkannten Regeln der Sicherheitstechnik in Hinblick auf die geotechnische Sicherheit von Tagebauen. Die an Europa- und Bundesrecht angepasste Sächsische Bergverordnung geht vielmehr davon aus, dass die geotechnische Sicherheit von Bergbauaktivitäten immer im Einzelfall durch Standsicherheitseinschätzungen und –nachweise zu belegen ist, die regelmäßig durch einen dafür anerkannten Sachverständigen für Geotechnik zu erstellen oder zu prüfen sind. Dies gilt gleichermaßen für die Prüfung von Betriebsplananträgen, also die Planungsphase, wie auch für Abnahmen bestehender Böschungssysteme in der Betriebsphase.

2.3 Untergesetzliche Regeln der Technik

Der Verzicht auf detaillierte Regeln der Technik auf normativer Ebene bezweckt nicht nur eine Entbürokratisierung, sondern soll die notwendige Flexibilität, die Aktualität der technischen Entwicklung und letztlich die situationsgerechte Anwendung technischer Standards sicherstellen. Dem Geotechniker oder der Prüfingenieurin kommt daher nicht nur ein Bewertungsspielraum zu, welche konkreten technischen Maßstäbe oder Berechnungsverfahren angewendet werden, sondern gleichermaßen die Verantwortung zur Begründung der verwendeten Normen oder anderer wissenschaftlicher Konventionen. Die vom Gesetzgeber und Verordnungsgeber nicht hoheitlich ausgefüllten Technikregeln konkretisiert also letztlich der oder die Sachverständige in Form des jeweiligen Standsicherheitsnachweises. Die privatrechtliche Normung auf europäischer oder nationaler Ebene bietet hierbei die Gewähr, dass keine willkürlichen oder individuell abweichenden Grundsätze herangezogen werden, da gerade die im Bergrecht angewendete Technikrechtsklausel der „allgemein anerkannten Regeln der Sicherheitstechnik“ davon bestimmt ist, dass diese der herrschenden Meinung unter den kompetenten Fachleuten entspricht und in der Praxis bewährt ist (Kappes, § 55 RN 40).

3 Geotechnische Standsicherheitsberechnungen in der bergaufsichtlichen Praxis

Das eben skizzierte Regelungssystem zur geotechnischen Sicherheit im Bergrecht führt in der Praxis zu unterschiedlichen Fällen, wie geotechnische Berechnungen mit unternehmerischen Betriebsplanpflichten und bergaufsichtlichen Befugnissen verknüpft sind.

3.1 Standsicherheitsnachweise als Abnahme mit hoheitlichem Charakter

Die rechtlich am weitesten gehende Qualität einer Standsicherheitsberechnung hat eine durch Gesetz oder Verordnung vorgeschriebene Abnahme und Prüfung durch einen hierfür anerkannten Sachverständigen. In Sachsen ist dies durch § 8 Absatz 2 in Verbindung mit den Fallkriterien der Anlage 1 der Sächsischen Bergverordnung ausdrücklich für die Standsicherheit von Böschungssystemen gefordert. Die Standsicherheitsberechnung muss in diesen Fällen von einem hierfür anerkannten Sachverständigen geprüft werden, wenn sie nicht bereits durch einen Sachverständigen erstellt wurde. Das Ergebnis der Prüfung bedarf insoweit keiner Entscheidung der Bergbehörde, die Abnahme durch Prüfvermerk eines Sachverständigen hat vielmehr unmittelbar hoheitlichen Charakter, da die Erfüllung der gesetzlichen Anforderungen durch die Standsicherheitsberechnung oder den Prüfvermerk abschließend bestätigt wird. Juristisch wird dies mit dem Begriff der Verleihung hoheitlicher Rechte an einen privaten Dritten umschrieben; der anerkannte Sachverständige nimmt in seiner Prüffunktion damit letztlich hoheitliche Aufgaben wahr, die ansonsten staatlichen Behörden vorbehalten sind. Vergleichbar ist dies mit der gesetzlich vorgeschriebenen

Hauptuntersuchung für ein Kraftfahrzeug. Die Prüfplakette des Prüfingenieurs von der Dekra oder dem TÜV ist rechtlich auch nichts anderes als die hoheitliche Bestätigung der Betriebssicherheit des Fahrzeugs.

3.2 Standsicherheitsnachweise aufgrund von bergbehördlichen Entscheidungen im Einzelfall

Auch in den Ländern, in denen keine Bergverordnung Abnahmen und Prüfungen von Böschungen durch einen hierfür anerkannten Sachverständigen für Geotechnik regelt, kann eine Sachverständigenprüfung im Einzelfall durch eine Auflage in der Betriebsplanzulassung oder durch Anordnung im Rahmen der Bergaufsicht gefordert werden. Der Unterschied zur hoheitlichen Abnahme und Prüfung durch einen hierfür anerkannten Sachverständigen nach sächsischem Landesrecht besteht letztlich darin, dass die zuständige Bergbehörde sowohl für die Begründung, warum im Einzelfall eine Sachverständigenprüfung in Form einer Standsicherheitsberechnung beauflagt oder angeordnet wird als auch für die Ergebnisse der dann vorgelegten Sachverständigenprüfung hoheitlich verantwortlich bleibt. Die Bergbehörde kann im Übrigen dann auch entscheiden, welche sachverständigen Personen für die jeweiligen Aufgaben beauftragt werden sollen. Eine bergrechtliche Anerkennung für das Fachgebiet ist nicht erforderlich, wobei nichts dagegen spricht, wenn Bundesländer ohne eigene Rechtsgrundlagen für die Anerkennung von Sachverständigen nach § 23 a ABBergV Positivlisten zu geeigneten Personen vorhalten, die dann der Unternehmer beauftragen kann. Für die fachliche Qualität der geotechnischen Berechnungen und die fachlichen Maßstäbe der allgemein anerkannten Regeln der Sicherheitstechnik gibt es im Übrigen keine Unterschiede in Hinblick auf den Rechtsgrund der Forderung zur Vorlage einer Standsicherheitsberechnung. Entscheidend ist nur, dass bei bergbehördlich im Einzelfall beauflagten oder angeordneten Standsicherheitsnachweisen nie der beauftragte Sachverständige abschließend entscheidet, sondern die Bergbehörde, die sich auf die fachliche Expertise des Sachverständigen stützen kann, aber die hoheitliche Verantwortung für das Ergebnis und weitere Konsequenzen selbst übernehmen muss.

3.3 Standsicherheitsberechnungen als Bestandteil der Betriebsplanunterlagen

In weiteren Fällen werden Sachverständige für Geotechnik nicht für eine Prüfung und Abnahme bestehender Anlagen oder Einrichtungen tätig, sondern im Vorfeld geplanter Bergbauaktivitäten, insbesondere bei der Erstellung von Planungsunterlagen. Hierbei geht es oftmals weniger um die Abbauplanung für neue Vorhaben, sondern um die Umsetzung von Handlungsempfehlungen der Sachverständigen, die in Reaktion auf kritische Betriebszustände erarbeitet wurden. Standsicherheitsberechnungen haben insoweit den Charakter von Antragsinhalten, der Bearbeiter befindet sich deshalb letztlich auf der Ebene des Bergbauunternehmers als Antragsteller für ein Zulassungsverfahren. Bergrechtlich verantwortlich für die Betriebsplanung und Antragstellung bleibt ausschließlich der Unternehmer (§ 61 Absatz 1 BBergG, § 51 Absatz 1 BBergG), verantwortlich für die Zulassungsentscheidung ist die zuständige Bergbehörde. Auch wenn sich beide Seiten auf eine sachverständig erstellte Standsicherheitsberechnung stützen, ersetzt der Sachverständige weder die unternehmerische Verantwortlichkeit für die Sicherheit des Betriebs noch die hoheitliche Zulassungsentscheidung der Bergbehörde, mit der die Rechtskonformität der bergbaulichen Maßnahmen festgestellt wird. Zulässig und für die tägliche Praxis auch schlichtweg notwendig ist hingegen ein „Sich-zu-eigen-machen“, das heißt, sich den Wertungen einer sachverständig erstellten Betriebsplanunterlage anzuschließen. Dies gilt sowohl für den Unternehmer als auch für die Zulassungsbehörde, deren eigene Verantwortlichkeiten aber auf Ebene einer qualifizierten Plausibilität erhalten bleibt. Denn plausibel und für eigene Entscheidungen übernahmefähig sind Standsicherheitsberechnungen nur dann, wenn der Bearbeiter die erforderliche Fachkunde aufweist, also insbesondere im Falle einer Anerkennung als Sachverständiger für das

Fachgebiet, der zu beurteilende Sachverhalt zum Zulassungszeitpunkt dem in der Standsicherheitsberechnung zugrunde gelegten Zustand entspricht und dass weitere fachliche Informationen z.B. aus einem behördlichen Zulassungsverfahren widerspruchsfrei berücksichtigt werden können. Letzteres kommt vor allem in den Bundesländern zum Tragen, in denen der staatliche geologische Dienst Prüfaufgaben in Hinblick auf geotechnische Sachverhalte wahrnimmt.

4 Zwischenergebnis

Standsicherheitsberechnungen, die von hierfür fachlich qualifizierten Personen erstellt werden, kommt eine zentrale Bedeutung bei der Beurteilung bergrechtlicher Sachverhalte zu. Sie konkretisieren die gesetzlich nur nach Schutzzielen und Grundanforderungen bestimmten allgemein anerkannten Regeln der Sicherheitstechnik und gewährleisten damit die notwendige Flexibilität und fachgerechte Anwendung auf den zu beurteilenden Einzelsachverhalt. Die rechtliche Qualität und die Verschränkung mit Verantwortlichkeiten auf Ebene des Unternehmers und auf Ebene der Bergbehörde ist dabei durchaus differenziert. Unmittelbar hoheitlich werden nur Standsicherheitsnachweise wirksam, die als Abnahme und Prüfung durch Gesetz oder Verordnung einem hierfür anerkannten Sachverständigen vorbehalten sind. In allen anderen Fällen bedürfen Standsicherheitsberechnungen einer behördlichen Entscheidung, wenn sie Grundlage von konkreten Maßnahmen im Betrieb oder bergaufsichtlichen Entscheidungen werden sollen. Im folgenden Teil werden Fallbeispiele aus der täglichen Praxis vorgestellt, die die Vielfalt der Konstellationen mit Schwerpunkt im Festgestein ohne Anspruch auf Vollständigkeit beschreiben.

5 Praxisbeispiele

Nachdem die rechtlichen Grundlagen und Anforderungen behandelt wurden, welche an einen Sachverständigen für Geotechnik gestellt werden, werden im nächsten Teil ein paar Beispiele aus dem praktischen Alltag vorgestellt. Die Beispiele sollen verdeutlichen wie häufig in der Praxis das Heranziehen eines Sachverständigen für Geotechnik erforderlich ist und welch vielfältige Aufgaben diesem dabei zu kommen.

5.1 Direktversturz über die Tagebaukante

Viele Festgesteinstagebaue werden, wenn die unterste Tagebausohle ganz oder zumindest bereits teilweise abgebaut wurde, mit bergbaulichen und nichtbergbaulichen Abfällen und Abraum verfüllt.

Der Einbau der Verfüllmassen kann dabei sowohl von unten nach oben, als auch von oben nach unten erfolgen. Bei der letztgenannten Einbauweise werden die Verfüllmaterialien von der Tagebaukante auf die Tagebausohle verstürzt. Der Vorteil bei dieser Methode ist, dass sich der Unternehmer die Kosten für den Transport der Verfüllmassen in das Tagebaustiefste spart. Für den Versturz der Verfüllmassen gibt es hierbei zwei Methoden. Zum einen können die Verfüllmassen mit einem Förderband, welches über die Bruchkante hinausragt direkt verstürtzt werden oder sie werden von einem Kipper an der Tagebaukante abgeladen und mittels eines Radladers über die Kante geschoben.

In beiden Fällen ist im Vorfeld die Standsicherheit der Kippstellen durch einen Sachverständigen für Geotechnik zu ermitteln um die geforderte Sicherheit zu gewährleisten.

Die Errichtung solcher Kippstellen können beim OBA unter Vorlage der Standsicherheitsberechnungen und -einschätzung des Sachverständigen beantragt werden.

Im folgenden Fallbeispiel wurde bei einer Routinebefahrung eines Festgesteinstagebaus festgestellt, dass der Unternehmer, ohne die dafür nötige Zulassung, drei Kippstellen zum Direktversturz betrieb. Hierauf wurde umgehend eine Anordnung gemäß § 72 Abs. 1 BBergG zur Verhinderung unerlaubter Tätigkeiten erlassen, um mögliche Personen- und/oder Sachschäden zu verhindern. Im anschließenden Gespräch wurde dem Unternehmer dargelegt, dass er zur Neuaufnahme der Versturztätigkeit einen Antrag auf Betriebsplanergänzung stellen muss. Dieser muss eine Standsicherheitseinschätzung eines Sachverständigen für Geotechnik enthalten, in welcher Aussagen getroffen werden ob die Böschungsschulter überhaupt tragfähig genug für die Verkipptätigkeit ist.

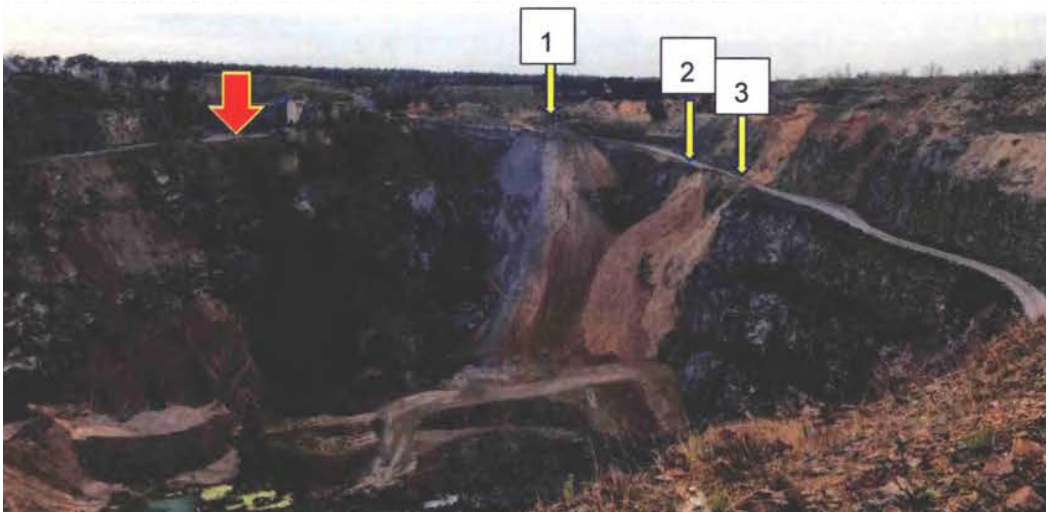

Abb. 1: Die drei ungesicherten Kippstellen.

Da der Unternehmer die drei Kippstellen weiter betreiben wollte, reichte er einen Antrag inklusive der besagten Standsicherheitseinschätzung ein. Somit wurde der Sachverständige in diesem Fall auf Bestreben des Unternehmers tätig und die Standsicherheitsberechnungen wurden als Bestandteil der Betriebsplanunterlagen eingereicht.

Der Sachverständige stellte fest, dass das Festgestein eine geringe Trennflächenhäufigkeit und vergleichsweise große Trennflächenabstände aufweist. Hierfür wurden zur detaillierten Auswertung des Kluftsystems sowie zur Beurteilung der Standsicherheit und Einschätzung bestehender Gefährdungen mehr als 2.000, teilweise schon vorliegende, Einzelmessungen ausgewertet.

Aufgrund der Messungen und den daraus abgeleiteten Berechnungen sowie der Vor-Ort-Komtrolle der geplanten Kippstellen kommt der Gutachter zum Ergebnis, dass die geotechnischen Voraussetzungen für das Betreiben der Kippstellen gegeben sind.

Allerdings betont der Gutachter dabei auch, dass die Ergebnisse von Standsicherheitsberechnungen im geklüfteten Felsgestein generell Unsicherheiten aufweisen. Einige wichtige Eingangsparameter können nicht berücksichtigt werden, der Einfluss der Böschungsneigungen, Bermen, Trennflächenneigungen und Trennfächenfestigkeiten kann aber ermittelt bzw. abgeschätzt werden. Die Raumlage und Einfallsbeträge der Trennflächen, als primäre Eingangsdaten können, soweit diese sichtbar sind, vor Ort gemessen werden, aber der sehr entscheidende Durchtrennungsgrad kann nur abgeschätzt bzw. angenommen werden. Dabei haben diese Kriterien direkten Einfluss auf die Standfestigkeit einer Böschung.Daher kann man nur direkt auf solche Schwächezonen reagieren, wenn man solche antrifft.

Die Bewertung der Standsicherheit beinhaltet damit immer einen erheblichen Bewertungsspielraum des Sachverständigen aufgrund seiner Fachkunde und eigener Erfahrungswerten.

5.2 Böschungsbruch während der Gewinnungsarbeit

Wie bereits beim ersten Beispiel ausgeführt wurde, können nicht alle Parameter, die Einfluss auf die Standsicherheit einer Böschung haben, im Vorfeld ermittelt werden. Auf manche lokalen Gegebenheiten, wie z.B. nicht sichtbare Störungszonen muss reagiert werden, wenn sie erkannt, bzw. angetroffen werden. Leider ist dies in einigen Fällen erst der Fall, wenn es bereits zu einem Ereignis gekommen ist. Initial für solche Ereignisse sind häufig durchgeführte Gewinnungssprengungen. In diesen Fällen ist es die Aufgabe des Sachverständigen, die bereits eingetretene Situation vor Ort zu begutachten und mögliche Schritte zum weiteren Vorgehen vorzuschlagen. Erst im Anschluss an die Beseitigung der akuten Gefahrensituation werden weitergehende Berechnungen durchgeführt um die Standsicherheit der Böschung neu zu bewerten.

Im folgenden Beispiel kam es im Rahmen einer planmäßigen Gewinnungssprengung zu einem Böschungsabbruch im Bereich der Berme auf der 2. Sohle eines Festgesteinstagebaus. Der Böschungsabbruch wurde dem Sächsischen Oberbergamt ordnungsgemäß gemeldet.

Das Sächsische Oberbergamt forderte daraufhin eine Begutachtung der entsprechenden Böschung durch einen Sachverständigen für Geotechnik. Bei der gemeinsamen Befahrung des Tagebaus durch das Oberbergamt, sowie Vertreter des Unternehmers, als auch eines Sachverständigen für Geotechnik wurde die Situation vor Ort bewertet.

Anders als im ersten Beispiel wurde der Sachverständige für Geotechnik in diesem Fall nicht auf Bestreben des Unternehmers tätig, sondern auf Grundlage einer behördlichen Entscheidung im Einzelfall.

Der Teilabbruch der Böschung ereignete sich im Bereich der mobilen Aufbereitungsanlage, obwohl die Anzahl der Bohrungen und die Menge des eingesetzten Sprengstoffes auf die komplizierten und ungünstigen Kluftverhältnisse der Südböschung angepasst wurde.

Abb. 2: Teilabbruch der Berme mit mobiler Aufbereitung.

Durch den Teilabbruch der Berme war der vorhandene Fahrweg im Böschungsbruchbereich weitgehend abgerutscht. Die Breite des Abbruches betrug etwa 30 - 35 m. Die Berme wurde in diesem Bereich bis auf eine Restbreite von ca. 3 - 4 m zerstört.

Abb. 3: bereits umgesetzte Teilverwallung des Böschungsfuß.

Bei der Befahrung stellte der Gutachter durch in Augenscheinnahme fest, dass die oberhalb der 2. Sohle im Abbruchbereich anschließende Teilböschung gegenwärtig standsicher ist und keine erkennbaren größeren oder durchgehenden Trennflächen aufweist, so dass ein Nachbrechen im Bereich der Böschung oberhalb aktuell nicht zu befürchten sei. Auf Anraten des Sachverständigen wurde auf der Berme der 2. Sohle eine Verwallung hergestellt, um eine Annäherung von Fahrzeugen an den abgebrochenen, nicht mehr befahrbaren Bereich zu verhindern. Auch am Böschungsfuß wurde ebenfalls mit der Herstellung einer Verwallung, zur Absperrung, begonnen. Weiter wurde auf Anraten des Gutachters das abgesprengte und abgerutschte Gestein am Fuß der Böschung auf der 3. Sohle beräumt und im Zuge der Beräumung offensichtlich lockere und überhängende Steine und Blöcke an der Abbauwand mit dem Bagger berissen.

Im Nachgang an die Befahrung führte der Sachverständige in seiner Stellungnahme aus, dass ursächlich für den Böschungsabbruch die, für den Tagebau prägenden, Lagerungsverhältnisse waren. Weiter wird in der Stellungnahme ausgeführt, dass eine Wiederherstellung der ursprünglichen Bermenbreite durch Rückverlagerung der oberen Teilböschung zwischen 1. und 2. Sohle nicht möglich ist, da es sich bei der Böschung um eine Endböschung handelte und sich die Aufbereitungsanlagen und Tagesanlagen des Tagebaus an der Böschungsoberkante befanden.

Der Gutachter betonte in seiner Stellungnahme, dass die Böschung zwar derzeit standsicher sei, aber durch regelmäßige in Augenscheinnahme zu kontrollieren ist, da abgleitende Steine und Blöcke aufgrund des Fehlens der Berme auf der 2. Sohle ungehindert bis auf die 3. Sohle herabstürzen könnten. Um zukünftige Ereignisse auszuschließen wurde die Verwallung am Fuß der Böschung auf der 3. Sohle nach Beendigung der Beräumung über die gesamte Breite des Abbruches zuzüglich beidseitig 20 m vervollständigt. Auf Vorgabe des Sachverständigen wurde die Verwallung mit einer Höhe von ca. 1,5 m hoch und in einem Abstand von ca. 9 m vom Böschungsfuß hergestellt.

Die weitere Abbauplanung auf der 3. Sohle war so anzupassen, dass im betreffenden Bereich eine ausreichende Bermenbreite belassen werden konnte.

5.3 Erstellung von Endböschungen

Für die Erstellung von Endböschungen sind im Zuge der Antragsstellung grundsätzlich Standsicherheitsberechnungen vorzulegen, welche von einem anerkannten Sachverständigen geprüft oder erstellt wurden.
In diesem Praxisbeispiel wurde die Standsicherheitsuntersuchung zur Gestaltung des Endböschungssystems in der Zulassung des Hauptbetriebsplans vom Sächsischen Oberbergamt gefordert. Wie bereits im rechtlichen Teil gesagt ist in § 8 Absatz 2 in Verbindung mit den Fallkriterien der Anlage 1 der Sächsischen Bergverordnung geregelt, dass diese Standsicherheitsuntersuchung durch einen anerkannten Sachverständigen für Geotechnik durchzuführen oder zu prüfen ist. Daher wurden die Standsicherheitsnachweise als Abnahme mit hoheitlichem Charakter erstellt.

Bei den Standsicherheitsuntersuchungen von Endböschungen im Festgestein ist eine der Schwierigkeiten, dass das Festgestein häufig von einer Abraumschicht aus Lockergestein überdeckt ist und diese unterschiedlichen Bodentypen teilweise im Zusammenspiel betrachtet werden müssen.
Problematisch war, dass es im vorliegenden Fall im Bereich des Lockergesteins bereits zu lokalen Rutschungen gekommen war.

In seiner Stellungnahme kam der Sachverständige zum Schluss, dass die Gesamtstandsicherheit des bisher bestehenden Böschungssystems zwar nicht gefährdet, aber lokal teilweise verringert ist. Ursächlich hierfür sind allgemeine Störungen des Gebirgsverbandes und der Aufbau des bisher erstellten Böschungssystems im Lockergestein. Im Besonderen die derzeit teilweise übersteile Böschung im Bereich der Rutschungen.

Abgleitungen im Festgestein lassen sich nicht immer vorhersehen und verhindern. Daher betont der Sachverständige wie wichtig Bermen als Stauraum für etwaige hinabfallende Felsteile sind. In diesem Fall ist bei den Böschungen im Fels mit einem Winkel von $\beta = 70°$ daher eine Mindestbermenbreite 5 m einzuhalten. Der Sachverständige wies in seiner Standsicherheitsuntersuchung daher explizit darauf hin, dass derzeit die Vorgaben an die Böschungshöhe und die Bermenbreite im Felsgestein nicht eingehalten werden, wodurch ein erhöhtes Risiko bezüglich eines Steinschlages vorliegt. Sollte dieser Zustand an der Böschung in ihrem Endzustand immer noch vorherrschen könnte diesem nur noch durch einen breiten Schutzstreifen oder Fangzäunen am Böschungsfuß begegnet werden.

Bezüglich des Böschungssystems im Lockergestein gab der Sachverständige eine Anpassung der bisherigen Fahrweise vor. Er führte aus, dass das geforderte Sicherheitsniveau im Bereich der Rutschungen im Abraum mit einer mittleren Böschungsneigung von ca. 1:1,5 bis 15 m Höhe erdstatisch nachweisbar ist. Dies wäre aber nur der Fall, wenn zum einen die vorhandenen Versteilungen an der Böschungsoberkante gebrochen werden und zum anderen eine weitere Berme auf der gesamten Böschungsbreite eingezogen wird. Die Berme sollte auf einer Höhe von ca. 2,5 m und mit einer Breite von ebenfalls ca. 2,5 m als Kopfentlastung angelegt werden. Weiter sollte die gesamte Böschungsoberkante insgesamt um 7 m rückverlegt und abgeflacht werden, da bei derzeitigem Zustand mit unkontrollierten Nachbrüchen mit Abbrüchen bis mindestens 4 m hinter die Böschungskante zu rechnen sei. Um die Dauerstandfestigkeit der Böschung zu sichern muss auf Dauer das Ausspülen des Materials durch eindringendes Oberflächenwasser verhindert werden. Um dies zu erreichen sollten zwei Dinge umgesetzt werden. Zum einen sollte die Böschung durch eine Auflage aus Blockhaufwerk gesichert werden, zum anderen sollte sie vollflächig begrünt werden, da eine schnelle Selbstbegrünung der Böschungsoberflächen zu erkennen ist.

Ausgangspunkt dieser Sachverständigentätigkeit war damit der durch die Sächsische Bergverordnung geforderte Standsicherheitsnachweis des bestehenden Böschungssystems, der im vorliegenden Fall nicht geführt werden konnte. Durchaus typisch für die angewandte Praxis im Steine-Erden-Bergbau ist dann aber auch die weitere Problemlösung, für die der Sachverständige Empfehlungen und Randbedingungen vorgibt, die anschließend im Verhältnis Bergbauunternehmer und Bergbehörde im Betriebsplanverfahren umgesetzt werden.

6 Zusammenfassung

Gerade im Festgestein kommt den fachlichen Einschätzungen eines Geotechnikers eine erhebliche Bedeutung bei, da die für einen Standsicherheitsnachweis erforderlichen Randbedingungen und Kennwerte immer nur im Einzelfall anhand der örtlichen Verhältnisse bewertet werden können. Die gesetzlichen Maßstäbe orientieren deshalb zurecht im Wesentlichen auf die Ziele der geotechnischen Sicherheit, während der Nachweis im Einzelfall aufgrund der allgemein anerkannten Regeln für Standsicherheitsberechnungen zu führen ist. Dem Sachverständigen für Geotechnik, der dies im jeweiligen Einzelfall leisten soll, kommt daher eine hohe Bedeutung im System zu – sowohl im Fall des abschließenden Standsicherheitsnachweises nach § 8 der Sächsischen Bergverordnung als auch in den Fällen, in denen er Vorschläge für betriebsplanpflichtige Maßnahmen oder bergbehördliche Anordnungen macht, denen sich die Bergbehörde im Regelfall anschließt. Die Praxisbeispiele verdeutlichen, dass beide Ebenen der Sachverständigentätigkeit oftmals eng miteinander verbunden sind. Im Freistaat Sachsen kommt im Übrigen der besonderen Fachkunde von anerkannten Sachverständigen für Geotechnik eine besondere Bedeutung bei, da der in den westlichen Bundesländern stärker ausgebaute geologische Dienst in den ostdeutschen Bundesländern keine ausreichenden Kapazitäten für Bergbaubetriebe hätte. Sowohl für den Bergbauunternehmer als auch für die Bergbehörde besteht aber ein Bedarf, eigene Planungen oder Entscheidungen in wesentlichen geotechnischen Fragestellungen auf eine unabhängige fachliche Bewertung stützen zu können, um der eigenen Verantwortung gerecht werden zu können. Dies ist letztlich die zentrale Rechtfertigung einer Sachverständigentätigkeit aufgrund staatlicher Anerkennung wie in Sachsen oder unmittelbar durch geologische Landesbehörden.

7 Literatur:

Bergverordnung für alle bergbaulichen Bereiche (Allgemeine Bundesbergverordnung – ABBergV) vom 23. Oktober 1995 (BGBl. I S. 1466)

Bundesberggesetz (BBergG) vom 13. August 1980 (BGBl. I S. 1310)

Herrmann in: Kühne/von Hammerstein/Keienburg/Kappes/Wiesendahl, BBergG, 3. Auflage 2023

Kappes in: Kühne/von Hammerstein/Keienburg/Kappes/Wiesendahl, BBergG, 3. Auflage 2023

Keusgen, Allgemeine Bundesbergverordnung – Entstehen, Konzeption, Regelungsinhalt, ZfB 1996, S. 60

Sächsische Bergverordnung vom 16. Juli 2009 (SächsGVBl. S. 489)

Geotechnical challenges during excavation of the shaft landing station Konrad 2

Geotechnische Herausforderungen bei der Auffahrung des Einlagerungsfüllortes Schacht Konrad 2

Stephan Gehne[1] (Editor), Mirko Polster[2], Mike Lieske[1], Rainer Weißmann[1]
[1] BGE GmbH, Eschenstr. 55, 31224 Peine
[2] BGE TECHNOLOGY GmbH, Eschenstr. 55, 31224 Peine

Abstract

The former Konrad iron ore mine is being converted for the storage of low and intermediate level radioactive waste. This article gives an overview of the geotechnical challenges during the construction of the shaft landing station, including the geotechnical assessment and stabilisation of a critical geotechnical development with locally increased deformations, and how numerical simulations were used for safety analysis and predictive simulations prior to the start of excavation. The results of the numerical simulation were used for a preliminary design of the excavation cross-section and support system. Locally increased deformations illustrate the need for geotechnical monitoring in combination with numerical simulations to ensure geotechnical safety during the construction phase. The monitoring allowed the early detection of a critical geotechnical behaviour and the timely implementation of the necessary safety measures, designed with numerical simulations ahead of construction.

Zusammenfassung

Die ehemalige Eisenerzgrube Konrad wird für die Einlagerung von schwach- und mittelradioaktiven Abfällen umgerüstet. Dieser Artikel gibt einen Überblick über die geotechnischen Herausforderungen bei der Erweiterung des Füllortes, einschließlich der geotechnischen Bewertung und Stabilisierung einer kritischen geotechnischen Entwicklung mit lokal erhöhten Verformungen. Weiterhin wurden numerische Simulationen für Sicherheitsanalysen und Vorhersagesimulationen vor Beginn der Bautätigkeiten eingesetzt. Die Ergebnisse der numerischen Simulation wurden für einen vorläufigen Entwurf des Baugrubenquerschnitts und des Ausbausystems verwendet. Lokal erhöhte Verformungen verdeutlichten die Notwendigkeit eines geotechnischen Monitorings in Kombination mit numerischen Simulationen, um die geotechnische Sicherheit während der Bauphase zu gewährleisten. Die Überwachung ermöglichte die frühzeitige Erkennung des kritischen geotechnischen Verhaltens und die rechtzeitige Umsetzung der erforderlichen Sicherheitsmaßnahmen, die mit numerischen Simulationen vor Baubeginn entworfen wurden.

1 Introduction

The Konrad mine in Salzgitter, Lower Saxony, is Germany's first licensed repository for low- and intermediate-level radioactive waste. The former iron ore mine is being converted for this purpose under the management of the Federal Company for Radioactive Waste Disposal (BGE).

Iron ore has been mined in the Konrad mine from 1964 and mining ceased in 1976 for economic reasons. From 1976 to 1982, the mine has been investigated for its suitability as a potential repository for low and intermediate level radioactive waste due to its favourable geology. Planning for a repository began as soon as the results of the studies indicated suitability.

The licensing procedure for the use of the site as a repository for low and intermediate level radioactive waste began in 1982 and was completed in 2007. Following, the process started to convert the former iron ore mine into a repository site. After completion, the Konrad repository will hold a total of up to 303,000 cubic metres of radioactive waste with a maximum radioactivity of 5 - 1018 Becquerel (5 trillion decayed atomic nuclei per second). Figure 1 gives an overview of the surface facility of the Konrad repository after its completion. The waste containers are transported underground via shaft Konrad 2. At the shaft landing station at a depth of 850 m, the containers are transferred onto a transport vehicle (see Figure 2), which transports the containers to the final storage chambers. This has required a significant expansion and re-equipping of the existing shaft landing station. Upon completion of the storing operation, all voids in the mine are backfilled and sealed for long term closure and security.

Fig. 1: 3D graphic of the surface facility of the Konrad repository after its completion.

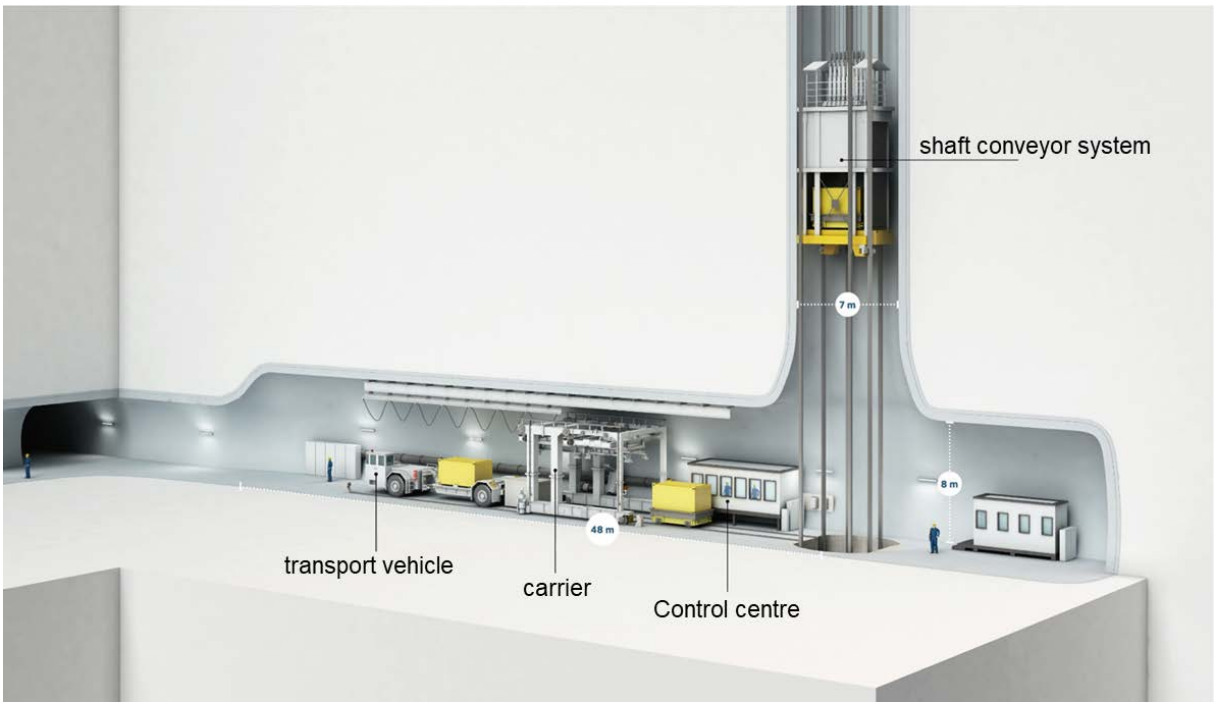

Fig. 2: 3D graphic of the emplacement site on level 2 with the emplacement area and the Konrad 2 shaft.

This article gives an overview of the geotechnical challenges during construction of the shaft landing station as a central component of the future storing phase. This includes the geological and mining conditions, the monitoring concept, as well as the geotechnical assessment and handling of a critical geotechnical development with locally increased deformations. Furthermore, this article shows how numerical simulations were used to aid the planning and design process and how the numerical model developed based on in-situ measurements.

2 Site Conditions at the Konrad 2 shaft landing station

Knowledge of the geological and mining conditions of the mine are crucial to the construction works, the design of a geotechnical monitoring concept and numerical simulations. The mining conditions also include the excavation works with the corresponding construction phases.

2.1 Geological conditions

Stratigraphically, the landing station is located in the Korallenoolith. From bottom to top, this consists of the 15 m - 25 m thick series of the Trümmerkalk, the Fladentonstein and the Erzkalk. The area of the shaft landing station is dominated by the Trümmerkalk series in the footwall, the Erzkalk series in the hanging wall and the Fladentonstein series in between.

The Fladentonstein series consists mainly of clay to clay-marl or marl-claystones, interspersed with three limestone beds of about 1 to 2 m thickness with intercalated marl-claystone beds. Particularly characteristic are the brown to ochre-coloured clayey ironstone pebbles and flakes. The rock is characterised by small prismatic fractures on the impact surface and by its sensitivity to water. Samples of Fladentonstein show very low strength with a mean value of UCS below 10 MPa (9.6 +/- 4.8 MPa) and only little tensile strength (59 +/- 38 kPa).

The Trümmerkalk series consists of bedded, partly oolitic limestones alternating with claystone beds of several centimetres thickness. The Erzkalk series is formed by an alternating sequence of clay-marlstone and limestone beds (partly oolitic and limonitic).

The rocks of the Erzkalk Series consist of laminated brown iron oxides and also fine sandy, predominantly thin-bedded, oolitic, shaly, grey to dark grey limestone. The benching is caused by numerous intercalated layers and beds of dark grey to black claystone and clay marl, mm to dm thick.

The rock mass is highly stratified and, particularly in the Fladentonstein series, strongly cut. There are N-S striking and approx. 45° to 60° west-dipping faults as well as parallel slip surfaces with strongly developed bench-like structure. The stratification strikes N-S and dips on average about 20° to the west. Other fault planes strike almost perpendicular to the stratigraphy and dip to the north. Several fault zones with offsets in the dm-range but also up to 1.3 m have been exposed.

2.2 Mining and construction conditions

The landing station of shaft Konrad 2 is constructed or extended at a depth of approximately 850 m (- 763 m NN). The whole landing station, with a final diameter of approximately 13 m, comprises of two sections: one section to the north-west of the shaft with a length of approximately 47.5 m and another section to the south-east of the shaft with a length of approximately 14.5 m.

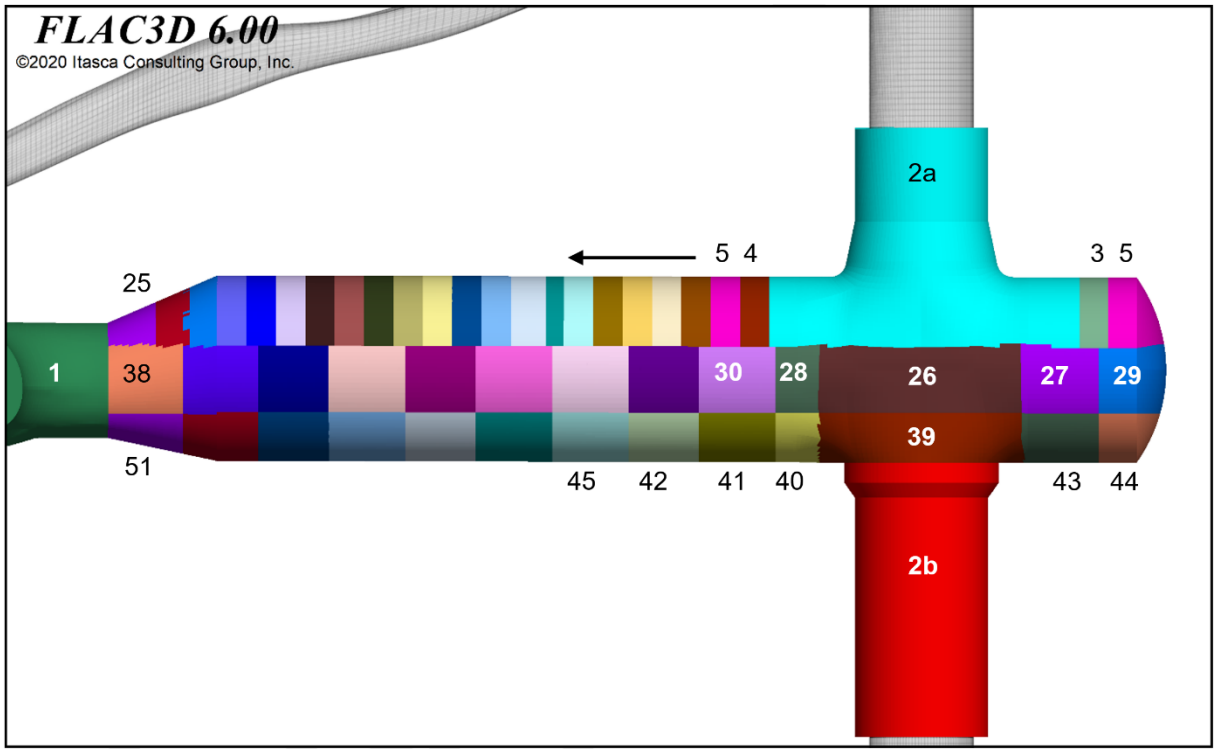

Fig. 3: Excavation steps of the shaft landing station.

The New Austrian Tunnelling Method (NATM) has been used to excavate the tunnel in three successive stages. It started with excavating of the crown area, followed by the bench and ended with excavation of the floor. The excavation of the extension has been carried out in several steps (Figure 3). The driving direction was horizontal and away from the shaft. Due to the geotechnical conditions, i.e. high initial stresses of approximately 20 MPa vertically and 10 - 12 MPa horizontally, combined with a low strength clayey rock, a rock convergence with magnitudes of up to several dm were expected over a long period of time. Therefore, a special

temporary support concept was chosen, which uses the existing (inherent) load-bearing capacity of the rock. A rigid lining system, installed immediately after excavation, would not have been able to support the predicted convergence very long. Therefore, a two-stage lining system has been planned, consisting of a reinforced anchor/shotcrete outer lining and a subsequently installed inner rigid concrete lining. The structural flexibility of the outer lining was achieved by compression slots in the shotcrete shell and the use of sliding head anchors. This allows for stress redistribution (resulting from the excavation) to take place with no or little damage to the support system and minimizes the support load. As a result of the mobilised bearing capacity of the rock, the rock pressure is only partly applied to the rigid support shell. Once the main convergences have subsided, the final lining is constructed with reinforced concrete as a quasi-rigid inner shell.

Figure 4 shows the outer shotcrete shell with anchors (sliding anchors) and the open compression slots after excavation of the bench section.

Fig. 4: Shotcrete shell with anchors and open compression slots.

An approximately 15 m high excavation, with the shape of a bell, is mined where the shaft (7 m diameter) and the landing station meet. The bottom of the shaft is accommodating the concrete foundation for the equipment and machinery within the shaft. The equipment will be installed afterwards.

3 Geotechnical monitoring

The excavation of the shaft landing station has been accompanied by an extensive geotechnical monitoring programme. The geotechnical monitoring consists of a system of geotechnical and mine surveying measurements. The measured values obtained need to be processed to provide unambiguous and immediately interpretable results for an assessment regarding geotechnical stability. For that, the results are also been compared with numerical predictions.

3.1 Monitoring concept

For the monitoring during construction, a monitoring concept is developed based on the observation method according to DIN EN 1997-1 (Eurocode 7). The instruments are arranged in monitoring cross sections (see Figure 5), which allow direct correlation with the numerical predictions and cover the entire construction area.

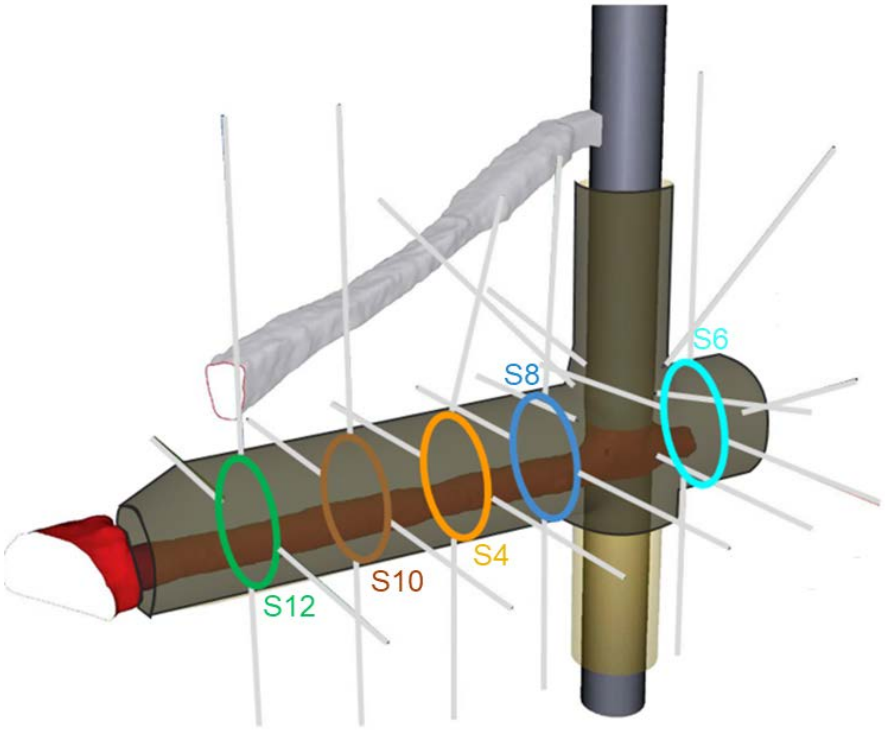

Fig. 5: Monitoring cross section shaft landing station.

The geotechnical monitoring programme at the shaft landing station consists of temperature, extensometer, convergence and tachymeter systems to monitor rock deformation. Measurements are taken close to the rock mass contour and deep into the rock mass.
In order to record the deformations, the cross sections are set up as early as possible so that the first measurements can be taken immediately after excavation. Therefore, several planned extensometers are installed prior to the start of construction in order to monitor all construction induced rock deformations. Further extensometers and convergence points are installed early after excavation. Temperature measurements are also taken in each extensometer borehole. In order to minimise the disturbance of the excavation works caused by the monitoring, measurements are automated. The extensometer and temperature data are automatically recorded and transmitted remotely. The convergence measurements are carried out regularly using several automated measuring stations that are permanently installed for the monitoring period. The automatically recorded data is remotely transmitted and automatically geodetically analysed. The results are three-dimensional point displacements from which displacements of the rock mass and changes in height can be derived.

4 Numerical modelling of excavation and support measures

4.1 Objectives

Numerical simulations have been carried out in conjunction with the extensive geotechnical monitoring programme. They are carried out as a prediction-calibration model and are based on the EC7 observation method. They were used to predict and verify the existing design of the shaft landing station and, if necessary, to adjust the design of the support system. For this purpose, 3D numerical models were generated and calibrated. In addition, these models were used for safety analysis and prediction simulations prior to the start of excavation to obtain deformation values indicating normal or critical conditions to ensure a safe structural design for both intermediate and final construction stages.

Prior to excavation, the analyses were carried out on the basis of in-situ data from older tunnels, which are not site-specific. The results of the numerical simulation were used for a preliminary design of the excavation cross-section and support system. During the construction phase, in-situ displacements and convergence measurements were compared with the results of the numerical prediction. Based on the new information (geology, structural geology, displacements and convergence) and the as-built process, the numerical model was recalibrated and final simulations were performed to derive the final support system.

These analyses were carried out using the finite difference code FLAC3D by CIC (a subcontractor of BGE).

4.2 Geology and tectonics

The modelling domain includes the shaft and filling station (former and enlarged diameters before/after excavation) as well as the adjacent drifts and a ramp crossing above the crown (Figure 3). As more geological information became available during the excavation, the model was successively refined and adapted to in-situ observations of stratigraphy and tectonics (Figure 6). In particular, the transition zones between the soft and weak Fladentonstein series and the significantly stiffer and harder rock layers above (Erzkalk series) and below (Trümmerkalk series) showed distinct clayey interlayers and a higher degree of fracturing. Consequently, these 2m thick layers were included in the calibration process.

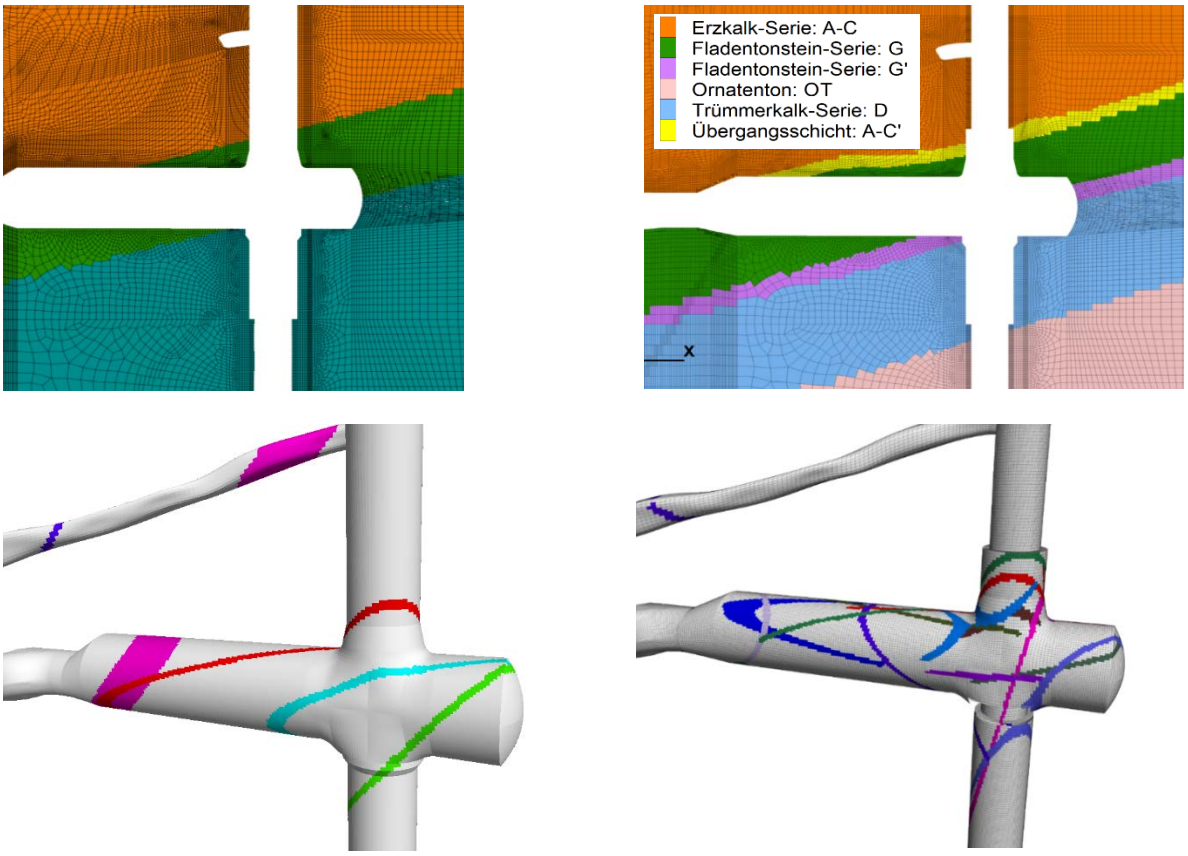

Prediction model (2017) prior to excavation **Calibration model (2022)**

Fig. 6: Geological model set up (above) and faults (below) taken into account.

4.3 Modeling of rock behavior –constitutive model used

An elasto-plastic model with anisotropic strength and strain softening (softening ubiquitous joint model) was used for the numerical analyses. The elastic deformation component was modelled as isotropic, linear elastic (Hooke). For the plastic part, the Mohr-Coulomb shear strength and a tension cut-off are used. To account for the anisotropy of strength, a distinction was made between matrix and stratification (bedding) strength (Figure 7). In addition to the peak shear strength, a softening dependent on the accumulated plastic strains to a residual value was considered for both the matrix and the bedding. After reaching the residual strength at 1% accumulated plastic shear or tensile strain, the strength level remains constant.

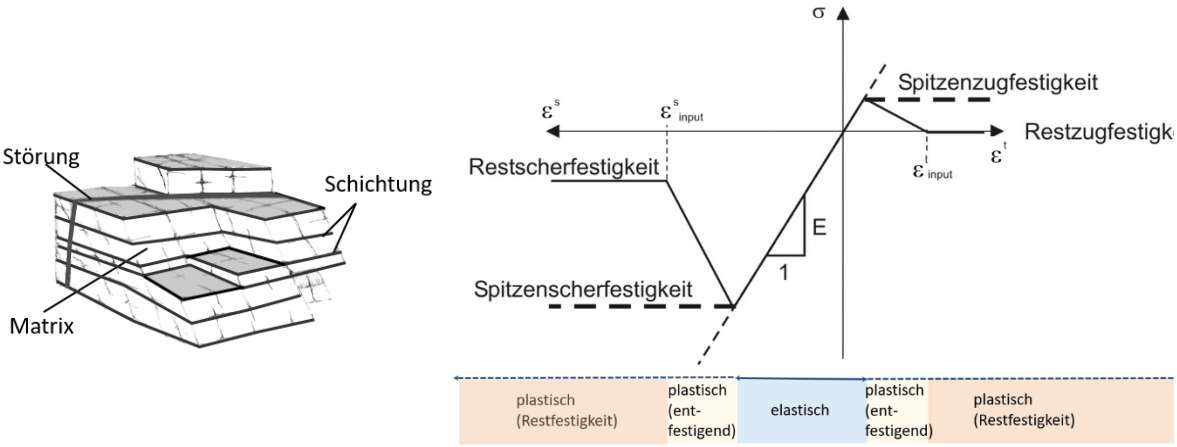

Fig. 7: Schematic representation of the used rock mass model. left: considered features, modified after WITTKE 1984, right: stress-strain diagram showing shear and tensile strain relief as a function of strain (pressure with negative sign).

4.4 Modeling of support measures

Several approaches were used to model the support components: The initial stabilisation by the shotcrete consolidation layer and short GRP anchors (2.0 m) was achieved by applying a normal stress of a few tens of kPa to the contour - according to the anchor spacing/pattern and the calculated radial rock deformation in this area. Discrete 1D structural (cable) elements were used to incorporate the 12...18 m long anchors. The implementation takes into account different anchor types according to the anchor plan and their characteristic load curves. A total of 4,750 FLAC3D cable elements were used (Figure 8). The outer slotted shotcrete shell was not modelled due to its limited tangential bearing capacity. The final (inner) shotcrete shell was modelled using 2D elements (liner and shell-elements respectively) with a thickness of 30 cm (40 cm near the shaft) and an additional levelling layer of approximately 28 cm to achieve the target diameter.

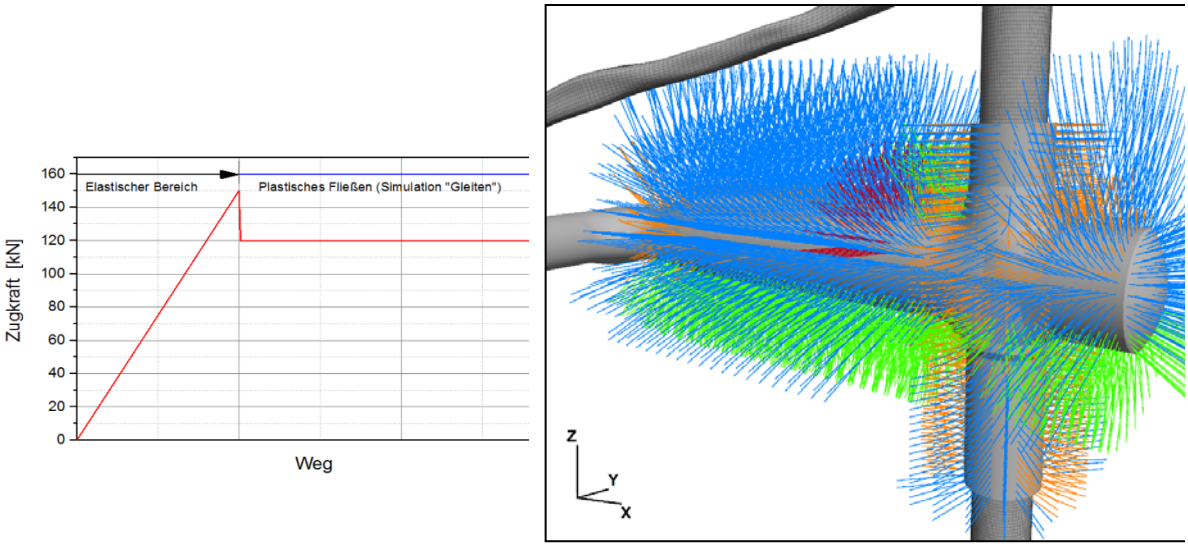

Fig. 8: Modelling of the anchors left: characteristic load curve for sliding anchor; right: anchor arrangement (blue – sliding anchors, orange – GRP anchors, green – fully glued steel anchors (hollow), brown - fully glued steel anchors (solid)).

4.5 Modeling sequence and results

The modelling sequence was chosen to follow the construction process in 51 steps (Figure 3). The support followed close to excavation for the crown and bench and one or two steps after the face for anchoring / shotcreting and ring closure during floor excavation.

Comparison of the measured data with the modelling results showed that the parameter sets initially used - derived from calibration using non-site specific data (i.e. horseshoe shaped drifts with short anchors) - were too conservative and overestimated the convergence values. Therefore, as part of the calibration process, the strength parameters were increased, with the exception of the transition layers mentioned above.

Nevertheless, the sliding wedge was identified at an early stage of modelling (non-converging simulation during the first steps of crown excavation with high displacements). The reason for this was found to be the combination of a geological interface, a fault intersecting this area and the cavities of the landing station and the shaft. This led to the planning and specification of support measures to stabilise this area prior to excavation. Specifically, resin injections and an additional anchorage pattern with a higher load-bearing capacity, fully bonded steel anchors, were specified. These were found to be statically effective in the calculations and were ultimately used on site.

After re-calibrating the model, the numerical results are in good agreement with the vertical/horizontal convergences and deformation measurements (Figure 9). The re-calibrated model is now being used to predict the cutting forces and the structural design of the final (inner) lining.

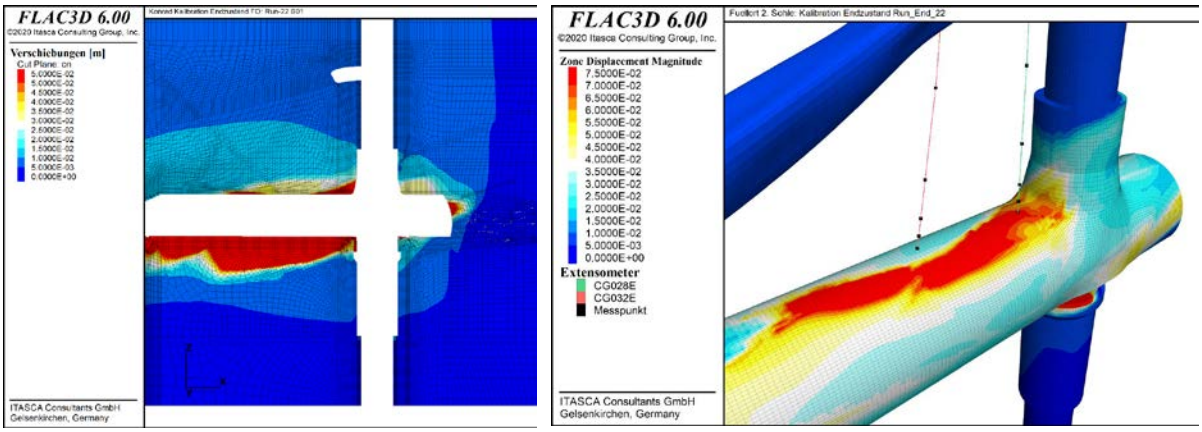

Fig. 9: Displacement magnitude [m] for the re-calibrated model; left: longitudinal section before floor excavation; right: perspective view (extensometers CG028E and 032E depicted).

5 Monitoring results and geotechnical measures to control locally increased deformations

In the following, the geotechnical monitoring carried out during the mine workings in the shaft landing station is illustrated using an example with localised increased deformations.
During the excavation, the geology in the tunnel roof opposed a geotechnical challenge, as the geology changes from the Fladentonstein series to the Erzkalk series as we go away from the shaft (see Figure 10). The particular challenge lies in the Fladentonstein series. It has a high degree of segregation and this area of rock is predominantly post-fractured. The combination of the geological interface between the Erzkalk Series and the Fladentonstein Series and the cavities of the landing station and the shaft creates a wedge in the roof area of the landing station near the shaft. Figure 10 shows the wedge and the monitoring cross-sections along the shaft landing station. The wedge is also cross-cut by several faults, which provides additional instability to the area. These conditions mean that the wedge was considered to be of particular concern and the monitoring cross-sections S8 and S4 were used to monitor this wedge.

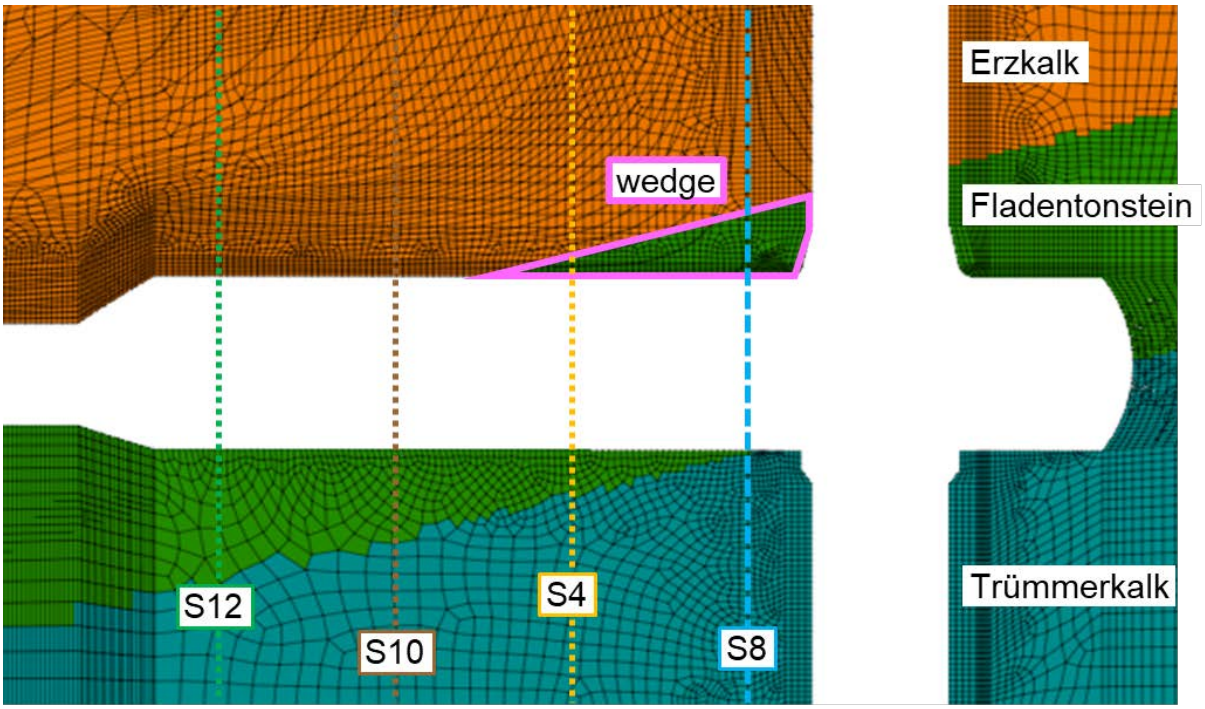

Fig. 10: Numerical model showing the geology and the wedge area.

Numerical simulations already predicted a critical rock behaviour in the area and pre-injections ahead of excavation were designed to stabilise the rock mass. For excavation steps in the crown area near the shaft, the excavation face has been pre-injected with a 2-component silicate resin in the area of the wedge. The pre-injections improve the rock mass and therefore increase stability as the injection material is intended to bond the fractures in the rock mass. Therefore, the bond between the rock and the injection material improves the strength of the rock. The injected section was then excavated and the outer concrete shell and anchors were installed. Figure 11 shows the tunnel face with injection boreholes as well as the outer concrete shell with anchors and open compression slots of the previous excavation step.

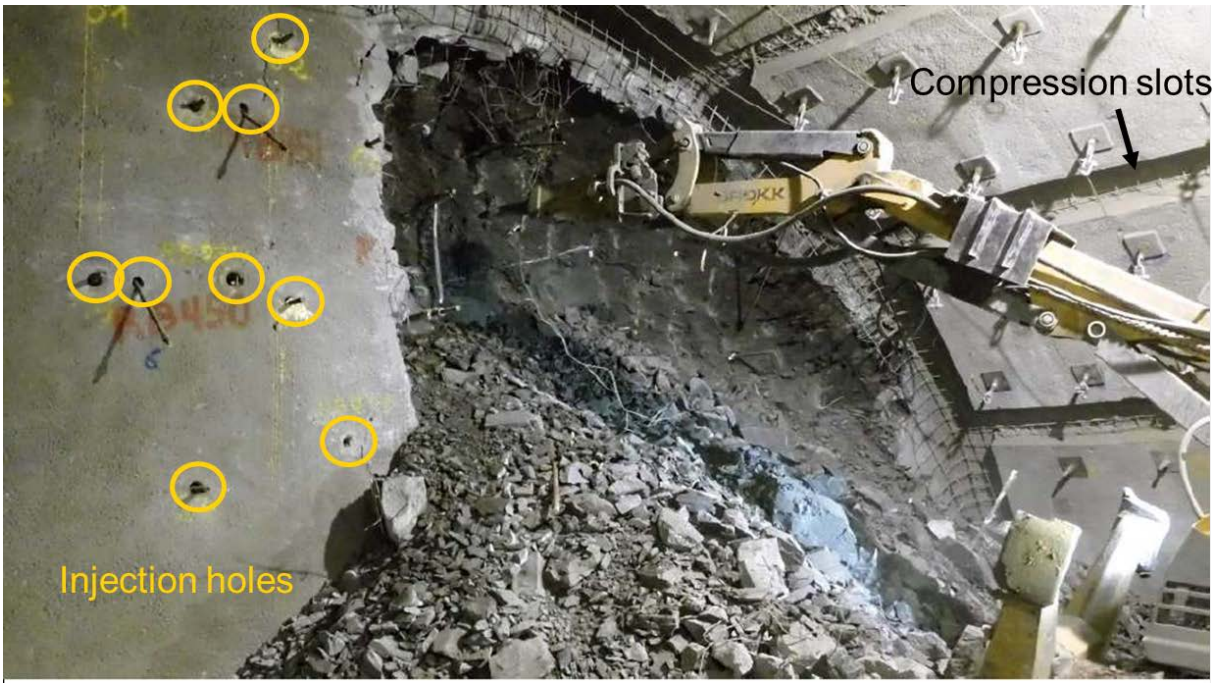

Fig. 11: Picture from the excavations works (injection holes to the left and compression slots to the right).

The displacement behaviour of the rock contour of the wedge due to the tunnelling work is shown and explained below on the basis of the monitoring results. The selected starting point for the following observations is excavation step 4, as displacements and deformation rates started to increase significantly when excavation started in this section. At this point, excavation steps 1, 2a, 2b and 3 have already been completed (see Figure 3).

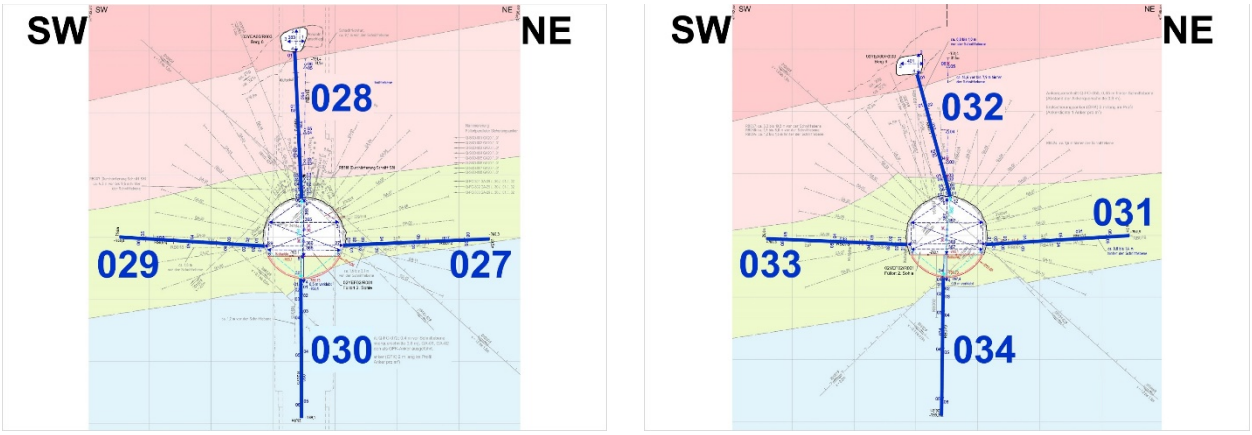

Fig. 12: Monitoring cross sections S8 und S4 including extensometers.

Figure 13 shows the displacements [mm] (blue line) and the deformation rates [(mm/m)/a] (green line) of roof extensometers 028 (monitoring section S8) and 032 (monitoring section S4) (Figure 12). There is a sharp increase in the deformation rate and a significant increase in the displacement in monitoring section S8 near the shaft during excavation of step 4 and following steps. At the start of step 10, there is a sudden increase in the displacement in monitoring section S4 and a sharp increase in the deformation rates.

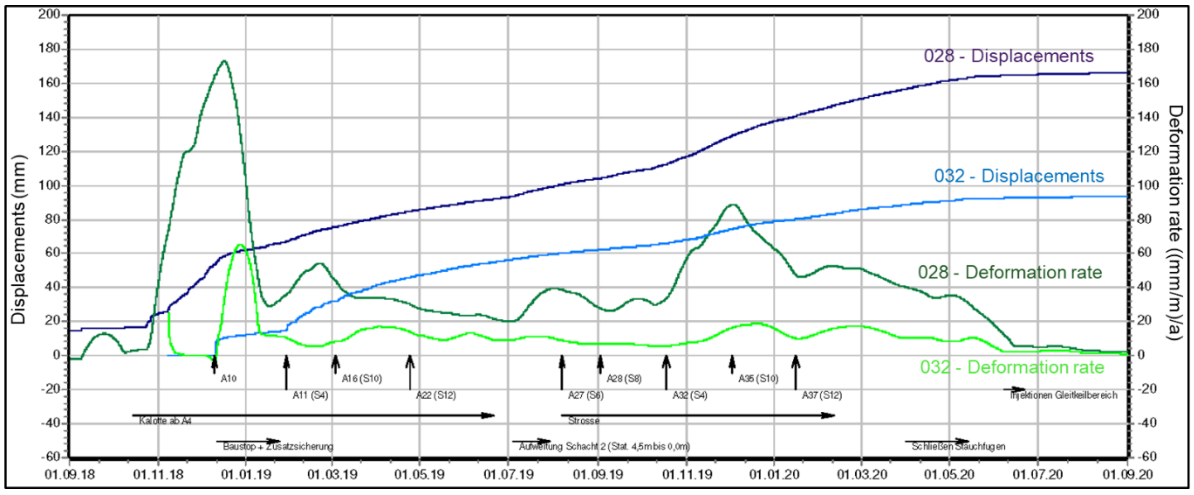

Fig. 13: Displacements and deformation rates of the roof extensometers 028 and 032.

Despite of the installation of structural support in excavation steps 4 to 9 including the outer concrete shell and anchoring, no reduction or stabilisation of the deformation rates and displacements in the near shaft section S8 can be seen. Therefore, construction was stopped and further structural support measures were carried out to secure the wedge. This consisted of additional anchoring and grouting to improve the rock mass in the excavated part of the crown area of the landing station.

The success of the stabilisation of the wedge with the additional support measures can be clearly seen in the reduced gradient of the displacements and the reduction in deformation rates in both sections. Based on the monitoring data, the geotechnical stability of the wedge is restored and construction continued. As off excavation step 16 all the way to the end of excavation of the crown area, a stable deformation rate can be seen in section S8 and an almost constant rate in monitoring section S4. The deformation rate in monitoring section S8 increases moderately again with the start of bench excavation and another significant increase in deformation rate can be seen during the excavation of step 32, which is located at the proposed end of the wedge. However, deformation rates in monitoring section S4 increase only slightly.

As the installation of the structural support measures proceeded and the excavation of the bench area is completed, the deformation rate in monitoring section S8 near the shaft decreases but remains at a significantly higher level than before excavation. Due to the high displacement and the very low stabilisation of rock displacements in monitoring section S8, additional structural support measures are carried out to ensure geotechnical stability. The support measures include the following steps to increase the rock support:

1. closing of the compression slots prior to excavation of the floor
2. further grouting to improve the rock mass around the wedge
3. construction of a foundation to transfer forces
4. floor excavation without compression slots to create the ring closure for increased stability
5. installation of fully grouted anchors in the floor area.

The monitoring results in Figure 13 show that the first three support measures had a clear stabilising effect on the deformation rates and that the rates in monitoring sections S8 and S4 are close to zero. The displacements flatten significantly, so that only very small displacements are present. The results of the geotechnical monitoring therefore show that the completed outer concrete shell without compression slots is taking the load and transferring them to the rock mass. Support measures 4 and 5 are used to adapt the subsequent construction sequence in order to create the ring closure of the shotcrete outer shell and use it as a load-bearing support element. Figure 14 shows the shaft landing station with compression slots closed.

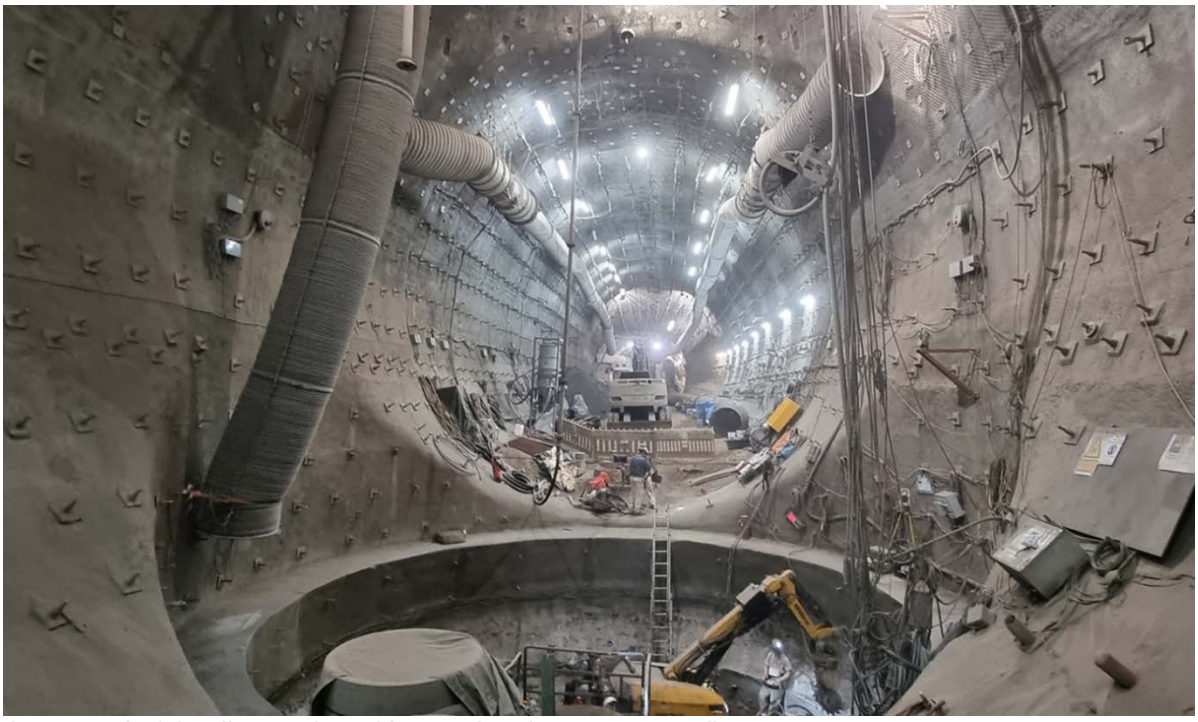

Fig. 14: Shaft landing station with completed outer support liner.

6 Summary

This article highlights the importance of geotechnical monitoring during the construction of underground structures in combination with numerical predictions. The appropriate approach to monitoring specific geological and mining conditions is a key element in the safe construction of underground structures. Instrumentation must be selected according to the environmental conditions and the duration of monitoring to ensure uninterrupted monitoring throughout the monitoring period. Wherever possible, instrumentation should be installed before or as soon as possible after excavation in order to fully record construction-induced deformations. This data is also used to calibrate the numerical model and improve the results. Monitoring data must be recorded, transmitted and analysed at defined intervals to assess geotechnical stability and respond to unexpected situations.

Another key element of safety were numerical simulations, which were used for safety analysis and predictive simulations prior to the start of excavation to obtain deformation values indicating normal or critical conditions to ensure a safe structural design for both interim and final construction phases. Numerical simulations can predict critical areas already ahead of construction and the monitoring concept can be designed accordingly, to focus on these critical areas. The article uses the example of locally increased deformation to illustrate the need for geotechnical monitoring combined with numerical simulations. Through geotechnical monitoring, a critical geotechnical behaviour was detected at an early stage and necessary safety measures, designed ahead using numerical simulations, were implemented promptly. In this way, geotechnical safety has been ensured during the construction phase.

The challenges of underground geological exploration mean that not all geotechnical conditions can be considered in advance during design. Geotechnical monitoring during the construction and numerical simulations, are therefore an important element of safe operation in underground structures.

Specific experiments on the material behavior of rock salt: creep, damage, healing

Spezifische Versuche zum Materialverhalten von Steinsalz: Kriechen, Schädigung, Verheilung

S. Lerche, N. Saruulbayar, A. Laatigue
Chair for Geomechanics and Multiphysics Systems, TU Clausthal

Abstract

The Chair for Geomechanics and multiphysics Systems, TU Clausthal, (TUC) is commissioned by the Ministry of Science, Energy, Climate Protection and Environment of the State of Saxony-Anhalt within the framework of planning approval process for the closure of radioactive waste repository in Morsleben (ERAM) for the accompanying expert assessment. In this context, a comprehensive laboratory program to characterize the properties of the occurring rock salt in ERAM was developed and executed by TUC during 2020-2023. 8 different salt types were investigated, with at least 13 short-term tests and 2 long-term tests performed per salt type. The total scope of the program comprises 148 tests with ca. 2900 machine days.

This paper focuses on the scientific aspects of experiment planning and evaluation. The emphasis is on the specific load condition of individual tests as well as the appropriate combinations of different types of tests in the design of the overall laboratory program (TUC-specific combination of short-term and long-term tests) aimed at optimizing the determination of material properties. The optimization pertains to the precision, reliability, robustness, and transferability of the determined material properties while minimizing the required realization time.

Specific multi-stage creep tests, developed by TUC, are presented. The load configuration allows for the scatter-free capture of creep, damage and healing processes using a single sample. Noteworthy advantage of the conducted long-term tests is the ability to isolate and thus precisely capture the damage-induced deformation during the damage phase as well as the creep deformation during the healing phase. In the case of the investigated carnallite, it was possible to induce intensive damage up to acceleration and subsequently capture the healing phase with measurement of increased creepability.

Finally, the goals, practical significance, and some results of the systematic analysis of the determined material parameters in terms of categorizing the material parameters of individual salt types into creep, strength, and damage classes are briefly described.

The extensive systematic experimental database produced can thus be used not only for engineering purposes to capture and quantify the differences in material properties of individual salt types but also for scientific purposes for the validation and (further) development of advanced constitutive models that capture all significant deformation processes such as creep, damage as well as healing.

Zusammenfassung

Im Rahmen des Planfeststellungsverfahrens zur Stilllegung des Endlagers für radioaktive Abfälle Morsleben (ERAM) wurde Arbeitsgruppe Morsleben vom Ministerium für Wissenschaft, Energie, Klimaschutz und Umwelt des Landes Sachsen-Anhalt (MWU) für begleitende Prüfungsarbeiten beauftragt. In diesem Zusammenhang wurde seitens TUC ein umfangreiches Laborversuchsprogramm zur Charakterisierung der Materialeigenschaften der im ERA Morsleben anstehenden Salzgesteine im Zeitraum 2020-2023 erarbeitet und realisiert. Der Untersuchungsumfang beläuft sich auf 148 Kurzzeit- und Langzeitversuche mit ca. 2900 Anlagentagen mit jeweils zumindest 13 Kurzzeitversuchen und zumindest 2 Langzeitversuchen pro Fazies. Insgesamt wurden 8 Salzfazies untersucht.

Es wird in diesem Beitrag auf die wissenschaftlichen Aspekte der Versuchsplanung und Auswertung eingegangen. Im Fokus stehen dabei spezifische Versuchsfahrweisen einzelner Versuche sowie geeignete Kombinationen unterschiedlicher Versuchsarten beim Design des gesamten Laborprogramms (TUC-spezifische Kombination von Kurzzeit- und Langzeitversuchen), die zur Optimierung der Ermittlung der Materialkennwerte dienen. Die Optimierung bezieht sich auf die Präzision, Zuverlässigkeit, Robustheit und Übertragbarkeit der ermittelten Materialkennwerte sowie zeitgleich auf den zu investierenden Zeitaufwand.

Es werden spezifische mehrstufige Kriechversuche – TUC-Eigenentwicklung –vorgestellt, die erlauben streubreitenfrei anhand einer Probe Kriech-, Schädigungs- sowie Schädigungsrückbildungsprozesse zu erfassen. Insbesondere hervorzuheben ist die Möglichkeit einer isolierten und somit präzisen Erfassung schädigungsinduzierter Deformationen während der Schädigungsphase sowie der Kriechdeformationen während der Verheilungsphase im Rahmen von Langzeitversuchen. Bemerkenswerterweise konnte im Fall von der untersuchten Fazies Kalisalz erst eine intensive Schädigung bis zur Akzeleration erzeugt werden und anschließend eine Verheilungsphase mit erhöhter messtechnisch isoliert eindeutig erfasster Kriechfähigkeit realisiert werden.

Schließlich werden kurz Ziele, praktische Bedeutung und einige Ergebnisse der durchgeführten systematischen Analyse zum Zweck der Kategorisierung der Materialeigenschaften einzelner Salzfazies in Kriech-, Festigkeits- und Schädigungsgruppen geschildert.

Die produzierte umfangreiche systematische Versuchsdatenbank kann somit nicht nur zur ingenieur-technischen Erfassung und Quantifizierung der Unterschiede in den Materialkennwerten einzelner Fazies, sondern auch für wissenschaftliche Zwecke der Validierung, Entwicklung bzw. Weiterentwicklung von fortgeschrittenen Stoffmodellen mit Erfassung aller wesentlichen Deformationsprozesse – Kriechen, Schädigung und Verheilung – verwendet werden.

1 Motivation and objectives

The motivation for the design and realization of the extensive laboratory program was the determination of the material parameter datasets for eight different salt types from the site of radioactive waste repository in Morsleben (ERAM) for the phenomenological constitutive model *Lux/Wolters/Lerche* that captures deformation processes elasticity, creep, damage and healing.

These laboratory investigations were initiated with the following objectives:

- Generation of an experimental database
  - to capture and characterize the material behavior of individual salt types involving the creep, damage and healing processes
  - with an optimized design of the laboratory program regarding the precision, reliability, robustness, and transferability of the material parameter
  - while minimizing the required realization time;
- Determination of individual material parameter datasets for the constitutive model *Lux/Wolters/Lerche* for eight different rock salt types from ERAM – z3LS, z3OS, z2HS3, z3AM, z3SS, z2HG, z2SF, z4;
- Systematic analysis of the created laboratory database regarding a possibility of categorization of the parameter sets – introduction of creep classes, strength classes, and damage classes
  - to reduce the modeling effort in regard to discretization and the number of elements when applying the determined material properties to geological layers in complex large-scale 3D discretized models with a mesh of several million elements and thus
  - to reduce the overall modeling effort in numerical simulations with application of the created 3D-meshes foreseen to use for the long-term safety assessment.

2 Overview and special Features of the laboratory program

2.1 Structure of the optimized laboratory program

A schematic overview of the complete laboratory program for determining the creep, strength, damage and healing parameter sets for the *Lux/Wolters/Lerche* model is shown in Figure 1.
As shown in Figure 1, the strength and damage parameter sets for individual salt types are derived from short-term test series at a relatively high strain rate of $\dot{\varepsilon}_1 = 3.6\, d^{-1} = 0.25\%/min$ (factor 1 → F1), whereas the confining pressure is varied and each test is sustained until an axial strain of up to the post-failure range ($\rightarrow \varepsilon_1 = 40\%$). As a result, the failure, dilatancy and residual strength can be determined as a function of the confining stress. With the exception of the short-term tests with a confining pressure of $\sigma_3 = 20\ \mathrm{MPa}$, which are considered to be nearly damage-free, all short-term tests with a strain rate of F1 were supplemented by a repeat test to assess the natural variability of the material behavior. Also, the choice of the minimum stress levels was made considering the in situ conditions in the vicinity of the underground openings, where the quantification of the dilatancy in the excavation damaged zone is essential for the safety analysis.

To validate and verify the transferability of the obtained damage parameters to the tests with lower strain rate, complementary short-term test series with successively reduced strain-rates with $\dot{\varepsilon}_1 = 0.36\, d^{-1} = 0.025\%/min$ (factor 10 slower → F10) and $\dot{\varepsilon}_1 = 0.036\, d^{-1} = 0.0025\%/min$ (factor 100 slower → F100) are conducted.

Finally, the single stress-controlled long-term test for each salt type is completed (supplemented by a repeat test to assess the natural variability) to further verify/demonstrate the transferability of the determined parameter sets to long-term behavior, as shown in Figure 1.

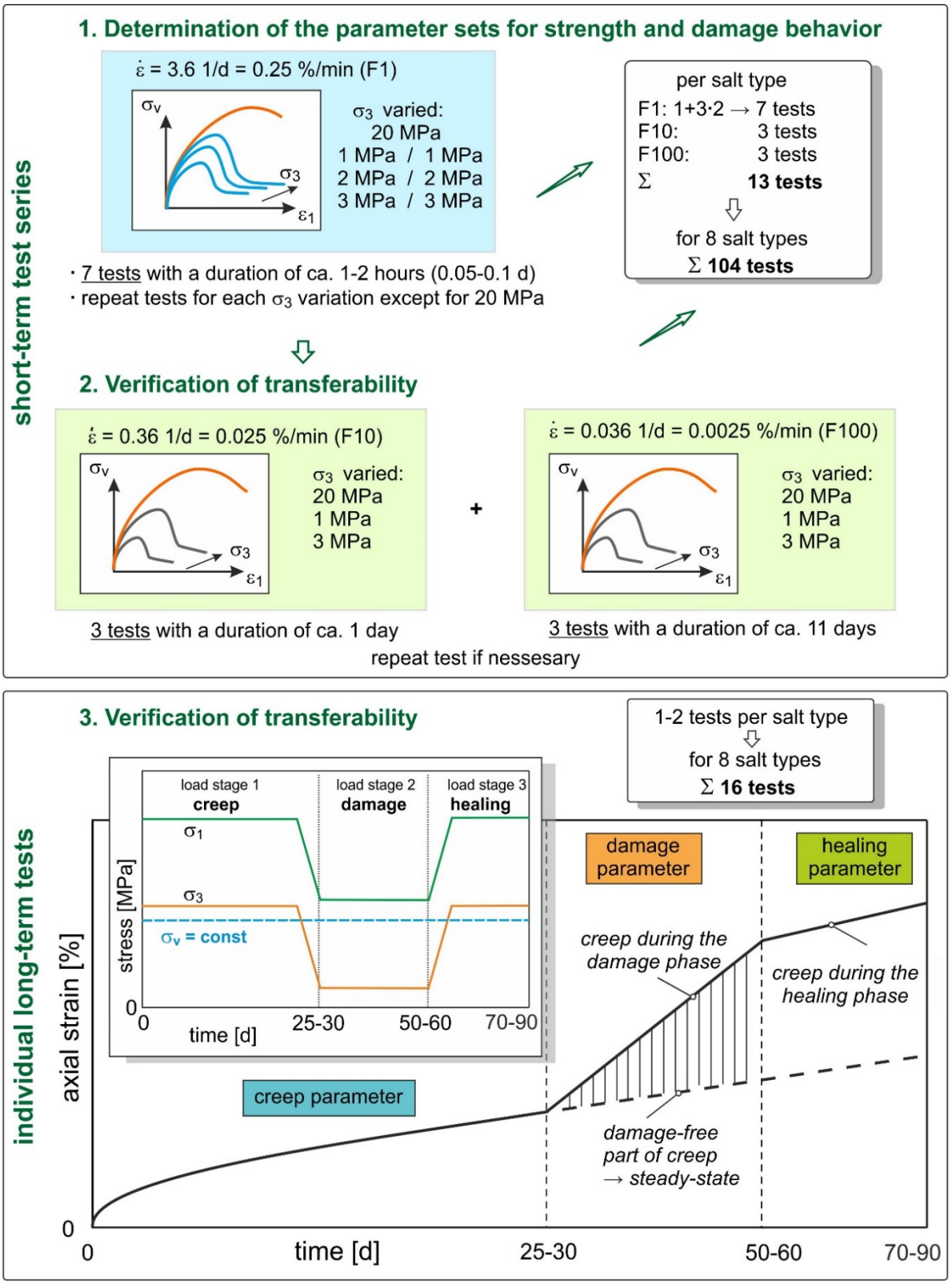

Fig. 1: Structure of the laboratory program from TUC to create a database for a reliable determination of the creep, strength, damage and healing parameter sets with the optimized effort.

The structure of the laboratory program outlined above ensures, through the variation of all parameters influencing strength and damage behavior, the generation of an extensive database for deriving robust and reliable material parameter datasets with optimized effort. Unlike the previous approach by TUC, which involved conducting both a series of short-term tests to determine strength properties and a series of long-term tests (→ extremely time-consuming) to determine creep and especially damage development, the current structure combines numerous short-term test series for the rapid development of moderate to intensive damage with single long-term tests for the low damage development rates, similar to in situ conditions.

Further details and complete documentation of the entire laboratory program can be found in *AG Morsleben (2024)*.

2.2 Specific long-term creep tests

Although the determination of individual creep parameter sets for each salt type was initially not formulated as one of the objectives (since the focus of the program was on the strength, damage and healing behavior), the triaxial long-term tests were mostly supplemented with an additional creep stage to enable the determination of the complete parameter set for the damage-free creep behavior of individual salt types.

Figure 2 shows exemplarily the variations of load conditions used in the long-term creep tests. All these variations are based on the one specific type of long-term test, developed by TUC, with the maintaining constant deviatoric stress when transitioning from damage-free stage to the damage-affected load stage. Further explanations to the specific tests can be found in *Lux et al. (2016)*, *Lux et al. (2018a)*, and *Lux et al. (2018b)*.

Accordingly, four variations of load conditions for this type of long-term test, realized in the frame of this laboratory program, can be differentiated as follows:

I. 3-stage long-term test C-D-H
   This test includes one damage-free creep stage (creep phase), one creep stage in the damage regime (damage phase) and one creep stage in the healing regime (healing phase).
II. 4-stage long-term test C-D-2H
   This test includes one creep phase, one damage phase and two healing phases. The two healing phases are used to capture the healing behavior for different loading regimes – deviatoric and isotropic regimes.
III. 5-stage long-term test 2C-D-2H
   This test includes two creep phases, one damage phase and two healing phases. The two creep phases are used to determine the complete creep parameter set for different deviatoric stress levels (not for one load level, as is the case in variant I).
IV. 6-stage long-term 2C-2D-2H
   This test includes two creep phases, two damage phases and two healing phases. The two damage phases are used, if necessary, to calibrate the intensity of the damage. Since the dilatancy limit of the specimen must be estimated before the start of each test, adjustments to the loading (due to the natural variability/scattering of the behavior) are required if the measured dilatancy significantly deviates from the expected values (increasing the minimal stress if the measured dilatancy is significantly greater than the expected value, or decreasing the minimal stress if the damage intensity measured by the dilatancy is too low). A target dilatancy of approximately 0.5-1.5% at the end of the damage phase was aimed for as optimally measurable damage intensity.

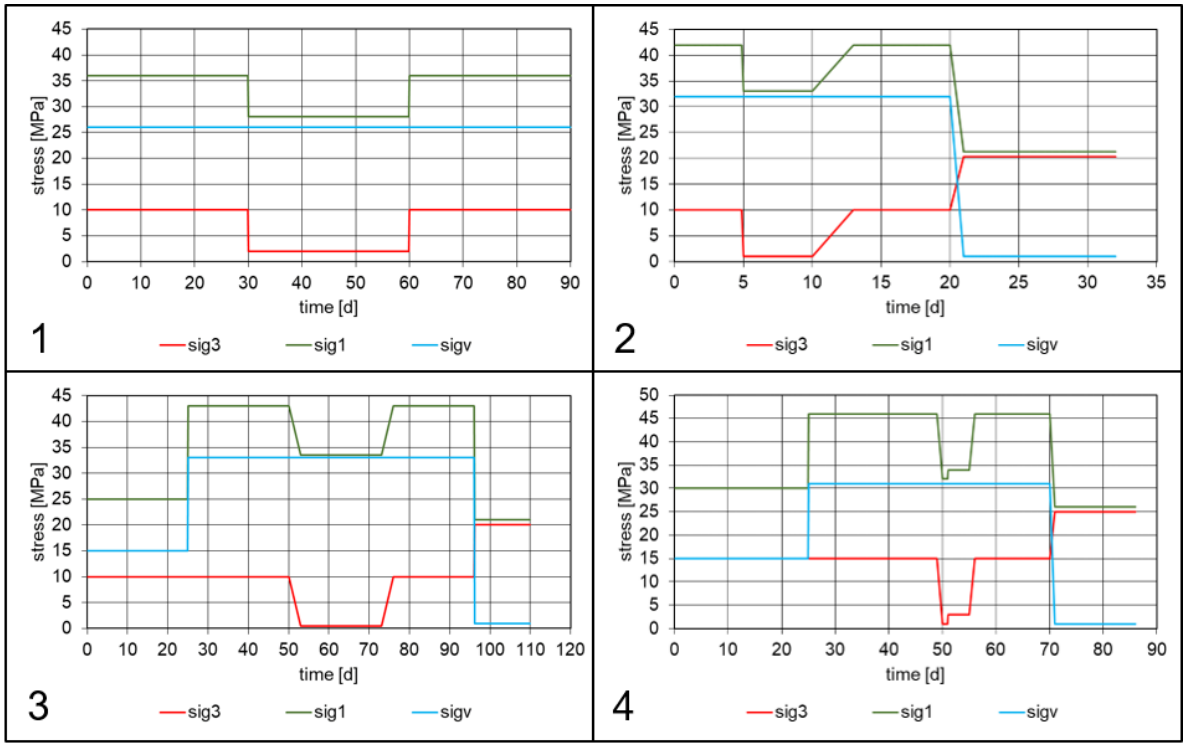

Fig. 2: Variations of the specific type of long-term creep test.

Figure 3 illustrates exemplary schematic diagram of the five-stage 2C-D-2H long-term test with the consecutive load history and the objectives of each load stage. Of particular importance is that the first two load stages represent specified stress levels localized below the dilatancy strength boundary. Consequently, the transient and steady-state creep deformations resulting from stages 1 and 2 are damage-free, allowing the determination of creep parameters for damage-free steady-state and transient creep. The subsequent stages 3 and 4 are characterized by a deviatoric stress corresponding to the level of the last damage-free load stage (→ stage 2). Therefore, any measured increase in creep rate from the level observed in the second load stage is expected to be exclusively due to the damage processes (→ no additional transient creep, since no deviatoric stress change). This method developed by TUC enables precise determination of damage-induced and healing-induced creep rates. Analogously, concerning the representation in Figure 3, for the fourth stage, the reduction in the creep rate compared to the rate observed in the damage phase can only occur if the stress level is lowered below the dilatancy strength boundary (still being in the steady-state regime due to maintaining constant deviatoric stress).

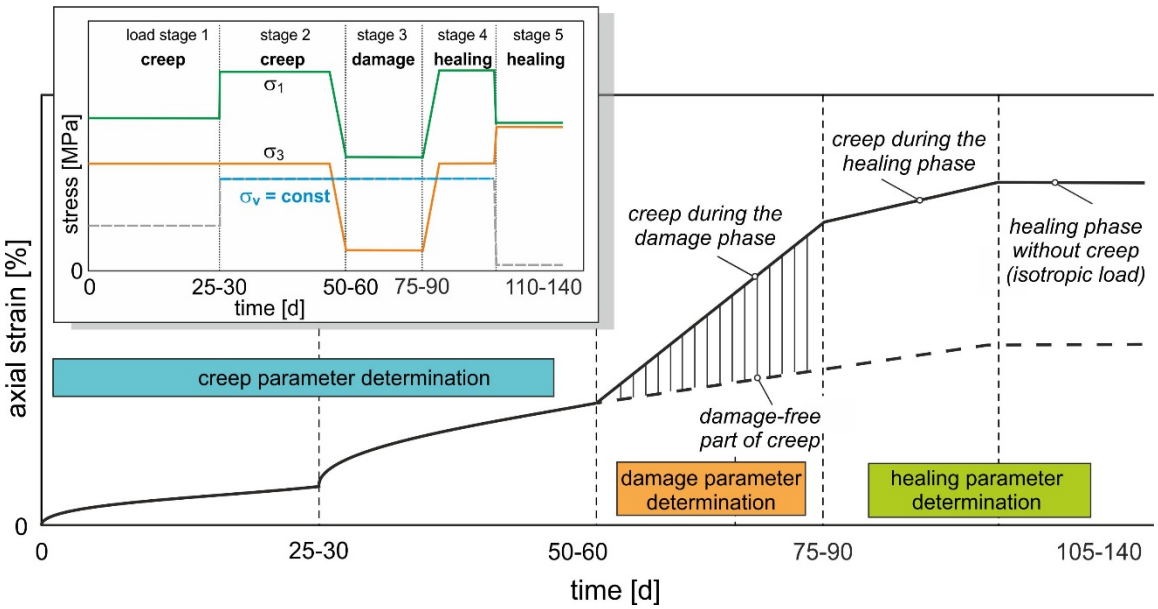

Fig. 3: Specific long-term creep test for optimized quantification of creep, damage and healing behavior.

3 Exemplary presentation of different test types for different processes

3.1 Optimized parameter determination procedure for the creep behavior

An improved approach for determining creep parameter set for the model *modLubby2* capturing the damage-free creep behavior (part of the model *Lux/Wolters/Lerche*) was developed while analyzing the created laboratory database. In contrast to the previous procedure, which uses the cumulative strain, the new approach utilizes strain-rates for the analysis and parameter determination. This ensures more precise results, less dependent on the analyzing person evaluating the tests.

First, the strain rate $\dot{\varepsilon}_1$ is derived from the measured values for axial strain $\varepsilon_{zz} = \varepsilon_1$, see Figure 4. Then, for each load stage, the level of the maximum strain rate occurring at the beginning of the load stage, as well as the level of the minimum strain rate occurring at the end of the load stage, are identified. These determined levels can be interpreted as transient (maximum) $\dot{\varepsilon}_{max}^{tr}$ and steady-state (minimum) creep rates $\dot{\varepsilon}^{st}$, assuming that the elastic portion of the deformations at the beginning of the load stage is negligibly small compared to the viscous strains, or after subtracting the elastic portion from the measured total strain and assuming that the duration of the load stage is sufficient to reach a nearly stationary state at the end of the load stage. Although, it is established that a complete decay of the transient creep rate occurs after several hundred days, based on lab test experience, a significant reduction in the transient creep rate to very small values can be observed already within about 30 days after loading (the transient strain rate is expected to be lower compared to the stationary creep rate).

For a more precise measurement of the transient and steady-state strain components, the laboratory test configuration developed and successfully applied by IfG (→ the combined test pairs with forward and reverse creep stages) is suitable, see e.g. *Günther et al. (2016)*. However, this type of the test combination with additional effort was not implemented in this laboratory program.

As shown in Figure 4, the viscosity moduli $\bar{\eta}_k$ and $\bar{\eta}_m$ can be derived from the determined minimum and maximum strain-rates of each load stage to quantify damage-free creep for the given deviatoric stress σ_v of the load stage. By subtracting the elastic strain (→ Hooke's law) and the stationary creep strain, which is determined by multiplying the duration of the load stage by the stationary creep rate $\varepsilon^{st} = \Delta t \cdot \dot{\varepsilon}^{st}$, from the total strain, the transient strain component can be calculated. As a result, the *Kelvin* shear modulus G_k can be derived as the quotient of the deviatoric stress and the maximum transient strain.

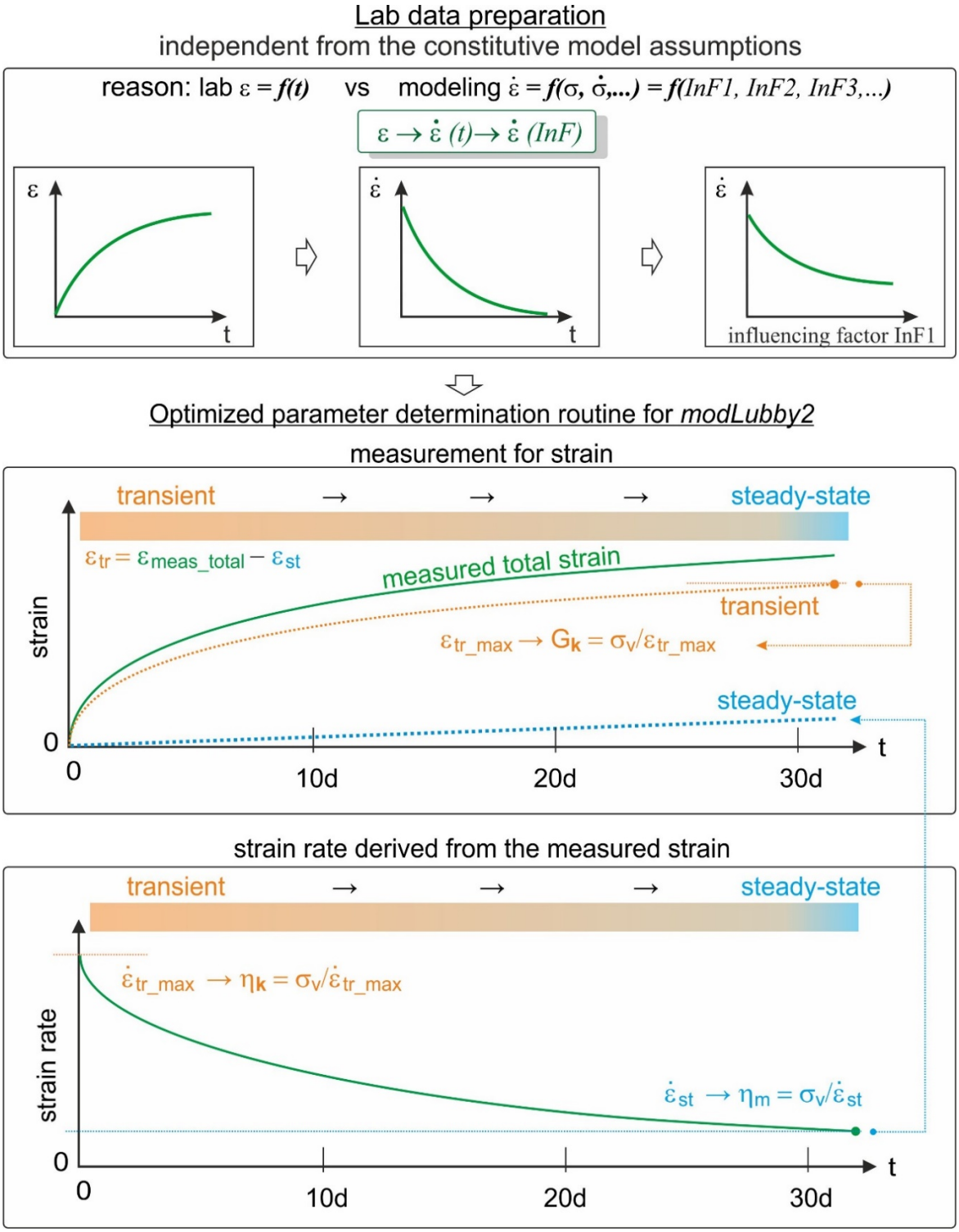

Fig. 4: Schematic visualization of the optimized procedure for the creep parameter determination for the model *modLubby2* as well as the general guidelines for the measurement preparation for the analysis independently from the chosen model (upper part).

By repeating the same process for a second or further load stages, the complete set of base parameters for *modLubby2* can be obtained, which characterizes the dependency of the creep behavior from deviatoric stress, temperature, and cumulated strains. The detailed description of the constitutive model *Lux/Wolters/Lerche* (*modLubby2*) is omitted and can be found e.g. in *AG Morsleben (2022) or Düsterloh et al. (2018)*.

Figure 5 shows exemplarily the final parameter determination diagrams for several long-term tests for the salt type z3LS.

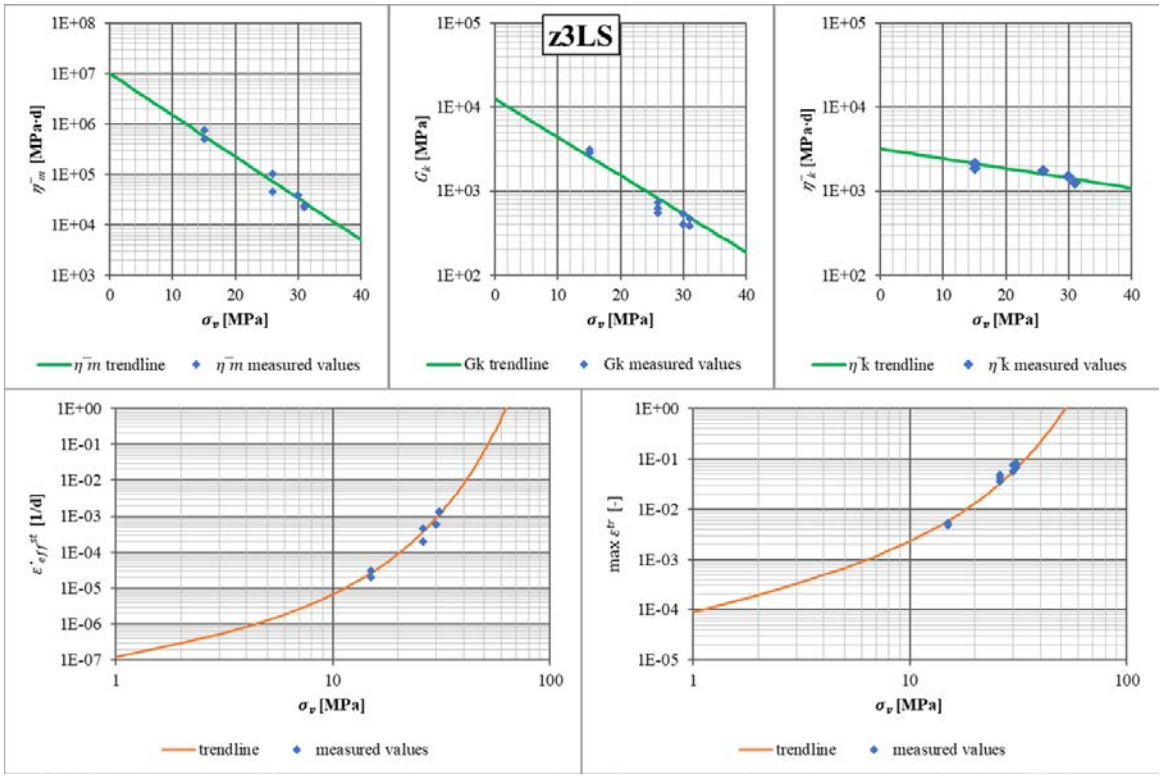

Fig. 5: Parameter determination diagrams for several long-term-tests for the salt type z3LS for the model *modLubby2*.

In the context of numerical simulations, it is necessary to demonstrate long-term secure containment of the radioactive waste in a repository for a period of up to 1 million years. Consequently, to ensure a sufficiently reliable prediction of the long-term behavior of underground systems in rock salt, it is particularly important to consider the effects of pressure solution creep at low deviatoric stresses. The scarcity of tests conducted at low deviatoric stresses leads to significant uncertainties, and thus the laboratory investigation for the creepability of rock salt at low deviatoric stresses has been the research focus in recent years, see e.g. *Hampel et al. (2022)*, *Bérest et al. (2022)*, *Spiers et al. (2021)* and *Spiers et al. (2022)*.

Within the framework of the project KRIECHTECH, TUC has developed and demonstrated a new experimental design to accurately capture the creep behavior under low deviatoric stresses in the TUC laboratory (*Düsterloh et al. (2024)*). However, the new experimental design was not included in the scope of the laboratory program for ERAM, and TUC intends to conduct a sensitivity analysis to address the above-mentioned uncertainties instead. Figure 6 illustrates variations in steady-state creep behavior for the example of salt type z3LS using *modLubby2, one-power-law* (*BGRa,* creep class four *CC4*) and *two-power-law* model, compared to the obtained measured data. This also underscores the capabilities of the *modLubby2* model, which allows for flexible variation of the dependency between creep-rate and deviatoric stress (→ due to the variation of the parameter a in the power-function-part of the model) in the area between *one-power-law* to *two-power-law* assumptions.

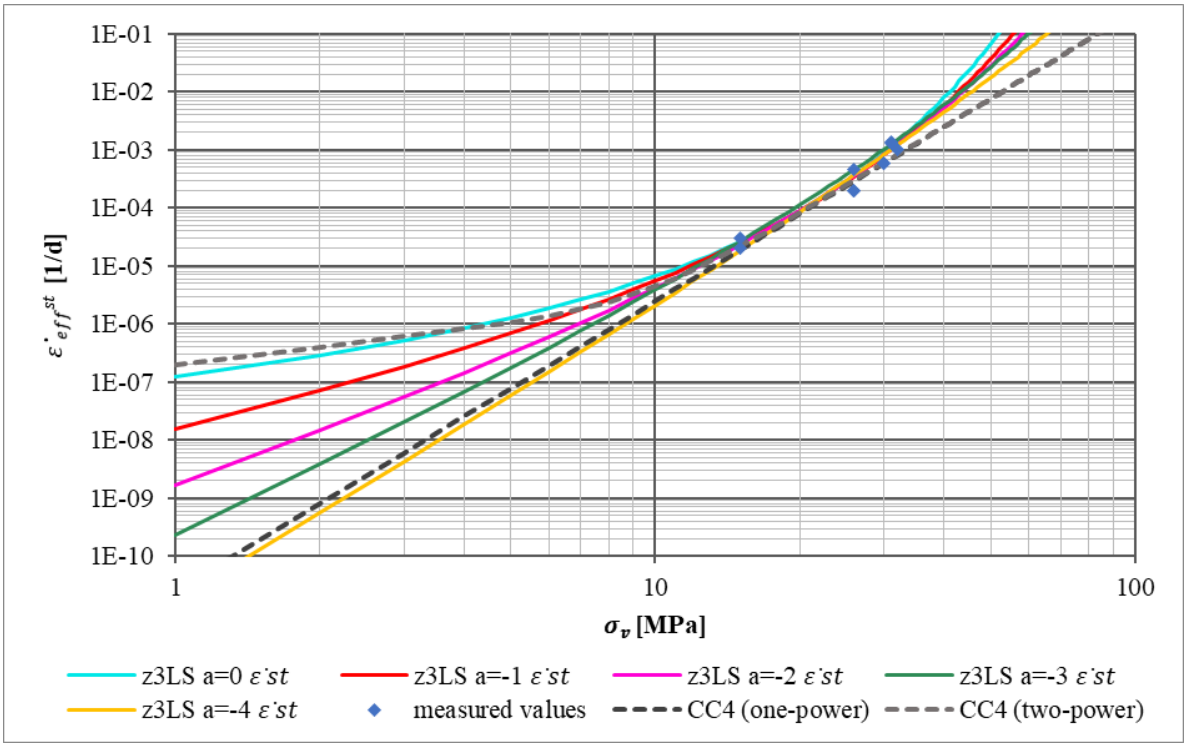

Fig. 6: Variation of the parameter a in *modLubby2* for the flexibility in the area of pressure solution creep (→ in situ relevant) while maintaining suitability in the area of dislocation creep (→ good agreement with lab measurements, z3LS) in comparison to the *one-power-law* and *two-power-law*

3.2 Short-term test to capture damage process

The parameter sets for failure, dilatancy, and residual strengths are determined as a function of confining stress as well as the damage parameter set for model *Lux/Wolters/Lerche* which can be derived from the short-term test series. With reference to *AG Morsleben (2024)*, a detailed description of the determination procedure for the strength and damage parameter sets is omitted here.

Figure 7 shows the results of the back-analysis of the short-term test series exemplarily for salt type z3LS. This last step does not serve to determine the parameters directly, but to subsequently demonstrate/check the suitability of the parameter sets determined in the previous steps. As shown in Figure 7, the results of the back-analysis for F1 tests demonstrate good agreement with the measurements. Furthermore, the derived parameter set confirms very well its transferability to F10 and F100 tests, as depicted in Figure 8.

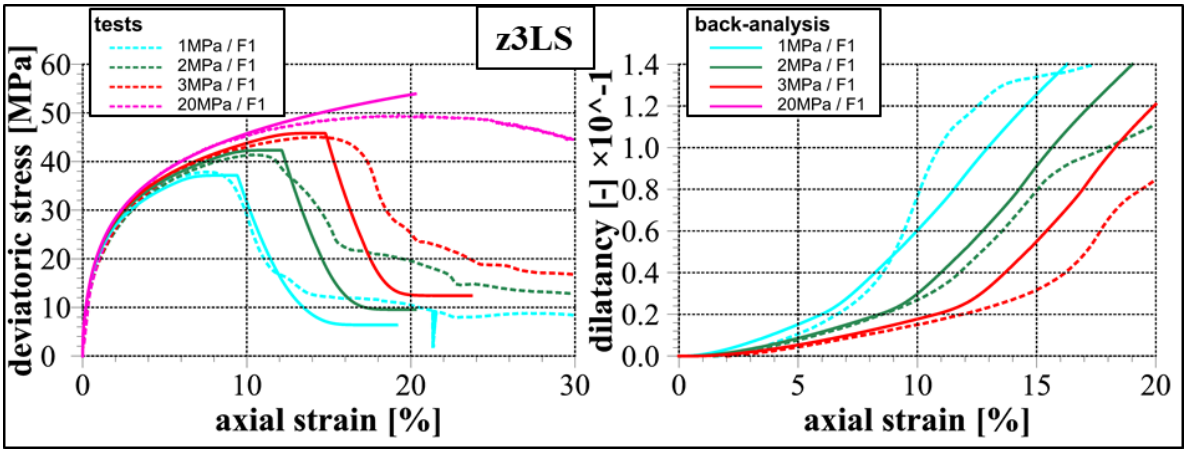

Fig. 7: Back-analysis of the short-term test series with the variation of the confining stress for salt type z3LS with the use of the derived strength and damage parameter sets.

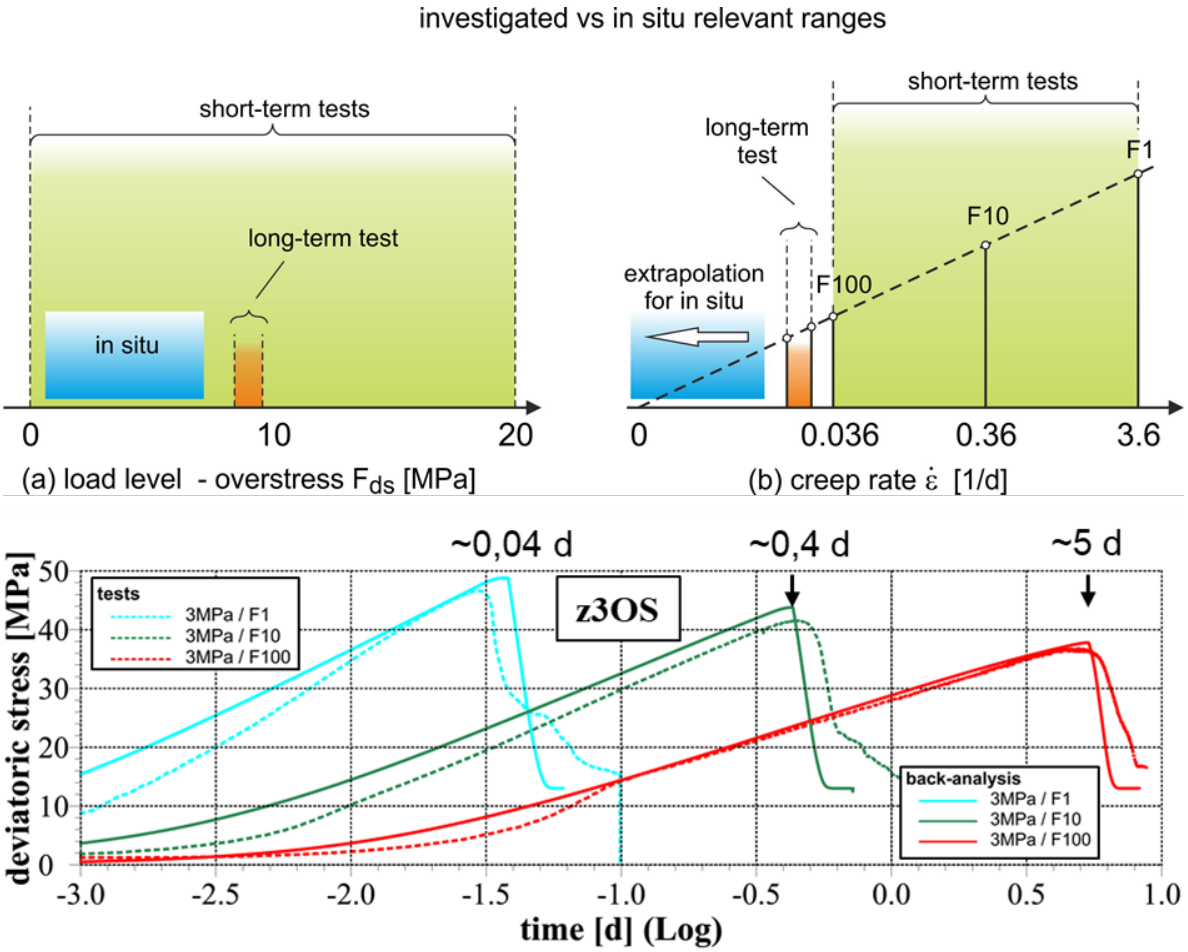

Fig.8: Back-analysis of the short-term test series with the variation of the strain-rate for salt type z3LS as well as the schematic visualization of the sufficient increase in the amount of information due to the involving of the short-term test series for different strain-rates and single long-term-tests.

The upper part of Figure 8 depicts in a schematic overview the ranges investigated in the laboratory program in comparison to the in situ relevant ranges of stress and strain-rate. The short-term test series with different strain-rates (F1, F10, F100) in combination with the individual long-term tests on the one hand enhances the confidence level in extrapolating the data (→ compared to the usual praxis of the use of only short-term tests with one defined strain-rate) and on the other hand save the realization time for the complete program (→ compared to the previous concept of TUC with the use of the long-term test series for the determination of the damage parameters).

3.3 Specific long-term creep test to capture creep and damage processes

The load configuration of the specific long-term tests presented in Figures 2 and 3 with one to two damage-free creep stages allows for the determination of the specimen-specific creep parameters set (section 3.1). Thus, the influence of natural variability in the material properties can be avoided while transitioning to the following damage phase. The damage parameters derived from a short-term test series (section 3.2) are then applied for the back-analysis of the damage-affected load stage to be assessed for their transferability to the long-term creep test.

Figure 9 presents a comparison of the measured axial strain, dilatancy and dilatancy rate with the calculated strain and damage behavior for the first 3 stages of a 5-stage long-term test 2C-D-2H using *Lux/Wolters/Lerche*. The dilatancy rates were derived from the smoothed curve of the measured data to reduce scatter and enhance interpretability. The accuracy of the back-analyses can be considered as satisfactory. Therefore, the damage parameters derived from the short-term tests and applied to the back-analysis of the long-term tests are validated and deemed suitable for representing long-term behavior.

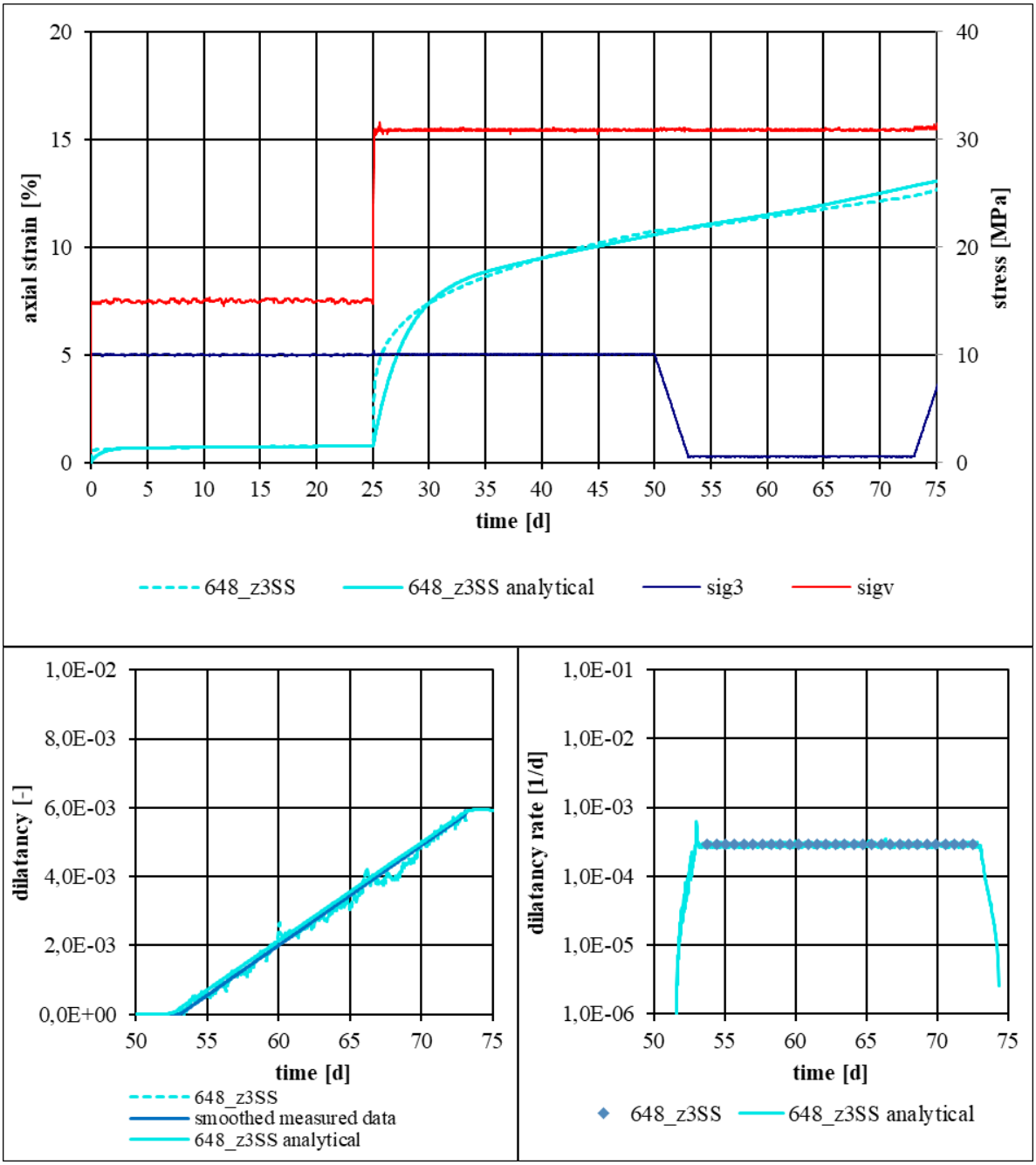

Fig. 9: Comparison of measured and calculated vertical strain and dilatancy development exemplarily for one long-term test on the salt type z3SS.

3.4 Specific long-term creep tests on carnallite to capture creep, damage and healing processes

Figure 10 and 11 show the measurement results and back analysis of two long-term tests on carnallite z2SF under the loading condition 2C-2D-2H.

The results of the back-analysis of test No.°677 (see Figure 10) show strong agreement with the measured data. This indicates that the phenomenological constitutive model *Lux/Wolters/Lerche* can be applied to represent the mechanical behavior of z2SF, despite carnallite indicating rather brittle damage behavior in contrast to rock salt with ductile behavior.

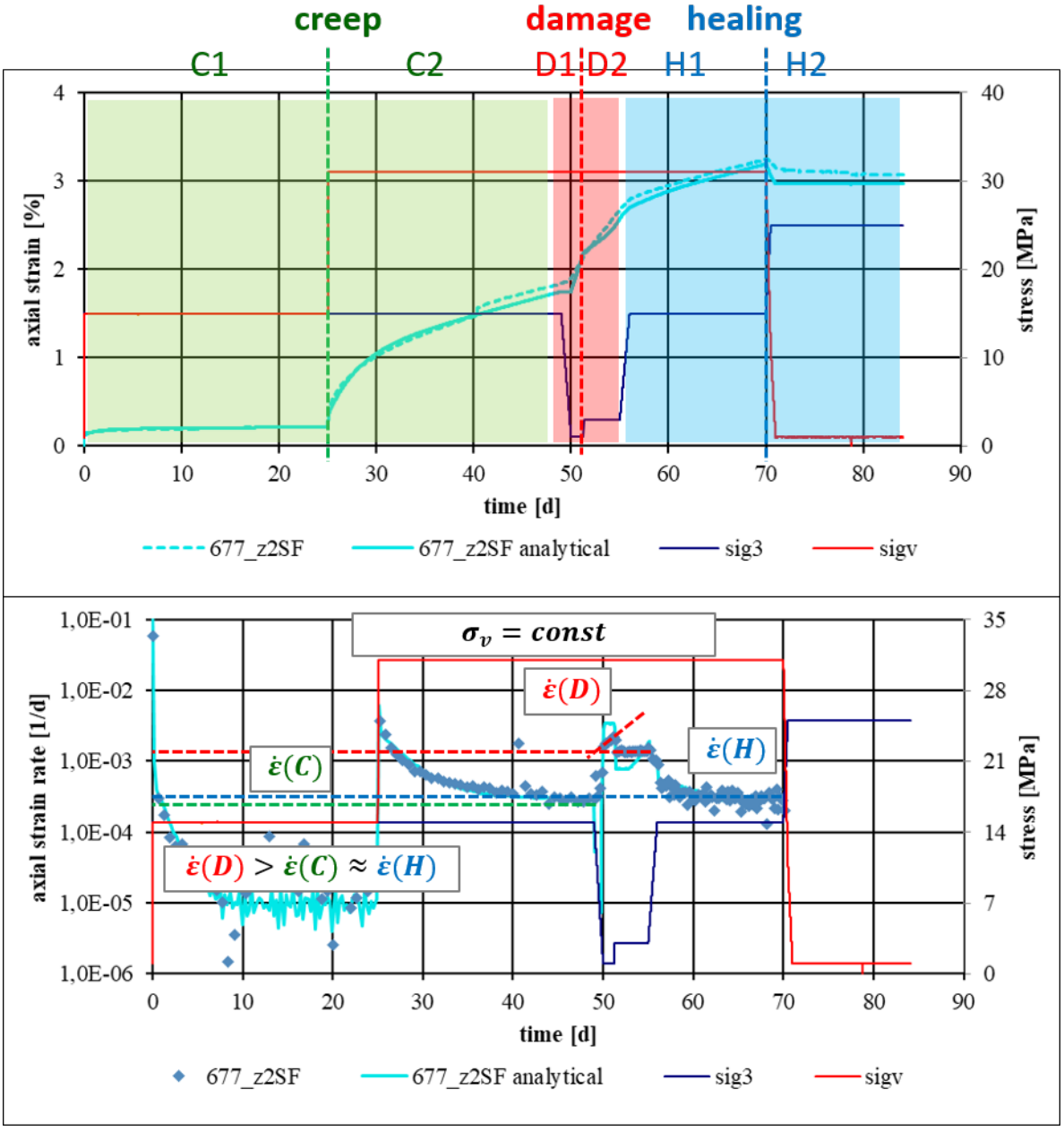

Fig. 10: Comparison of measured and calculated vertical strain development for test No.°677 on carnallite z2SF.

In the long-term tests on carnallite z2SF, due to its intensive damage development, the load was reduced during the damage phase (→ the confining stress was increased) while maintaining the deviatoric stress constant to prevent premature failure of the specimens (→ implementation of loading condition 2C-2D-2H). Due to the natural variability of the material, the specimen-specific strength boundary can vary from the average representative salt type-specific strength behavior, thus the damage development can deviate significantly from expected behavior, leading to a correction of the load that can be necessary during the test.

In both tests No.°677 and No.°620 on carnallite z2SF, the correction of load conditions during the damage phase allowed to save the samples from breaking. However, both samples cumulated intensive damage up to acceleration in the post-failure range. After transitioning to the healing phase, it was possible to observe the healing of a previously damaged specimen, for the first time in the frame of the long-term test, as shown in Figures 10 and 11. During the healing phase, a distinctly increased creepability of the intensely damaged specimen was observed compared to the undamaged state of the same specimen under the same deviatoric stress. This clear and unambiguous observation was made possible only under the following conditions:

- The experiment was conducted in the TUC configuration with the same deviatoric stress applied in all three phases: the creep phase C2, the damage phase D1 and D2, and the healing phase H1. Consequently, nearly steady-state creep behavior was expected during the damage and healing phases (no transient creep), making all deviations from the steady-state creep rate attributable to damage or healing and thus clearly quantifiable.
- The loading in the healing phase was deviatoric (in contrast to the previously common isotropic loading). Therefore, viscous creep strains could be observed during the healing phase.
- The induced damage in the specimen has reached up to the post-failure range (acceleration phase) in the damage phase. In previous tests of this kind on rock salts, the damage-induced strain was rather significantly less than the damage-free creep strain, so that during the subsequent healing phase, only the creepability of the undamaged specimen could be measured almost instantaneously. An increased creepability during the healing phase was not measurable in those cases.

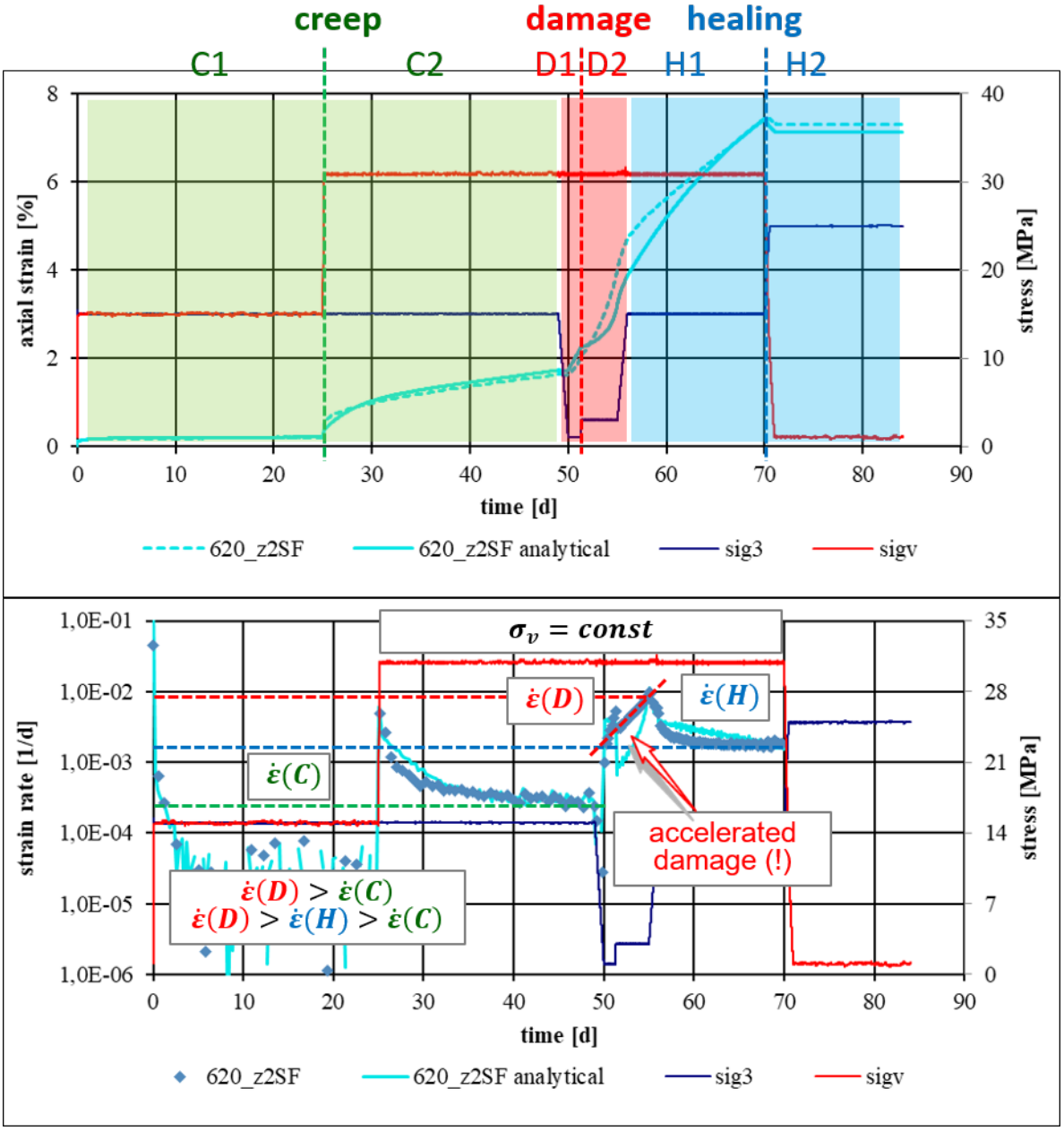

Fig. 11: Comparison of measured and calculated vertical strain development for test No.°620 on carnallite z2SF.

The influence of damage development on the viscous creep properties is described in *Lux/Wolters/Lerche* through a functional dependency, where the viscous creep behavior is defined based on the current state of damage or the current dilatancy. The significantly increased viscosity after reaching the residual strength was already accounted for in the constitutive model. This dependency has not yet been validated through systematic laboratory tests and was estimated phenomenologically. Thus, these new test results give the first confirmation of the assumptions made in the model approach. From the scientific point of view, these test results give the possibility to validate model assumptions for the advanced constitutive model, which considers creep, damage as well as healing processes.

4 Systematizing analysis of the test results for all salt types

Once the parameter sets for the complete constitutve model *Lux/Wolters/Lerche* (creep, strength, damage, healing) were determined for all individual salt types, as a final step a systematic comparative analysis and systematization of the determined parameters (as well as of the measurement results) for their optimized application in numerical simulations and long-term predictions. The aimed result was the identification and definition of classification for the creepability, the strength as well as the damage behavior.

The need for this comparative analysis and systematization arose from the complex geometric configuration of the geology and the underground cavities in ERAM and the search for possibilities to reduce the number of geological layers in the large-scale 3D-models for ERAM with highly realistic idealization of the cavities and geological information in regard to the foreseen numerical simulations. An insight into several large-scale 3D-models created by TUC is shown in Figure 12. Detailed information to the procedures for the idealization and discretization of complex large-scale 3D-models can be found in *Düsterloh et al. (2022)*.

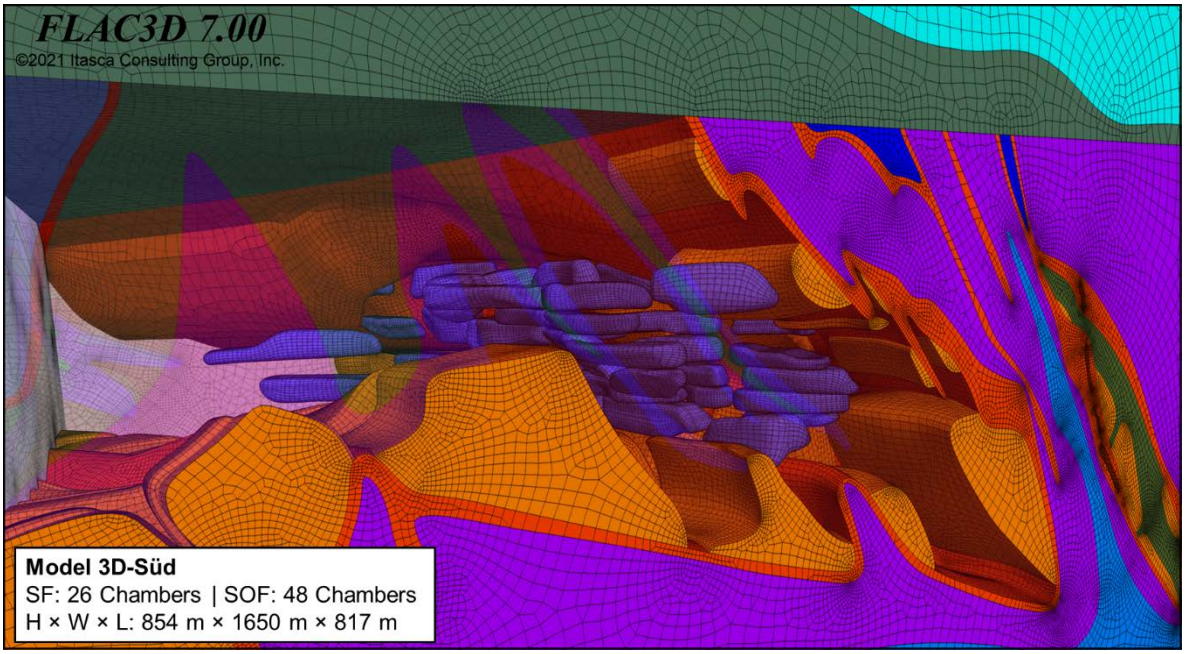

Fig. 12: Large-scale complex 3D-Model with highly realistic idealisation of the cavities (filigree structures) and geological informations (large-scale structures).

Figure 13 (top) depicts the functional dependency of the steady-state creep rate from deviatoric stress for the *modLubby2* approach for each investigated rock salt type, alongside the respective measured data.
Based on the comparative analysis, the eight specific homogenous areas were categorized into five creep groups as follows (Figure 13, bottom):

S-K: weakly creepable (→ z2HG, z3AM)
SM-K: weakly to moderately creepable (→ z2SF)
M-K: moderately creepable (→ z3LS, z3SS)
HM-K: moderately to highly creepable (→ z3OS, z4)
H-K: highly creepable (→ z2HS3)

The correlation between the parameter dataset of each creep group for *modLubby2* was described by the following equations:

$$Ref\ \bar{\eta}_m^{**}(CG_i) = \bar{\eta}_m^{**}(CG_1)/{F_1}^{i-1}$$
$$Ref\ m(CG_i) = m(CG_1) \cdot \left(F_2 - {F_3}^{i-1}\right)$$
$$Ref\ a(CG_i) = a(CG_1) \cdot {F_4}^{6-i}$$

with

$$F_1 = 1.8,\ F_2 = 2,\ F_3 = 0.85,\ F_4 = 1.03;$$

CG – creep group;
$\bar{\eta}_m^{**}$, m, a – parameter set for the steady-state creep in *modLubby2.*

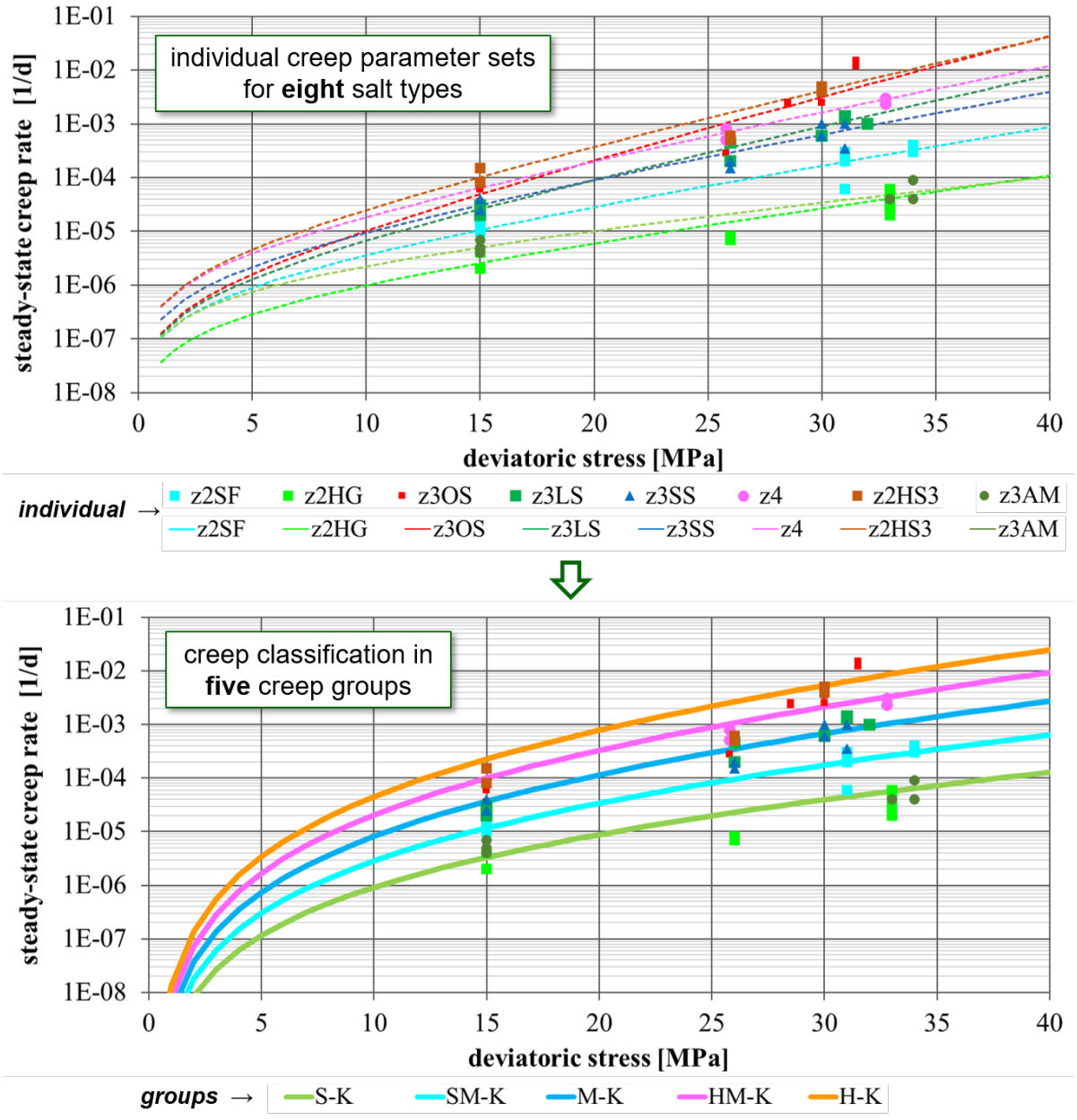

Fig. 13: Comparison of the steady-state creep behavior and measured data of individual salt types to identify salt facies with similar material behavior (top) and derived TUC creep groups, each with a reference creep characteristic.

The concept of classifying rock salts based on similar material behavior is not new in the field of salt mechanics. The classification of creep behavior of the rock salts introduced by BGR, has been well-established and practiced for many years. However, this classification only captures one deformation mechanism of rock salt – steady-state dislocation creep.

The special and expanding aspects of the classification developed and introduced by TUC compared to the BGR-classification are the extended scope of validity according to the models corresponding to the state of the art: (a) the classification for the creepability is prepared to be usable for more realistic model approaches taking into account dislocation creep as well as pressure solution creep; (b) the classification is prepared to be usable for more realistic model approaches taking into account creepability as well as strength and damage behavior, i.e. not only creep classes (steady-state as well as transient) but also strength classes and damage classes were defined.

The results of the classification in more detail can be found in *AG Morsleben (2024)*.

5 Summary and outlook

An extensive laboratory program was executed to investigate the mechanical behavior of different rock salt types z3LS, z3OS, z2HS3, z3AM, z3SS, z2HG, and z4, as well as carnallite z2SF from ERAM. The program encompassed 148 long-term and short-term tests, totaling over 2900 machine days. This resulted in the creation of an extensive systematic experimental database obtained through an optimized design of the laboratory program regarding the precision, reliability, robustness, and transferability of the determined material parameter datasets while minimizing the required realization time.

It was demonstrated that the implemented laboratory program, which combines short- and long-term tests with a wide variety of load conditions, effectively covers broad range of validity compared to in situ relevant conditions and delivers well representative material parameter datasets.

The specific long-term creep tests from TUC with the maintaining of the deviatoric load level constant during the transition from the damage-free creep stage to the damage-affected load stage as well as during the transition from the damage-affected load stage to the healing stage were successfully conducted for each salt type. Furthermore, the original design of this test type with three stages C-D-H was extended to different variations with one to two load stages for each process (creep, damage, healing), e.g. C-D-2H, 2C-D-2H, 2C-2D-2H. In the case of the investigated carnallite z2SF, it was possible to induce intensive damage up to acceleration in the post-failure range in the damage phase and subsequently capture the healing phase with an isolated measurement of increased creepability for the first time.

A classification regarding the material properties of individual salt types into creep groups (stationary and transient), strength groups and damage groups was introduced. Furthermore, correlations between these individual material groups were identified and ultimately leading to the definition of five material groups MG-1 to MG-5, which can (substantially) accurately represent the behavior of the eight investigated salt types. The derived material parameter datasets will be applied in the numerical simulations with the use of large-scale 3D-models in the frame of long-term safety assessment of the radioactive waste repository in Morsleben.

6 References

Günther et al. (2016): Verbundprojekt – Vergleich aktueller Stoffgesetze und Vorgehensweisen anhand von Modellberechnungen zum thermo-mechanischen Verhalten und zur Verheilung von Steinsalz, Teilvorhaben 2, IfG, Leipzig, 2016.

Lux, K.-H.; Düsterloh, U.; Lerche, S.; Dyogtyev, O. (2016): Energy Storage in Salt Cavities – some Aspects with Respect to Load-bearing Behavior as well as Documentation of Geotechnical Safety. 76. Jahrestagung der Deutschen Geophysikalischen Gesellschaft e.V., Münster, 2016.03.16, p. 3-24, 2016.

Düsterloh, U.; Lerche, S.; Dyogtyev, O.; Feierabend, J. (2018): Abschlussbericht – Langzeitsicheres Abdichtungselement aus Salzschnittblöcken – Bautechnische Realisierung Technikumsprüfstand mit Durchführung und Auswertung erster Versuche – BMWi-Forschungsvorhaben FKZ 02E 11425 76, Clausthal, 2018.

Lux, K.-H.; Lerche, S.; Dyogtyev, O. (2018a): Ein neuer Ansatz zu physikalischer Modellierung und numerischer Simulation intensiver Schädigungsprozesse im Salinargebirge mit exemplarischer Anwendung auf den Belastungsfall blow out einer Gasspeicherkaverne, Erdöl Erdgas Kohle, Heft 1-2, 2018.

Lux, K.-H.; Lerche, S.; Dyogtyev, O. (2018b): Intense damage processes in salt rocks – a new approach for laboratory investigations, physical modelling and numerical simulation. Saltmech IX, BGR Hannover, 2018.

Spiers, Ch. et al. (2021): Salt Mechanics Webinar, Part 1 – Creep at low deviatoric stresses, Universiteit Utrecht, hosted by Chris Spiers and Suzanne Hangx, 12.10.2021.

AG Morsleben (2022): Düsterloh, U.; Lerche, S. – Zwischenbericht zu AP1.2 – Dokumentation der verwendeten Gleichungen und Parameter für Homogenbereiche, Bestell-Nr. 0108/03-42-2740, Lehrstuhl für Geomechanik und multiphysikalische Systeme, TU Clausthal, Clausthal, 2022.

Bérest, P. et al. (2022): Creep tests on salt samples performed at very small stresses, SMRI Spring 2022 Technical Conference, Rapid City, USA, 4-5 May 2022.

Düsterloh, U.; Lerche, S.; Saruulbayar, N. (2022): Crushed salt compaction - a new approach for lab test analysis, physical modeling and numerical simulation. 10.1201/9781003295808-30. Saltmech X, Utrecht, 2022.

Hampel, A. et al. (2022): Verbundprojekt – Weiterentwicklung und Quantifizierung der gebirgsmechanischen Modellierung für HAW-Endlagerung im Steinsalz (WEIMOS) – Synthesebericht zum BMWi-geförderten Forschungsprojekt – FKZ 02E11446A bis 02E11446E, Zeitraum 01.04.2016-31.12.2022.

Spiers, Ch. et al. (2022): Salt Mechanics Webinar, Part 2 – Creep at low deviatoric stresses, Impact of low-stress creep laws in numerical modelling at the field scale, Universiteit Utrecht, hosted by Chris Spiers and Bart van Oosterhout, 08.02.2022.

AG Morsleben (2024): Düsterloh, U.; Lerche, S.; Saruulbayar, N. – Schlussbericht zu Prüfkomplex 6 – Schachtverschlusssystem der Schächte Bartensleben und Marie – Laborversuche zur Bestimmung der Schädigungs- und Verheilungsparameter für das Stoffmodell *Lux/Wolters/Lerche* an standortspezifischem Bohrkernmaterial, Lehrstuhl für Geomechanik und multiphysikalische Systeme, TU Clausthal, Clausthal, 2024.

Düsterloh et al. (2024): Düsterloh, U.; Lerche, S. – Entwicklung und Validation einer neuartigen Versuchstechnik für triaxiale Kriechversuche bei geringer deviatorischer Belastung. 4. Tage der Standortauswahl 18./19.04.2024 in Goslar, Clausthal-Zellerfeld, p. 36-37, 2024.

Experience with monitoring of unstable quarry slopes using continuous InSAR radar.

Erfahrungen beim Monitoring einer instabilen Tagebauböschung mittels kontinuierlichem InSAR Radar

Jindřich Šancer, Lubomír Chlebek, Tomáš Široký and Vlidimír Krenžel
VSB – Technical University of Ostrava, Faculty of Mining and Geology
17. listopadu 2172/15, 708 00 Ostrava – Poruba, Czech Republic

Abstract

In March 2022, a massive rockslide occurred on the final slope of a limestone quarry in the Czech Republic. In order to ensure the safety of the workers, to enable the continuation of mining in the quarry and to carry out remediation work on the final slope, it was necessary to design appropriate geotechnical monitoring. This monitoring must meet relatively high demands for accuracy, speed of measurement and evaluation, must operate in a continuous and on-line mode and monitor the entire relatively large area of the damaged slope. For this reason, it was decided to purchase a modern monitoring system - a geo-radar with interferometric technology (InSAR), namely the IDS GeoRadar Hydra X, equipped with the Guardian evaluation software. The article below summarizes the practical experience gained from more than one year of monitoring the damaged final slope of the quarry with this technology.

Zusammenfassung

Im März 2022 fand ein großer Felssturz an einer finalen Böschung eines Kalksteintagebaus in der Tschechischen Republik statt. Um die Arbeitssicherheit und den Fortgang der bergmännischen Arbeiten zu gewährleisten sowie die Beräumungs- und Sicherungsarbeiten an der Felsböschung auszuführen, war es notwendig ein geeignetes geotechnisches Monitoring zu planen. Dieses Monitoring muss relativ hohe Anforderungen an Genauigkeit sowie Schnelligkeit der Messungen und Auswertungen erfüllen. Es muss kontinuierlich und im online Modus arbeiten und das gesamte, relativ große Areal der geschädigten Böschung erfassen. Aus diesen Gründen wurde sich für ein modernes Monitoringsystem entschieden – ein Georadar mit Interferometrik (InSAR), namentlich IDS GeoRadar Hydra X, ausgerüstet mit Guardian Auswertesoftware. Der Artikel beschreibt praktische Erfahrungen aus dem mehr als 1-jährigen Monitoring der geschädigten Böschung mit dieser Technologie.

1 Introduction

Open pit mining and quarrying of minerals is a risky activity in which a danger situation can occur that can endanger the health of workers and mining technology. One of the most serious and common risks in surface mining is associated with the instability of slopes and rock faces. In March 2022, the final slope of a limestone quarry in the Czech Republic experienced instability (the owners of this quarry do not wish to publish the specific location or detailed information about this quarry). This was a massive movement of the entire final slope which directly threatened the health of the quarry's employees and operations.

It was a relatively fast and massive rock slide. Only about 10 days elapsed between the first signs of the landslide (tension cracks in the crown of the slope) and the massive landslide that occurred on 12 March 2022. In the most advanced phase of the landslide, almost the entire final slope with a maximum height of approx. 155 m and a length of approx. 850 m was displaced by approx. 7 m in the vertical direction within one day.

In the main body of rockslide, the the main scarp of the rockslide was visible, on which the shear surface (surface of rupture) could be traced. At that time, the drop of the terrain in the detachment area was in the order of units of metres. The surface of rupture in the detachment area was flat, smooth, falling steeply into the body of the rockslide, probably taking advantage of the natural predisposition - the geological rock interface. In this part of the rockslide we can assume a planar shear surface. In the accumulation zone it was possible to observe the toe of the rockslide, which was manifested by the 'uplift' of the original quarry floor in front of the base of the original final wall, which could indicate the unbearing bedrock of the final wall of the quarry and the rotational shape of the shear surface in this part of the rockslide. Based on this orientation survey, the slope deformation could be evaluated as the result of a rotational-planar rock slide. Due to the demonstrable movement of the rocks along the shear surface, as evidenced by both subsequent in situ visual inspections and surface measuring by mine gauger, it was possible to classify the slide as an active slide, threatening the safe operation of the quarry, particularly in the immediate vicinity of the unstable quarry closing wall.

In order to deal with this emergency and preserve the possibility of at least limited mining on this site, it was necessary to first mark out a danger area beyond which any movement of persons was prohibited and to ensure slope monitoring that would be able to react in time to the accelerating movement of the slope and to warn employees in time of the approaching danger of a slope slide. In the first stage of the monitoring, after inspecting the slope deformation, it was decided to continuously monitor the slope during the mining period from a safe distance by an instructed patrol and to monitor the surface movements of the slope by means of an unmanned aerial vehicle (drone) using the photogrammetry method. With this monitoring it was possible to monitor slope movements quite reliably with an accuracy of a few centimetres, which was sufficient in the developed phase of the landslide. The imaging was carried out according to the climatic conditions at approximately 14-day intervals.

Due to the need to ensure safe and regular operation of the quarry, it was decided to provide continuous monitoring of the unstable wall, working in on-line mode with access to the control room and authorized persons. Currently, there are a number of geotechnical monitoring options for unstable slopes [1], however, few of them allow to continuously monitor such a large area with sufficiently high accuracy and under all light and climatic conditions. A method using interferometric radar (InSAR) technology was chosen as the most appropriate method for such monitoring. The system allows virtually continuous monitoring of an unstable wall with a resolution of motion in the tens to units of millimetres (depending on the location and distance of the radar and weather conditions).

Monitoring of surface movements of the slope by an unmanned aerial vehicle (drone) using photogrammetry with a monthly frequency was retained as an additional monitoring method. In addition, 2 inclinometric boreholes were constructed on the current quarry floor to monitor the possible extension of the landslide during the possible deepening of the quarry in the safe zone.

2 Geotechnical monitoring of the final slope of quarry

As mentioned above, there are currently 3 main methods used for geotechnical monitoring of unstable quarry stopes. These are the monitoring of the surface movements of the slope by means of an unmanned system (drone) by photogrammetry, inclinometric measurements in boreholes carried out at an interval of 3 times a year and continuous scanning by interferometric radar (InSAR). It is the last method of monitoring that is considered the main method, therefore it will be given the most attention in this article.

2.1 Monitoring by an unmanned aerial vehicle (drone) using photogrammetry

For at least an indicative verification of the extent of the rockslide and the rate of movement in the developed phase of the landslide of the closing slope, a monitoring method of photogrammetric targeting using a drone from DJI company, supplemented by a special camera, was proposed. Using this monitoring, it was possible to monitor the slope movements quite reliably with an accuracy of units of cm, which was sufficient in the developed phase of the landslide. The measuring was carried out according to the climatic conditions at approximately 14-day intervals. And in the most developed phase of the landslide, vertical movements were recorded in units of m per 14 days. Gradually, the rate of wall movement slowed down to tens to units of cm (see Table 1). At present, the measured movements are irregular (after intense rains, etc.) in the order of max. units of cm. In this method it is advisable to have clearly defined points in the monitored slope to which the direction and magnitude of movement is defined. Originally, the slope contained monitoring points - monitoring and targeting of the wall was carried out by this method even before the rockslide occurred, with a frequency at least of once a year. However, during the landslide and in the post-landslide period, some points were lost or destroyed by the landslide. Another problem and increasing error is caused by the growing vegetation on some benches and the accumulation of fallen rock blocks.

Tab. 3: Measured data (stabilized points) by drone using photogrammetry.

	21.12.2021	17.03.2022	20.04.2022	27.04.2022	11.05.2022	27.05.2022	03.06.2022	08.06.2022	total landslide [m]
C0	351,39	343,8	342,5	341,8	341,6	340,1	339,1	337,86	**13,53**
C1	364,95	356,1	354,6	353,9					
C2	377,58	368,0	366,5	365,7					
C3	390,62	381,0	379,6	378,7					
C4	405,39	395,0	394,3	393,4	392,9	391,5	389,7	388,36	**17,03**
B1	364,60	357,2	355,6	354,6	354,2	352,5	352,2	350,01	**14,59**
B2	377,31	369,5	367,9	366,8					
B3	390,43	382,6	381,1						
B4	405,47	397,7	396,1	395,0					

By periodically scanning the entire unstable damaged rock wall and comparing the images, or cross sections created from these images, it is possible to determine the direction and magnitude of the wall movement. An example of such a comparison is shown in Figure 1. Only a section of the lower part of the wall is shown for illustrative purposes. The figure shows how the direction of movement changes (see red arrows). While in the higher parts of the slope the motion is translational - approximately parallel to the slope gradient, in the lower parts near the base of the slope the motion is almost horizontal, indicating rotational movement in this part of the slope.

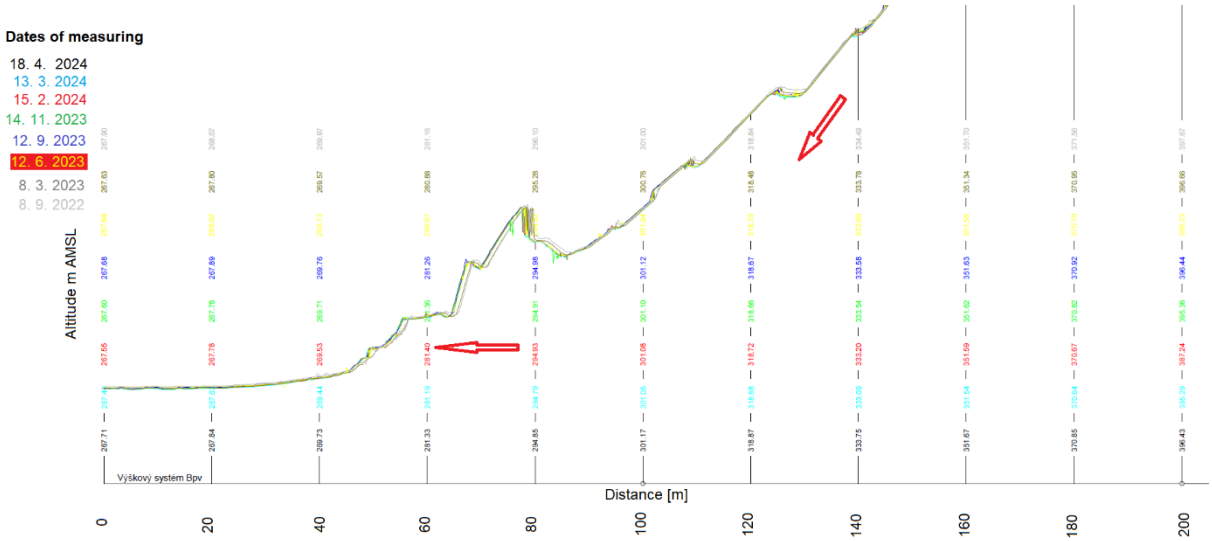

Fig. 22: Crosscut created from measured data by drone using photogrammetry.

2.2 Monitoring of inclinometric boreholes

As part of the regular measurements, two inclinometer boreholes with a depth of about 30 m were built in the foreground of the damaged rock slope and are regularly measured. Their aim is to check whether a shear surface is not forming in the foreground of the slope, which could indicate a future extension of the rockslide. To date, however, the measurements have not shown any movement.

2.3 Monitoring of final slope by Georaradar with InSAR technology

Due to the need to ensure safe and regular operation of the quarry, it was necessary to ensure continuous monitoring that would alert the dispatcher to any movements of the damaged slope so that he could recall in time the workers working near the slope or on its rehabilitation. Another condition was that the monitoring should be able to work in all normal weather conditions that may occur in the area (rain, snow, fog, darkness, frost, etc.).
The most suitable method for this purpose was chosen to be the Interferometric Synthetic Aperture Radar, a measurement method specially developed for this purpose. There are several companies on the market offering these radars. For the monitoring in the described quarry, a radar from IDS GeoRadar, type Hydra-X, was selected.

2.3.1 IDS GeoRadar Hydra-X

HYDRA-X is a high-resolution, high-accuracy, rapid deployment radar monitoring system designed to improve safety in surface mines, coal mines, tailings ponds and industrial mineral processing operations.

HYDRA-X provides spatial resolution twice as fine as any other slope tracking radar on the market. By closely monitoring the etages above working faces or hazardous features in quarries, HYDRA-X can measure sub-scale instability. With a maximum scanning range of 800 meters, risk areas can be safely monitored even with the slightest rock movement [2].

HYDRA-X features on-site processing and alarm, an HD optical camera with visual imagery linked to radar data and refreshed scans every 30 seconds. Information is always available for quick response even in the event of sudden acceleration and people are immediately alerted in the field [2].

The radar is equipped with additional Guardian software. Guardian provides an easy-to-use and powerful tool for visualizing and interpreting radar data and performing trend analysis of ground movement displacements. Alarms can be completely customized and set based on specific speed thresholds, alerts activated via pop-ups, email, text messages and audio-visual siren.

2.3.2 Installation, setup and monitoring with IDS GeoRadar Hydra-X

For the measurement and monitoring itself, it is very important to select a suitable place for the installation of the measuring apparatus and to choose the appropriate sensing settings so that the subsequent monitoring and interpretation of the data is as little burdened as possible by measurement error and incorrect setting of the apparatus.

When selecting a suitable location for the GPR, it is necessary to take into account a direct and unobstructed view of the entire monitored area. A suitable distance from the slope to be monitored is also important. As the distance increases, the resolution of the radar decreases (the radar divides the scanned area into a predetermined number of pixels), and as the distance increases, the area of the monitored slope per pixel increases.

It is also important that the radar is positioned and fixed in a fixed location, protected against excessive wind and possible vibrations (e.g. from blasting, dumper transport, etc.) that could lead to unwanted movement of the radar. Furthermore, the radar should not impede the development of the quarry and block the balance of the reserves. For this reason, the radar was placed in the crown of the opposite slope. The radar was fixed to a floor consisting of concrete panels. A wooden shed protects the radar from the weather. The photograph of the radar located at the addressed site is shown in figure 2. On the left you can see a detail of the radar, on the right the location of the radar in a wooden hut on the opposite slope.

Fig. 23: Position of IDS Georadar HYDRA – X on Quarry.

After creating and calibrating the 3D digital terrain model, the area to be monitored is set and the scanning frequency of this area is determined. In the case of monitoring a damaged slope in the location, the settings were made so that practically the entire final slope of the quarry was scanned. Scanning this entire area takes about 150 seconds. After this time, the radar returns to its initial position and starts a new scan. It is therefore possible to state that the monitoring takes place continuously and every approx. 3 minutes it is possible to make a comparison with the previous image. All scanned images are automatically saved on the HDD in the control PC and can be further processed by Guardian software.

The processing takes place in a special sw called Guardian. This sw enables a full range of scanned image display and evaluation. It is possible to separately evaluate the average speed, or deformation of an arbitrarily selected surface or specific point. An example of the division of the monitored area into several areas can be seen in Figure 3. The software can monitor the development of deformations in the selected time interval, set limits and different alarm levels, etc. One of the important functions is the possibility of sending SMS messages or emails to specified contacts if the set limits are exceeded. When the values that have been set as critical are exceeded, it is possible to activate the siren, which alerts all quarry employees to this crisis situation.

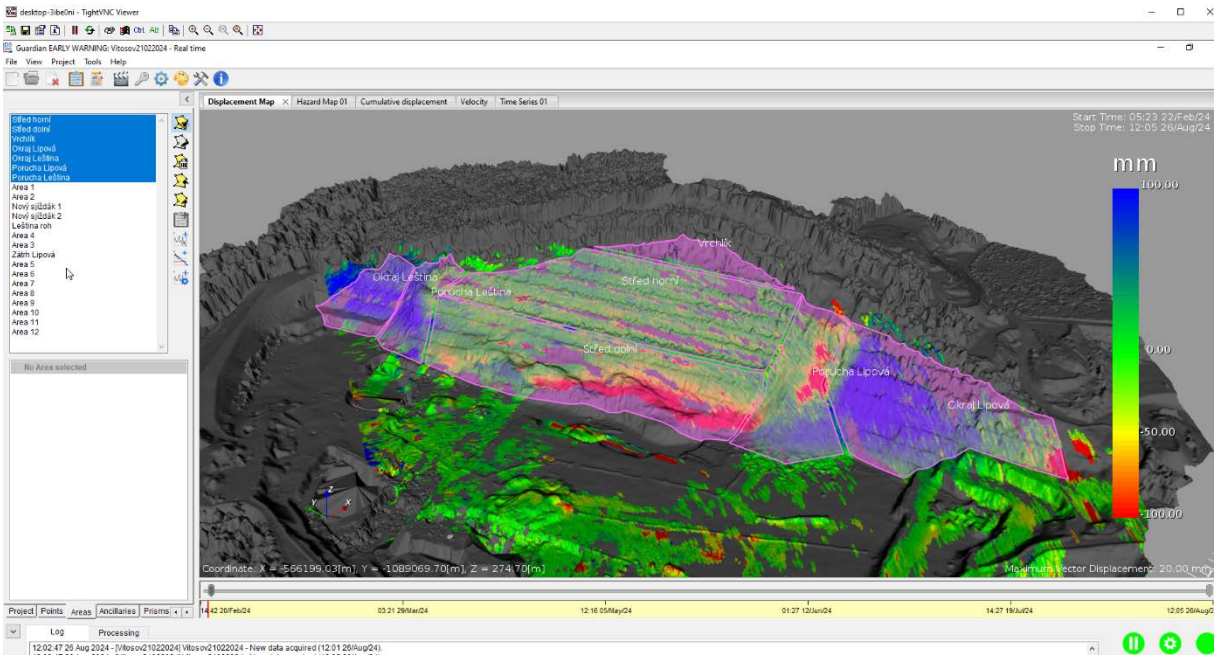

Fig. 24: Division of the monitored area into several areas.

The following early warning system was set up at the addressed location:
The final slope was divided into six logical units - monitored areas (sum of measured points). For all monitored areas, 4 marginal safety limits of slope movement were set, defining 5 operating conditions in the quarry from the point of view of work safety. When these limits are exceeded, safety procedures are activated leading to informing the responsible persons, ascertaining the safety situation and ensuring the maximum safety of people and equipment in the quarry.

Stage 1. Normal condition

State definition: wall without movement, or very small movements at the level of measurement sensitivity, negligible movement or movement of encroaching vegetation

Stage 2. Condition requiring attention (2.5 mm/h)

Status definition: motion detected, or movement speed exceeding normal status limit
Designated persons: geotechnician and radar technical supervisor
Action: designated persons will check the measured data, consult their findings and start more frequent monitoring of the trend development. In case of mitigation of danger, it goes to state 1. In case of increasing danger, they inform the racing quarry, without waiting for point 3.

Stage 3. Vigilance (5 mm/h)

Status definition: motion detected, or movement speed exceeding normal status limit
Designated persons: geotechnician, technical supervision of the radar, quarry operation manager and production manager
Action: designated persons will check the measured data, consult their findings and start more frequent monitoring of the trend development. If the danger is reduced, it goes to state 2. In the case of an increasing danger, they proceed to point 4 without waiting.

Stage 4. Threat (10 mm/h)
Status definition: the value of the movement limit has been exceeded, or movement speed exceeding the wakefulness interval
Designated persons: geotechnician, radar technical supervisor, quarry operations manager, production manager and executive/CEO
Action: convened a meeting of all persons (can be online), evaluate the trend of the measured values, evaluate and monitor the trend of the inverse value of the speed of movement (estimate when the slope could theoretically collapse) and choose the next procedure according to the results (e.g. constant supervision during work, limited access to the quarry, etc.)

Stage 5. Danger (25 mm/h)
Status definition: alarm value exceeded
Designated persons: geotechnician, radar technical supervisor, quarry operations manager, production manager, executive/CEO and shift technicians
Action: closure of traffic, ban on entry to the threatened area, convening of an expert group to decide on the next course of action.

2.3.3 Evaluation and interpretation of data

In the first stage of monitoring, an approx. ½ year test operation of monitoring the damaged wall with the IDS GeoRadar Hydra X system leased by the manufacturer was started at the addressed location. It was a demonstration (demo) version of the radar, which is mainly used for promotional and verification purposes. Based on the positive experience with this radar and the analysis of the measured data, the above-mentioned early warning system was designed and a completely new radar was purchased at the beginning of 2024. This new radar has been monitoring the damaged wall continuously since February 2024. An image showing the total movement of the damaged slope in about 7 months is shown in figure 4.

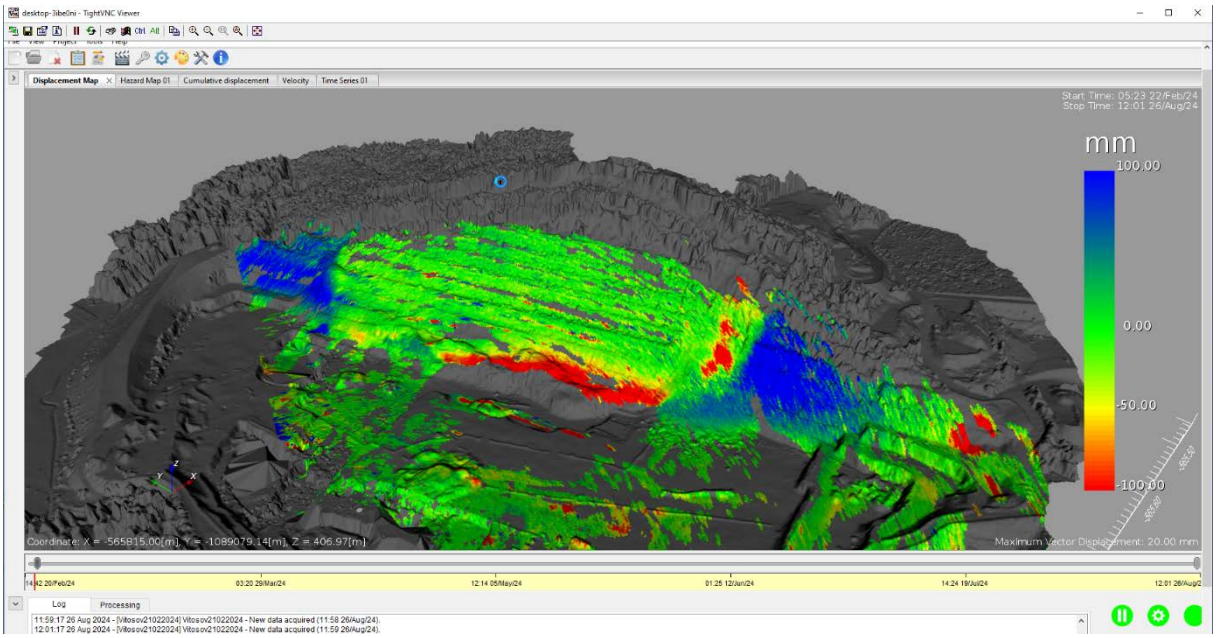

Fig. 25: Total movement of the monitored damaged slope.

It is clear from the figure 4 that during the monitored period there were movements of the order of cm in the damaged wall. It is necessary to realize that the radar measures the horizontal change in distance, i.e. whether the wall is "approaching" the radar or, on the contrary, "moving away" from the radar. Approaching in is represented by a negative sign (minus) in red, on the contrary "moving away" is represented in blue (positive values). The green area represents areas with no apparent motion.

The apparently illogical measured movement can be explained by rotational-planar sliding, which was confirmed by photogrammetric measurement with the help of a drone, see Fig. 1. The heel of the slope is pushed out almost horizontally and is therefore reliably captured by the radar and shown in red. On the contrary, the higher parts of the wall slide planarly along the shear surface, which is almost parallel to the rock wall, therefore horizontal movement is not evaluated by the radar, which is why these parts are shown in green. The blue-colored edges of the quarry correspond to geological faults in the quarry, and the "opposite" movement of rocks in these parts is probably due to the fact that the central part of the quarry moves quicker and moves along the geological faults at the edge of quarry, where the faulted rocks are consolidated by pressure and as would "push" into the wall.

The red area in the right corner of the local overburden landslide, which the radar detected in time, approximately two days in advance, when the 2nd and then the 3rd stage of the waring system (see above) were reported.

A sample of one of the outputs from SW Guardian is shown in Figure 5. This figure shows the time evolution of the deformation in the individual evaluated surfaces. It is necessary to know that these are average values from evaluated surfaces therefore absolute values, cannot be directly compared (due to difference between surfaces). However, the influence of the rotation-planar landslide can be clearly seen when the higher and marginal parts of the wall seem to be moving away, while the landslide front (red curve) is approaching.

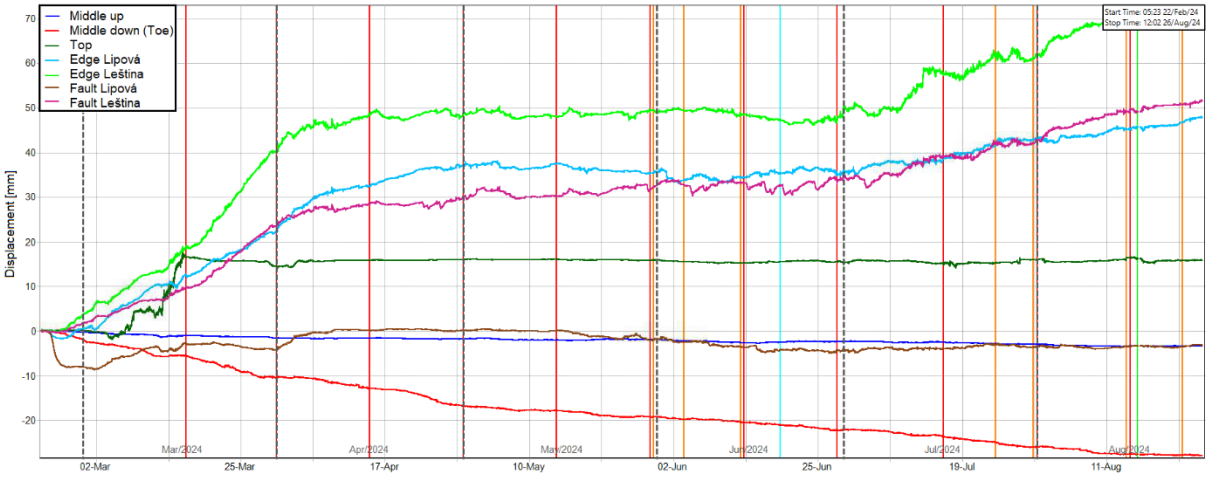

Fig. 26: Time evolution of the deformation in the individual evaluated surfaces of monitored slope.

3 Conclusion

The aim of the article was to inform readers about the first experiences with interferometric georadar for monitoring the unstable rock slope of a quarry in the Czech Republic. It is clear from experience that this is a very suitable method, the main advantage of which is the possibility of continuous scanning of the entire monitored area and online display of measured data in a 3D terrain model. Thanks to the continuous measurement and online connection, the early warning system for workers can also be used with advantage.

However, similar to other methods of monitoring unstable slopes, it is necessary to have some experience with monitoring and rock mechanics when evaluating and interpreting the measured data. For a better interpretation of the measured data, it is advisable to supplement the monitoring with other independent methods of monitoring the movement of unstable slopes, which will allow a better understanding of the mechanism of movement and the interpretation of potentially illogical data. In the case of the addressed locality, it involved regular geodetic surveying of stabilized points, monitoring by the method of photogrammetric surveying using a drone and inclinometric measurement in boreholes.

An automatic meteorological station and measurements of hydrogeological boreholes are also used at the given location, which indicate that the speed of movement of the rock walls with a certain delay of about 7-10 days affecting excessive precipitation and changes in the groundwater level.

4 References

[1] Masood, Maneeb, Raju Gunda, Verma Tarun: Slope Monitoring and Failure Prediction Techniques in Mines: A Review, Journal of Mines, Metals and Fuels, 70(8) : 171-181; 2022. DOI: 10.18311/jmmf/2022/29942

[2] IDS HYDRA-X Brochure available at https://idsgeoradar.com/products/interferometric-radar/hydra-x

Temperature-dependent behavior of ice-filled rock joints – Laboratory study of strength and deformation of ice-filled rock joints

Temperaturabhängiges Verhalten eisgefüllter Klüfte – Versuchsreihe zu Festigkeits- und Verformungsverhalten eisgefüllter Klüfte

Friederike Tiedtke, Max Friedel, Heinz Konietzky
Geotechnical Institut, TU Bergakademie Freiberg
Gustav-Zeuner-Str. 1, 09599 Freiberg, Germany

Abstract

Rising ground temperatures in cold and alpine permafrost regions trigger increased rock slope movements and instabilities. Failure inducing mechanisms are often rooted in joints and fractures. In this study, the investigated temperature-dependent mechanical behavior of ice-filled rock joints is documented. Constant strain-rate tests are performed to determine the shear strength of ice-filled joints under temperatures ranging from -10°C up to -1°C. A decrease of shear strength with increasing temperature is observed. The failure mechanism changes from “brittle” for cold temperatures to ductile for temperatures close to the melting point. Constant stress tests are conducted to evaluate the time-dependent creep behavior. The formation of (micro-)cracks has a strong influence on the creep rates. The damaged-controlled creep rates superimpose the temperature dependency of creep for pure (and unfractured) ice.

Zusammenfassung

Die stetige Erwärmung des Untergrunds in kaltem und alpinen Permafrostregionen führt vermehrt zu Instabilitäten von Felshängen. Um diese Versagensprozesse, die oft in Kluftbewegungen begründet sind, besser zu verstehen, wurden zwei Versuchsreihen zum temperaturabhängigen Verhalten eisgefüllter Klüfte durchgeführt. Die erste Versuchsreihe untersucht die Kluftscherfestigkeit bei Temperaturen zwischen -10°C und -1°C. Die Laborergebnisse zeigen eine Abnahme der Scherfestigkeit mit steigenden Temperaturen. Die Versagensart wechselt von „spröde“ bei kalten Temperaturen zu „duktil“ bei Temperaturen nahe dem Schmelzpunkt. Kriechversuche sind durchgeführt worden, um die zeitabhängige Verformung der Klüfte zu untersuchen. Erkennbar ist der starke Einfluss der (Mikro-)Rissbildung im Eis auf die Kriechraten. Die Schädigungen führen auch bei kalten Temperaturen zu hohen Kriechraten. Die schadensbedingte Erhöhung der Kriechraten überlagert die Temperaturabhängigkeit der Kriechrate von reinem Eis.

1 Introduction

1.1 Motivation

In the last decades, climate change in terms of generally increasing temperature is also observed in cold and alpine regions. A steady rise of air temperature has occurred since the 1990s (e.g. (PERMOS, 2022)). As a result, the annual ground temperatures increase as well (Fig. 1). A rise of ground temperatures is critical for cold permafrost regions, since the change of temperature is accompanied with alterations of mechanical ground properties and behavior.

As monitoring in alpine regions shows, the risk of landslides and other mass movements is highly increased under melting permafrost conditions (e.g. (PERMOS, 2022), (Mamot et al., 2018)). Beside the dangerous destabilization of mountain slopes, maintenance of infrastructure and buildings in cold and alpine regions is another important aspect that is influenced by rock-ice interaction. Mechanisms causing damage and critical movement are often based on failure processes along rock joints/fractures. To better understand the temperature-dependent behavior of ice-filled rock joints, laboratory tests are conducted to evaluate the alterations of shear strength as well as joint creep for temperatures between -10°C and -1°C.

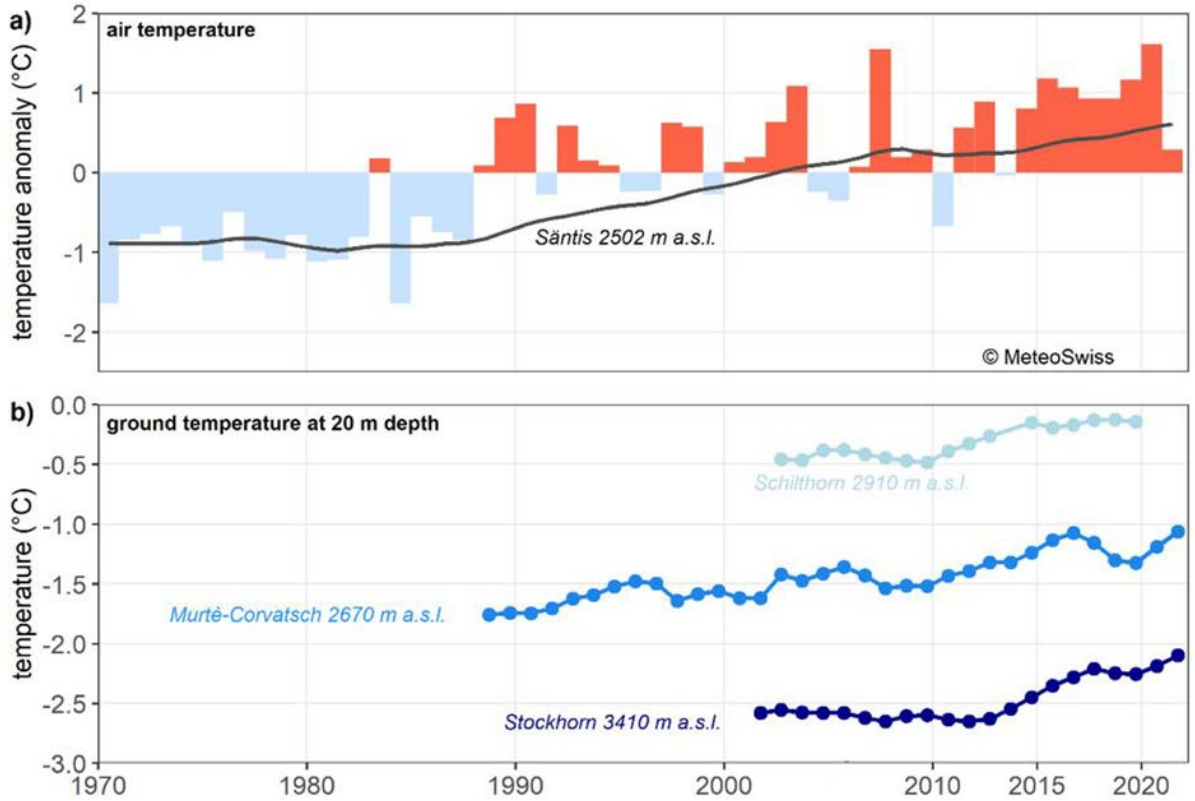

Fig. 1: Changes of air and ground temperature over time. Monitored in the Swiss Alps. Modified from PERMOS (2022).

1.2 Scope of Laboratory Experiments

Two laboratory studies were performed to characterize the mechanical behavior of ice-filled rock joints. The first study focuses on joint shear strength and the analysis of the temperature-dependent transition from brittle to ductile failure mechanism. The second study concentrates on joint deformation under constant load evaluating temperature-dependent creep behavior.

1.3 State-of-the-Art Review

Ice as a solid material is characterized by its internal (poly-)crystalline structure, that can cause large creep deformations. Lattice imperfections occurring in the crystalline structure control ice viscosity, plasticity and strength (e.g. (Gold, 1970). The steady-state creep rate of ice can be fitted to Glen's Law of creep ((Glen,1955), (Homer and Glen 1978), (Weertman,1983)):

$$\dot{\varepsilon} = B * \sigma^n \, exp\left(\frac{-Q}{k\,T}\right) \qquad \text{Eq. (1)}$$

B… (temperature-dependent) constant
Q… 134 kJ/mol (for T > -10°C)
n… 2…4
k… 1.380649e-23 J/K (= Boltzmann-Constant)

The steady-state strain-rate of ice is temperature-dependent, as Eq. (1) shows. The strain-rate increases with increasing temperatures. Weertman (1983) reports a strain-rate ratio of

$$\frac{\varepsilon'(-1°C)}{\varepsilon'(-10°C)} = 7.6$$

for polycrystalline ice.

Due to a relatively low diffusion rate, ice exhibits a tendency for intergranular cracking (Sinha, 1988). The minimum stress for cracking decreases with increasing temperatures (Sinha, 1988). Sinha (1988), highlights the importance of crack-enhanced creep for the description of time-dependent ice behavior. A crack-enhanced deformation process is especially pronounced under high strain-rates. The formation of micro-cracks during loading under high strain-rates (or $\varepsilon' > \varepsilon'_{crit}$) lead to "yield-type" failures. If the strain-rate is low ($\varepsilon' < \varepsilon'_{crit}$), viscous flow and the asymptotical approach to a flow stress dominates the ice deformation process (Sinha, 1988). The estimation of the ice strength depends therefore on the transition point from brittle to ductile behavior, which itself depends on temperature, stress and strain rate ((Gold,1970), (Sinha, 1988)).

The complex material behavior of ice receives growing attention as a research field in rock mechanics. For geotechnical issues, the influence of ice on the rock mass strength is primarily important. At low ice temperatures, rock-ice interlocking and adhesion can result in high shear strength and stabilization of rock slopes ((Davies et al., 2001), (Mamot et al., 2018)). This stabilization effect vanishes at higher temperatures close to the ice melting point (Fig. 2).

Krautblatter et al. (2013) developed an ice-mechanical model for potential sliding planes in alpine regions that incorporates creep and fracturing of ice. They performed constant shear stress tests on concrete samples with an ice-filled layer. The starting temperature was -4°C and the temperature was increased at a constant rate, until failure of the sample. They observed a linear relation between shear stress at failure and temperature. The shear stress at which failure occurs is decreasing with higher temperatures. The experiments from Krautblatter et al. (2013) therefore confirm the destabilization of rock mass during warming.

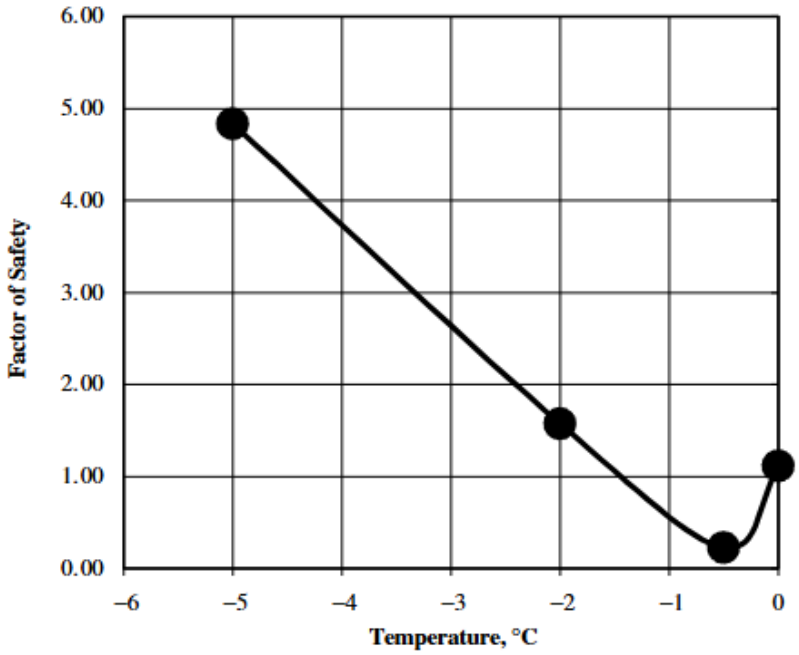

Fig. 2: Factor of safety for an ice-filled joint (slope angle = 70°, joint inclination = 40°). From Davies et al. (2001).

Recent studies further investigate the impact of temperature on the shear strength of ice-filled rock joints. Mamot et al. (2018) perform constant-strain shear tests on rock-ice samples focusing on brittle shear failure. To observe brittle failure, a relatively high strain-rate (10^{-3} sec^{-1}) is used. The tests are conducted for temperatures ranging from -10°C to -0.5°C and normal stresses between 100 kPa and 800 kPa. From their experimental results, they derive a temperature dependent failure criterion for ice-filled rock joints based on the Mohr-Coulomb law. They observe a decrease of the shear parameters (cohesion and friction) with increasing temperature. After the experiments, Mamot et al. (2018) analyze the failure type of the ice-filled joints. They report a transition from failure in the ice layer to failure along the rock-ice interface with increasing temperatures.

Huang et al. (2023) perform constant-strain tests to investigate the influence of joint roughness on the shear strength of ice-filled rock joints. They vary the temperature (-15°C, -5°C, -1°C and -0.5°C), normal stress (between 0 MPa and 2 MPa), shear rate, joint opening and joint roughness. In their experiments, Huang et al. (2023) see a temperature dependency of shear and normal displacement before failure. With increasing temperatures, the shear displacements increase indicating a transition from brittle to ductile behavior. Shear dilatancy and normal displacement on the other hand decrease with higher temperatures due to the decreasing elastic modulus of ice with higher temperatures. A decrease of shear strength with increasing shear rates was observed, since the adjusting of the ice crystal structure (or “self-healing potential”) at high strain rates is more difficult. Huang et al. (2023) chose relatively high shear-rates ($1.6*10^{-3}$ – $6.0*10^{-3}$ sec^{-1}) and were therefore not able to capture the transition point from brittle to ductile joint behavior.

Su et al. (2024) investigated the influence of joint roughness on the shear strength of ice-filled rock joints at lower temperatures (between -50°C and -10°C). They observed brittle failure in their specimen with a distinct hardening effect after exceeding the peak shear strength. This effect leads to the recording of several strength peaks during one experiment.

Li et al. (2024) present an experimental study on the shear behavior of (planar) ice-filled joints. They use a shear apparatus that is able to perform THMC coupled shear tests. Li et al. (2024) compared the shear behavior of dry and wet joints (at a temperature of +25°C) with the behavior of ice-filled rock joints at temperatures ranging from -20°C to -5°C. They ice-layers had a thickness between 0.1 mm and 5 mm. Applying the Mohr-Coulomb law on their experimental results they see that the cohesion is the strength dominating parameter for ice thickness between 1 mm and 3 mm. With higher ice-thicknesses, they see ice-rock interface debonding as relevant failure mechanism and a strong reduction of the cohesion (Fig. 3).

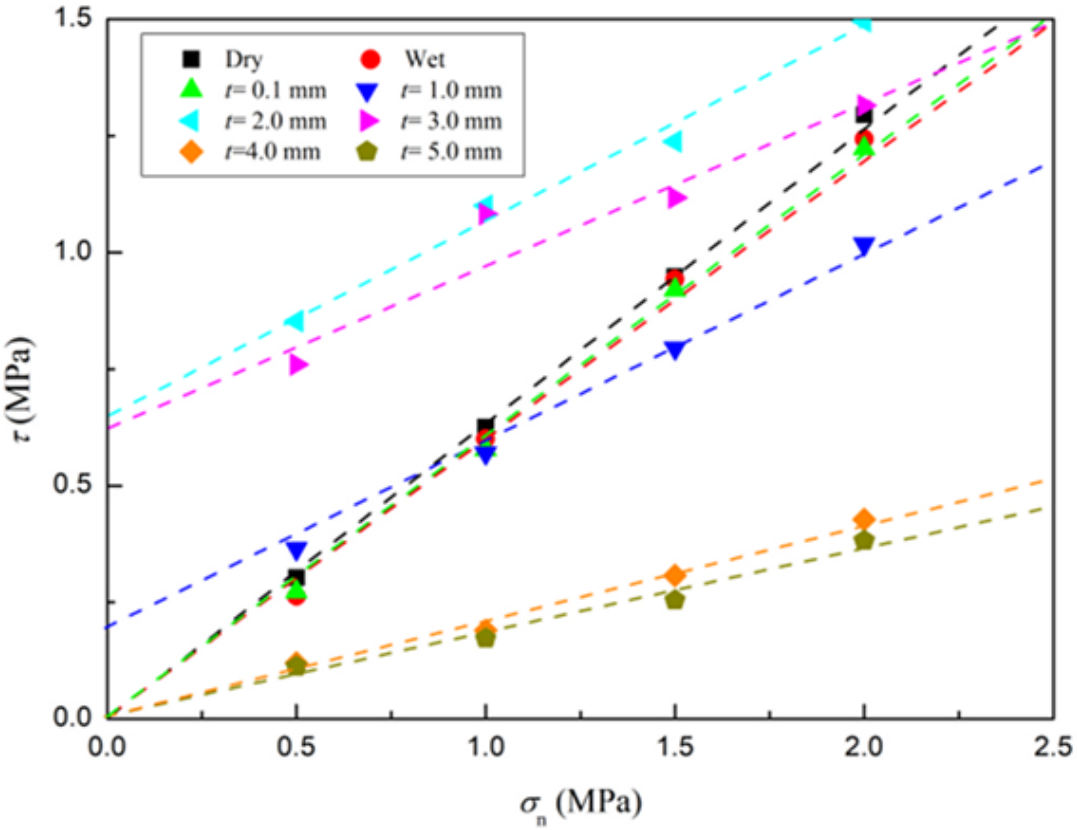

Fig. 3: Shear strength in dependence of normal stress for ice-filled rock joints at T = -20°C. From Li et al. (2024)

The literature review shows that in respect to shear strength of ice-filled rock joints several factors influencing the shear strength have already been investigated. The following aspects are still not yet resolved:

- **The systematical determination of the transition point from brittle to ductile behavior for ice-filled rock joints.** Most of the studies focus on investigating brittle joint failure and used relatively high strain rates. We know that the transition from brittle to ductile behavior of ice depends on strain rate, temperature and stress regime, but no study has been conducted to systematically analyzing the transition point for ice-filled rock joints.

- **Time- and temperature dependent joint behavior under creep conditions.** Creep behavior of pure ice (e.g (Weertman, 1983), (Sinha, 1988)) and ice-soil mixtures (e.g. (Arenson and Springman, 2005) has been investigated for several decades and is well understood. But the long-term behavior of ice-filled rock joints and the temperature-dependent potential for deformation (even without failure) are still an open field. Knowledge about the deformation of rock joints are crucial to predict rock slope movement and to mitigate/minimize damage on engineered structures.

2 Laboratory Tests

2.1 Test Equipment

The laboratory tests were carried out in the HP Inspekt 400 universal testing machine equipped with a climate chamber to conduct tests under fixed temperature and moisture conditions. For both studies, five different temperatures were tested: **-10°C, -5°C, -3°C, -2°C and - 1°C.** Stresses/strains on the samples are produced by uniaxial compression. During the tests, the axial loading force F_{axial} [kN] as well as the vertical specimen displacement Δh [mm] are monitored.

Based on the joint plane inclination α and the (uni)axial compression stress σ_1, normal stress σ_N and shear stress τ along the joint plane are calculated:

$$\sigma_N = \sigma_0 - \tau_{max} \cos(2\beta) \quad \text{Eq. (2)}$$

$$\tau = \tau_{max} \sin(2\beta) \quad \text{Eq. (3)}$$

With:

β… 90-α

σ_0 … ½ * (σ_1 + σ_2)

τ_{max}… ½ * (σ_1 - σ_2)

Based on the vertical displacement Δh, shear displacement (and shear strain) of the ice-filled joint are derived in dependence of the joint inclination. The shear displacement *s* is defined as the relative displacement of upper and lower specimen half (Fig. 5). It is calculated from the vertical displacement Δh of the loading plate. Vertical compression of the ice-layer itself is neglected for this analysis.

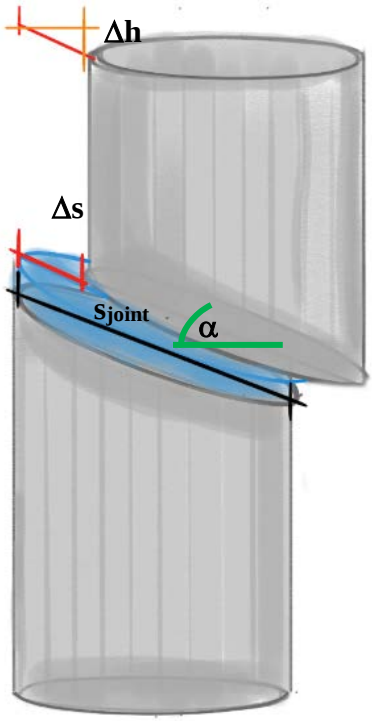

Fig. 5: Shear Displacement of the ice-filled rock joint.

$$\Delta s = \frac{\Delta h}{\sin \alpha} \quad \text{Eq. (4)}$$

$$\varepsilon_{shear} = \frac{\Delta s}{s_{joint}} \quad \text{Eq. (5)}$$

2.2 Sample Preparation

Cylindrical concrete test specimens (D= 50 mm, H= 100 mm) were used for the experiments. The first step in preparing the test specimens was to produce a (smooth) joint plane. Two different joint angles (α=30° and α =45°) are used for the test series.

To create the ice-layer inside the joint plane, a waterproof coating was necessary to prevent the outflow of the water before freezing. Therefore, a shrinking tube was attached to the lower half of the concrete sample. To fixate the upper half of the sample (and to prevent distortion/relative movement of the test specimen halves due to the tightening of the shrinking tube), wooden rods were attached to the specimen halves. The joint plane between specimen halves sealed by the shrinking tube was filled with water and placed in the climate chamber at -10°C (for about 6-8 hours) (Fig. 4). The aim was to achieve a 3 mm wide ice filling of the interface.

After the freezing process, the shrinking tube was removed. To avoid accumulation effects, surplus ice has been (mechanically) cleared from the outer specimen sides before testing. Once the ice layer has been produced, the temperature in the climate chamber was set to the planned test temperature. The tests were carried out as soon as the specimen temperature had adjusted to the new desired temperature.

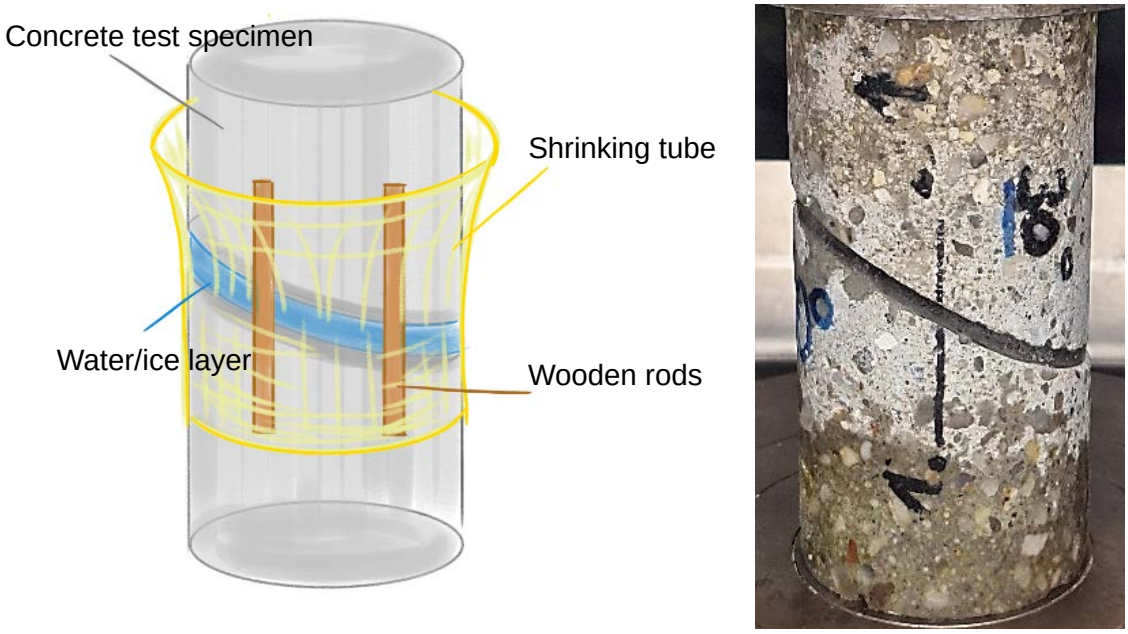

Fig. 4: Left: Sketch of the sample preparation and picture of a sample ready for testing. Right: Prepared sample.

2.3 Test Methods

2.3.1 Constant Strain Rate Tests

Tests with constant strain rates were carried out to investigate the failure behavior of ice-filled rock joints. Pre-Tests were performed to determine a loading velocity leading to a brittle yield-type failure at a temperature level of -5°C. The loading velocity (=Δh/Δt) was set to 0.5 mm/min*****. Overall, 36 specimens were tested. Tab. 1 gives an overview of the conducted tests and Fig. 6 shows typical results.

Tab. 1: Overview of conducted constant strain rate tests.

Temp.	Joint Angle	Sample Name			
-10°C	30°	T-10_30-2	T-10_30-3	T-10_30-5	T-10_30-6
	45°	T-10_45-3	T-10_45-5	T-10_45-6	T-10_45-8
-5°C	30°	T-5_30-1	T-5_30-8	T-5_30-9	
	45°	T-5_45-1	T-5_45-2		
-3°C	30°	T-3_30-1	T-3_30-7	T-3_30-9	
	45°	T-3_45-1	T-3_45-2	T-3_45-4	T-3_45-6
-2°C	30°	T-2_30-3	T-2_30-5	T-2_30-6	T-2_30-8
	45°	T-2_45-3	T-2_45-5	T-2_45-6	T-2_45-8
-1°C	30°	T-1_30-1	T-1_30-6	T-1_30-7	T-1_30-9
	45°	T-1_45-1	T-1_45-2	T-1_45-4	T-1_45-6

*****The same loading rate was applied for both joint angles (α=30° and α =45°). The shear rates are $2.83*10^{-4}$ sec^{-1} and $1.67*10^{-4}$ sec^{-1}, respectively.

2.3.2 Constant Stress Tests

Tests with constant stresses were carried out to investigate the creep behavior of ice-filled rock joints. For the constant stress tests, only test specimen with joint inclination α=30° were used. The applied stress for each temperature was set to 50% of the determined shear strength. Overall, 26 specimens were tested. Tab. 2 gives an overview of the conducted constant stress tests. Each test was conducted for app. 1 hour.

Tab. 2: Overview of conducted constant stress tests.

Temp.	τ_{load}	Sample Name			
-10°C	0.95 MPa	T-10_30-1	T-10_30-3	T-10_30-5	T-10_30-8
		T-10_30-1n	T-10_30-2n	T-10_30-3n	T-10_30-5n
-5°C	1.10 MPa	T-5_30-3	T-5_30-6	T-5_30-8	
-3°C	1.10 MPa	T-3_30-1	T-3_30-2	T-3_30-3	T-3_30-6
		T-3_30-8	T-3_30-1n	T-3_30-2n	T-3_30-6n
-2°C	0.55 MPa	T-2_30-2	T-2_30-5	T-2_ 30-6	T-2_ 30-8
-1°C	0.45 MPa	T-1_30-2	T-1_30-3	T-1_30-5	

3 Temperature-dependent joint behavior

3.1 Shear Strength and Failure Behavior

To evaluate the failure behavior of the ice-filled joints, the stress-displacement curves of the constant strain rate tests have been categorized into three categories:

a) Brittle behavior with peak and residual strength
b) Brittle behavior without residual strength
c) Ductile behavior

The stress-displacements curves show predominantly brittle behavior (category a and b) for temperatures between -10°C and -3°C. Low temperatures (T=-10°C and T=- 5°C) result in (plastic) hardening of the residual strength. Ductile behavior can be seen at -2°C and -1°C (Tab. 3). Fig. 6 shows for comparison of both failure regimes (brittle vs. ductile) the stress-displacement curves for - 3°C and - 2°C. The transition from brittle to ductile behavior is clearly visible in the laboratory results.

Tab. 3: Overview of the failure types.

Temp.	Joint Angle	Sample Name			
-10°C	30°	T-10_30-2	T-10_30-3	T-10_30-5	T-10_30-6
	45°	T-10_45-3	T-10_45-5	T-10_45-6	T-10_45-8
-5°C	30°	T-5_30-1	T-5_30-8	T-5_30-9	
	45°	T-5_45-1	T-5_45-2		
-3°C	30°	T-3_30-1	T-3_ 30-7	T-3_30-9	
	45°	T-3_45-1	T-3_45-2	T-3_45-4	T-3_45-6
-2°C	30°	T-2_ 30-3	T-2_ 30-5	T-2_ 30-6	T-2_ 30-8
	45°	T-2_45-3	T-2_ 45-5	T-2_ 45-6	T-2_ 45-8
-1°C	30°	T-1_30-1	T-1_30-6	T-1_30-7	T-1_ 30-9
	45°	T-1_45-1	T-1_45-2	T-1_45-4	T-1_ 45-6

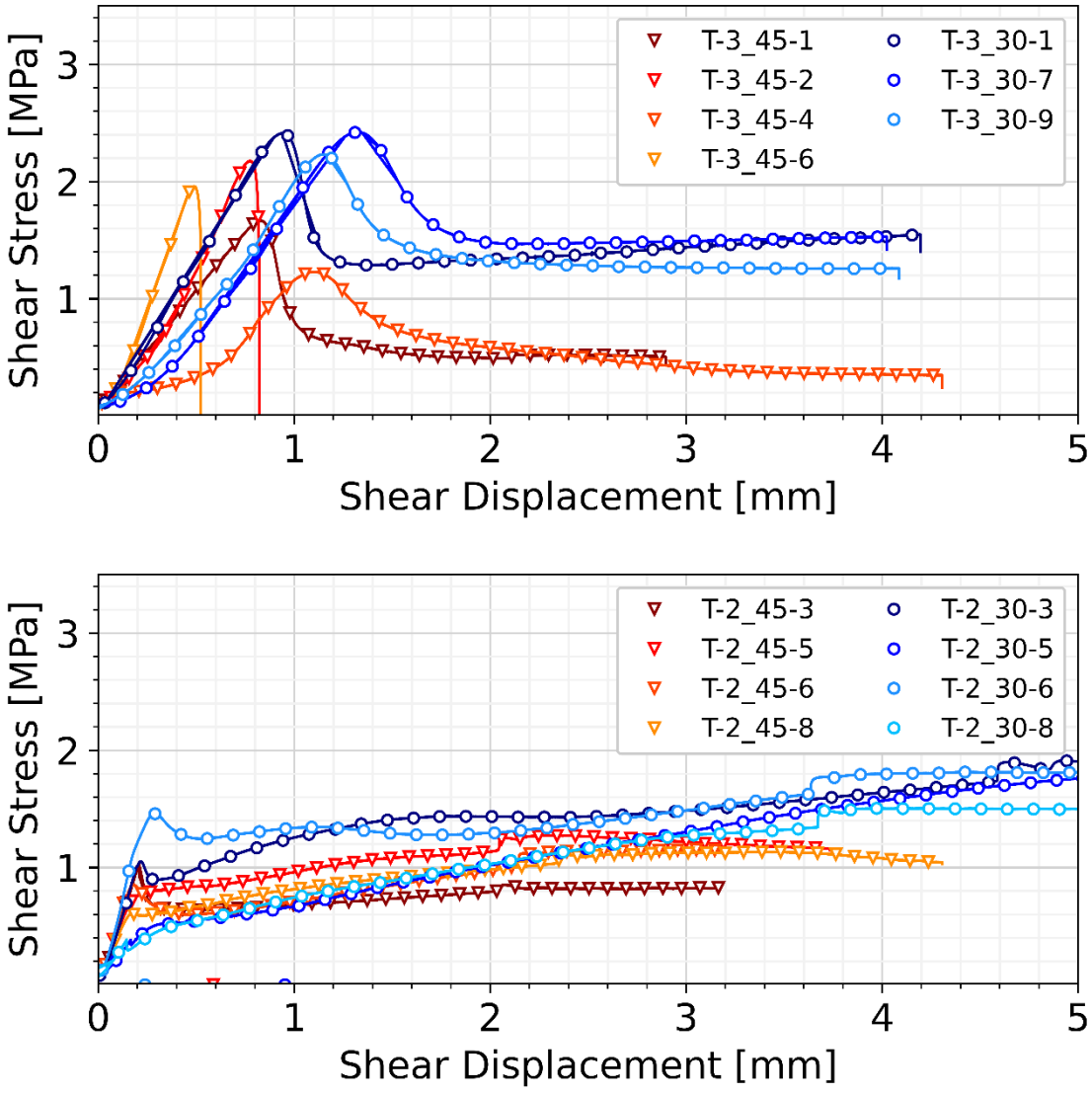

Fig. 6: Shear Stress-Shear Displacement curves for T = -3°C (above) and T= -2°C (below). The transition from brittle to ductile behavior is clearly visible.

Fig. 7 shows the temperature-dependent shear strength (= maximum observed shear stress). For brittle type failures, the peak strength is plotted. For ductile behavior, the maximum viscous flow stress is plotted. Highest shear strength, but also highest variation of the strength values is obtained for -10°C. This link can be explained by the governing brittle failure type. The reorganization of the crystal structure ("self-healing potential") is limited and therefore cracks and other inhomogeneities (e.g. air bubbles) in the ice-layer have a strong influence on the ice strength. A clear decrease of shear strength is observed in the temperature interval from - 3°C to -1°C. This interval corresponds to the transition from brittle to ductile behavior. The ductile behavior leads to low variability of the strength values due to the improved possibility for self-healing.

For each temperature, a linear Mohr-Coulomb failure criterion is derived (Fig. 8). The high variability of the shear strength for low temperatures and brittle failure types is also visible in the relatively low coefficient of determination (R^2=0.438 and R^2=0.679) for -10°C and -5°C. Very good coefficient of determination are obtained for -2°C and -1°C (R^2=0.952 and R^2=0.968, respectively).

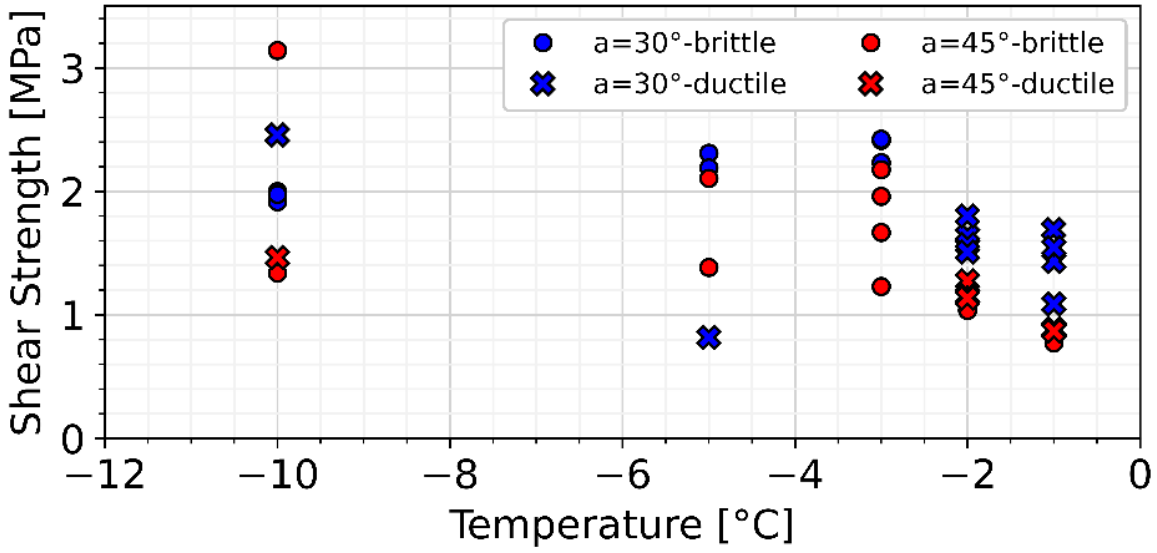

Fig. 7: Temperature-dependent shear strength. Values for specimen with joint angle α = 45° in red, joint angle α = 30° in blue.

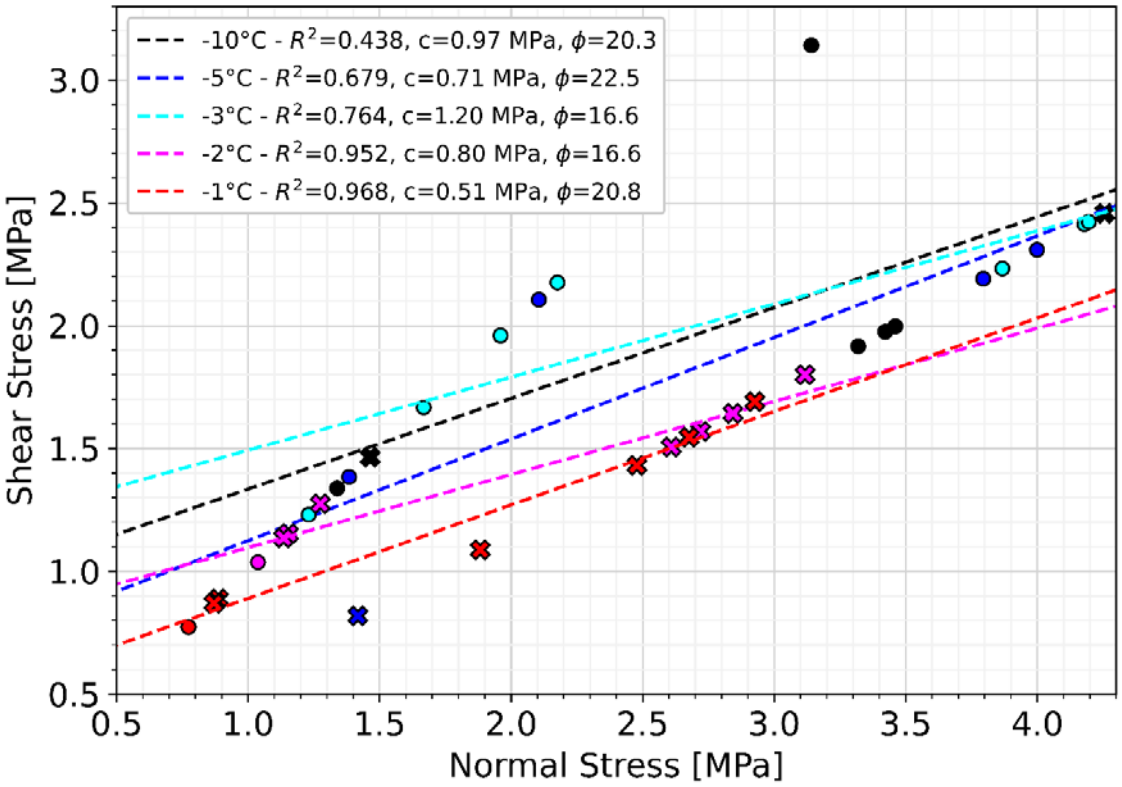

Fig. 8: Shear Stress-Normal Stress plot. A Mohr-Coulomb failure criterion is determined for each temperature interval. Peak strength is marked with a circle. Maximum viscous flow stress is marked with a cross.

3.2 Time-dependent joint creep

For each temperature, an average shear strength has been calculated. The constant stress tests have been conducted under a load of 50% of the average shear strength. The load has been applied with the same velocity. The test results show three main trends:

1) For the applied strain rate and stress, constant secondary creep occurs in all tests with temperature of -1°C and -2°C ("viscous flow"-dominated regime). The maximum displacement after one hour is under 1 mm. The displacement rates range from around 5e-5 mm/s and 1e-4 mm/s. No visible change/fracturing occurred in the ice-layer (Fig. 9 and Fig. 11)

2) Lower temperatures (-3°C, -5°C, "brittle"-dominated regime) show a different behavior. They show maximum displacements in the order of several millimeter with high constant secondary creep rates (between 1e-3 mm/s and 1e- 2 mm/s) and transitions from secondary creep to accelerated, tertiary creep. Fracturing in the ice-layer is clearly visible (Fig. 10)

3) For -10°C, the behavior is different. Some tests show extremely low displacement rates (~1e- 5 mm/s), which corresponds to the expected behavior of pure ice: The creep rate for low temperatures is lower than for higher temperatures (Fig. 9). The other tests show high displacement rates (~1e- 3 mm/s) (Fig. 10 and Fig. 12). The two different creep processes can be explained by the higher strength at -10°C. If a strong ice-layer is created, no fracturing occurs, and therefore the creep rate is low. If micro-cracks could form (e.g. due to impurities/bubbles in the ice-layer), a strong crack-enhanced creep process starts. The constant-stress tests show, that the displacement rate is not only temperature-dependent but also strongly "damaged controlled".

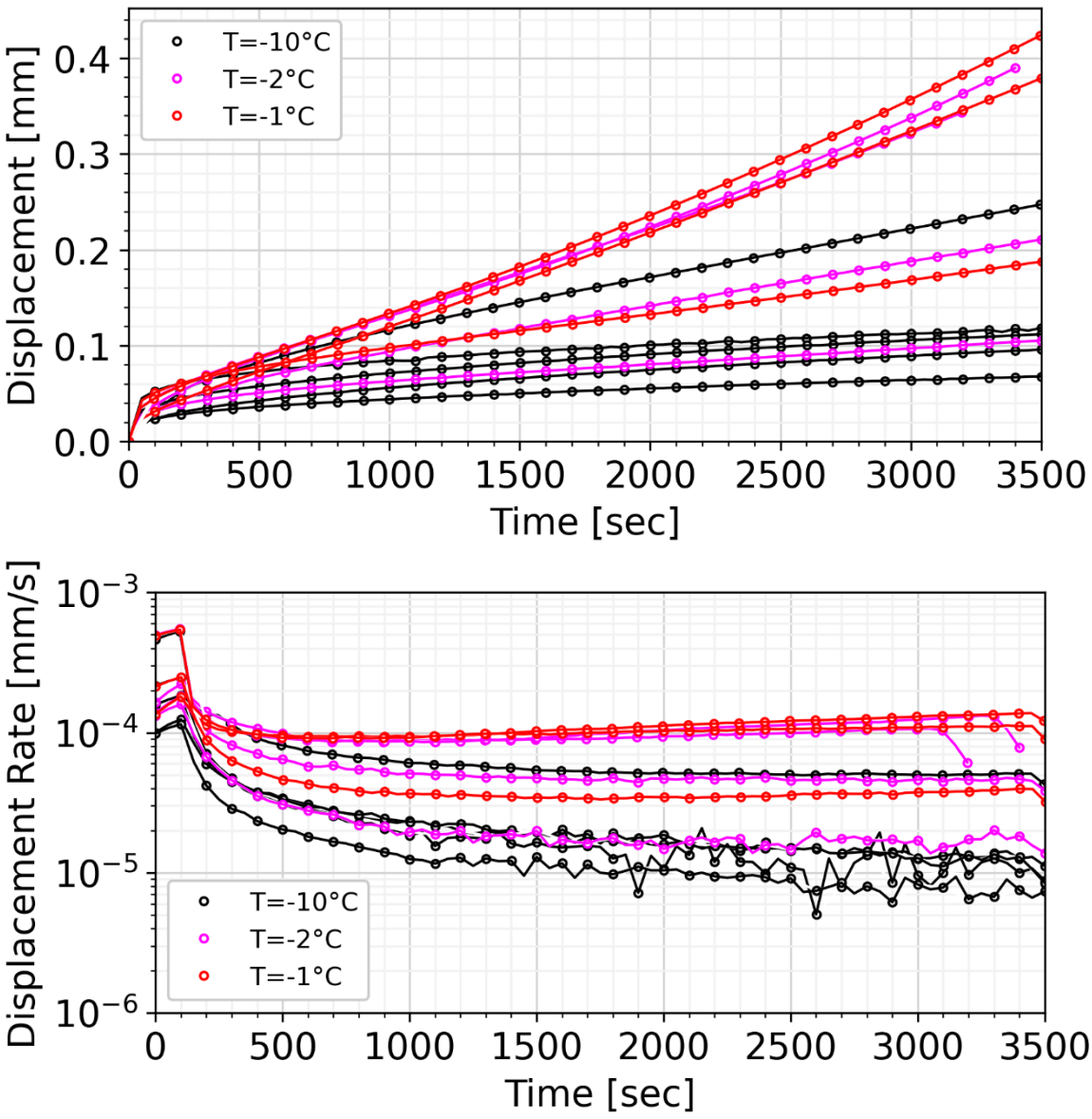

Fig. 9: Low displacements and displacement rates for “viscous flow”-dominated temperature regime (T=-2°C and T=-1°C) and unfractured ice-layers for temperature T=- 10°C. The ratio of the average stationary displacement rates for -10°C and -10°C is around 4.

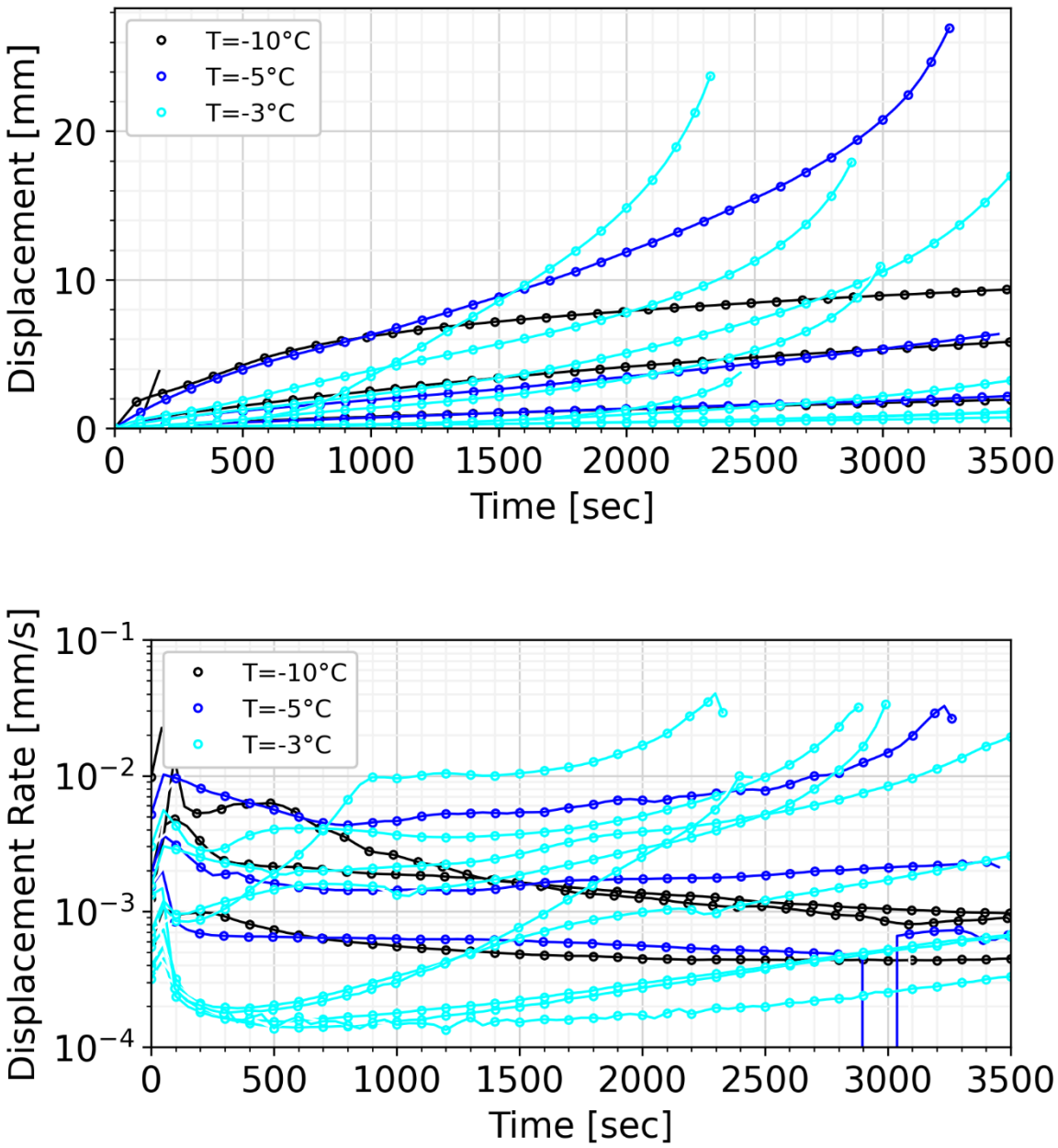

Fig. 10: Large displacements and displacement rates for “brittle”-dominated temperature regime (T=-10°C, T=-5°C and T=-3°C). Fractured ice-layers show enhanced creep rates.

t_0 t_1 t_2

Fig. 11: Pictures made during the creep test of T-2_30-6 for temperature T = - 1°C. The ice-layer is clear, no fracturing occurred.

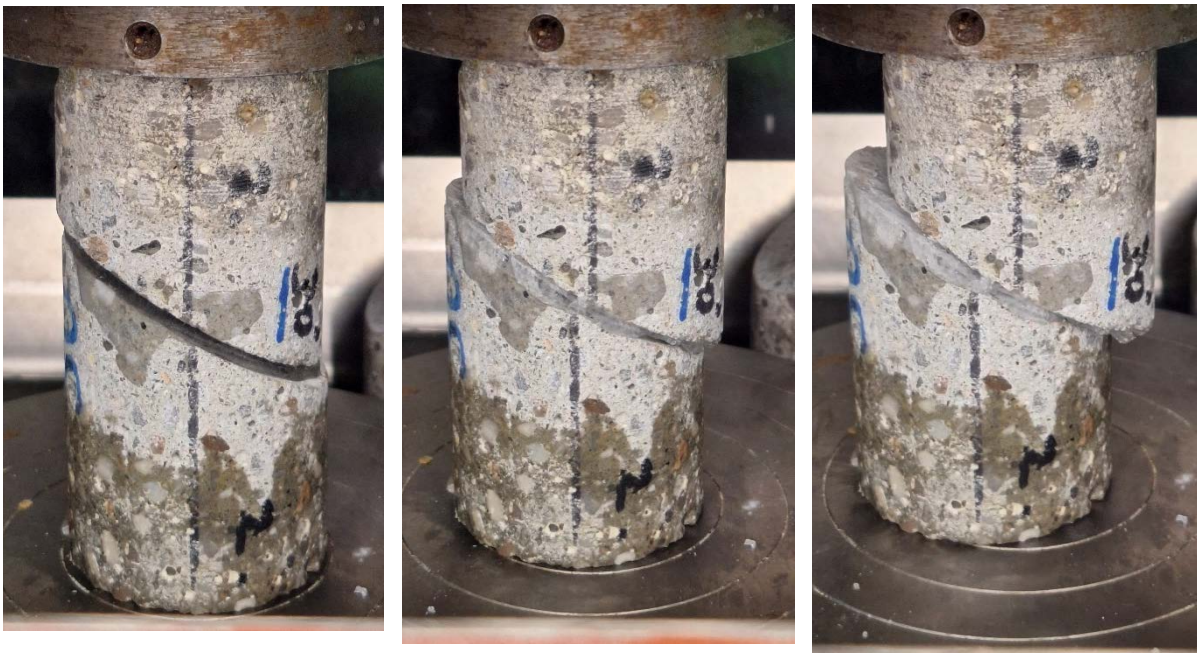

t_0 t_1 t_2

Fig. 12: Pictures made during the creep test of T-10_30-2n for temperature T=- 10°C. Fracturing occurred in the ice-layer.

4 Discussion and Conclusion

Two test series have been performed to characterize the temperature-dependent behavior of ice-filled rock joints.

Constant strain-rate tests were used to analyze shear strength and failure behavior of the joints. For the selected loading velocity, a transition from brittle to ductile behavior can be seen between -3°C and -2°C. For low temperatures, the obtained strength values fluctuate widely. The fluctuation of those values should be further investigated. Here, the sample preparation processes should be scrutinized to create uniform ice qualities.

Constant stress tests were performed to analyze the time-dependent creep behavior of ice-filled rock joints. The tests were conducted under a load level of 50% of the short-term peak load. The results show, that the transition from brittle to ductile behavior also influences the creep behavior. Crack-enhanced creep with high displacement rates predominately occurs under brittle conditions. The applied load for each temperature has been derived from the previously determined shear strength values. This might lead to inaccuracy for low temperatures (-10°C, -5°C), due to the fluctuation of the strength values.

Aspects for further studies are the investigation of the governing failure mechanism (rock-ice interface or ice-layer fracturing) and the influence of micro-cracking (use of AE sensors) to evaluate the damage evolution during the loading process.

5 Acknowledgements

The series of experiments were carried out as part of student projects. We would like to thank the students C. Sadri and J. Bräutigam for the careful realization and documentation of the experiments!

6 References

PERMOS (2022) Swiss Permafrost Monitoring Network. https://www.permos.ch/fileadmin/Files/publications/swiss_permafrost_bulletin/PERMOS_bulletin_2021.pdf.

P. Mamot, S. Weber, T. Schröder, M.Krautblatter (2018). A temperature- and stress-controlled failure criterion for ice-filled permafrost rock joints. *The Cryosphere,12, 3333-3353, 2018*. https://doi.org/10.5194/tc-12-3333-201.

L. Gold, (1970). The failure process in columnar-grained ice. *PHD Thesis.* Montreal.

W. Glen (1955). The creep of polycrystalline ice. Available at https://royalsocietypublishing.org .

D. R. Homer and J. W. Glen (1978). The creep activation energies of ice. *Journal of Glaciology*. Vol. 21, No. 85,1978.

J. Weertman (1983). Creep deformation of ice*. Ann. Rev. Earth Planet. Sci.* 1983. 11:215-240.

N. K. Sinha (1988). Crack-enhanced creep in polycrystalline material: strain-rate sensitive strength and deformation of ice*. Journal of Material Science* 23 (1988) 4415-4428.

Davies, M. C. R., Hamza, O. & Harris, C. (2001). The effect of rise in mean annual temperature on the stability of rock slopes containing ice-filled discontinuities*. Permafrost and Periglacial Processes*, 12(1), 137–144. https://doi.org/10.1002/ppp.378.

M. Krautblatter, D. Funk, F. K. Günzel (2013). Why permafrost rocks become unstable: a rock–ice-mechanical model in time and space. *Earth Surf. Process. Landforms* 38, 876–887 (2013). DOI: 10.1002/esp.3374.

S. Huang, H. Cai, Z. Xin, G. Liu (2023). The temperature-dependent shear strength of ice-filled joints in rock mass considering the effect of joint roughness, opening and shear rates. *The Cryosphere*, 17, 1205–1223, 2023 https://doi.org/10.5194/tc-17-1205-2023

Z. Su et al. (2024). Experimental and theoretical study of the shear strength of ice-rock interface. *Cold Regions Science and Technology.* https://doi.org/10.1016/j.coldregions.2023.104076

B. Li, X. Gong, G. Wang, J. Qiao (2024). Benchmark experiment on shear behavior of ice-filled planar rock joints using a novel direct shear testing apparatus. *International Journal of Rock Mechanics and Mining Sciences.* https://doi.org/10.1016/j.ijrmms.2024.105757

L. U. Arenson and S. M. Springman (2005): Triaxial constant stress and constant strain rate tests on ice-rich permafrost samples*, Can. Geotech. J.*, 42, 412–430, https://doi.org/10.1139/t04-111.

Non-explosive damage initiation in rock: From Soundless Cracking Demolition Agents to Shape Memory Alloys

Explosionsfreie Gesteinszerlegung: von Quellzementen zu Formgedächnismaterialien

Radhika de Silva, Jordan Aaron
Department of Earth Science and Planetary Science, ETH Zürich
Sonneggstrasse 5, 8092 Zürich, Switzerland

Abstract

Soundless Cracking Demolition Agents (SCDA) have been picking up traction as a safe, non-explosive method of inducing damage in rock for applications such as deep earth resource recovery and storage, and underground excavations. Historically, predicting the fracturing potential of SCDA has been done by performing laboratory testing under in-situ stress conditions and numerical modelling of SCDA expansion. However, these modelling methods largely simplify the expansion mechanism of SCDA and often produce unrealistic results. A new modelling approach to simulate SCDA expansion considering the strain-energy density of SCDA (~3.7 MJ/m^3) is presented in this study. The model implemented in 3-Dimensional Discrete Element Code, 3DEC 9.0 shows that once calibrated, fractures initiated by SCDA expansion can be simulated under various in-situ stress conditions without requiring the recalibration of the model. The results presented in this study highlight the limitations of SCDA based on its finite strain energy release during the fracturing process. Therefore, a potential alternative for SCDA use is presented to initiate fractures around an injection well using Shape Memory Alloy (SMA) actuators. Compared to SCDA, SMA is thermally triggered, reusable, and has a strain energy density nearly an order of magnitude greater compared to conventional SCDA. Finally, the proposed strain energy-dependent modelling methodology was applied to SMA to simulate fracture propagation 3DEC as a preliminary assessment of the SMA induced fracturing in rock under in-situ stress conditions.

Zusammenfassung

Quellzemente (Soundless Cracking Demolition Agents = SCDA) sind interessant als sichere, explosionsfreie Methode zur Schädigungsinitiierung in Gesteinen mit Anwendungen bei der Erschließung von Ressourcen in größeren Tiefen inkl. der Speicherung sowie für unterirdische Hohlräume. Historisch gesehen basiert die Vorhersage des Bruchpotentials von SCDA auf Labortests unter in-situ Spannungsbedingungen und numerischen Simulationen der SCDA-Expansion. Diese Modellierungsmethoden vereinfachen allerdings den Expansionsmechanismus von SCDA stark und erzeugen oft unrealistische Ergebnisse. Diese Studie stellt eine neue Modellierungsstrategie der SCDA-Expansion unter Beachtung der Deformationsenergiedichte von SCDA (~3.7 MJ/m^3) vor. Das Modell, implementiert in den 3-dimensionalen Discrete Element Code 3DEC 9.0, zeigt nach Kalibrierung, dass die Rissinitiierung durch die SCDA-Expansion unter verschiedenen in-situ Spannungsbedingungen ohne erneute Kalibrierung des Modells erfolgt. Die Ergebnisse dieser Studie zeigen die Limitierungen von SCDA basierend auf der begrenzten Deformationsenergiefreisetzung während des Bruchprozesses. Deshalb wird eine potentielle Alternative zum SCDA zur Rissinitiierung in einem Injektionsbohrloch mittels eines Materials mit Formgedächtnis (Shape Memory Alloy = SMA) vorgestellt. Verglichen mit SCDA, ist SMA thermisch getriggert, wiederverwendbar, und hat eine etwa 10-fach höhere Deformationsenergiedichte verglichen mit konventionalem SCDA. Abschließend wird die vorgeschlagene Deformationsenergie-abhängige Modellierungsstrategie auf SMA angewandt, um Rissausbreitung in 3DEC als vorläufige Abschätzung zur SMA-induzierten Rissausbreitung in Gesteinen unter in-situ Spannungsbedingungen zu simulieren.

1 Introduction

1.1 Soundless cracking demolition agents

Non-explosive demolition agents were introduced in the 1970s as a rock fracturing compound (Hinze and Brown, 1994). They mainly consist of Calcium Oxide (CaO) and other cementing compounds such as $CaSO_4$, $3CaO{\cdot}Al_2O_3$ and $3CaO{\cdot}SiO_2$ are marketed under many names: Soundless Cracking Demolition Agents (SCDA), Static Cracking Agents (SCA), and Non-Explosive Expansion Materials (NEEM).

SCDA is mixed with water and formed into a slurry, which is then poured/injected into pre-drilled holes in a target rock. The exothermic hydration reaction of CaO (Eq.1) results in a volumetric expansion and produces an expansive pressure within the confines of the injected borehole (Goto et al., 1988).

$$CaO\ (s) + H_2O\ (l) \leftrightarrow Ca(OH)_2\ (s)\ \Delta H,\ 298K = -104\ kJ/\ mol \qquad (1)$$

The expansive pressure produced by SCDA is limited to the strain energy density of SCDA, which is approximately 3.7MJ/m^3 (De Silva and Ranjith, 2019b). This is also dependent on the water content (typically 30% by weight of SCDA) used to produce the SCDA slurry.

1.2 Mechanism of fracturing during non-explosive demolition

SCDA expansion within an injection well produces a radial compressive stress field and a tangential tensile stress field around the SCDA injection well. When the tensile stress developed at the borehole boundary exceeds the tensile strength of the rock multiple radial fractures are formed (Fig. 1a). The extent of fracture propagation is confined to the tensile hoop stress field around an SCDA injected well (Harada et al., 1989). Therefore, SCDA fracturing allows for the controlled initiation of multiple radial fractures over several hours by gradually increasing the expansive pressure (Fig. 1) without noise and vibrations. This rock fracture initiation and propagation by SCDA charging can be idealized with quasi-static fracture propagation (de Silva et al., 2016).

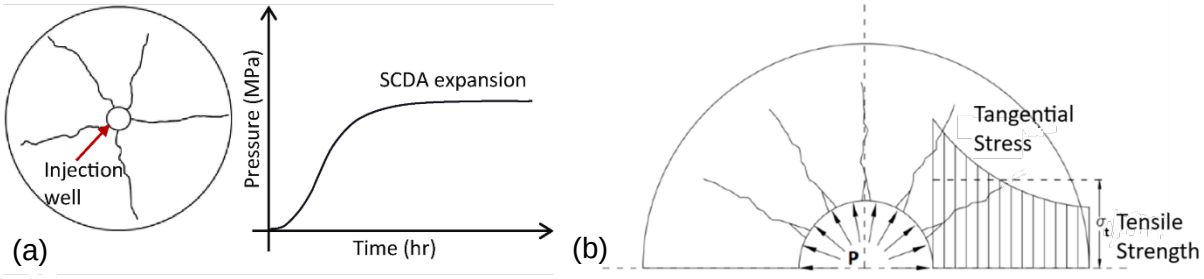

Fig.1: (a) SCDA-induced fracturing and the expansive pressure development around an injection well (De Silva et al., 2024), and (b) radial fracture propagation and termination with tensile strength (de Silva et al., 2016)

1.3 Recent developments in SCDA

Gamage and De Silva (2020) introduced a patented hydrophobic SCDA variant that has high fluidity and injectability. Manatunga et al. (2022) further improved the SCDA by improving its injectability and hydrophobicity. Maneenoi et al. (2022) improved the reaction rate of SCDA with the addition of $MgCl_2$. Sakhno and Sakhno (2024) introduced a method for directional fracturing using SCDA cartridges. De Silva and Ranjith (2019a) and Zhong et al. (2023) investigated borehole optimization methods for initiating fractures during SCDA charged stimulations. Xu et al. (2021) introduced a self-swelling SCDA cartridge that can be used in place of conventional SCDA slurries. The impact of lateral restraint on the expansive pressure produced by SCDA was also investigated in many studies (De Silva et al., 2019, Tang et al., 2017, Li et al., 2021). Some studies were also performed to increase the peak expansive pressure produced by SCDA systems (Liyanage and Gamage, 2021, Liyanage et al., 2022).

Following the development of SCDA systems, its applicability in engineering applications such as rock quarrying (Arshadnejad, 2019), selective demolition (Natanzi et al., 2020), directional roof cutting (Zhang et al., 2020), stress release in underground excavations (Chen et al., 2023) and permeability enhancement in Enhanced Coal Bed Methane (ECBM) systems (Zhai et al., 2018) and shale gas reservoirs (Guo et al., 2015) were assessed.

2 Numerical simulation methods for SCDA charged fracturing

As the industry shows increasing interest in SCDA applications, numerical simulations of SCDA-induced fracture propagation have been conducted using both continuum and discontinuum modelling techniques to better understand its fracturing performance.

2.1 Continuum and discontinuum modelling methods

Continuum methods of SCDA expansion simulation allow the measurement of the deformation and the stresses developed in underground structures. Tang et al. (2017) investigated the stress-strain development in roof rock structures in underground mines when SCDA is injected into boreholes at inclined angles. In this model, the effect of SCDA on the surrounding rock mass was assessed by applying an expansive stress boundary to the wall of the injection well. Abaqus was used to assess the fracturing potential of SCDA using a modified cohesive element method implemented in Abaqus (Wang et al., 2018). Other studies have simulated SCDA expansion in boreholes utilizing the thermal expansion of materials using the software package RFPA (Liu et al., 2021) and Abaqus (Cho et al., 2018). A cohesive zone model was implemented in the extended finite element method (XFEM) by Tiam et al. (2020) to simulate crack propagation between two boreholes. Using FLAC3D, Xu et al. (2022) simulated the strains developed by SCDA in a steel cylinder by applying a pressure boundary condition to the internal walls of SCDA.

SCDA charged fracture propagation was implemented in discontinuum modelling methods using PFC3D (De Silva et al., 2018, De Silva and Ranjith, 2020) to predict the fracture propagation pattern. However, these methods apply a constant velocity boundary condition to the inner wall of the boreholes to mimic SCDA expansion. In another study, the Continuous-discontinuous element method (CDEM) was used to simulate SCDA expansion by implementing the strain applied by SCDA (Wang et al., 2024). The strain applied in the model was calibrated against a laboratory experiment. Li (2017) simulated the expansive pressure applied by SCDA with the implementation of a swelling law originally defined for expansive rocks (Grob, 1972) in UDEC. However, these models are only applicable to the material and confining boundary conditions at which they were calibrated.

2.2 Limitations of current models and a new approach

When using pressure boundary applications in numerical simulations of SCDA within injection wells, there can be discrepancies between experimental outcomes and numerical results, even if the fracture patterns appear similar. One key limitation is the use of pressure boundary conditions at the injection well to simulate the expansive pressure of SCDA, which falls short of accurately assessing the pressure at the injection hole boundary. The expansive pressure generated by SCDA depends on the strain on the rock, the confining pressure, and material stiffness, (Tang et al., 2017, Wang et al., 2018, De Silva et al., 2018) and therefore should not be an input parameter for simulations focused on stress distribution around injection wells. Furthermore, applying a constant strain rate to the injection well boundary, by leveraging the thermal expansion coefficient or a velocity boundary condition, may lead to inaccuracies due to the absence of a physical limit on the strain induced by SCDA expansion.

Considering these limitations a novel simulation method for SCDA expansion is presented in this study, integrating boundary strain application to model fracture initiation and propagation across various geometries, such as infilled rock joints. Implemented in 3DEC, this approach introduces strain rate decay functions, derived from experimental expansive pressure measurements, to limit SCDA expansion in rock joints and boreholes. Additionally, the total strain energy from SCDA expansion is calculated in the model to terminate fracture propagation when the peak expansive potential is reached. This energy-based method overcomes the need for experimentally determining peak expansive pressures for different rock types under varying stress conditions prior to simulations and offers the flexibility to be applied in other mechanically induced fracturing methods.

3 Methods

3.1 Numerical approximation of expansive pressure generated by SCDA in an injection well and a rock joint

The strain applied by SCDA expansion inside a steel cylinder (Fig. 2a) can be approximated using the theory of elasticity for thick-walled cylinders as shown in Eq. 2.

$$\varepsilon = \frac{2r_o^2}{E_s \cdot (r_o^2 - r_i^2)} \cdot P = D \cdot P \tag{2}$$

where, ε is the tangential strain, r_o is the outer radius of the pipe, r_i is the inner radius of the pipe, E_s is the Young's modulus of the steel cylinder and P is the expansive pressure applied by SCDA expansion. A typical expansive pressure curve generated by SCDA using the outer pipe method is presented in Fig. 2b and the expansive pressure, P in MPa can be approximated with a negative exponential function as shown in Eq. 2.

$$P = a \cdot [1 - c \cdot e^{(-b \cdot t)}] \tag{3}$$

where, t is the time in hours. The three shape factors a (peak pressure factor), b (reactivity factor), and c (onset delay factor) govern the expansive pressure development of SCDA under any given lateral restraint or ambient temperature condition. For expansive pressure measured in a steel cylinder using the outer pipe method at an ambient temperature of 25 °C (Fig. 2a), these factors are 47, 1.5 and 0.1 for a, b, and c respectively. Combining Eqs. 2 and 3, and taking its time derivative, an exponential decay function is obtained for the strain rate applied by SCDA in the time domain.

$$\dot{\varepsilon} = D \cdot \dot{P} = D \cdot a \cdot c \cdot b \cdot e^{-b \cdot t} \tag{4}$$

In Eq.(4), $\dot{\varepsilon}$ is the strain rate decay in the borehole, and $\dot{P}$ is the expansive pressure generation decay rate.

Similarly, an approximate function was developed to simulate SCDA expansion within a joint by considering expansion between two parallel boundaries. In the experiment, SCDA was placed in a horizontal joint in sandstone, propped open with ceramic proppants to maintain a 2 mm fracture aperture. An axial stress of 10 MPa was applied, and the top and bottom boundaries were fixed to measure the additional expansive pressure (Fig. 2c). The shape factors in Eq. 3 for the joint expansion pressure (Fig.2d) were calculated as 14.5 (peak pressure factor), 0.038 (reactivity factor), and 0.38 (onset delay factor).

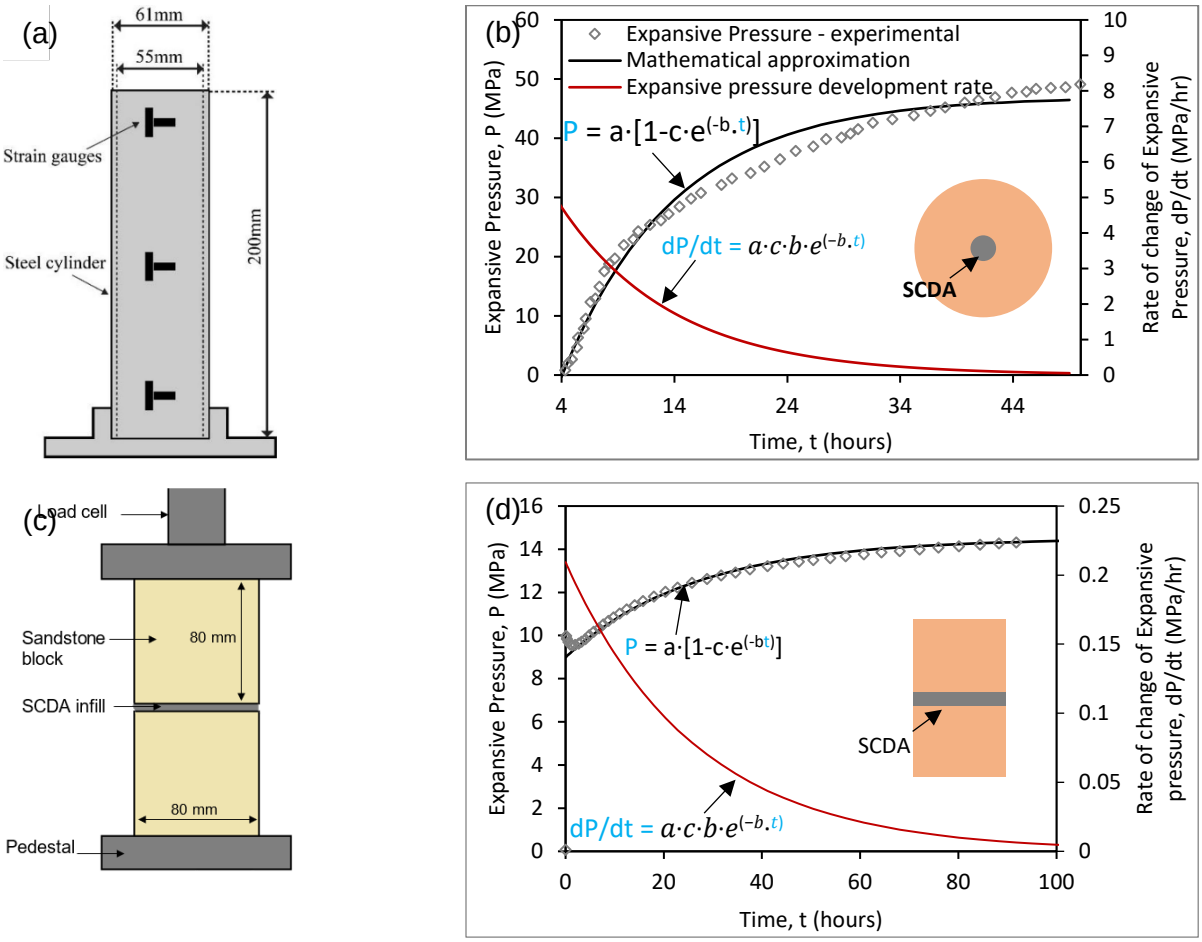

Fig. 2: Expansive pressure, (a) Outer pipe method used to measure SCDA expansion, (b) fitting curve and the expansive pressure generation rate in a cylinder, (c) experimental setup used to measure SCDA expansive pressure in a rock joint, and (d) expansive pressure, fitting curve and the expansive pressure generation rate in an SCDA infilled joint

These values were lower than those for SCDA expansion in an injection well due to the lack of confinement. The calibration of SCDA expansion in the rock joint indicates that the curve fitting strain energy simulation method presented in this study can be applied to various models, independent of the geometry of the expanding volume.

Therefore, the strain response of the rock at the joint interface due to axial expansive pressure is given by,

$$P = E_r \cdot \varepsilon_a \tag{5}$$

where, E_r is the Young's modulus of the sandstone, and ε_a is the strain perpendicular to the joint plane. The time derivative of this relationship yields an exponential decay function for the strain rate, of SCDA expansion in a joint.

$$\dot{\varepsilon} = E_r \cdot \dot{P} = E_r \cdot a \cdot c \cdot b \cdot e^{-b \cdot t} \quad (6)$$

The empirical relationships between the expansive pressure and the strain rate will be used in the 3DEC numerical model to simulate SCDA expansion.

3.2 Fracturing experiments

Fracturing experiments were performed on massive silicate cemented homogeneous fine-grained sandstone specimens to qualitatively validate the numerical simulations.

The sandstone consisted of 87% Quartz, 7% Kaolinite, 3 % Muscovite, 1 % Siderite, and 2% of other mineral species. The specimens tested had a uniaxial compressive strength (UCS) of 50.36 MPa, a Brazilian disk tensile strength (BTS) of 6.57 MPa, and a Young's modulus of 6.57 MPa.

For the fracturing experiment, a sandstone block (80 mm x 80 mm x 160 mm) with an artificial horizontal joint (JRC 2-4) was created using waterjet cutting. A 10 mm diameter central injection well was drilled vertically to a depth of 120 mm. Ceramic proppants with mesh size 16/30 were placed in the joint to maintain a 2 mm fracture aperture. Then SCDA mixed with a viscosifier, and superplasticizer (Manatunga et al., 2022), was injected into the horizontal fracture via the central injection well. Following the SCDA injection, an axial stress of 10 MPa was applied to provide additional resistance to fracturing and facilitate expansive pressure development. Acoustic Emission (AE) monitoring and strain measurements were used to track the fracture propagation. The final fracture pattern was obtained using X-ray CT scanning at the Hutch 3B Imaging and Medical Beamline of the Australian Synchrotron, utilizing a 150 keV X-ray beam with a 32 µm resolution.

3.3 Numerical implementation of the model

Simulation of SCDA expansion was performed on a calibrated grain-scale rock mass assembly simulating Sandstone. Next, the SCDA filled in the injection well and the rock joint was modelled as solid elements. Finally, SCDA expansion was simulated for the infilled joint and the injection well using the derived strain rate decay functions.

3.3.1 Grain-based rock mass assemblies

The grain-based rock mass was assembled by generating a Voronoi grain structure in 3DEC. Individual grains were modelled as linear elastic elements and the grain contacts were modelled using the Coulomb slip model. Sandstone was modelled as a homogenous material. The model was calibrated against experimentally observed UCS and BTS values (De Silva et al., 2024, De Silva et al., 2023). The models only simulated intergranular fracturing between grain contact boundaries. The calibrated model parameters are shown in Table 1. The comparison of the mechanical properties between the experimental values and the calibrated models is shown in Table 2.

Tab. 1: Calibrated model parameters for sandstone (De Silva et al., 2024).

Zone constitutive model	Isotropic Elastic
Young's modulus (GPa)	57.00
Poisson's ratio	0.22
Joint Constitutive model	Mohr-Coulomb
Friction angle, φ (°)	33.00
Cohesion, C (MPa)	17.00
Tensile strength, σ_t (MPa)	6.60
Joint normal stiffness, K_n (GPa/m)	1200
Joint shear stiffness, K_s (GPa/m)	1200

Tab. 2: Comparison of experimental and numerical results.

Model	UCS_{Exp} (MPa)	UCS_{sim} (MPa)	$Error_{UCS}$ (%)	BTS_{exp} (MPa)	BTS_{sim} (MPa)	$Error_{BTS}$ (%)
Sandstone	50.36	51.11	1.49	3.39	3.41	0.56

3.3.2 SCDA expansion simulation in 3DEC

The numerical model for SCDA expansion in a borehole and flat joint was implemented in 3DEC using FISH scripts to simulate fracture evolution and stress distribution. The 3DEC model simulated SCDA expansion in a vertical borehole intersected by a horizontal joint infilled with SCDA (Fig.3). The model assumed constant Young's modulus for SCDA elements and expansion perpendicular to boundary surfaces. The strain rate decay functions, Eqs. 4 and 6 were applied to simulate SCDA expansion, using experimentally derived strain rates. The strain rates were converted to velocities that were applied to the model in the SCDA-rock interface (Eq.7).

$$V = \frac{\Delta r}{\Delta t} = \frac{r \cdot \varepsilon}{\Delta t} = r \cdot \dot{\varepsilon} \tag{7}$$

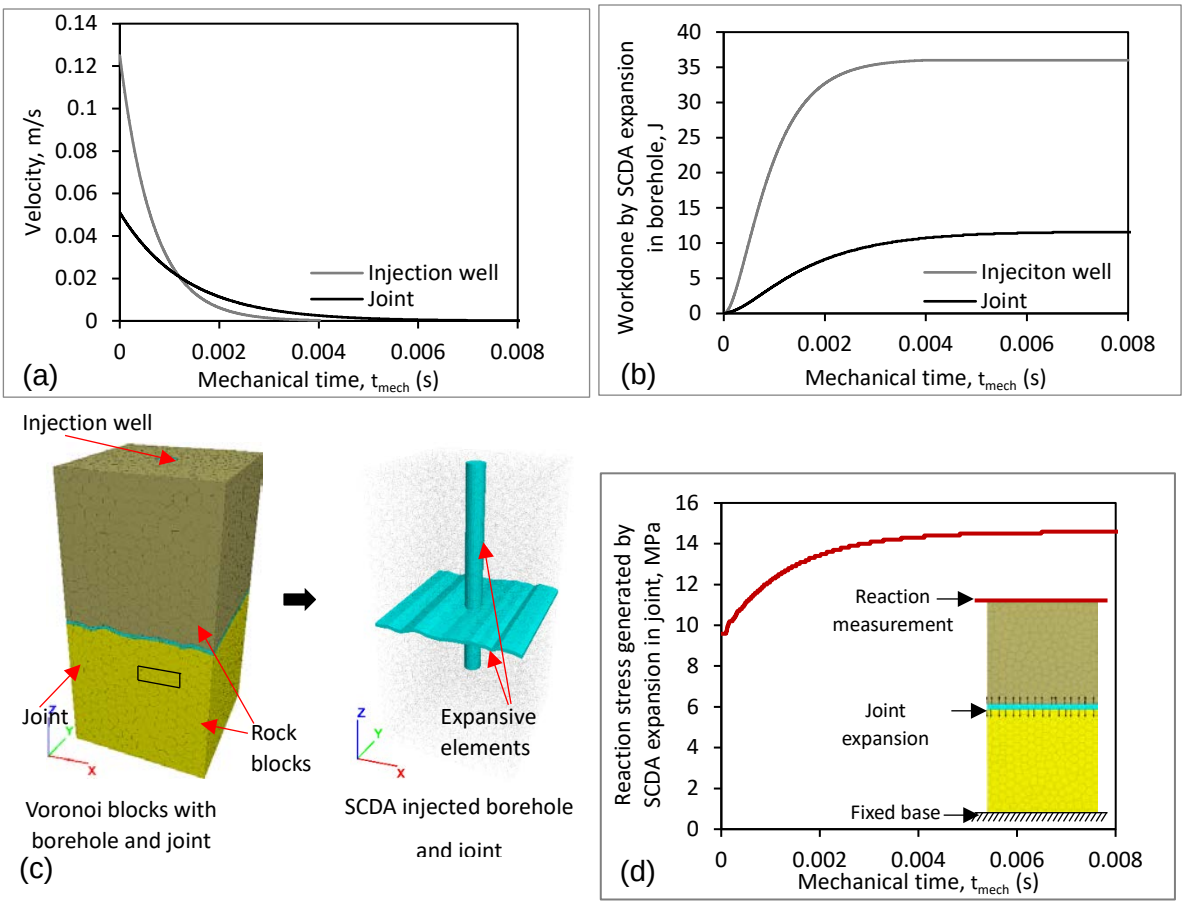

Fig. 3: Strain rate decay and SCDA strain energy application. (a) Velocity boundary decay function for SCDA expansion in the injection well and in the joint, (b) total strain energy input from SCDA expansion in the injection well and in joint, (c) numerical assembly with rock and SCDA elements, and (d) reaction stress generated by SCDA expansion in rock joint.

In Eq.7, V is the velocity applied at each grid point of the SCDA rock boundary, and r is either the diameter of the SCDA injection well or the SCDA infill thickness. The strain rates given in Eqs. 4 and 6 can be converted from the time domain t to the mechanical simulation time in 3DEC, t_{mech}. This allows the experimentally observed strain energy to be applied in the 3DEC model within a specified me chanical time (set to 0.008 s). A simple mechanical time-dependent exponentially decaying velocity boundary can be obtained to Simulate SCDA expansion, by combining Eqs. 4 and 6 with Eq.7, and collapsing all parameters to an equivalent single value, V_{ini} (Eq. 8). In Eq.8, V_{ini} is the initial velocity applied to the rock-SCDA boundary, t_{mech} is the current mechanical time of the 3DEC model, and b' is an adjusted reactivity factor in the simulation time of the numerical model. Further details of the proposed model and calibration method are described by De Silva et al. (2024).

$$V = V_{ini} \cdot e^{-b' \cdot t_{mech}} \tag{8}$$

By calibrating V_{ini}, and b' in Eq.8 for the SCDA expansion in the rock joint and the borehole, the total work done in the simulation can be calibrated to match the experimental observations. The velocity decay functions and the corresponding work done in the calibrated model are shown in Fig. 3a and b respectively. Fig. 3c shows the numerical assembly with rock blocks and the SCDA expansion regions and the reaction stress produced by SCDA expansion in the rock joint is shown in Fig. 3d, which is similar to the experimental observations (Fig. 2d). The calibrated model was first compared against a laboratory SCDA fracturing test performed under uniaxial compressive stress of 10 MPa. The model was used to simulate SCDA expansion under different in-situ stress conditions after the comparison.

4 Results of SCDA simulation

4.1 Laboratory scale fracturing tests under uniaxial compression

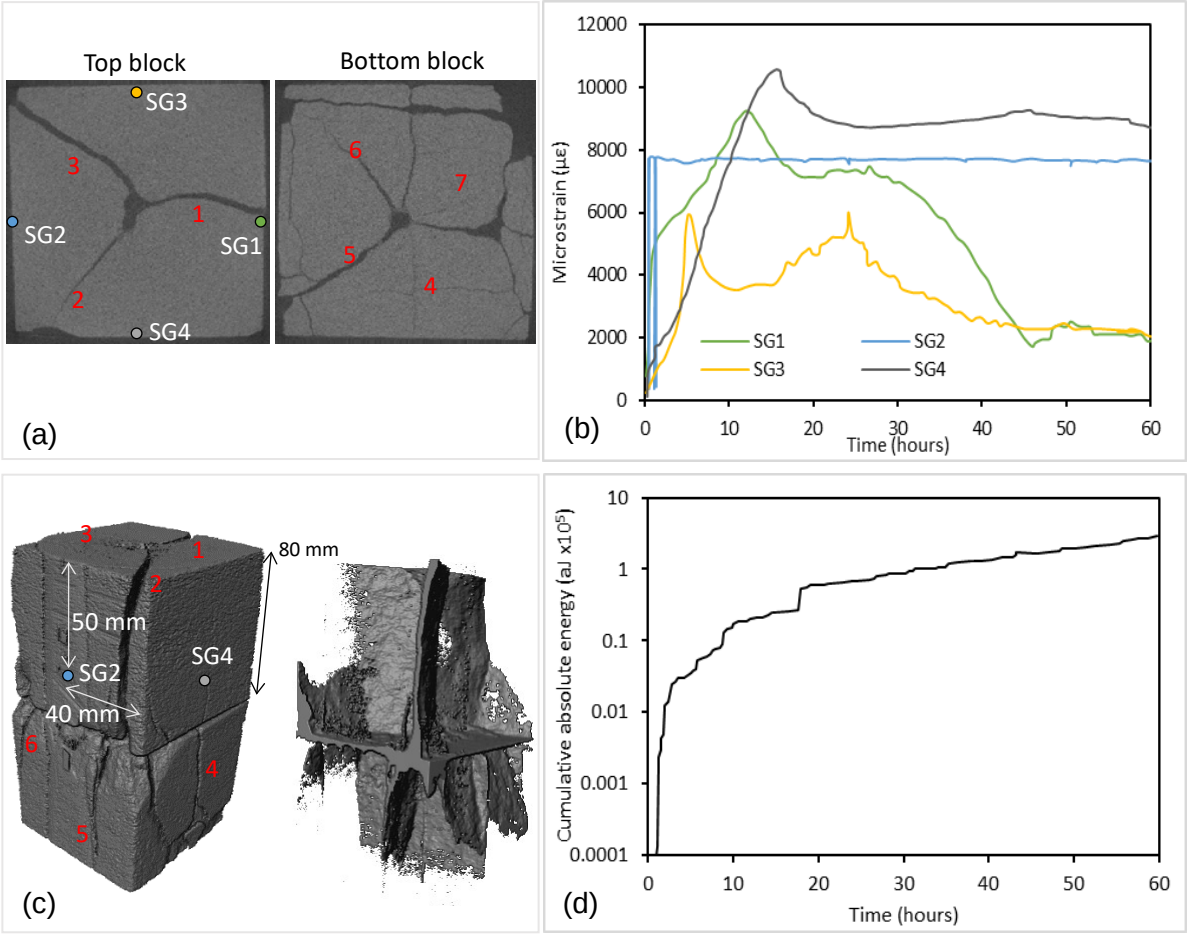

Fig. 4: Fracture test experimental results, (a) Fracture pattern of the top and bottom blocks (b) Strain measurements in SG1-SG4, (c) CT reconstruction of the fractured specimen (left) and the fracture network (right), and (d) Cumulative AE measurement during fracture test. Strain gauge positions are indicated by SG1-4 in white, and the main fractures are denoted by 1-7 in red (De Silva et al., 2024).

The laboratory fracturing experiment under uniaxial stress of 10 MPa fractured the sandstone specimen, as illustrated in Fig. 4. X-ray Computer Tomography (CT) scans revealed three main fractures in the top block and four in the bottom block, independent of each other, with additional minor axial splitting observed at the specimen boundary (Fig. 4a). Lateral strain measurements (SG1 to SG4) on the top block indicated localized strain peaks followed by a drop in the strain (Fig. 4b). This indicates elastic strain energy releases in the rock specimen during fracture propagation. SG1 and SG4 showed simultaneous fracture growth, while SG3 recorded lower, double peaks. SG2 exhibited an abrupt strain increase likely due to axial splitting near the joint. SG4 displayed gradual fracture propagation, with peak microstrain observed 16 hours after test initiation. Acoustic Emission (AE) monitoring showed initial accumulation due to fracture initiation and propagation, followed by steady growth from fracture opening (Fig. 4d). X-ray CT reconstructions highlighted larger millimetre-scale fracture apertures resulting from SCDA expansion (Fig. 4c).

4.2 Numerical simulation of the fracturing test under uniaxial compression

A numerical simulation replicating the laboratory conditions was conducted to understand SCDA expansion in rock joints and its effect on rock fracturing performance. The simulation applied an axial displacement boundary condition to achieve a 10 MPa vertical stress, then ran the SCDA expansion in the injection well and rock joint for 48,000 steps over a mechanical time of 0.004 seconds. The SCDA expansion was capped by strain energy densities of 3.7 MJ/m³ for the injection well and 0.91 MJ/m³ for the infilled joint. This was achieved by setting the SCDA-rock boundary velocities to zero when the work done by SCDA expansion reached 36 J in the borehole and 15 J in the rock joint. The simulation revealed a vertical stress distribution due to the expansion of the rock joint (Fig. 5a). Four main radial fractures in the top block and three in the base block were observed (Fig. 5b and c), differing from the experimental pattern. This discrepancy is mainly due to the predefined crack paths around the injection well boundary in the numerical model. Nevertheless, the typical Y-shaped and Star-shaped fracture patterns produced by SCDA charging were simulated in the model. The expansive pressure development and the tensile and shear cracks formed in the model are shown in Fig.5d.

The simulated fracture patterns, cumulative crack count (tensile and shear) and strain responses were comparable to experimental observations. Strain measurements in SG1 to SG4 (Fig. 5e) indicated similar strain responses, with peak strain increments observed as fractures propagated to the specimen boundary. The model also captured the characteristic double peak event in SG4, reflecting fracture propagation and bifurcation. The tensile and shear crack count evolution (Fig. 5d) showed a similar trend to what was observed in the AE results. Overall, the Strain energy based simulation method of expanding bodies effectively replicated SCDA charging characteristics and provided a foundation for further investigation.

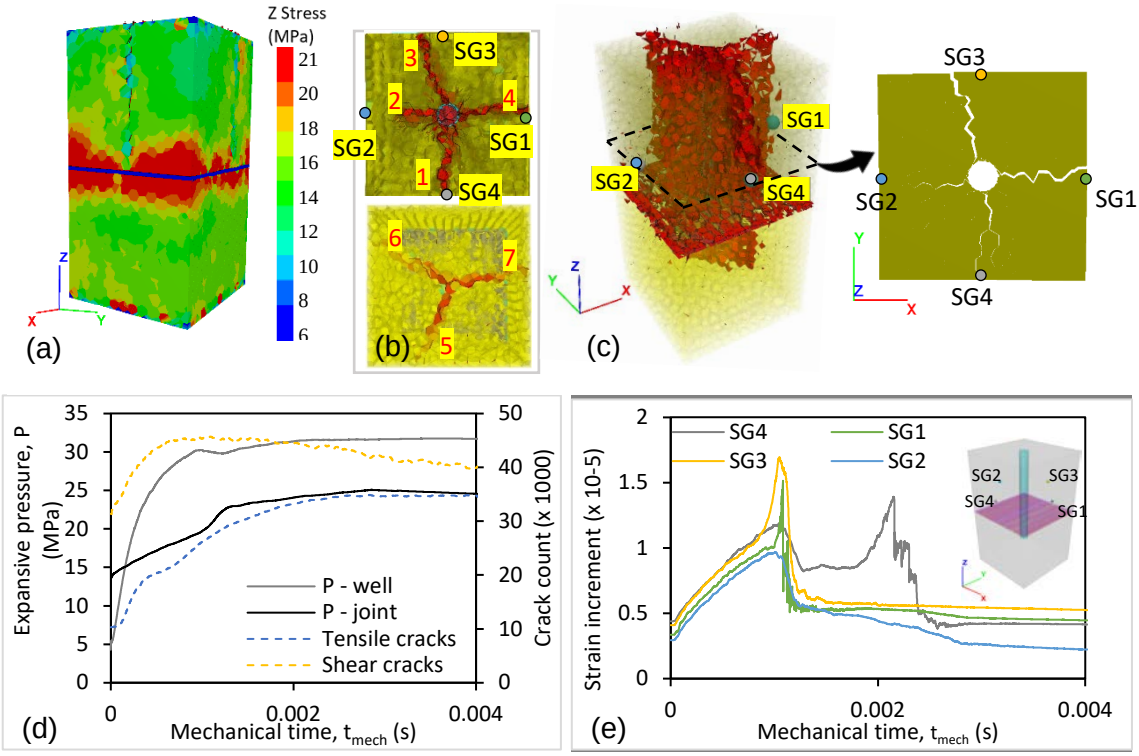

Fig. 5: SCDA charged fracturing in the numerical model. (a) Vertical stress distribution due to SCDA expansion in the joint, (b) final fracture pattern at the top (above) and base (below) blocks, (c) fracture pattern of the specimen. Strain measurement positions are indicated by SG1 to SG4, and the main fractures are denoted by 1 to 7 in red. (d) Expansive pressure in the joint and the injection well, and crack counts, (e) lateral strain measurements at SG1 to SG4.

4.3 Model sensitivity to confining pressure

SCDA expansion in jointed rock exhibited significant variations under lateral confinement pressures of 0 MPa, 0.5 MPa, and 1.5 MPa (Fig. 6a). At 0 MPa confinement, the specimen experienced complete splitting, with abrupt plummeting of strain increments at the boundaries (Fig. 6b), indicating rapid fracture propagation and the highest tensile crack count, reflecting extensive radial fractures and the lowest shear cracking (Fig. 6c). Expansive pressure buildup in the injection well also sensitive to the applied confinement, where the peak expansive pressure increased with confinement applied to the specimen (Fig. 6d). Under 0.5 MPa confinement, the extent of radial fractures was reduced, strain increments initially increased and then stabilized, and the expansive pressure moderately increased. The tensile crack count significantly dropped, while shear cracks gradually increased. At 1.5 MPa confinement, the extent of radial fractures further decreased and became more localized around the injection well, with lower peak strain increments stabilizing more quickly. The expansive pressure showed a marginal increase, and the shear crack count continued to rise due to restricted strain energy release through tensile failure, leading to more pronounced shear fracturing.

The extent of the fractures seems to be dominated by the tensile hoop stress field applied around the injection well by the SCDA expansion as shown in Fig.6b. Overall, increasing lateral confinement increased the peak expansive pressure, shifted the dominant fracturing mode from tensile to shear, and reduced radial fractures as the finite strain energy release of the SCDA is insufficient to propagate fractures.

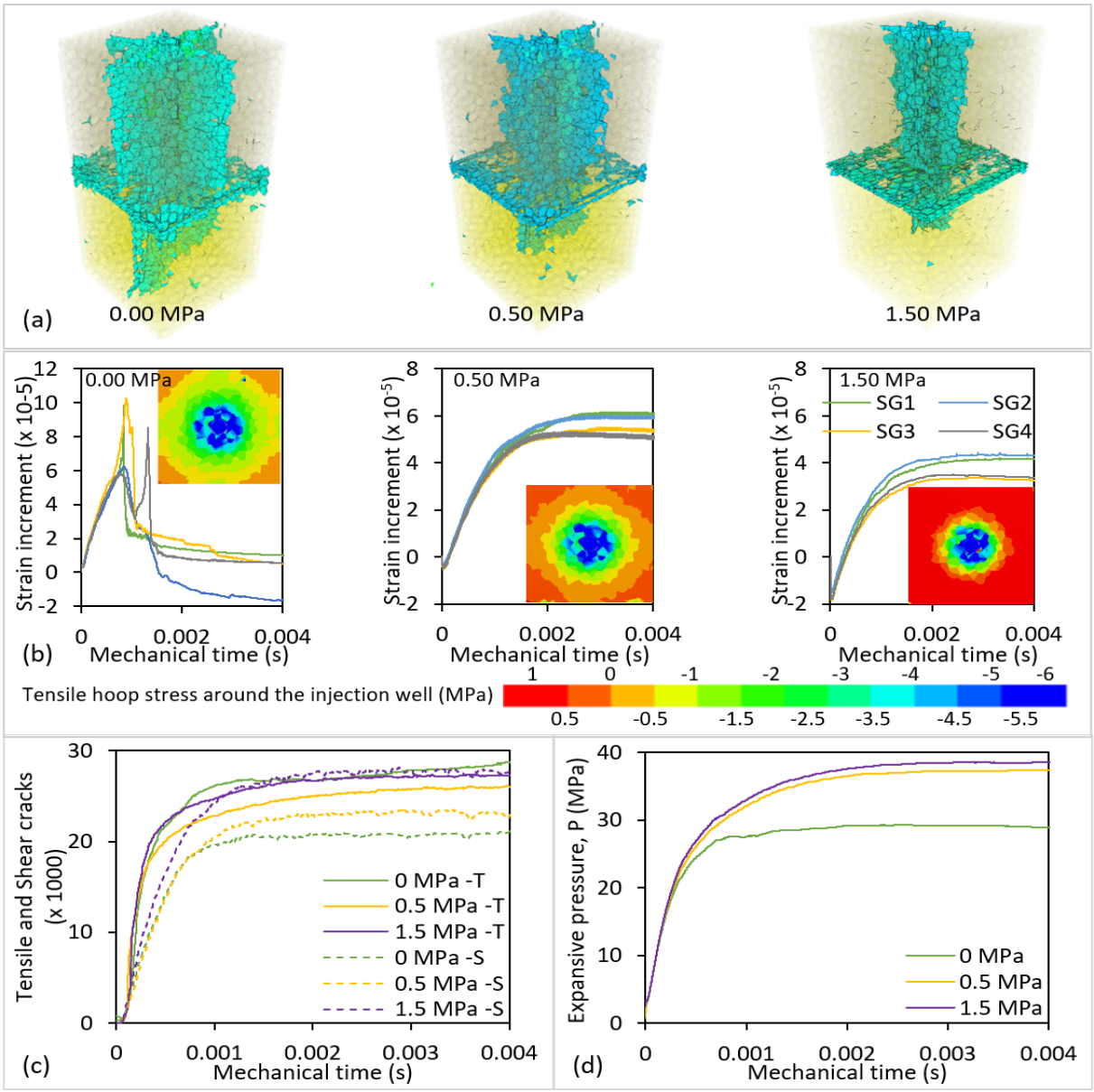

Fig.6: Fracture propagation in confined conditions (0 MPa, 0.5 MPa, and 1.5 MPa), (a) final fracture pattern, (b) strain increment (SG1 – SG4), (c) tensile and shear crack count and, (d) expansive pressure development in the borehole

5 Limitations of SCDA and a possible alternative

As demonstrated in the numerical simulations, with the low strain energy density of SCDA, the fracturing performance greatly reduces when the confining stress increases around the injection well. Furthermore, once expanded the SCDA cannot be removed easily from the injection well, although there have been some studies to dilute and remove injected SCDA (Manatunga, 2023), this hasn't been achieved in an injection well filled with SCDA. In addition, SCDA is not reusable and the production of SCDA has a carbon footprint equivalent to that of cement production. The extreme sensitivity to temperature is another critical factor, where at high temperatures (generally in excess of 40°C ambient temperature) SCDA violently reacts with uncontrollable expansion making it unsuitable in some underground applications unless further modified.

5.1 Shape Memory Alloys (SMA)

Considering the limitations of SCDA, Shape memory alloy (SMA) actuators are a possible alternative for subsurface rock fracture stimulation applications requiring repeated cyclic loading, such as near well-bore fracture activation in geothermal reservoirs for efficient heat transfer. SMA undergo a solid phase transition Martensite, Ma (low energy) to Austenite, As (high energy) state when thermally triggered (Benafan et al., 2014) allowing plastic deformation at low temperatures (Twinned to Detwinned Martensite, black path in Fig 8a) and then recovering its original state once heated above the As transition temperature (red path in Fig 8a), giving 'Shape Memory' properties. This reversible property of SMA makes it a heat engine capable of converting heat into mechanical motion. Furthermore, if the Ma -As transition is restricted during heating, SMA produces large reaction stresses in the order of several hundred Megapascals (Du et al., 1995). These recovery stresses produced by SMA during its linear actuation are sufficient to fracture intact rock.

Binary SMA cylinders with a 10 mm height and 8.8 mm diameter, consisting of $NiTi_{50}$ were used in this study to investigate its potential in rock fracturing applications. The thermal hysteresis in the SMA between Austenite and Martensite phase transitions and the resultant extension and contraction of the specimen observed due to heating and cooling is shown in Fig.8b. SMA also exhibits excellent fatigue life with minimal plastic deformation under cyclic loading in the Martensite state (Fig 8c). Following the fatigue life estimation, the SMA elements were conditioned for axial expansion by thermal cycling between 20 and 120°C at 330 MPa axial stress to impart the shape memory effect. The axial deformation of SMA elements during this process termed isobaric training (Benafan et al. 2016; Karakoc et al. 2020) is shown in Fig. 8d.

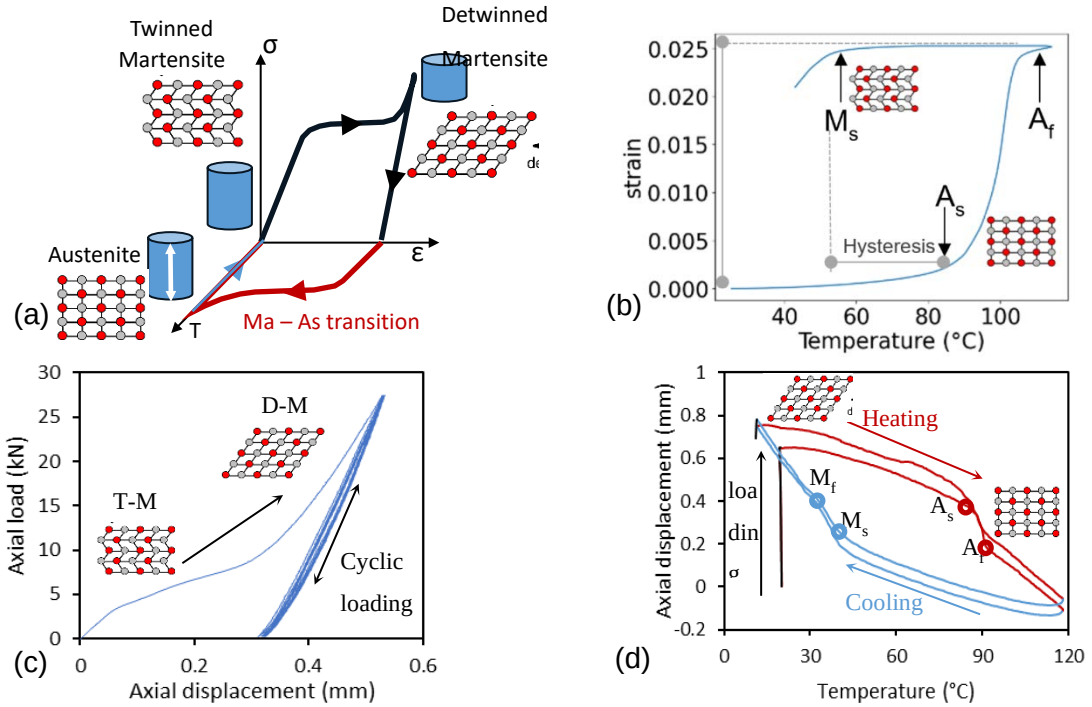

Fig. 8: Shape Memory effect of $NiTi_{50}$ (a) Phase transition of SMA, (b) thermal hysteresis of SMA phase transition, (c) transition from Twinned Martensite, T-M to Detwinned Martensite, D-M and fatigue response under cyclic loading, and (d) isobaric training of SMA elements at 330 MPa under cyclic heating and cooling.

Following the training process, the SMA elements are axially compressed to 9.4 mm under room temperature to reach the Detwinned Martensite state (Fig.8a) in preparation for fracturing tests. A mechanical splitter housing four SMA elements encased in two steel contact plates was produced to apply the actuation strain inside a pre-drilled borehole (Fig. 9a). The splitter was then placed in a sandstone specimen and heated to 140°C to trigger the phase transition.

Fig. 9b shows the fabricated SMA splitter for the fracturing experiments.

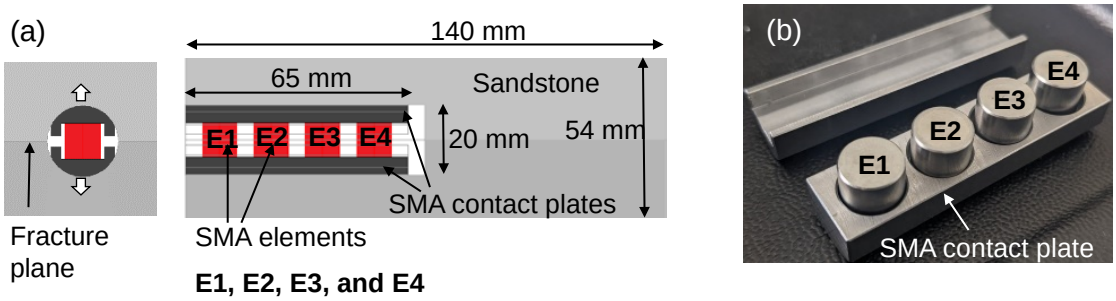

Fig.9: SMA splitter in borehole (a) schematic diagram of the splitter in a sandstone specimen with a 20 mm diameter borehole, and (b) SMA splitter.

5.2 Strain energy density of SMA and fracture testing.

The strain energy density of SMA was estimated during the isobaric training process. The extension and the contraction of the specimen during thermal cycling are shown in Fig. 10a (compression positive). First, the SMA element was compressed (i-ii) to reach an axial stress of 330 MPa, then subjected to two thermal cycles between 20°C and 120°C (ii-vi), and finally unloaded (vii). The loading path of a single SMA element during isobaric training is shown in Fig. 10b. Measuring the SMA deformation during isobaric training allows the strain energy in SMA to be calculated under the applied normal load (20.9 kN ~ 330 MPa in applied stress) as shown in Fig. 10b. Considering a mean actuation displacement of 0.7 mm during thermal cycling under the applied normal load, the strain energy density of SMA is approximately 23.1 MJ/m^3 compared to the strain energy density of SCDA at approximately 3.7 MJ/m^3 (De Silva and Ranjith 2019b). In addition to the repeated possibility of actuation by thermal cycling, SMA exhibits a strain energy density approximately 7 times greater than that of modified SCDA systems.

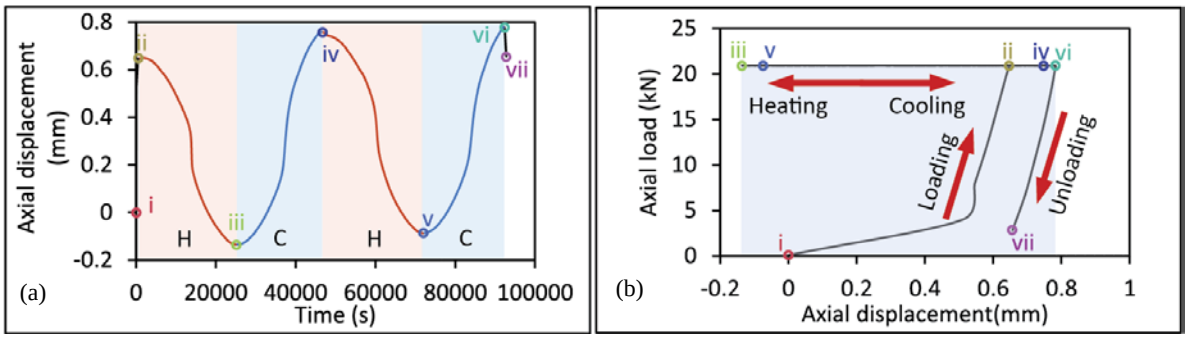

Fig. 10: Isobaric deformation of SMA (a) Expansion and contraction of SMA during thermal cycling (Red indicates heating up to 120°C, blue indicates cooling down to 20°C and compression is taken as positive) and (b) axial load vs. displacement for strain energy calculation. The initial loading point, heating and cooling inversion points and the final unloading points are indicated by i – vii in the figures.

5.3 Fracture Experiment and Numerical simulations of SMA.

Adopting the previously proposed strain-energy dependent numerical simulation method for SCDA systems, a numerical model was produced to simulate rock fracturing using SMA actuation. The expansion of the SMA elements in the numerical model was constrained by the strain energy and the maximum actuation strain of the SMA elements. The approximate function for the expansion of SMA during the heating cycle can be written as shown in Eq. 9.

$$y = A\,(\cos(\omega t + \phi)) \tag{9}$$

where, Y is the displacement, A is the amplitude, ω is the frequency, t is the time and ϕ is the phase shift in the curve. Considering the displacement of the SMA element from ii to iii in Fig. 10a (1/2 wavelength), the velocity of the SMA boundary during the expansion can be written as

$$V = \frac{dy}{dt} = -A.\omega(\sin(\omega t + \phi)) \tag{10}$$

The approximate functions for the expansion and the corresponding boundary velocity as shown in Fig.11a for the first expansion of the SMA were obtained with the coefficients A=0.39, ω=1.27e^{-4}, ϕ=0. This velocity boundary function was then applied in 3DEC at the SMA contact interface to simulate expansion. However, the mechanical simulation time in 3DEC, t_{mech} was limited to 0.001 s by changing the frequency and the strain energy was calibrated by fine-tuning the amplitude in Eq.10 to apply the finite strain energy of the SMA element to the surrounding rock. The strain energy of a single SMA element tested is 16.09 J (see Fig. 10b). The calibration was done by tuning the A, ω parameters to match the strain energy applied by a single SMA element expanding under uniaxial compression of 330 MPa in the 3DEC model. In this paper, the maximum SMA element actuation strain in the numerical model was limited to 2.3%. This is because the actuation strain of SMA in practical application is between 2% to 4% (Saikrishna et al., 2013). Thus, the expansion boundary velocity function due to the thermally triggered phase transition was calibrated as shown in Eq.11 in which $A.\omega$= 0.174, and ω=3140.

$$V = 0.174 \cdot \sin(3140 \cdot t_{mech}) \tag{11}$$

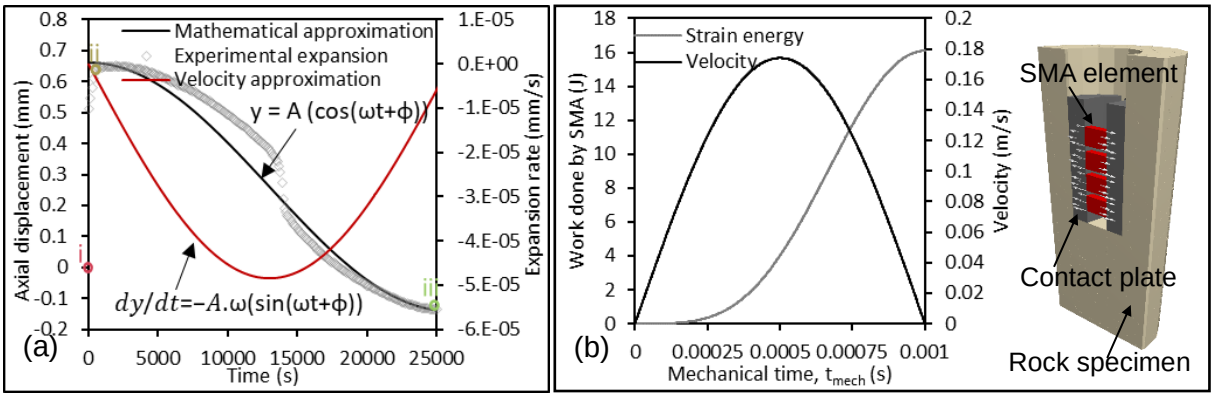

Fig. 11: SMA expansion (a) fitting curve for the thermally triggered expansion of SMA due to phase transition, (b) equivalent boundary velocity application at the SMA plug interface in the numerical model, and the corresponding strain energy per SMA element. The applied velocity at the SMA elements (red) and the splitter contact plates (grey) in the borehole are indicated by the white arrows.

The fracturing experiment was performed in a 54 mm diameter 160 mm length sandstone specimen with a 20 mm diameter borehole drilled to a depth of 70 mm. The trained splitter was then placed in the borehole and heated to 120°C to actuate the splitter. The observed fracture pattern of the experiment is shown in Fig.12a. Compared to SCDA, due to the linear actuation of the SMA, a single diametrical tensile fracture is produced perpendicular to the actuation direction (indicated by the white arrows in Fig.12a) of the SMA splitter. Although similar experiments have been performed previously (Nishida et al., 1990, Yamauchi et al., 1992, Benafan et al., 2016) the calibrated SMA model in addition to successfully simulating the fracturing process in 3DEC (Fig.12b) provided insights into the total strain energy released, applied stress and strain by each element as shown in Figs. 12c-e. This facilitates the assessment of SMA performance under various in-situ stress conditions as this aspect has not been previously investigated, particularly considering underground applications.

As indicated by Fig.12b, SMA induced fractures are mainly tensile with some shear induced fractures initiating mainly due to the slip of the splitter in the borehole. The diametral strain is highest at the free surface of the rock specimen at E1, and the lowest is at the base of the borehole at E4 (Fig.12c). Consequently, the largest normal fracture aperture was observed at the top of the specimen at 0.64 mm (Fig.12b fracture aperture) which is consistent with the experimental observation of 0.52 mm. However, in contrast, the greatest actuation stress and the strain energy release were recorded at the base (E4) of the splitter owing to the additional lateral restraint provided by the surrounding rock. In addition, once fully actuated, the reaction stress on the elements E1, E2, and E3 diminished to near zero, while the reaction stress on E4 remained at 20 MPa (Fig.12d). The residual reaction stress in E4 is resultant of the lateral restraint of the specimen at the base of the borehole, where the fracture did not fully split the specimen. The diametrical fracture propagation was therefore limited by the actuated length of the SMA elements in the splitter, which was also seen in the fracturing experiment. Following these observations, the numerical model was then extended to simulate rock fracturing under confined conditions.

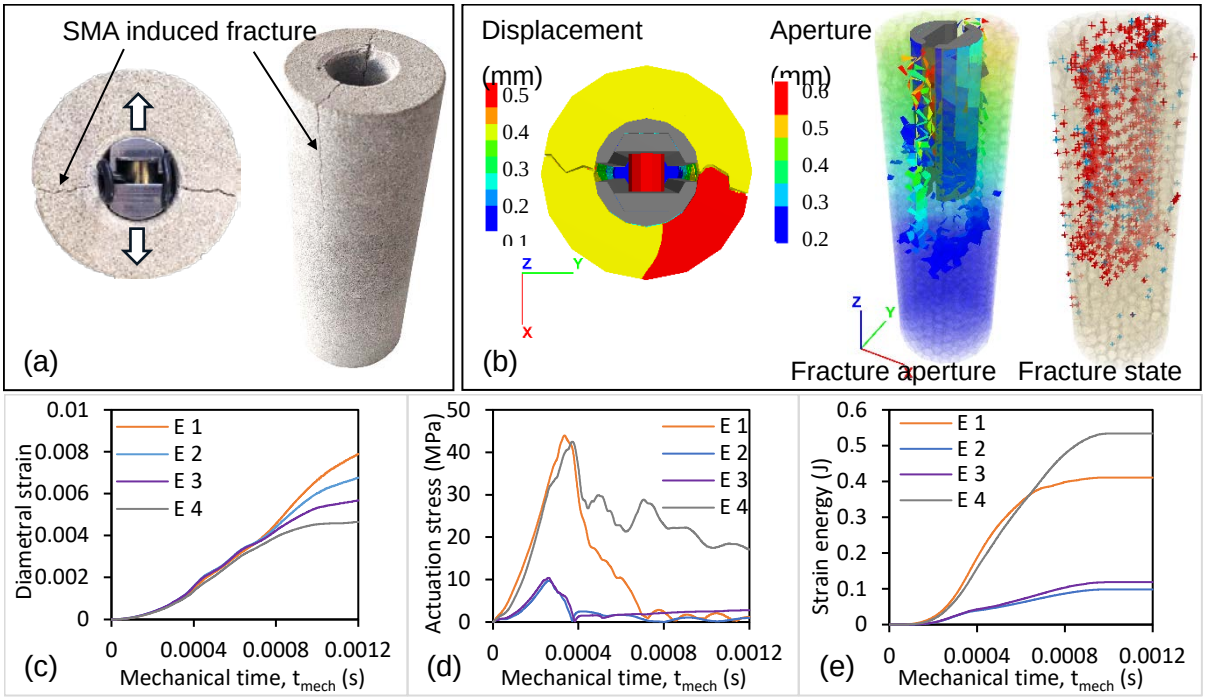

Fig.12: Rock fracturing using the SMA splitter. (a) the experimentally observed diametrical fracture terminating at specimen mid-depth, (b) numerically simulated fracture pattern, with fracture aperture and fracture state (tensile fractures in red, and shear fractures in blue), numerical simulation results, (c) diametral strain around the specimen at SMA element positions, (d) actuation stress produced by SMA elements, and (e) strain energy released by SMA elements.

5.4 SMA fracturing under in-situ stress conditions

For a direct comparison of the fracturing performance with SCDA, SMA induced fracturing was simulated under the same stress conditions and block geometry was simulated for SCDA charged fracturing in Section 4.3. The fracturing performance of the SMA splitter is shown in Fig.13 in a rock block under uniaxial stress of 1 MPa (Similar to Fig.6a). The splitter was positioned at the base of the 20 mm diameter borehole at a depth of 120 mm from the specimen top surface.

Under zero confinement, SMA produced a single planar fracture (Fig.13a), compared to the two fracture planes observed in SCDA charging. The single planar fracture observed in SMA induced fracturing is due to the unidirectional load application by the splitter as opposed to the radial expansion applied by SCDA (Fig.1). Consequently, the strain measurements at SG1 to SG 4 in the specimen vary from what was observed for SCDA. On the two planes perpendicular to the splitter actuation direction (SG2 and SG4), elastic strain gradually builds up (extension is positive) until the fracture reaches the specimen boundary. This is followed by a steep reduction in the strain increment as the elastic strain energy of the rock specimen is released (Fig.13b). Strain increment measurements in the planes parallel to the splitter actuation direction are first negative at the surface resultant from a bending action produced by the SMA splitter actuation orthogonal to the fracture plane (Fig. 13a). However, as the fracture propagates to the boundary, the extensional strain increment spikes as the specimen is split by the SMA actuators (Fig. 13b). The actuation stresses and the utilized strain energy is highest in the SMA elements E1 and E4 at the boundary of the splitter (Fig.13c and d). Under zero confinement, after splitting the specimen, the actuation pressure reduces to zero. The observations further indicate the central SMA elements (E2 and E3) in the splitter do not fully utilize the strain energy of the elements under low confinement.

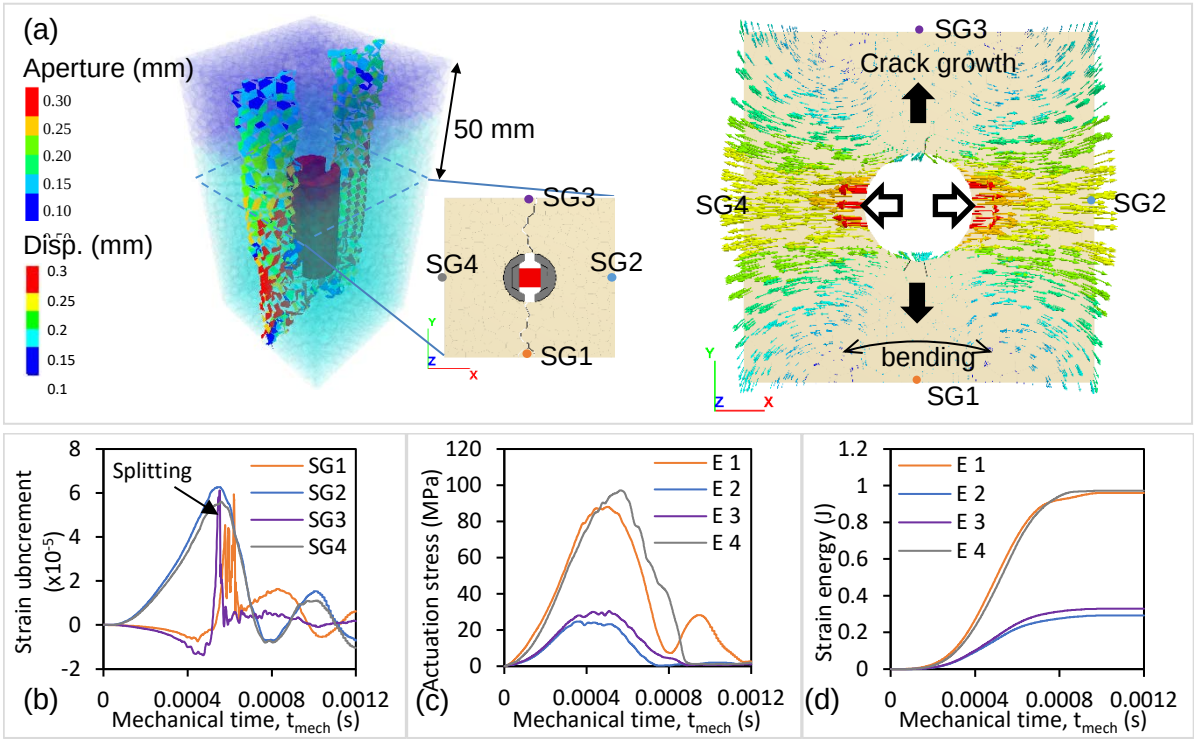

Fig.13: SMA induced fracturing in rock block (a) single planar fracture, the position of strain gauges and unidirectional strain application, (b) strain increment (SG1 – SG4), (c) actuation stress and (d) strain energy release in SMA elements (E1-E4)

Simulating SMA induced fracturing at a confining stress of 1.5 MPa (Fig.14a), shows a significant reduction in the fracture area produced, similar to the trend in the SCDA system (Fig.6). However, in contrast to the SCDA system, where the fracturing is restrained by the strain energy release of SCDA, the SMA induced fracture is restrained by the maximum actuation strain of SMA elements. This is evident by the maximum actuation stress and the utilized strain energy of the SMA element as shown in Figs. 14b and c, where neither the peak actuation stress (~ 600 MPa) (Du et al., 1995) nor the maximum strain energy per element (~ 16.1J) was reached. Despite its capability of repeated cyclic actuation and high strain energy density, the limited serviceable actuation strain of SMA elements is one of the main drawbacks.

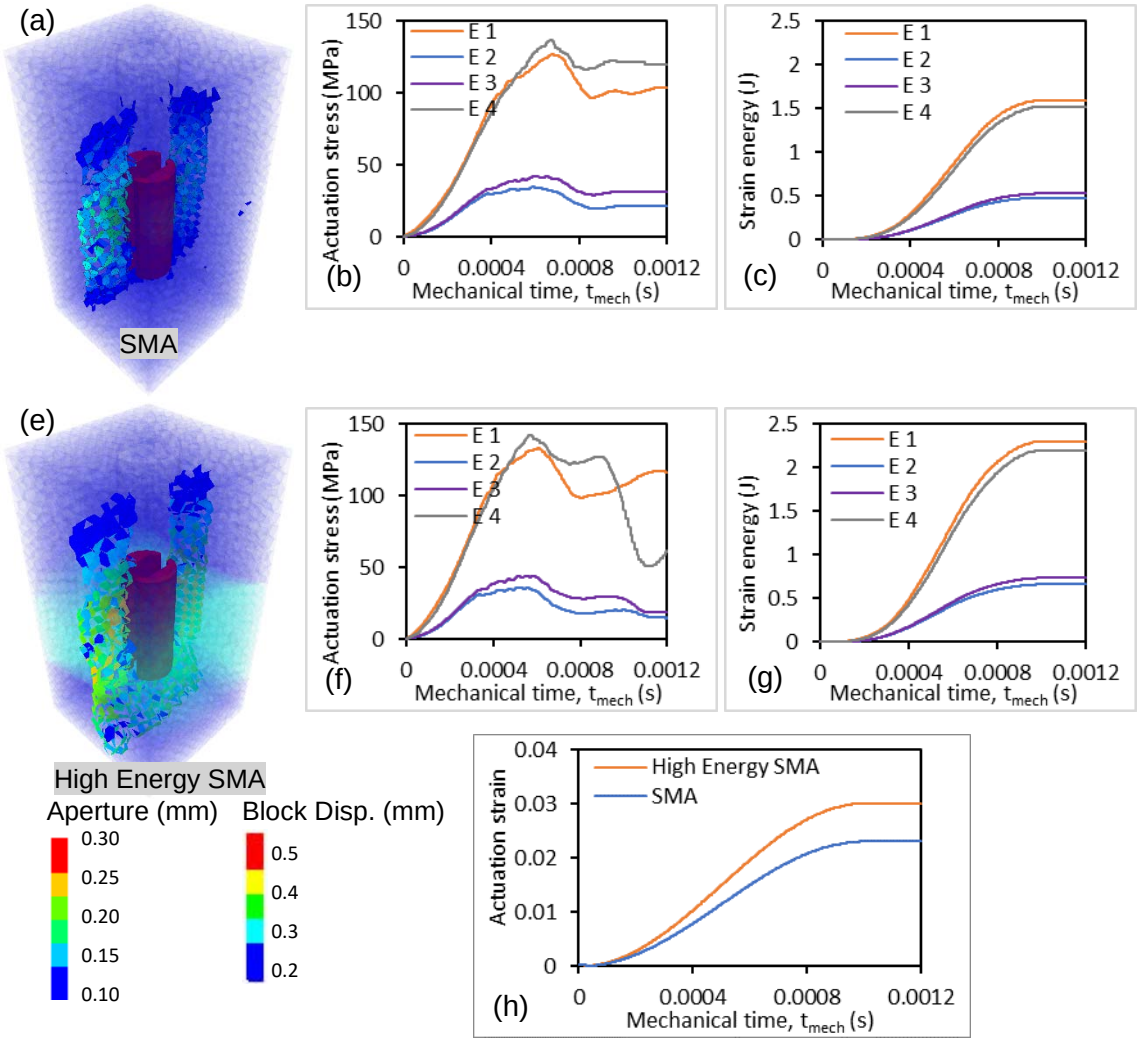

Fig.14: Mechanical splitter induced fracturing in rock block. Final fracture pattern, strain increment, actuation stresses, and strain energy released for SMA induced fracturing (a-c), High Energy SMA induced fracturing (d-g), and (h) actuation strains.

Fig.14e illustrates the same block at 1.5 MPa confinement, fractured with a simulated SMA having a higher strain energy density at 30 MJ/m^3 and, the maximum actuation strain at 3%. The increased energy density and the actuation were achieved by modifying the boundary velocity equation as shown in Eq.12 and the maximum strain energy of a single plug was capped at 20.85 J.

$$V = 0.227 \cdot \sin(3140 \cdot t_{mech}) \tag{12}$$

Despite having similar peak actuation stresses (Fig.14f), the strain energy release is greater in the simulation with the higher strain energy cap (Fig.14g). This is primarily due to the greater actuation strain allowed in the High Energy SMA model compared to the standard model (Fig. 13(h)).

6 Future directions for SMA actuated fracturing

The High Energy SMA simulated in Section 5.4 of this study is produced as a ternary alloy consisting of $Ni_{50.3}Ti_{29.7}Hf_{20}$ in practice and has been used for rock-splitting applications (Benafan et al., 2016). Although not commercially viable yet (Benafan et al., 2021), High Energy SMAs have demonstrated larger recovery stresses in excess of 1.5 GPa, and consistent actuation strains above 4%. The numerical models presented in this paper lay the foundation for further developing the SMA splitter concept for subsurface rock fracture actuation applications. Additionally, the proposed method may be used to prop open near wellbore pre-existing fractures for applications such as subsurface energy storage and extraction processes.

7 Conclusions

This study presented a novel strain energy based modelling method to numerically simulate the fracture initiation and propagation around an injection well filled with Soundless Cracking Demolition Agents (SCDA). The proposed simulation method relies on the strain energy density of SCDA to calculate the expansive pressure produced by SCDA when it is expanded in boreholes. The calibration of the SCDA expansion model which is implemented in 3D Discrete Element code is independent of the stress boundary conditions and the modelling method can be extended to other expansion bodies with varying geometries.

SCDA charged fracture simulations performed under increasing stress boundary conditions reveal the limitations of the SCDA charging method, mainly due to the low strain energy density of SCDA (3.7 MJ/m^3). In the second part of the study, to tackle the limitations of SCDA charged fracturing, a novel method of utilizing high energy (23 MJ/m^3) rock splitters produced by Shape Memory Alloy (SMA) actuators to induce fractures around boreholes is presented. The strain energy based modelling method was successfully extended SCDA to simulate fracture initiation and propagation using the SMA rock splitters. The numerical simulation results provided insights into the mechanics of fracture initiation and propagation with SMA rock splitters.

SMA rock splitters, while having limitations of their own, show potential to be used for subsurface rock fracture actuation applications such as underground energy storage and recovery. The numerical modelling methods presented in this study lay the foundation for the design and execution of laboratory scale experiments to further assess the applicability of SMA rock splitters for underground applications.

8 References

ARSHADNEJAD, S. 2019. Design of hole pattern in static rock fracture process due to expansion pressure. *International Journal of Rock Mechanics and Mining Sciences,* 123**,** 104100.

BENAFAN, O., BIGELOW, G. S., GARG, A., NOEBE, R. D., GAYDOSH, D. J. & ROGERS, R. B. 2021. Processing and scalability of NiTiHf high-temperature shape memory alloys. *Shape Memory and Superelasticity,* 7**,** 109–165.

BENAFAN, O., GARG, A., NOEBE, R., BIGELOW, G., PADULA II, S., GAYDOSH, D., SCHELL, N., MABE, J. & VAIDYANATHAN, R. 2014. Mechanical and functional behavior of a Ni-rich Ni50. 3Ti29. 7Hf20 high temperature shape memory alloy. *Intermetallics,* 50**,** 94-107.

BENAFAN, O., NOEBE, R. D. & HALSMER, T. J. 2016. Static rock splitters based on high temperature shape memory alloys for planetary explorations. *Acta Astronautica,* 118**,** 137–157.
CHEN, T., VENNES, I. & MITRI, H. S. 2023. Biaxially Confined Rock Breakage with SCDA: Large-Scale Tests and Numerical Modelling. *Rock Mechanics and Rock Engineering***,** 1-17.

CHO, H., NAM, Y., KIM, K., LEE, J. & SOHN, D. 2018. Numerical simulations of crack path control using soundless chemical demolition agents and estimation of required pressure for plain concrete demolition. *Materials and Structures,* 51**,** 169.

DE SILVA, R. V., PATHEGAMA GAMAGE, R. & ANNE PERERA, M. S. 2016. An Alternative to Conventional Rock Fragmentation Methods Using SCDA: A Review. *Energies,* 9.

DE SILVA, V. R. S., KONIETZKY, H., MEARTEN, H., RANJITH, P. G. & KUMARI, W. G. P. 2023. A Hybrid Approach to Rock Pre-conditioning Using Non-explosive Demolition Agents and Hydraulic Stimulation. *Rock Mechanics and Rock Engineering*.

DE SILVA, V. R. S., KONIETZKY, H., RANJITH, P. G. & MANATUNGA, U. I. 2024. Strain energy dependent numerical simulation of rock fracture initiation and propagation using soundless cracking demolition agents (SCDA): Effects of SCDA-filled rock joints. *International Journal of Rock Mechanics and Mining Sciences,* 177**,** 105740.

DE SILVA, V. R. S. & RANJITH, P. G. 2019a. Evaluation of injection well patterns for optimum fracture network generation host-rock formations: An application in in-situ leaching. *Minerals Engineering,* 137**,** 319–333.

DE SILVA, V. R. S. & RANJITH, P. G. 2019b. Intermittent and multi-stage fracture stimulation to optimise fracture propagation around a single injection well for enhanced in-situ leaching applications. *Engineering Fracture Mechanics,* 220**,** 106662.

DE SILVA, V. R. S. & RANJITH, P. G. 2020. A study of rock joint influence on rock fracturing using a static fracture stimulation method. *Journal of the Mechanics and Physics of Solids,* 137**,** 103817.

DE SILVA, V. R. S., RANJITH, P. G., PERERA, M. S. A. & WU, B. 2019. Artificial fracture stimulation of rock subjected to large isotropic confining stresses in saline environments: application in deep-sea gas hydrate recovery. *Natural resources research,* 28**,** 563–583.

DE SILVA, V. R. S., RANJITH, P. G., PERERA, M. S. A., WU, B. & WANNIARACHCHI, W. A. M. 2018. A low energy rock fragmentation technique for in-situ leaching. *Journal of Cleaner Production,* 204**,** 586–606.

DU, Y., NIE, J., ZHANG, X. & ZHAO, C. Tests and Expressions of the Recovery Effect of NiTi Shape Memory Alloys. Turbo Expo: Power for Land, Sea, and Air, 1995. American Society of Mechanical Engineers, V005T12A016.

GAMAGE, R. P. & DE SILVA, R. S. V. 2020. Demolition agent. Google Patents.

GOTO, K., KOJIMA, K. & WATABE, K. 1988. The mechanism of expansive pressure and blow-out of static demolition agent. *Conference of Demolition and Reuse of Concrete and Masonry.*

GROB, H. 1972. Schwelldruck im belchentunnel. *Proc. Int. Symp. für Untertagebau, Luzern.*

GUO, T., ZHANG, S., GE, H. & QU, Z. 2015. A Novel" Soundless Cracking Agent Fracturing" for Shale Gas Reservoir Stimulation. *International Journal of Environmental Science and Development,* 6**,** 681.

HARADA, T., IDEMITSU, T., WATANABE, A. & TAKAYAMA, S.-I. 1989. The design method for the demolition of concrete with expansive demolition agents. *Fracture of Concrete and Rock.* Springer.

HINZE, J. & BROWN, J. 1994. Properties of Soundless Chemical Demolition Agents. *Journal of construction engineering and management,* 120**,** 816–827.

LI, F. 2017. *Discrete element based numerical simulation of crack formation in brittle material by swelling cement.* Ph.D, Technical University Bergakadamie Freiberg.

LI, R., YAN, Y., JIANG, Z., ZHENG, W. & LI, G. 2021. Impact of hole parameters and surrounding constraint on the expansive pressure distribution and development in soundless chemical demolition agents. *Construction and Building Materials,* 307**,** 124992.

LIU, J., ZHANG, L., WEI, Y. & WU, Z. 2021. Coupling Model of Stress–Damage–Seepage and Its Application to Static Blasting Technology in Coal Mine. *ACS Omega,* 6**,** 34920–34930.

LIYANAGE, J. B. & GAMAGE, R. P. 2021. The Hydration and Volume Expansion Mechanisms of Modified Expansive Cements for Sustainable In-Situ Rock Fragmentation: A Review. *Energies,* 14**,** 5965.

LIYANAGE, J. B., RANJITH, P. G. & KUMARI, W. G. P. 2022. A study of the short-term leaching behaviour of a modified expansive cement in groundwater for mining and mineral extraction. *Process Safety and Environmental Protection,* 166**,** 682–692.

MANATUNGA, U. I. 2023. *Preconditioning of mineral bearing rock formations for permeability enhanced in-situ leaching application.* PhD, Monash University.

MANATUNGA, U. I., RANJITH, P. G. & DE SILVA, V. R. S. 2022. Enhancing rheological properties of slow releasing energy material (SREMA) for rock fragmentation under submerged conditions. *Construction and Building Materials,* 327**,** 126935.

MANEENOI, N., BISSEN, R. & CHAWCHAI, S. 2022. Influence of admixtures on the performance of soundless chemical demolition agents and implications for their utilization. *Journal of Sustainable Mining,* 21.

NATANZI, A. S., LAEFER, D. F. & ZOLANVARI, S. M. I. 2020. Selective demolition of masonry unit walls with a soundless chemical demolition agent. *Construction and Building Materials,* 248**,** 118635.

NISHIDA, M., KANEKO, K., INABA, T., HIRATA, A. & YAMAUCHI, K. 1990. Static rock breaker using TiNi shape memory alloy. *Materials Science Forum.*

SAIKRISHNA, C. N., RAMAIAH, K. V., BHAGYARAJ, J., GOUTHAMA & BHAUMIK, S. K. 2013. Influence of stored elastic strain energy on fatigue behaviour of NiTi shape memory alloy thermal actuator wire. *Materials Science and Engineering: A,* 587**,** 65-71.

SAKHNO, I. & SAKHNO, S. 2024. Directional fracturing of rock by soundless chemical demolition agents. *Heliyon,* 10.

TANG, S. B., HUANG, R. Q., WANG, S. Y., BAO, C. Y. & TANG, C. A. 2017. Study of the fracture process in heterogeneous materials around boreholes filled with expansion cement. *International Journal of Solids and Structures,* 112**,** 1–15.

TIAM, F. F. K., DANWE, R. D., KONA, N. L. & MEVA¡¯A, L. 2020. Experimental Study and Numerical Simulation Using Extended Finite Element Method (XFEM) Combined with Cohesive Zone Model (CZM), of Crack Growth Induced by Non-Explosive Expansive Material on Two Neighboring Circular Holes of A Gneiss Rock. *Open Journal of Applied Sciences,* Vol.10No.10**,** 21.

WANG, J., NIE, W., ZHANG, Y., SHI, C., WANG, D. & ZHANG, D. 2024. 3D crack propagation in concrete induced by soundless cracking demolition agents. *Engineering Fracture Mechanics,* 306**,** 110135.

WANG, S., MITRI, H., LI, H., LI, D. & WANG, W. 2018. Study of SCA ‐ Induced Rock Crack Propagation under Different Stress Conditions Using a Modified Cohesive Element Method. *Advances in Civil Engineering,* 2018**,** 7936043.

XU, S., HOU, P., LI, R. & CAI, M. 2021. An Experimental Study on the Mechanical Properties and Expansion Characteristics of a Novel Self-Swelling Cartridge for Rock Breakage. *Rock Mechanics and Rock Engineering,* 54**,** 819–832.

XU, S., HOU, P., LI, R. & SUORINENI, F. T. 2022. An improved outer pipe method for expansive pressure measurement of static cracking agents. *International Journal of Mining Science and Technology,* 32**,** 27–39.

YAMAUCHI, K., INABA, T., NISHIDA, M. & KANEKO, K. 1992. Development of static rock breaker using TiNi shape memory alloy as pressure source. *Bull. Jpn. Inst. Met.,* 31**,** 550–552.

ZHAI, C., XU, J., LIU, S. & QIN, L. 2018. Fracturing mechanism of coal-like rock specimens under the effect of non-explosive expansion. *International Journal of Rock Mechanics and Mining Sciences,* 103**,** 145–154.

ZHANG, Q., HE, M., WANG, J., GUO, S., GUO, Z., LIU, X., HU, J., MA, Z., FAN, L. & GUO, P. 2020. Instantaneous expansion with a single fracture: A new directional rock-breaking technology for roof cutting. *International Journal of Rock Mechanics and Mining Sciences,* 132**,** 104399.

ZHONG, Z., ZHANG, H., HU, Y., LOU, R., TAO, P. & LIU, J. 2023. Experimental and numerical explorations on the optimized applications of SCDA in cracking concrete blocks. *Measurement,* 206**,** 112335.

Rockfall as a gravitational natural hazard - influencing factors and approaches to action at municipal level

Steinschlag als gravitative Naturgefahr – Einflussfaktoren und Handlungsansätze auf kommunaler Ebene

Rainer Kienreich, Luca Kammerer, Thomas Frühwirt, Thomas Marcher
Institute of Rock Mechanics and Tunnelling, Technical University Graz

Abstract

The article deals with the quantification of the rockfall risk on natural rock slopes. In a first step, the rock mechanical risk is determined and, in a second step, climate-related trigger factors are added. The process
s steps are the search for rock types (GA), the determination of slope behaviour types (BVT) and, in combination with climatic trigger factors, the system behaviour (SVT) of a slope. The random set method was used in the calculations and the risk was specified in bandwidths. A special focus is placed on the change in the strength behaviour of the rock types because of freeze-thaw cycles.

Zusammenfassung

Der Beitrag befasst sich mit der Quantifizierung des Steinschlagrisikos an natürlichen Felsböschungen. Dabei wird in einem ersten Schritt das felsmechanische Risiko ermittelt und in einem zweiten Schritt klimabedingte Auslösefaktoren ergänzt. Die Prozessschritte sind die Feststellung von Gebirgsarten (GA), die Ermittlung von Böschungsverhaltenstypen (BVT) und in Kombination mit klimatischen Auslösefaktoren das Systemverhalten (SVT) einer Böschung. In den Berechnungen wurde die Random Set Methode eingesetzt und das Risiko in Bandbreiten angegeben. Ein besonderer Fokus gilt der Änderung des Festigkeitsverhaltens der Gebirgsarten infolge von von Frost-Tau Zyklen.

1 Introduction

The use of the Alps as a recreational area has increased significantly in recent years. As a result, the alpine natural hazard of "rockfall" has statistically led to more accidents involving people.

To evaluate the rockfall risk, the inter-university project "STEInschlagRISiko (STEIRIS)" was therefore launched in 2021 and completed in 2022 (Marcher et al, 2022). The Graz University of Technology (Institute of Rock Mechanics and Tunnelling, Institute of Construction Economics and Construction Management) and the University of Graz (Institute of Domestic and Foreign Private Law and Civil Law, Institute of Public Law and Political Science) were involved with the support of the municipality of Schladming and Regionalmanagement Liezen GmbH.

Chapter 2 of this paper covers the processing methodology in the process steps of collecting rock mass types, slope behaviour types and system behaviour types. Data preparation using the randomised method (RSM) is described in a subchapter. A further subchapter is dedicated to the laboratory tests for the freeze-thaw tests. Chapter 3 presents the results of the rockfall risk assessment in individual cases or preventively for larger sections. The summary and outlook are summarised in chapter 4.

2 Methodology

The assessment method is mapped as a modular process taking into account uncertainties (risk management). In the first step, the rockfall risk (risk of occurrence of a rockfall) is determined in the fault tree analysis. In the second step, the extent of damage (probability of hitting a person and severity of injury) is determined using the event tree analysis.

The rockfall risk is determined in the fault tree analysis for a homogeneous area. This can be an entire slope section or partial areas. The process sequence is shown in Figure 1 and comprises the following steps:

1. The present rock mass type (GA) is to be determined by the technical-geological rock mass description.
2. The slope behaviour varies within the same rock mass type depending on local influencing factors (spatial position of the interface structure in relation to the slope face, rock water situation and primary stress behaviour). Rock type and influencing factors form a slope behaviour type (BVT), which is described with the rock mechanical failure risk (R_0).
3. The climatic situation and the vegetation come into play as trigger factors. Slope and trigger behaviour together result in the system behaviour types (SVT) and thus the rockfall risk (R_{Sys}) of a rock slope.

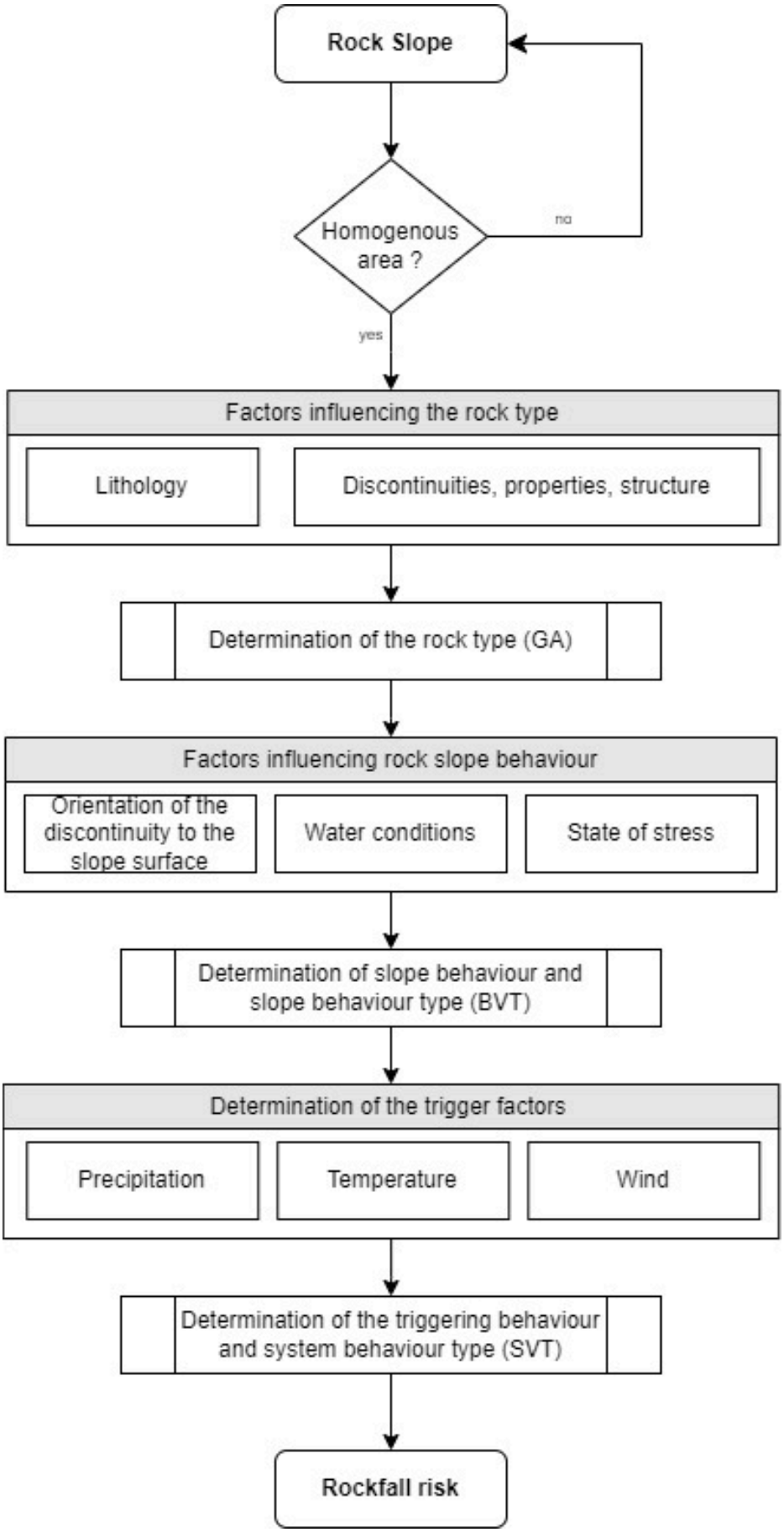

Fig. 1: Fault tree process sequence.

3 Rock Types (GA)

Rock types are rock volumes that have similar geological-mineralogical parameters, engineering geological discontinuities characteristics and rock mechanical parameters - separately for rock and rock mass (discontinuities). In the case study, 5 sedimentary rock types (limestones K.1 to K.5) and 7 metamorphic rock types with gneisses (G.1, G.2), mica schist (GlS), green schist (GrS), quartz phyllite (QzPhy), phyllites (Phy) and limestone marble (KM) were differentiated.

4 Slope Behaviour (BVT)

The slope behaviour describes the risk of failure for each rock mass type. For this purpose, the failure model is determined for each individual case using kinematic analysis from the spatial intersection of the discontinuities and rock surface. For unstable blocks, the stability is calculated as global safety according to ÖNORM B 1997-1-5 (Austrian Standardisation Institute 2021). The input data for the stability calculation is prepared using the random set method (RSM) (Peschl 2005; Schweiger and Peschl 2005; Schweiger et al. 2007). The result is a range (best case/worst case) of the rock mechanical failure risk. In order to reduce the complexity and computational effort of the data preparation, it must first be clarified which of the parameters should be subjected to the random set procedure. For this purpose, a sensitivity analysis (U.S. EPA 2002) was performed first:

- Significant sensitivity was found for the directly determined parameters. These are the block size, block shape (ratio of volume to slip surface), persistence and, to a lesser extent, the slip surface inclination. The RSM was used for these parameters.
- Low sensitivity was found for the indirectly determined shear parameters. This was based on the joint condition (Jc) (Palmström 1995) from the field recordings, empirical values from the rock mechanics laboratory and literature (Barton and Choubey 1977; Hoek and Bray 1981; Hoek 2007; Schön 2015). This meant that there were no large variations between the rock types and parameter bandwidths were used.

Due to the natural bandwidths of the directly determined parameters, the RSM is used for the reliability analysis. The theoretical basis of the method is the consideration of various sources of uncertainty. A distinction is made between pure randomness, also known as aleatory uncertainty, and epistemic uncertainty, which describes unknown correlations. This defines the functions of the envelope (Fig. 2). The step functions can be smoothed using statistical methods (e.g. chi-squared statistics) and thus be included in further calculations.

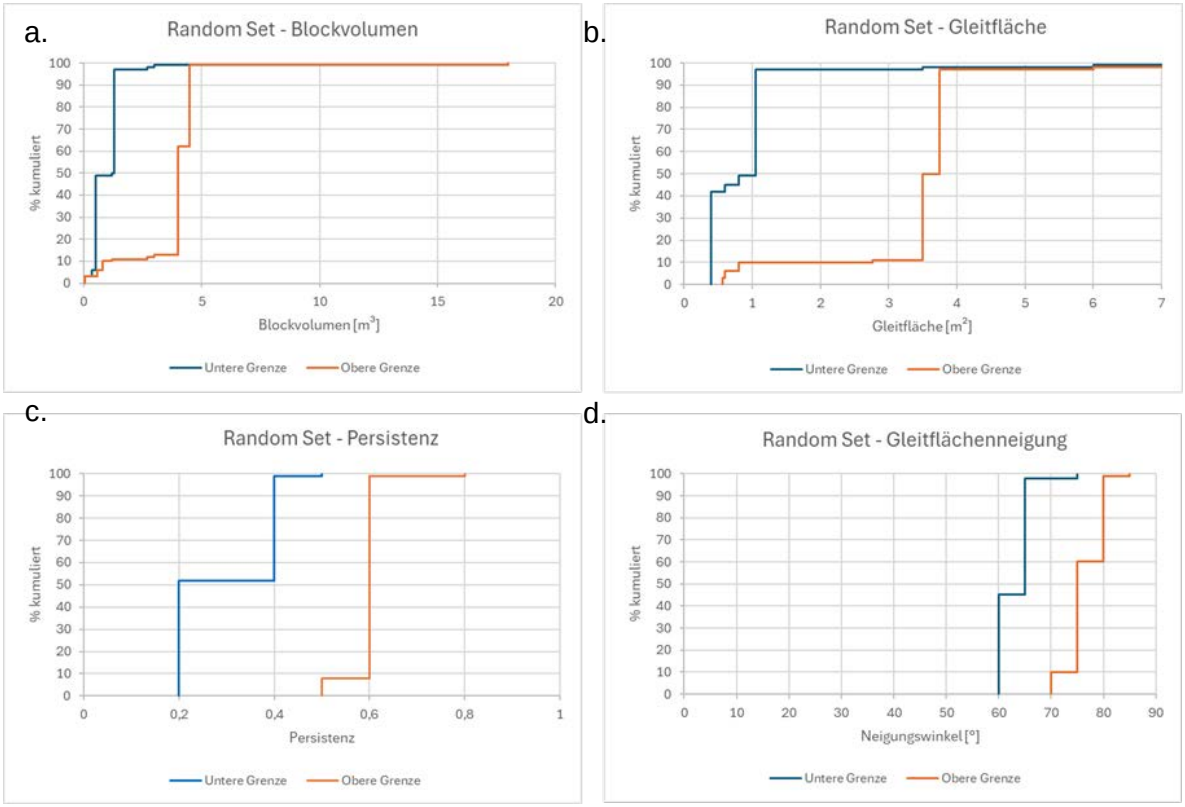

Fig. 2: Example of the evaluation of mountain type K.1: Random set representations of the Parameters; x-axis: block size (a.), sliding plane (b.), persistence (c.), dip-angle (d.); y-axis: share.

In geotechnical engineering, reliability models are safety analyses that determine the probability of failure. The block equilibrium and the safety definition (η) of the ratio of the restraining (R) to the driving (T) forces (Wyllie 2014) are used as the basic model:

$$\eta = \frac{R}{T} \tag{1}$$

When applying the limit equilibrium approach, the parameter combinations for the probability of failure typically result in a sigmoidal probability distribution function:

$$p(f) = p\,(g(x) \leq 1) = \int_{g(x)\leq 1} f(x)dx \tag{2}$$

The input values are, on the one hand, the decisive, uncertain parameters (block size, block shape, persistence, inclination angle of the sliding surface) resulting from the sensitivity analysis and, on the other hand, the parameters defined with fixed values (shear parameters, weights). Using the two distribution functions for the upper/lower parameter bandwidths, the risk of failure (Fig. 3) is determined and presented in a bandwidth.

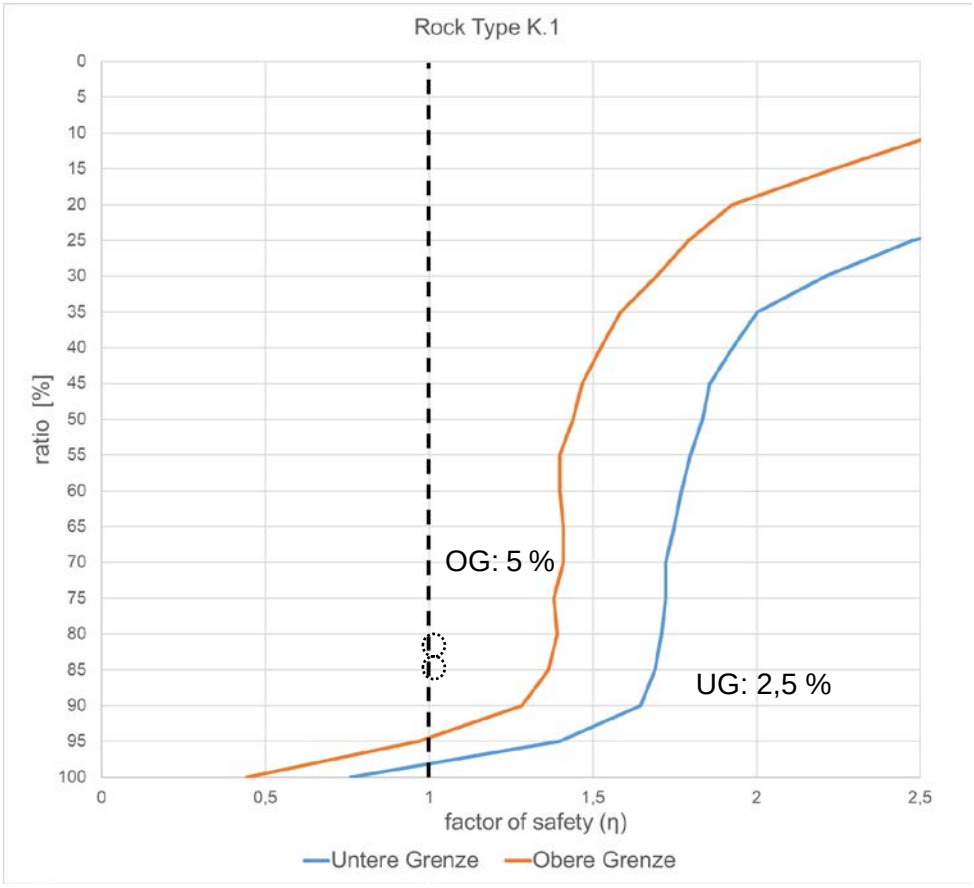

Fig. 3: Example of rock type K.1: Probability-density function (PDF) of failure with minimum (lower limit 2.5%) and maximum risk of failure (upper limit 5%). (OG: upper limit, UG: lower limit.

5 System Behaviour

Apart from geological and morphological causes, the main trigger factors for system behaviour are hydrological factors, ice pressure due to freeze-thaw cycles and wind throw. These factors increase the risk of failure.

In the course of a precipitation event, the amount of rainfall on the one hand and the runoff duration on the other are important for the water pressure. For calculations, design rainfall amounts are available from the national hydrographic services (in Austria eHYD - access to Austrian hydrographic data) (BML 2024). From ÖNORM B 2506-1 (Austrian Standardisation Institute 2013), the design principle of a 5-year rainfall event (q) is applied as a block rainfall model.

A freeze-thaw cycle is a temperature change around the freezing point of water. This is accompanied by a change taken together state of water, whereby a volume expansion of 9% (Matsuoka 1990) has been demonstrated in the rock during the freezing process under laboratory conditions. Actual rock softening because of freeze-thaw cycles was measured in the laboratory in porous sandstone samples after around 17 cycles (Jia et al. 2015). Frost-induced softening processes are only described to a lesser extent for less porous, metamorphic rocks, e.g. (Matsuoka 1990) states more than 100 cycles for loosening evidence. For this reason, a separate laboratory investigation was carried out (see Chapter 2.3.1). The effect of ice pressure in the rock mass was tested in artificial discontinuities in the metamorphic rock mass using laboratory tests (Draebing and Krautblatter 2019). It was found that the highest ice pressure of around 10 MPa occurs during "top-down" freezing processes and leads to the degradation of rock bridges (Persistence). Top-down freezing conditions occur when it

rains and temperatures then drop rapidly to -4°C to -8°C. Derived from this publication and the study (Section 2.3.1), this resulted in an increase in dissolution of 10% per cycle for rock types with UCS below 10 MPa.

The *Handbook of Tree Statics and Tree Inspection* (Wessolly and Erb 2014) provide the static approach for the stability assessment of trees (windthrow). The hurricane wind force is generally used as the measurement load. To determine the change in the trigger risk, the probability of occurrence of hurricane-force winds must be linked to the proportion of critical tree categories. The risk is therefore independent of the type of slope behaviour.
The system behaviour risk (R_{Sys}) results from the summation of the slope behaviour (R_0) and the trigger risk R_A (N, F, W). This calculation is to be shown for each slope behaviour type or rock type and season (Table 1).

Tab. 1: Determination of risk according to system behaviour.

BVT	Scenario	Rock Mechanical Risk	Trigger Risk (R_A)	System Behaviour Risk (R_{Sys})
A	precipitation	R_0	R_A(N)	R_0+ R_A(N)
	freeze-thaw cycles	R_0	R_A(F)	R_0+ R_A(F)
	wind throw	R_0	R_A(W)	R_0+ R_A(W)
	non scenario	R_0	0	R_0
…	…	…	…	…

5.1.1 Freeze-thaw cycles: influence of various thermomechanical effects on the strength of rock

The study (Kammerer 2024) deals with thermomechanical influences. The aim of the work was an in-depth laboratory study to investigate the influence of thermal fatigue on the strength of low-porosity rock. A test series of typical regional rock types (gneiss and limestone) was taken from the Schladming region. Test specimens were prepared in the laboratory and freeze-thaw tests were carried out in a programmable climate chamber under laboratory conditions with and without the influence of water.

A thermal fatigue process was set as a framework condition, which requires a controlled temperature change (ΔT) per time unit (t):

$$\frac{\Delta T}{t} \leq 2{,}0\ [^{\circ}\ C/min] \qquad (3)$$

The rock strength σ and the effective porosity e were analysed as mechanical parameters. Changes in σ and e represent the measured parameter of fatigue.

(1) Initially, the rock strength of selected rock samples was determined in the uniaxial compression test. The effective porosity was determined by determining the mass of the specimens in the fully saturated state in comparison to the subsequent measurement in the dried state. Only hydraulically connected pore spaces were determined using this method.
(2) After completion of the freeze-thaw cycles, comparative velocity measurements (DV) and unconfined compression tests were carried out. To measure the expected change in unconfined compressive strength with increasing number of tests, 6 specimens per rock type were tested in the laboratory at the beginning of the test series. Three specimens per rock type were saturated and three specimens per rock type were unsaturated. After completion of the freeze-thaw cycles between and at the end (15 cycles for water-saturated and 29 cycles for unsaturated specimens), uniaxial compression tests were carried out.

The test procedure (Fig. 4) was carried out separately with water influence (saturated) and without water influence (unsaturated). First, the half of the samples were saturated with water in a pressurised container at a pressure of 7 bar for 24 hours. The freezing cycle for saturated and unsaturated samples then began with freezing in the climate chamber for 12 hours, whereby the samples were initially cooled continuously to -10°C. The subsequent thawing phase took place over a period of 10 hours, during which the temperature was continuously increased to 20°C.

The change in the effective porosity of all rock samples was determined after each cycle using velocity measurement and back-calculated to the effective porosity using the transmission time. A greater reduction in rock strength and an associated greater increase in effective porosity compared to the non-water-saturated rock samples was expected.

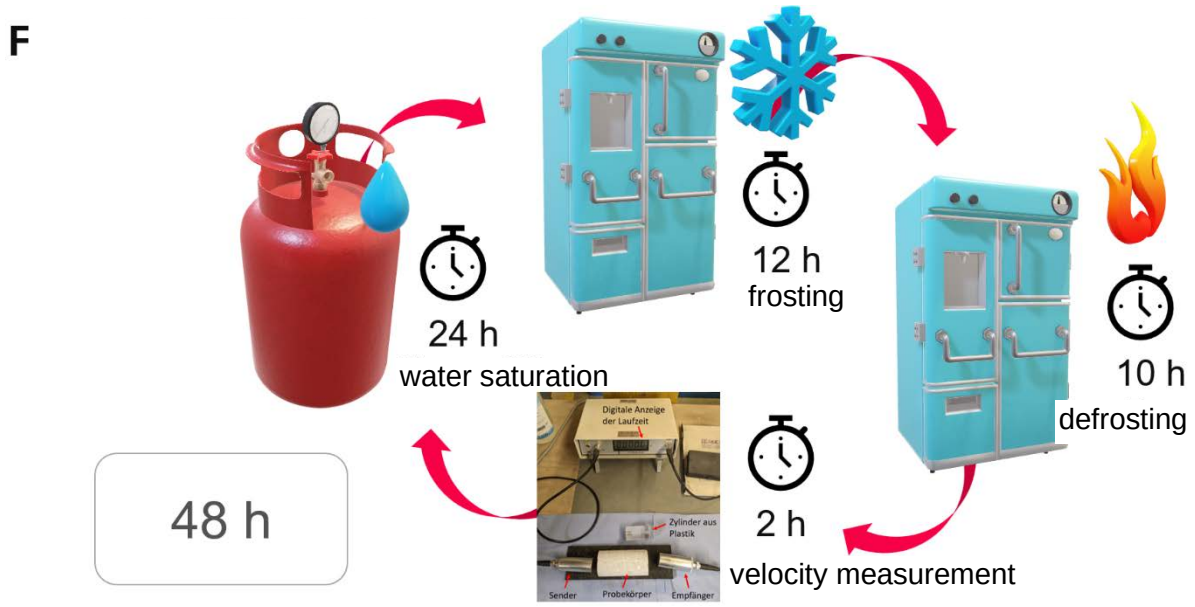

Fig. 4: Test procedure of freeze-thaw cycles for saturated test specimens.

The test specimens were drilled from the hand pieces collected in the field. The lime-stone samples (Fig. 5) showed healed cracks. During the processing of the rock blocks into cylindrical specimens, some specimens spalled off at pre-existing weak points.

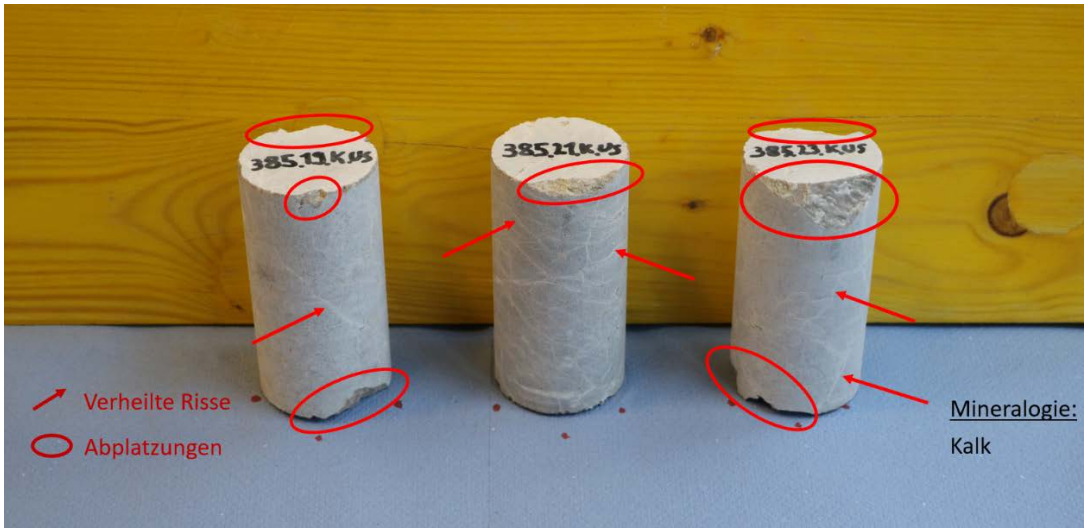

Fig. 5: Limestone samples in their original state: Spalling caused by processing the samples during cutting with a circular saw and/or grinding is circled in red in the image. Some of the healed cracks are marked with red arrows.

The gneiss samples (Fig. 6) are characterised by greater inhomogeneity. This inhomogeneity is determined by the diverse mineralogy and the existing weak points (healed cracks, spalling and layered pattern). In comparison to the limestone, the specimens showed less spalling.

Fig. 6: Gneiss in its original state: Spalling caused by processing the samples during cutting with a circular saw and/or grinding is circled in red in the image. Some of the healed cracks are marked with red arrows. The red lines represent foliations.

The results of the transmission tests (DV) are shown in the following diagrams (Fig. 8-13). The expected effect of the decrease in velocity (corresponding to the increase in porosity) with consecutive cycles could not be demonstrated. Only specimen gneiss weathered with the number 44 (GV44, see Fig. 13) shows a slight decrease.

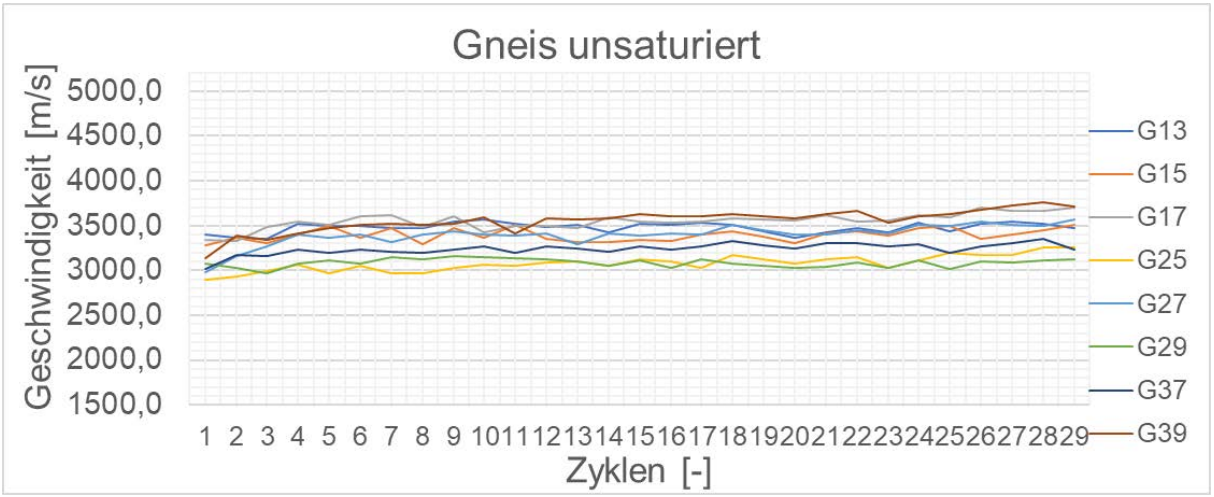

Fig. 7: Results of DV - gneiss unsaturated: y-axis: velocity, x-axis: cycles.

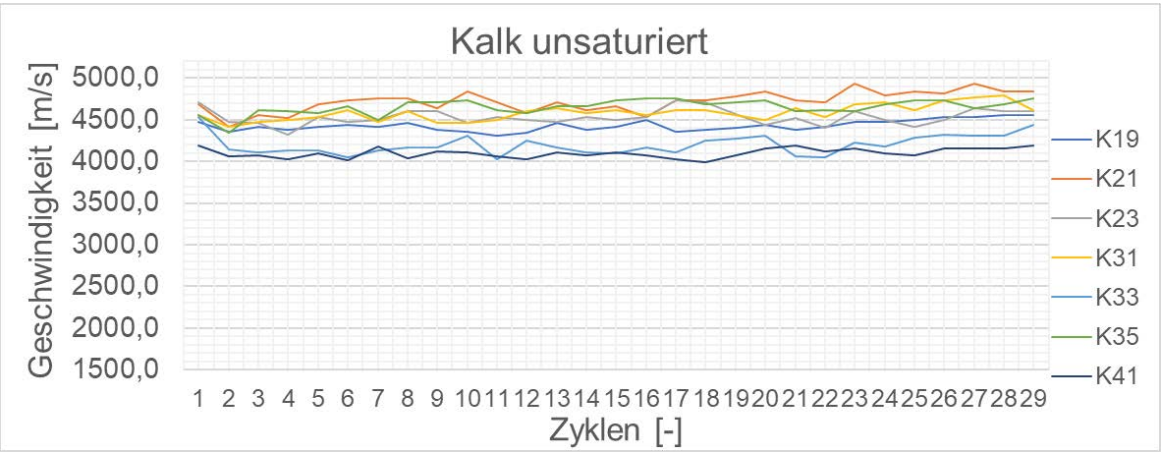

Fig. 8: Results of DV - limestone unsaturated: y-axis: velocity, x-axis: cycles.

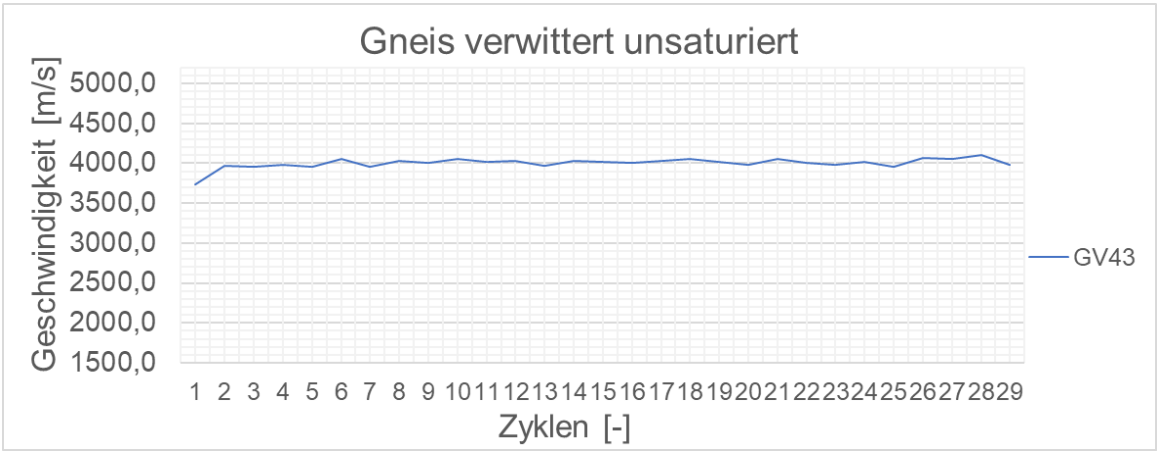

Fig. 9: Results of DV - Gneiss weathered unsaturated: y-axis: velocity, x-axis: cycles.

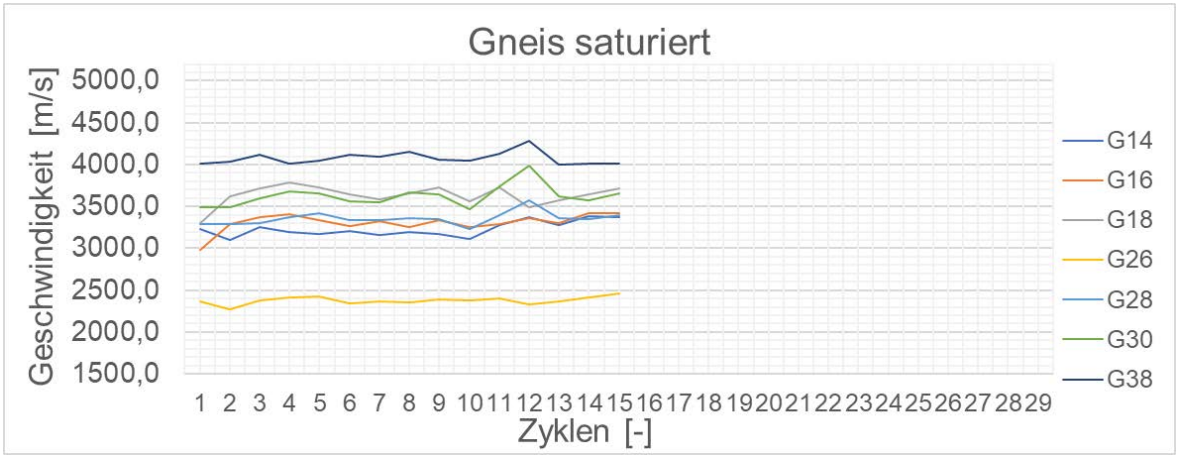

Fig. 10: Results of DV - Gneiss saturated: y-axis: velocity, x-axis: cycles.

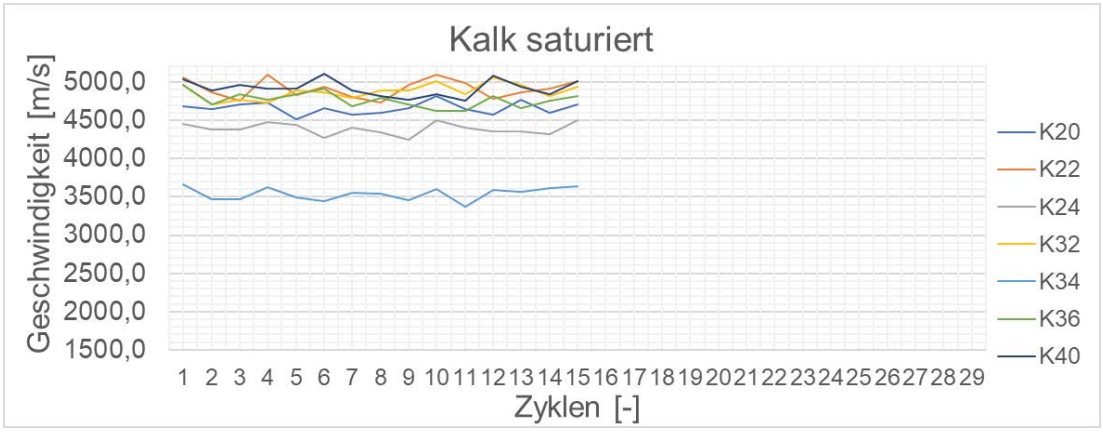

Fig. 11: Results of DV - limestone saturated: y-axis: velocity, x-axis: cycles.

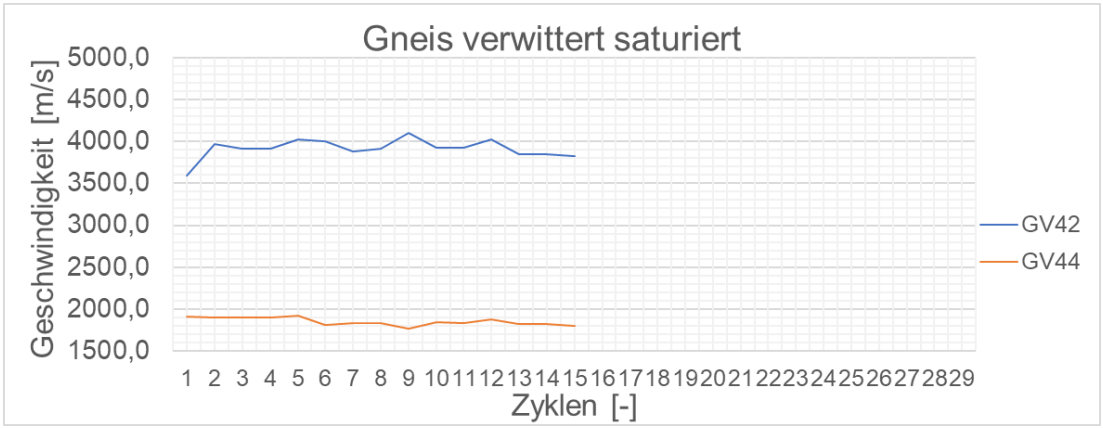

Fig. 12: Results of DV - Gneiss weathered saturated.

In the uniaxial compression tests, the compressive strengths of the individual rock types are first compared with each other in the initial and final state (see Figure 13). Basically, a significant decrease in compressive strength can be observed. The compressive strength in the final state is higher than in the initial state only for the test specimens of type Gs. In contrast to porous rocks (Jia et al. 2015), the influence of water is not recognisable at this low number of cycles.

Figure 14 shows the mean values of the compressive strengths of the respective rock types (Gus, Gs, Kus, Ks). The results show a reduction in the compressive strength of the Gus type samples by 26% after 29 cycles, of the Kus type samples by 28% after 29 cycles and of the Ks type samples by 30% after 15 cycles. The results for rock type Gs were not representative due to the sample preparation.

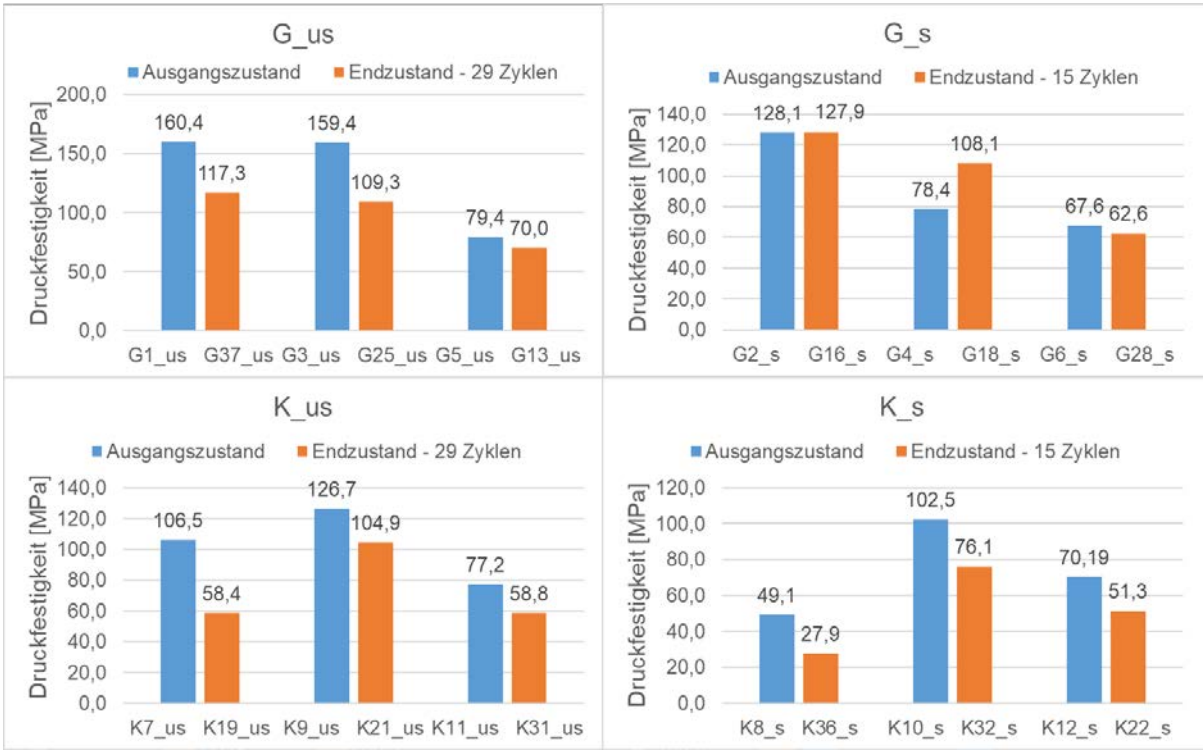

Fig. 13: Average compressive strength. In the individual diagrams, test specimens from the same group (e.g. gneiss unsaturated) are compared with each other in the initial (blue) and final (orange) state.

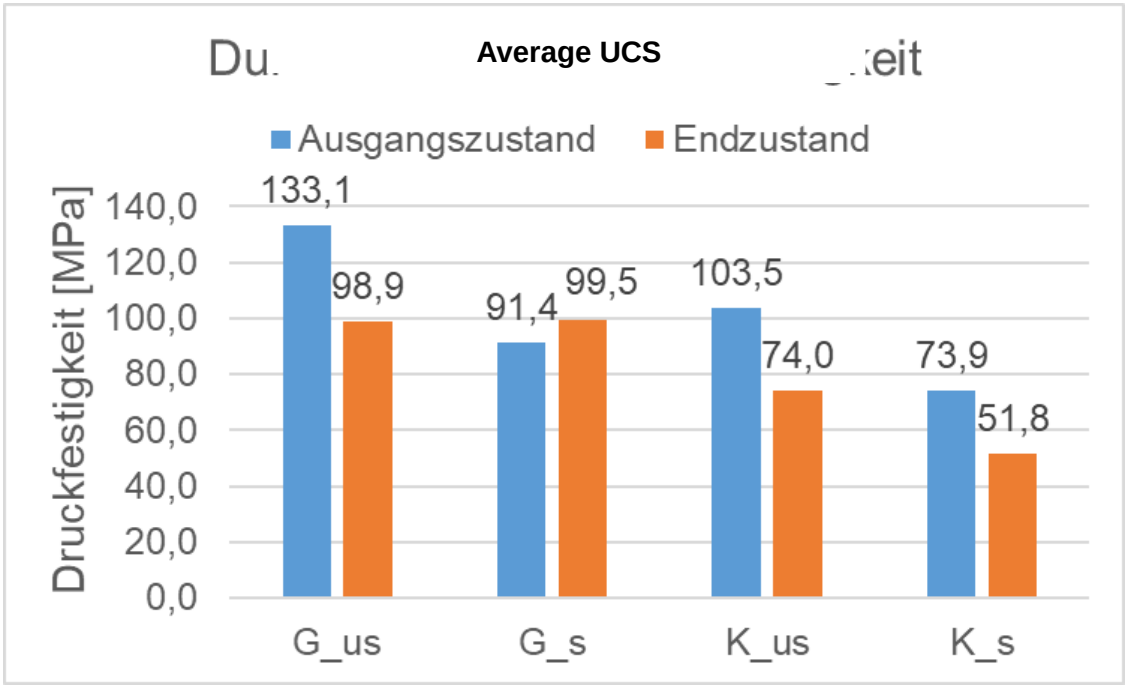

Fig. 274: Average UCS (G: Gneiss, K: Limestone; us: unsaturated, s: saturated).

The freeze-thaw cycle leads to a reduction in UCS of around 2% in gneiss and 3% in limestone. An experimental trend would therefore be - under the premise of increasing loosening with less solid rock types - a reduction increase of Δ1 % per 25 MPa. Taking into account the experimental results of frost blasting in discontinuities (Draebing and Krautblatter 2019), a decrease of 5-10% in rock strength or a break-up of rock fragments in a fissure can be derived for the rock group with UCS < 10 MPa.

6 Results

The method described in Chapter 2 was tested in a field study with around 1,200 natural rock slopes. The results can be used for individual assessments or as a preventive assessment with regard to rockfall hazard and personal risk.

7 Individual case analysis

The stability of fissure bodies (slope behaviour) can be shown graphically for the rock groups limestone (Fig. 15) and metamorphic rocks (Fig. 16) investigated in the case study.

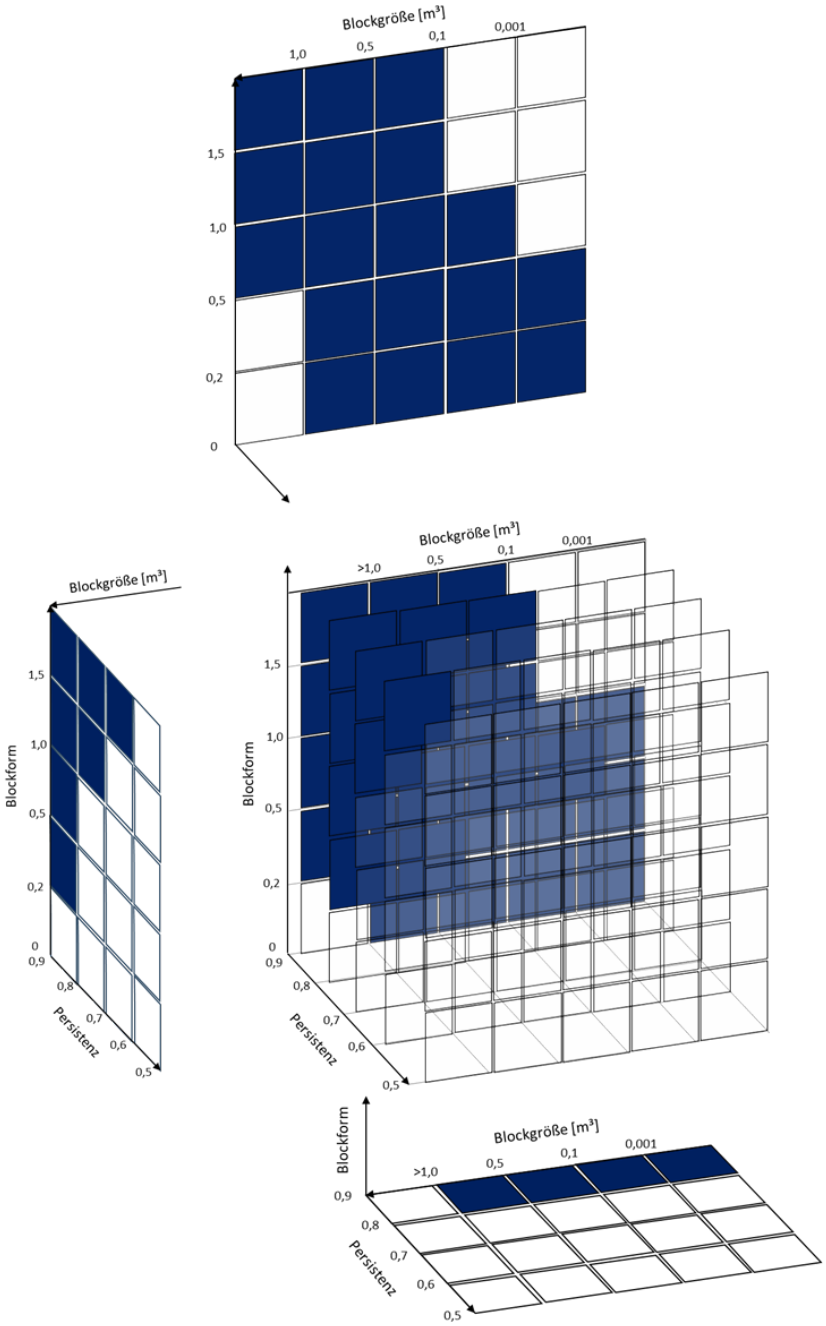

Fig. 15: Stability of sedimentary (carbonate) rock types: transparent squares: stable, blue squares: unstable (global safety); x-axis: persistence, y-axis: block size, z-axis: block shape.

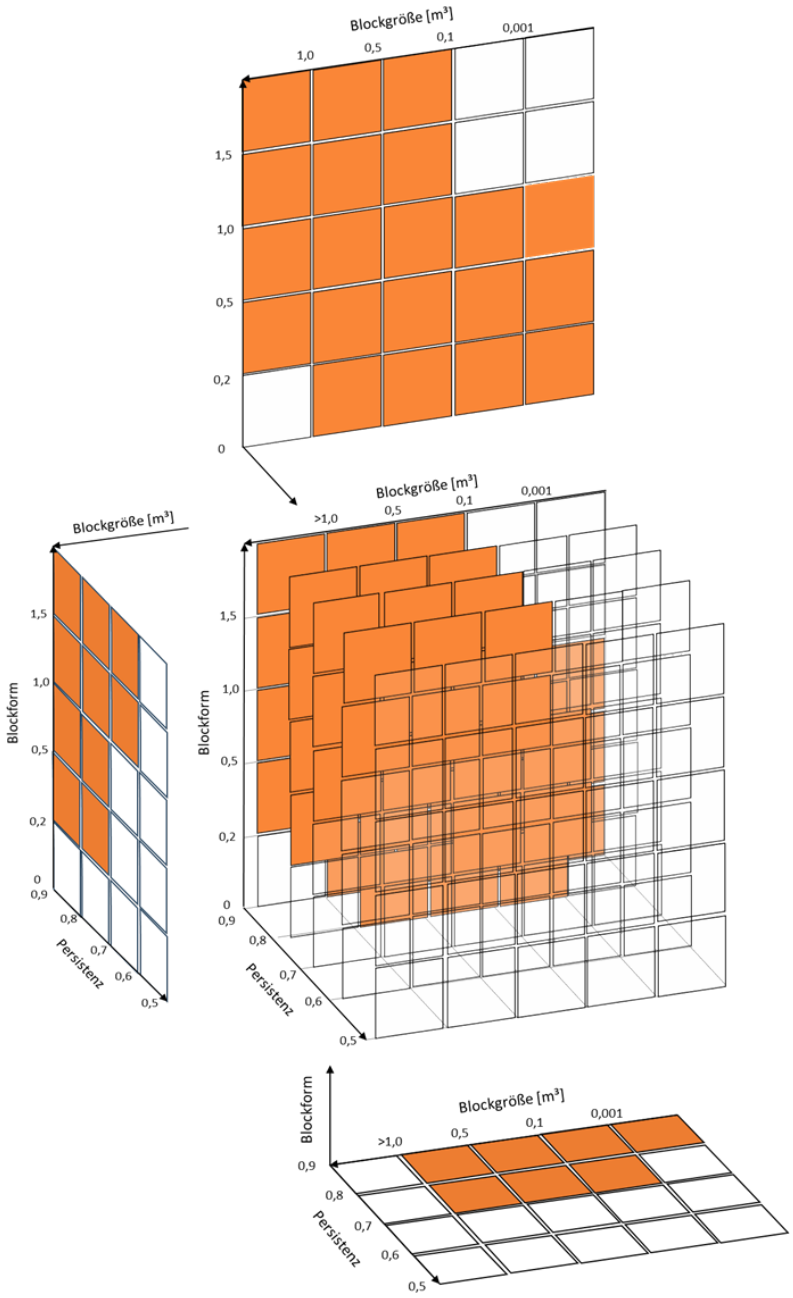

Fig. 16: 3D cube: stability of metamorphic rock types: transparent squares: stable, orange squares: unstable (global safety); x-axis: persistence, y-axis: block size, z-axis: block shape.

Figures 15 and 16 clearly show the different rock mechanical behaviour of the rock types. The block size and block shape are important; the more favourable shear parameters at the interfaces are usually decisive. Carbonate rock types are generally stable up to a degree of separation of 0.7, while metamorphic rock types are already unstable from of 0.6.

For precipitation events, a distinction was made between normal to heavy precipitation amounts of 25-50 mm (5-year event) and extreme events of 50-80 mm (>20-year event), 80-100 mm and over 100 mm. The risk increases are linked to precipitation amounts:

- Heavy rainfall ab 25 mm: Rock types G.1, G.2 by 5-8 %
- Extreme rainfall 80-100 mm: Rock types K.1, KM.1 by 5-15 %

At around 75 %, these rock types represent the largest proportion of the natural slopes surveyed. For all other rock types - due to the higher risk values of the slope behaviour higher precipitation amounts of well over 200 mm are necessary for a significant increase in risk.

Influences from the freeze-thaw cycle (top-down freezing) occur in autumn/winter in rock types K.4, K.5, G.2 (faulted), GrS.1 and Phy.1. The reduction in stability is caused by rupture of rock bridges in discontinuities near the surface. The increase in risk is around 5-30% per cycle.

Windthrow occurs in trees (spruces) in connection with gusty winds at hurricane force, the minimum trunk diameter is 10 cm at a height of 4 m, 15 cm at a height of 6 m, 20 cm at a height of 8 m, etc. Trees with a smaller trunk diameter are at risk of being blown down by the wind, so the risk of falling rocks in the event of an incident is 100%.

8 General Assessment

Slope behaviour types must be determined for the case of an annual forecast. These were derived in the field study in 4 clusters A, B, C and D (Fig. 11).

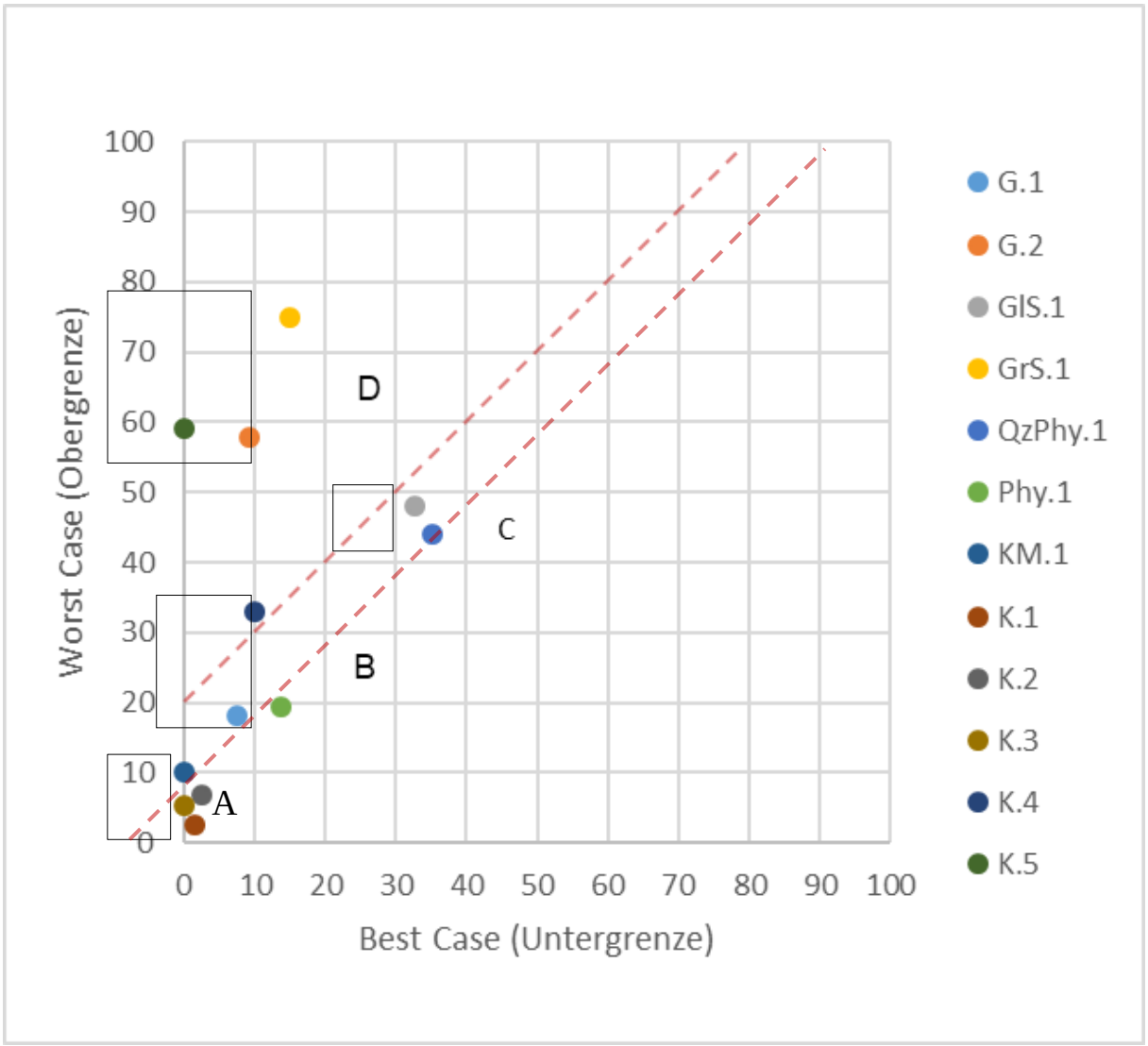

Fig. 11: Slope behaviour by rock type (GA) grouped into clusters A to D (rectangles).

These were described with regard to their classification and assigned to a slope behaviour (risk of failure R_0) (Table 2).

Tab. 2: Slope Behaviour Types (BVT).

Slope behaviour type	Description	Block size	Block shape	Persistence	Discontinuity surface	Risk of failure
A	Compact, wall-forming rock; irregular interface orientation, few outcrops with larger cubatures, good interlocking	0,4-2m³, (max. up to 5m³)	platy-banked or cubic	0,2-0,8	stepped-(very) rough, unweathered, Jc > 3	<10 %
B	Rocks with break-outs due to separation planes; steep slopes > 60°up to approx. 10 m high with small-grained fall and occasional larger blocks.	up to 1m³	platy-cubic	0,4-0,8	stepped-wavy, rough, slightly weathered Jc 0,8-2,5	10-20 %
C	Overstressed, interface-dominated rock with numerous secondary fractures with cubic volumes in the dm³ to m³ range. Slopes mostly below 60°; low interlocking	up to 0,7m³	platy	0,5-0,8	even-wavy, smooth; distinct weathering , Jc 0,38-2,5	30-50%
D	Difficult to predict mountains; medium-high, steep slopes with numerous, coarse blocks; karst; low interlocking.	0,001-5m³	Predominantly cubic	0,5-0,9	stepped-even, rough-smooth; clear weathering , Jc 0,38-1,5	10-80%

The trigger risk in annularity the probability of occurrence of the climate scenarios "precipitation", "freeze-thaw cycle" and "windthrow". The determination of the probabilities of occurrence was derived from typical regional frequencies, optimised using the Monte Carlo method and linked using combinatorics. The system behaviour risk (R_{Sys}) shown in Table 3 resulted from the example of the study area.

Tab. 3: System behaviour (R_{Sy}s).

Saison	Slope Behaviour Type	Rock Type	System Behaviour Risk ($R_{Sys.}$)	
			Best Case	**Worst Case**
Spring	A	K.1	1,8%	2,9%
		K.2	3,2%	7,2%
		K.3	0,2%	5,2%
		KM.1	0,2%	10,4%
	B	G.1	8,4%	19,1%
		K.4	15,0%	46,0%
		Phy.1	19,0%	25,7%
	C	GlS.1	33,3%	48,2%
		QZPhy.1	35,2%	44,2%
	D	K.5	2,0%	62,0%
		G.2	12,5%	61,3%
		GrS.1	25,4%	78,4%
Summer	A	K.1	1,8%	2,9%
		K.2	3,2%	7,2%
		K.3	0,2%	5,2%
		KM.1	0,2%	10,4%
	B	G.1	8,4%	19,1%
		K.4	10,2%	33,2%
		Phy.1	14,2%	19,3%
	C	GlS.1	33,3%	48,2%
		QZPhy.1	35,2%	44,2%
	D	K.5	0,4%	59,4%
		G.2	9,3%	58,8%
		GrS.1	15,8%	75,2%
Fall	A	K.1	1,8%	2,9%
		K.2	3,2%	7,2%
		K.3	0,2%	5,2%
		KM.1	0,2%	10,4%
	B	G.1	8,4%	19,1%
		K.4	10,2%	33,2%
		Phy.1	14,2%	19,3%
	C	GlS.1	33,3%	48,2%
		QZPhy.1	35,2%	44,2%
	D	K.5	0,4%	59,4%
		G.2	9,3%	58,8%
		GrS.1	15,8%	75,2%

Tab. 9 continued.

Winter	A	K.1	1,6%	2,6%
		K.2	3,1%	7,1%
		K.3	0,1%	5,1%
		KM.1	0,1%	10,1%
	B	G.1	8,1%	18,1%
		K.4	10,1%	33,1%
		Phy.1	14,1%	19,1%
	C	GlS.1	33,1%	48,1%
		QZPhy.1	35,1%	44,1%
	D	K.5	0,1%	59,1%
		G.2	9,1%	58,1%
		GrS.1	15,1%	75,1%

The slope behaviour, 4 basic types were derived for the superordinate risk assessment. These basic types range in three slope behaviour types (BVT A, B, and C) from favourable to unfavourable rock types. A fourth BVT (D) represents a type that is difficult to predict due to the highly scattered input parameters. In order to avoid time-consuming recalculations, these basic types are described with their main characteristics and presented in tabular form. For the detailed application, a graphic consisting of the main parameters (rock type, fissure body size, block shape and degree of separation) is provided in order to narrow down the specific risk.

The slope behaviour types are combined with region-specific climate data (e.g. Ramsau a. Dachstein measuring station) to produce system behaviour. Heavy precipitation from 25 mm/h in metamorphic mountains and 80 mm/h in carbonate mountains significantly increases the rockfall risk by 8 % and 20 % respectively. Freeze-thaw cycles cause the most pronounced reduction in stability, although only the gust behaviour types C and D are affected. The effect increases the risk by around 5-30% and occurs with a time delay during the snowmelt. Wind gusts of hurricane force generally result in windthrow and associated rockfall (risk: 100%).

In individual cases, the rockfall risk must be determined separately for carbonate and metamorphic rock types based on the influencing parameters of block size, block shape and degree of separation (persistence). In the event of heavy precipitation from 25 mm/h in metamorphic mountains or 80 mm/h in carbonate mountain types and/or wind gusts of hurricane force, it is generally not justifiable to stay.

9 Summary and Outlook

This article describes a transparent process for quantifying the alpine risk of rockfall on natural slopes.

The method draws on existing rock mechanics literature and extends it for a preventive assessment using the random set method (RSM). This makes it possible to describe the uncertainty in the assessment, which results from the sometimes large variations in the geological input parameters for each rock type. As a result, a bandwidth of the risk of failure can be specified from the distribution functions.

This is used to derive slope behaviour types, which are described using a table and assigned a failure risk.

The influence of the most important climatic factors was analysed. The results show that even heavy precipitation can significantly increase the risk of rockfall for the most common rock types (limestone, gneiss) in the investigated region. A very large effect results (karstified limestone, phyllites, faulted rock) from freeze-thaw cycles in the case of top-down freezing cycles in autumn, but the risk only becomes significant with a time delay during the thaw phase in spring. Windthrow due to strong winds or gale-force winds are independent of the mountain type and generally represent a high risk.

The quantification of the rockfall risk for personal injury depends on the frequency of visitors. Studies on this are still ongoing and are being carried out with the help of simulations of regional climatic trigger factors and visitor frequencies.

10 Literature

Barton, N.; Choubey, V. (1977): The Shear strength of rock joints in theory and practise. In: *Rock Mechanics* 10, p. 1-54.

BML (2024): Hydrographische Messstellen und Daten. Hg. v. Bundesministerium für Land- und Forstwirtschaft, Regionen und Wasserwirtschaft. Wien. Online verfügbar unter https://ehyd.gv.at, zuletzt geprüft am 12.04.2024.

David, F. N. (1962): Games, Gods and Gambling. University of London.
Draebing, Daniel; Krautblatter, Michael (2019): The Efficacy of Frost Weathering Processes in Alpine Rockwalls. In: *Geophysical Research Letters* 46 (12), S. 6516–6524. DOI: 10.1029/2019GL081981.

Draebing, Daniel; Krautblatter, Michael (2019): The Efficacy of Frost Weathering Processes in Alpine Rockwalls. In: *Geophysical Research Letters* 46 (12), S. 6516–6524. DOI: 10.1029/2019GL081981

Gabriel, J. (2022): Bewertung des Einflusses von Niederschlagswasser als Steinschlagauslöser. Bachelorarbeit. Technische Universität Graz. Institut für Felsmechanik und Tunnelbau.
Hacking, Ian (2013): The Emergence of Probability: Cambridge University Press.

Hoek, E. (2007): Practical Rock Engineering. Online verfügbar unter https://www.rocscience.com/assets/resources/learning/hoek/Practical-Rock-Engineering-Full-Text.pdf.

Hoek, Evert; Bray, John (1994): Rock slope engineering. 3. rev. ed., reprinted (twice). London: E & FN Spon.

Jia, H.; Xiang, W.; Krautblatter, M. (2015): Quantifying Rock Fatigue and Decreasing Compressive and Tensile Strength after Repeated Freeze-Thaw Cycles. In: *Permafrost & Periglacial* 26 (4), S. 368–377. DOI: 10.1002/ppp.1857.

Kammerer, L. (2024): Frost-Tau-Wechsel: Einfluss verschiedener thermomechanischer Einwirkungen auf die Festigkeit von Gestein. Masterarbeit. Technische Universität Graz. Institut für Felsmechanik und Tunnelbau.

Kienreich, R., Kluckner, A., Marcher, T. (2022). Rockfall Risk Projekt (STEIRIS). In T. Marcher, R. Kienreich, & A. Kluckner, *Beiträge zum Steinschlagsymposium 2022* (pp. 1-16). Schladming: NAWI Graz Geocenter.

Marcher,T., Kienreich, R. und Kluckner, A. (Hg.): Beiträge zum Steinschlagsymposium 2022. Steinschlag - Risikoeinschätzung und Maßnahmen aus Sicht kommunaler Verantwortlicher: 01. Dezember 2022, Congress Schladming. Graz: Technische Universität Graz (NAWI Graz Geocenter, Heft 12).

Matsuoka, Norikazu (1990): Mechanisms of rock breakdown by frost action: An experimental approach. In: *Cold Regions Science and Technology* 17 (3), S. 253–270. DOI: 10.1016/S0165-232X(05)80005-9.

ÖGG (2014): Empfehlungen für das Schutzziel bei gravitativen Naturgefahren in Österreich. Salzburg.

Österreichisches Normungsinstitut (2013): ÖNORM B 2506-1 Regenwasser-Sickeranlagen für Abläufe von Dachflächen und befestigten Flächen Teil 1: Anwendung, hydraulische Bemessung, Bau und Betrieb.

Österreichisches Normungsinstitut (2021): ÖNORM B 1997-1-5, Eurocode 7: Entwurf, Berechnung und Bemessung in der Geotechnik, Teil 1-5: Gesamtstandsicherheit von Böschungen, Hängen und Geländesprüngen. Nationale Festlegungen zu ÖNORM EN 1997-1 und nationale Ergänzungen, Artikel ICS 93.020.

Palmström, A. (1995): RMi - A system for characterizing rock mass strength for use in rock engineering. In: *J. of Rock Mech. & Tunnelling Tech.* 1 (2), p. 69-108.

Peine, J. (2022): Ingenieurgeologische Beurteilung einer Steinschlaggefährdung: Am Beispiel von vier Ereignissen im Bezirk Liezen, Steiermark. Master Arbeit. Technische Universität Graz, Graz. Institut für Felsmechanik und Tunnelbau.

Peschl, G. M. (2005): Reliability Analyses in Geotechnics with the Random Set Finite Element Method. Dissertation. Technische Universität Graz.

Schön, Jürgen H. (Hg.) (2015): Physical properties of rocks. Fundamentals and principles of petrophysics. Second edition. Amsterdam, New York: Elsevier (Developments in petroleum science, volume 65). Online verfügbar unter http://www.sciencedirect.com/science/bookseries/03767361/65.

Schweiger, H. F.; Peschl, G. M. (2005): Reliability analysis in geotechnics with the random set finite element method. In: *Computers and Geotechnics* 32 (6), S. 422–435. DOI: 10.1016/j.compgeo.2005.07.002.

Schweiger, H. F.; Peschl, G. M.; Pöttler, R. (2007): Application of the random set finite element method for analysing tunnel excavation. In: *Georisk: Assessment and Management of Risk for Engineered Systems and Geohazards* 1 (1), S. 43–56. DOI: 10.1080/17499510701204141.

U.S. EPA (2002): Total Risk Integrated Methodology, TRIM.FaTE Technical Support Document. Volume I: Description of Module. North Carolina. Online verfügbar unter https://www.epa.gov/fera/total-risk-integrated-methodology-trim-trimfate, zuletzt geprüft am 02.05.2024

Wessolly, L.; Erb, M. (2014): Handbuch der Baumstatik und Baumkontrolle. [Neuausg.]. Berlin, Hannover: Patzer.

Wyllie, Duncan C. (2014): Rock Slope Engineering. Fourth Edition. Unter Mitarbeit von Chris Mah. 4th ed. London: CRC Press.

Injection-driven seismic slip of saw-cut shale fractures

Injektionsinduzierte seismische Scherbewegung auf gesägten Schieferklüften

Wengang Dang[1], Chunpeng Wang[1] & Kang Tao[2]
[1]School of Civil Engineering, Sun Yat-sen University
Zhuhai 519082, China
[2]Geotechnical Institute, TU Bergakademie Freiberg
Freiberg 09599, Germany

Abstract

The instabilities of underground faults induced by fluid injection are common, and the related seismic activities can threaten human safety. This paper aims to experimentally investigate the mechanism of injection-induced instability of fractures. A series of triaxial slip tests was conducted on critically stressed saw-cut shale fractures with fluid injection of constant pressurization rate. Slip instabilities induced by fluid pressure injection were observed, and the fluid pressure for fracture activation is related to the initial stress state of the fracture surface. The greater the gap between the initial stress state and the critical stress state, the closer the experimental fluid injection pressure to the theoretical value. The induced slip events decreased with lower initial stress levels. The maximum seismic moments released by fast slip events were obtained via two theoretical models. Also, the energy released by the slip events can be predicted by the energy conversion rate of injected fluid energy.

Zusammenfassung

Instabilitäten von unterirdischen Störungszonen induziert von Fluidinjektionen ist ein typisches Phänomen und die damit verbundenen seismischen Aktivitäten können die Sicherheit von Menschen gefährden. Dieser Artikel hat zum Ziel, den Mechanismus der fluid-induzierten Instabilität von Bruchflächen experimentell zu untersuchen. Eine Reihe von triaxialen Slip-Tests wurden auf kritisch gespannten gesägten Bruchflächen mit konstanter Fluiddruckrate durchgeführt. Slip-Instabilitäten induziert durch den Fluiddruck wurden beobachtet, wobei der notwendige Fluiddruck zur Bruchaktivierung vom initialen Spannungszustand auf der Bruchfläche abhängt. Je größer der Unterschied zwischen dem initialen Spannungszustand und dem kritischen Spannungszustand, je näher war der experimentell ermittelte Injektionsdruck an der theoretischen Lösung. Die induzierten Slip-Ereignisse nehmen mit kleiner werdendem initialen Spannungsniveau ab. Die maximalen seismischen Momente erzeugt durch schnell ablaufende Slip-Ereignisse wurden mittels theoretischer Modelle erhalten. Die durch die Slip-Ereignisse freigesetzte Energie kann über die injezierte Fluidenergie prognostiziert werden.

1 Introduction

As an advanced clean energy with abundant reserves and widely used across the world, geothermal energy has been drawing increasing attention from the public (Chen et al. 2020). However, fluid injection during geothermal extraction usually links to unstable faults slips and substantial seismicity risks (Ellsworth 2013). Injection-induced seismicity has become a major obstacle for development of geothermal exploitation (De Simone et al. 2017, Rathnaweera et al. 2020).

Many laboratory injection experiments have been carried out to investigate the mechanism of fracture instability. According to the Mohr-Coulomb failure criterion and effective stress principle, fracture instability occurs when the shear stress on a rock fracture exceeds the product of the friction coefficient and effective normal stress that is given by the difference between the normal stress and fluid pressure. Elevating the fluid pressure during fluid injection decreases the effective normal stress, resulting in fracture instability. Nevertheless, some laboratory investigations have shown that the fluid pressure required to activate the fracture significantly exceeds that predicted by Mohr-Coulomb failure criterion (Ji et al. 2020). The diffusion of fluid overpressure significantly influences the local stress field and the subsequent fracture instability (Scuderi et al., 2017; Passelègue et al., 2018; Scuderi and Collettini, 2018; Wang et al., 2020). The main reason for the deviation between the predicted fluid pressure and the actual fluid pressure is the uneven distribution of fluid pressure on the fracture (Ji et al. 2021).

Laboratory studies on this problem usually assuming the unchanged initial stress state of fractures and focus on the injection strategy for seismicity mitigation. However, there are few researches on the role of different initial stress state on slip behavior of fractures. In this research, a triaxial shear-flow test system is used to carry out the injection-induced slip tests on saw-cut shale fractures subjected to different initial stress states with increasing fluid pressure. The injection induced earthquakes magnitude and the mechanisms leading to the reactivation of the fault are discussed.

2 Experimental configuration

2.1 Samples and apparatus

As shown in Fig. 1, we conducted a series of fluid injection tests on a saw-cut shale cylinder with a diameter of 50 mm and a height of 100 mm, which is sourced from Sichuan Basin, China. The sample is divided into upper and lower parts, and the sliding plane in the middle is at a 60° angle to the horizontal direction. We drilled two boreholes to facilitate distilled water flowing into the fault (Ji & Wu 2020; Fang & Wu 2022). The experiments were performed using a triaxial testing device, DYS-1000, coupled with a high-pressure syringe pump. The samples were fixed on the loading platform and axial load and confining load can be applied. It is assumed that the injected fluid flows through the fracture without penetrating into granite matrix because the permeability of granite matrix is extremely small (Ye & Ghassemi 2018; Ji et al. 2021).

Confining pressure and axial pressure during the experiment were servo-controlled and recorded by test system with a precision of 0.01 MPa. The displacement of the sample was recorded by a linear variable differential transformer (LVDT) with a precision of 0.1 μm. Normal and shear stress on the fracture were determined by Eqs. (1-2) The distilled water was injected through the borehole in the bottom and the fluid injection pressure was measured by the pump.

$$\tau = (\sigma_1 - \sigma_3)\frac{\sin 2\theta}{2} \tag{1}$$

$$\sigma_n = (\sigma_1 - \sigma_3)\cos^2\theta + \sigma_3 \tag{2}$$

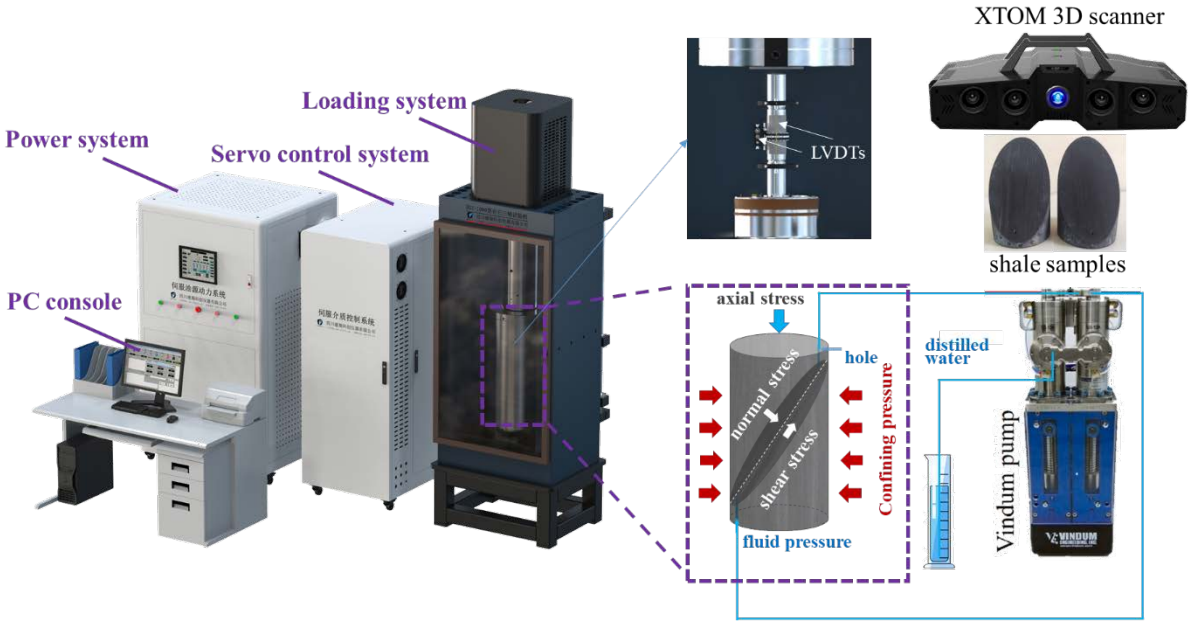

Fig. 1: Experimental configuration. Overview and main components of the loading device and the syringe pump.

2.2 Test procedure

At the beginning, we measured the friction coefficient of the fracture without fluid flow. The confining pressure was applied and then stabilized; the axial loading piston was set to the 'displacement control' mode. The fracture was sheared at a rate of 0.1 mm /min. The confining pressure was set as 5, 10 and 15 MPa, respectively. As a result, the critical axial stress (σ_m) is obtained based on the measured friction coefficient.

Afterwards we considered the fluid effects. The 10 MPa confining pressure was applied and then stabilized. First the axial loading mode is set to 'stress control' mode. The axial stress of the sample is gradually loaded to the desired values of 102%, 100%, 95%, 93% and 90% of σ_m, respectively (named Test 1, Test 2, Test 3, Test 4, Test 5). Then the axial stress is kept constant as 'initial stress'. The fluid pump is then turned on and distilled water is injected into the fracture using a pressure of 1 MPa. A relative long timespan should be reserved to make the flow rate stable. When the flow rate at the inlet is nearly equal the flow rate at the outlet, we believed the fracture flow has been stabilized. Finally, we increased the inlet injection pressure at a rate of 0.25 MPa /min until the unstable fast slip events occurred at the fracture.

3 Results

3.1 Shear strength without fluid flow

First, the test for determining the friction coefficient of the fracture was carried out. Before the experiment, X-TOM 3D scanner was used to scan and record the fracture roughness, as shown in Fig. 2a. It shows that there were no obvious morphological defects except water injection holes on the surfaces, which meets the test requirements. After the shear strength test, the same scanning treatment was carried out on the fracture surface, which shows that the wear of the surface was tiny, which ensured the repeatability of the test.

When the axial displacement reached 0.5 mm, we defined the shear stress at this moment as the fracture shear strength. Normal stress and shear stress on the fracture surface were calculated from σ_1 and σ_3. Since the confining pressure was 5, 10 and 15 MPa, three shear strength values were obtained. Linear fitting was used, as shown in Fig. 2b. The friction coefficient of the fracture surface is 0.4373. This line is also the strength envelope according to the Coulomb friction law in the original state at the fracture surface. When the confining pressure is 10 MPa, the theoretical value of σ_m was 7.34 MPa.

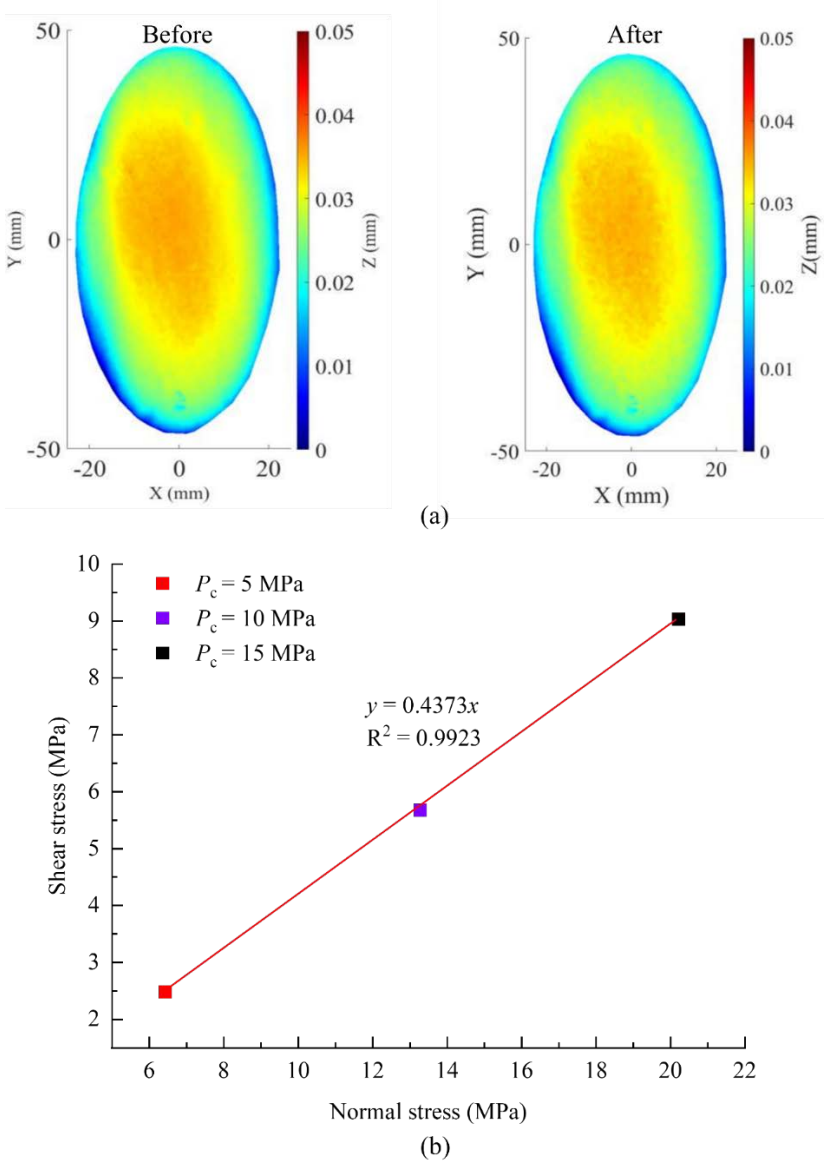

Fig. 2: (a) Vertical elevation of polished shale fracture before and after the test; (b) Coulomb's friction law fitting curve obtained from triaxial shear test without water.

3.2 Slip behavior during fluid pressurization

In the five injection-induced slip tests, the confining pressure remained constant (10 MPa), and the axial stress did not change before the fracture instability. After the flow rate was stabilized, the pressurization started. The water injection rate was 0.25 MPa/min. We recorded the change of injected fluid volume and the change of vertical displacement of the fracture, as shown in Fig. 3.

The green lines show the test results of Test 1 (initial stress = 102% σ_m). The axial stress was loaded to 7.48 MPa by stress control mode and keep unchanged. The fluid pressure increased gradually, and the frictional rupture occurred when the fluid pressure reached 8.08 MPa. The corresponding axial stress drop was 0.46 MPa, the slip of the fast slip event was 30 μm, and the cumulative injected fluid volume was 0.62 ml.

The red lines show the test results of Test 2 (initial stress = 100% σ_m). The axial stress was loaded to 7.34 MPa by stress control mode and keep unchanged. The frictional rupture occurred when the fluid pressure reached 5.15 MPa. The corresponding axial stress drop was 0.41 MPa, the slip of fast slip event was 22 μm, and the injected fluid volume was 0.48 ml.

The blue lines show the results of Test 3 (initial stress = 95% σ_m). The axial stress was loaded to 6.97 MPa by stress control mode and keep unchanged. The frictional rupture occurred when the fluid pressure reached 5.05 MPa. The corresponding axial stress drop is 0.36 MPa, the slip distance of fast slip event was 20 μm, and the volume of injected fluid was 0.45 ml.

The black lines show the test results of Test 4 (initial stress = 93% σ_m). The axial stress was loaded to 6.82 MPa by stress control mode and keep unchanged. The frictional rupture occurred when the fluid pressure reached 4.89 MPa. At the rupture moment, the axial stress drop is 0.30 MPa, the slip distance of fast slip event was 13 μm, and the cumulative injected fluid volume was 0.39 ml.

The purple lines show the test results of Test 5 (initial stress = 90% σ_m). The axial stress was loaded to 6.60 MPa by stress control mode and keep unchanged. Differently, when we gradually increased the injection pressure, it can be seen that the shear displacement of the sample raised continuously. When the fluid pressure increased to 7.6 MPa (much larger than the above 4 trails), it is considered that the frictional rupture of the fracture would never occur under this condition.

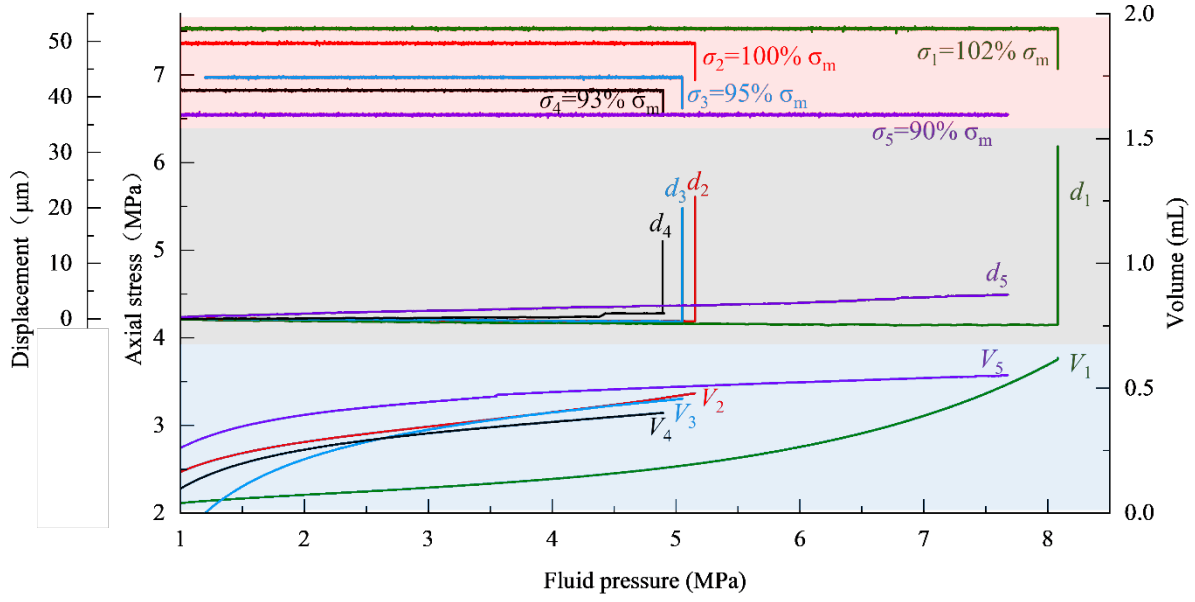

Fig. 3: Test results of injection-induced slip processes for a saw-cut shale fracture.

3.3 Injection-driven slip events

Fig. 4a shows the variation of slip versus injection pressure during the tests. It can be seen that in Test 1 ~ Test 3, due to the large initial stress, the displacement of the fracture slowly decreased in the process of increasing the fluid pressure. The reason is: when the fracture surface is in a local undrained state, the aperture expansion under the action of fluid pressure caused the specimen to expand. However, in Test 4 and Test 5, due to the smaller initial stress, the fracture surface was in a drained state, fluid was more evenly distributed on the fracture surface, and the fluid lubrication accelerated the slip rate of the fracture. Therefore, local instability was observed in Test 4. Under greater lubrication, the fracture of Test 5 slipped continuously, but because of the disappearance of local obstacles, the whole sliding process was stable without fast slip events.

As shown in Fig. 4b, triangle markers denote the initial stress state of the fracture. When the fluid is injected into the fracture at a constant injection rate, the effective normal stress continuously reduces until square markers representing the stress states at the onset of fracture instability overshoots the Coulomb failure envelope (blue line). The distances these markers moved to the left are the experimental pressure values for destabilizing the fracture.

According to Coulomb theory, the theoretical fluid pressure values of each test were calculated. They are 4.46, 4.57, 4.84, 4.95 and 5.11 MPa, respectively. We compared these values with real injection pressure at the onset of fracture instability in our tests. Without taking into account Test 5 where no instability slip occurred, we found that the experimental values exceeded the theoretical values by 81.1%, 12.7%, 4.3% and -1.2%, respectively. As the initial stress on the fracture surface decreases, the theoretical value gets gradually in agreement with the experimental values. The reason is: when the initial stress is large, the fracture surface is in a local undrained state and the fluid distribution was not uniform. In the process of fluid pressurization, the fluid pressure acts on some parts of the fracture surface, resulting in local-to-global instability, so the required fluid pressure is far exceeding the theoretical fluid pressure values.

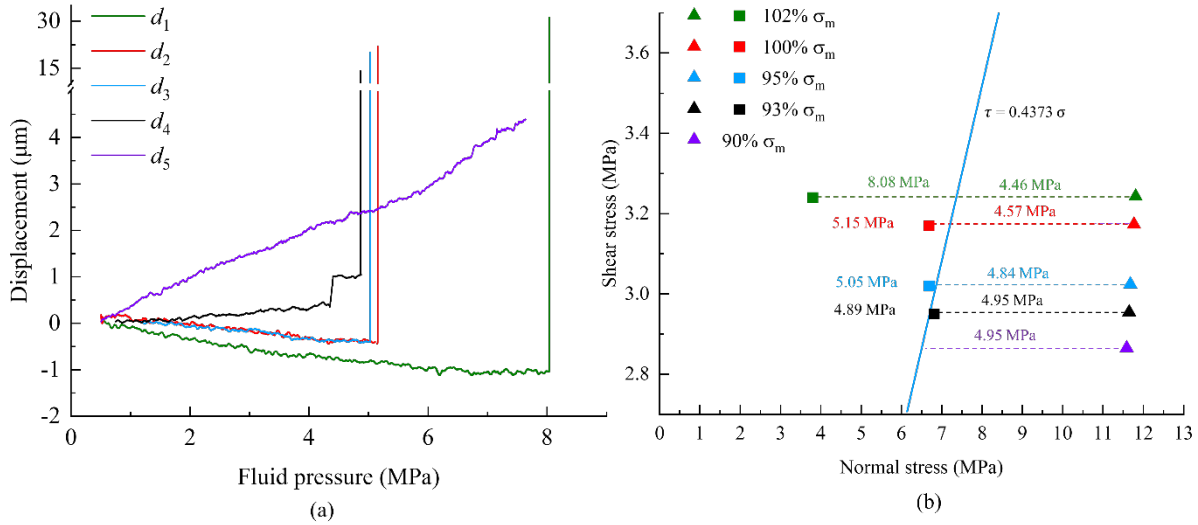

Fig. 4: (a) Slip displacement variation during fluid pressurization; (b) Stress state of each test before fluid injection and at instability onset.

4 Seismic characteristics

The seismic moment (M_0) is defined as the product of shear modulus (or rigidity) (G), fracture area (A), slip displacement (Δd) as Eq. (3).

$$M_0 = GA\Delta d \tag{3}$$

The magnitude of an earthquake is routinely reported using the moment magnitude (M_w), which is estimated from the seismic moment as Eq. (4).

$$M_w = \frac{2}{3}(\log M_0 - 9.1) \tag{4}$$

As a result, in Test 1~Test 4, M_0 is calculated as 53.06, 38.91, 35.37, 22.99 N·m, respectively, which can be seen in Fig. 5a as triangle markers. The same holds for the corresponding M_w values. In the relevant studies on earthquakes induced by fluid injections, in order to describe the seismic risk, McGarr (2014) proposed a model of maximum seismic moment (M_{0max}) prediction by using injected fluid volume as follows:

$$M_0(\max) = G_0\Delta V \tag{5}$$

Where G_0 is the shear modulus which can be estimated by the combined shear stiffness of loading apparatus and the saw-cut fracture. In our research, G_0 = 0.45 GPa. ΔV is the injected fluid volume.

Also, based on the similar idea of using fluid injection volume to predict earthquake magnitude, Gails et al. (2017) [110] established a new prediction mode as follows:

$$M_0(\max) = \gamma\Delta V^{1.5} \tag{6}$$

Where γ is the model parameter which is defined as:

$$\gamma = 0.4255\left(\frac{\kappa\mu}{h\sqrt[3]{\Delta\tau}}\right)^{1.5} \tag{7}$$

In Eq. (7), κ is the bulk modulus of the rock which is about 2/3 of combined shear modulus. h is the thickness of underground layer. Here, the ratio of sample volume to fracture surface area is about 0.05 m. $\Delta\tau$ is the shear stress drop of fast slip events.

In this model, the seismic moment is proportional to the 1.5 power of injected fluid volume. We obtain the trend lines of M_{0max} with ΔV for the McGarr and Galis models. As shown in Fig. 4a, compared with McGarr model, it can be seen that Galis model is more accurate in predicting seismic moment release for our lab tests. The star marks in the figure are the real data of the Pohang earthquake (one main shock, four aftershocks). Similarly, the Gails model shows better prediction with larger water injection volume in-situ.

In order to further describe the relationship between fluid injection and earthquake intensity, previous studies analyzed the ratio of seismic energy released by induced earthquakes to injected hydraulic energy (E_w) and defined this ratio as ‘seismic injection efficiency’ (Gómez et al., 2020). In the process of fluid injection, E_w of the fluid is given in Eq. (8) as integral for time.

$$E_w = \int_{t_0}^{t_1} P_w Q \mathrm{d}t \tag{8}$$

Where P_w is injected water pressure and Q id the flow rate. We calculated E_w for Test 1~Test 5 as 7.35, 3.68, 2.75, 2.41 and 3.23 J, respectively. Based on the theory proposed by McGarr (2012), the released seismic energy (E_e) was estimated by Eq. (9).

$$E_e = \frac{1}{4} \Delta\tau S_0 \Delta d \tag{9}$$

Where S_0 is the surface area of the saw-cut fracture. E_e released in Test 1~Test 4 is 0.0058, 0.0052, 0.0046 and 0.0038 J, respectively. The results are shown in Fig. 5b. It can be seen that the energy conversion rate of our tests is about 0.1%, which is close to the in-situ data.

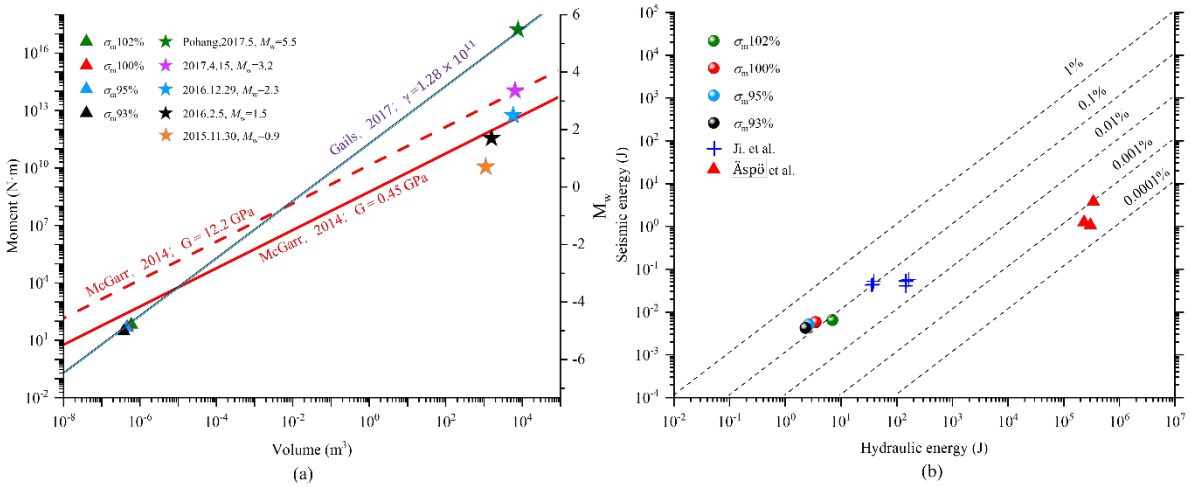

Fig. 5: (a) Seismic moment release as function of injected fluid volume; (b) Seismic injection efficiency.

5 Conclusions

The fluid pressure which activates fracture instability is related to the initial stress state at the fracture surface under monotonic-pressure fluid injection. The greater the difference between the initial stress state and the critical stress state, the closer the pressure of fracture activation to the theoretical value. The magnitude of induced slip events decreased with lower initial stress level. When the initial stress value was 90% σ_m, the fracture kept slowly sliding during fluid injection without any instability. The maximum seismic moment of the slip event was obtained by calculating fluid injection volume and system stiffness, respectively using different theoretical models. The Gails model is more accurate in predicting seismic moments. In addition, the released seismic energy can be predicted by fluid injection energy with energy conversion rate. The energy conversion rate of induced seismic events is about 0.1% in our tests.

6 References

Chen, S., Zhang, Q., Andrews-Speed, P. et al. 2020. Quantitative assessment of the environmental risks of geothermal energy: A review. J. Environ. Manage. 276: 0301-4797.

Ellsworth, W.L., 2013. Injection-induced earthquakes. Science 341, 6142.

Fang, Z. & Wu, W. 2022. Laboratory friction-permeability response of rock fractures: a review and new insights. Geomech. and Geophys. for Geo-Ener. and Geo-Res. 8,15.

Galis, M., Ampuero, J., Mai, P., et al. 2017. Induced seismicity provides insight into why earthquake ruptures stop. Sci. Adv. 3(12), eaap7528.

Gómez, A.S., Vargas, C, Zang, A. 2020. Evidencing the relationship between injected volume of water and maximum expected magnitude during the Puerto Gaitán (Colombia) earthquake sequence from 2013 to 2015. Geophy. J. Int. 220(1), 335-344.

Ji, Y. & Wu, W. 2020. Injection-driven fracture instability in granite: Mechanism and implications. Tectonophysics 791.

Ji, Y., Wanniarachchi, W.A.M., Wu, W. 2020. Effect of fluid pressure heterogeneity on injection-induced fracture activation. Comp. Geotech. 123, 103589.

Ji, Y., Zhuang L., Wu W., et al. 2021. Cyclic Water injection potentially mitigates seismic risks by promoting slow and stable slip of a natural fracture in granite. Rock Mech. Rock Eng. 54, 5389–5405.

McGarr, A. 2012. Relating stick-slip friction experiments to earthquake source parameter. Geophys. Res. Lett. 2012, 39(5).

McGarr, A. 2014. Maximum magnitude earthquakes induced by fluid injection. J. Geophys. Res. Solid Earth, 119(2), 1008-1019.

Passelègue, F.X., Brantut, N., Mitchell, T.M. 2018. Fault reactivation by fluid injection: Controls from stress state and injection rate. Geophys. Res. Lett. 45 (23), 12837–812846.

Rathnaweera, T.D., Wu, W., Ji, Y., Gamage, R.P. 2020. Understanding injection-induced seismicity in enhanced geothermal systems: From the coupled thermo-hydro-mechanical-chemical process to anthropogenic earthquake prediction. Earth-sci. Rev. 205, 103182.

Scuderi, M.M., Collettini, C. 2018. Fluid injection and the mechanics of frictional stability of shale-bearing faults. J. Geophys. Res. Solid Earth 123 (10), 8364–8384.

Scuderi, M.M., Collettini, C., Marone, C. 2017. Frictional stability and earthquake triggering during fluid pressure stimulation of an experimental fault. Earth Planet. Sci. Lett. 477, 84–96.

Wang, L., Kwiatek, G., Rybacki, E., Bonnelye, A., Bohnhoff, M., Dresen, G. 2020. Laboratory study on fluid-induced fault slip behavior: The role of fluid pressurization rate. Geophys. Res. Lett. 47(6), e2019GL086627.

Ye, Z. & Ghassemi, A. 2018. Injection-Induced shear slip and permeability enhancement in granite fractures. J. Geophys. Res. Solid Earth 123, 9009–9032.